Vol. 65 ■ No. 2 ■ February 2024

JNM

The Journal of Nuclear Medicine

FEATURED ARTICLE

Beyond Average: α-Particle Distribution and Dose Heterogeneity in Bone Metastatic Prostate Cancer. Nadia Benabdallah et al. See page 245.

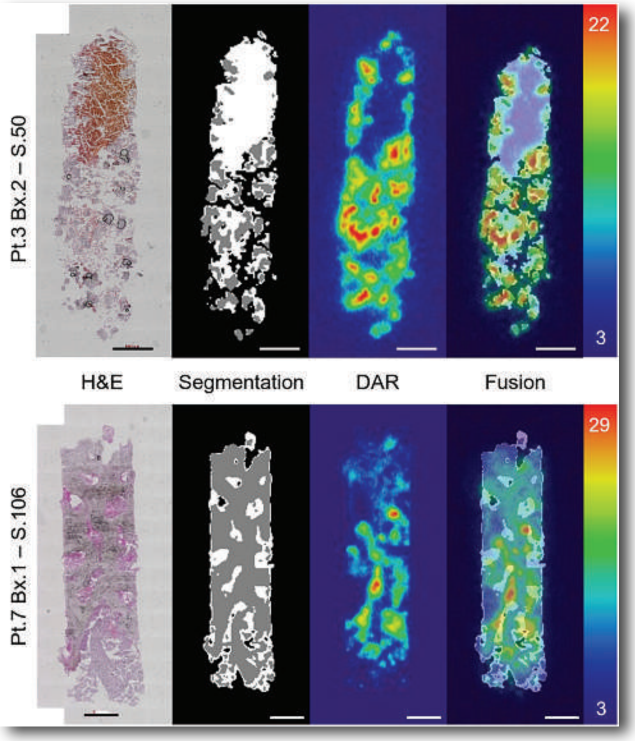

Preclinical cardiac study reproducibility: Enhancing multisite murine ^{68}Ga-labeled radiotracer imaging through standardized acquisition protocols. Maja Strunk et al. See page 287.

SNMMI
SOCIETY OF
NUCLEAR MEDICINE &
MOLECULAR IMAGING

SNMMI
SOCIETY OF
NUCLEAR MEDICINE &
MOLECULAR IMAGING

Thank You to our 2023 SNMMI Annual Fund, Heritage Fund, Lalita & Mathew Thakur Award Fund, Mars Shot, Paul Cole Technologist Scholarship Fund, PDEF, and Value Initiative: Transformative Leadership Donors

- Dixie Aaring, CNMT, BA
- Janet N. Alessi, CNMT, RT(N)
- Sydney M. Andrews, CNMT
- Twyla B. Bartel, DO, FACNM, FSNMMI
- Cheryl A. Beegle, JD, CRA
- Dominique Blanc
- Lori A. Blok, MBA, CNMT
- Thomas Boike, MD
- Julie Dawn Bolin, MS, CNMT
- Norman E. Bolus, MSPH, CNMT, FSNMMI-TS
- Thomas F. Cavanaugh
- Bonnie Clarke
- Patrick M. Colletti, MD, FACNM, FSNMMI
- Paul J. Crowe
- Cathy Sue Cutler, PhD, FSNMMI
- Ishani Dalal, MD
- Guido A. Davidzon, MD, SM
- Paresh B. Desai, MD
- Kevin J. Donohoe, MD
- Arlene M. Downs-Coleman
- Derek E. Fuerbringer, CNMT, BS
- Seyed Mohammad H. Gharavi, MD
- Munir Ghesani, MD, FACNM, FSNMMI
- C. David Gilmore, EdD, CNMT, FSNMMI-TS
- Edwin C. Glass, MD
- Krystle W. Glasgow, CNMT, NMTCB(CT), NMAA
- Linda D. Goforth, CNMT
- Leonard Gomella
- Frederick D. Grant, MD
- Bennett S. Greenspan, MD, FACNM, FACR, FSNMMI
- Denise Guerrero, CNMT
- Adriana G. Guillen Torres
- Gary P. Heald, CNMT
- Marcia L. Hess Smith, MEd, CNMT, FSNMMI-TS
- Judith E. Ho, MD, ABNM, ABP
- Arnold F. Jacobson, MD, PhD
- Hossein Jadvar, MD, PhD, MPH, MBA, FACNM, FSNMMI
- Frances L. Johnson, MD
- Peter V. Kamvosoulis, BS,PET,RT[N,CT,MR]
- Brian William Karam
- Ann Latham
- Hollie Anne Anne Lai, MD
- Steven M. Larson, MD
- Jason S. Lewis, PhD
- Lobular Breast Cancer Alliance Inc.
- Helmut R. Maecke, PhD
- Jose C. Mantil, MD, PhD, ABIM, ABNM
- Nancy McDonald, MHA, CRA, CNMT
- Theresa Gibbons McDonald, BS, CNMT
- Matthew C. McMahon, MS, CNMT, RT(CT)
- Darlene Metter, MD, FACNM, FSNMMI
- Beth T. Meysenburg, CNMT, PET, RT(N)(CT)
- Michael L. Middleton, MD
- Bettina M. Moore, CNMT
- Lyndsey A. Murray, CNMT
- Helen R. Nadel, MD, FRCPC, FSNMMI
- William J. Nahrwold, CNMT
- Frances L. Neagley, BA, CNMT, FSNMTS
- Dori L. Nelson, BHS, CNMT, NCT, FSNMMITS
- Gesa Neumann, MD
- Susan Odelson, CNMT
- Koon Pak
- Chris J. Palestro, MD
- Michele A. Panichi-Egberts, CNMT, RT(N), FSNMMI-TS
- Terry B. Pearl
- Scott B. Perlman, MD
- Lalitha Ramanna, MD, FACNM
- Natarajan Ranganathan
- Susan K. Riesau, CNMT
- Karin Salerno
- David J. Sallee, CNMT, RT(N)
- Hatice Savas, MD
- Devendra A. Sawant, MD, PhD
- Katherine L. Seifert, MBA
- ReidAnn Elizabeth Sever
- Barry L. Shulkin, MD, MBA
- Valerie L. Slaughter, CNMT
- Peggy Squires, BS, CNMT, FSNMMI-TS
- Lisa J. States, MD
- Yohaira G. Stavrou, CNMT
- Rodger A. Stinson, MS, CNMT, RT(N)
- Jacqueline Swaim, CNMT
- Edouard J. Trabulsi, MD
- Donna L. Vaughn, ARRT(R), BS
- Gary Ulaner, MD, PhD, FACNM
- Aaron R. White
- Kamaya Williams
- Terri Wilson, BS, CNMT, MBA
- David M.Y. Yeh, MD
- Hyungtae Yim, CNMT, NMTCB(CT)
- Dusty M. York, CNMT, PET, RT(N)(CT)
- John A. Zehner, BS
- Joyce K. Zimmerman, CNMT, MBA, FSNMMI-TS

Join your colleagues and donate today!

www.snmmi.org/donate

012024-8

JNM

Volume 65 • Number 2 • February 2024

STATE OF THE ART

HOT TOPICS

IS IT REALLY HAPPENING?

ONCOLOGY

Clinical

THERANOSTICS

Clinical

RADIONUCLIDE THERAPY

Clinical

CARDIOVASCULAR

Clinical

Basic

MOLECULAR IMAGING

Basic

NEUROLOGY

Clinical

AI/ADVANCED IMAGE ANALYSIS

Clinical

PHYSICS AND INSTRUMENTATION

Clinical

ILLUSTRATED POST

LETTERS TO THE EDITOR

IN MEMORIAM

DEPARTMENTS

JNM The Journal of
NUCLEAR MEDICINE

The Official Publication of **SNMMI**

MISSION STATEMENT: *The Journal of Nuclear Medicine* advances the knowledge and practice of molecular imaging and therapy and nuclear medicine to improve patient care through publication of original basic science and clinical research.

JNM (ISSN 0161-5505 [print]; ISSN 2159-662X [online]) is published monthly by SNMMI, 1850 Samuel Morse Drive, Reston, VA 20190-5316. Periodicals postage is paid at Herndon, VA, and additional mailing offices. Postmaster, send address changes to *The Journal of Nuclear Medicine,* 1850 Samuel Morse Drive, Reston, VA 20190-5316. The costs of publication of all nonsolicited articles in *JNM* were defrayed in part by the payment of page charges. Therefore, and solely to indicate this fact, these articles are hereby designated “advertisements” in accordance with 18 USC section 1734.

DISCLOSURE OF COMMERCIAL INTEREST: Johannes Czernin, MD, editor-in-chief of *The Journal of Nuclear Medicine,* has indicated that he is a founder of Sofie Biosciences and holds equity in the company and in intellectual property invented by him, patented by the University of California, and licensed to Sofie Biosciences. He is also a founder and board member of Trethera Therapeutics and holds equity in the company and in intellectual property invented by him, patented by the University of California, and licensed to Triangle. He also serves on the medical advisory board of Actinium Pharmaceuticals and on the scientific advisory boards of POINT Biopharma, RayzeBio, and Jubilant Pharma and is a consultant for Amgen. No other potential conflicts of interest were reported. Manuscripts submitted to *JNM* with potential conflicts are handled by a guest editor.

EDITORIAL COMMUNICATIONS should be sent to: Editor-in-Chief, Johannes Czernin, MD, *JNM* Office, SNMMI, 1850 Samuel Morse Drive, Reston, VA 20190-5316. Phone: (703) 326-1185; Fax: (703) 708-9018. To submit a manuscript, go to https://submit-jnm.snmjournals.org.

BUSINESS COMMUNICATIONS concerning permission requests should be sent to the publisher, SNMMI, 1850 Samuel Morse Drive, Reston, VA 20190-5316; (703) 708-9000; home page address: jnm.snmjournals.org. Subscription requests and address changes should be sent to Membership Department, SNMMI at the address above. Notify the Society of change of address and telephone number at least 30 days before date of issue by sending both the old and new addresses. Claims for copies lost in the mail are allowed within 90 days of the date of issue. Claims are not allowed for issues lost as a result of insufficient notice of change of address. For information on advertising, contact Team SNMMI (Kevin Dunn, Rich Devanna, and Charlie Meitner; (201) 767-4170; fax: (201) 767-8065; TeamSNMMI@cunnasso.com). Advertisements are subject to editorial approval and are restricted to products or services pertinent to nuclear medicine. Closing date is the first of the month preceding the date of issue.

INDIVIDUAL SUBSCRIPTION RATES for the 2024 calendar year are $665 within the United States and Canada; $714 elsewhere. Make checks payable to the SNMMI. CPC IPM Sales Agreement No. 1415158. Sales of individual back copies from 1999 through the current issue are available for $60 at http://www.snmmi.org/subscribe (subscriptions@snmmi.org; fax: (703) 667-5134). Individual articles are available for sale online at http://jnm.snmjournals.org.

JNM | The Journal of Nuclear Medicine | Editorial Board

EDITOR-IN-CHIEF
Johannes Czernin, MD
University of California at Los Angeles
Los Angeles, California

IMMEDIATE PAST EDITOR
Dominique Delbeke, MD, PhD
Vanderbilt University Medical Center
Nashville, Tennessee

ASSOCIATE EDITORS, CONTINUING EDUCATION
Hossein Jadvar, MD, PhD, MPH, MBA, FACNM, FSNMMI
University of Southern California
Los Angeles, California
Lale Kostakoglu, MD, MPH
University of Virginia Health System
Charlottesville, Virginia

ASSOCIATE EDITORS
Ramsey Derek Badawi, PhD
UC Davis Medical Center
Sacramento, California
Henryk Barthel, MD, PhD
Leipzig University
Leipzig, Germany
Frank M. Bengel, MD
Hannover Medical School
Hannover, Germany
Lisa Bodei, MD, PhD
Memorial Sloan Kettering Cancer Center
New York, New York
Irene Buvat, PhD
Université Paris Sud
Orsay, France
Jérémie Calais, MD
University of California at Los Angeles
Los Angeles, California
Sharmila Dorbala, MBBS
Brigham and Women's Hospital
Lexington, Massachusetts
Alexander E. Drzezga, MD
University Hospital of Cologne
Cologne, Germany
Jan Grimm, MD, PhD
Memorial Sloan Kettering Cancer Center
New York, New York
Ken Herrmann, MD, MBA
Universitätsklinikum Essen
Essen, Germany
Thomas A. Hope, MD
University of California, San Francisco
San Francisco, California
Jason S. Lewis, PhD
Memorial Sloan Kettering Cancer Center
New York, New York
David A. Mankoff, MD, PhD
University of Pennsylvania
Philadelphia, Pennsylvania
Heiko Schöder, MD
Memorial Sloan Kettering Cancer Center
New York, New York
Wolfgang Weber, MD
Technical University of Munich
München, Germany

SERIES EDITOR, FOCUS ON MI
Carolyn J. Anderson, PhD
University of Missouri
Columbia, Missouri

SERIES EDITOR, HOT TOPICS
Heinrich R. Schelbert, MD, PhD
University of California at Los Angeles
Los Angeles, California

CONSULTING EDITORS
Nancy Knight, PhD
University of Maryland School of Medicine
Baltimore, Maryland
Barry A. Siegel, MD
Mallinckrodt Institute of Radiology
St. Louis, Missouri
Arnold M. Strashun, MD
SUNY Downstate Medical Center
Scarsdale, New York
H. William Strauss, MD
Memorial Sloan Kettering Cancer Center
New York, New York

ASSOCIATE EDITORS (INTERNATIONAL)
Gerald Antoch, MD
Dusseldorf, Germany
Richard P. Baum, MD, PhD
Bad Berka, Germany
Ambros J. Beer, MD
Ulm, Germany
François Bénard, MD, FRCPC
Vancouver, Canada
Thomas Beyer, PhD
Vienna, Austria
Andreas K. Buck, MD, PhD
Würzburg, Germany
Ignasi Carrió, MD
Barcelona, Spain
June-Key Chung, MD
Seoul, Korea
Stefano Fanti, MD
Bologna, Italy
Markus Hacker, MD
Wien, Austria
Rodney J. Hicks, MD, FRACP
Melbourne, Australia
Michael S. Hofman, MBBS, FRACP
Melbourne, Australia
Ora Israel, MD
Haifa, Israel
Andreas Kjaer, MD, PhD, DMSc
Copenhagen, Denmark
Adriaan A. Lammertsma, PhD
Amsterdam, The Netherlands
Michael Lassman, PhD
Würzburg, Germany
Helmut R. Mäcke, PhD
Freiburg, Germany
Wim J.G. Oyen, MD, PhD
Milan, Italy
John O. Prior, MD, PhD
Lausanne, Switzerland
Osman Ratib, MD, PhD
Geneva, Switzerland
Mike Sathekge, MBChB, MMed, PhD
Pretoria, South Africa
Markus Schwaiger, MD
München, Germany
Andrew M. Scott, MD
Heidelberg, Australia
Nagara Tamaki, MD, PhD
Kyoto, Japan
Jia-He Tian, PhD
Beijing, China
Mei Tian, MD, PhD
Hangzhou, China

EDITORIAL CONSULTANTS
Martin S. Allen-Auerbach, MD
Los Angeles, California
Magnus Dahlbom, PhD
Los Angeles, California
Andrew Quon, MD
Los Angeles, California
Christiaan Schiepers, MD, PhD
Los Angeles, California
Daniel H. Silverman, MD, PhD
Los Angeles, California
Roger Slavik, PhD
Winterthur, Switzerland

EDITORIAL BOARD
Diane S. Abou, PhD
St. Louis, Missouri
Hojjat Ahmadzadehfar, MD
Dortmund, Germany
Valentina Ambrosini, MD, PhD
Bologna, Italy
Norbert Avril, MD
Cleveland, Ohio
Shadfar Bahri
Los Angeles, California
Jacques Barbet, PhD
Saint-Herbalin, France
Bradley Jay Beattie, PhD
New York, New York
Freek J. Beekman, PhD
Delft, The Netherlands
Matthias Richard Benz, MD
Los Angeles, California
Elie Besserer-Offroy, PhD, FACSc
Los Angeles, California
Pradeep Bhambhvani, MD
Birmingham, Alabama
Angelika Bischof-Delaloye, MD
Lausanne, Switzerland
Christina Bluemel, MD
Würzburg, Germany
Ronald Boellaard, PhD
Groningen, The Netherlands
Nicolaas Bohnen, MD
Ann Arbor, Michigan
Wesley E. Bolch, PhD
Gainesville, Florida
Elias H. Botvinick, MD
San Francisco, California
Winfried Brenner, MD, PhD
Berlin, Germany
Richard C. Brunken, MD
Cleveland, Ohio
Ralph Buchert, PhD
Hamburg, Germany
Alfred Buck, MD
Menzingen, Switzerland
Denis B. Buxton, PhD
Bethesda, Maryland
Weibo Cai, PhD
Madison, Wisconsin
Federico Caobelli, MD
Basel, Switzerland
Giuseppe Carlucci, PhD
Los Angeles, California
Richard E. Carson, PhD
New Haven, Connecticut
Paolo Castellucci, MD
Bologna, Italy
Franscesco Ceci, MD, PhD
Turin, Italy
Juliano J. Cerci
Curitiba, Brazil
Delphine Chen, MD
Seattle, Washington
Xiaoyuan Chen, PhD
Singapore
Simon R. Cherry
Davis, California
Arturo Chiti, MD
Rozzano, Italy
Peter M. Clark, PhD
Los Angeles, California
Christian Cohade, MD
Montreal, Canada
Ekaterina (Kate) Dadachova, PhD
Saskatoon, Canada
Issa J. Dahabreh, MD
Boston, Massachusetts
Heike Elisabeth Daldrup-Link, MD, PhD
Stanford, California
Farrokh Dehdashti, MD
St. Louis, Missouri
Robert C. Delgado-Bolton, MD, PhD
Logroño, Spain
Thorsten Derlin, MD
Hannover, Germany
Elisabeth G.E. de Vries, PhD
Groningen, The Netherlands
Marcelo F. Di Carli, MD
Boston, Massachusetts
David W. Dick, PhD
Iowa City, Iowa
Vasken Dilsizian, MD
Baltimore, Maryland
Jacob Dubroff, MD, PhD
Philadelphia, Pennsylvania
Janet F. Eary, MD
Bethesda, Maryland
W. Barry Edwards, PhD
Columbia, Missouri
Matthias Eiber, MD
Munich, Germany
David Eidelberg, MD
Manhasset, New York
Georges El Fakhri, PhD
Boston, Massachusetts
Peter J. Ell, MD
London, United Kingdom
Louise M. Emmett, MD
Sydney, Australia
Keigo Endo, MD
Nantan, Japan
Einat Even-Sapir, MD, PhD
Tel Aviv, Israel
Frederic H. Fahey, DSc
Boston, Massachusetts
Melpomeni Fani, PhD, MSc
Basel, Switzerland

EDITORIAL BOARD, continued
Andrea Farolfi, MD
Bologna, Italy
Wolfgang Peter Fendler, MD
Essen, Germany
James W. Fletcher, MD
Indianapolis, Indiana
Amy M. Fowler, MD, PhD
Madison, Wisconsin
Kirk A. Frey, MD, PhD
Ann Arbor, Michigan
Andrei Gafita
Los Angeles, California
Victor H. Gerbaudo, PhD, MSHCA
Boston, Massachusetts
Frederik L. Giesel, MD, PhD, MBA
Düsseldorf, Germany
Karolien Goffin, MD, PhD
Leuven, Belgium
Serge Goldman, MD, PhD
Brussels, Belgium
Stanley J. Goldsmith, MD
New York, New York
Martin Gotthardt, MD, PhD
Nijmegen, The Netherlands
Michael Graham, MD, PhD
Iowa City, Iowa
David Groheux, MD, PhD
Paris, France
Uwe A. Haberkorn, MD
Heidelberg, Germany
Mathieu Hatt, PhD, HDR
Brest, France
Wolf-Dieter Heiss, MD
Cologne, Germany
Karl Herholz, MD
Manchester, United Kingdom
Thomas F. Heston, MD
Las Vegas, Nevada
John M. Hoffman, MD
Salt Lake City, Utah
Carl K. Hoh, MD
San Diego, California
Jason P. Holland, DPhil
Zurich, Switzerland
Roland Hustinx, MD, PhD
Liege, Belgium
Andrei H. Iagaru, MD
Stanford, California
Masanori Ichise, MD
Chiba, Japan
Amir Iravani, MD
Seattle, Washington
Heather A. Jacene, MD
Boston, Massachusetts
Francois Jamar, MD, PhD
Brussels, Belgium
Jae Min Jeong, PhD
Seoul, Korea
John A. Katzenellenbogen, PhD
Urbana, Illinois
Zohar Keidar, MD, PhD
Haifa, Israel
Kimberly A. Kelly, PhD
Charlottesville, Virginia
Laura M. Kenny, MD, PhD
London, United Kingdom
Fabian Kiessling, MD
Aachen, Germany
E. Edmund Kim, MD, MS
Orange, California
Francoise Kraeber-Bodéré, MD, PhD
Nantes, France
Clemens Kratochwil, MD
Heidelberg, Germany
Kenneth A. Krohn, PhD
Portland, Oregon
Brenda F. Kurland, PhD
Pittsburgh, Pennsylvania
Constantin Lapa, MD
Augsburg, Germany
Suzanne E. Lapi, PhD
Birmingham, Alabama
Steven M. Larson, MD
New York, New York
Dong Soo Lee, MD, PhD
Seoul, Korea
Jeffrey Leyton, PhD
Sherbrooke, Canada
Xiang-Guo Li, PhD
Turku, Finland
Hannah M. Linden, MD
Seattle, Washington
Martin A. Lodge, PhD
Baltimore, Maryland
Katharina Lückerath, PhD
Los Angeles, California
Susanne Lütje, MD, PhD
Bonn, Germany
Umar Mahmood, MD, PhD
Boston, Massachusetts
H. Charles Manning, PhD
Nashville, Tennessee
Giuliano Mariani, MD
Pisa, Italy
Chester A. Mathis, PhD
Pittsburgh, Pennsylvania
Alan H. Maurer, MD
Philadelphia, Pennsylvania
Jonathan McConathy, MD, PhD
Birmingham, Alabama
Alexander J.B. McEwan, MD
Edmonton, Canada
Yusuf Menda, MD
Iowa City, Iowa
Philipp T. Meyer, MD, PhD
Freiburg, Germany
Matthias Miederer, MD
Mainz, Germany
Jasna Mihailovic, MD, PhD
Sremska Kamenica, Serbia
Erik Mittra, MD, PhD
Portland, Oregon
Christine E. Mona, PhD
Los Angeles, California
Dae Hyuk Moon, MD
Seoul, Korea
Jennifer Murphy, PhD
Los Angeles, California
Helen Nadel, MD, FRCPC
Stanford, California
Matthias Nahrendorf, MD, PhD
Boston, Massachusetts
Yuji Nakamoto, MD, PhD
Kyoto, Japan
David A. Nathanson, PhD
Los Angeles, California
Nghi C. Nguyen, MD, PhD
Dallas, Texas
Sridhar Nimmagadda, PhD
Baltimore, Maryland
Egbert U. Nitzsche, MD
Aarau, Switzerland
Daniela E. Oprea-Lager, MD, PhD
Amsterdam, The Netherlands
Medhat M. Osman, MD, PhD
Saint Louis, Missouri
Christopher J. Palestro, MD
New Hyde Park, New York
Miguel Hernandez Pampaloni, MD, PhD
San Francisco, California
Neeta Pandit-Taskar, MD
New York, New York
Ashwin Singh Parihar, MBBS, MD
Saint Louis, Missouri
Michael E. Phelps, PhD
Los Angeles, California
Gerold Porenta, MD, PhD
Vienna, Austria
Sophie Poty, PhD
Montpellier, France
Edwin (Chuck) Pratt, PhD, MS Eng
New York, New York
Daniel A. Pryma, MD
Philadelphia, Pennsylvania
Valery Radchenko, PhD
Vancouver, Canada
Caius G. Radu, MD
Los Angeles, California
Isabel Rauscher, MD
Munich, Germany
Nick S. Reed, MBBS
Glasgow, United Kingdom
Mark Rijpkema, PhD
Nijmegen, The Netherlands
Steven P. Rowe, MD, PhD
Baltimore, Maryland
Mehran Sadeghi, MD
West Haven, Connecticut
Orazio Schillaci, MD
Rome, Italy
Charles Ross Schmidtlein, PhD
New York, New York
David M. Schuster, MD
Atlanta, Georgia
Travis Shaffer, PhD
Stanford, California
Sai Kiran Sharma, PhD
New York, New York
Anthony F. Shields, MD, PhD
Detroit, Michigan
Barry L. Shulkin, MD, MBA
Memphis, Tennessee
Yu Shyr, PhD
Nashville, Tennessee
Albert J. Sinusas, MD
New Haven, Connecticut
Riemer H.J.A. Slart, MD, PhD
Groningen, The Netherlands
Piotr Slomka, PhD, FACC
Los Angeles, California
Simon John Christoph Soerensen, MD
Stanford, California
Ida Sonni, MD
Los Angeles, California
Michael G. Stabin, PhD
Richland, Washington
Lisa J. States, MD
Philadelphia, Pennsylvania
Sven-Erik Strand, PhD
Lund, Sweden
Rathan M. Subramaniam, MD, PhD, MPH
Dunedin, New Zealand
John Sunderland, PhD
Iowa City, Iowa
Suleman Surti, PhD
Philadelphia, Pennsylvania
Julie Sutcliffe, PhD
Sacramento, California
David Taieb, MD, PhD
Marseille, France
Laura H. Tang, MD, PhD
New York, New York
Ukihide Tateishi, MD, PhD
Tokyo, Japan
James T. Thackeray, PhD
Hannover, Germany
Mathew L. Thakur, PhD
Philadelphia, Pennsylvania
Alexander Thiel, MD
Montreal, Canada
Daniel L.J. Thorek, PhD
St. Louis, Missouri
David W. Townsend, PhD
Singapore
Timothy Turkington, PhD
Durham, North Carolina
Gary A. Ulaner, MD, PhD
Irvine, California
David Ulmert, MD, PhD
Los Angeles, California
Lena M. Unterrainer, MD, MHBA
Munich, Germany
Christopher H. van Dyck, MD
New Haven, Connecticut
Douglas Van Nostrand, MD
Washington, District of Columbia
Patrick Veit-Haibach, MD
Toronto, Canada
Nerissa Viola-Villegas, PhD
Detroit, Michigan
John R. Votaw, PhD
Atlanta, Georgia
Richard L. Wahl, MD
St. Louis, Missouri
Anne Marie Wallace, MD
La Jolla, California
Martin A. Walter, MD
Geneva, Switzerland
Rudolf A. Werner, MD
Wuerzburg, Germany
Andreas G. Wibmer, MD
New York, New York
Anna M. Wu, PhD
Duarte, California
Randy Yeh, MD
New York, New York
Hyewon (Helen) Youn, PhD
Seoul, Korea
Pat B. Zanzonico, PhD
New York, New York
Brian M. Zeglis, PhD
New York, New York
Robert Zeiser, MD
Freiburg, Germany
Hong Zhang, MD, PhD
Hangzhou, China
Hongming Zhuang, MD, PhD
Philadelphia, Pennsylvania
Sibylle I. Ziegler, PhD
Munich, Germany

ASSISTANT TO THE EDITOR
Joshua N. Wachtel
Los Angeles, California

THIS MONTH IN JNM

Theranostics in brain tumors: Tolboom and European colleagues provide a state-of-the-art overview of theranostic approaches in neurooncology, including specific tumor entities, potential molecular targets, and strategies to enhance effectiveness.. . . . . ***Page 167***

α-Synuclein assays in PD: Seibyl looks at expanding promise for α-synuclein seeding amplification assays in earlier diagnosis of Parkinson disease and timely management of therapies that target synucleinopathies.. ***Page 174***

^{212}Pb: a post-^{177}Lu/^{225}Ac blockbuster? Zimmermann reviews current progress in large-scale supply of ^{212}Pb and surveys current industry involvement in development and production, highlighting the potential for future replacement of ^{225}Ac with ^{212}Pb in α-emitter therapies. . . . . ***Page 176***

HER2-sdAb phase II trial: Gondry and colleagues analyze trial results on the repeatability of uptake quantification and extended safety of the [^{68}Ga]Ga-NOTA-anti-human epidermal growth factor receptor 2 single-domain antibody in PET/CT imaging of locally advanced or metastatic breast carcinoma. . . . . ***Page 178***

Discordant volume in GEP NENs: Chan and colleagues investigate differing tumor volumes on [^{18}F]FDG and [^{68}Ga]Ga-DOTATATE PET/CT as a potential prognostic biomarker in patients with advanced gastroenteropancreatic neuroendocrine neoplasms. . . . . ***Page 185***

[^{18}F]TFB PET/CT in recurrent DTC: Ventura and colleagues compare [^{18}F]tetrafluoroborate PET with high-activity posttherapeutic [^{131}I]iodine whole-body scintigraphy and SPECT/CT in recurrent differentiated thyroid cancer and with [^{18}F]FDG PET/CT in suspected dedifferentiation . . . . ***Page 192***

^{68}Ga-FAP-2286 PET in bladder cancer: Koshkin and colleagues present experience with the novel fibroblast activation protein–peptide binder ^{68}Ga-FAP-2286 in PET imaging and staging of patients with muscle-invasive bladder cancer. . . . ***Page 199***

^{18}F-FAPI-04 PET/CT in pancreatic cancer: Li and colleagues explore the ability of ^{18}F-fibroblast activation protein inhibitor–04 PET/CT to diagnose and stage pancreatic ductal adenocarcinoma and compare findings with those from ^{18}F-FDG PET. . . . . ***Page 206***

^{68}Ga-FAPI PET/CT in gastric cancer: Miao and colleagues ask whether imaging parameters from ^{18}F-FDG and ^{68}Ga-fibroblast activation protein inhibitor–04 PET/CT can predict early pathologic response to neoadjuvant chemotherapy in patients with locally advanced gastric cancer. . . ***Page 213***

[^{18}F]FES PET breast procedure guideline: Mankoff, Balogová, and coauthors offer a summary of their recently published SNMMI procedure standard/European Association of Nuclear Medicine practice guideline for estrogen receptor imaging with 16α-[^{18}F]fluoro-17β-estradiol PET in breast cancer. . . . . ***Page 221***

Radioligand therapy in prostate cancer: Rahbar and Boegemann underscore the need for robust studies of targeted radioligands, including comparisons with established clinical treatments, taking as an example ^{177}Lu-PSMA-617 in metastatic castration-resistant prostate cancer. . . . . ***Page 224***

PSMAfore trial design: Sartor and colleagues respond to commentary by Rahbar and Boegemann and discuss critical factors in the design of the PSMAfore phase 3 trial of ^{177}Lu-PSMA-617 in taxane-naïve patients with metastatic castration-resistant prostate cancer. . . . . ***Page 226***

PRRT in metastatic insulinoma: Friebe and colleagues study somatostatin receptor–positive metastatic malignant insulinoma, evaluating the efficacy of peptide receptor radionuclide therapy for hypoglycemia, changes in medication after therapy, and resulting progression-free and overall survival.. . . . . ***Page 228***

PRRT outcome prediction in GEP NETs: Mileva and colleagues use multimodality imaging and tumor dosimetry to identify factors predicting outcomes in peptide receptor radionuclide therapy of gastroenteropancreatic neuroendocrine tumors . . . . ***Page 236***

^{223}Ra dose within bone biopsy specimens: Benabdallah and colleagues determine the distribution of clinically approved [^{223}Ra]RaCl$_2$ in bone metastatic castration-resistant prostate cancer to inform activity distribution and dose at the near-cell scale.. . . . . ***Page 245***

Role of FAPα in SFTs: Hamacher and colleagues report on the expression pattern of fibroblast activation protein α in solitary fibrous tumors and its potential use as a radiotheranostic target . . . . ***Page 252***

^{177}Lu-DOTATATE and mesenteric mass: Al Mansour and colleagues look at the question of whether desmoplastic mesenteric masses, present in most small-intestinal neuroendocrine tumors, are refractory to ^{177}Lu-DOTATATE peptide receptor radionuclide therapy.. . . . . ***Page 258***

Updated DOSISPHERE-01 trial analysis: Garin and colleagues describe long-term results on overall survival from this study that showed improvement in response and survival with personalized dosimetry of ^{90}Y-loaded glass microspheres in nonoperable locally advanced hepatocellular carcinoma.. . . . . ***Page 264***

Personalizing ^{90}Y radioembolization dosimetry: Soulen and Rilling provide perspective on history and challenges that have accompanied the approval for ^{90}Y radioembolization techniques and offer commentary on a related article in this issue of *JNM*. . . . . ***Page 270***

SIRT particles for ICC: Wagemans and colleagues compare absorbed doses, toxicities, and responses with ^{90}Y-glass, ^{90}Y-resin, and ^{166}Ho-labeled poly(L-lactic acid) microspheres for selective internal radiation therapy in locally advanced intrahepatic cholangiocarcinoma. . . . . . ***Page 272***

Combined FFR/iFR: de Winter and colleagues compare [^{15}O]H$_2$O PET–derived absolute myocardial perfusion between vessels with concordant and discordant fractional flow reserve and instantaneous wave-free ratio measurements to elucidate the hemodynamic significance of discordance . . . . ***Page 279***

Multicenter molecular imaging after MI: Strunk and colleagues report on the reproducibility of murine quantitative inflammation and fibroblast activation images acquired after myocardial infarction at 2 facilities. . . . . ***Page 287***

CD69 PET in inflammatory arthritis: Puuvuori and colleagues evaluate a CD69-targeting PET agent for early disease detection in a mouse model of inflammatory arthritis, with clinical promise for identification of activated immune cells in rheumatoid arthritis onset.. . . . . ***Page 294***

(*R*)-[^{18}F]YH134 PET of MAGL: He and colleagues explore in mouse and rat brains the kinetic properties of this [^{18}F]T-401 derivative as a novel PET tracer for imaging monoacylglycerol lipase . . . . ***Page 300***

CBF from florbetaben and water PET/MRI: Fettahoglu and colleagues detail a quantitative cerebral blood flow imaging method combining early [^{18}F]florbetaben with phase-contrast MRI using simultaneous PET/MRI, providing CBF and amyloid burden measurement in 1 session in memory disorders.. . . . . ***Page 306***

Tumor location and prognosis in DLBCL: Girum and colleagues determine whether identification of tumor locations relative to spleen location in baseline [^{18}F]FDG PET/CT images predicts survival in diffuse large B-cell lymphoma and improves the predictive value of other metrics.. . . . . . . ***Page 313***

Portable PET comparisons in humans: Bartlett and colleagues perform a within-participant comparison of fully quantified [^{18}F]FDG dynamic scans in healthy volunteers using a standard Biograph mCT scanner and a portable CerePET scanner. . . . . ***Page 320***

^{11}C-Met PET in acromegaly: Haberbosch and colleagues present a case study illustrating the dual role of ^{11}C-Met PET in acromegaly, confirming remission and detecting recurrence. . . . . ***Page 327***

Theranostics in Neurooncology: Heading Toward New Horizons

Nelleke Tolboom[1], Antoine Verger[2], Nathalie L. Albert[3], Francesco Fraioli[4], Eric Guedj[5], Tatjana Traub-Weidinger[6], Silvia Morbelli[7,8], Ken Herrmann[9], Pietro Zucchetta[10], Sabine L.A. Plasschaert[11], Igor Yakushev[12], Michael Weller[13], Martin Glas[14], Matthias Preusser[15], Diego Cecchin[16], Henryk Barthel[17], and Donatienne Van Weehaeghe[18]

[1]Department of Radiology and Nuclear Medicine, University Medical Centre Utrecht, Utrecht, The Netherlands; [2]IADI, INSERM, UMR 1254, Department of Nuclear Medicine and Nancyclotep Imaging Platform, CHRU-Nancy, Université de Lorraine, Nancy, France; [3]Department of Nuclear Medicine, University Hospital of Munich, Munich, Germany; [4]Institute of Nuclear Medicine, University College London, London, United Kingdom; [5]Département de Médecine Nucléaire, Hôpital de la Timone, CERIMED, Institut Fresnel, Aix Marseille University, APHM, CNRS, Centrale Marseille, Marseille, France; [6]Department of Biomedical Imaging and Image-Guided Therapy, Medical University of Vienna, Vienna, Austria; [7]IRCCS Ospedale Policlinico San Martino, Genoa Italy; [8]Nuclear Medicine Unit, Department of Health Sciences, University of Genoa, Genoa, Italy; [9]Department of Nuclear Medicine, University of Duisburg–Essen and German Cancer Consortium–University Hospital Essen, Essen, Germany; [10]Department of Nuclear Medicine, University Hospital of Padova, Padova, Italy; [11]Princess Máxima Center for Pediatric Oncology, Utrecht, The Netherlands; [12]Department of Nuclear Medicine, School of Medicine, Technical University of Munich and Munich Center for Neurosciences–Brain and Mind, Munich, Germany; [13]Department of Neurology, University Hospital and University of Zurich, Zurich, Switzerland; [14]Division of Clinical Neurooncology, Department of Neurology and Center for Translational Neuro- and Behavioral Sciences, University Medicine Essen, University Duisburg–Essen and German Cancer Consortium, Essen, Germany; [15]Division of Oncology, Department of Medicine I, Medical University of Vienna, Vienna, Austria; [16]Nuclear Medicine Unit, Department of Medicine–DIMED, University Hospital of Padua, Padua, Italy; [17]Department of Nuclear Medicine, Leipzig University Medical Centre, Leipzig, Germany; and [18]Department of Radiology and Nuclear Medicine, Ghent University Hospital, Ghent, Belgium

Therapeutic approaches to brain tumors remain a challenge, with considerable limitations regarding delivery of drugs. There has been renewed and increasing interest in translating the popular theranostic approach well known from prostate and neuroendocrine cancer to neurooncology. Although far from perfect, some of these approaches show encouraging preliminary results, such as for meningioma and leptomeningeal spread of certain pediatric brain tumors. In brain metastases and gliomas, clinical results have failed to impress. Perspectives on these theranostic approaches regarding meningiomas, brain metastases, gliomas, and common pediatric brain tumors will be discussed. For each tumor entity, the general context, an overview of the literature, and future perspectives will be provided. Ongoing studies will be discussed in the supplemental materials. As most theranostic agents are unlikely to cross the blood–brain barrier, the delivery of these agents will be dependent on the successful development and clinical implementation of techniques enhancing permeability and retention. Moreover, the international community should strive toward sufficiently large and randomized studies to generate high-level evidence on theranostic approaches with radioligand therapies for central nervous system tumors.

Key Words: radionuclide therapy; brain tumor; neurooncology; radionuclide therapy; theranostics; blood–tumor barrier

J Nucl Med 2024; 65:167–173
DOI: 10.2967/jnumed.123.266205

In the last decade, we have observed a huge step forward in treatment options for a wide range of tumors in terms of both survival and quality of life. However, therapeutic approaches to brain tumors remain a challenge, with considerable limitations regarding delivery of drugs. Because of the recent success of theranostics in oncology with ^{177}Lu-DOTATATE for neuroendocrine tumors and ^{177}Lu-prostate specific antigen (PSMA) for prostate cancer, resulting in Food and Drug Administration and European Medicines Agency approvals, there has been renewed and increasing interest in translating the theranostic approach to neurooncology (*1–3*). Extracranially, such approaches are generally well tolerated, delivering a high absorbed dose with a low dose rate, specifically to the tumor, even on anatomically complex lesions, with a targeting that preserves the surrounding parenchyma. The latter is of course of high critical importance for brain interventions. Theranostics are also particularly adapted to treating multiple tumoral lesions in the whole body at the same time, for example, in metastatic disease. An added benefit is the possibility of identifying patients with high target availability using the corresponding imaging ligand, often the diagnostic twin, such as the positron-emitting version (suitable for PET) of the therapeutic ligand.

In this paper, theranostic approaches to brain tumors will be discussed. For each tumor entity, the general context and future perspectives will be provided. In the supplemental materials (available at http://jnm.snmjournals.org), an overview of the literature and ongoing studies is provided. Table 1 gives an overview of potential molecular targets for theranostic applications in neurooncology. Moreover, strategies to overcome the blood–brain barrier (BBB) and blood–tumor barrier (BTB) will be briefly discussed.

BBB AND BTB

The main obstacle in neurooncology compared with other solid tumors is getting therapeutics through the BBB. Brain tumors are known to alter the physiologic BBB integrity, some producing a highly heterogeneous vasculature—the BTB. This altered physiologic

---

Received Jun. 21, 2023; revision accepted Oct. 23, 2023.

For correspondence or reprints, contact Donatienne Van Weehaeghe (donatienne.vanweehaeghe@uzgent.be).

TABLE 1
Overview of Molecular Targets for Radionuclide Therapy in Meningioma, Brain Metastases, Glioma, and Pediatric Brain Tumors

Molecular target	Meningioma	Glioma	Brain metastases	Pediatric brain tumors
SSTR	O (phase 1–2) (NCT03971461, NCT04997317, NCT03273712, NCT04082520, NCT05278208)	O (phase 1) (NCT05109728)		O (phase 1–2) (NCT05278208, NCT03273712)
Tenascin		X	O (phase 1–2) (NCT00002752)	
EGFR		X		
NK1R		X		
GRPR		O (phase 1–2) (NCT03872778, NCT05739942)		X
LAT-1		O (phase 1–2) (NCT03849105, NCT05450744)		
Carbonic anhydrase XII		O (phase 1) (NCT05533242)		
Integrins		X		
PARP1		X		
PSMA		X	X	
MMP		X	X	
DNAH1		X		
Chemokine receptor 4		X		
Fibronectin			X	
HER2			O (phase 1–2) (NCT04467515)	
PCSP			X	
Disialoganglioside (GD2)			O (phase 2) (NCT00445965)	X
B7-H3				O (phase 1) (NCT00089245, NCT05063357)
$CuCl_2$				X
FAP		X		

O = ongoing studies; X = target that has been investigated in previous studies; EGFR = epidermal growth factor receptor; NK1R = neurokinin type 1 receptor; GRPR = gastrin-releasing peptide receptor; PARP1 = poly(adenosine diphosphate ribose) polymerase 1; PSMA = prostate-specific antigen; MMP = matrix metalloproteinase; DNAH1 = DNA histone ^{1}H complex; HER2 = human epidermal growth factor receptor 2; PCSP = proteoglycan chondroitin sulfate-associated protein; FAP = fibroblast activation protein.

NOTEWORTHY

- In this paper, we describe the general context of, an overview of the literature for, and future perspectives on radionuclide therapy for meningiomas, gliomas, brain metastases, and pediatric brain tumors.
- Preliminary research on theranostics in meningiomas and leptomeningeal spread of certain pediatric brain tumors is encouraging. To date, other entities fail to impress.
- Successful development of other principles enabling BBB passage is crucial for the future success of radionuclide therapy for brain tumors.

BBB and BTB integrity is heterogeneous between metastatic lesions and various primary tumor types and shown by contrast enhancement on MRI (*4*). Several strategies have been developed to bypass the BBB and BTB (*4–6*): local administration (including intraventricular administration), convection-enhanced delivery (CED), focused ultrasound (FUS), and innovatively designed monoclonal antibodies and neural stem cells. We will describe some of these mechanisms in more detail (Fig. 1). Most of these techniques are complex and, as such, can be performed only in expert centers.

Therapeutics can be directly administered into the tumor or into surgical or anatomic cavities (such as intraventricular administration using a catheter). Compared with systemic therapy, the toxicity to the body is thereby reduced. Nevertheless, a certain grade of

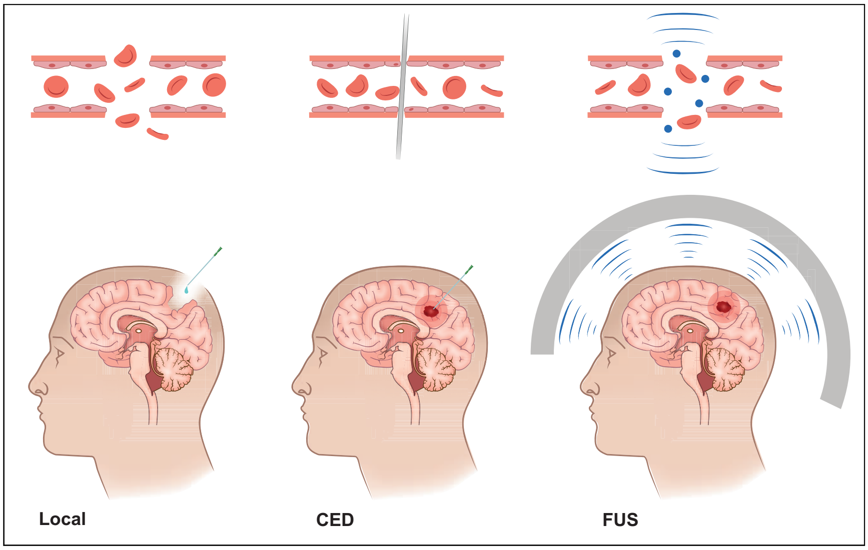

FIGURE 1. Example of interventional approaches to bypass physiologic BBB and BTB. Normal transport in BBB is not included. (Left) Local delivery with administration of radioactivity directly into resection cavity. (Middle) CED: microcatheter is implanted into tumor, and hydraulic pressure is used to distribute drugs in brain parenchyma. (Right) FUS reshapes BBB using targeted ultrasonic wave. This in turn causes interaction between administered microbubbles and capillary bed, resulting in enhanced vessel permeability.

hematologic and neurologic toxicity can still be present through dissemination of the compound into the blood, catheter dislocation and leakage in other vital areas (*7*).

CED represents a well-studied way to bypass the BBB in which one or more microcatheters are implanted into and around the tumor. CED, mostly of chemo- and immunotherapeutic drugs, has a long history and has been repeatedly used safely in clinical trials in both adult and pediatric patients (*8*,*9*). However, no durable clinical impact has been seen, despite multiple clinical trials (*10*). Because of the complex nature of CED, studies vary with respect to agent, infusion volume, and rate and cannula design, for example. CED has specific issues due to slow and continuous delivery with varying clearance via the interstitial fluid and back into the bloodstream over the BBB. Personalized image-guided drug delivery using PET before, during, and after CED could increase the potential of this technique. Upfront pharmacokinetic imaging, especially for large drugs such as monoclonal antibodies, using imaging ligands with a long half-life could be applied for patient selection, treatment planning, and dose scheduling. A recent study in murine models of diffuse intrinsic pontine glioma revealed significant variability in post-CED clearance within and across injection cohorts with post-CED PET. This was probably due to the heterogeneity of the tumors and from inherent technical variance. The use of PET-guided CED dosing schedules did, however, prolong survival (*11*). Clinical studies combining CED with labeled drugs have recently been performed. Safety and feasibility were shown in a study evaluating CED of ^{124}I-8H9, a monoclonal antibody targeting the glioma-associated B7-H3 antigen in children with diffuse midline glioma (*5*). Safety and feasibility were also confirmed in glioblastoma (*6*). For ligands with simultaneous diagnostic–theranostic characteristics such as ^{124}1-8H9 (*12*), posttherapy dosimetry can be used not only to validate the principles of CED but also to verify and adjust the dosing schedule and treatment plan.

An alternative method to enhance radioisotope-labeled drug delivery to the brain is FUS-mediated BBB opening, which uses low-frequency ultrasound waves inducing stable cavitation of intravenously injected microbubbles (*13*) Mechanical interaction of microbubbles with the BBB temporarily dislocates tight junctions between endothelial cells and increases transcytosis, thereby enhancing permeability into the brain parenchyma (*13*,*14*).

This technique has been explored only in limited clinical trials (*15*,*16*), and different technical implementations of this technology exist. Technical implementations are diverse, ranging from implanted ultrasound transducer designs (*17*) appearing favorable for cost-effective repetitive openings of the supratentorial brain to fully MRI-guided transcranial (and thus noninvasive) devices (*18*), which appear favorable for deep-seated lesions in the brain stem or thalamus. Although this technology has not yet been used clinically in combination with a theranostic approach, preclinical studies demonstrating enhanced delivery of monoclonal antibodies to the parenchyma have shown considerable promise (*19*–*21*).

Innovatively designed monoclonal antibodies also show promise to pass the physiologic BBB, such as single-domain antibodies and antibodies modified into a bispecific format (*22*,*23*). Additionally, various transporters such as the L-type amino acid transporter 1 (LAT-1) are present on the physiologic BBB. These transporters deliver essential nutrients and energy and can be used in a carrier-mediated manner to cross the BBB. LAT-1 is promising for carrier-mediated brain drug delivery: it has a rapid BBB exchange and accepts various amino acids and analogs, and a transient disruption in essential amino acid transport will not cause irreversible brain damage (*24*). The use of LAT-1 targets is further discussed in the glioma section.

MENINGIOMAS

Context

Meningiomas are the brain tumors for which peptide receptor radionuclide therapy (PRRT) has been most performed. They represent 30% of primary intracranial tumors. Although approximately 80% of these tumors are benign (central nervous system [CNS] World Health Organization [WHO] grade 1), the remaining cases are classified as high-grade meningiomas (related to CNS WHO grades 2 and 3) (*25*,*26*). Treatment options encompass mainly neurosurgical resection and external-beam irradiation. PRRT is currently considered in meningiomas that cannot be treated by surgery or conventional radiation therapy regardless of their grade (*27*,*28*). PRRT targets somatostatin receptor (SSTR) type 2, since meningiomas almost invariably express SSTR type 2 (*29*) which can be monitored with SSTR-targeted PET imaging. Patients with grade 1 well-differentiated and thus generally less aggressive meningiomas exhibit higher levels of SSTR and may have the best responses to PRRT (*30*). ^{90}Y-SSTR–targeted PRRT and ^{177}Lu-SSTR–targeted PRRT similarly combine a molecular vector targeting the SSTR receptor with a β-emitting radioactive label and are used in PRRT of meningiomas.

Perspectives

Most of the available data on PRRT in meningiomas are from patients at a late stage of the disease (*27*,*30*), when the efficacy of the treatment is potentially limited. Achieving a partial response after PRRT (*31*) or other systemic therapies (*32*) in meningiomas is rare. It might therefore be advantageous to start PRRT earlier in the disease course (after surgery)—that is, before patients develop treatment-refractory, progressive, and extensive disease. Moreover, identification of potentially dedifferentiated meningiomas with a poorer prognosis (lesions with high ^{18}F-FDG uptake and low SSTR uptake) with multitracer pretherapeutic SSTR PET and ^{18}F-FDG PET (*33*) could help to select patients for whom PRRT could provide more benefit. Meningiomas are considered a heterogeneous group, and even the pathologically benign subtypes (grade 1) can have a high recurrence risk depending on their molecular alterations (*34*,*35*). PRRT should be investigated not only in refractory (end-stage) meningioma but also in surgically inoperable, high-grade, and high–recurrence-risk meningioma. In high-grade meningioma, because additional value for dedifferentiated meningioma can be expected, pretherapeutic ^{18}F-FDG PET will be critical (*36*). Future efforts should include the development of criteria for appropriate use of PRRT in the specific subtypes (with the current insight on molecular alterations and the risk of recurrence) and the determination of efficacy in randomized prospective trials.

Moreover, SSTR-targeted PRRT in meningiomas has been based on the standard approach in neuroendocrine tumors, that is, sequential treatment by multiple doses. This paradigm requires reevaluation in meningiomas, ideally including personal tumor dosimetry and alternative administration modes. For the latter, promising preliminary results were reported for intraarterial administration boosts of ^{177}Lu-SSTR–targeted PRRT in salvage meningioma patients (*37*). Moreover, as β-emitters (^{177}Lu and ^{90}Y) have been used in all studies, the efficiency of labeling STTRs with α-emitters should be investigated.

Lastly, future studies should also focus on treatment combinations. The combination of external-beam radiation therapy and PRRT, for instance, could improve the absorbed dose while limiting the organ-at-risk irradiation. This improvement would be due to the difference in radiation fields between the 2 modalities, thereby potentially providing better local disease control than PRRT alone (*38*,*39*). In a study of Kreissl et al. (*38*), one cycle of PRRT was administered in combination with external radiation therapy, bringing us to the point mentioned above. A randomized controlled trial comparing the effect of 1 cycle versus 4 cycles of PRRT with or without external-beam radiation therapy should be investigated in terms of safety and efficacy. Also, because radiation exposure increases SSTR type 2 expression, pre-PRRT external radiation therapy might be able to boost the antitumor effects of PRRT (*40*). As another example, PRRT and targeted therapies such as everolimus, an inhibitor of mammalian target of rapamycin, may potentially act synergistically without potentiating adverse effects (*41*). Phase II trial results with a combination of everolimus and nonradiolabeled octreotide have been encouraging in terms of progression-free survival (55% after 6 mo) in a study population of whom 90% had WHO grade 2 and 3 meningiomas (*42*).

GLIOMAS

Context

Gliomas are the most common malignant brain tumors. They include diffuse gliomas such as astrocytomas, oligodendrogliomas, and glioblastomas, as well as ependymomas. Around 80% are high-grade gliomas. They are classified according to the WHO as CNS WHO grade 2, 3, or 4 (*43*). Currently, a combined approach of maximal safe surgical resection, external-beam radiation therapy, and chemotherapy represents the standard of care for diffuse gliomas, but new therapeutic approaches are needed (*44*).

Gliomas are characterized by a high level of treatment resistance, immune escape, and temporospatial heterogeneity. It is not surprising that although considerable effort has been put into the development of new treatment options, the last few decades have revealed only a few significant changes in the outcome of glioma patients. The limited overall survival, especially for patients with glioblastoma, underlines the need for new therapeutic concepts in the management of glioma patients (*45*). Many potential theranostic targets for gliomas have been investigated, with variable but mostly discouraging results: tenascin, epidermal growth factor receptor, neurokinin type 1 receptor, SSTR, gastrin-releasing peptide receptor, LAT-1, carbonic anhydrase XII, PSMA, matrix metalloproteinase, DNA histone ^{1}H complex, poly(adenosine diphosphate ribose) polymerase 1, integrins, chemokine receptor 4, disialoganglioside, and fibroblast activation protein.

Perspectives

Similar to the situation in meningiomas, most theranostic studies on gliomas have been performed either after incomplete surgery or as a second line in recurrent disease, the latter most often being in combination with chemotherapy or radiation therapy (*46*). The main weaknesses of the current studies are selection bias in patient inclusion, small patient numbers, or lack of efficacy data. All planned and performed glioma studies based on systemic administration of a non–BBB-penetrant compound have failed or are likely to fail, and all performed studies that include direct tumor administration have been discouraging. Therefore, currently, the most promising studies are trials targeting LAT-1, although the low residence time and radiation burden to normal brain parenchyma should be closely investigated. Moreover, future studies should focus on using multimodal approaches combining theranostic agents with techniques enhancing BBB or BTB permeability.

BRAIN METASTASES

Context

Brain metastases are diagnosed in 50% of patients with advanced primary lung cancer and melanoma and 20% of patients with breast cancer (*47*). The presence of brain metastases is associated with a poor prognosis. The current therapeutic options consist of a combination of surgery, external radiation therapy, and targeted and immune-modulating therapies (*48*). As primary cancer control is advancing dramatically, brain metastases across many cancer types occur more frequently, illustrating the need for more effective therapies.

Perspectives

Radionuclide therapy for brain metastases has scarcely been investigated. As in primary brain tumors, in brain metastases the physiologic BBB is usually altered with formation of a BTB (*49*). An advantage of radionuclide therapy over immune therapy is that the effective targeting of all lesions can be visualized using intratherapy scanning (*1*,*2*). Although studies of radionuclide therapy in brain metastases are scarce and efficacy needs to be proven, there are very preliminary data on example cases in breast cancer, prostate cancer, and melanoma.

The added value of radionuclide therapy for metastasis is the simultaneous treatment of most tumor localizations in the body when using intravenous or intraarterial administration. Moreover, the effective targeting of brain metastases can be noninvasively—that is, repeatedly—monitored by PET imaging. These features might translate into an advantage over the current standard of care in terms of clinical benefit. With regard to the development of theranostic radiopharmaceutical pairs to treat brain metastases, these must focus on specific targets for specific cancer types.

PEDIATRIC BRAIN TUMORS

Context

Brain tumors are the most frequent solid malignancy in childhood and account for around 20% of all pediatric tumors (the second most frequent after leukemias). They differ in many aspects from the disease in adults, both in site (pediatric brain tumors are more often infratentorial [≤60% of cases]) and in histology (*50*), as has been recognized in the most recent WHO classification of CNS tumors (fifth edition, 2021), in which specific pediatric variants have been added (e.g., pediatric-type low-grade and high-grade diffuse gliomas) (*51–53*). Recent advances in molecular and genetic characterization have detected many peculiarities of pediatric CNS tumors, significantly impacting spreading, response to treatment, and survival (*54*,*55*).

Surgery is the mainstay in many pediatric brain tumors. It offers a prospective cure in the noninfiltrating forms but is often performed also to treat diffuse infiltrating disease, because debulking can improve survival and quality of life. Surgery can be combined with adjuvant therapy (external radiation therapy or chemotherapy) when complete resection is not achievable or when microscopic persistence of disease is probable (*56*).

Surgical options are often heavily limited by the anatomic relationships between lesions and critical structures, as is often the case for H3-K27–altered diffuse midline gliomas (formerly known as diffuse intrinsic pontine gliomas), for which external radiation therapy offers the best chance for palliation. External radiation therapy increases survival in many high-grade tumors, as in medulloblastoma, one of the most frequent CNS neoplasms in childhood, typically located in the posterior fossa. However, radiation therapy can have devastating long-term effects (neurocognitive, endocrine, etc.), particularly in younger patients (0–3 y) (*57*). Therefore, external radiation therapy is often avoided when prolonged survival is expected in younger patients, despite its efficacy.

Chemotherapy is used in combination with surgery or external radiation therapy, considering the interactions of the drug with the BBB. Intraventricular administration is often used in young children with embryonal tumors (atypical teratoid rhabdoid tumor, medulloblastoma), who cannot receive external radiation, to treat or prevent meningeal spread or dissemination through the cerebrospinal fluid circulation. Pediatric CNS tumors remain the leading cause of cancer-related death in childhood, despite much progress in comprehension of their molecular bases, and greatly need alternative treatment options, as in the case of the theranostic approach.

Perspectives

Considering the field, a relatively large amount of literature is available on theranostic approaches toward radioligands in pediatric neurooncology. One of the best-documented and promising approaches is the use of intracranioventricular [^{131}I]omburtamab via an intrathecal Ommaya reservoir in metastatic neuroblastoma, recurrent medulloblastoma, and ependymoma for treatment of leptomeningeal disease (*58*).

In leptomeningeal disease, cancer cells are located in the cerebrospinal fluid space. Intracranioventricular administration enables targeted treatment with high regional tracer concentrations and a low systemic distribution, confirmed by pretherapeutic [^{131}I]omburtamab scans (*58*).

It is too early to know which radionuclide therapy shows the greatest potential, and as in adults, more research must be done with innovative techniques to resolve the issue of penetrability of the physiologic BBB and BTB. Several preclinical and clinical studies are in progress and will soon show whether theranostic approaches will be able to serve as the desperately needed tools to improve patient care in neurooncology.

CONCLUSION

Theranostics is an exciting field of nuclear medicine with proven efficacy in, up to now, mainly thyroid cancer, prostate cancer, and neuroendocrine tumors. The theranostic concept is increasingly also being tested in brain tumors, with preliminary encouraging results for meningiomas and leptomeningeal spread of pediatric brain tumors but discouraging results for gliomas. To date, no studies have proven clinical efficacy. Existing concepts from extracranial malignancies—such as ^{177}Lu-DOTATATE for neuroendocrine tumors—are being translated to the brain tumor setting. In parallel, new theranostic targets are being explored. However, unlike extracranial malignancies, the BBB and BTB form a significant hurdle in the development of effective therapies for primary and secondary brain tumors. Respective therapeutics that can cross the intact or partially intact BBB and BTB are desired. Although some therapeutics do, in fact, actively cross these barriers, the success of most agents will depend on the successful development and clinical implementation of other principles that increase the permeability of the BBB in combination with agents that decrease efflux. These techniques are still under development, without proven efficacy, and are found in multiple versions. Here, nuclear medicine techniques can aid and potentially speed development by enabling visualization and verification of the principle, such as imaging after FUS with radiolabeled monoclonal antibodies, which are large by nature and normally would not cross the BBB (*59*,*60*). Besides standalone therapy, synergistic approaches with external-beam radiation or immunotherapy could potentially be even more effective and are being evaluated. Additionally, as with all theranostic approaches, the optimal timing (e.g., phase of treatment) should be explored. Another major limitation of substantial progress is the use of underpowered and uncontrolled clinical trial designs. The international community should strive toward sufficiently large and randomized studies to generate high-level evidence on radioligand therapies for CNS tumors. More basic and clinical research is certainly necessary.

DISCLOSURE

Matthias Preusser has received honoraria for lectures, consultation, or advisory board participation from the following for-profit companies: Bayer, Bristol-Myers Squibb, Novartis, Gerson Lehrman Group (GLG), CMC Contrast, GlaxoSmithKline, Mundipharma, Roche, BMJ Journals, MedMedia, Astra Zeneca, AbbVie, Lilly, Medahead, Daiichi Sankyo, Sanofi, Merck Sharp & Dohme, Tocagen, Adastra, Gan & Lee Pharmaceuticals, and Servier. Nathalie Albert has received honoraria for consultation or advisory board participation from Novartis and Telix and research funding from Novocure. Antoine Verger has received honoraria for lectures from General Electric, Curium, and Eisai. Ken Herrmann reports personal fees from Bayer, personal fees and other from Sofie Biosciences, personal fees from SIRTEX, nonfinancial support from ABX, personal fees from Adacap, personal fees from Curium, personal fees from Endocyte, grants and personal fees from BTG, personal fees from IPSEN, personal fees from Siemens Healthineers, personal fees from GE Healthcare, personal fees from Amgen, personal fees from Novartis, personal fees from ymabs, personal fees from Aktis Oncology, personal fees from Theragnostics, personal fees from Pharma15, personal fees from Debiopharm, personal fees from AstraZeneca, and personal fees from Janssen. Martin Glas reports honoraria from Roche, Novartis, UCB, Abbvie, Daiichi Sankyo, Novocure, Bayer, Janssen-Cilag, Medac, Merck, and Kyowa Kirin; travel support from Novocure and Medac; and a research grant from Novocure. Michael Weller has received research grants from Quercis and Versameb and honoraria from Bayer, Curevac, Medac, Novartis, Novocure, Orbus, Philogen, Roche, and Sandoz. Michael Weller is part of the EORTC board and the president of the Swiss Neuro-Oncology Society. Henryk Barthel received reader honoraria from Life Molecular Imaging and dosing committee honoraria from Pharmtrace. Igor Yakushev receives speaker honoraria from Piramal and consultant fees from ABX-CRO and Blue Earth Diagnostics. Igor Yakushev receives research funding from the Federal Ministry of Education and Research, Germany (grant 031L0200B; principal investigator, 2020–2022); the German Research Foundation (grant 491096247; principal investigator, 2021–2024); the International Brain Research Organization (meeting support award, 2022); and the International Society for Cerebral Blood Flow and Metabolism (satellite symposia sponsorship, 2022). No other potential conflict of interest relevant to this article was reported.

ACKNOWLEDGMENTS

We thank Drs. Dannis Van Vuurden and Mario Ries for their valuable contribution.

REFERENCES

1. Kratochwil C, Fendler WP, Eiber M, et al. EANM procedure guidelines for radionuclide therapy with ^{177}Lu-labelled PSMA-ligands (^{177}Lu-PSMA-RLT). *Eur J Nucl Med Mol Imaging.* 2019;46:2536–2544.
2. Bodei L, Mueller-Brand J, Baum RP, et al. The joint IAEA, EANM, and SNMMI practical guidance on peptide receptor radionuclide therapy (PRRNT) in neuroendocrine tumours. *Eur J Nucl Med Mol Imaging.* 2013;40:800–816.
3. Pasciak AS, Manupipatpong S, Hui FK, et al. Yttrium-90 radioembolization as a possible new treatment for brain cancer: proof of concept and safety analysis in a canine model. *EJNMMI Res.* 2020;10:96.
4. Arvanitis CD, Ferraro GB, Jain RK. The blood-brain barrier and blood-tumour barrier in brain tumours and metastases. *Nat Rev Cancer.* 2020;20:26–41.
5. Benmelouka AY, Munir M, Sayed A, et al. Neural stem cell-based therapies and glioblastoma management: current evidence and clinical challenges. *Int J Mol Sci.* 2021;22:2258.
6. Aboody KS, Brown A, Rainov NG, et al. Neural stem cells display extensive tropism for pathology in adult brain: evidence from intracranial gliomas. *Proc Natl Acad Sci USA.* 2000;97:12846–12851.
7. Chaichana KL, Pinheiro L, Brem H. Delivery of local therapeutics to the brain: working toward advancing treatment for malignant gliomas. *Ther Deliv.* 2015;6: 353–369.
8. Song DK, Lonser RR. Convection-enhanced delivery for the treatment of pediatric neurologic disorders. *J Child Neurol.* 2008;23:1231–1237.
9. Shi M, Sanche L. Convection-enhanced delivery in malignant gliomas: a review of toxicity and efficacy. *J Oncol.* 2019;2019:9342796.
10. Mehta AM, Sonabend AM, Bruce JN. Convection-enhanced delivery. *Neurotherapeutics.* 2017;14:358–371.
11. Tosi U, Kommidi H, Adeuyan O, et al. PET, image-guided HDAC inhibition of pediatric diffuse midline glioma improves survival in murine models. *Sci Adv.* 2020;6:eabb4105.
12. Souweidane MM, Kramer K, Pandit-Taskar N, et al. Convection-enhanced delivery for diffuse intrinsic pontine glioma: a single-centre, dose-escalation, phase 1 trial. *Lancet Oncol.* 2018;19:1040–1050.
13. Burgess A, Shah K, Hough O, Hynynen K. Focused ultrasound-mediated drug delivery through the blood–brain barrier. *Expert Rev Neurother.* 2015;15:477–491.
14. Sheikov N, McDannold N, Sharma S, Hynynen K. Effect of focused ultrasound applied with an ultrasound contrast agent on the tight junctional integrity of the brain microvascular endothelium. *Ultrasound Med Biol.* 2008;34:1093–1104.
15. Mainprize T, Lipsman N, Huang Y, et al. Blood-brain barrier opening in primary brain tumors with non-invasive MR-guided focused ultrasound: a clinical safety and feasibility study. *Sci Rep.* 2019;9:321.
16. Lipsman N, Meng Y, Bethune AJ, et al. Blood–brain barrier opening in Alzheimer's disease using MR-guided focused ultrasound. *Nat Commun.* 2018;9:2336.
17. Idbaih A, Canney M, Belin L, et al. Safety and feasibility of repeated and transient blood–brain barrier disruption by pulsed ultrasound in patients with recurrent glioblastoma. *Clin Cancer Res.* 2019;25:3793–3801.
18. Meng Y, Pople CB, Budiansky D, et al. Current state of therapeutic focused ultrasound applications in neuro-oncology. *J Neurooncol.* 2022;156:49–59.
19. Antoniou A, Stavrou M, Evripidou N, et al. FUS-mediated blood–brain barrier disruption for delivering anti-Aβ antibodies in 5XFAD Alzheimer's disease mice. *J Ultrasound.* July 29, 2023 [Epub ahead of print].
20. Shi L, Palacio-Mancheno P, Badami J, et al. Quantification of transient increase of the blood–brain barrier permeability to macromolecules by optimized focused ultrasound combined with microbubbles. *Int J Nanomedicine.* 2014:9:4437–4448.
21. Tran VL, Novell A, Tournier N, et al. Impact of blood-brain barrier permeabilization induced by ultrasound associated to microbubbles on the brain delivery and kinetics of cetuximab: an immunoPET study using ^{89}Zr-cetuximab. *J Controlled Release.* 2020;328:304–312.
22. Hultqvist G, Syvänen S, Fang XT, Lannfelt L, Sehlin D. Bivalent brain shuttle increases antibody uptake by monovalent binding to the transferrin receptor. *Theranostics.* 2017;7:308–318.
23. Johnsen KB, Bak M, Melander F, et al. Modulating the antibody density changes the uptake and transport at the blood-brain barrier of both transferrin receptor-targeted gold nanoparticles and liposomal cargo. *J Controlled Release.* 2019;295:237–249.
24. Rautio J, Gynther M, Laine K. LAT1-mediated prodrug uptake: a way to breach the blood-brain barrier? *Ther Deliv.* 2013;4:281–284.
25. Louis DN, Perry A, Wesseling P, et al. The 2021 WHO classification of tumors of the central nervous system: a summary. *Neuro Oncol.* 2021;23:1231–1251.
26. Goldbrunner R, Minniti G, Preusser M, et al. EANO guidelines for the diagnosis and treatment of meningiomas. *Lancet Oncol.* 2016;17:e383–e391.
27. Salgues B, Graillon T, Horowitz T, et al. Somatostatin receptor theranostics for refractory meningiomas. *Curr Oncol.* 2022;29:5550–5565.
28. Minczeles NS, Bos EM, de Leeuw RC, et al. Efficacy and safety of peptide receptor radionuclide therapy with [^{177}Lu]Lu-DOTA-TATE in 15 patients with progressive treatment-refractory meningioma. *Eur J Nucl Med Mol Imaging.* 2023;50:1195–1204.
29. Dutour A, Kumar U, Panetta R, et al. Expression of somatostatin receptor subtypes in human brain tumors. *Int J Cancer.* 1998;76:620–627.
30. Seystahl K, Stoecklein V, Schüller U, et al. Somatostatin-receptor-targeted radionuclide therapy for progressive meningioma: benefit linked to ^{68}Ga-DOTATATE/-TOC uptake. *Neuro Oncol.* 2016;18:1538–1547.
31. Mirian C, Duun-Henriksen AK, Maier A, et al. Somatostatin receptor–targeted radiopeptide therapy in treatment-refractory meningioma: individual patient data meta-analysis. *J Nucl Med.* 2021;62:507–513.
32. Kaley T, Barani I, Chamberlain M, et al. Historical benchmarks for medical therapy trials in surgery- and radiation-refractory meningioma: a RANO review. *Neuro Oncol.* 2014;16:829–840.
33. Mairal E, Chevalier E, Imbert L, Boursier-Joppin C, Verger A. Multiparametric ^{18}F-FDG and ^{68}GA-DOTATOC PET imaging in bone metastatic meningioma before radionuclide therapy. *Clin Nucl Med.* 2022;47:e321–e322.
34. Maggio I, Franceschi E, Tosoni A, et al. Meningioma: not always a benign tumor. A review of advances in the treatment of meningiomas. *CNS Oncol.* 2021;10: CNS72.
35. Patel AJ, Wan YW, Al-Ouran R, et al. Molecular profiling predicts meningioma recurrence and reveals loss of DREAM complex repression in aggressive tumors. *Proc Natl Acad Sci USA.* 2019;116:21715–21726.
36. Lee JW, Kang KW, Park SH, et al. ^{18}F-FDG PET in the assessment of tumor grade and prediction of tumor recurrence in intracranial meningioma. *Eur J Nucl Med Mol Imaging.* 2009;36:1574–1582.
37. Vonken EP, Bruijnen RCG, Snijders TJ, et al. Intraarterial administration boosts ^{177}Lu-HA-DOTATATE accumulation in salvage meningioma patients. *J Nucl Med.* 2022;63:406–409.

38. Kreissl MC, Hänscheid H, Löhr M, et al. Combination of peptide receptor radionuclide therapy with fractionated external beam radiotherapy for treatment of advanced symptomatic meningioma. *Radiat Oncol.* 2012;7:99.
39. Hartrampf PE, Hänscheid H, Kertels O, et al. Long-term results of multimodal peptide receptor radionuclide therapy and fractionated external beam radiotherapy for treatment of advanced symptomatic meningioma. *Clin Transl Radiat Oncol.* 2020; 22:29–32.
40. Oddstig J, Bernhardt P, Nilsson O, Ahlman H, Forssell-Aronsson E. Radiation induces up-regulation of somatostatin receptors 1, 2, and 5 in small cell lung cancer *in vitro* also at low absorbed doses. *Cancer Biother Radiopharm.* 2011;26:759–765.
41. Claringbold PG, Brayshaw PA, Price RA, Turner JH. Phase II study of radiopeptide ^{177}Lu-octreotate and capecitabine therapy of progressive disseminated neuroendocrine tumours. *Eur J Nucl Med Mol Imaging.* 2011;38:302–311.
42. Graillon T, Sanson M, Campello C, et al. Everolimus and octreotide for patients with recurrent meningioma: results from the phase II CEVOREM trial. *Clin Cancer Res.* 2020;26:552–557.
43. Osborn AG, Louis DN, Poussaint TY, Linscott LL, Salzman KL. The 2021 World Health Organization classification of tumors of the central nervous system: what neuroradiologists need to know. *AJNR.* 2022;43:928–937.
44. Weller M, van den Bent M, Preusser M, et al. EANO guidelines on the diagnosis and treatment of diffuse gliomas of adulthood. *Nat Rev Clin Oncol.* 2021;18:170–186.
45. Weller M, Wick W, Aldape K, et al. Glioma. *Nat Rev Dis Primers.* 2015;1:15017.
46. Riva P, Franceschi G, Frattarelli M, et al. Loco-regional radioimmunotherapy of high-grade malignant gliomas using specific monoclonal antibodies labeled with ^{90}Y: a phase I study. *Clin Cancer Res.* 1999;5(suppl)3275s–3280s.
47. Aizer AA, Lamba N, Ahluwalia MS, et al. Brain metastases: a Society for Neuro-Oncology (SNO) consensus review on current management and future directions. *Neuro Oncol.* 2022;24:1613–1646.
48. Le Rhun E, Guckenberger M, Smits M, et al. EANO-ESMO clinical practice guidelines for diagnosis, treatment and follow-up of patients with brain metastasis from solid tumours. *Ann Oncol.* 2021;32:1332–1347.
49. Upton DH, Ung C, George SM, Tsoli M, Kavallaris M, Ziegler DS. Challenges and opportunities to penetrate the blood-brain barrier for brain cancer therapy. *Theranostics.* 2022;12:4734–4752.
50. Sturm D, Pfister SM, Jones DTW. Pediatric gliomas: current concepts on diagnosis, biology, and clinical management. *J Clin Oncol.* 2017;35:2370–2377.
51. Jaimes C, Poussaint TY. Primary neoplasms of the pediatric brain. *Radiol Clin North Am.* 2019;57:1163–1175.
52. Udaka YT, Packer RJ. Pediatric brain tumors. *Neurol Clin.* 2018;36:533–556.
53. Thomas DL. 2021 updates to the World Health Organization classification of adult-type and pediatric-type diffuse gliomas: a clinical practice review. *Chin Clin Oncol.* 2023;12:7.
54. Rosenberg T, Bandopadhayay P. Molecular genetics of paediatric brain tumours and opportunities for precision medicine: a focus on infant tumours. *Curr Opin Neurol.* 2022;35:772–778.
55. Monteiro JM, Reis Ramos JI, Teixeira E Sousa I, Bighetti-Trevisan RL, Ribas Filho JM, Isolan GR. Identification of CD114 membrane receptors as a molecular target in medulloblastomas. *Int J Mol Sci.* 2023;24:5331.
56. Pollack IF, Agnihotri S, Broniscer A. Childhood brain tumors: current management, biological insights, and future directions. *J Neurosurg Pediatr.* 2019;23:261–273.
57. Baudou E, Pollidoro L, Iannuzzi S, et al. A review of long-term deficits in memory systems following radiotherapy for pediatric posterior fossa tumor. *Radiother Oncol.* 2022;174:111–122.
58. Pandit-Taskar N, Grkovski M, Zanzonico PB, et al. Radioimmunoscintigraphy and pretreatment dosimetry of ^{131}I-omburtamab for planning treatment of leptomeningeal disease. *J Nucl Med.* 2023;64:946–950.
59. Yang FY, Chang WY, Li JJ, Wang HE, Chen JC, Chang CW. Pharmacokinetic analysis and uptake of ^{18}F-FBPA-Fr after ultrasound-induced blood–brain barrier disruption for potential enhancement of boron delivery for neutron capture therapy. *J Nucl Med.* 2014;55:616–621.
60. Liu HL, Hsu PH, Lin CY, et al. Focused ultrasound enhances central nervous system delivery of bevacizumab for malignant glioma treatment. *Radiology.* 2016;281:99–108.

α-Synuclein Seeding Amplification Assay: A Breakthrough in Diagnosing Parkinson Disease?

John P. Seibyl

Institute for Neurodegenerative Disorders and Yale University School of Medicine, New Haven, Connecticut

Research over the last several decades implicates brain accumulations of misfolded proteins as a primary pathologic feature of neurodegenerative diseases. These brain deposits can now be interrogated in vivo in some neurodegenerative diseases using PET imaging or fluid biomarkers (*1*). In our diagnostic algorithms for clinical research trials, these new biomarkers are generating a nosologic shift that may improve the accuracy and timeliness of diagnosis and provide more consistency for monitoring effects of treatment (*2*). The conceptual framework for diagnosis and monitoring of neurodegenerative disorders is undergoing a revolutionary paradigm shift—from diagnoses based on clinical signs and symptoms described by eponymic syndromes to a definition of disease guided by a biologic understanding of the primary pathophysiology as demonstrated by highly specific biomarkers.

A recent example of this trend is the integration of imaging and nonimaging biomarkers of Alzheimer disease into clinical treatment trials. PET imaging biomarkers for amyloid β and tau now serve important roles in enrolling cohorts for trials of amyloid-targeting treatments, as well as in detecting changes in amyloid or tau burden in the brain as a measure of drug target engagement. The amyloid/tau/neurodegeneration system (*3*) is based on the presence and timing of biomarkers over the course of disease rather than strictly the severity of cognitive impairment for diagnosing and staging Alzheimer disease. Most important, a diagnosis can be made very early, when the impact of a disease-modifying treatment may be greatest, even before the manifestation of common clinical symptoms.

Clinical researchers on Parkinson disease (PD) now have access to biomarkers of the primary disease process, α-synuclein (a-syn) brain deposition in the form of Lewy bodies. The systematic spread of Lewy bodies in brain deduced from cross-sectional post-mortem data focuses the field on targeting a-syn for therapies that may potentially slow disease progression. This offers the challenge and the opportunity to make an earlier, more accurate diagnosis for timely management with therapies that target a-syn.

It is now logistically feasible to assay in vivo the presence of brain a-syn. Recent work has shown that the method referred to as the a-syn seeding amplification assay (SAA) provides a highly sensitive and accurate test for synucleinopathies (*4*,*5*). The test takes advantage of the characteristic property of misfolded a-syn fibrils—promotion of misfolding of the normal protein. These misfolded a-syn fibrils spread along specific neural networks to other neurons, moving across synapses. This is a process thought to occur in vivo as the mechanism for spreading of Lewy bodies over the course of disease progression. When a small sample of cerebrospinal fluid is coincubated with normally folded recombinant a-syn, the latter misfolds, creating more aberrant protein that goes on in serial fashion to amplify the assay to the point that it may be detectable through standard histochemical techniques. SAAs have also been pursued with serum and tissue, most notably skin biopsy, with the presence of small amounts of a-syn being found in PD patients (*6*). These latter approaches are not as sensitive as the cerebrospinal fluid but are improving and moving toward the goal of having a simple assay that may provide binary information or even semiquantitative data regarding the a-syn status of the patient.

Preliminary data on a large PD patient cohort ($n = 1{,}123$) with cerebrospinal fluid samples from the Parkinson Disease Progression Marker Initiative evaluated a-syn SAA at baseline presentation of idiopathic PD participants ($n = 545$), healthy controls ($n = 173$), participants with clinical signs or symptoms but without evidence of dopaminergic deficits ($n = 54$), participants with prodromal PD based on either rapid-eye-movement sleep behavior disorder or olfactory impairment ($n = 51$), and nonmanifesting genetic carriers of LRRK2 or GBA ($n = 310$) (*7*). The sensitivity for detection of clinically well-characterized PD was 88%, whereas specificity was 96% for healthy controls. When evaluated in PD participants with an olfactory deficit, a-syn SAA was positive in 98.6%. In the prodromal cohort, rapid-eye-movement sleep behavior disorder or hyposmic/anosmic participants were positive in 86% of cases. Within the prodromal group, there were subjects who were a-syn SAA–positive and dopamine transporter imaging–negative but not a-syn SAA–negative and dopamine transporter imaging–positive. This finding suggests that the a-syn SAA may be more sensitive than dopaminergic imaging with ^{123}I-ioflupane SPECT and is consistent with the fact that motor symptoms do not appear until the nigrostriatal pathways are affected by Braak stage 3, well after the process of Lewy body formation has begun (*8*).

The rapid development of a-syn SAAs has motivated groups to develop biologically based diagnostic schemes. Höglinger et al., in preliminary work, propose a system based on defined gene variants, a-syn pathology, and imaging evidence of neurodegeneration, with the associated clinical syndrome defined by ranked, high-specificity features (*9*).

In fall 2022, a working group was formed to incorporate these advances in a paradigm-shifting, biologically based, and functionally relevant staging of PD. This group includes academic physicians

---

Received Sep. 8, 2023; revision accepted Nov. 7, 2023.

For correspondence or reprints, contact John P. Seibyl (jpseibyl@seibyl.com).

DOI: 10.2967/jnumed.123.266191

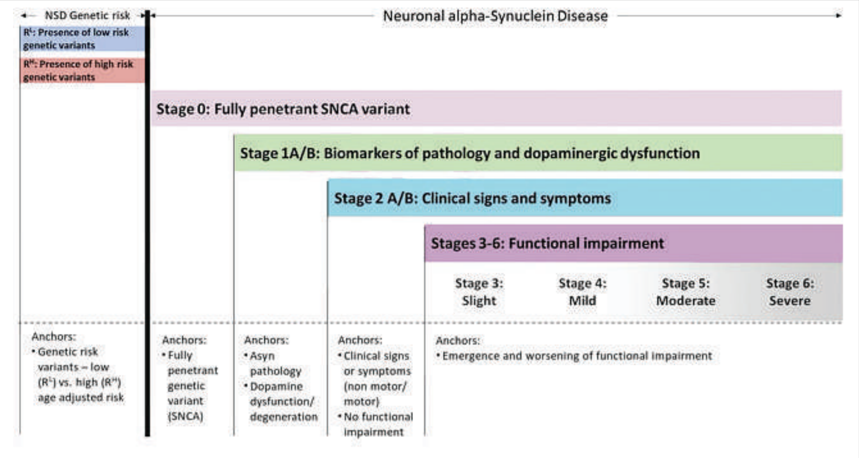

FIGURE 1. Schematic of neuronal NSD-ISS, biologically rooted, evidence-based hybrid staging schema for clinical research on neuronal synucleinopathies, PD, and Lewy body dementia. (Reprinted with permission of (*11*).)

and movement disorder specialists, basic scientists, pharmaceutical company scientists, regulatory scientists, PD patients, and nonprofits such as the Critical Paths Institute under the organizational umbrella of the Michael J. Fox Foundation. Interest in such a staging system comes from, first, the immediate clinical trial requirement for testing PD as early in the course as possible, even before motor manifestations required of the current clinically based diagnosis; second, a lack of evidence-based measures of progressing functional impairment with more specificity than Hoehn–Yahr staging for a more patient-relevant and standardized way to assess the impact of novel, disease-targeting therapeutics on longitudinal evaluation of clinical trial participants; and third, more accurate prognoses for patients and caretakers, despite phenotypic heterogeneity.

The conceptual framework keys off the premise that neuronal a-syn pathology and dopaminergic dysfunction measured with biomarkers are the sine qua non of PD diagnosis and that the functional impact of symptoms is more important than taxonomic symptom classification per se to patients, their caregivers, and regulatory authorities. These considerations resulted in an initial iteration of the neuronal a-syn disease integrated staging system (NSD-ISS). The NSD-ISS is a hybrid system of biologically based diagnosis and functional staging that is designed to reflect the current state of the art in understanding of the pathophysiology of neuronal a-syn disease, which includes PD and Lewy body dementia. The other disorder associated with a-syn is multiple-system atrophy, which features glial cell involvement as its primary pathology and hence is excluded from this classification and staging (*10*). This conceptual schema is described in Figure 1.

Briefly, there are 6 stages. Stage 1 is a-syn pathology and dopaminergic dysfunction demonstrated by a-syn SAA and ^{123}I-ioflupane SPECT, respectively, without any clinical signs or symptoms. At stage 2, clinical signs and symptoms are evident but cause no functional impairment. At stage 3, there is some slight functional impairment, which progresses to mild in stage 4, moderate in stage 5, and finally severe in stage 6. Both biologic and functional stages are evidence-based. The particular biomarkers for the targeted pathology—indeed, even the pathologic target—may change as new information becomes available.

Although offering some advantages, the NSD-ISS does represent a paradigm shift that will challenge some individuals. The diagnosis of PD in the absence of motor symptoms may feel counterintuitive to some clinicians and patients. The bundling of PD and Lewy body dementia under one classification schema will be challenging to others. The fact is that the terms *PD* and *Lewy body dementia* will still be used referring to patients; the NSD-ISS parses along lines of biology, which in the end is critical to drug development.

These are research staging criteria currently, but it is conceivable that biologically based phenotype classification may have wider utility for clinical purposes such as ensuring the appropriateness of a treatment or offering more accurate prognoses that allow care providers to better plan resources and families to better manage expectations. The consequence of these developments for the nuclear medicine community may also be profound, with the high sensitivity of scintigraphy, the information about spatial extent in the brain, and the possibility of quantification being critical aids in the effort to slow progression or even prevent clinical expression of these α-synucleinopathies.

DISCLOSURE

No potential conflict of interest relevant to this article was reported.

REFERENCES

1. Seibyl JP. Imaging biomarkers for central nervous system drug development and future clinical utility: lessons from neurodegenerative disorders. *J Nucl Med.* 2023; 64:12–19.
2. van Dyck CH, Swanson CJ, Aisen P, et al. Lecanemab in early Alzheimer's disease. *N Engl J Med.* 2023;388:9–21.
3. Hampel H, Cummings J, Blennow K, Gao P, Jack CR Jr, Vergallo A. Developing the ATX(N) classification for use across the Alzheimer disease continuum. *Nat Rev Neurol.* 2021;17:580–589.
4. Grossauer A, Hemicker G, Krismer F, et al. Alpha-synuclein seed amplification assays in the diagnosis of synucleinopathies using cerebrospinal fluid: a systematic review and meta-analysis. *Mov Disord Clin Pract (Hoboken).* 2023;10:737–747.
5. Concha-Marambio L, Pritzkow S, Shahnawaz M, Farris CM, Soto C. Seed amplification assay for the detection of pathologic alpha-synuclein aggregates in cerebrospinal fluid. *Nat Protoc.* 2023;18:1179–1196.
6. Kuzkina A, Rossle J, Seger A, et al. Combining skin and olfactory alpha-synuclein seed amplification assays (SAA): towards biomarker-driven phenotyping in synucleinopathies. *NPJ Parkinsons Dis.* 2023;9:79.
7. Siderowf A, Concha-Marambio L, Lafontant DE, et al. Assessment of heterogeneity among participants in the Parkinson's Progression Markers Initiative cohort using alpha-synuclein seed amplification: a cross-sectional study. *Lancet Neurol.* 2023;22:407–417.
8. Chahine LM, Beach TG, Adler CH, et al. Central and peripheral alpha-synuclein in Parkinson disease detected by seed amplification assay. *Ann Clin Transl Neurol.* 2023;10:696–705.
9. Höglinger GU, Adler CH, Berg D, et al. Towards a biological definition of Parkinsons disease. Preprints.org website. Published April 7, 2023. Accessed November 13, 2023.
10. Kim A, Martinez-Valbuena I, Li J, Lang AE, Kovacs GG. Disease-specific alpha-synuclein seeding in Lewy body disease and multiple system atrophy are preserved in formaldehyde-fixed paraffin-embedded human brain. *Biomolecules.* 2023;13:936.
11. Simuni T, Chahine L, Poston K, et al. Biological definition of neuronal alpha-synuclein disease: towards an integrated staging system for research. Zenodo website. https://zenodo.org/records/10001310. Published September 27, 2023. Accessed November 13, 2023.

Is ^{212}Pb Really Happening? The Post-^{177}Lu/^{225}Ac Blockbuster?

Richard Zimmermann

Chrysalium Consulting, Lalaye, France; MEDraysintell, Louvain-la-Neuve, Belgium; and Oncidium Foundation, Mont-Saint-Guibert, Belgium

Interest in α-emitters for radiotherapeutic applications is on the rise. However, the number of options for α-emitters with midterm industrial availability remains limited. Currently, only ^{225}Ac, ^{212}Pb, and ^{211}At have realistic chances to reach the market within the next 10 y. A review published in 2022 (*1*) extensively describes the history of development of ^{212}Pb and related technologies. Because industrialization processes and realistic production costs are also important criteria, the aim of this editorial is to confirm that, as for ^{225}Ac (*2*), the industry is seriously tackling the challenge of a large-scale supply of ^{212}Pb with a short-term answer. I conducted a survey among different industrial entities claiming their involvement in such development. Surprisingly, more than 15 companies have made progress in ^{212}Pb production, although some of them are still keeping their work confidential.

ALMOST IDEAL PROFILE

^{212}Pb has a half-life of 10.64 h but is a β-emitter. ^{212}Pb decays into ^{212}Bi (half-life, 60.5 min), which is the α-emitter in the further decay sequence, but only at 36% in ^{208}Tl; the other 64% of the decay arm produces ^{212}Po through another β^--emission. ^{212}Po is a pure α-emitter that decays into stable ^{208}Pb in 0.3 μs, whereas ^{208}Tl is both a β^--emitter and a γ-emitter (half-life, 3.06 min), which also leads to stable ^{208}Pb. Indeed, ^{212}Pb also does not show the expected ideal profile, as it needs to be strongly trapped in the cancer cell to keep all the benefits from the α-emission. The high-energy γ-ray emitted by the ^{208}Tl daughter is an identified drawback that can be solved by lowering doses and shielding health care personnel from high-energy γ-rays. On the other hand, the short half-life maximizes the energy deposition in the tumor cell. Compared with ^{225}Ac, this shorter half-life also eliminates the potential issue of storing radioactive waste, indirectly solving the question of a hospital stay and containment of patients' biologic radioactive waste versus ambulatory treatment. For a specific clinical indication, at equal efficacy, any ^{212}Pb-labeled molecule will have the potential to displace any ^{177}Lu- or ^{225}Ac-labeled analog from the market on the basis of the simple marketing advantage of a lower environmental impact from patients.

DEDICATED CHELATING AGENTS

To really benefit from the efficient secondary α-emission of the radionuclide, the first decay radionuclide, ^{212}Bi, needs to stay trapped within the original lead-atom chelating agent. Significant improvements have been made in this area, and several groups have developed chelating agents that also strongly keep ^{212}Bi attached to the vector (*1*). Since the first emission is a β-emission, the recoil effect that could eject the decay metal out of the chelating cage remains limited and is in no way comparable to the recoil effect of the emission of an α-particle, for which such trapping remains close to impossible.

AN ALTERNATIVE TO COCKTAIL THERAPIES

The evolution of radiotherapeutics is expected to follow the same trend as chemotherapeutics given as cocktails—that is, use of mixtures of radiotherapeutics instead of consecutive treatments—and has already been explored with tandem therapies (mixtures of ^{177}Lu and ^{225}Ac similars). Obviously, the evolution of therapies will combine molecules labeled with different energies of β-emitters and α-emitters or even Auger/conversion electron–emitting radionuclides. By maintaining both the β-emitter and the α-emitter in or next to the cancer cell, the use of ^{212}Pb brings an additional advantage over mixtures with simultaneous efficacy in larger tumors and micrometastases. The ^{212}Pb β-particle contribution has already been proven to be nonnegligible (*3*), and this effect could lead to a reduction in both the doses and their number.

IMAGING WITH LEAD

Quantitative SPECT/CT imaging of ^{212}Pb proved feasible (*4*) but will probably remain used only for development purposes. ^{203}Pb, a γ-emitter with a half-life of 51.87 h, has been presented as the ideal ^{212}Pb surrogate for imaging. However, cyclotron production of ^{203}Pb may not receive industry favor because it would require the creation of a large and expensive network of dedicated tools for access (*5*). Certainly, in the same way as for ^{177}Lu-labeled therapeutic agents, imaging agents used for patient selection will be based on radiodiagnostics labeled with more commonly available radionuclides such as ^{18}F, ^{64}Cu, ^{68}Ga, or ^{99m}Tc.

^{212}PB PRODUCTION ROUTES

Orano Med was the first company to believe strongly in the future of ^{212}Pb and has developed a full production process and started investing in ^{212}Pb-labeled drugs. The company is presently

---

Received Nov. 5, 2023; revision accepted Dec. 19, 2023.

For correspondence or reprints, contact Richard Zimmermann (richard.zimmermann@chrysalium.com).

DOI: 10.2967/jnumed.123.266774

building 2 industrial facilities called α-therapy laboratories (https://www.oranomed.com/en/industrial-platform) in Indianapolis and Valenciennes with a capacity of 10,000-plus doses per year by 2025 and anticipating more than 10 times this number by the end of the decade.

^{212}Pb is most easily produced through a generator based on the decay of ^{228}Th (*1*). ^{228}Th has a 1.91-y half-life and decays successively into ^{224}Ra (half-life, 3.66 d), ^{220}Rn (56 s), and ^{216}Po (0.14 s), eventually leading to ^{212}Pb through α-emissions in each step. Generators can be based on 3 different processes.

In the first process, ^{212}Pb can be extracted directly from the ^{228}Th decay solution, but this process is the most cumbersome, as it involves handling of the long–half-life ^{228}Th and can therefore be used only in an industrial environment. The first players (Orano Med [France] and TRIUMF [Canada]) originally used this technology but later gave preference to the 2-step processes. Orano Med opted to keep control of the overall process from the production and isolation of thorium to the final radiolabeling and distribution of drugs and therefore does not intend to sell generators. ATOX (Japan), Oncoinvent (Norway), and the Kurchatov Institute (Russia) are also exploring this route.

The second of the 3 processes utilizes the fact that in the decay sequence of ^{228}Th, ^{224}Ra can easily be extracted for loading of ^{224}Ra/^{212}Pb generators. Major players (Perspective Therapeutics [United States], United Well [China], and Pacific Northwest National Laboratory [United States]) use this technology now because generators containing shorter–half-life parent radionuclides will be easier to distribute from a regulatory point of view.

The third process utilizes ^{220}Rn, a gas that can easily be separated from the ^{228}Th/^{224}Ra mixture as soon as it is generated and then left to decay into ^{212}Pb in a second container (*6*). The companies AdvanCell (Australia), AlphaGen Therapeutics (China), ARTBIO (United States), NRG-PALLAS, FutureChemistry (The Netherlands), and Oncoinvent are developing industrial processes based on this technology. ARTBIO claims that its manufacturing approach is poised to scale comfortably to deliver 20,000-plus doses per year once its first program reaches the commercial stage.

^{212}Pb could also be produced directly, without a generator, by using the precursor ^{226}Ra. The conversion reaction in the same tools as those developed for the production of ^{225}Ac or ^{67}Cu (linear accelerator or Rhodotron [IBA Industrial Solutions]) can lead to large amounts of ^{212}Pb, on the basis of the reaction [^{226}Ra(γ,2n)^{224}Ra→^{212}Pb]. In the ^{225}Ac production process based on photoconversion, up to 6 times more ^{212}Pb than ^{225}Ac is generated as a by-product and could be separated. Such a separation process would affect the yields in ^{225}Ac and would be useful only locally. No company is presently developing such a separation process.

Investment in central industrial-scale production centers could remain low, in the range of an ^{18}F manufacturing site investment. Because the half-life of ^{212}Pb will allow overnight shipment to a distance of several thousand kilometers, not only could production costs remain low but individual radiopharmaceutical companies could keep control of their production.

ACCESS TO THE PRECURSORS ^{228}TH AND ^{226}RA

^{228}Th is not considered of concern and is presently available from several governmental or private sources supporting access to ^{212}Pb and recovery of parent isotopes from legacy nuclear material (Department of Energy [United States], Eckert & Ziegler [Germany], Orano [France], Rosatom [Russia], and National Nuclear Laboratory [U.K.]). The nongenerator production route needs access to ^{226}Ra, which should not be an issue in the near future, as it is the main starting material for the production of ^{223}Ra and ^{225}Ac (*2*).

Industrial access to ^{212}Pb is not yet ready, but an impressive number of new players have entered this field over the past 3 y, with several of them proposing new alternatives for access to ^{212}Pb. At the same time, several ^{212}Pb molecules are under development (>20 identified), with 7 having already reached the clinical stage (*7*). There is strong optimism that industrial solutions for large-scale production of ^{212}Pb will be in place before 2028, opening an avenue for a radionuclide that could replace ^{225}Ac over the period 2035–2045.

DISCLOSURE

No potential conflict of interest relevant to this article was reported.

ACKNOWLEDGMENTS

I thank Simon Puttick (AdvanCell), Conrad Wueller (ARTBIO), Mizuki Nagarekawa (ATOX), James Hill (FutureChemistry), Tim Tinsley (NNL), Nicolas Bozovic (Orano Med), and Bernhard Sixt and Michael Schultz (Perspective Therapeutics) for sharing information about the stage of development in their respective companies.

REFERENCES

1. Kokov KV, Egotov BV, German MN, et al. ^{212}Pb: production approaches and targeted therapies applications. *Pharmaceutics.* 2022;14:189.
2. Zimmermann R. Is actinium really happening? *J Nucl Med.* 2023;64:1516–1518.
3. Lee D, Li M, Bednarz B, Schultz MK. Modeling cell and tumor-metastasis dosimetry with the Particle and Heavy Ion Transport Code System (PHITS) software for targeted alpha-particle radionuclide therapy. *Radiat Res.* 2018;190:236–247.
4. Kvassheim M, Revheim MER, Stokke C. Quantitative SPECT/CT imaging of lead-212: a phantom study. *EJNMMI Phys.* 2022;9:52.
5. McNeil BL, Robertson AKH, Fu W, et al. Production, purification, and radiolabeling of the ^{203}Pb/^{212}Pb theranostic pair. *EJNMMI Radiopharm Chem.* 2021;6:6.
6. Li RG, Stenberg VY, Larsen RH. An experimental generator for production of high-purity ^{212}Pb for use in radiopharmaceuticals. *J Nucl Med.* 2023;64:173–176.
7. Goethals PE, Zimmermann R. *Nuclear Medicine Report and Directory.* 10th ed. MEDraysintell; September 2023.

Phase II Trial Assessing the Repeatability and Tumor Uptake of [^{68}Ga]Ga-HER2 Single-Domain Antibody PET/CT in Patients with Breast Carcinoma

Odrade Gondry[1,2], Vicky Caveliers[1,2], Catarina Xavier[1], Laurens Raes[2], Marian Vanhoeij[3], Guy Verfaillie[3], Christel Fontaine[4], Katrien Glorieus[3], Jacques De Grève[4], Sofie Joris[4], Ine Luyten[4], Karen Zwaenepoel[5], Frederik Vandenbroucke[6], Wim Waelput[7,8], Sheeno Thyparambil[9], Ilse Vaneycken[2], Julie Cousaert[2], Sophie Bourgeois[2], Nick Devoogdt[1], Lode Goethals[6], Hendrik Everaert[2], Frank De Geeter[10], Tony Lahoutte[1,2], and Marleen Keyaerts[1,2]

[1]Department of Medical Imaging, Vrije Universiteit Brussel, Brussels, Belgium; [2]Department of Nuclear Medicine, Universitair Ziekenhuis Brussel, Brussels, Belgium; [3]Department of Surgical Oncology, Universitair Ziekenhuis Brussel, Brussels, Belgium; [4]Department of Medical Oncology, Universitair Ziekenhuis Brussel, Brussels, Belgium; [5]Centre for Oncological Research, University of Antwerp, Wilrijk, Belgium; [6]Department of Radiology, Universitair Ziekenhuis Brussel, Brussels, Belgium; [7]Department of Pathology, Universitair Ziekenhuis Brussel, Brussels, Belgium; [8]Experimental Pathology, Vrije Universiteit Brussel, Brussels, Belgium; [9]mProbe, Rockville, Maryland; and [10]Department of Nuclear Medicine, Algemeen Ziekenhuis Sint-Jan Brugge Oostende, Bruges, Belgium

Human epidermal growth factor receptor 2 (HER2) status is used for decision-making in breast carcinoma treatment. The status is obtained through immunohistochemistry or in situ hybridization. These two methods have the disadvantage of necessitating tissue sampling, which is prone to error due to tumor heterogeneity or interobserver variability. Whole-body imaging might be a solution to map HER2 expression throughout the body. **Methods:** Twenty patients with locally advanced or metastatic breast carcinoma (5 HER2-positive and 15 HER2-negative patients) were included in this phase II trial to assess the repeatability of uptake quantification and the extended safety of the [^{68}Ga]Ga-NOTA-anti-HER2 single-domain antibody (sdAb). The tracer was injected, followed by a PET/CT scan at 90 min. Within 8 d, the procedure was repeated. Blood samples were taken for antidrug antibody (ADA) assessment and liquid biopsies. On available tissues, immunohistochemistry, in situ hybridization, and mass spectrometry were performed to determine the correlation of HER2 status with uptake values measured on PET. If relevant preexisting [^{18}F]FDG PET/CT images were available (performed as standard of care), a comparison was made. **Results:** With a repeatability coefficient of 21.8%, this imaging technique was repeatable. No clear correlation between PET/CT uptake values and pathology could be established, as even patients with low levels of HER2 expression showed moderate to high uptake. Comparison with [^{18}F]FDG PET/CT in 16 patients demonstrated that in 7 patients, [^{68}Ga]Ga-NOTA-anti-HER2 shows interlesional heterogeneity within the same patient, and [^{18}F]FDG uptake did not show the same heterogeneous uptake in all patients. In some patients, the extent of disease was clearer with the [^{68}Ga]Ga-NOTA-anti-HER2-sdAb. Sixteen adverse events were reported but all without a clear relationship to the tracer. Three patients with preexisting ADAs did not show adverse reactions. No new ADAs developed. **Conclusion:** [^{68}Ga]Ga-NOTA-anti-HER2-sdAb PET/CT imaging shows similar repeatability to [^{18}F]FDG. It is safe for clinical use. There is tracer uptake in cancer lesions, even in patients previously determined to be HER2-low or -negative. The tracer shows potential in the assessment of interlesional heterogeneity of HER2 expression. In a subset of patients, [^{68}Ga]Ga-NOTA-anti-HER2-sdAb uptake was seen in lesions with no or low [^{18}F]FDG uptake. These findings support further clinical development of [^{68}Ga]Ga-NOTA-anti-HER2-sdAb as a PET/CT tracer in breast cancer patients.

Key Words: HER2; sdAb; PET/CT; phase II; breast carcinoma

J Nucl Med 2024; 65:178–184
DOI: 10.2967/jnumed.123.266254

Worldwide, the most common cancer in women is breast cancer (*1*). The expression of both hormone receptors and human epidermal growth factor receptor 2 (HER2) is important for prognosis and therapy choices (*2*). Therapies targeting HER2 have been developed over the last 2 decades, including kinase inhibitors, trastuzumab, pertuzumab, and trastuzumab-based antibody–drug conjugates (*3*). Receptor expression and genome status are predictive biomarkers for these therapies; in HER2-positive breast carcinoma patients, these therapies improve the overall survival (*4–6*). Following the guidelines of the American Society of Clinical Oncology and College of American Pathologists, HER2-positive patients were defined as those with an immunohistochemistry score of 3+ or those with an immunohistochemistry score of 2+ but a positive score on in situ hybridization (ISH). In recent years, a new category emerged, termed *HER2-low* (1+ and 2+ with negative ISH), as these patients also benefit from the second-generation antibody–drug conjugates trastuzumab–deruxtecan (*7*). This makes the correct assessment of HER2 expression levels and the identification of such HER2-low disease even more important, as the detection of low levels of HER2 expression could be key for selecting the right drug for the right patient (*5,7*).

HER2 status is determined by immunohistochemistry or ISH on biopsy specimens (*8*). Biopsies are invasive but allow the assessment of many required molecular parameters, albeit in only

---

Received Jul. 5, 2023; revision accepted Nov. 3, 2023.

For correspondence or reprints, contact Odrade Gondry (odrade.gondry@uzbrussel.be) or Marleen Keyaerts (marleen.keyaerts@vub.be).

a small fragment of the disease present in the patient. With increasing data confirming the heterogeneous expression of HER2 within and between cancer lesions, whole-body assessment may circumvent the need for multiple biopsies (*5,9,10*).

Several targeting molecules can be used as imaging tracers: monoclonal antibodies and their fragments, peptides, protein scaffolds, and others (*11–13*). Each has its own specific pharmacokinetic characteristics, which influences the choice of radionuclide (*14*). A single-domain antibody (sdAb) targeting HER2 (2Rs15D) has been developed (*15,16*). The sdAbs are small (12–15 kDa); they have high stability, a nanomolar affinity, and low immunogenicity (*17,18*). Radiolabeled sdAbs target their antigen rapidly and are eliminated by the kidneys. This implies that they can be labeled with short-lived radionuclides such as ^{68}Ga or ^{18}F, reducing the radioactive dose to the patient in comparison with the longer-lived radionuclides needed for radiolabeling of monoclonal antibodies. Therefore, these sdAbs allow for same-day imaging, making them ideal probes for molecular imaging.

A phase I study confirmed that [^{68}Ga]Ga-NOTA-anti-HER2-sdAb PET/CT is a safe procedure with a radiation dose similar to that of other short-lived PET/CT tracers. The tracer accumulates in HER2-positive metastases, with optimal image quality at 90 min after injection (*15*).

The phase II trial reported here aimed to evaluate the repeatability of [^{68}Ga]Ga-NOTA-anti-HER2-sdAb uptake in breast carcinoma patients (*19*). Additionally, tracer uptake was correlated with HER2 expression in tissues, if available, and safety and immunogenicity data for the investigational medicine were evaluated beyond phase I (*17,20*). Furthermore, if [^{18}F]FDG PET/CT images were available, a retrospective comparison was made.

MATERIALS AND METHODS

Complete materials and methods can be found in the supplemental material (available at http://jnm.snmjournals.org) (*15,21–23*). The protocol of this prospective open-label phase II study (EudraCT 2016-002164-13) was approved by the Belgian Federal Agency for Medicines and Health Products, the local ethics committee, and the Federal Agency for Nuclear Control. The study was performed in accordance with the declaration of Helsinki and the International Conference on Harmonization Guidelines for Good Clinical Practice. Informed consent was obtained from all subjects at inclusion. Twenty women with locally advanced or metastatic breast carcinoma (5 HER2-positive and 15 HER2-negative patients) were included between April 15, 2019, and January 12, 2021.

To assess the repeatability of this technique, patients were injected intravenously twice with [^{68}Ga]Ga-NOTA-anti-HER2-sdAb with a maximal interval of 8 d and a minimal interval of 18 h, with each injection followed by a PET/CT scan after 90 min. The SUV_{peak} in selected tumor lesions (minimum diameter, 12 mm; maximum of 2 lesions per organ system and 5 per patient) and SUV_{mean} in the liver and in the left ventricle were assessed after both scans by a central reviewer. Bland–Altmann plots and calculations of the repeatability coefficient and the mean absolute percentage difference (Supplemental Table 1) were performed as described by Lodge et al. (*19*).

To correlate uptake values and HER2 expression within lesions, patients were given the option of undergoing a biopsy, the location of which was chosen on the basis of the SUV and feasibility. In patients who declined biopsy, other relevant tissues that were obtained as the standard of care were used if available. Immunohistochemistry analysis and ISH on the tissues were assessed in-house and reassessed elsewhere (Anapath Services). Mass spectrometry for HER2 quantification was performed by mProbe (*24*). Blood samples were taken to assess circulating free DNA and RNA for the presence of the HER2 gene or its transcript.

For the exploratory endpoint of interlesion heterogeneity in tracer uptake, the number of patients in the first PET/CT scan with differences in SUV_{peak} above an arbitrary threshold of 3 g/mL is reported. As no comparison at the histologic level was available, a comparison with [^{18}F]FDG uptake was made in a subset of patients to evaluate if the observed difference could be purely related to partial-volume effects. Patients in whom the interlesional difference of 3 g/mL was not in line with at least a similar 50% difference in [^{18}F]FDG were considered to have a potential interlesional heterogeneity.

[^{18}F]FDG PET/CT, performed as the standard of care within 8 wk from [^{68}Ga]Ga-NOTA-anti-HER2-sdAb PET/CT, was available for 16 patients and used for comparison.

Adverse events (AEs) were documented, and blood samples were collected before each scan and 60–365 d after the last scan to determine the presence of antidrug antibodies (ADAs). To exclude false-positive ADA results induced by the presence of the HER2 protein in the serum sample, the latter was evaluated.

RESULTS

Patient Characteristics

Twenty adult women (mean age, 58.6 y) were included (5 HER2-positive and 15 HER2-negative patients). Table 1 summarizes the patient characteristics.

Patients were injected intravenously with 121.3 ± 15.7 MBq (50.2 ± 13.9 μg) of [^{68}Ga]Ga-NOTA-anti-HER2-sdAb (range, 98.3–153.0 MBq) for the first PET/CT scan and 126.1 ± 16.9 MBq (45.3 ± 7.6 μg) of [^{68}Ga]Ga-NOTA-anti-HER2-sdAb (range, 104.3–166.9 MBq) for the second PET/CT scan. Three of 20 patients were scanned only once because of withdrawal of consent ($n = 2$) or because of the severe acute respiratory syndrome coronavirus 2 pandemic ($n = 1$). In 18 of 20 patients, active metastatic disease was confirmed, either by biopsy or, in the absence of biopsy, by patient follow-up using medical imaging data or clinical examination in the case of skin metastases. In patients 13 and 17, the suggestive lesions were finally diagnosed as a relapse of tuberculosis (Supplemental Fig. 1) and lung atelectasis (Supplemental Fig. 2), respectively, rather than breast carcinoma.

Tracer Biodistribution and Uptake in Normal Tissues

Figure 1 shows 2 HER2-negative patients who were injected twice with [^{68}Ga]Ga-NOTA-anti-HER2-sdAb. The main uptake in the kidneys, liver, and intestines was in line with the results of the phase I trial (*15*). For all 20 patients, the SUV_{mean} in healthy liver tissue was 11.7 ± 4.6 g/mL (range, 2.6–19.9 g/mL). In the left ventricle, with an approximation of blood-pool activity, the SUV_{mean} was 1.4 ± 0.2 g/mL (range, 0.9–2.0 g/mL).

Tracer Uptake in Tumor Lesions and Repeatability Assessment

For each patient with cancer lesions ($n = 18$), the mean SUV_{peak} for selected lesions, as well as the maximal and minimal SUV_{peak} among the lesions, is presented in Table 2. Tracer uptake in cancer lesions ranged from an SUV_{peak} of 1.5 g/mL, which is close to blood-pool activity, to an SUV_{peak} of 18.0 g/mL. Uptake could be evaluated in 5 liver lesions in 3 patients, all with HER2-negative disease. Here, lesional uptake tended to be lower than in the surrounding liver tissue with an SUV_{peak} of 3.9 ± 2.4 g/mL (range, 1.6–7.2 g/mL), as measured on the first PET/CT scan.

In total, 39 lesions in 16 patients were included in the repeatability analysis. The mean time interval between scans was 4.2 ± 1.4 d

TABLE 1
Patient Characteristics and Lesional Uptake Values

Patient	Age (y)	HER2 status at inclusion (IHC)	Type	ER/PR at inclusion	Optional biopsy	Mean SUV_{peak} (PET1/PET2)	Lowest SUV_{peak} (PET1/PET2)	Highest SUV_{peak} (PET1/PET2)
1	62	p (3+)	Ductal	n/n	No	2.7/2.4	1.7/1.6[*]	3.7/3.2[*]
2	81	n (0)	Ductal	p/p	No	5.4/4.9	2.2/2.3[†]	11.6/9.9[‡]
3	50	p (3+)	Ductal	p/p	No	6.6/6.1	5.2/4.5[§]	8.0/7.6[‖]
4	70	n (1+)	Ductal	p/n	Yes	8.3/8.4	6.4/6.2[¶]	10.2/10.6[¶]
5	72	n (1+)	Ductal	p/p	No	6.4/7.0	5.6[#]	7.2[#]
6	63	n (0)	Lobular	p/p	Yes	5.3/5.6	2.9/3.4[†]	7.6/7.7[‡]
7	75	n (0)	Lobular	p/p	No	9.2[*]	—	—
8	37	n (2+)	Ductal	p/p	No	7.3/7.4	5.4/5.3[*]	10.7/11.4[¶]
9	53	n (1+)	Lobular	p/p	Yes	5.1/5.3	2.4/2.4[¶]	7.8/8.2[¶]
10	73	n (2+)	Ductal	p/p	No	1.8/1.8	1.6/1.5[*]	1.8/2.0[¶]
11	58	n (1+)	Ductal	n/n	No	2.6/2.5	2.4/2.2[†]	2.7/2.6[#]
12	62	n (1+)	Ductal	p/p	No	8.3/7.7	8.0/7.5[¶]	8.6/7.8[¶]
13	33	p (3+)	Ductal	p/n	Yes	—	—	—
14	65	n (2+)	Ductal	p/p	Yes	12.9/11.6	7.7/7.2[¶]	18.0/16.0[¶]
15	51	n (1+)	Ductal	p/p	No	3.5/3.3	3.1/2.7[¶]	3.9/4.0[¶]
16	46	n (1+)	Ductal	p/p	Yes	4.3[¶]	—	—
17	56	p (3+)	Ductal	n/n	Yes	—	—	—
18	57	p (3+)	Ductal	n/n	Yes	4.4[‡]	—	—
19	62	n (2+)	Ductal	n/n	No	5.3/5.8	3.5/3.8[‖]	8.8/9.3[‡]
20	46	n (2+)	Ductal	p/n	No	2.0/1.7	1.6/1.3[#]	2.4/2.2[#]

---

[*] Lung.
[†] Primary breast.
[‡] Lymph node.
[§] Thoracic wall.
[‖] Breast (not primary lesion).
[¶] Bone.
[#] Liver.

IHC = immunohistochemistry; ER = estrogen receptor; PR = progesterone receptor; PET1 = first PET/CT scan; PET2 = second PET/CT scan; p = positive; n = negative.

In patients in whom only 1 lesion was assessed, values of lesions are described. Data for lesions of patient 13 and patient 17 are not included as relevant lesion was nonmalignant.

(range, 1–7 d). Lesions were located in the breasts ($n = 8$), lungs ($n = 6$), bones ($n = 14$), liver ($n = 4$), lymph nodes ($n = 5$), or elsewhere ($n = 2$). Figure 1 shows that the images were comparable visually. The distribution of the relative differences was normal, which allowed analysis via the Bland–Altman plot shown in Figure 2. The repeatability coefficient of the SUV_{peak} was 21.8%, and the mean absolute percentage difference was 9.2%.

HER2 Assessment on Tissue Samples and Liquid Biopsies

Table 2 provides an overview of histopathologic data, from both previously obtained and contemporary biopsies, and allows head-to-head comparison with tracer uptake values of [^{68}Ga]Ga-NOTA-anti-HER2-sdAb in lesions with contemporary biopsy results. Eight patients consented to a study-specific but optional biopsy. Eight patients had biopsies performed as the standard of care within 4 wk from the first PET/CT scan, enabling a relevant comparison in a total of 16 patients.

Remarkably, 2 of 15 patients with HER2-negative disease, in whom a biopsy of a lesion with high tracer uptake was performed, were recategorized as HER2-positive on the basis of a positive HER2 ISH score in combination with an immunohistochemistry result of at least 2+ (patients 4 and 10). In 3 patients with the highest lesional SUV_{peak} (>10 g/mL), 2 had an immunohistochemical score of 2+, but with a negative ISH result, therefore categorizing them as HER2-negative, whereas the remaining patient was HER2-positive. On the other hand, in lesions with an SUV_{peak} below 10 g/mL, immunohistochemistry scores ranged from 0 to 3+, without any correlation between SUV_{peak} and immunohistochemistry results (Table 2). Because of insufficient tissue, few mass spectrometry data were available (Supplemental Table 2). Assessment of circulating free DNA (Supplemental Table 3) for the presence of the HER2 gene could not confirm any positive status.

Heterogeneity

In 16 patients, more than 1 lesion was assessed for tracer uptake, and these data were used to study the secondary study

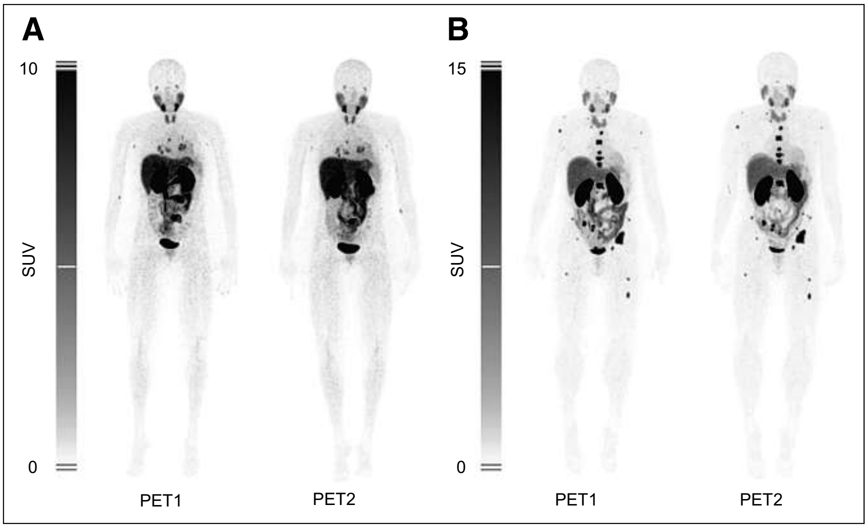

FIGURE 1. Patient 8 (A) and patient 14 (B) are both HER2-negative patients. In both patients, similar physiologic uptake in liver, kidneys, intestines, bladder, and salivary glands can be seen. Not only physiologic biodistribution but also uptake in lesions is similar between first PET/CT scan (PET1) and second PET/CT scan (PET2). In patient 8 (A), tracer uptake in lung metastases and metastases in mediastinal lymph nodes is visible. In patient 14 (B), tracer uptake in diffuse bone metastases is present.

objective of interlesional heterogeneity in tracer uptake. In 7 of these patients, the difference in the SUV_{peak} between lesions was larger than 3 g/mL (Table 1; Supplemental Table 4). Patient 8 and patient 4 are presented in Figure 3 and in Supplemental Figure 3, respectively.

Comparison with $[^{18}F]FDG$

In 16 patients, $[^{18}F]FDG$ PET/CT, performed within 8 wk of the first PET/CT scan, was available for comparison. In 8 patients, lesional uptake with $[^{68}Ga]$Ga-NOTA-anti-HER2-sdAb PET/CT could be seen in CT-graphic lesions that were not $[^{18}F]FDG$-avid: in patients 2, 3, 12, and 19 (Supplemental Fig. 4), the $[^{68}Ga]$Ga-NOTA-anti-HER2-sdAb PET/CT image showed additional adenopathies; in patients 4, 6, 7, and 14, additional bone metastases were revealed (Fig. 4). Two patients with suggestive $[^{18}F]FDG$ uptake in ultimately noncancerous lesions did not show HER2 tracer uptake above the blood-pool activity in these lesions (patient 14, inflammation around breast prosthesis; patient 13, tuberculosis) (Supplemental Fig. 1).

Extended Safety Assessment

Sixteen AEs were documented and are described in Supplemental Table 5. Six AEs were reported as possibly related to $[^{68}Ga]$Ga-NOTA-anti-HER2-sdAb; they were of mild intensity, and the patients recovered spontaneously. In retrospect, no clear relationship between these AEs and $[^{68}Ga]$Ga-NOTA-anti-HER2-sdAb could be determined.

ADAs were detected in the serum of 3 patients, with titers ranging from 1:2 (patient 9) and 1:8 (patient 2) to 1:512 (patient 1).

TABLE 2

Correlation Between Tissue and Images for Individual Lesions with Contemporary Biopsy

Patient	HER2 status at inclusion	IHC/ISH at inclusion	IHC (UZB/APS)	ISH (UZB/APS)	SUV_{peak} (PET1/PET2)
2	n	0/*	0/0	—/p	2.2/2.3
			0/0	—/n	11.6/9.9
4	n	1+/*	2+/1+	p/p	6.4/6.2
5	n	1+/n	1+/1+	n/p	7.2/7.0
6	n	0/*	0/2+	n/—	7.6/7.7
7	n	0/*	0/0	n/n	9.2/†
8	n	2+/n	2+/3+	n/n	10.7/11.4
9	n	1+/*	1+/—	n/n	7.8/8.2
10	n	2+/n	2+/—	n/p	1.4/1.4
11	n	1+/*	0/—	—/—	2.7/2.6
		1+/*	1+/—	—/—	2.4/2.2
12	n	1+/*	1+/—	—/—	8.6/7.8
14	n	2+/n	2+/—	—/—	18.0/16.0
15	n	1+/n	0/—	—/—	3.9/4.0
16	n	1+/*	2+/2+	—/—	5.7/†
18	p	3+/*	3+/—	p/—	4.4/†
19	n	2+/n	2+/—	n/—	3.5/3.8

*Not determined in clinical routine.

†No second PET/CT scan was performed.

IHC = immunohistochemistry; UZB = Universitair Ziekenhuis Brussel; APS = Anapath Services; n = negative; p = positive; — = data not available; PET1 = first PET/CT scan; PET2 = second PET/CT scan.

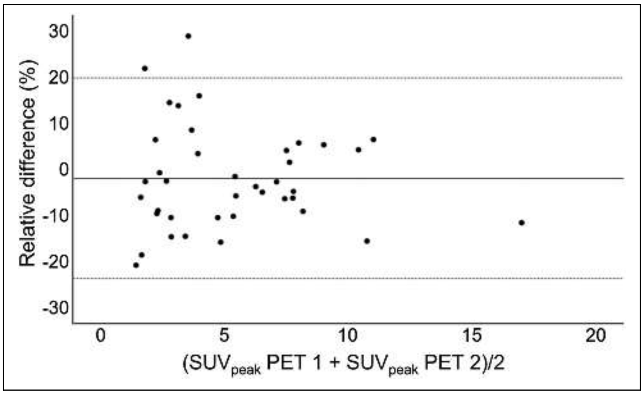

FIGURE 2. Bland–Altman plot showing SUV_{peak} difference data in relative units as function of mean. Gray dotted lines show 95% CI. PET 1 = first PET/CT scan; PET 2 = second PET/CT scan.

All 3 patients had preexisting ADAs, but no rise in the titers was observed after tracer injection. Patient 1, a HER2-positive patient, had unexpectedly low tracer uptake in metastatic lesions, but contemporary tissue analysis was not able to assess if this could be due to the loss of HER2 expression over the course of the disease or the presence of preexisting ADAs.

In patients with preexisting ADAs, the presence of circulating HER2 protein in the blood was excluded as a possible cause of false positivity. No related AEs were documented in these patients.

None of the patients without ADAs before injection developed ADAs afterward.

DISCUSSION

The classification of patients according to HER2 status is based on immunohistochemistry analysis and ISH results. The problem of accurate HER2-status assessment, however, is compounded by the dynamics of receptor expression during the disease course and by expression heterogeneity (*25*). This may lead to sampling errors. Even with a current standard ERBB2 immunohistochemistry assay and following the American Society of Clinical Oncology and College of American Pathologists score, which allows different expression levels to be distinguished, the scoring accuracy in the low range (0 vs. 1+) is poor (*26,27*). These inaccuracies might entail giving a treatment with possible AEs to patients who will not benefit or denying patients a potentially efficacious treatment. That is why other techniques to assess the HER2 status are currently being developed using compounds ranging from mass spectrometry to molecular imaging (*28–30*).

The present prospective phase II study on [^{68}Ga]Ga-NOTA-anti-HER2-sdAb PET/CT confirmed the overall biodistribution previously observed in the phase I trial (*15*), that is, normal uptake in the kidneys, liver, and intestines (*16*).

Evaluation of the repeatability of the SUV_{peak} in tumor lesions in 16 patients resulted in a repeatability coefficient of 22.8%. This is in line with repeatability coefficients reported for [^{18}F]FDG SUV_{peak}, ranging between 16% and 37%, as well as with those reported for ^{68}Ga-PSMA-HBED-CC SUV_{peak} (repeatability coefficient, 33%–38%) or for [^{68}Ga]GaABY-025 (a HER2-targeting Affibody [Affibody AB]) SUV_{max} (repeatability coefficient, 18%) (*19,31,32*). Our data thus demonstrate a high repeatability of [^{68}Ga]Ga-NOTA-anti-HER2-sdAb, justifying its future quantitative use in patients.

Differences between local and central immunohistochemistry results were observed (patients 4, 6, and 8 in Table 2), in keeping with the reported lower accuracy of immunohistochemistry results in the lower range (*26*).

Overall, tracer uptake above background is seen in many patients with classic HER2-negative disease, mainly in HER2-low disease but also in some cases of HER2-null disease. We hypothesize that tracer uptake in HER2-null disease might reflect cases of HER2-ultralow disease that could be detected by this sensitive imaging tracer (*33*). However, it remains to be investigated in further clinical trials whether [^{68}Ga]Ga-NOTA-anti-HER2-sdAb PET/CT imaging could outperform immunohistochemistry and ISH analyses as a method to predict treatment outcome in HER2-low breast cancer patients.

Differences were noted between the immunohistochemistry results at inclusion and at concurrent biopsies, regardless of HER2 status (Table 2). In patient 4 (HER2-negative disease at inclusion), the study-specific biopsy, performed in a lesion with high tracer uptake, yielded an immunohistochemistry score of 2+, with HER2 amplification assessed on ISH, recategorizing this patient as HER2-positive and resulting in the subsequent change to HER2-targeted treatment. This image-guided biopsy therefore had a therapeutic impact in this patient.

In 7 of 16 patients, differences in SUVs of more than 3 g/mL were found between lesions, which points at interlesional heterogeneity in tracer uptake within the same patient. It remains to be further investigated if this also correlates with heterogeneity in HER2 expression. Nevertheless, these findings already suggest a possible role for [^{68}Ga]Ga-NOTA-anti-HER2-sdAb PET/CT to assess heterogeneity and to follow the dynamics of HER2 expression in the course of the disease. Tumor heterogeneity has been suggested as an explanation for the development of resistance to anti-HER2 therapies in breast carcinoma patients and might be the cause of a so-called mixed response to HER2-targeted therapy (*34*).

The imaging data of 16 patients were compared with routinely obtained [^{18}F]FDG PET/CT images. In 3 of these patients, the earlier reported differences in [^{68}Ga]Ga-NOTA-anti-HER2-sdAb uptake, which point at interlesional heterogeneity, were not found in [^{18}F]FDG uptake of those same lesions, confirming that such differences are more likely due to heterogeneous expression of HER2 rather than other effects such as partial volume. In 2 patients, no uptake of [^{68}Ga]Ga-NOTA-anti-HER2-sdAb

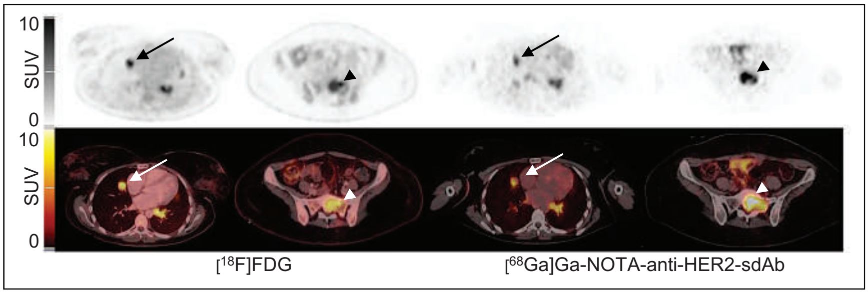

FIGURE 3. Patient 8 had bone (arrowhead), liver, and lung (arrow) metastases. SUV_{peak} with [^{18}F]FDG in bone lesion (arrowhead) and in lung lesion (arrow) was 7.8 and 7.9, respectively. With [^{68}Ga]Ga-NOTA-anti-HER2-sdAb, SUV_{peak} was 10.7 and 5.6, respectively, indicating difference in uptake that was not seen with [^{18}F]FDG.

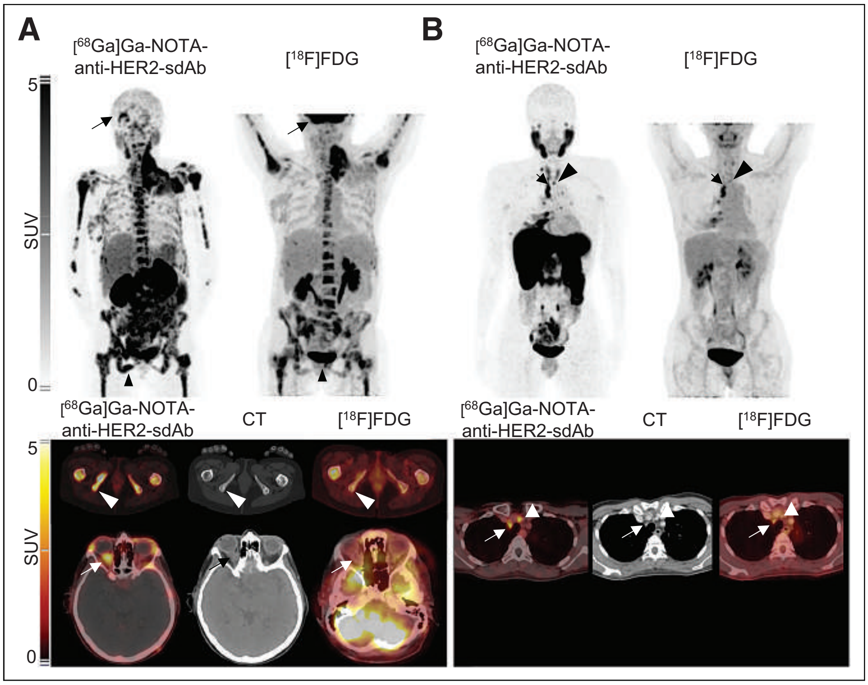

FIGURE 4. For patient 6 (A) and patient 3 (B), [^{18}F]FDG (top right) and [^{68}Ga]Ga-NOTA-anti-HER2-sdAb (top left) maximum-intensity projection PET images and additional axial CT (bottom center) and PET/CT (bottom left and right) images. Patient 6 was HER2-negative patient with bone metastases, with mass in neck and recent right exophthalmia. In [^{68}Ga]Ga-NOTA-anti-HER2-sdAb image, uptake in these regions was confirmed, but metastatic lesions in os ischium (arrowhead) and right orbita (arrow) were better identified than on [^{18}F]FDG. Patient 3 was HER2-positive patient with [^{18}F]FDG-avid lymph nodes in mediastinum. Extent of disease to cervical lymph node (arrow) was better delineated on [^{68}Ga]Ga-NOTA-anti-HER2-sdAb PET.

PET/CT was found in lesions that took up [^{18}F]FDG, but these lesions were finally confirmed to be inflammatory lesions, suggesting a higher specificity for [^{68}Ga]Ga-NOTA-anti-HER2-sdAb than for [^{18}F]FDG. In addition, [^{68}Ga]Ga-NOTA-anti-HER2-sdAb showed improved detection of cancer lesions in 8 patients. Although [^{18}F]FDG has a good detection potential in highly proliferative breast tumors, such as triple-negative and HER2-positive tumors, it might not be as sensitive in tumors with low proliferation and low metabolic activity. As [^{68}Ga]Ga-NOTA-anti-HER2-sdAb uptake is seen even in lesions with a low immunohistochemistry score, this tracer might help to assess the disease extent in breast carcinoma with lower [^{18}F]FDG avidity.

In comparison with [^{18}F]FDG, [^{68}Ga]Ga-NOTA-anti-HER2-sdAb showed uptake in lesions that were not found in 9 of 16 patients with [^{18}F]FDG, suggesting a complementary value of both tracers, of which the clinical value remains to be determined in future trials. Other tracers relevant for breast carcinoma have been investigated for their ability to assess the extent of disease in breast carcinoma patients as well. [^{68}Ga]GaABY-025, a HER2-targeting Affibody tracer, has been reported to be superior to [^{18}F]FDG in a murine model (*35*).

In general, sdAbs are suggested to have a low immunogenicity risk profile (*36*). The extended safety assessment could not identify patients who developed ADAs after tracer injection and confirmed the low incidence of low-level preexisting ADAs without clinical safety concerns, as was also concluded by Ackaert et al. on the basis of the phase I study data of this compound (*17*).

Other small proteins targeting the HER2 that have advanced into clinical trials include Affibody molecules. Their biodistribution is similar to that of the sdAbs described here. [^{68}Ga]GaABY-025 PET/CT had a more dichotomous distribution of SUVs in the first trial, because it could determine a threshold to distinguish HER2-positive from HER2-negative lesions (*32*). However, this threshold was not confirmed in a more recent trial, and their results showed a lack of correlation of [^{68}Ga]GaABY-025 with immunohistochemistry data, similar to our current findings. [^{68}Ga]GaABY-025 uptake did, however, predict metabolic response to HER2-targeted therapy in patients with metastatic breast carcinoma with 56% sensitivity and 66% specificity (*37*). [^{89}Zr]Zr-trastuzumab PET/CT is able to distinguish HER2-positive from HER2-negative disease but suffers from the tracer's long biologic half-life, necessitating scanning after several days (*38*).

The clinical potential of [^{68}Ga]Ga-NOTA-anti-HER2-sdAb in other HER2-expressing tumor types is currently being assessed in another cohort of this phase II trial (EudraCT 2016-002164-13). An advantage of [^{68}Ga]Ga-NOTA-anti-HER2-sdAb PET/CT might be its high sensitivity, with the potential to better discriminate the level of HER2 expression in a lower range than immunohistochemistry.

CONCLUSION

[^{68}Ga]Ga-NOTA-anti-HER2-sdAb PET/CT shows similar repeatability to that of [^{18}F]FDG. It is safe for clinical use. It can detect HER2-expressing lesions, even in patients previously determined to be HER2-low or -negative. The tracer shows potential in the assessment of interlesional heterogeneity of HER2 expression. [^{68}Ga]Ga-NOTA-anti-HER2-sdAb showed more sensitive and more specific determination of disease extent than did [^{18}F]FDG in a subset of the investigated patients. Together with the ability to acquire images 90 min after injection, these findings support further clinical development of [^{68}Ga]Ga-NOTA-anti-HER2-sdAb as a PET/CT tracer in breast cancer patients.

DISCLOSURE

This project was funded by Kom op tegen Kanker (Stand Up to Cancer), the Flemish Cancer Society, and by IWT TBM (IWT150198). Odrade Gondry received an Emmanuel Van der Schueren grant funded by Kom op tegen Kanker (Stand Up to Cancer), the Flemish Cancer Society. Nick Devoogdt and Tony Lahoutte are shareholders and consultants for Precirix. Nick Devoogdt, Tony Lahoutte, and Marleen Keyaerts are shareholders and consultants for Abscint NV/SA, which has licensed a patent on the diagnostic HER2-sdAb tracer described in this study. Sheeno Thyparambil works for mProbe. Catarina Xavier, Nick Devoogdt, Tony Lahoutte, and Marleen Keyaerts hold patents related to sdAb imaging and therapy. Tony Lahoutte and Marleen

Keyaerts have an FWO clinical mandate. No other potential conflict of interest relevant to this article was reported.

ACKNOWLEDGMENT

We express our gratitude to Yasmine De Maeyer for all her logistic work and data management; Gratienne Van Holsbeeck, Sonja Van Den Block, Martine Van den Broeck, and Steffi De Triff for the radiotracer preparations; Janik Puttemans for the graphical abstract; the Central Biobank UZ Brussel for the processing and storage of blood samples; nurses Wendy Kemps, Nadine Eersels, Carl Van Halewijn, Nele Risch, Cedric Roels, Petra Aalders, Brecht Segers, Kathleen Op Debeeck, and Tjibbe De Haan for study patient caretaking; and Annie Van Broekhoven, Marc Peeters, Bart Dehaes, and Mia Callens for their guidance in the advisory committee.

KEY POINTS

QUESTION: The aim of this trial is to assess the repeatability, the safety, and the clinical potential of [^{68}Ga]Ga-NOTA-anti-HER2-sdAb PET/CT as an imaging technique in breast carcinoma.

PERTINENT FINDINGS: This phase II clinical trial indicates that the technique is safe and repeatable and warrants further investigation into its clinical potential, especially in HER2-low patients.

IMPLICATIONS FOR PATIENT CARE: This technique allows us to assess the presence of HER2 overexpression in a sensitive way throughout the whole body, helping to identify patients eligible for new HER2-targeting therapies.

REFERENCES

1. Sung H, Ferlay J, Siegel RL, et al. Global cancer statistics 2020: GLOBOCAN estimates of incidence and mortality worldwide for 36 cancers in 185 countries. *CA Cancer J Clin.* 2021;71:209–249.
2. Slamon DJ, Leyland-Jones B, Shak S, et al. Use of chemotherapy plus a monoclonal antibody against HER2 for metastatic breast cancer that overexpresses HER2. *N Engl J Med.* 2001;344:783–792.
3. Tarantino P, Carmagnani Pestana R, Corti C, et al. Antibody-drug conjugates: smart chemotherapy delivery across tumor histologies. *CA Cancer J Clin.* 2022;72: 165–182.
4. Kunte S, Abraham J, Montero AJ. Novel HER2-targeted therapies for HER2-positive metastatic breast cancer. *Cancer.* 2020;126:4278–4288.
5. Ferraro E, Drago JZ, Modi S. Implementing antibody-drug conjugates (ADCs) in HER2-positive breast cancer: state of the art and future directions. *Breast Cancer Res.* 2021;23:84.
6. Seshadri R, Firgaira FA, Horsfall DJ, McCaul K, Setlur V, Kitchen P. Clinical significance of HER-2/neu oncogene amplification in primary breast cancer. The South Australian Breast Cancer Study Group. *J Clin Oncol.* 1993;11:1936–1942.
7. Modi S, Jacot W, Yamashita T, et al. Trastuzumab deruxtecan in previously treated HER2-low advanced breast cancer. *N Engl J Med.* 2022;387:9–20.
8. Wolff AC, Hammond MEH, Allison KH, et al. Human epidermal growth factor receptor 2 testing in breast cancer: American Society of Clinical Oncology/College of American Pathologists clinical practice guideline focused update. *J Clin Oncol.* 2018;36:2105–2122.
9. Hamilton E, Shastry M, Shiller SM, Ren R. Targeting HER2 heterogeneity in breast cancer. *Cancer Treat Rev.* 2021;100:102286.
10. Seban R-D, Champion L, Bellesoeur A, Vincent-Salomon A, Bidard FC. Clinical potential of HER2 PET as a predictive biomarker to guide the use of trastuzumab deruxtecan in breast cancer patients. *J Nucl Med.* 2023;64:1164–1165.
11. Capala J, Bouchelouche K. Molecular imaging of HER2-positive breast cancer: a step toward an individualized 'image and treat' strategy. *Curr Opin Oncol.* 2010; 22:559–566.
12. Perik PJ, Lub-De Hooge MN, Gietema JA, et al. Indium-111-labeled trastuzumab scintigraphy in patients with human epidermal growth factor receptor 2-positive metastatic breast cancer. *J Clin Oncol.* 2006;24:2276–2282.
13. Altunay B, Morgenroth A, Beheshti M, et al. HER2-directed antibodies, affibodies and nanobodies as drug-delivery vehicles in breast cancer with a specific focus on radioimmunotherapy and radioimmunoimaging. *Eur J Nucl Med Mol Imaging.* 2021;48:1371–1389.
14. Lub-de Hooge MN, Kosterink JG, Perik PJ, et al. Preclinical characterisation of ^{111}In-DTPA-trastuzumab. *Br J Pharmacol.* 2004;143:99–106.
15. Keyaerts M, Xavier C, Heemskerk J, et al. Phase I study of ^{68}Ga-HER2-nanobody for PET/CT assessment of HER2 expression in breast carcinoma. *J Nucl Med.* 2016;57:27–33.
16. Xavier C, Vaneycken I, D'huyvetter M, et al. Synthesis, preclinical validation, dosimetry, and toxicity of ^{68}Ga-NOTA-anti-HER2 nanobodies for iPET imaging of HER2 receptor expression in cancer. *J Nucl Med.* 2013;54:776–784.
17. Ackaert C, Smiejkowska N, Xavier C, et al. Immunogenicity risk profile of nanobodies. *Front Immunol.* 2021;12:632687.
18. Muyldermans S, Atarhouch T, Saldanha J, Barbosa JA, Hamers R. Sequence and structure of VH domain from naturally occurring camel heavy chain immunoglobulins lacking light chains. *Protein Eng.* 1994;7:1129–1135.
19. Lodge MA. Repeatability of SUV in oncologic ^{18}F-FDG PET. *J Nucl Med.* 2017; 58:523–532.
20. Mire-Sluis AR, Barrett YC, Devanarayan V, et al. Recommendations for the design and optimization of immunoassays used in the detection of host antibodies against biotechnology products. *J Immunol Methods.* 2004;289:1–16.
21. Vaneycken I, Devoogdt N, Van Gassen N, et al. Preclinical screening of anti-HER2 nanobodies for molecular imaging of breast cancer. *FASEB J.* 2011;25: 2433–2446.
22. Xavier C, Blykers A, Laoui D, et al. Clinical translation of [^{68}Ga]Ga-NOTA-anti-MMR-sdAb for PET/CT imaging of protumorigenic macrophages. *Mol Imaging Biol.* 2019;21:898–906.
23. Nuciforo P, Thyparambil S, Aura C, et al. Quantitative measurement of HER2 levels by multiplexed mass spectrometry from FFPE tissue predicts survival in patients treated with anti-HER2 based therapy [abstract]. *Cancer Res.* 2015;75(suppl): P4-11-29.
24. De Angelis C, Nagi C, Hoyt CC, et al. Evaluation of the predictive role of tumor immune infiltrate in patients with HER2-positive breast cancer treated with neoadjuvant anti-HER2 therapy without chemotherapy. *Clin Cancer Res.* 2020;26:738–745.
25. Miglietta F, Griguolo G, Bottosso M, et al. Evolution of HER2-low expression from primary to recurrent breast cancer. *NPJ Breast Cancer.* 2021;7:137.
26. Fernandez AI, Liu M, Bellizzi A, et al. Examination of low ERBB2 protein expression in breast cancer tissue. *JAMA Oncol.* 2022;8:1–4.
27. Roulot A, Héquet D, Guinebretière JM, et al. Tumoral heterogeneity of breast cancer. *Ann Biol Clin (Paris).* 2016;74:653–660.
28. Gebhart G, Lamberts LE, Wimana Z, et al. Molecular imaging as a tool to investigate heterogeneity of advanced HER2-positive breast cancer and to predict patient outcome under trastuzumab emtansine (T-DM1): the ZEPHIR trial. *Ann Oncol.* 2016;27:619–624.
29. Gebhart G, Flamen P, De Vries EG, Jhaveri K, Wimana Z. Imaging diagnostic and therapeutic targets: human epidermal growth factor receptor 2. *J Nucl Med.* 2016; 57(suppl 1):81S–88S.
30. Moutafi M, Robbins CJ, Yaghoobi V, et al. Quantitative measurement of HER2 expression to subclassify ERBB2 unamplified breast cancer. *Lab Invest.* 2022;102: 1101–1108.
31. Pollard JH, Raman C, Zakharia Y, et al. Quantitative test–retest measurement of ^{68}Ga-PSMA-HBED-CC in tumor and normal tissue. *J Nucl Med.* 2020;61: 1145–1152.
32. Sörensen J, Velikyan I, Sandberg D, et al. Measuring HER2-receptor expression in metastatic breast cancer using [^{68}Ga]ABY-025 affibody PET/CT. *Theranostics.* 2016;6:262–271.
33. Venetis K, Crimini E, Sajjadi E, et al. HER2 low, ultra-low, and novel complementary biomarkers: expanding the spectrum of HER2 positivity in breast cancer. *Front Mol Biosci.* 2022;9:834651.
34. Ocaña A, Amir E, Pandiella A. HER2 heterogeneity and resistance to anti-HER2 antibody-drug conjugates. *Breast Cancer Res.* 2020;22:15.
35. Kramer-Marek G, Bernardo M, Kiesewetter DO, et al. PET of HER2-positive pulmonary metastases with ^{18}F-Z$_{\text{HER2:342}}$ affibody in a murine model of breast cancer: comparison with ^{18}F-FDG. *J Nucl Med.* 2012;53:939–946.
36. Papadopoulos KP, Isaacs R, Bilic S, et al. Unexpected hepatotoxicity in a phase I study of TAS266, a novel tetravalent agonistic Nanobody® targeting the DR5 receptor. *Cancer Chemother Pharmacol.* 2015;75:887–895.
37. Alhuseinalkhudhur A, Lindman H, Liss P, et al. Human epidermal growth factor receptor 2–targeting [^{68}Ga]Ga-ABY-025 PET/CT predicts early metabolic response in metastatic breast cancer. *J Nucl Med.* 2023;64:1364–1370.
38. Dehdashti F, Wu N, Bose R, et al. Evaluation of [^{89}Zr]trastuzumab-PET/CT in differentiating HER2-positive from HER2-negative breast cancer. *Breast Cancer Res Treat.* 2018;169:523–530.

[^{18}F]FDG PET/CT–Avid Discordant Volume as a Biomarker in Patients with Gastroenteropancreatic Neuroendocrine Neoplasms: A Multicenter Study

David L. Chan[1,2], Aimee R. Hayes[3], Ioannis Karfis[4], Alice Conner[1], Magdalena Mileva[4], Elizabeth Bernard[5], Geoffrey Schembri[5], Shaunak Navalkissoor[3,6], Gopinath Gnanasegaran[3,6], Nick Pavlakis[1,2], Clémentine Marin[4], Bruno Vanderlinden[7], Patrick Flamen[4], Paul Roach[5], Martyn E. Caplin[3], Christos Toumpanakis[3], and Dale L. Bailey[1,5]

[1]Faculty of Medicine and Health, University of Sydney, Sydney, New South Wales, Australia; [2]Medical Oncology, ENETS Centre of Excellence, Royal North Shore Hospital, Sydney, New South Wales, Australia; [3]Neuroendocrine Tumour Unit, ENETS Centre of Excellence, Royal Free Hospital, London, United Kingdom; [4]Nuclear Medicine Department, Institut Jules Bordet, ENETS Centre of Excellence, Hôpital Universitaire de Bruxelles, Université Libre de Bruxelles, Brussels, Belgium; [5]Nuclear Medicine, ENETS Centre of Excellence, Royal North Shore Hospital, Sydney, New South Wales, Australia; [6]Nuclear Medicine, ENETS Centre of Excellence, Royal Free Hospital, London, United Kingdom; and [7]Medical Physics Department, Institut Jules Bordet, ENETS Centre of Excellence, Hôpital Universitaire de Bruxelles, Université Libre de Bruxelles, Brussels, Belgium

---

[^{18}F]FDG PET/CT and [^{68}Ga]Ga-DOTATATE PET/CT are both used to predict tumor biology in neuroendocrine neoplasms. Although the presence of discordant ([^{18}F]FDG-avid/non–[^{68}Ga]Ga-DOTATATE–avid) disease predicts poor prognosis, the significance of the volume of such discordant disease remains undetermined. The aim of this study is to investigate discordant tumor volume as a potential biomarker in patients with advanced gastroenteropancreatic neuroendocrine neoplasms (GEPNENs). **Methods:** A multicenter retrospective study in patients with advanced GEPNENs and paired [^{18}F]FDG and [^{68}Ga]Ga-DOTATATE PET/CT no more than 85 d apart was conducted. Patients with discordant disease were identified by the NET-PET score, and discordant lesions were contoured with a flat [^{18}F]FDG SUV cutoff of 4. The primary variable of interest was the total discordant volume (TDV), which was the sum of the volumes of discordant lesions. Patients were dichotomized into high- and low-TDV cohorts by the median value. The primary endpoint was overall survival. **Results:** In total, 44 patients were included (50% men; median age, 60 y), with primary cancers in the pancreas (45%), small bowel (23%), colon (20%), and other (12%). Of the patients, 5% had grade 1 disease, 48% had grade 2 disease, and 48% had grade 3 disease (24% well differentiated, 67% poorly differentiated, 10% unknown within the grade 3 cohort). The overall median survival was 14.1 mo. Overall survival was longer in the low-TDV cohort than in the high-TDV cohort (median volume, 43.7 cm^3; survival time, 23.8 mo vs. 9.4 mo; hazard ratio, 0.466 [95% CI, 0.229–0.948]; $P = 0.0221$). Patients with no more than 2 discordant intrahepatic lesions survived longer than those with 2 or more lesions (31.8 mo vs. 10.2 mo, respectively; hazard ratio, 0.389 [95% CI, 0.194–0.779]; $P = 0.0049$). **Conclusion:** TDV is a potential prognostic biomarker in GEPNENs and should be investigated in future neuroendocrine neoplasm trials.

Key Words: prognostic biomarker; discordance; [^{18}F]FDG; dual PET; tumor volume

J Nucl Med 2024; 65:185–191
DOI: 10.2967/jnumed.123.266346

Neuroendocrine neoplasms (NENs) are a heterogeneous group of tumors that may produce vasoactive hormones. Although NENs are currently uncommon, recent data show that the incidence and prevalence of NENs are significantly increasing (*1*). Because of the insidious and nebulous symptoms of NENs, many patients present with disease at an advanced stage (*2*) and are treated with systemic therapy without curative intent. Prognostication in these patients is of the utmost importance as it helps patients make difficult life decisions while assisting physicians in the selection of the optimal systemic therapy. Patients with low-grade disease tend to have poor response rates to chemotherapy (*3*) and are instead preferentially treated with somatostatin analogs, targeted therapies, and peptide receptor radionuclide therapy. Conversely, patients with high-grade disease exhibit poor response rates to the aforementioned treatments and are generally treated with chemotherapy (*4*).

Diagnosing a patient with low- or high-grade disease requires histologic analysis of biopsied or resected tissue. However, tissue is often taken from a single lesion, in a disease in which patients commonly have multiple tumor sites (*5*) that are biologically heterogeneous. The use of repeat tissue sampling is limited by the risk of complications, and the lack of tissue from a fine-needle biopsy limits accurate grade determination (*6*). This potentially results in grading misclassification, resulting in suboptimal therapy selection. Finally, the histologic grade alone cannot explain the observed clinical heterogeneity in patients with NENs. Therefore, there is a pressing need for repeatable and ideally noninvasive biomarkers to accurately stratify NEN tumor behavior in vivo.

PET/CT has entered the mainstream clinical practice in NEN imaging. Particularly, the combined interpretation of [^{68}Ga]Ga-DOTATATE PET and [^{18}F]FDG PET (dual PET) is emerging as a highly informative clinical tool in patients with metastatic

---

Received Aug. 17, 2023; revision accepted Oct. 25, 2023.

For correspondence or reprints, contact David L. Chan (david.chan@sydney.edu.au).

gastroenteropancreatic NENs (GEPNENs) (*7*). [^{68}Ga]Ga-DOTATATE PET utilizes somatostatin receptors (particularly subtype 2) as targets, which are overexpressed in well-differentiated and typically low-grade NENs. Accordingly, high [^{68}Ga]Ga-DOTATATE avidity is associated with lower-grade, well-differentiated histology and better prognosis (*8*). [^{18}F]FDG PET avidity reflects glycolysis and hence areas of increased metabolic activity. This avidity is associated with higher-grade, poorly differentiated histology and poorer prognosis (*9*). We previously developed a 5-grade scoring system (known colloquially as the NETPET score) (*10*) to succinctly capture the complexity of dual PET findings to guide prognostication. We demonstrated that patients with [^{68}Ga]Ga-DOTATATE–avid disease only (without any [^{18}F]FDG avidity) have the best prognosis, that those with concordant disease ([^{18}F]FDG avidity corresponding with [^{68}Ga]Ga-DOTATATE avidity) have intermediate prognosis, and that those with any degree of discordant disease have the worst prognosis (*11*). This work suggests that discordant disease may be considered a poor prognostic marker. Although research investigating [^{68}Ga]Ga-DOTATATE PET or [^{18}F]FDG PET as a prognostic biomarker is promising, most studies (including those cited above) have largely concentrated on point measures or SUVs (SUV$_{max}$ and SUV$_{peak}$), without incorporating tumor volume as a separate prognostic biomarker.

Several studies have established the prognostic value of PET-avid tumor volume on [^{18}F]FDG PET and [^{68}Ga]Ga-DOTATATE PET separately (*12–14*). These studies showed that increased tumor volume on either scan is associated with an increasingly worse prognosis, but these findings have not yet been applied to dual PET imaging.

Given the lack of data to date integrating the concepts of discordant disease and tumor volume, we sought to investigate the discordant tumor volume as a potential new imaging-based biomarker. We conducted a retrospective analysis to investigate the prognostic impact of this discordant tumor volume in patients with advanced NENs.

MATERIALS AND METHODS

Patient Cohort

Consecutive patients with a histologically confirmed GEPNEN and dual PET/CT scans no more than 85 d apart were identified on retrospective review across 3 institutions, as previously published (*10,15,16*). Of these patients, only those with a NETPET score of P4b/P5 (indicating the presence of discordant disease) were selected for analysis in this study. A follow-up period of at least 30 d was necessary for inclusion in this study.

This study was approved by the institutional review boards of the Northern Sydney Local Health District Human Research Ethics Committee (2019/ETH14060), the Royal Free Hospital NHS Foundation Trust Quality Governance and Clinical Audit Committee, and the Ethics Committee of Jules Bordet Institute (CE2531). Each committee waived the need for informed consent.

PET-Based Analysis

Imaging data were acquired as reported previously (*11*) on comparable current-generation PET/CT scanners at each center with time-of-flight capabilities as whole-body scans (vertex of skull to mid thigh). Physicians had full access to software tools and clinical history at the time of the scan, reflecting the normal clinical practice. Dual PET scans were anatomically coregistered and displayed on a dedicated nuclear medicine–reporting workstation in transverse, coronal, and sagittal planes with rotating maximum-intensity projection cine images. All software tools were available for use, including window adjustment, color tables, and distance-defining calipers. Positivity on each scan was defined as an uptake visually greater than background uptake for the specific tissue surrounding the region of interest. Experienced nuclear medicine physicians reviewed each pair of PET scans qualitatively to derive the NETPET score (*10*).

Discordant lesions showing [^{18}F]FDG avidity but no [^{68}Ga]Ga-DOTATATE avidity were identified by experienced nuclear medicine physicians on simultaneous review of both scans. The images were manually contoured on the [^{18}F]FDG PET using a flat threshold SUV of 4 (MIM software, version 7.2.7; MIM Software Inc.). An example of a discordant lesion can be seen in Figure 1. Imaging variables of interest included SUV$_{max}$, SUV$_{mean}$, metabolic tumor volume, total lesion glycolysis, and the number and location of discordant lesions.

Clinicopathologic Variables

Clinical data were collected at each site by a retrospective chart review. Age at diagnosis, sex, primary site of GEPNEN, histologic grade (by World Health Organization 2017–2019 criteria) (*6*), the presence or absence of extrahepatic disease, and clinical outcomes were recorded.

The primary endpoint of this study was overall survival. Overall survival was calculated from the latter of the dual PET scans to the date of death, with data censored at the last known follow-up.

Statistical Analysis

The total discordant volume (TDV) of all lesions, the discordant metastatic lesion volume, and the discordant primary volume (in patients with tumors > 0 cm^3) were dichotomized by the median value of each variable. Similarly, the [^{18}F]FDG SUV$_{mean}$ and SUV$_{max}$ across all discordant lesions in each patient were calculated, and patients were dichotomized by their respective median values. Patients were also dichotomized by the presence of no more than 2 or more than 2 total discordant lesions, and no more than 2 or more than 2 discordant intrahepatic lesions as exploratory analyses (with 2 as an arbitrarily chosen cutoff). The overall survival of the resulting 2 groups from each dichotomization was compared using the log-rank test, with an α of 0.05 applied to the primary outcome measurement of TDV and Bonferroni adjustment used for all secondary outcomes.

Cohorts formed by histologic grade and by differentiation status (in patients with grade 3 disease only) were assessed using the log-rank test in groups with n greater than 5. This resulted in the exclusion of grade 1 patients from this analysis. The TDVs of grade 2 and grade 3 patients were additionally compared using an unpaired t test, with TDV as a continuous variable. Multivariate analysis was not performed because of the relatively small number of patients in this cohort.

RESULTS

In total, 44 patients with discordant disease were identified from the report by Chan et al. (NETPET P4b/P5) (*11*) across 3 participating centers in Sydney, London, and Brussels. The median age at diagnosis was 60 y, and 50% of the patients were men (n = 22/44). Scans were performed a maximum of 85 d apart, with a median scan interval of 8 d and an interquartile range of 1.75–22.5 d. No patients had progressive disease between the 2 scans. The median mitotic count was 3.5 per 2 mm^2, and the median Ki-67 index was 15%. The most common primary sites were the pancreas (45%, n = 20/44), small bowel (23%, n = 10/44), and colon (20%, n = 9/44). Using the World Health Organization 2019 criteria, we determined that 5% of patients were grade 1 (n = 2/44), 48% were grade 2 (n = 21/44), and 48% were grade 3 (n = 21/44). Within the grade 3 cohort, 24% were well differentiated (n = 5/21), 67% were poorly differentiated (n = 14/21), and 10% had unknown differentiation (n = 2/21). The median follow-up period of surviving patients was 40 mo. The median overall

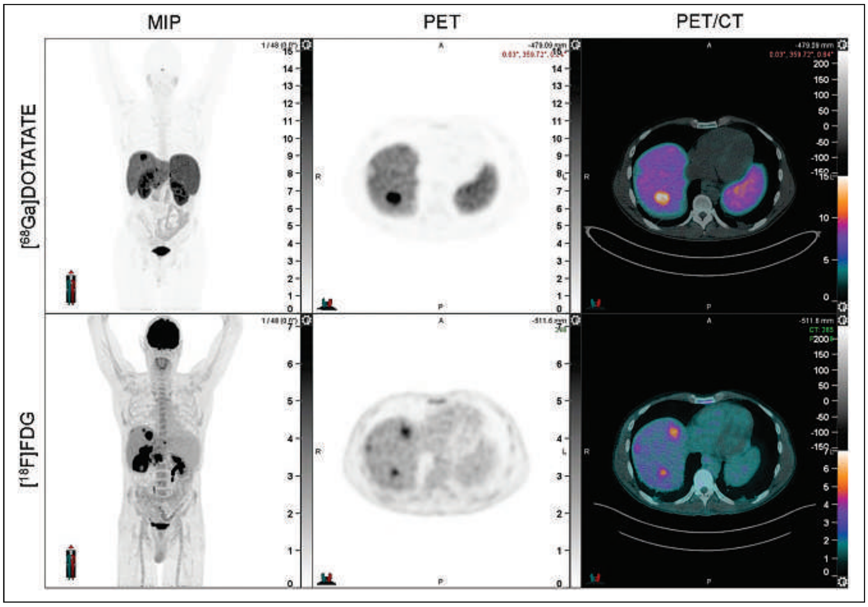

FIGURE 1. Example of discordant lesion, which is [^{18}F]FDG PET–positive but [^{68}Ga]Ga-DOTATATE PET–negative. From left to right, panels reflect maximum-intensity projection (MIP) image, PET, and PET/CT fusion.

survival of the cohort was 14.1 mo. Summarized cohort demographic data are available in Table 1.

Regarding the distribution of discordant lesions, 15 patients (34%) had discordant disease confined to the liver, 9 patients (20%) had discordant disease in extrahepatic sites only, and 20 patients (45%) had discordant disease both inside and outside the liver. The median discordant tumor volume used for dichotomization was 43.7 cm^3. The median TDVs of the low-TDV group and high-TDV group were 6.75 and 137.22 cm^3, respectively. There was no statistically significant difference in post-PET therapy choices between the 2 groups.

Overall survival was longer in the cohort with low TDV than in the cohort with high TDV, with median survival of 23.8 mo versus 9.4 mo, respectively (cohort median volume, 43.7 cm^3; hazard ratio, 0.466 [95% CI, 0.229–0.948]; $P = 0.0221$; Fig. 2A).

Using a Bonferroni adjustment, the adjusted α-value for secondary outcomes had a P value of 0.006. There was no significant difference in overall survival when using the Bonferroni adjustment and dichotomizing by metastatic volume ($P = 0.049$; Fig. 2B) or primary volume ($P = 0.1724$). The SUV$_{\text{mean}}$ and SUV$_{\text{max}}$ across all lesions were not significantly associated with overall survival on a patient-level basis ($P = 0.1243$ and 0.0936, respectively; Figs. 2C and 2D). The total number of discordant lesions of no more than 2 or more than 2 was not significantly associated with survival ($P = 0.1200$; Fig. 3A); however, patients with a maximum of 2 discordant intrahepatic lesions had significantly longer survival than those with more than 2 such lesions (31.8 mo vs. 10.2 mo; hazard ratio, 0.389 [95% CI, 0.194–0.779]; $P = 0.0049$; Fig. 3B). There was a significant difference between the survival of grade 2 and the survival of grade 3 patients ($P = 0.0002$; Fig. 3C) but not between those with poorly differentiated and well-differentiated grade 3 histology ($P = 0.0457$). Given the focus on [^{18}F]FDG PET over [^{68}Ga]Ga-DOTATATE PET in grade 3 poorly differentiated neuroendocrine carcinoma, we conducted a sensitivity analysis restricting the cohort of patients to those with well-differentiated disease alone (i.e., grade 1, grade 2, and grade 3 well-differentiated NENs) and redichotomizing the median TDV of this new cohort (19.1 cm^3). There was no significant difference in the overall survival of low- versus high-TDV patients in this subgroup (38.6 and 10.7 mo, respectively; $P = 0.1373$), likely due to the lower number of patients. Detailed statistical results for the overall survival of patients with these variables are presented in Table 2. There was no significant correlation between the TDV of grade 2 and grade 3 patients ($P = 0.2279$; Fig. 4).

DISCUSSION

The current study demonstrates for the first time, to our knowledge, that higher volumes of discordant disease on dual

TABLE 1
Cohort Summary Characteristics

Characteristic	Patients ($n = 44$)
Sex	
Male	22 (50%)
Female	22 (50%)
Primary site of tumor	
Pancreas	20 (45%)
Midgut	10 (23%)
Colorectal	9 (20%)
Other	3 (12%)
Histologic grade	
Grade 1	2 (5%)
Grade 2	21 (48%)
Grade 3 (differentiation)	21 (48%; 24% well differentiated, 67% poorly differentiated, 10% unknown)
Extrahepatic disease	
Yes	34 (77%)
No	10 (23%)
Functional disease	
Yes	9 (20%)
No	26 (59%)
Unknown	9 (20%)

Mean age at diagnosis was 60 y (range, 24–82 y).

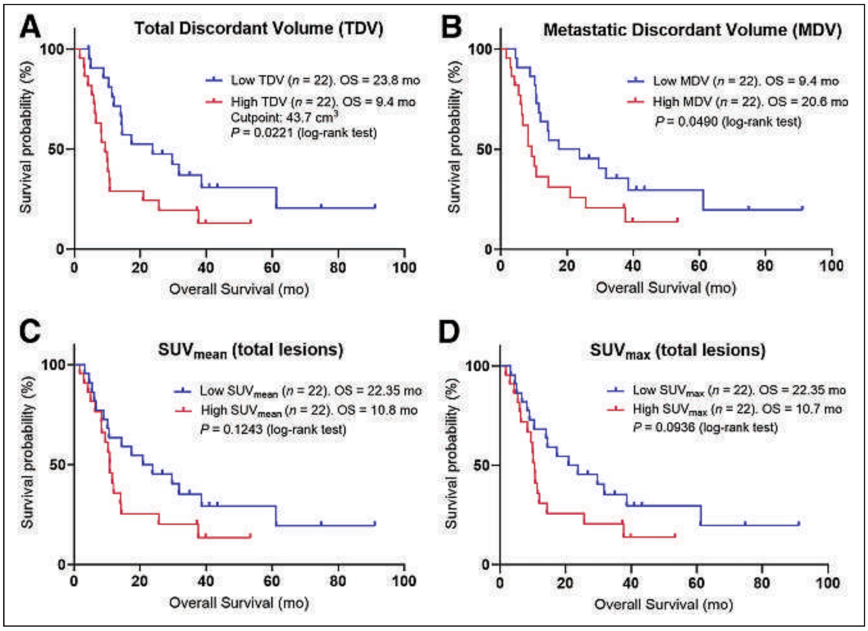

FIGURE 2. Kaplan–Meier curves for overall survival (OS) are shown for each variable. Patients were dichotomized into 2 groups based on median value of TDV (A) (43.7 cm^3), metastatic discordant volume (B) (30.2 cm^3), SUV$_{mean}$ of all discordant lesions (C) (dichotomization SUV, 6), and SUV$_{max}$ of all discordant lesions (D) (dichotomization SUV, 12.6).

PET imaging are a prognostic biomarker in patients with metastatic GEPNENs. Although our group has previously shown that the presence of discordant disease predicts poor prognosis (P5 cohort (*11*)), the current study further stratifies these patients into cohorts of high- and low-volume discordant disease. Although prior studies have looked at tumor volume on [^{68}Ga]Ga-DOTATATE PET and [^{18}F]FDG PET in isolation (*10,14*), the volumetric implications from overlaying the 2 scans have not previously been considered. For instance, the patient in Figure 5 displays multiple [^{68}Ga]Ga-DOTATATE–avid and [^{18}F]FDG-avid lesions. However, dual PET analysis highlights that a low volume of this disease is discordant. We note that both flat cutoffs and adaptive cutoffs have been used in prior studies (*12–14*). We elected to use a flat cutoff for the current study, in keeping with previous work investigating [^{18}F]FDG PET (*12*). We note that dual PET has been used successfully in the prediction of tumor aggressiveness and clinical outcomes in patients with resectable pancreatic NENs (*17,18*).

Patients were included in this multicenter study regardless of their age, histologic grade, or GEPNEN primary site, resulting in a representative real-world cohort. Our cohort contained 2 patients with grade 1 histology who also demonstrated discordant disease. This is not entirely unexpected, as a significant minority of patients diagnosed with grade 1 histology (on initial biopsy) exhibit [^{18}F]FDG avidity (*19*). Our findings reinforce the role of dual PET in metastatic GEPNENs, even in a low-grade population. Although analysis of the well-differentiated cohort did not show a significant association between TDV and overall survival, the smaller numbers in this cohort might explain the lack of statistical significance, as we note that the 28-mo numeric difference in overall survival between high- and low-TDV cohorts remains clinically significant and mirrored that of the overall population. The exploratory analysis showing possibly poorer prognosis for patients with a higher number of discordant intrahepatic lesions may reflect the difficulty in giving liver-directed therapy to such patients. Whether this is true may be investigated in future studies. The findings may be because patients with a high number of discordant intrahepatic lesions may not be effectively targeted by liver-directed therapy, meaning that only systemic therapies are available to keep this more biologically aggressive disease under control. However, given the exploratory nature of such analyses, no firm conclusions regarding the use of these metrics in clinical practice can be made at this point.

The findings of this study carry practical implications for the practicing NEN physician. Patients with low-volume discordant disease have a significantly better prognosis than those with high-volume disease but may require a variety of treatment approaches. For example, patients with 1–2 oligodiscordant metastases in the setting of mostly [^{68}Ga]Ga-DOTATATE–avid disease may still benefit from peptide receptor

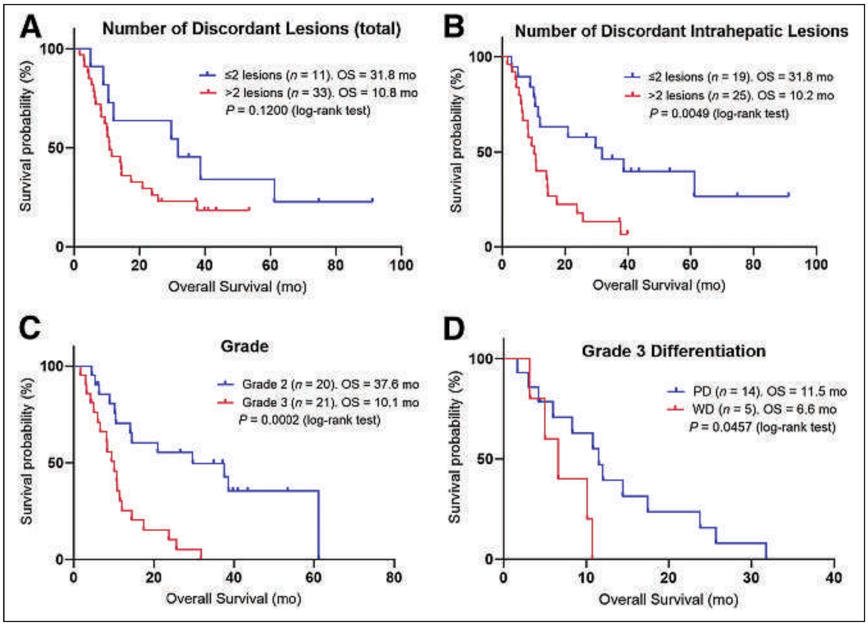

FIGURE 3. Kaplan–Meier curves for overall survival (OS) are shown for each variable. Patients were dichotomized by number of discordant lesions (A) (≤2 or >2), number of discordant intrahepatic lesions (B) (≤2 or >2), tumor grade (C) (grade 1 patients were excluded as $n < 5$), and differentiation of grade 3 patients (D) (well differentiated [WD] and poorly differentiated [PD]).

TABLE 2
Statistical Results for Each Variable Using Log-Rank Test

Variable	Value used to dichotomize cohort	Median overall survival (mo) of group below/above dichotomization	Hazard ratio*	*P*
TDV	43.7 cm^3	23.8/9.4	0.466 (0.229–0.948)	0.0221
Metastatic discordant volume	30.2 cm^3	20.6/9.4	0.516 (0.253–1.053)	0.0490
Primary discordant volume	12.1 cm^3	11.5/10.7	1.272 (0.380–4.261)	0.1724
SUV$_{\text{mean}}$	6	22.35/10.8	0.596 (0.296–1.200)	0.1243
SUV$_{\text{max}}$	12.6	22.35/10.7	0.569 (0.282–1.151)	0.0930
Discordant lesions	≤2 lesions, >2 lesions	31.8/10.8	0.550 (0.271–1.116)	0.1200
Intrahepatic lesions	≤2 lesions, >2 lesions	31.8/10.2	0.389 (0.194–0.779)	0.0049
Grade	Grade 2, grade 3	29.7/10.1	0.303 (0.146–0.631)	0.0002
Grade 3 differentiation	Well differentiated, poorly differentiated	6.6/11.5	2.568 (0.651–10.130)	0.0457

---

*Hazard ratio with 95% CI.

radionuclide therapy, but with the addition of a simultaneous anatomically targeted therapy (e.g., stereotactic body radiotherapy) to specifically target low-volume discordant lesions. This is particularly the case with discordant disease limited to the liver, for which liver-directed therapy in addition to simultaneous therapy (perhaps even peptide receptor radionuclide therapy) may deal effectively with non–[^{68}Ga]Ga-DOTATATE–avid NEN lesions. The better prognosis of this subgroup justifies the complexity, health resource use, and potential complications of this combination treatment. On the other hand, patients with high-volume discordant disease have a significantly shorter survival (median survival was 9.4 mo in the current cohort), suggesting that more aggressive treatments should be considered. Given the significant amount of non–[^{68}Ga]Ga-DOTATATE–avid aggressive disease in this cohort, patients should most likely be treated with chemotherapy and be prioritized for clinical trials because of their anticipated poor outcome.

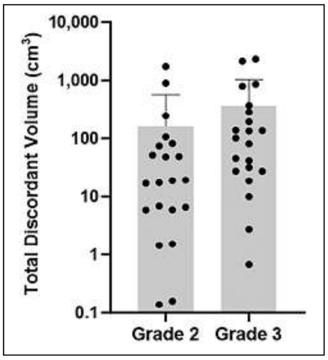

FIGURE 4. TDV by histologic grade. Groups (*n* = 21 each) were not significantly different (grade 2 mean, 166.4 cm^3; grade 3 mean, 367.3 cm^3; *P* = 0.2279, unpaired *t* test). Patients with grade 1 disease were excluded from analysis because of small sample (*n* < 5). Gray bars represent mean value, and error bars represent SD.

Our study had the strength of pooling data across multiple centers using similar scanners, paving the way for clinical translation to practice across multiple NEN practices globally. This collaboration allowed a significant number of patients to be identified in an uncommon subset of an uncommon tumor. We prespecified the study methodology to ensure that scan analysis was conducted similarly across geographically disparate areas. We acknowledge the limitations of the current study arising from the retrospective design and the relatively small sample size. As mentioned above, whereas the 44 patients identified in the present study represent a significant cohort in discordant advanced NENs, multivariate analysis is not feasible in a cohort of this size.

The current study suggests several paths forward for future research. Although the NETPET system (*10*) assumes lesion-level homogeneous uptake (or lack of uptake), future studies may elucidate the prognostic significance of lesions with heterogeneous uptake within the tumor. Particularly, lesions with heterogeneous discordance (Fig. 6) should be explored to determine whether a small amount of discordance within an otherwise [^{68}Ga]Ga-DOTATATE–avid lesion truly represents discordant disease and carries its associated poor prognosis. Additionally, an analysis of the lesions with [^{68}Ga]Ga-DOTATATE avidity but not [^{18}F]FDG avidity may yield additional information (e.g., when compared in volume against that of the discordant disease). Further correlative studies may elucidate the biology underlying discordant PET findings—whether grade migration, development of poorly differentiated neuroendocrine carcinoma, or hypoxia may be contributory to these appearances.

From a technical viewpoint, dual PET analysis presents some difficulties. Typically, the 2 scans are completed on separate days, with the intervening (and unstandardized) period introducing an opportunity for tumor growth or shrinkage and anatomic shift. This may complicate accurate colocalization and limit high-quality reporting. Recent advances such as novel radiotracers and whole-body PET may allow for reduced imaging times and reduced injected radiotracer activity and may facilitate same-day scanning. Additionally, the application of artificial intelligence and machine-learning methods to dual PET data may decrease some of these technical difficulties in the future.

Validation of the current findings in a larger prospective study would further strengthen the quality of evidence surrounding discordant lesions. Such a large-scale study will require significant international cooperation, including formal imaging harmonization. However, given the lack of existing methods to identify patients with discordant disease before dual PET imaging, this will likely involve many patients scanned de novo, with its attendant feasibility and cost implications. Although larger-scale retrospective collaborations would be a desirable way to make progress

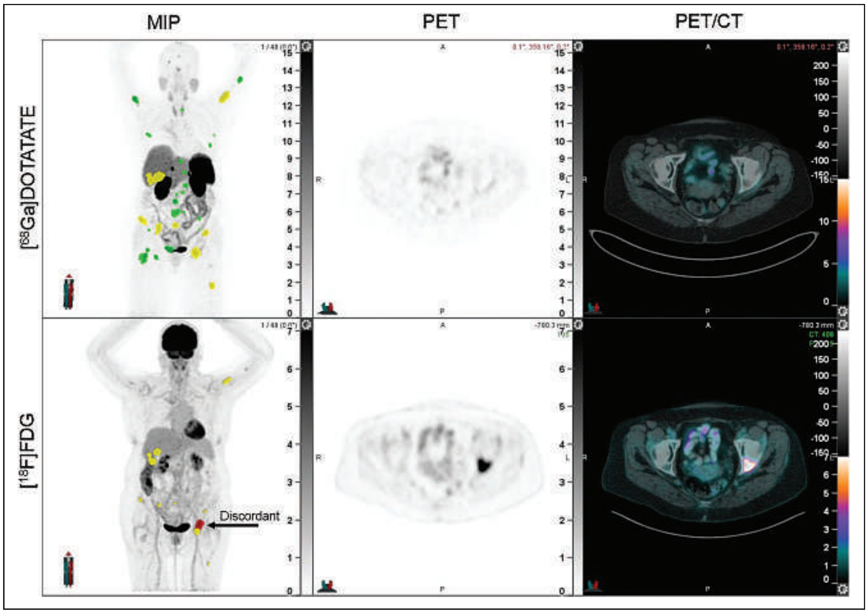

FIGURE 5. Example patient in low-TDV group with TDV of 9.91 cm^3. Patient has 31 [^{68}Ga]Ga-DOTATATE–positive lesions, 21 of which are avid on [^{68}Ga]Ga-DOTATATE only (green) and 10 of which have corresponding [^{18}F]FDG avidity (yellow). Of 11 [^{18}F]FDG-avid lesions with SUV of at least 4, 1 is discordant ([^{68}Ga]Ga-DOTATATE–negative, in red). From left to right, panels reflect the maximum-intensity projection (MIP) image, PET, and PET/CT fusion.

in an uncommon disease, the challenges associated with this approach include the heterogeneity of practice patterns across different jurisdictions, the differential cost of PET (particularly dual PET), and the privacy issues related to data sharing. Finally, an in-depth quantitative analysis of imaging characteristics, perhaps assisted by machine learning, may yield insights into potential biomarkers. Particularly, further defining the cohort of patients with concordant [^{68}Ga]Ga-DOTATATE and [^{18}F]FDG avidity (without any discordant disease) would provide a holistic examination of dual PET expression and further the goal of using dual PET as a virtual biopsy to predict tumor biology and disease course. The advent of multiple potential biomarkers for PET-aided prognostication in NENs (together with the need to integrate both [^{68}Ga]Ga-DOTATATE PET and [^{18}F]FDG PET metrics) also raises the question of potential statistical collinearity, which will have to be carefully considered in future work that compares candidate biomarkers.

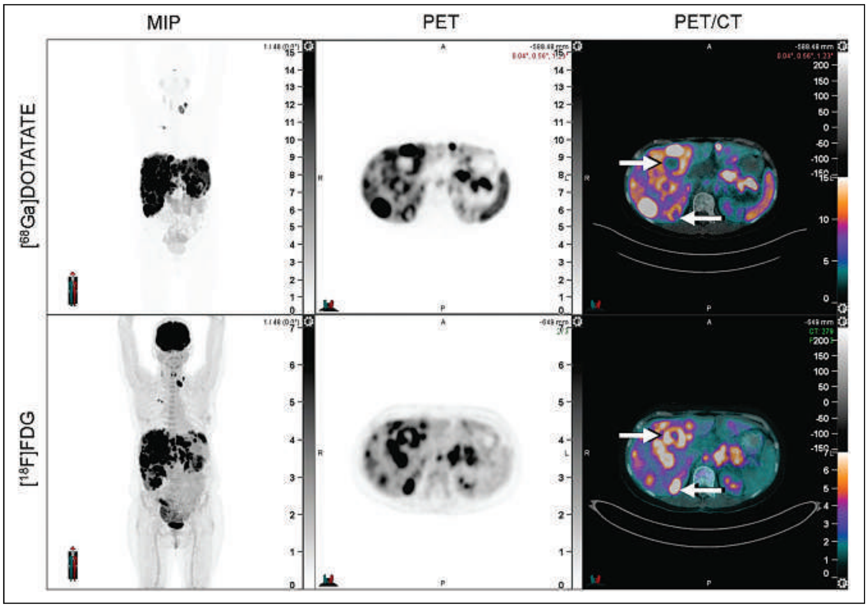

FIGURE 6. Example of heterogeneous discordance. Arrows highlight areas of [^{18}F]FDG discordance in a lesion that otherwise displays concordant [^{68}Ga]Ga-DOTATATE and [^{18}F]FDG avidity. From left to right, panels reflect the maximum-intensity projection (MIP) image, PET, and PET/CT fusion.

CONCLUSION

We have identified discordant tumor volume as a potential novel imaging biomarker and have shown that higher discordant tumor volume is associated with poorer prognosis in patients with advanced GEPNENs. This prognostication may be used to guide treatment choice. Patients with lower discordant tumor volumes (particularly those with only 1–2 sites of discordant disease) could be considered for ablative approaches for discordant disease sites while simultaneously proceeding with traditional modalities (such as peptide receptor radionuclide therapy) for the bulk of their [^{68}Ga]Ga-DOTATATE–avid tumor burden. Despite the challenges associated with a prospective study to validate this biomarker, we hope that the coming postpandemic years will usher in a new era of international collaboration to yield further progress in this challenging disease and ultimately to optimize the outcomes of patients affected by NENs.

DISCLOSURE

David Chan was funded by the National Health and Medical Research Council of Australia (GNT1175788) and also reports honoraria from Ipsen, Novartis, and Camurus and research support from EMD Serono, outside the submitted work. Gopinath Gnanasegaran reports personal fees from Advanced Accelerator Applications, a Novartis company, and received honoraria for lectures outside the submitted work. Nick Pavlakis reports personal fees from AstraZeneca, Bayer, Boehringer Ingelheim, Merck Serono, Ipsen, Amgen, Bayer Healthcare Pharmaceuticals, Bristol-Myers Squibb, Eli Lilly, Pfizer, Novartis, Roche Pharma AG, Merck, Baxalta, and Specialised Therapeutics, outside the submitted work. Martyn Caplin reports personal fees from Ipsen, Novartis, AAA, Lexicon, and Pfizer and grants from AAA and Ipsen, outside the submitted work.

Christos Toumpanakis reports personal fees from Ipsen, Novartis, and AAA and education grants from Ipsen, Novartis, and AAA, outside the submitted work. No other potential conflict of interest relevant to this article was reported.

ACKNOWLEDGMENT

This study was presented as a poster and accompanying abstract at the 20th Annual ENETS Conference (March 22–24, 2023, Vienna, Austria).

KEY POINTS

QUESTION: What is the prognostic impact of discordant tumor volume in patients with advanced GEPNENs imaged with dual [^{68}Ga]Ga-DOTATATE and [^{18}F]FDG PET?

PERTINENT FINDINGS: This retrospective multicenter study of 44 patients with discordant ([^{18}F]FDG-avid/non–[^{68}Ga]Ga-DOTATATE–avid) disease showed that those with low discordant tumor volume had statistically better overall survival than those with high discordant tumor volume on univariate analysis.

IMPLICATIONS FOR PATIENT CARE: Discordant tumor volume may be a prognostic biomarker in patients with advanced GEPNENs.

REFERENCES

1. Wyld D, Wan MH, Moore J, Dunn N, Youl P. Epidemiological trends of neuroendocrine tumours over three decades in Queensland, Australia. *Cancer Epidemiol.* 2019;63:101598.
2. Dasari A, Shen C, Halperin D, et al. Trends in the incidence, prevalence, and survival outcomes in patients with neuroendocrine tumors in the United States. *JAMA Oncol.* 2017;3:1335–1342.
3. Wong MH, Chan DL, Lee A, et al. Systematic review and meta-analysis on the role of chemotherapy in advanced and metastatic neuroendocrine tumor (NET). *PLoS One.* 2016;11:e0158140.
4. Sorbye H, Welin S, Langer SW, et al. Predictive and prognostic factors for treatment and survival in 305 patients with advanced gastrointestinal neuroendocrine carcinoma (WHO G3): the NORDIC NEC study. *Ann Oncol.* 2013;24:152–160.
5. Hallet J, Law CHL, Cukier M, Saskin R, Liu N, Singh S. Exploring the rising incidence of neuroendocrine tumors: a population-based analysis of epidemiology, metastatic presentation, and outcomes. *Cancer.* 2015;121:589–597.
6. Nagtegaal ID, Odze RD, Klimstra DS, et al. The 2019 WHO classification of tumours of the digestive system. *Histopathology.* 2020;76:182–188.
7. Muffatti F, Partelli S, Cirocchi R, et al. Combined ^{68}Ga-DOTA-peptides and ^{18}F-FDG PET in the diagnostic work-up of neuroendocrine neoplasms (NEN). *Clin Transl Imaging.* 2019;7:181–188.
8. Campana D, Ambrosini V, Pezzilli R, et al. Standardized uptake values of ^{68}Ga-DOTANOC PET: a promising prognostic tool in neuroendocrine tumors. *J Nucl Med.* 2010;51:353–359.
9. Binderup T, Knigge U, Loft A, Federspiel B, Kjaer A. ^{18}F-fluorodeoxyglucose positron emission tomography predicts survival of patients with neuroendocrine tumors. *Clin Cancer Res.* 2010;16:978–985.
10. Chan DL, Pavlakis N, Schembri GP, et al. Dual somatostatin receptor/FDG PET/CT imaging in metastatic neuroendocrine tumours: proposal for a novel grading scheme with prognostic significance. *Theranostics.* 2017;7:1149–1158.
11. Chan DL, Hayes AR, Karfis I, et al. Dual [^{68}Ga]DOTATATE and [^{18}F]FDG PET/CT in patients with metastatic gastroenteropancreatic neuroendocrine neoplasms: a multicentre validation of the NETPET score. *Br J Cancer.* 2023;128:549–555.
12. Chan DL, Bernard EJ, Schembri G, et al. High metabolic tumour volume on 18-fluorodeoxyglucose positron emission tomography predicts poor survival from neuroendocrine neoplasms. *Neuroendocrinology.* 2020;110:950–958.
13. Langen Stokmo H, Aly M, Bowitz Lothe IM, et al. Volumetric parameters from [^{18}F]FDG PET/CT predicts survival in patients with high-grade gastroenteropancreatic neuroendocrine neoplasms. *J Neuroendocrinol.* 2022;34:e13170.
14. Tirosh A, Papadakis GZ, Millo C, et al. Prognostic utility of total ^{68}Ga-DOTATATE-avid tumor volume in patients with neuroendocrine tumors. *Gastroenterology.* 2018;154:998–1008.e1.
15. Karfis I, Marin G, Levillain H, et al. Prognostic value of a three-scale grading system based on combining molecular imaging with ^{68}Ga-DOTATATE and ^{18}F-FDG PET/CT in patients with metastatic gastroenteropancreatic neuroendocrine neoplasias. *Oncotarget.* 2020;11:589–599.
16. Hayes AR, Furtado O'Mahony L, Quigley AM, et al. The combined interpretation of ^{68}Ga-DOTATATE PET/CT and ^{18}F-FDG PET/CT in metastatic gastroenteropancreatic neuroendocrine tumors: a classification system with prognostic impact. *Clin Nucl Med.* 2022;47:26–35.
17. Mapelli P, Partelli S, Salgarello M, et al. Dual tracer ^{68}Ga-DOTATOC and ^{18}F-FDG PET/computed tomography radiomics in pancreatic neuroendocrine neoplasms: an endearing tool for preoperative risk assessment. *Nucl Med Commun.* 2020;41:896–905.
18. Mapelli P, Partelli S, Salgarello M, et al. Dual tracer ^{68}Ga-DOTATOC and ^{18}F-FDG PET improve preoperative evaluation of aggressiveness in resectable pancreatic neuroendocrine neoplasms. *Diagnostics (Basel).* 2021;11:192.
19. Bahri H, Laurence L, Edeline J, et al. High prognostic value of ^{18}F-FDG PET for metastatic gastroenteropancreatic neuroendocrine tumors: a long-term evaluation. *J Nucl Med.* 2014;55:1786–1790.

Diagnostic Performance of [^{18}F]TFB PET/CT Compared with Therapeutic Activity [^{131}I]Iodine SPECT/CT and [^{18}F]FDG PET/CT in Recurrent Differentiated Thyroid Carcinoma

David Ventura*[1,2], Matthias Dittmann*[1,3], Florian Büther[1,4], Michael Schäfers[1,2,4], Kambiz Rahbar[1,2],
Daniel Hescheler[1,2], Michael Claesener[1], Philipp Schindler[2,5], Burkhard Riemann[1,2], Robert Seifert†[1,2,6,7], and
Wolfgang Roll†[1,2]

[1]Department of Nuclear Medicine, University Hospital Münster, Münster, Germany; [2]West German Cancer Centre, Münster, Germany; [3]Department of Nuclear Medicine, St. Marien Hospital Lünen, Lünen, Germany; [4]European Institute for Molecular Imaging, University of Münster, Münster, Germany; [5]Clinic for Radiology, University and University Hospital Münster, Münster, Germany; [6]Department of Nuclear Medicine, University Hospital Essen, Essen, Germany; and [7]West German Cancer Centre, Essen, Germany

[^{18}F]tetrafluoroborate ([^{18}F]TFB) is an emerging PET tracer with excellent properties for human sodium iodide symporter (NIS)–based imaging in patients with differentiated thyroid cancer (DTC). The aim of this study was to compare [^{18}F]TFB PET with high-activity posttherapeutic [^{131}I]iodine whole-body scintigraphy and SPECT/CT in recurrent DTC and with [^{18}F]FDG PET/CT in suspected dedifferentiation. **Methods:** Twenty-six patients treated with high-activity radioactive [^{131}I]iodine therapy (range, 5.00–10.23 GBq) between May 2020 and November 2022 were retrospectively included. Thyroid-stimulating hormone was stimulated by 2 injections of recombinant thyroid-stimulating hormone (0.9 mg) 48 and 24 h before therapy. Before treatment, all patients underwent [^{18}F]TFB PET/CT 40 min after injection of a median of 321 MBq of [^{18}F]TFB. To study tracer kinetics in DTC lesions, 23 patients received an additional scan at 90 min. [^{131}I]iodine therapeutic whole-body scintigraphy and SPECT/CT were performed at a median of 3.8 d after treatment. Twenty-five patients underwent additional [^{18}F]FDG PET. Two experienced nuclear medicine physicians evaluated all imaging modalities in consensus. **Results:** A total of 62 suspected lesions were identified; of these, 30 lesions were [^{131}I]iodine positive, 32 lesions were [^{18}F]TFB positive, and 52 were [^{18}F]FDG positive. Three of the 30 [^{131}I]iodine-positive lesions were retrospectively rated as false-positive iodide uptake. Tumor-to-background ratio measurements at the 40- and 90-min time points were closely correlated (e.g., for the tumor-to-background ratio for muscle, the Pearson correlation coefficient was 0.91; $P < 0.001$; $n = 49$). We found a significant negative correlation between [^{18}F]TFB uptake and [^{18}F]FDG uptake as a potential marker for dedifferentiation (Pearson correlation coefficient, -0.26; $P = 0.041$; $n = 62$). **Conclusion:** Pretherapeutic [^{18}F]TFB PET/CT may help to predict the positivity of recurrent DTC lesions on [^{131}I]iodine scans. Therefore, it may help in the selection of patients for [^{131}I]iodine therapy. Future prospective trials for iodine therapy guidance are warranted. Lesion [^{18}F]TFB uptake seems to be inversely correlated with [^{18}F]FDG uptake and therefore might serve as a dedifferentiation marker in DTC.

Key Words: [^{18}F]TFB; radioactive iodine therapy; DTC; [^{18}F]FDG; PET

J Nucl Med 2024; 65:192–198
DOI: 10.2967/jnumed.123.266513

The incidence of differentiated thyroid carcinoma (DTC) is currently increasing at a rate of approximately 3% per year, with papillary thyroid carcinoma being the major histologic tumor entity, followed by follicular thyroid carcinoma (*1,2*). After standard treatment with thyroidectomy and radioactive [^{131}I]iodine therapy (RAI), approximately 90% of DTC patients have a normal life expectancy. However, up to 50% will develop lymph node metastases and about 10% will develop distant metastases (*3*). Importantly, dedifferentiation may occur in the course of the disease, accompanied by a decrease or loss of expression of the sodium iodide symporter (NIS) and the subsequent failure of [^{131}I]iodine-based theranostics (*4*). These radioiodine-refractory DTC (RRDTC) patients have poorer survival rates (*2*). Therefore, a multimodal approach including various imaging modalities is recommended in patients with tumor recurrence or suspected RRDTC to guide treatment decisions (*5*).

NIS-based imaging is a standard procedure for the detection of suspected DTC recurrence with the therapeutic/diagnostic application of [^{131}I]iodine for whole-body scintigraphy (WBS) and SPECT/CT (WBS-SPECT/CT) (*6*). However, the low signal-to-noise ratio and the low spatial resolution of WBS-SPECT/CT in combination with [^{131}I]iodine limit their sensitivity. This issue may cause the “thyroglobulin elevated and negative scintigraphy” (TENIS) syndrome (*7*). In addition, [^{131}I]iodine as a β-emitter involves comparably high radiation exposure (*8*). As yet, positron-emitting [^{124}I]iodine is only available in a few centers and, again, is associated with a low signal-to-noise ratio (*9*). A promising alternative PET radiotracer for targeting NIS is [^{18}F]tetrafluoroborate ([^{18}F]TFB), which has a high signal-to-noise ratio and involves lower radiation exposure (*10*). It was shown previously that [^{18}F]TFB PET/CT offers equivalent diagnostic accuracy as [^{124}I]iodine PET/CT (*11*). We recently demonstrated that [^{18}F]TFB

Received Aug. 7, 2023; revision accepted Nov. 1, 2023.

For correspondence or reprints, contact David Ventura (david.ventura@ukmuenster.de).

*Contributed equally to this work.

†Contributed equally to this work.

TABLE 1
Patient Characteristics

Characteristic	*n*	%	Median	Range	95% CI
Patients*	26				
Sex					
Women	12	46.2			
Men	14	53.8			
Histology					
PTC	11	42.3			
FTC	13	50			
OTC	2	7.7			
UICC TNM (*33*)					
pT1	4	15.4			
pT2	7	27			
pT3	9	34.6			
pT4	3	11.5			
pTx	3	11.5			
pN0	5	19.2			
pN1	7	27			
pNx	14	53.8			
cM0	5	19.2			
cM1	16	61.5			
cMx	5	19.2			
PUL	5	19.2			
OSS	7	27			
OTH	4	15.4			
Laboratory analysis					
TG† (ng/mL)			10.1	0.15–10,807	
Anti-TG† (IU/mL)			17.2	<15–230	
TSH (μU/mL)			0.1	0.02–2.36	
TSH after stimulation (μU/mL)			122	51.8–424.1	
TG after stimulation (ng/mL)			61.9	0.46–21,200	
8 wk after RAI					
TG†			6.7	0.15–10,780	
Anti-TG†			15.6	<15–238	
RAI and PET/CT					
GBq of [^{131}I]iodine			6,023		5,032–6,497
MBq of [^{18}F]TFB			321		297–342
MBq of [^{18}F]FDG			326		270–317

*Median age was 64.5 y, and range was 38–87.

†If measurable.

PTC = papillary thyroid carcinoma; FTC = follicular thyroid carcinoma; OTC = oncocytic carcinoma of thyroid; PUL = pulmonary metastases; OSS = bone metastases; OTH = other-side metastases; anti-TG = antibodies against thyroglobulin.

PET/CT has high accuracy compared with [^{131}I]iodine-based diagnostic SPECT/CT (*12*). However, there is a lack of knowledge regarding the clinically relevant comparison of [^{18}F]TFB PET/CT with posttherapeutic SPECT/CT in recurrent DTC (*13*).

Differentiated metastases of thyroid cancer still express NIS and thereby show iodide uptake with low glucose metabolism, whereas dedifferentiated metastases have lost NIS expression and do not trap iodide sufficiently but have a high glucose consumption (*14,15*). [^{18}F]FDG PET/CT uptake correlates with the degree of DTC dedifferentiation and therefore has already established its diagnosis (*16*). The performance of [^{18}F]TFB PET/CT in dedifferentiating DTC is unknown. In addition, there is a lack of evidence regarding the optimal imaging time point after tracer injection for [^{18}F]TFB PET/CT (*10*).

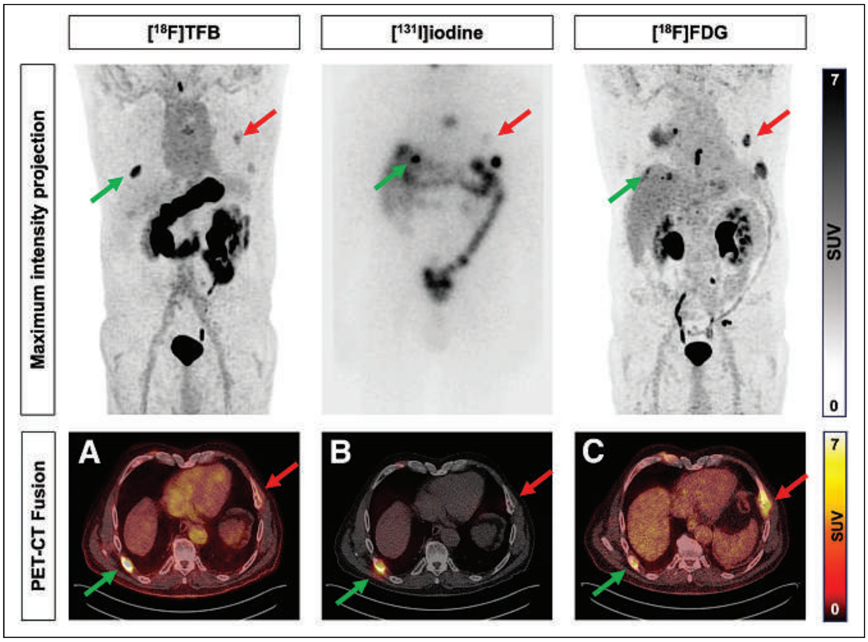

FIGURE 1. Heterogeneous disease pattern. 71-y-old man with follicular thyroid carcinoma and various bone metastases. Rib metastases show heterogeneous disease pattern: intense [^{18}F]TFB (A) and [^{131}I]iodine (B) uptake but low [^{18}F]FDG (C) uptake (green arrow); intense [^{18}F]FDG (C) uptake but no relevant [^{18}F]TFB (A) and [^{131}I]iodine (B) uptake (red arrows).

Therefore, the aim of this retrospective study was to evaluate the accuracy and optimal time point of [^{18}F]TFB PET/CT in patients with suspected recurrence of DTC in comparison to clinically approved therapeutic WBS-SPECT/CT (TxWBS-SPECT/CT). In addition, [^{18}F]TFB PET/CT is also compared with [^{18}F]FDG PET/CT to assess dedifferentiation in DTC.

MATERIALS AND METHODS

Patients

This single-center retrospective study included 26 patients with recurrent DTC treated with high-activity RAI (range, 5.00–10.23 GBq) between May 2020 and November 2022. Before RAI, all included patients underwent [^{18}F]TFB PET/CT, with its previously demonstrated higher diagnostic accuracy, in routine clinical practice to evaluate potential localized treatment options. High-activity therapeutic RAI was recommended by the local tumor board on the basis of international guidelines (*5*). All patients underwent TxWBS-SPECT/CT after RAI. Additional [^{18}F]FDG PET/CT was performed if dedifferentiation was suspected. Detailed characteristics of the patients are summarized in Table 1.

All patients gave written and informed consent before treatment and imaging acquisition in accordance with the Declaration of Helsinki. This retrospective study was approved by the local ethic committee (2019-615-f-S; Ethik-Kommission Westfalen-Lippe).

[^{18}F]TFB PET/CT and [^{131}I]Iodine TxWBS-SPECT/CT

All patients received 2 intramuscular injections of thyrotropin alfa (Thyrogen; Sanofi) (0.9 mg) 48 and 24 h before [^{18}F]TFB PET/CT and RAI. Thyroid-stimulating hormone (TSH) was assessed immediately before PET and RAI. [^{18}F]TFB was produced in-house as described in detail previously (*12*) and administered intravenously at 3 MBq/kg of body weight. Whole-body PET acquisitions from the head to the proximal femur (acquisition speed, 2 min/bed position or 1.1 mm/s) were performed 40 min (all patients) and 90 min (23/26 patients) after injection using a Siemens Biograph 128 mCT scanner (Siemens Healthcare). A low-dose CT scan was performed for attenuation correction and anatomic correlation.

A median activity of 6.02 GBq (range, 5.00–10.23 GBq) of [^{131}I]iodide was administered orally (Curium Germany GmbH) immediately after PET acquisition. Planar TxWBS scans were acquired using a high-energy parallel-collimator matrix with a 2.21-mm pixel size at a speed of 10 cm/min and a photopeak at 364 keV (±10%). Also, all patients underwent SPECT/CT from the skull base to the diaphragm and, on the basis of the TxWBS scans, SPECT/CT of additional regions using a Discovery NM/CT 670 Pro System (General Electric Co.). SPECT was acquired with a high-energy collimator matrix of 128 × 128 in the step-and-shoot mode with 20 s/step and a photopeak at 364 keV (±10%).

Tumor-to-Background (TBR) Ratios in [^{18}F]TFB PET

The maximum TBR was measured with 3 reference organs to reliably compare tracer kinetics in DTC lesions. The maximum TBR was calculated as the quotient of lesion SUV_{max} and reference SUV_{mean} (*17*). The reference SUV_{mean} was measured using a spheric 1.0-cm-diameter volume of interest in the thoracic aorta (blood-pool TBR) or a 3.0-cm-diameter volume of interest in the left gluteus maximus muscle (muscle TBR) or in the right apical lung lobe (lung TBR). This procedure was done for both 40- and 90-min PET scans.

[^{18}F]FDG PET/CT

[^{18}F]FDG PET/CT was performed if dedifferentiated disease was suspected (*5*). Eligible patients were imaged after at least 6 h of fasting with

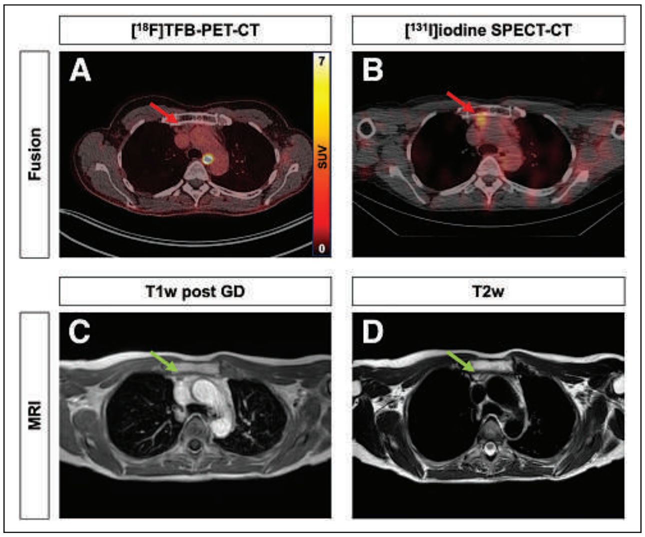

FIGURE 2. False-positive thymus uptake in [^{131}I]iodine SPECT/CT. 49-y-old woman with follicular thyroid cancer. Absent [^{18}F]TFB uptake (A) in [^{131}I]iodine-positive (B) mediastinal mass (red arrow). Subsequent contrast-enhanced MRI showed thymus rebound (green arrow) in T1-weighted (after gadolinium) (T1w post GD) and T2-weighted (T2w) (C and D) sequences. [^{131}I]iodine uptake therefore was considered to be false-positive, a conclusion that was also confirmed by further follow-up.

blood glucose of less than 6.7 mM. Images were acquired at 60 min after the intravenous administration of body weight–adapted [^{18}F]FDG (3 MBq/kg) (acquisition speed, 2 min/bed position or 1.1 mm/s) using a Siemens Biograph 128 mCT scanner. Whole-body images from the head to the proximal femur were acquired and, for attenuation correction, an additional low-dose CT scan was performed.

Image Analysis

All available image acquisitions were reviewed in consensus by 2 experienced nuclear medicine physicians. Nonphysiological focal uptake above the background uptake of [^{131}I]iodine in TxWBS and correlative SPECT/CT was considered suspicious. Similarly, nonphysiological focal [^{18}F]TFB uptake was defined as uptake exceeding the background uptake (e.g., muscular uptake for cervical lesions) and considered suspicious. Focal [^{18}F]FDG uptake was considered suspicious when the uptake was over the liver background uptake (*18*). For lesion-based analysis, the SUV$_{max}$ was measured in each lesion for [^{18}F]FDG and [^{18}F]TFB at both 40 and 90 min. Image analysis for PET/CT and TxWBS-SPECT/CT was performed with Syngo.via (Siemens Healthcare).

Biochemical Analysis

Free triiodothyronine, free thyroxine, TSH, thyroglobulin (TG), and antibodies against TG were measured on the first day before the intramuscular injection of thyrotropin alfa. Verification of stimulated TSH was performed before the application of [^{18}F]TFB and [^{131}I]iodide. Stimulated TG was measured 3 d after a second injection with thyrotropin alfa (Elecsys assays and cobas e 801 [Roche Diagnostics]; TG, assay, and high-sensitive TG Kryptor [BRAHMS GmbH; Thermo Fisher Scientific]).

Statistical Analysis

Clinical and demographic parameters are presented as total number, percentage, range, and 95% CI. The Pearson correlation coefficient (r_p) and the φ-coefficient (r_φ) were used for continuous and binary variables, respectively. Values of greater than 0.10, 0.30, and 0.50 for $|r_p|$ and $|r_\varphi|$ correspond to low, intermediate, and strong positive correlations and vice versa for negative correlations. The null hypothesis was rejected if the *P* value was less than 0.05 (2-sided). Statistical analysis was performed using SPSS Statistics version 26 (SPSS Inc.).

RESULTS

Patient-Based Analysis

A total of 26 patients who received [^{18}F]TFB PET/CT, RAI, and [^{131}I]iodine TxWBS-SPECT/CT were included in this retrospective study. The indication for high-activity RAI was imaging evidence of lymph node or distant metastases on [^{18}F]FDG PET/CT (22/26; 84.6%), ultrasound (2/26; 7.7%), MRI (1/26; 3.9%), and [^{131}I]iodine diagnostic WBS (1/26; 3.9%). Of the 22 patients with available [^{18}F]FDG PET/CT, local recurrence (3/22; 13.6%), lymph node metastases (5/22; 22.7%), lung metastases (9/22; 30.9%), bone metastases (8/22; 36.3%), or metastases to other organs (2/22; 9.1%) as well as [^{18}F]FDG-positive and -negative findings were identified. The ultrasound or MRI findings were suspected cervical lymph node metastases. Local recurrence was suspected in the patient with [^{131}I]iodine diagnostic WBS imaging.

The median time between [^{18}F]TFB PET/CT/RAI and [^{131}I]iodine TxWBS-SPECT/CT was 3.8 d (95% CI, 3.3–4.2 d). A total of 25 of 26 patients (96%) underwent [^{18}F]FDG PET/CT for suspicion of dedifferentiated disease. The median time between [^{18}F]TFB PET/CT/RAI and [^{18}F]FDG PET/CT was 32.8 d (95% CI, 18.3–47.3 d). [^{18}F]TFB-, [^{131}I]iodine-, and [^{18}F]FDG-positive lesions were seen in 11 of 26 patients (42%), 12 of 26 patients (46%), and 11 of 25 patients (42%), respectively. On a per-patient basis, cross-tabulation with the χ^2 test revealed a strong and significant correlation (r_φ) between [^{18}F]TFB and [^{131}I]iodine findings ($r_\varphi = 0.61$; $P < 0.001$; $n = 26$) and a low, nonsignificant correlation between [^{18}F]TFB and [^{18}F]FDG findings ($r_\varphi = 0.06$; $P = 0.902$; $n = 25$). A heterogeneous disease pattern is illustrated in Figure 1.

Lesion-Based Analysis

A total of 62 tracer-avid lesions were found in all imaging modalities; of these, 32 of 62 (52%) were [^{18}F]TFB positive, 30 of 62 (48%) were [^{131}I]iodine positive, and 52 of 62 (84%) were [^{18}F]FDG positive. A detailed lesion-based analysis is illustrated in Supplemental Table 1 (supplemental materials are available at http://jnm.snmjournals.org). False-positive [^{131}I]iodide uptake was confirmed in 3 of 26 patients (11%), as illustrated for 2 patients in Figure 2 and Figure 3.

Without the aforementioned false-positive [^{131}I]iodine uptake, [^{18}F]TFB PET/CT detected 5 of 62 additional lesions (8%) compared with [^{131}I]iodine imaging. Detailed findings for patients, including the description of false-positive and [^{131}I]iodine mismatch findings, are summarized in Table 2.

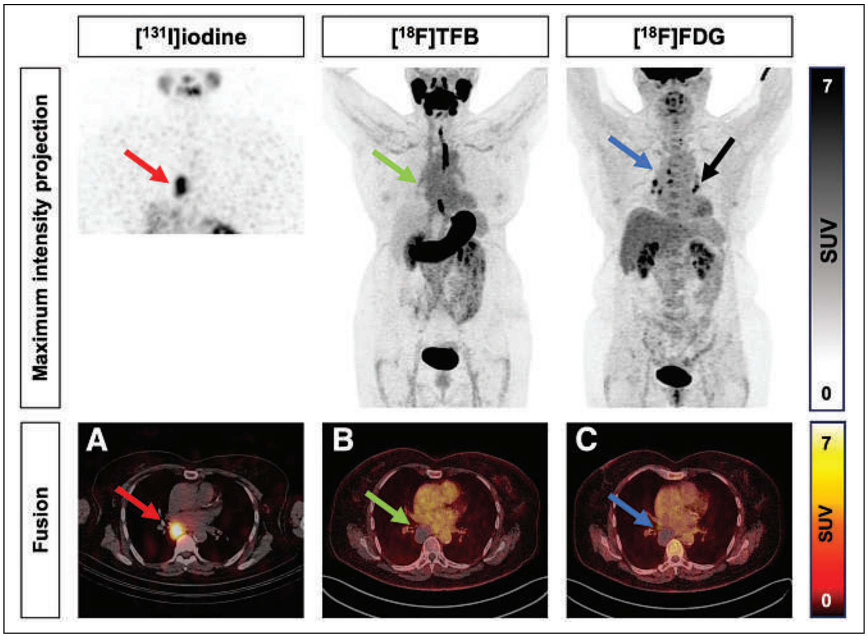

FIGURE 3. False-positive low mediastinal mass in [^{131}I]iodine SPECT/CT. 67-y-old woman with papillary thyroid cancer. Intense [^{131}I]iodine uptake in low mediastinal mass (red arrow, A) with absent uptake of [^{18}F]TFB (green arrow, B) and [^{18}F]FDG (blue arrow, C). CT scan revealed probably benign hypodense lesion. Histologic confirmation was recommended due to intense [^{131}I]iodine uptake. Samples were obtained by endobronchial ultrasound-guided transbronchial needle aspiration, which revealed benign soft-tissue cells, suggesting hemorrhagic cyst. Additionally, [^{18}F]FDG-positive (black arrow) and [^{18}F]TFB/[^{131}I]iodine–negative mediastinal lymph node metastases were visualized by maximum-intensity-projection imaging.

TABLE 2
Findings Per Patient

Patient identification	Finding	[^{18}F]TFB	[^{131}I]iodine TxWBS-SPECT/CT	[^{18}F]FDG	Dominant tumor burden
1	Cervical and mediastinal lymph nodes	N	P	P	[^{18}F]FDG
2	Lung nodules	N	N	N	N/A
3	Bone lesions and lung nodules	P	N	P	[^{18}F]FDG
4	N/A	N	N	N	N/A
5	Lung nodules	N	N	P	[^{18}F]FDG
6	Glottis and cervical lymph nodes	P	P	N	[^{18}F]TFB/[^{131}I]iodine
7	Local recurrence	P	N	P	[^{18}F]TFB
8	High mediastinal lymph nodes and low mediastinal mass	N	fP[*]	P	[^{18}F]FDG
9	Lung nodules	N	N	N	N/A
10	Local recurrence on right	P	P	N	[^{18}F]TFB/[^{131}I]iodine
11	Lung nodules	P	P	N	[^{18}F]TFB/[^{131}I]iodine
12	Lung nodules and inflammation	N	fP[†]	N	N/A
13	Lung nodules	P	P	P	[^{18}F]FDG
14	Bone lesions	P	P	P	[^{18}F]FDG
15	Local recurrence on right and bone lesions	P	P	N	[^{18}F]TFB/[^{131}I]iodine
16	N/A	N	N	N	N/A
17	Lung nodules and bone lesions	N	P	P	[^{18}F]FDG
18	Bone lesions	P	P	N	[^{18}F]TFB/[^{131}I]iodine
19	Bone lesions	P	P	N	[^{18}F]TFB
20	Lung lesions and soft-tissue lesion	N	P	P	[^{131}I]iodine
21	N/A	N	N	N	N/A
22	N/A	N	N	N	N/A
23	N/A	N	N	N/A	N/A
24	Thymus and cervical lymph nodes	N	fP[‡]	P	[^{18}F]FDG
25	Bone lesions	P	P	P	[^{18}F]TFB/[^{131}I]iodine
26	N/A	N	N	N	N/A

[*] Histologic verification: no malignancy was found in [^{131}I]iodine-positive low mediastinal mass.

[†] Primary pulmonary inflammation due to chronic obstructive pulmonary disease.

[‡] Follow-up: [^{131}I]iodine accumulation in projection onto thymus, verification by MRI.

N = negative; P = positive; N/A = not available; fP = false-positive.

[^{131}I]iodine-positive mismatch detailed patient analysis: patient 1—predominantly [^{18}F]FDG-positive (SUV$_{\text{max}}$, 8.3) tumor burden with low [^{131}I]iodine uptake in solitary mediastinal lymph node metastases; patient 17—predominantly [^{18}F]FDG-positive (SUV$_{\text{max}}$, 15.8) tumor burden with low [^{131}I]iodine uptake in solitary lung and bone metastases; patient 20—predominantly [^{18}F]FDG-positive (SUV$_{\text{max}}$, 5.2) tumor burden with intermediate [^{131}I]iodine uptake in solitary soft-tissue metastasis.

Quantitative Analysis of Lesion Differentiation

The SUV$_{\text{max}}$ was measured in all suspected lesions ($n = 62$) to evaluate [^{18}F]TFB uptake as a potential surrogate marker of differentiation. The SUV$_{\text{max}}$ of [^{18}F]TFB was lower and inverse compared with that of [^{18}F]FDG (3.97 [95% CI, 3.1–4.9] vs. 6.23 [95% CI, 5.9–9.1]; $P < 0.001$). The SUV$_{\text{max}}$ of [^{18}F]TFB and [^{18}F]FDG showed a statistically significant, intermediate negative correlation ($r_p = -0.26$; $P = 0.041$; $n = 62$) (Fig. 4).

Comparison of [^{18}F]TFB PET/CT Acquisition Time Points

Whole-body static imaging was performed 40 and 90 min after [^{18}F]TFB administration ($n = 23$; 88%; 49 lesions) to evaluate the tracer kinetics. The SUV$_{\text{max}}$ of suspected lesions declined from the 40-min to the 90-min time point (4.18 [95% CI, 3.1–5.3] vs. 3.9 [95% CI, 2.8–4.9]). The Pearson coefficient showed a highly significant, strong linear correlation between both time points ($r_p = 0.94$; $P < 0.001$; $n = 49$) (Supplemental Fig. 1). Also, there was a highly significant, strong linear correlation between the 40-min and 90-min time points for normalized lesion uptake: blood-pool TBR ($r_p = 0.88$; $P < 0.001$), muscle TBR ($r_p = 0.91$; $P < 0.001$), and lung TBR ($r_p = 0.90$; $P < 0.001$). Detailed results of quantification of [^{18}F]TFB PET at 40 and 90 min after injection are illustrated in Supplemental Table 2.

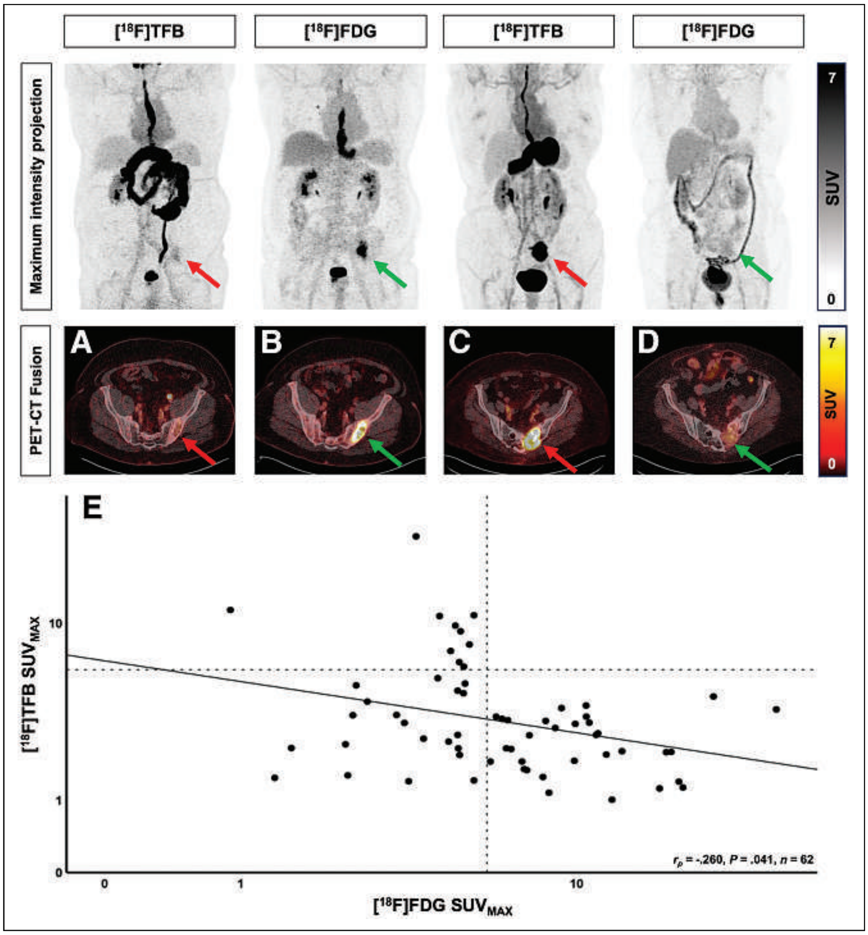

FIGURE 4. Lesion [^{18}F]TFB vs. [^{18}F]FDG uptake. 70-y-old man with follicular thyroid carcinoma and singular bone metastasis in left ilium. Dedifferentiation was demonstrated with low [^{18}F]TFB uptake (A) and intense [^{18}F]FDG uptake (B). 75-y-old woman with follicular thyroid carcinoma and singular differentiated bone metastasis in left-side sacrum. High NIS expression was demonstrated with intense [^{18}F]TFB uptake (C) and low [^{18}F]FDG uptake (D). (E) Inverse Pearson correlation representing significant inverse relationship between NIS expression (differentiation) and glucose consumption ([^{18}F]FDG) in lesion SUV$_{max}$ of [^{18}F]TFB and [^{18}F]FDG.

DISCUSSION

Despite multiple imaging options, accurate diagnosis of recurrent DTC remains challenging (*19*). Appropriate therapeutic decisions are especially difficult to make in cases of incipient dedifferentiation or TENIS syndrome (*20,21*). Here, 26 patients who received [^{18}F]TFB PET/CT and [^{131}I]iodine TxWBS-SPECT/CT have been analyzed. The detection rate of both tracers was relatively similar, but slightly more lesions could be identified positive on [^{18}F]TFB PET/CT. This indicates that [^{18}F]TFB PET/CT might help in the selection of DTC patients for RAI.

[^{131}I]iodine diagnostic WBS with SPECT/CT was clearly inferior to [^{18}F]TFB PET/CT in our previous study (*12*). In contrast, [^{131}I]iodine TxWBS-SPECT/CT is an excellent imaging modality and has previously not been compared with [^{18}F]TFB-based imaging (*22*). However, patients are exposed to significantly higher radiation levels from [^{131}I]iodine, and WBS-SPECT/CT has limited spatial resolution (*23*). Moreover, RAI has a variety of dose-dependent acute and long-term side effects, like adverse effects on the salivary and lacrimal glands up to secondary malignancies after repeated high activity of RAI (*24,25*). Also, it is well known that with increasing [^{131}I]iodine activity, more nontumor-related accumulations occur (*26,27*). These false-positive findings may lead to unnecessary further invasive procedures as biopsies (Fig. 3). In contrast, lesions with false-positive [^{131}I]iodine uptake did not show increased uptake of [^{18}F]TFB in our cohort. Considering the detection rates and correct identification of false-positive [^{131}I]iodine uptake by [^{18}F]TFB, we see great potential in the implementation of [^{18}F]TFB PET in the clinical routine before RAI for optimal treatment planning and decision making in recurrent DTC.

Several genetic alterations leading to decreased expression of NIS are the major contributors to RRDTC (*28*). The decrease in iodine uptake is often correlated with an increase in glucose metabolism, thereby providing a rationale for the higher sensitivity of [^{18}F]FDG PET/CT in dedifferentiated disease (*16*). We show here for the first time that the lesion differentiation can be quantified using [^{18}F]TFB and [^{18}F]FDG PET/CT with a significant inverse correlation between [^{18}F]TFB and [^{18}F]FDG uptake. This has previously been demonstrated for [^{124}I]iodine and [^{18}F]FDG PET/CT (*29*). However, [^{124}I]iodine imaging is only available at a few centers and has many disadvantages in clinical practice (*5*) like high-energy γ-rays degrading spatial resolution and a long half-life of 4.2 d resulting in higher radiation exposure (*30*). In contrast, [^{18}F]TFB is easy to synthesize in any cyclotron-based radiochemistry and has favorable physical properties for PET imaging (*13,31*). The presented data underscores the complexity and heterogeneity of advanced disease in DTC and RRDTC. In particular, TENIS syndrome or dedifferentiation complicates clinical routine and the use of [^{18}F]TFB and [^{18}F]FDG may establish a new differentiation/dedifferentiation score in DTC.

The biodistribution and kinetics of [^{18}F]TFB have already been investigated using dynamic whole-body imaging in healthy adults. The results showed a rapid blood clearance and a good background-to-target ratio of NIS-expressing organs after 30–45 min (*10*). However, studies illustrating the biodistribution of recurrent DTC metastases are still lacking (*32*). In the presented study, between 40 and 90 min after injection, maximum TBR values showed a decreasing trend and a significant correlation. This result may simply reflect washout due to nontrapping/nonmetabolization of [^{18}F]TFB. Like [^{99m}Tc]TcO$_4^-$, [^{18}F]TFB is rapidly taken up by the NIS and concentrated in the cell, but it is not metabolized like radioactive iodine (*31*). Therefore, imaging at a later time point does not appear to be useful or necessary for the detection of DTC lesions.

The present study has some limitations due to its retrospective design and small patient cohort. Due to the heterogeneous disease pattern of recurrent DTC, there were many patients with partially dedifferentiated disease and therefore fewer pure [^{18}F]TFB- or [^{131}I]iodine-positive findings. Prospective studies in predefined patient cohorts are needed to define the role of [^{18}F]TFB PET in recurrent DTC compared with [^{131}I]iodine imaging and [^{18}F]FDG PET. Change in management due to [^{18}F]TFB PET is another point to be addressed needing consistent follow-up and prospective datasets. Thus, to identify potential false-positive enrichments and pitfalls. Response per lesion was not feasible as RRDTC patients undergo different non-RAI therapies in further follow-up.

CONCLUSION

[^{18}F]TFB PET might offer a noninferior diagnostic performance compared with [^{131}I]iodine imaging with therapeutic activities. Together with [^{18}F]FDG PET, [^{18}F]TFB PET might establish a new quantitative measure of differentiation/dedifferentiation for optimal therapeutic management of recurrent DTC with suspicion of dedifferentiation. Further prospective studies on the clinical implementation of [^{18}F]TFB are warranted.

DISCLOSURE

Robert Seifert received research support from Boehringer Ingelheim Fonds and Else Kröner-Fresenius-Stiftung. Philipp Schindler and Wolfgang Roll received funding from the Maria-Möller-Stiftung. No other potential conflict of interest relevant to this article was reported.

ACKNOWLEDGMENT

We thank the staff of the Department of Nuclear Medicine of the University Hospital Münster.

KEY POINTS

QUESTION: Does [^{18}F]TFB PET/CT provide detection rates in patients with recurrent DTC similar to those provided by the gold standard [^{131}I]iodine WBS-SPECT/CT at therapeutic doses?

PERTINENT FINDINGS: The detection rate of [^{18}F]TFB PET/CT in recurrent DTC is comparable to that of [^{131}I]iodine WBS-SPECT/CT, with fewer false-positive lesions. [^{18}F]FDG PET is recommended as an additional imaging tool to detect dedifferentiation of tumor lesions.

IMPLICATIONS FOR PATIENT CARE: The pretherapeutic use of [^{18}F]TFB PET before radioactive iodine therapy may guide the use of high-dose treatment in patients with recurrent DTC.

REFERENCES

1. Jung CK, Bychkov A, Kakudo K. Update from the 2022 World Health Organization Classification of Thyroid Tumors: a standardized diagnostic approach. *Endocrinol Metab (Seoul).* 2022;37:703–718.
2. Lim H, Devesa SS, Sosa JA, Check D, Kitahara CM. Trends in thyroid cancer incidence and mortality in the United States, 1974-2013. *JAMA.* 2017;317:1338–1348.
3. Schmidbauer B, Menhart K, Hellwig D, Grosse J. Differentiated thyroid cancer-treatment: state of the art. *Int J Mol Sci.* 2017;18:1292.
4. Liu J, Liu Y, Lin Y, Liang J. Radioactive iodine-refractory differentiated thyroid cancer and redifferentiation therapy. *Endocrinol Metab (Seoul).* 2019;34:215–225.
5. Haugen BR, Alexander EK, Bible KC, et al. 2015 American Thyroid Association management guidelines for adult patients with thyroid nodules and differentiated thyroid cancer: the American Thyroid Association Guidelines Task Force on Thyroid Nodules and Differentiated Thyroid Cancer. *Thyroid.* 2016;26:1–133.
6. Schlumberger M, Leboulleux S. Current practice in patients with differentiated thyroid cancer. *Nat Rev Endocrinol.* 2021;17:176–188.
7. Khoo ACH, Fong LY, Hamzah F. A review of TENIS syndrome in Hospital Pulau Pinang. *Indian J Nucl Med.* 2018;33:284–289.
8. Hicks RJ, Hofman MS. Is there still a role for SPECT-CT in oncology in the PET-CT era? *Nat Rev Clin Oncol.* 2012;9:712–720.
9. Herzog H, Tellmann L, Scholten B, Coenen HH, Qaim SM. PET imaging problems with the non-standard positron emitters yttrium-86 and iodine-124. *Q J Nucl Med Mol Imaging.* 2008;52:159–165.
10. Jiang H, Schmit NR, Koenen AR, et al. Safety, pharmacokinetics, metabolism and radiation dosimetry of ^{18}F-tetrafluoroborate (^{18}F-TFB) in healthy human subjects. *EJNMMI Res.* 2017;7:90.
11. Samnick S, Al-Momani E, Schmid JS, Mottok A, Buck AK, Lapa C. Initial clinical investigation of [^{18}F]tetrafluoroborate PET/CT in comparison to [^{124}I]iodine PET/CT for imaging thyroid cancer. *Clin Nucl Med.* 2018;43:162–167.
12. Dittmann M, Gonzalez Carvalho JM, Rahbar K, et al. Incremental diagnostic value of [^{18}F]tetrafluoroborate PET-CT compared to [^{131}I]iodine scintigraphy in recurrent differentiated thyroid cancer. *Eur J Nucl Med Mol Imaging.* 2020;47:2639–2646.
13. Verburg FA, Giovanella L, Hoffmann M, et al. New F-18-based PET/CT for sodium-iodine-symporter-targeted imaging. *Eur J Nucl Med Mol Imaging.* 2020; 47:2484–2486.
14. Isoda T, BaBa S, Maruoka Y, et al. Impact of patient age on the iodine/FDG “flip-flop” phenomenon in lung metastasis from thyroid cancer. *Ann Nucl Med.* 2016;30:518–524.
15. Duarte PS, Marin JFG, De Carvalho JWDA, Sapienza MT, Buchpiguel CA. Iodine/FDG “flip-flop” phenomenon inside a large metastatic thyroid cancer lesion better characterized on SPECT/CT and PET/CT studies. *Clin Nucl Med.* 2018;43: 436–438.
16. Riemann B, Uhrhan K, Dietlein M, et al. Diagnostic value and therapeutic impact of ^{18}F-FDG-PET/CT in differentiated thyroid cancer. results of a German multicentre study. *Nuklearmedizin.* 2013;52:1–6.
17. Meric K, Killeen RP, Abi-Ghanem AS, et al. The use of ^{18}F-FDG PET ratios in the differential diagnosis of common malignant brain tumors. *Clin Imaging.* 2015; 39:970–974.
18. Hofman MS, Hicks RJ. How we read oncologic FDG PET/CT. *Cancer Imaging.* 2016;16:35.
19. Brauckhoff K, Biermann M. Multimodal imaging of thyroid cancer. *Curr Opin Endocrinol Diabetes Obes.* 2020;27:335–344.
20. Sacks W, Braunstein GD. Evolving approaches in managing radioactive iodine-refractory differentiated thyroid cancer. *Endocr Pract.* 2014;20:263–275.
21. Silberstein EB. The problem of the patient with thyroglobulin elevation but negative iodine scintigraphy: the TENIS syndrome. *Semin Nucl Med.* 2011;41:113–120.
22. Xue YL, Qiu ZL, Song HJ, Luo QY. Value of ^{131}I SPECT/CT for the evaluation of differentiated thyroid cancer: a systematic review of the literature. *Eur J Nucl Med Mol Imaging.* 2013;40:768–778.
23. Ahmadi S, Coleman A, de Morais NS, et al. Clinical experience following implementation of routine SPECT-CT imaging following 131-iodine administration for thyroid cancer. *Endocr Connect.* 2022;11:e210371.
24. Lang BHH, Wong IOL, Wong KP, Cowling BJ, Wan KY. Risk of second primary malignancy in differentiated thyroid carcinoma treated with radioactive iodine therapy. *Surgery.* 2012;151:844–850.
25. Yu CY, Saeed O, Goldberg AS, et al. A systematic review and meta-analysis of subsequent malignant neoplasm risk after radioactive iodine treatment of thyroid cancer. *Thyroid.* 2018;28:1662–1673.
26. Oral A, Yazıcı B, Eraslan C, Burak Z. Unexpected false-positive I-131 uptake in patients with differentiated thyroid carcinoma. *Mol Imaging Radionucl Ther.* 2018;27:99–106.
27. Barbaro D, Campennì A, Forleo R, Lapi P. False-positive radioiodine uptake after radioiodine treatment in differentiated thyroid cancer. *Endocrine.* 2023;81:30–35.
28. Oh JM, Ahn BC. Molecular mechanisms of radioactive iodine refractoriness in differentiated thyroid cancer: impaired sodium iodide symporter (NIS) expression owing to altered signaling pathway activity and intracellular localization of NIS. *Theranostics.* 2021;11:6251–6277.
29. Grabellus F, Nagarajah J, Bockisch A, Schmid KW, Sheu SY. Glucose transporter 1 expression, tumor proliferation, and iodine/glucose uptake in thyroid cancer with emphasis on poorly differentiated thyroid carcinoma. *Clin Nucl Med.* 2012;37: 121–127.
30. Zampella E, Klain M, Pace L, Cuocolo A. PET/CT in the management of differentiated thyroid cancer. *Diagn Interv Imaging.* 2021;102:515–523.
31. Jiang H, DeGrado TR. [^{18}F]tetrafluoroborate ([^{18}F]TFB) and its analogs for PET imaging of the sodium/iodide symporter. *Theranostics.* 2018;8:3918–3931.
32. O’Doherty J, Jauregui-Osoro M, Brothwood T, et al. ^{18}F-tetrafluoroborate (^{18}F-TFB), a PET probe for imaging sodium-iodide symporter expression: whole-body biodistribution, safety, and radiation dosimetry in thyroid cancer patients. *J Nucl Med.* 2017;58:1666–1671.
33. Brierley J, Gospodarowicz MD, Wittekind CT. *TNM Classification of Malignant Tumors International Union Against Cancer.* 8th ed. Wiley; 2017:57–62.

Initial Experience with ^{68}Ga-FAP-2286 PET Imaging in Patients with Urothelial Cancer

Vadim S. Koshkin*[1,3], Vipul Kumar*[1], Brad Kline[2], Domenique Escobar[4], Maya Aslam[2], Matthew R. Cooperberg[4], Rahul R. Aggarwal[1,3], Ivan de Kouchkovsky[1,3], Jonathan Chou[1,3], Maxwell V. Meng[4], Terence Friedlander[1,3], Sima Porten[3,4], and Thomas A. Hope[2,3]

[1]Division of Hematology/Oncology, Department of Medicine, University of California San Francisco, San Francisco, California; [2]Department of Radiology and Biomedical Imaging, University of California San Francisco, San Francisco, California; [3]Helen Diller Family Comprehensive Cancer Center, University of California San Francisco, San Francisco, California; and [4]Department of Urology, University of California San Francisco, San Francisco, California

Improved imaging modalities are needed to accurately stage patients with muscle-invasive bladder cancer (MIBC) and metastatic urothelial carcinoma. Imaging with small-molecule ligands or inhibitors of fibroblast activation protein (FAP) is a promising modality that has demonstrated initial efficacy across a broad range of tumors. We present our experience with the novel FAP-peptide binder ^{68}Ga-FAP-2286 in patients with MIBC. **Methods:** Patients with histopathologically confirmed bladder cancer who had either localized disease at diagnosis (localized cohort, $n = 13$) or known metastatic disease (metastatic cohort, $n = 8$) were imaged with ^{68}Ga-FAP-2286 PET as part of a clinical trial (NCT04621435). The SUV$_{\text{max}}$ of ^{68}Ga-FAP-2286 PET–positive lesions and lesion size were documented. In patients who had available ^{18}F-FDG PET performed within 45 d of ^{68}Ga-FAP-2286 PET ($n = 5$), uptake on the 2 scans was compared. When there was a discrepancy between imaging modalities on retrospective review, biopsy of suggestive lesions was performed as the standard of care. **Results:** In the metastatic and localized cohorts, 36 and 18 ^{68}Ga-FAP-2286–avid lesions, respectively, were identified across multiple anatomic locations, including lymph nodes, visceral metastases, and bones. Fourteen of 36 lesions in the metastatic cohort and 14 of 18 lesions in the localized cohort were lymph nodes measuring less than 1 cm. Among lesions measuring less than 0.5 cm, 0.5–1 cm, and more than 1 cm, average SUV$_{\text{max}}$ was 5.2 ± 2.6, 9.6 ± 3.7, and 13.0 ± 4.3, respectively, in the metastatic cohort and 10.5 ± 5.1, 10.8 ± 5.7, and 9.9 ± 5.4, respectively, in the localized cohort. Five patients had ^{18}F-FDG PET available for comparison. The average SUV$_{\text{max}}$ for lesions avid on ^{68}Ga-FAP-2286 PET and ^{18}F-FDG PET was 9.9 ± 3.4 versus 4.2 ± 1.9, respectively ($n = 16$ lesions). For 3 patients in the localized cohort, ^{68}Ga-FAP-2286 PET informed clinical management, including identification of both false-positive findings on ^{18}F-FDG PET and false-negative findings on conventional CT. **Conclusion:** ^{68}Ga-FAP-2286 imaging is highly sensitive in patients with urothelial cancer and is effective in identifying metastatic lesions across a variety of anatomic sites, including subcentimeter lymph nodes that would not have raised suspicion on conventional scans. This novel imaging modality may inform clinical decision-making in patients with MIBC both by refining local nodal staging and by defining metastatic disease that would otherwise be undetectable on conventional imaging.

Key Words: FAP; bladder cancer; PET imaging

J Nucl Med 2024; 65:199–205
DOI: 10.2967/jnumed.123.266390

Bladder cancer is an aggressive and potentially life-threatening disease. At diagnosis, most cases (~75%) are identified as non–muscle-invasive (non-MIBC) which can be treated with intravesical treatments alone such as *Bacillus* Calmette–Guérin intravesical therapy. Although the response rate to *Bacillus* Calmette–Guérin therapy is high, many patients experience recurrence in the first 5 y (*1*). Additionally, a significant fraction (~20%) has MIBC at diagnosis, and 5%–10% present with de novo metastatic disease (*2*). The standard-of-care treatment for localized MIBC is neoadjuvant cisplatin-based chemotherapy followed by radical cystectomy with curative intent (*3*). In those who are not candidates for cystectomy, a combination of maximal resection, chemotherapy, and localized radiation can also be used. Among several key prognostic factors, involvement of regional lymph nodes portends inferior outcomes, including decreased overall survival (*4*). Thus, to aid in treatment planning with either approach, as well as possible adjuvant therapy after treatment, timely and accurate nodal staging and identification of any metastatic lesions are critical.

Currently accepted imaging modalities (i.e., conventional imaging) for staging rely on size criteria or metabolic activity for accurate staging and include contrast-enhanced CT of the chest, abdomen, and pelvis; contrast-enhanced MRI of the abdomen and pelvis; and ^{18}F-FDG PET. The criteria for identifying malignant lymph nodes in pelvic tumors are an active area of discussion and investigation. For example, on the basis of the widely used RECIST, lymph nodes can be deemed as malignant (target lesions) at initial staging if they measure more than 1.5 cm in the short axis, irrespective of tumor type or anatomic location (*5*). However, anatomic location and tumor type likely influence whether a node is involved by tumor. In this context, it is increasingly appreciated that pelvic lymph nodes across multiple tumor types, such as rectal cancer and MIBC, may contain malignancy despite measuring less than 1 cm (*6*). Accordingly, conventional scans are estimated to have approximately 50% sensitivity to accurately define nodal disease in MIBC (*7*). To obviate the limitations of using size-based criteria alone, ^{18}F-FDG PET has also been evaluated for initial staging of MIBC. However, sensitivity estimates for ^{18}F-FDG PET remain at approximately 50% (*7–9*). Because of physiologic ^{18}F-FDG

Received Aug. 24, 2023; revision accepted Nov. 7, 2023.

For correspondence or reprints, contact Vadim S. Koshkin (vadim.koshkin@ucsf.edu).

*Contributed equally to this work.

excretion in urine, ^{18}F-FDG PET provides limited information about tumors within the urinary tract. Thus, there is a critical need for improved imaging modalities in patients with MIBC (*7*).

Fibroblast activation protein (FAP) is a transmembrane serine protease that is overexpressed on cancer-associated fibroblasts that are present in the microenvironment of diverse tumor types of epithelial, mesenchymal, and even lymphoid origin (*10–12*). Expression of FAP appears to be specific to cancer-associated fibroblasts, as well as a subset of fibroblasts involved in wound healing and potentially inflammatory states (*11*,*12*). Thus, FAP is an attractive pan-cancer target for both diagnostic and therapeutic applications.

Several classes of FAP-targeting molecules, including small-molecule inhibitors (FAPIs) and peptide binders, are being developed for this purpose. The FAPI family of compounds has been the best studied and has identified lesions associated with diverse epithelium-based tumors (*13*,*14*). The cyclic peptide binder FAP-2286 was recently developed to improve tumor residence time relative to FAPI (*15*). First-in-humans diagnostic studies of FAP-2286 have shown preliminary efficacy in staging multiple tumor types, including head-and-neck, gastric, and pancreatic cancers (*16*). Therapeutically, the LUMIERE trial (NCT04939610) is currently testing application of ^{177}Lu-FAP-2286 in patients with various solid tumors, with no dose-limiting toxicities or serious adverse advents observed and a partial response noted in at least 1 enrolled patient (*17*).

Immunohistochemical studies have revealed high expression of FAP in urothelial carcinomas (*18*), with minimal expression in normal urothelium and stroma and generally high signal-to-background expression, suggesting potential diagnostic efficacy of FAP-based imaging in MIBC and metastatic urothelial carcinoma. Two initial studies showed that FAPI-46 and FAPI-04 could accurately identify bladder cancer metastases (*19*,*20*). Therefore, in this study, we investigated the ability of ^{68}Ga-FAP-2286 to stage MIBC.

MATERIALS AND METHODS

Study Design

This is a report on a subset of patients with solid tumors prospectively enrolled in a single-arm trial (NCT04621435) evaluating the efficacy and safety of ^{68}Ga-FAP-2286 PET from December 2020 to February 2023. This study was approved by the University of California San Francisco institutional review board, and all patients provided written informed consent. The main eligibility criteria were an age of at least 18 y, histopathologically confirmed solid tumors, and conventional imaging within 8 wk of ^{68}Ga-FAP-2286 PET. The cohorts reported for this study include patients with metastatic, RECIST (version 1.1)-measurable disease (metastatic cohort) and patients with localized invasive bladder cancer without RECIST-measurable disease (localized cohort). Two patients with known metastatic disease before enrollment in the study were without RECIST-measurable disease at the time of imaging because of prior systemic treatment; these patients were assigned to the metastatic cohort. One patient had high-grade T1 disease with ^{18}F-FDG PET–avid nodes clinically suggesting at least muscle-invasive disease; this patient underwent ^{68}Ga-FAP-2286 PET despite noninvasive disease (case 2 in "Impact on Clinical Management"). The histology of the primary tumor was based on the dominant histologic pattern (e.g., >50%) of the tumor as determined by board-certified pathologists.

Imaging Protocol

All patients underwent ^{68}Ga-FAP-2286 PET. Radiosynthesis was conducted in an iQS ^{68}Ga fluidic labeling module and cassette (ITM Pharma Solutions GmbH). The precursor, FAP-2286, was provided by Clovis Oncology, Inc. ^{68}Ga was eluted from a ^{68}Ge/^{68}Ga generator (Galliapharm; Eckert and Ziegler). Radiolabeling was performed at 120°C for 10 min. The injected activity ranged from 111 to 296 MBq (3–8 mCi), and the patients received a mean of 219.04 ± 51.8 MBq (5.92 ± 1.4 mCi). The target uptake period was 60 min (allowed range, 50–100 min), and image acquisition began at a mean of 106 ± 26 min after injection. Patients were imaged using either PET/CT (16 patients) or PET/MRI (5 patients). For PET/CT, a unenhanced diagnostic CT scan with 5-mm slice thickness was performed. For PET/MRI, abbreviated pelvic PET/MRI was followed by whole-body MRI. Whole-body PET images were acquired from pelvis to vertex. All PET images were corrected for attenuation, dead time, random events, and scatter.

Image Interpretation

All images were interpreted by a board-certified nuclear medicine physician. Uptake was considered positive if it was 1.5 times higher than blood pool activity in the mediastinum and not due to known physiologic causes. Because of physiologic excretion of the radiotracer in the bladder, lesions outside the primary bladder tumor were selected for further analysis. Up to 5 lesions per patient were included for analysis. For each lesion, the SUV$_{max}$, short-axis diameter of lymph nodes, and long-axis diameter of soft-tissue lesions were measured. In patients (n = 5) who underwent ^{18}F-FDG PET within 45 d of ^{68}Ga-FAP-2286 PET, paired SUV$_{max}$ was measured on the ^{18}F-FDG PET images.

Change in Management

In the localized cohort, a post hoc analysis of each patient was performed to assess for the potential impact of ^{68}Ga-FAP-2286 PET on clinical management. Patients were categorized as those for whom ^{68}Ga-FAP-2286 PET was concordant with conventional imaging, those for whom ^{68}Ga-FAP-2286 PET was discordant with conventional imaging but did not alter clinical management, or those for whom ^{68}Ga-FAP-2286 PET was discordant with conventional imaging and altered clinical management. When suggestive lesions were identified either on conventional imaging or on ^{68}Ga-FAP-2286 PET and biopsy would influence treatment planning, biopsy was performed as the standard of care to evaluate the presence of malignancy.

Statistical Analysis

Statistical analysis was performed using GraphPad Prism software, version 9.0. For analyses comparing SUV$_{max}$ across different lesion sizes within either the localized or the metastatic cohort, 1-way ANOVA with a Tukey posttest was performed. For analyses of paired SUV$_{max}$ obtained from ^{68}Ga-FAP-2286 PET versus ^{18}F-FDG PET, a paired t test was performed.

RESULTS

Eight patients were enrolled in the metastatic cohort and 13 in the localized cohort. All had tumors with a urothelium-predominant histology (>50% urothelial) (Tables 1 and 2).

Metastatic Cohort

To assess the feasibility of ^{68}Ga-FAP-2286 PET for identifying bladder cancer lesions as a proof of concept, we first evaluated avidity in the metastatic cohort. All 8 patients had at least 3 and at most 5 ^{68}Ga-FAP-2286–avid lesions. In total, 36 ^{68}Ga-FAP-2286–avid lesions were identified in various anatomic locations ranging from lymph nodes to visceral metastases (Fig. 1A). Notably, in addition to RECIST-measurable disease obtained on conventional imaging, 14 of 36 ^{68}Ga-FAP-2286–avid lesions measured less than 1 cm, including 12 lymph nodes, 1 lung metastasis, and 1

TABLE 1
Clinical Features of Metastatic Cohort

Parameter	Data
Sex	
Male	7
Female	1
Age	72.5 (68–87)
Primary site of disease	
Bladder	6
Upper tract	2
Race	
White	3
Hispanic	1
Asian	4
Prior definitive treatment	
Nephroureterectomy	2
Cystectomy	5
Systemic treatments before/at time of scan	
Chemotherapy	8
Immune checkpoint inhibitors	7
Antibody–drug conjugate	4
Histologic subtype	
Urothelium-predominant	8
Variant histology	0
Metastatic site	
Lymph node only	3
Any visceral disease (not lymph nodes only)	4
Bones	4
Liver	1
Concurrent ^{18}F-FDG PET available	3

Qualitative data are number (*n* = 8 patients total); continuous data are median and range.

TABLE 2
Clinical Features of Localized Cohort

Parameter	Data
Sex	
Male	12
Female	1
Age (y)	67 (28–90)
Race	
White	12
Asian	1
Clinical stage (conventional imaging)	
cT2N0	11
cT2N1	1
cT1Nx	1
Treatment before scan	
Neoadjuvant chemotherapy	6
Bacillus Calmette–Guérin	5
Neoadjuvant immune checkpoint inhibition	2
Treatment after scan	
Cystectomy	7
Trimodality therapy (maximal resection, chemotherapy, and localized radiation)	2
Bacillus Calmette–Guérin treatment	1
Immune checkpoint inhibitor	3
Histologic subtype	
Urothelium-predominant	13
Variant histology	0
Concurrent ^{18}F-FDG PET available	2

Qualitative data are number (*n* = 13 patients total); continuous data are median and range.

osseous metastasis. Among these, 5 measured less than 0.5 cm. The average SUV$_{max}$ in lesions measuring less than 0.5 cm, 0.5–1 cm, and more than 1 cm was 5.2 ± 2.6, 9.6 ± 3.7, and 13.0 ± 4.3, respectively, compared with an average blood pool SUV$_{max}$ of 1.4 ± 0.06. Moreover, the average SUV$_{max}$ of lesions smaller than 0.5 cm was significantly lower than those larger than 1 cm ($P = 0.001$; Fig. 1A).

Localized Cohort

Of the 13 patients with localized disease at initial staging, 7 had a total of 18 ^{68}Ga-FAP-2286–avid lesions (range, 1–5 lesions per patient). Almost all ^{68}Ga-FAP-2286–avid lesions (17/18, 94%) were lymph nodes, with 1 remaining lesion a possible perineal metastasis (biopsy not performed). Similar to findings in the metastatic cohort, ^{68}Ga-FAP-2286 PET detected subcentimeter lymph nodes (14/18 total lesions), including 4 of 18 lymph nodes measuring less than 0.5 cm. For lesions measuring less than 0.5 cm, 0.5–1.0 cm, and more than 1 cm, the average SUV$_{max}$ was 10.5 ± 5.1, 10.8 ± 5.7, and 9.9 ± 5.4, respectively. The average SUV$_{max}$ in lesions less than 0.5 cm did not significantly differ from that in lesions measuring 0.5–1 cm or more than 1 cm ($P = 0.995$ and 0.986, respectively; Fig. 1B).

Six of 7 patients with ^{68}Ga-FAP-2286–avid lesions underwent standard-of-care biopsy of at least 1 of the lymph nodes, either as part of standard lymph node dissection during cystectomy or for biopsy of a suggestive lesion (case 1 in "Impact on Clinical Management"). Of the 7 patients, malignancy was present in at least 1 of the lymph nodes in 4 patients; in the 3 remaining patients, 1 patient underwent maximal resection, chemotherapy, and localized radiation (and therefore no pelvic lymph node sampling), and 2 patients had ypT0N0 pathology in the postcystectomy specimens. The patients who were to receive neoadjuvant therapy underwent ^{68}Ga-FAP-2286 PET before that therapy.

^{68}Ga-FAP-2286 PET Versus ^{18}F-FDG PET

Across both cohorts, 5 total patients (3 from the metastatic cohort and 2 from the localized cohort) had paired ^{18}F-FDG PET available for comparison. In these patients, all 16 ^{68}Ga-FAP-2286–avid lesions were also ^{18}F-FDG–avid. The average SUV$_{max}$ for ^{68}Ga-FAP-2286–avid lesions was 9.9 ± 3.4, which was

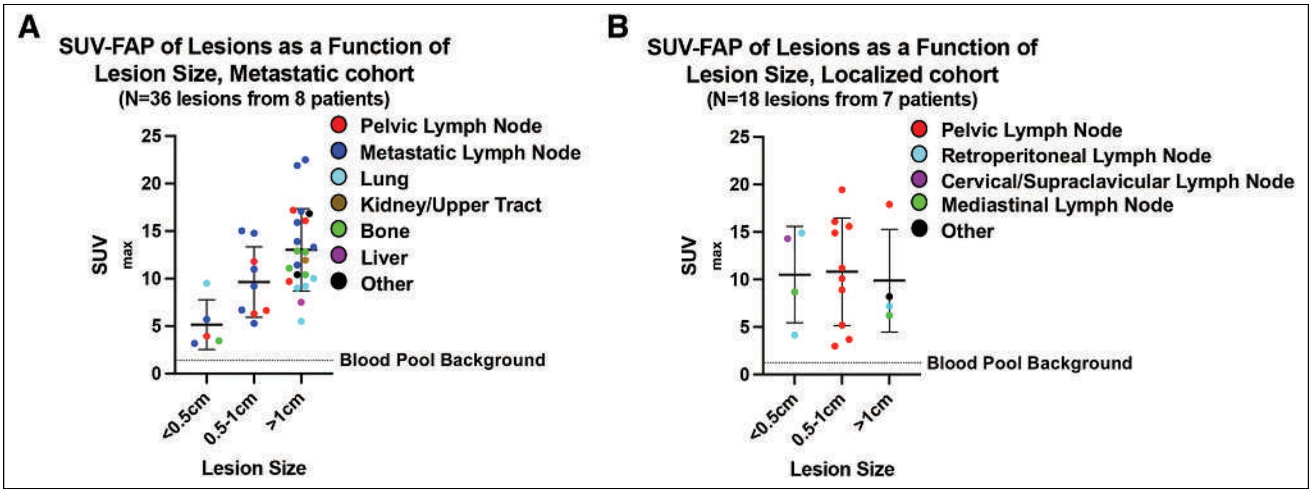

FIGURE 1. SUV_{max} of lesions in patients undergoing ^{68}Ga-FAP-2286 PET. Lesions beyond bladder identified by ^{68}Ga-FAP-2286 PET were categorized by size (<0.5, 0.5–1, and >1 cm) and are displayed for metastatic cohort (A) and localized cohort (B). Anatomic locations of lesions, including lymph nodes measuring <1 cm, are color-coded by location. Dotted line indicates blood pool background SUV averaged across all patients in cohort. Means and SDs are plotted. For metastatic cohort, range of lesion sizes was 0.3–5.5 cm; for localized cohort, range was 0.4–1.2 cm. Anatomic locations for "other" were abdominal wall (SUV, 16.8) and chest wall (SUV, 10.4) for metastatic cohort and perineum (SUV, 8.2) for localized cohort. SUV_{mean} differed significantly between lesions measuring <0.5 cm and >1 cm ($P = 0.001$) in metastatic cohort. Otherwise, there was no statistically significant difference between SUV_{mean} across different size subsets in either cohort. Of 13 patients in localized cohort, only 7 had ^{68}Ga-FAP-2286–avid lesions.

significantly greater than the average SUV_{max} of ^{18}F-FDG PET–avid lesions, 4.2 ± 1.9 ($P < 0.0001$) (Fig. 2). Of 16 total lesions, 1 (located in the lung) had higher uptake on ^{18}F-FDG PET, whereas the remainder had higher uptake on ^{68}Ga-FAP-2286 PET. In 1 case, a patient had indeterminate pelvic nodes on ^{18}F-FDG PET that were negative on ^{68}Ga-FAP-2286 PET; at the time of surgery, the nodes were negative for malignancy (Supplemental Fig. 1; supplemental materials are available at http://jnm.snmjournals.org).

Impact on Clinical Management

We performed a post hoc analysis to assess the concordance of ^{68}Ga-FAP-2286 PET with conventional imaging in the localized cohort and ascertain potential clinical implications. Among the 13 patients, ^{68}Ga-FAP-2286 PET was concordant with conventional imaging in 5, nonconcordant with conventional imaging but did not change management in 5, and nonconcordant with conventional imaging but did change clinical management in 3. We describe these 3 cases below.

Case 1. A 76-y-old man presented with clinically localized disease based on conventional imaging (Fig. 3). CT did not demonstrate enlarged lymph nodes, and the patient was originally scheduled for a radical cystectomy. ^{68}Ga-FAP-2286 PET demonstrated numerous avid nodes (SUV_{max} and size of detected lymph nodes: 16.1 and 0.6 cm, respectively) extending to the left supraclavicular region, suggesting metastatic disease. Biopsy of the left supraclavicular node confirmed the presence of metastatic urothelial cancer. Radical cystectomy was deferred, and the patient was instead referred for systemic therapy to treat metastatic disease.

Case 2. A 28-y-old man presented with a history of high-volume, rapidly recurrent, high-grade T1 bladder cancer (high-risk non-MIBC) with 6- to 7-mm pelvic lymph nodes identified on CT urography but with otherwise presumed organ-confined disease (Fig. 4). He had undergone intravesical *Bacillus* Calmette–Guérin treatment 2 mo before the scans. ^{18}F-FDG PET demonstrated uptake in these nodes, raising suspicion of muscle-invasive disease and nodal metastasis. ^{68}Ga-FAP-2286 PET, however, showed no uptake in these lymph nodes, raising the possibility that this uptake on ^{18}F-FDG PET was false-positive. The patient underwent excisional lymph node sampling (robot-assisted) because percutaneous biopsy was deemed unsafe. The sampling demonstrated that none of the 13 evaluated nodes were positive for tumor, including the lymph nodes in question. It is likely that his prior extensive transurethral resections and subsequent intravesical *Bacillus* Calmette–Guérin treatment may have led to benign inflammation of these nodes, thereby leading to the false-positive findings on ^{18}F-FDG PET.

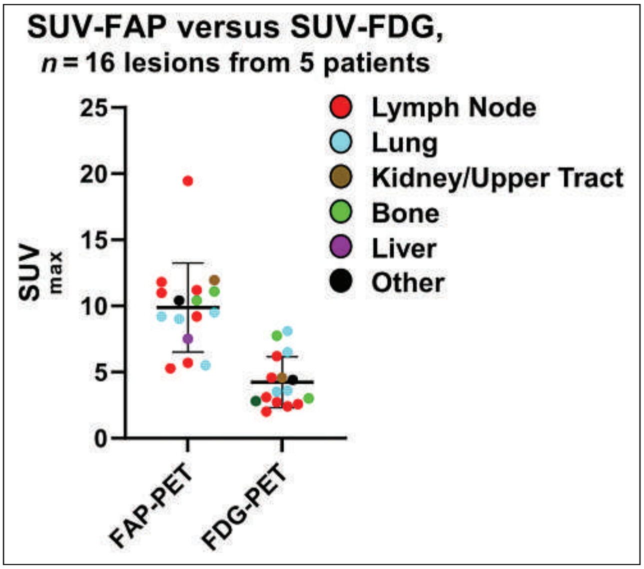

FIGURE 2. SUV_{max} of lesions from ^{68}Ga-FAP-2286 vs. ^{18}F-FDG PET. SUVs of lesions beyond bladder were identified by ^{68}Ga-FAP-2286 PET or paired ^{18}F-FDG PET in 5 patients (3 from metastatic cohort; 2 from localized cohort). Means and SDs are plotted. SUV_{max} differed significantly between ^{68}Ga-FAP-2286 PET and ^{18}F-FDG PET ($P < 0.0001$).

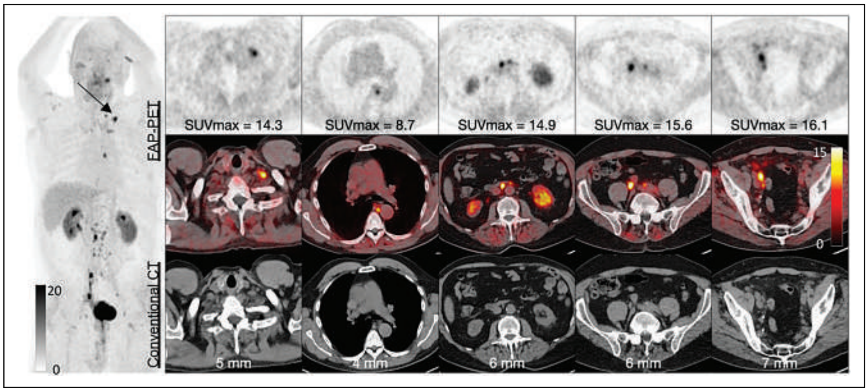

FIGURE 3. ^{68}Ga-FAP-2286 PET (top and maximal-intensity projection at left), PET/CT (middle), and CT (bottom) in 76-y-old man with MIBC. Imaging revealed metastatic disease in subcentimeter lymph node not detectable by conventional CT, including disease in supraclavicular node (arrow), which was biopsy-confirmed to contain bladder cancer.

Case 3. A 78-y-old man presented with MIBC without nodal disease on conventional imaging. However, ^{68}Ga-FAP-2286 PET identified avid pelvic and paracaval lymph nodes (Fig. 5). Because of hearing loss and neuropathy, he was ineligible for cisplatin-based chemotherapy. Thus, he underwent upfront radical cystectomy with bilateral extended pelvic lymphadenectomy (up to the aortic bifurcation), an approach generally beyond the standard anatomic boundaries used for pelvic lymph node dissection, as pathology was anticipated to be aggressive. Final pathology revealed pT3aN3 disease with 12 of 38 lymph nodes involved. The nodal distribution confirmed the findings noted on ^{68}Ga-FAP-2286 PET (not seen on conventional imaging), with involvement of the paracaval, right and left common iliac, right external iliac, and left obturator lymph nodes. The patient subsequently underwent adjuvant systemic immunotherapy given his nodal status (*21*) and remained disease-free at 8 mo after surgery.

DISCUSSION

In this study, we applied ^{68}Ga-FAP-2286, a novel peptide binder of FAP, to image patients with either metastatic or clinically localized urothelial cancer. In the metastatic cohort, ^{68}Ga-FAP-2286 PET identified subcentimeter lymph nodes that would not otherwise meet RECIST criteria for malignancy. In the localized cohort, ^{68}Ga-FAP-2286 PET confirmed the nodal status defined on conventional imaging and additionally identified a significant number of subcentimeter lymph nodes, leading to a change in clinical management for several patients.

We demonstrate that ^{68}Ga-FAP-2286 PET was able to identify both false-positive and false-negative results on conventional imaging, with biopsy confirmation. For cases 1 and 2, the morbidity of cystectomy was avoided and a more appropriate treatment pursued. In the third case, ^{68}Ga-FAP-2286 PET more accurately identified locally advanced or metastatic lymph nodes before surgery, leading to a modified surgical plan with extended lymph node dissection. Thus, in our cohorts with either localized or metastatic urothelial cancer, ^{68}Ga-FAP-2286 PET demonstrated the ability to stage local and metastatic disease more reliably than conventional imaging. We envision that ^{68}Ga-FAP-2286 PET will ultimately play an important role in identifying patients with MIBC who may not benefit from radical surgery.

Our results meaningfully add to the growing body of studies on ^{68}Ga-FAP-2286-based imaging in various tumor types (*22*)—studies that have shown several potential advantages over ^{18}F-FDG PET. Consistent with a prior study using FAPI imaging in bladder cancer (*20*), ^{68}Ga-FAP-2286 uptake was on average higher than ^{18}F-FDG uptake. This feature leads to an improved tumor-to-background ratio and finer resolution of nodal disease, as we report in Supplemental Figure 1. Our results also highlight the ability of ^{68}Ga-FAP-2286 PET to potentially address the long-standing challenge of improving sensitivity to define pelvic nodal metastasis using criteria beyond size or metabolism, with potentially less susceptibility to false positives (as highlighted in case 2). Finally, given the lack of patient preparation required the night before imaging, ^{68}Ga-FAP-2286 PET may also be advantageous over ^{18}F-FDG PET from the perspective of patient preparation and workflow.

Use of this imaging modality in bladder cancer more broadly highlights potential benefits in imaging specific cancers with unique cell-surface protein antigens, which may allow for more accurate and sensitive staging. Two relevant examples include prostate-specific membrane antigen PET, which is widely used in men with biochemically recurrent prostate cancer and has been shown to identify small metastases not otherwise seen on conventional imaging (*23*), and ^{89}Zr-deferoxamine-girentuximab, a carbonic-anhydrase binder that more accurately stages renal cell carcinoma (*24*).

The generally high SUV$_{\text{max}}$ and tumor-to-background ratio of ^{68}Ga-FAP-2286 across all lesion sizes raises the possibility that ^{68}Ga-FAP-2286 can be effective therapeutically. Previous studies using ^{90}Y-FAPI-46 demonstrated safety and some efficacy in stabilizing advanced disease in patients with various malignancies, though at the expense of hematologic toxicity (*25*). It will be important to evaluate ongoing therapeutic studies targeting FAP in bladder cancer, including the metastatic

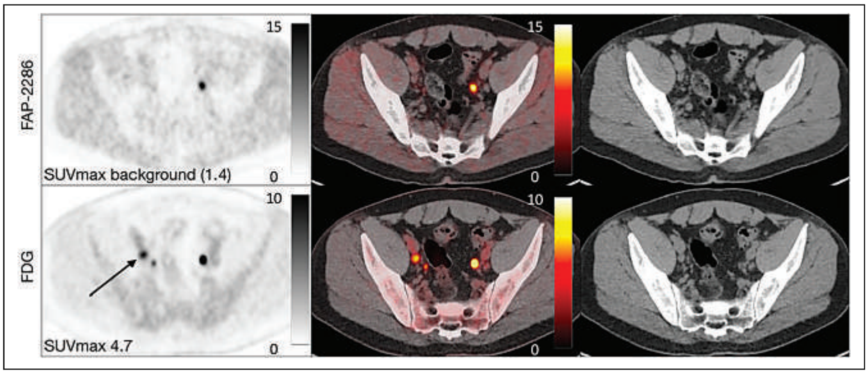

FIGURE 4. ^{68}Ga-FAP-2286 and ^{18}F-FDG PET (left), PET/CT (middle), and CT (right) in 28-y-old man with non-MIBC. ^{18}F-FDG PET showed positive nodes concerning for metastatic disease, whereas ^{68}Ga-FAP-2286 PET showed no uptake. Lymph node dissection confirmed absence of cancer in lymph nodes. Avidity seen on ^{68}Ga-FAP-2286 PET is from excretion of tracer into left ureter.

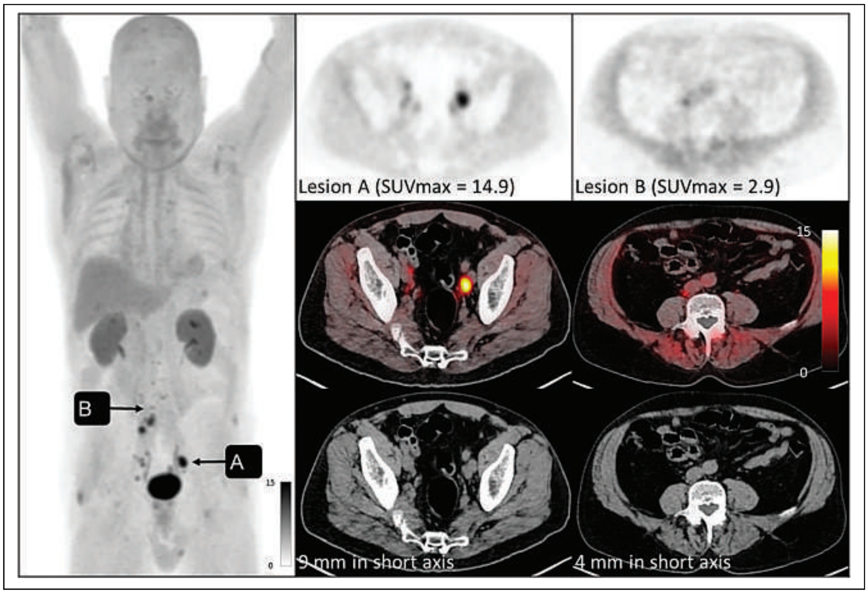

FIGURE 5. 78-y-old man presenting with lymph node–negative, localized MIBC on initial staging ^{68}Ga-FAP-2286 PET (top and maximum-intensity projection at left), PET/CT (middle), and CT (bottom). Imaging revealed multiple paracaval and pelvic lymph nodes (denoted by arrows). Patient underwent radical cystectomy with extended lymph node dissection, which confirmed spread of cancer at time of surgery.

bladder cohort of LUMIERE (*17*), as well as parallel studies of ^{177}Lu-FAP-2286 reported in an initial cohort (*26*).

This study had several limitations, including the small sample size and lack of central pathology or masked radiology review. Moreover, this study was not specifically designed to detect false positives or false negatives using ^{68}Ga-FAP-2286 PET. Specifically, the neoadjuvant treatment that some patients in the localized cohort had undergone before lymph node sampling during cystectomy would be expected to influence nodal status by potentially downstaging them (*3*). Finally, the results are more difficult to generalize to the broader population of bladder cancer patients because of the lack of histologic variants (e.g., squamous, neuroendocrine, or small cell). Nonetheless, a future larger prospective cohort addressing these concerns using ^{68}Ga-FAP-2286 would be valuable.

CONCLUSION

^{68}Ga-FAP-2286 is a promising FAP ligand for the initial staging of MIBC, a disease that is difficult to accurately stage with conventional imaging. ^{68}Ga-FAP-2286 PET identifies metastatic lymph nodes smaller than 1 cm and may have higher specificity than ^{18}F-FDG PET. Although these results need to be validated prospectively and in larger cohorts, ^{68}Ga-FAP-2286 imaging may have an important role in initial staging, disease monitoring, and appropriate treatment selection for patients with MIBC.

DISCLOSURE

Thomas Hope has grant funding from Clovis Oncology (used to complete this study), Philips, GE Healthcare, Lantheus, Janssen, the Prostate Cancer Foundation, and the National Cancer Institute (R01CA235741 and R01CA212148). He received personal fees from Ipsen, Bayer, and BlueEarth Diagnostics and received fees from and has an equity interest in RayzeBio and Curium. Vadim Koshkin reports serving in a consulting or advisory role for AstraZeneca, Clovis, Janssen, Pfizer, EMD Serono, Seagen, Astellas, Dendreon, Guidepoint, GLG, and ExpertConnect; has received research funding for the institution from Endocyte, Nektar, Clovis, Janssen, and Taiho; and is supported by the Prostate Cancer Foundation. Terence Friedlander reports serving in a consulting or advisory role for AstraZeneca, Aadi Biosciences, Seagen, Merck, and Astellas and has received research funding for the institution from Roche-Genentech, Seagen, and Bristol-Meyers-Squibb. Sima Porten reports receiving research funding from Photocure, serving as a consultant for Stryker and Photocure, receiving an honorarium from Pacific Edge, and serving on the advisory board for Oncuria and AstraZeneca. No other potential conflict of interest relevant to this article was reported.

KEY POINTS

QUESTION: Is ^{68}Ga-FAP-2286 PET an effective imaging modality in the initial staging of MIBC?

PERTINENT FINDINGS: ^{68}Ga-FAP-2286 PET is effective at identifying bladder cancer that has spread outside the bladder, including small lesions that appear unremarkable on conventional imaging. In several cases, this imaging modality meaningfully influenced patient management.

IMPLICATIONS FOR PATIENT CARE: Imaging patients with newly diagnosed bladder cancer using ^{68}Ga-FAP-2286 PET improves staging and potentially improves patient management.

REFERENCES

1. Matulay JT, Li R, Hensley PJ, et al. Contemporary outcomes of patients with nonmuscle-invasive bladder cancer treated with bacillus Calmette-Guérin: implications for clinical trial design. *J Urol.* 2021;205:1612–1621.
2. Siegel RL, Miller KD, Wagle NS, Jemal A. Cancer statistics, 2023. *CA Cancer J Clin.* 2023;73:17–48.
3. Grossman HB, Natale RB, Tangen CM, et al. Neoadjuvant chemotherapy plus cystectomy compared with cystectomy alone for locally advanced bladder cancer. *N Engl J Med.* 2003;349:859–866.
4. Vieweg J, Gschwend JE, Herr HW, Fair WR. The impact of primary stage on survival in patients with lymph node positive bladder cancer. *J Urol.* 1999;161:72–76.
5. Eisenhauer EA, Therasse P, Bogaerts J, et al. New response evaluation criteria in solid tumours: revised RECIST guideline (version 1.1). *Eur J Cancer.* 2009;45:228–247.
6. McMahon CJ, Rofsky NM, Pedrosa I. Lymphatic metastases from pelvic tumors: anatomic classification, characterization, and staging. *Radiology.* 2010;254:31–46.
7. Galgano SJ, Porter KK, Burgan C, Rais-Bahrami S. The role of imaging in bladder cancer diagnosis and staging. *Diagnostics (Basel).* 2020;10:703.
8. Girard A, Reyes HV, Shaish H, et al. The role of ^{18}F-FDG PET/CT in guiding precision medicine for invasive bladder carcinoma. *Front Oncol.* 2020;10:565086.

9. Moussa M, Chakra MA, Saad W, Dellis A, Papatsoris A. The role of ^{18}F-FDG PET/CT scan compared to CT-scan alone for lymph node staging before radical cystectomy in patients with bladder cancer. *Urol Oncol.* 2021;39: 833.e9–833.e17.
10. Jin X, Wei M, Wang S, et al. Detecting fibroblast activation proteins in lymphoma using ^{68}Ga-FAPI PET/CT. *J Nucl Med.* 2022;63:212–217.
11. Kalluri R. The biology and function of fibroblasts in cancer. *Nat Rev Cancer.* 2016;16:582–598.
12. Sahai E, Astsaturov I, Cukierman E, et al. A framework for advancing our understanding of cancer-associated fibroblasts. *Nat Rev Cancer.* 2020;20:174–186.
13. Kratochwil C, Flechsig P, Lindner T, et al. ^{68}Ga-FAPI PET/CT: tracer uptake in 28 different kinds of cancer. *J Nucl Med.* 2019;60:801–805.
14. Lindner T, Giesel FL, Kratochwil C, Serfling SE. Radioligands targeting fibroblast activation protein (FAP). *Cancers (Basel).* 2021;13:5744.
15. Zboralski D, Hoehne A, Bredenbeck A, et al. Preclinical evaluation of FAP-2286 for fibroblast activation protein targeted radionuclide imaging and therapy. *Eur J Nucl Med Mol Imaging.* 2022;49:3651–3667.
16. Pang Y, Zhao L, Meng T, et al. PET imaging of fibroblast activation protein in various types of cancer using ^{68}Ga-FAP-2286: comparison with ^{18}F-FDG and ^{68}Ga-FAPI-46 in a single-center, prospective study. *J Nucl Med.* 2023;64:386–394.
17. McConathy J, Dhawan M, Goenka AH, et al. LuMIERE: a phase 1/2 study investigating safety, pharmacokinetics, dosimetry, and preliminary antitumor activity of ^{177}Lu-FAP-2286 in patients with advanced or metastatic solid tumors [abstract]. *Cancer Res.* 2022;82(suppl):CT251.
18. Hemida AS, Aiad HAES, Hassan NA, Sharaky DRA. Fibroblast activation protein (FAP) expression in CK5/6 expressed (basal subtype) & CK20 expressed (luminal subtype) urothelial bladder carcinoma: an immunohistochemical study. *J Immunoassay Immunochem.* 2022;43:618–633.
19. Unterrainer LM, Lindner S, Eismann L, et al. Feasibility of [^{68}Ga]Ga-FAPI-46 PET/CT for detection of nodal and hematogenous spread in high-grade urothelial carcinoma. *Eur J Nucl Med Mol Imaging.* 2022;49:3571–3580.
20. Novruzov E, Dendl K, Ndlovu H, et al. Head-to-head intra-individual comparison of [^{68}Ga]-FAPI and [^{18}F]-FDG PET/CT in patients with bladder cancer. *Mol Imaging Biol.* 2022;24:651–658.
21. Galsky MD, Bajorin DF, Witjes JA, et al. Disease-free survival analysis for patients with high-risk muscle-invasive urothelial carcinoma from the randomized CheckMate 274 trial by PD-L1 combined positive score and tumor cell score. *Eur Urol.* 2023;83:432–440.
22. Gilardi L, Farulla LSA, Demirci E, Clerici I, Salè EO, Ceci F. Imaging cancer-associated fibroblasts (CAFs) with FAPi PET. *Biomedicines.* 2022;10:523.
23. Ferdinandus J, Fendler WP, Farolfi A, et al. PSMA PET validates higher rates of metastatic disease for European Association of Urology biochemical recurrence risk groups: an international multicenter study. *J Nucl Med.* 2022;63:76–80.
24. Shuch BM, Pantuck AJ, Bernhard J-C, et al. Results from phase 3 study of ^{89}Zr-DFO-girentuximab for PET/CT imaging of clear cell renal cell carcinoma (ZIRCON) [abstract]. *J Clin Oncol.* 2023;41(suppl):LBA602.
25. Fendler WP, Pabst KM, Kessler L, et al. Safety and efficacy of ^{90}Y-FAPI-46 radioligand therapy in patients with advanced sarcoma and other cancer entities. *Clin Cancer Res.* 2022;28:4346–4353.
26. Baum RP, Schuchardt C, Singh A, et al. Feasibility, biodistribution, and preliminary dosimetry in peptide-targeted radionuclide therapy of diverse adenocarcinomas using ^{177}Lu-FAP-2286: first-in-humans results. *J Nucl Med.* 2022;63:415–423.

^{18}F-FAPI-04 Outperforms ^{18}F-FDG PET/CT in Clinical Assessments of Patients with Pancreatic Adenocarcinoma

Xiang Li*[1,2], Na Lu*[1,2], Lili Lin[3], Yiwen Chen[1,2], Shuye Yang[3], Huatao Wang[3], Xinyuan Liu[1,2], Chengyi Wu[1,2], Xing Xue[4], Xinhui Su[3], Xueli Bai†[1,2], and Tingbo Liang†[1,2,5]

[1]Department of Hepatobiliary and Pancreatic Surgery, First Affiliated Hospital, School of Medicine, Zhejiang University, Hangzhou, China; [2]Zhejiang Provincial Key Laboratory of Pancreatic Disease, Hangzhou, China; [3]Department of Nuclear Medicine, First Affiliated Hospital, School of Medicine, Zhejiang University, Hangzhou, China; [4]Department of Radiology, First Affiliated Hospital, School of Medicine, Zhejiang University, Hangzhou, China; and [5]Zhejiang University Cancer Center, Hangzhou, China

Accurate diagnosis and staging are crucial for selecting treatment for patients with pancreatic ductal adenocarcinoma (PDAC). The desmoplastic responses associated with PDAC are often characterized by hypometabolism. Here, we investigated ^{18}F-fibroblast activation protein inhibitor (FAPI)–04 PET/CT in evaluation of PDAC and compared the findings with those obtained using ^{18}F-FDG. **Methods:** Sixty-two PDAC patients underwent ^{18}F-FAPI-04 PET/CT and ^{18}F-FDG PET/CT. Identification of primary lesions, lymph node (LN) metastasis, and distant metastasis (DM) by these methods was evaluated, and TNM staging was performed. Correlation between $\mathrm{SUV}_{\max}$ of the primary lesion and treatment response was explored in patients who received systemic therapy. **Results:** ^{18}F-FAPI-04 PET/CT identified all patients with PDAC; ^{18}F-FDG PET/CT missed 1 patient. Tracer uptake was higher in ^{18}F-FAPI-04 PET/CT than in ^{18}F-FDG PET/CT in primary tumors (10.63 vs. 2.87, $P < 0.0001$), LN metastasis (2.90 vs. 1.43, $P < 0.0001$), and DM (liver, 6.11 vs. 3.10, $P = 0.002$; peritoneal, 4.70 vs. 2.08, $P = 0.015$). The methods showed no significant difference in the T staging category, but the N and M values were significantly higher for ^{18}F-FAPI-04 PET/CT than for ^{18}F-FDG PET/CT ($P = 0.002$ and 0.008, respectively). Thus, 14 patients were upgraded, and only 1 patient was downgraded, by ^{18}F-FAPI-04 PET/CT compared with ^{18}F-FDG PET/CT. A high $\mathrm{SUV}_{\max}$ of the primary tumor did not correlate with treatment response for either ^{18}F-FAPI-04 or ^{18}F-FDG. **Conclusion:** ^{18}F-FAPI-04 PET/CT performed better than ^{18}F-FDG PET/CT in identification of primary tumors, LN metastasis, and DM and in TNM staging of PDAC.

Key Words: ^{18}F-FAPI-04; ^{18}F-FDG; PET/CT; pancreatic ductal adenocarcinoma; staging

J Nucl Med 2024; 65:206–212
DOI: 10.2967/jnumed.123.266283

Pancreatic ductal adenocarcinoma (PDAC) is one of the most lethal malignancies (*1*). Accurate diagnosis and initial staging are crucial for optimal treatment selection. Imaging techniques, including CT and MRI, are the most frequently used methods for tumor detection, staging, treatment response evaluation, and tumor surveillance (*2,3*). CT scans, which offer good resolution and wide anatomic coverage, are routinely used for tumor staging and assessment of resectability. Both local and distant diseases can be assessed in a single session (*4*). However, the detection of micrometastases with CT scans remains a major challenge. MRI has proved to be outstanding for detection of small lesions, including identification of local pancreatic tumors and screening for hepatic or peritoneal micrometastases. However, screening-range limitations restrict the application of MRI in the detection of distant metastases (DMs) (*5*).

PET/CT is a hybrid imaging technique with wide anatomic coverage that allows the depiction of all possible small metastases throughout the body. ^{18}F-FDG is the most widely used radiotracer for PET/CT. Although hypermetabolic tumors are known to demonstrate particularly high ^{18}F-FDG uptake, the desmoplastic reaction associated with PDAC usually shows hypometabolic characteristics, which is a well-known limitation of ^{18}F-FDG PET/CT in PDAC diagnosis and staging (*6–8*).

The tumor cells in PDACs exist within a dense stroma, which is composed of an extracellular matrix, vasculature, and cancer-associated fibroblasts (*9*). Fibroblast activation protein (FAP) is a membrane protease that is highly expressed on the surface of cancer-associated fibroblasts (*10,11*). Therefore, a radioactively labeled FAP inhibitor (FAPI) is a promising PET tracer in PDAC (*12,13*). Moreover, PDAC is expected to show intensive uptake of ^{68}Ga-conjugated FAPI (^{68}Ga-FAPI). The clinical value of ^{68}Ga-FAPI for PDAC has been preliminarily investigated, and the studies have shown promising results (*14,15*).

Nevertheless, storage and long-distance transit of ^{68}Ga are difficult because of its relatively short half-life. In addition, the availability of ^{68}Ga-labeled tracers from ^{68}Ge/^{68}Ga generators is limited. In contrast, ^{18}F is the most widely used radionuclide in PET; therefore, it can be easily produced in larger doses and delivered over longer distances at a relatively lower cost than ^{68}Ga. Thus, ^{18}F-labeled FAPI-targeting tracers are strongly desired in clinical practice (*16*). However, the advantages of ^{18}F-AlF-NOTA-FAPI-04 (^{18}F-FAPI-04) over ^{18}F-FDG have not yet been systematically evaluated in PDAC. Our purpose was to explore the potential efficacy of ^{18}F-FAPI-04 PET/CT for PDAC

Received Jul. 21, 2023; revision accepted Nov. 7, 2023.

For correspondence or reprints, contact Tingbo Liang (liangtingbo@zju.edu.cn) or Xueli Bai (shirleybai@zju.edu.cn).

*Contributed equally to this work.

†Contributed equally to this work.

tumor staging and compare the results with those obtained using ^{18}F-FDG PET/CT.

MATERIALS AND METHODS

Enrollment and Treatment

Sixty-two patients with PDAC were enrolled prospectively between August 2021 and February 2023 at the First Affiliated Hospital, School of Medicine, Zhejiang University. The hospital's ethics committee approved this study (NCT05884463; ClinicalTrials.gov), and all patients gave written informed consent. For comparative analyses, both ^{18}F-FAPI-04 PET/CT and ^{18}F-FDG PET/CT were performed at enrollment. The inclusion criteria were as follows: patients who were suspected to have PDAC by radiologic imaging; patients who had scheduled paired ^{18}F-FAPI-04 PET/CT and ^{18}F-FDG PET/CT for metastasis screening, recurrence confirmation, or tumor staging; and patients who were willing to participate in clinical trials and who signed an informed-consent form. The exclusion criteria were as follows: patients who were not pathologically diagnosed as PDAC, pregnant patients, and patients with the inability or unwillingness of the research participant, parent, or legal representative to provide written informed consent. After systemic treatment, surgical treatment was performed if the patients met the criteria for a conversion operation. The decision to complete preoperative PET/CT was based on the patient's willingness. The treatment response was evaluated bimonthly according to RECIST version 1.1. Final clinical staging was conducted by our tumor board and based on clinical, pathologic, and all imaging data.

Radiopharmaceuticals

^{18}F-FAPI-04 was prepared as described previously (*17,18*). The NOTA-FAPI-04 precursor was purchased from Beijing PET Technology Co. Ltd. ^{18}F was produced from a medical cyclotron (Siemens Medical Solutions). The synthesis of ^{18}F-FAPI-04 was performed in an AllInOne synthesis module (Trasis). The final product was reconstituted in saline and passed through a 0.22-μm syringe filter (Pall Corp.). The radiochemical purity of ^{18}F-FAPI-04 was analyzed by radio–high-performance liquid chromatography (1200 series; Agilent) and was more than 95%. ^{18}F-FDG was synthesized automatically and routinely in a ^{18}F-FDG synthesizer module (FDG4 Explora; Siemens) and was purified to radiochemical purity of more than 95% before clinical use.

PET/CT Imaging

PET/CT imaging with both ^{18}F-FAPI-04 and ^{18}F-FDG was performed on a PET/CT scanner (Biograph version 600; Siemens Healthineers). All images were acquired from top of skull to mid thigh 60–90 min after intravenous administration of ^{18}F-FAPI-04 or ^{18}F-FDG at a dose of 3.7–4.44 MBq/kg (0.1–0.12 mCi/kg). Fasting and normal blood glucose levels were obtained for ^{18}F-FDG PET/CT. ^{18}F-FAPI-04 PET/CT and ^{18}F-FDG PET/CT were performed within 2 wk, and both were conducted before treatment. The PET scan was performed with 3 min/frame three-dimensional acquisition. The CT parameters were 120 kV, 160 mA, pitch of 1.3, slice thickness of 2.5 mm, and rotation time of 0.5 s, and these were used to conduct PET attenuation correction. PET images were reconstructed using a Siemens workstation (syngo.via Client 4.1) with TrueX plus time of flight (UltraHD PET [Siemens]; 10 iterations, 5 subsets, gaussian filter with full width at half maximum of 4 mm, 440 × 440 matrix).

PET/CT Image Analysis

Two nuclear medicine physicians, both of whom have more than 10 y of experience in nuclear oncology, independently analyzed all images using a MedExsystem nuclear medical information system (MedEx Technology Limited Corp.), and discordant results were resolved by consensus. Image interpretation included visual analysis and quantitative assessments. Focal ^{18}F-FAPI-04 or ^{18}F-FDG accumulations showing activity higher than the background, except for physiologic uptake, were considered potential positive lesions. The uptake of ^{18}F-FAPI-04 or ^{18}F-FDG in primary tumors and metastatic lesions was semiquantified by SUV_{max}. To ensure that SUV_{max} was relatively comparable, the tumor-to-background (T/B) ratio was performed according to the following formula: T/B ratio = tumor SUV_{max}/background SUV_{mean}. Average SUV_{mean} of the liver was set as the background to SUV_{max} of the local tumor. Background SUV_{mean} of hepatic or bone metastasis was average SUV_{mean} of normal liver tissue or bone tissue, respectively. For lymph node (LN), pleural, and peritoneal lesions, background SUV_{mean} was set as average SUV_{mean} of the descending aorta. Average background SUV_{mean} was calculated for 3 random regions. If there were fewer than 5 lesions in a single organ, all lesions were quantitatively assessed. Otherwise, the 5 lesions with the highest activity were quantitatively evaluated.

Statistical Analysis

Continuous variables were expressed as mean ± SD, whereas categoric variables were expressed as frequency and proportion. ^{18}F-FAPI-04 and ^{18}F-FDG uptake were compared using the paired *t* test. The McNemar–Bowker test was used to assess significant differences between ^{18}F-FAPI-04 and ^{18}F-FDG PET/CT for TNM staging. All statistical analyses were conducted using SPSS (version 18.0; IBM).

RESULTS

Participant Characteristics

All patients were pathologically diagnosed as showing PDAC by biopsy or surgery. Fifty-eight patients were newly diagnosed and treatment-naïve, whereas the other 4 patients underwent PET/CT for restaging after initial treatment. Our cohort consisted of 43 men and 19 women, with a median age of 63 y. Finally, 54 patients received further treatment at our institution, including surgery treatment (n = 4) and systemic treatment (n = 50). In addition, 48 patients who received systemic treatment underwent radiologic response evaluation; these patients were included to investigate the value of the 2 tracers in treatment response prediction. More details about the patients' concurrent symptoms, comorbidities, tumor location, carbohydrate antigen 19-9 values, and other pertinent data are recorded in Supplemental Table 1 (supplemental materials are available at http://jnm.snmjournals.org).

Adverse Events

^{18}F-FAPI-04 and ^{18}F-FDG were tolerated by all participants without physical discomfort or adverse effects.

Diagnostic Performance of ^{18}F-FAPI-04 and ^{18}F-FDG in Primary Tumors

^{18}F-FDG PET/CT showed a sensitivity of 98.4% (61/62 patients) for identification of primary tumors, whereas ^{18}F-FAPI-04 PET/CT identified all local lesions (62/62 patients). ^{18}F-FAPI-04 SUV_{max} was almost 2 times greater than ^{18}F-FDG SUV_{max}, increasing from a mean of 8.00 (range, 3.70–55.20) to 15.65 (range, 3.70–34.50) in the semiquantitative parametric analysis (Table 1) and showing that the uptake of ^{18}F-FAPI-04 in primary tumors was significantly greater than that of ^{18}F-FDG ($P < 0.0001$). The difference of T/B ratio in uptake between ^{18}F-FAPI-04 and ^{18}F-FDG was more pronounced (10.63 vs. 2.87, $P < 0.0001$). The typical PET/CT images obtained with the 2 tracers and the corresponding CT/MR images are shown in Figure 1.

TABLE 1
Comparison of ^{18}F-FDG and ^{18}F-FAPI Uptake in Lesions

		^{18}F-FDG uptake				^{18}F-FAPI-04 uptake				
Parameter	Patients (*n*)	Median SUV_{max}	Range of SUV_{max}	Patients (*n*)	Positive lesions (*n*)	Median SUV_{max}	Range of SUV_{max}	Patients (*n*)	Positive lesions (*n*)	^{18}F-FDG SUV vs. ^{18}F-FAPI-04 SUV *P* value
Primary tumor	62			61	61			62	62	
Original		8.00	3.70–55.20			15.65	3.70–34.50			<0.0001
T/B ratio		2.87	1.02–16.61			10.63	1.91–37.06			<0.0001
LNs	44			40	151			44	203	
Original		2.30	0.97–5.92			3.56	1.43–10.23			<0.0001
T/B ratio		1.43	0.65–4.28			2.90	0.91–12.06			<0.0001
Metastasis										
Liver	12			5	19			12	35	
Original		6.10	4.34–6.85			7.04	1.30–10.30			0.388
T/B ratio		3.10	2.10–3.68			6.11	1.50–19.99			0.002
Peritoneal	12			11	103			12	158	
Original		2.82	2.10–7.94			6.00	3.10–10.83			0.016
T/B ratio		2.08	0.99–4.14			4.70	1.90–12.85			0.015
Bone	3			1	4			3	6	
Original		8.92	ND			7.00	4.90–13.25			0.925
T/B ratio		7.28	ND			8.00	5.76–40.60			0.678
Pleural	1			1	18			1	26	
Original		3.00	ND			6.00	ND			ND
T/B ratio		4.31	ND			7.32	ND			ND

ND = not determined.

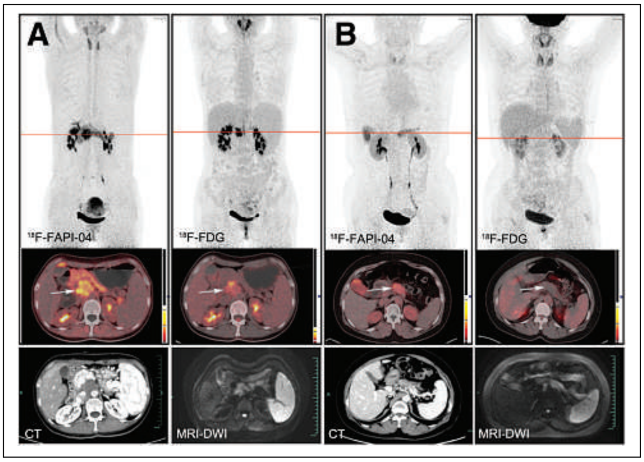

FIGURE 1. Typical PET (top), PET/CT (middle), and CT and MR (bottom) images of primary tumor obtained using 2 tracers in representative patients (A and B). Tumor is marked by arrows. DWI = diffusion-weighted imaging.

Diagnostic Performance of ^{18}F-FAPI-04 and ^{18}F-FDG for LN Assessments

In total, 44 patients showed large LN shadowing with high metabolism after performing PET/CT. Among these, 40 patients showed abnormal LN findings on ^{18}F-FDG PET/CT, whereas the remaining 4 patients showed suggestive findings on ^{18}F-FAPI-04 PET/CT alone (Table 1). ^{18}F-FAPI-04 showed an obvious advantage over ^{18}F-FDG in terms of the number of positive LNs identified (203 vs. 151). In the semiquantitative study, median SUV_{max} and maximum SUV_{max} for ^{18}F-FAPI-04 uptake were 3.56 and 10.32, respectively, which were higher than the values for ^{18}F-FDG (median SUV_{max}, 2.30; maximum SUV_{max}, 5.92), with a P value of less than 0.0001. The difference in uptake between ^{18}F-FAPI-04 and ^{18}F-FDG was more pronounced in the T/B ratio (2.90 vs. 1.43, $P < 0.0001$). The 2 examination approaches showed a substantial difference for the identification of LN metastases (Fig. 2).

Diagnostic Performance of ^{18}F-FAPI-04 and ^{18}F-FDG for DM

The data for the number of positive hepatic, peritoneal, bone, and pleural metastases and the semiquantitative parameters of ^{18}F-FAPI-04 PET/CT and ^{18}F-FDG PET/CT are presented in Table 1. ^{18}F-FDG and ^{18}F-FAPI-04 confirmed hepatic metastasis in 5 and 12 patients, respectively, implying that ^{18}F-FAPI-04 surpassed ^{18}F-FDG in the detection of hepatic lesions. SUV_{max} in hepatic metastases was slightly higher for ^{18}F-FAPI-04 than for ^{18}F-FDG (7.04 vs. 6.10), but the difference was not significant ($P = 0.388$). To exclude background effects, the T/B ratio of ^{18}F-FAPI-04 was higher than that of ^{18}F-FDG (6.11 vs. 3.10, $P = 0.002$). Altogether, ^{18}F-FAPI-04 PET/CT showed better sensitivity and accuracy than ^{18}F-FDG PET/CT for detection of hepatic metastases. The images of representative cases are presented in Figure 3. Similar results were obtained for patients with peritoneal metastasis. Although the sample size of patients with bone or pleural lesions was limited, ^{18}F-FAPI-04 PET/CT demonstrated higher detection rates of these lesions than did ^{18}F-FDG PET/CT (Fig. 4).

TNM Staging

Sixty-two patients were staged according to the eighth edition American Joint Committee on Cancer tumor staging criteria (Supplemental Table 2). The distribution of T staging was similar between the 2 tracers. Assessment of vascular involvement based on enhanced CT was more accurate than that based on PET/CT. Therefore, the T4 staging proportion based on CT/MRI (58.1%) was significantly greater than that based on PET/CT.

N staging was more variable between ^{18}F-FDG and ^{18}F-FAPI-04. Four patients without LN metastases, according to ^{18}F-FDG, were categorized as N1 by ^{18}F-FAPI-04, and 11 patients who were categorized as N1 according to ^{18}F-FDG were categorized as N2 by ^{18}F-FAPI-04. Moreover, preoperative ^{18}F-FAPI-04 PET/CT was performed in 13 patients. Pathologic examination confirmed 290 LNs. Of these, 23 positive LNs were confirmed in 6 patients. LN involvement included 18 true-positive, 26 false-positive, 241 true-negative, and 5 false-negative findings with ^{18}F-FAPI-04 PET/CT. The sensitivity, specificity, and accuracy for the diagnosis of LN metastasis were 78.3%, 90.3%, and 89.3%, respectively (Supplemental Table 3).

^{18}F-FDG PET/CT revealed DM in 17 patients, whereas ^{18}F-FAPI-04 PET/CT showed DM in 24 patients. ^{18}F-FAPI-04 PET/CT upgraded the M stage in 7 patients. Five of them were confirmed to have hepatic metastasis by ^{18}F-FAPI-04 PET/CT, whereas the remaining 2 patients were found to have peritoneal metastases and bone metastases.

Figure 5 illustrates how, in comparison with ^{18}F-FDG PET/CT, ^{18}F-FAPI-04 PET/CT upgraded the staging of 14 patients: 1 from Ia to IIb, 1 from Ib to IIa, 1 from Ib to IIb, 2 from IIa to IV, 4 from IIb to III, 4 from IIb to IV, and 1 from III to IV. However, only 1 patient was downstaged from III to IIb after ^{18}F-FAPI-04 PET/CT (Supplemental Tables 4 and 5).

Treatment Response Evaluation

Forty-eight patients received systemic treatment, and the best treatment response was recorded. The correlations between SUV_{max} or T/B ratio and response were analyzed (Fig. 6). Median SUV_{max} and median T/B ratio values of ^{18}F-FDG and ^{18}F-FAPI-04, respectively, were identified as the cutoff values. Patients were divided into response group (complete and partial response) and nonresponse group (stable and progressive disease). Patients showing higher uptake of ^{18}F-FDG (≥ 8.00) or ^{18}F-FAPI (≥ 15.70) showed response rates similar to those of patients with lower SUV_{max} (^{18}F-FDG, 25.0% vs. 21.7%, $P = 0.798$; ^{18}F-FAPI, 25.0% vs. 20.8%, $P = 0.786$). Similarly to SUV_{max}, a lower ^{18}F-FAPI-04 T/B ratio

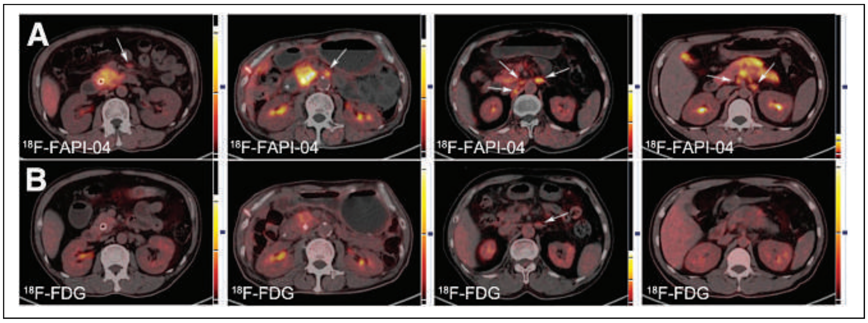

FIGURE 2. Typical LN PET/CT images obtained with ^{18}F-FAPI-04 (A) and ^{18}F-FDG (B) from 4 patients. Lesion is marked by arrows.

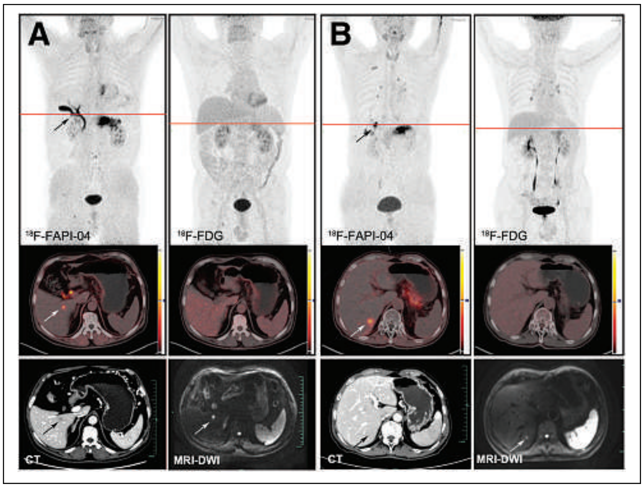

FIGURE 3. Typical PET (top), PET/CT (middle), and CT and MR (bottom) images of hepatic metastases obtained using 2 tracers in 2 patients (A and B). Lesion is marked by arrows. DWI = diffusion-weighted imaging.

was not significantly associated with an increased response rate (29.2% vs. 16.7%, $P = 0.303$). Therefore, the level of uptake of ^{18}F-FAPI-04 or ^{18}F-FDG failed to predict the response to systemic treatment.

DISCUSSION

Diagnosis and proper staging based on imaging assessments are essential for choosing treatment plans for tumor patients. Unfortunately, CT, MRI, and other routinely used imaging examinations frequently fall short in various aspects, especially in assessments of PDAC. Our results demonstrate that ^{18}F-FAPI-04 PET/CT is significantly superior to ^{18}F-FDG PET/CT in detecting both primary and metastatic lesions.

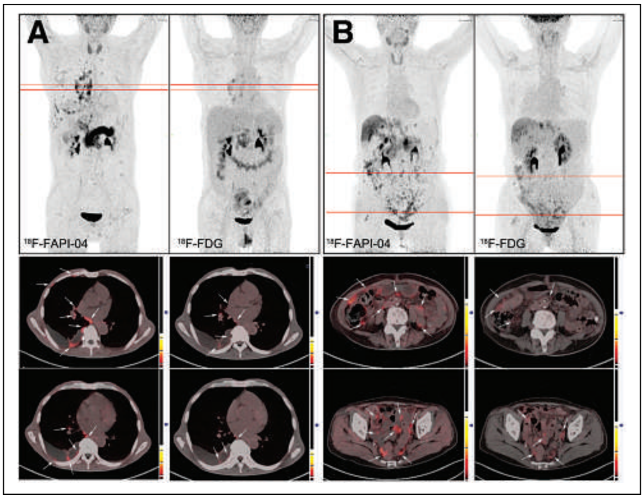

FIGURE 4. Typical PET (top) and PET/CT (middle and bottom) images showing pleural (A) and peritoneal (B) metastasis obtained with 2 tracers. Axial PET/CT images correspond to red lines in coronal PET images. Lesion is marked by arrows.

The most widely used PET tracer is ^{18}F-FDG, which relies on functional activity to distinguish metabolically active proliferative lesions, because tumors frequently accumulate ^{18}F-FDG (*19*). However, the use of ^{18}F-FDG PET/CT for the detection and staging of suspected PDAC remains debatable (*6*). The sensitivity of ^{18}F-FDG PET/CT in the initial diagnosis of PDAC ranges from 73% to 94% (*20*), and our study results were slightly higher than this range (~98.4%). In contrast to ^{18}F-FDG, the tracer ^{18}F-FAPI-04 offers a new method for identification of malignancies (*11,12*). Pang et al. (*12*) reported that ^{68}Ga-FAPI was more sensitive than ^{18}F-FDG for the identification of PDAC, although their study included only 26 patients. Our study had a larger sample size: 62 PDAC patients were enrolled. In our investigation, ^{18}F-FAPI-04 had a remarkably higher T/B ratio than that of ^{18}F-FDG, although its identification of primary tumors was similar to that of ^{18}F-FDG. A previous study demonstrated that ^{68}Ga-FAPI PET/CT can be used to determine the expression of FAP and further guide ^{177}Lu-FAPI radionuclide therapy in patients with breast cancer (*21*). Our study confirmed that PDAC shows high uptake of ^{18}F-FAPI-04, which may also indirectly represent the high expression of FAP in PDAC, giving a diagnostic and clinical strategy for treatment.

LN metastasis is one of the independent factors affecting the prognosis (*22*). Particular importance should be placed on preoperative examination and prediction of LN status. However, ^{18}F-FDG shows limited utility in assessing LN metastasis. In a study by Wang et al. (*23*), the accuracy of ^{18}F-FDG in determining LN metastasis of PDAC in 160 patients was only 39.4%. The authors theorized that this may be related to LN size. Positive LNs often have a large number of cancer-associated

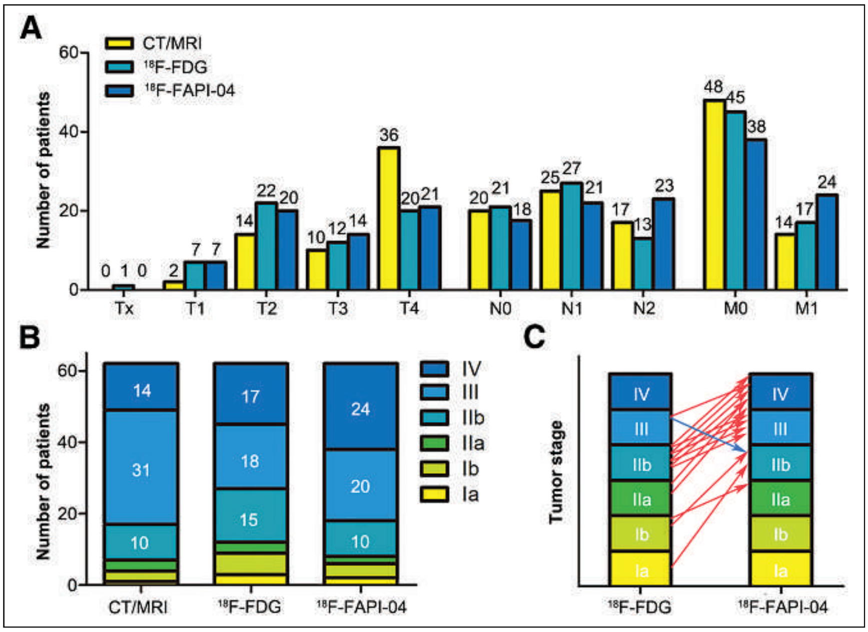

FIGURE 5. Staging based on CT/MRI, ^{18}F-FAPI-04 PET/CT, and ^{18}F-FDG PET. Shown are number of patients in T, N, and M categories (A); prognostic stage groups based on CT/MRI, ^{18}F-FAPI-04 PET/CT, and ^{18}F-FDG PET/CT (B); and differences in prognostic staging of patients between 2 tracers (C).

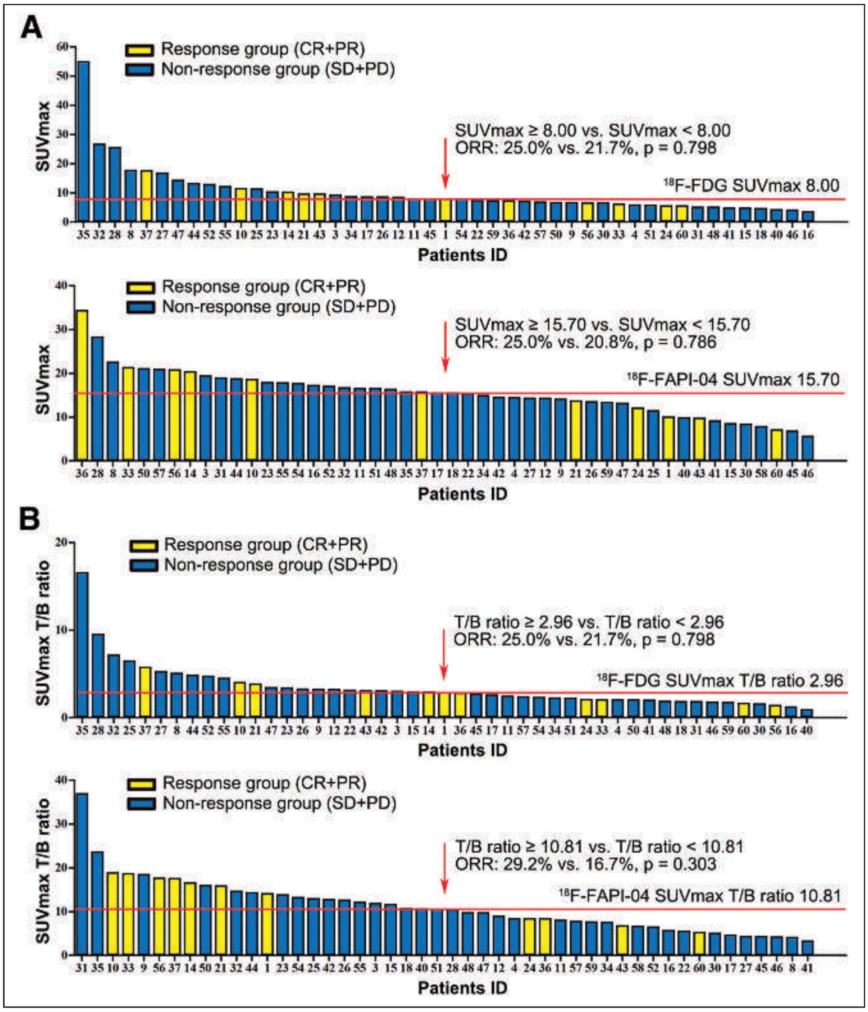

FIGURE 6. Relationship between SUV_{max} and treatment response. Shown are ^{18}F-FDG and ^{18}F-FAPI-04 SUV_{max} (A) and ^{18}F-FDG SUV_{max} and ^{18}F-FAPI-04 SUV_{max} T/B ratio (B) based on primary tumor and related treatment response in patients. CR+PR = complete response and partial response; ORR = objective response rate; SD+PD = stable disease and progressive disease.

fibroblasts, which can be combined with ^{18}F-FAPI for visualization (*24*). In our investigation, ^{18}F-FAPI-04 showed an obvious advantage over ^{18}F-FDG in terms of the number of positive LNs detected and higher tracer uptake, suggesting that ^{18}F-FAPI-04 is more sensitive than ^{18}F-FDG in the identification of metastatic LNs. In our study, 13 patients who received tumor resection underwent ^{18}F-FAPI-04 PET/CT preoperatively, and 290 LNs were confirmed with pathologic examination. The sensitivity, specificity, and accuracy of the diagnosis of LN metastasis based on ^{18}F-FAPI-04 PET/CT were 78.3%, 90.3%, and 89.3%, respectively, which implies that ^{18}F-FAPI-04 PET/CT performed well in detecting metastatic LNs. However, we did not find pathologic evidence to support the advantages of ^{18}F-FAPI-04 PET/CT over ^{18}F-FDG PET/CT in the assessment of LN metastasis, because preoperative paired PET/CT was not essential according to our study design.

The ^{18}F-FDG detection findings for hepatic metastases are equally unsatisfactory (*25,26*). Pang et al. (*12*) and Deng et al. (*15*) have demonstrated that ^{68}Ga-FAPI is more effective than ^{18}F-FDG in distinguishing hepatic metastases from PDAC and gastrointestinal cancers, respectively. Similarly, hepatic metastasis was indicated by ^{18}F-FDG alone in only 5 patients in our study. ^{18}F-FAPI-04 and ^{18}F-FDG had a similar SUV_{max}. High uptake of ^{18}F-FDG in the liver background may cover the uptake in some micrometastases. In contrast, ^{18}F-FAPI-04 showed better background contrast with lower uptake in the liver. Similar results were observed for peritoneal, bone, and pleural lesions. Thus, ^{18}F-FAPI-04 upstaged 14 patients in comparison with ^{18}F-FDG findings. Although detection of metastatic lesions by PET/CT has improved greatly, the assessment of vascular involvement based on enhanced CT is more accurate.

Some studies have already shown that the high expression of FAP on cancer-associated fibroblasts is strongly associated with aggressive tumor behavior and poor prognoses (*27,28*). PDAC patients with moderate or strong FAP expression experience shorter overall survival than those with negative or weak expression (*29*). Pancreatic tumor cells are known to exist within a dense stroma, which accounts for nearly 90% of the tumor mass. Therefore, ^{18}F-FAPI-04 uptake is better than ^{18}F-FDG uptake as a possible indicator of tumor prognosis. Moreover, the presence of an abundant stromal compartment may create a physical barrier to decrease microvascularity and drug delivery in the tumor, thereby reducing the sensitivity to systemic therapy. In this regard, the visualization of FAP expression using ^{18}F-FAPI-04 seems to be a promising approach to predict the response to systemic treatment. In our study, we evaluated the correlation between ^{18}F-FAPI-04 uptake and treatment response, but no significant difference was observed in the objective response rate in relation to differences in ^{18}F-FAPI-04 versus ^{18}F-FDG uptake. This may result from the limitation of the radiologic response for PDAC: it is difficult to observe obvious tumor shrinkage even in cases showing significant tumor cell regression. Because all stages of PDAC were included in our study and some patients underwent conversion surgery after treatment, we failed to analyze the correlation of SUV_{max} with progression survival, which is an obvious limitation. Thus, additional studies are required to validate the prognostic value of ^{18}F-FAPI-04.

This study had some other limitations. First, we included only patients with pathologically diagnosed PDAC, and the assessment of ^{18}F-FAPI-04 was limited to evaluating the sensitivity of this technique, with no assessments of the specificity and other indicators. Disease lesions such as those presenting in IgG4-related disease are known to show significant fibrosis, as well as the potential for high ^{18}F-FAPI uptake (*30*). Furthermore, pathologic evidence to support the advantages of ^{18}F-FAPI-04 over ^{18}F-FDG in the assessment of LN metastasis was insufficient, because all enrolled patients underwent ^{18}F-FAPI-04 and ^{18}F-FDG PET/CT at diagnosis, and preoperative PET/CT was not essential according to our study design.

CONCLUSION

Our results show that ^{18}F-FAPI-04 performed better than ^{18}F-FDG in identifying the primary tumor, LN metastasis, and DM and for TNM staging in PDAC. In the future, ^{18}F-FAPI-04 PET/CT may play a greater role in the actual clinical management of PDAC.

DISCLOSURE

This work was supported by the National Key Research and Development Program (2019YFC1316000 to Tingbo Liang), the National Natural Science Foundation of China (U20A20378, 81830089, and 82188102 to Tingbo Liang; 81871925 and 82071867 to Xueli Bai; 82071965 to Xinhui Su; 82071916 to Xiang Li; and 82172859 to Yiwen Chen), the Key Research and Development Program of Zhejiang Province (2019C03019 to Tingbo Liang and 2020C03117 to Xueli Bai), the Fundamental Research Funds for the Zhejiang Provincial Universities (2021XZZX031 to Xueli Bai), and Huadong Medicine Joint Funds of the Zhejiang Provincial Natural Science Foundation of China (LHDMZ22H300010 to Xinhui Su). No other potential conflict of interest relevant to this article was reported.

KEY POINTS

QUESTION: Is ^{18}F-FAPI-04 PET/CT more effective than ^{18}F-FDG PET/CT at identifying primary lesions, LN metastases, and DMs of PDAC?

PERTINENT FINDINGS: In this 62-patient prospective study, ^{18}F-FAPI-04 PET/CT showed performance superior to that of ^{18}F-FDG PET/CT in the detection of primary lesions and metastases of PDAC and eventually upgraded the TNM stage in 14 patients.

IMPLICATIONS FOR PATIENT CARE: ^{18}F-FAPI-04 PET/CT is expected to assist in the detection of PDAC, offer more accurate staging, and help patients choose surgery or other treatment options.

REFERENCES

1. Siegel RL, Miller KD, Fuchs HE, Jemal A. Cancer statistics, 2022. *CA Cancer J Clin.* 2022;72:7–33.
2. Baliyan V, Kordbacheh H, Parakh A, Kambadakone A. Response assessment in pancreatic ductal adenocarcinoma: role of imaging. *Abdom Radiol (NY).* 2018;43:435–444.
3. Ha J, Choi SH, Byun JH, et al. Meta-analysis of CT and MRI for differentiation of autoimmune pancreatitis from pancreatic adenocarcinoma. *Eur Radiol.* 2021;31:3427–3438.
4. Brennan DD, Zamboni GA, Raptopoulos VD, Kruskal JB. Comprehensive preoperative assessment of pancreatic adenocarcinoma with 64-section volumetric CT. *Radiographics.* 2007;27:1653–1666.
5. Raman SP, Horton KM, Fishman EK. Multimodality imaging of pancreatic cancer—computed tomography, magnetic resonance imaging, and positron emission tomography. *Cancer J.* 2012;18:511–522.
6. Lytras D, Connor S, Bosonnet L, et al. Positron emission tomography does not add to computed tomography for the diagnosis and staging of pancreatic cancer. *Dig Surg.* 2005;22:55–62.
7. Leppänen J, Lindholm V, Isohookana J, et al. Tenascin C, fibronectin, and tumor–stroma ratio in pancreatic ductal adenocarcinoma. *Pancreas.* 2019;48:43–48.
8. Kauhanen SP, Komar G, Seppänen MP, et al. A prospective diagnostic accuracy study of ^{18}F-fluorodeoxyglucose positron emission tomography/computed tomography, multidetector row computed tomography, and magnetic resonance imaging in primary diagnosis and staging of pancreatic cancer. *Ann Surg.* 2009;250:957–963.
9. Hosein AN, Brekken RA, Maitra A. Pancreatic cancer stroma: an update on therapeutic targeting strategies. *Nat Rev Gastroenterol Hepatol.* 2020;17:487–505.
10. Sahai E, Astsaturov I, Cukierman E, et al. A framework for advancing our understanding of cancer-associated fibroblasts. *Nat Rev Cancer.* 2020;20:174–186.
11. Bughda R, Dimou P, D'Souza RR, Klampatsa A. Fibroblast activation protein (FAP)–targeted CAR-T cells: launching an attack on tumor stroma. *ImmunoTargets Ther.* 2021;10:313–323.
12. Pang Y, Zhao L, Shang Q, et al. Positron emission tomography and computed tomography with [^{68}Ga]Ga-fibroblast activation protein inhibitors improves tumor detection and staging in patients with pancreatic cancer. *Eur J Nucl Med Mol Imaging.* 2022;49:1322–1337.
13. Röhrich M, Naumann P, Giesel FL, et al. Impact of ^{68}Ga-FAPI PET/CT imaging on the therapeutic management of primary and recurrent pancreatic ductal adenocarcinomas. *J Nucl Med.* 2021;62:779–786.
14. Gong W, Yang X, Wu J, Ou L, Zhang C. ^{68}Ga-FAPI PET/CT imaging of multiple muscle metastases of pancreatic cancer. *Clin Nucl Med.* 2022;47:73–75.
15. Deng M, Chen Y, Cai L. Comparison of ^{68}Ga-FAPI and ^{18}F-FDG PET/CT in the imaging of pancreatic cancer with liver metastases. *Clin Nucl Med.* 2021;46:589–591.
16. Hu K, Li J, Wang L, et al. Preclinical evaluation and pilot clinical study of [^{18}F]AlF-labeled FAPI-tracer for PET imaging of cancer associated fibroblasts. *Acta Pharm Sin B.* 2022;12:867–875.
17. Jiang X, Wang X, Shen T, et al. FAPI-04 PET/CT using [^{18}F]AlF labeling strategy: automatic synthesis, quality control, and in vivo assessment in patient. *Front Oncol.* 2021;11:649148.
18. Wei Y, Zheng J, Ma L, et al. [^{18}F]AlF-NOTA-FAPI-04: FAP-targeting specificity, biodistribution, and PET/CT imaging of various cancers. *Eur J Nucl Med Mol Imaging.* 2022;49:2761–2773.
19. Singer E, Gschwantler M, Plattner D, et al. Differential diagnosis of benign and malign pancreatic masses with ^{18}F-fluordeoxyglucose–positron emission tomography recorded with a dual-head coincidence gamma camera. *Eur J Gastroenterol Hepatol.* 2007;19:471–478.
20. Rijkers AP, Valkema R, Duivenvoorden HJ, van Eijck CH. Usefulness of F-18-fluorodeoxyglucose positron emission tomography to confirm suspected pancreatic cancer: a meta-analysis. *Eur J Surg Oncol.* 2014;40:794–804.
21. Ballal S, Yadav MP, Kramer V, et al. A theranostic approach of [^{68}Ga]Ga-DOTA.-SA.FAPi PET/CT-guided [^{177}Lu]Lu-DOTA.SA.FAPi radionuclide therapy in an end-stage breast cancer patient: new frontier in targeted radionuclide therapy. *Eur J Nucl Med Mol Imaging.* 2021;48:942–944.
22. Morales-Oyarvide V, Rubinson DA, Dunne RF, et al. Lymph node metastases in resected pancreatic ductal adenocarcinoma: predictors of disease recurrence and survival. *Br J Cancer.* 2017;117:1874–1882.
23. Wang S, Shi H, Yang F, Teng X, Jiang B. The value of ^{18}F-FDG PET/CT and carbohydrate antigen 19-9 in predicting lymph node micrometastases of pancreatic cancer. *Abdom Radiol (NY).* 2019;44:4057–4062.
24. Polack M, Hagenaars SC, Couwenberg A, et al. Characteristics of tumour stroma in regional lymph node metastases in colorectal cancer patients: a theoretical framework for future diagnostic imaging with FAPI PET/CT. *Clin Transl Oncol.* 2022;24:1776–1784.
25. Izuishi K, Yamamoto Y, Sano T, Takebayashi R, Masaki T, Suzuki Y. Impact of 18-fluorodeoxyglucose positron emission tomography on the management of pancreatic cancer. *J Gastrointest Surg.* 2010;14:1151–1158.
26. Diederichs CG, Staib L, Vogel J, et al. Values and limitations of ^{18}F-fluorodeoxyglucose–positron-emission tomography with preoperative evaluation of patients with pancreatic masses. *Pancreas.* 2000;20:109–116.
27. Liao Y, Ni Y, He R, Liu W, Du J. Clinical implications of fibroblast activation protein-α in non-small cell lung cancer after curative resection: a new predictor for prognosis. *J Cancer Res Clin Oncol.* 2013;139:1523–1528.
28. Sandberg TP, Stuart M, Oosting J, Tollenaar R, Sier CFM, Mesker WE. Increased expression of cancer-associated fibroblast markers at the invasive front and its association with tumor–stroma ratio in colorectal cancer. *BMC Cancer.* 2019;19:284.
29. Kawase T, Yasui Y, Nishina S, et al. Fibroblast activation protein-α–expressing fibroblasts promote the progression of pancreatic ductal adenocarcinoma. *BMC Gastroenterol.* 2015;15:109.
30. Kamisawa T, Zen Y, Pillai S, Stone JH. IgG4-related disease. *Lancet.* 2015;385:1460–1471.

Value of ^{68}Ga-FAPI-04 and ^{18}F-FDG PET/CT in Early Prediction of Pathologic Response to Neoadjuvant Chemotherapy in Locally Advanced Gastric Cancer

Ying Miao*[1], Runhua Feng*[2], Teng Yu[3], Rui Guo[1], Min Zhang[1], Yue Wang[1], Wangxi Hai[1], Chengfang Shangguan[4], Zhenggang Zhu†[2], and Biao Li†[1,5]

[1]Department of Nuclear Medicine, Ruijin Hospital, Shanghai Jiao Tong University School of Medicine, Shanghai, China; [2]Department of General Surgery, Ruijin Hospital, Shanghai Jiao Tong University School of Medicine, Shanghai, China; [3]Department of Pathology, Ruijin Hospital, Shanghai Jiao Tong University School of Medicine, Shanghai, China; [4]Department of Oncology, Ruijin Hospital, Shanghai Jiao Tong University School of Medicine, Shanghai, China; and [5]Collaborative Innovation Center for Molecular Imaging of Precision Medicine, Ruijin Center, Shanghai, China

This prospective study investigated whether PET parameters from ^{18}F-FDG and ^{68}Ga-fibroblast activation protein inhibitor (FAPI)-04 PET/CT can predict a pathologic response to neoadjuvant chemotherapy (NAC) early in patients with locally advanced gastric cancer (LAGC). **Methods:** The study included 28 patients with LAGC who underwent ^{18}F-FDG PET/CT and ^{68}Ga-FAPI-04 PET/CT at baseline and after 1 cycle of NAC. PET parameters including SUV and tumor-to-background ratio (TBR), as well as the change rate of SUV and TBR, were recorded. Patients were classified as major or minor pathologic responders according to postoperative pathology findings. We compared the PET parameters between the 2 pathologic response groups and different treatment regimens and analyzed their predictive performance for tumor pathologic response. **Results:** Major pathologic responders had significantly lower ^{68}Ga-FAPI change rates (percentage SUV_{max} [%SUV_{max}], percentage SUV_{peak} [%SUV_{peak}], and percentage TBR [%TBR]) than minor pathologic responders. Among the PET parameters, ^{68}Ga-FAPI %SUV_{max} (area under the curve, 0.856; $P = 0.009$), %SUV_{peak} (area under the curve, 0.811; $P = 0.022$), and %TBR (area under the curve, 0.864; $P = 0.007$) were significant parameters for early prediction of pathologic response to NAC in LAGC; they had the same predictive accuracy of 89.29%, with the thresholds of decrease to at least 52.43%, 60.46%, and 52.96%, respectively. In addition, ^{68}Ga-FAPI %SUV_{max} and %TBR showed significant differences between the different treatment regimens. **Conclusion:** In this preliminary study, ^{68}Ga-FAPI-04 PET change rate parameters were preferable to ^{18}F-FDG in predicting pathologic response to NAC at an early stage in LAGC. ^{68}Ga-FAPI %SUV_{max} and %TBR may be better predictors of therapeutic response between different treatment regimens. These findings may help optimize the treatment for patients with LAGC.

Key Words: fibroblast activation protein inhibitor; PET/CT; neoadjuvant chemotherapy; locally advanced gastric cancer

J Nucl Med 2024; 65:213–220
DOI: 10.2967/jnumed.123.266403

In patients with locally advanced gastric cancer (LAGC) before radical surgery, neoadjuvant chemotherapy (NAC) is increasingly being applied because it may help control focal lesions, downstage tumors, increase R0 resection rates, and improve the disease-free and overall survival of patients (*1–4*). However, the role of preoperative NAC in LAGC remains controversial (*5,6*). For patients with poor sensitivity to chemotherapy, NAC may not only increase treatment-related adverse effects but also delay the optimal timing of surgery. Tumor regression grade (TRG) is an indicator of pathologic response to NAC and an important prognostic factor after NAC in gastric cancer (*7–9*). However, TRG can be determined only by postoperative pathology after completion of NAC treatment. Therefore, early prediction of patients with a suboptimal pathologic response and timely adjustment of their treatment plan are clinically important.

^{18}F-FDG PET aids in assessing treatment response in various malignancies (*10–13*). However, the interference of physiologic or inflammatory accumulation of ^{18}F-FDG in the gastric wall, as well as the low ^{18}F-FDG uptake in signet ring cell carcinoma (SRCC), mucinous adenocarcinoma, and some poorly differentiated carcinomas with a high mucinous component, limits its use for assessing treatment response in patients with gastric cancer (*14*).

^{68}Ga-labeled fibroblast activation protein inhibitor (FAPI), an emerging PET tracer, targets fibroblast activation protein overexpressed on cancer-associated fibroblasts, which are predominant in the tumor microenvironment (*15*). The use of FAPI-based tracers has shown promise in the assessment of digestive system tumors, particularly gastric cancer (*16,17*). Our recent study has substantiated that ^{68}Ga-FAPI-04 PET/CT is better than ^{18}F-FDG in detecting primary gastric cancer lesions and peritoneal metastases, particularly in poorly cohesive carcinoma (PCC) (including SRCC) (*18*). However, the value of ^{68}Ga-FAPI PET/CT in the assessment of treatment response is still unclear.

Hence, this prospective study aimed to investigate whether PET parameters from ^{18}F-FDG and ^{68}Ga-FAPI-04 PET/CT can be used to predict pathologic response to NAC early. The results would help personalize the treatment for patients with LAGC.

MATERIALS AND METHODS

Patients

This prospective clinical study was approved by the Ruijin Hospital Ethics Committee of Shanghai Jiao Tong University School of Medicine

---

Received Jul. 24, 2023; revision accepted Nov. 7, 2023.

For correspondence or reprints, contact Biao Li (lb10363@rjh.com.cn) or Zhenggang Zhu (zzg1954@hotmail.com).

*Contributed equally to this work.

†Contributed equally to this work.

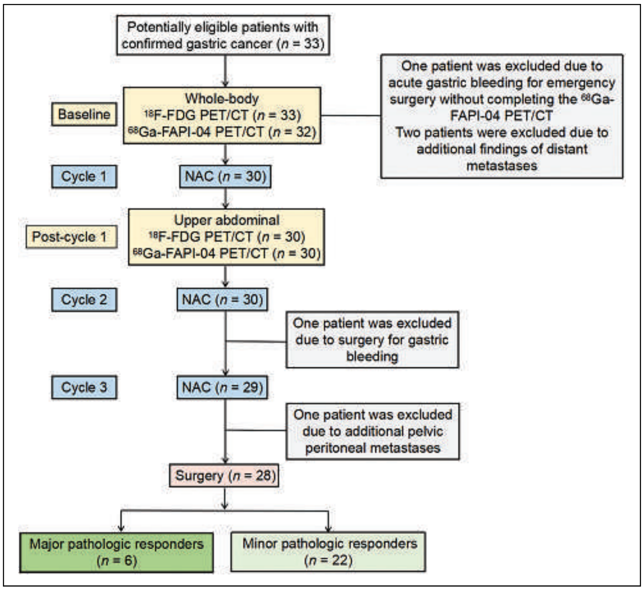

FIGURE 1. Flowchart of study.

and registered at ClinicalTrials.gov (NCT05140746). Patients were enrolled consecutively from September 2020 to October 2022, and all provided written informed consent. The inclusion criteria were as follows: age of 18–75 y; gastric adenocarcinoma histologically confirmed through gastroscopy; resectable gastric cancer; Eastern Cooperative Oncology Group performance status of 0–1; white blood count greater than 4×10^9/L; absolute neutrophil count greater than 2×10^9/L; hemoglobin greater than 90 g/L; platelets greater than 100×10^9/L; ejection fraction greater than 50%; serum bilirubin less than 1.5 times the upper level of normal; alanine-transaminase and aspartate-transaminase less than 1.5 times the upper level of normal; serum creatinine no more than 1.5 times the upper level of normal or glomerular filtration rate more than 60 mL/min; a signed informed consent form; willingness and ability to comply with the protocol throughout the study period; and no childbearing plan within 6 mo. Conversely, the exclusion criteria included the following: a second primary malignant disease in the past 5 y, except for basal cell and squamous cell carcinoma of the skin that have been cured; a known hypersensitivity reaction to chemotherapy drugs or with contraindications; severe disease or other unsuitable conditions determined by investigators and inadequate organ function; uncontrollable diabetes or a fasting blood glucose level of at least 11 mmol/L on the test day; severe mental symptoms, unconsciousness, or inability to complete the examination; pregnancy or possible pregnancy; breastfeeding; and noncompliance.

Treatment Schemes

The NAC treatment was based on the SOX regimen (tegafur gimeracil oteracil potassium capsule for 2 wk with oxaliplatin on day 1, every 3 wk for 3 courses). According to randomization, 16 received the SOX regimen alone, 4 received the SOX regimen combined with apatinib, and 8 received the SOX regimen combined with apatinib and camrelizumab. Surgery was performed at a median of 30.5 d (range, 3–6 wk) after NAC completion.

TABLE 1
Clinical and Pathologic Characteristics of Patients

Characteristic	*n*	%
Patients	28	
Sex		
Male	21	75.00
Female	7	25.00
Histologic type		
Containing PCC	14	50.00
Without PCC	14	50.00
Pathologic tumor staging		
ypT0	1	3.57
ypT1	2	7.14
ypT2	5	17.86
ypT3	12	42.86
ypT4	8	28.57
Pathologic lymph node staging		
ypN0	15	53.57
ypN1	8	28.57
ypN2	3	10.72
ypN3	2	7.14
Degree of differentiation		
Well	0	0.00
Moderately	9	32.14
Poorly	18	64.29
Not applicable	1	3.57
Lauren classification		
Intestinal subtype	12	42.86
Mixed subtype	3	10.71
Diffuse subtype	11	39.29
Not applicable	2	7.14
TRG		
0	1	3.57
1	5	17.86
2	16	57.14
3	6	21.43

Median age is 61 y (range, 38–75 y). Pathologic staging is according to eighth American Joint Committee on Cancer Post–Neoadjuvant Therapy Classification system.

PET/CT Imaging

^{68}Ga-FAPI-04 was prepared according to a previous procedure (*18*). Briefly, radioactive gallium (^{68}Ga) was extracted from a ^{68}Ge/^{68}Ga generator and added to a reactor vial with 20 μg of DOTA-FAPI-04 (CSBio) and then mixed with NaOAc (1 mol/L, 1 mL) to achieve a pH of 4. An automated synthesis module (Trasis) was used to react the mixture further at 100°C for 10 min. ^{18}F-FDG was routinely synthesized. Patients underwent ^{18}F-FDG PET/CT and ^{68}Ga-FAPI-04 PET/CT imaging covering the whole body (from the top of the head to the upper thigh) at baseline and the upper abdomen after 1 NAC cycle. The interval between ^{18}F-FDG and ^{68}Ga-FAPI-04 PET/CT scans was within 7 d, and the interval between the first cycle of NAC treatment and the postcycle 1 PET/CT scan was 15–20 d. After being injected with ^{18}F-FDG (3.7–4.44 MBq/kg) or ^{68}Ga-FAPI-04 (1.85–2.96 MBq/kg), patients rested for 60–90 or 30–60 min, respectively. Patients with excluded contraindications were then administered 20 mg of hyoscine-*N*-butylbromide intravenously and then drank approximately 500 mL of water to distend the stomach before scanning. PET/CT scans

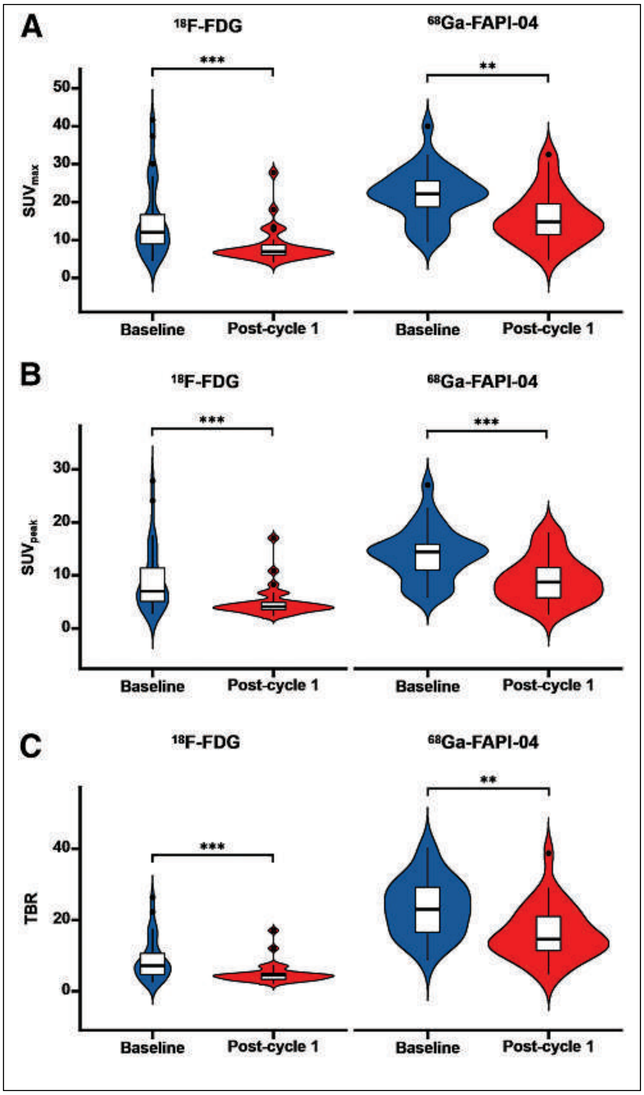

FIGURE 2. Changes in PET parameters at baseline and after 1 NAC cycle: SUV_{max} (A), SUV_{peak} (B), and TBR (C) from ^{18}F-FDG and ^{68}Ga-FAPI-04 PET. $^{**}P < 0.01$. $^{***}P < 0.001$.

were performed using a dedicated PET/CT scanner (Biograph Vision 450; Siemens Healthineers). CT images were captured using CARE Dose4D (Siemens) technique (120 kV, automatic mA-modulation), whereas PET images were captured in 3-dimensional mode and reconstructed in a 440 × 440 matrix (iterations, 4, subsets, 5) using the TrueX + TOF (ultraHD-PET; Siemens) method.

Image Analysis

All PET/CT images were independently evaluated by 2 experienced nuclear medicine physicians. Both baseline and postcycle 1 ^{18}F-FDG PET/CT and ^{68}Ga-FAPI-04 PET/CT images were analyzed using the syngo.via software (Siemens Molecular Imaging). A spheric region of interest was drawn around tumor lesions, and it was automatically adjusted to a 3-dimensional volume of interest at 60% isocontour (*19*). PET parameters including the SUV_{max} and the SUV_{peak} were recorded. To measure the SUV_{mean} of the mediastinal blood pool background, we set a 10-mm-diameter volume of interest on the descending aorta. Furthermore, we calculated the tumor-to-background ratio (TBR) as tumor lesion SUV_{max}/mediastinal blood pool background SUV_{mean}; the change rate of SUV (%SUV) as [postcycle 1 SUV – baseline SUV]/baseline SUV × 100%; and the change rate of TBR (%TBR) as [postcycle 1 TBR – baseline TBR]/baseline TBR × 100%.

Pathologic Assessment

The postoperative specimens were examined histopathologically, and the TRG was based on the following: grade 0, complete regression with no viable cancer cells; grade 1, moderate regression with single cancer cells or a small cluster of cancer cells; grade 2, minimal regression with residual cancer but less than fibrosis; grade 3, poor regression with extensive residual cancer, or minimal or no cancer cell death (*20*). Grades 0 and 1 indicate a major pathologic response, whereas grades 2 and 3 indicate a minor pathologic response.

Statistical Analysis

Statistical analysis was performed using the IBM SPSS Statistics 26.0 software. Continuous variables for SUV, TBR, %SUV, and %TBR are presented as medians and interquartile ranges, whereas categoric variables are expressed as numbers and percentages. The Wilcoxon signed-rank test was used to compare ^{18}F-FDG and ^{68}Ga-FAPI-04 PET parameters, as well as PET parameters at baseline and after 1 NAC cycle. The Mann–Whitney *U* test was used to compare PET parameters between the major and minor pathologic responders. The Kruskal–Wallis test was used to compare PET parameters between the different regimens. The correlation between variables was assessed using the Spearman rank correlation coefficient. The area under the curve (AUC) was obtained using the receiver operating characteristic curve, and the optimal predictive threshold was further calculated using the Jorden index (i.e., sensitivity + specificity − 1). The predictive performance for tumor pathologic response, including sensitivity, specificity, positive predictive value, negative predictive value, and accuracy, was also analyzed. All statistical data were analyzed using the 2-tailed test, and a *P* value of less than 0.05 was considered statistically significant.

RESULTS

Patients

Of the 33 potentially eligible patients, 28 were ultimately enrolled and succeeded in completing the study. Figure 1 presents the study's flowchart. Within the cohort, 6 patients were major pathologic responders, whereas 22 were minor pathologic responders. Table 1 summarizes the clinical and pathologic characteristics of the 28 patients.

Comparison of PET Parameters at Baseline and 1 Cycle After NAC in Patients with LAGC

At baseline, all 28 patients were ^{68}Ga-FAPI-04–avid, whereas 23 of 28 were ^{18}F-FDG–avid. Five patients with non–^{18}F-FDG–avid tumors were confirmed as having PCC (with partial SRCC). Moreover, baseline ^{68}Ga-FAPI-04 SUV_{max} was significantly higher than ^{18}F-FDG SUV_{max} (22.15 [18.44–26.59] vs. 12.05 [8.25–19.32], $P = 0.007$), as well as SUV_{peak} (14.43 [10.73–15.90] vs. 7 [5.05–13.00], $P = 0.003$) and TBR (23.01 [15.93–29.24] vs. 7.17 [4.51–11.54], $P < 0.001$). After 1 NAC cycle, ^{18}F-FDG PET parameters (SUV_{max}, SUV_{peak}, and TBR) significantly decreased ($P < 0.001$, $P < 0.001$, and $P < 0.001$, respectively), as did ^{68}Ga-FAPI-04 PET parameters ($P = 0.001$, $P < 0.001$, and $P = 0.001$, respectively). Figure 2 shows the changes in ^{18}F-FDG and ^{68}Ga-FAPI-04 PET parameters at baseline and after 1 NAC cycle in patients with LAGC.

Correlations Between PET Parameters and Pathologic Features

Figure 3 presents the correlations between ^{18}F-FDG and ^{68}Ga-FAPI-04 PET parameters and the pathologic features. First, the

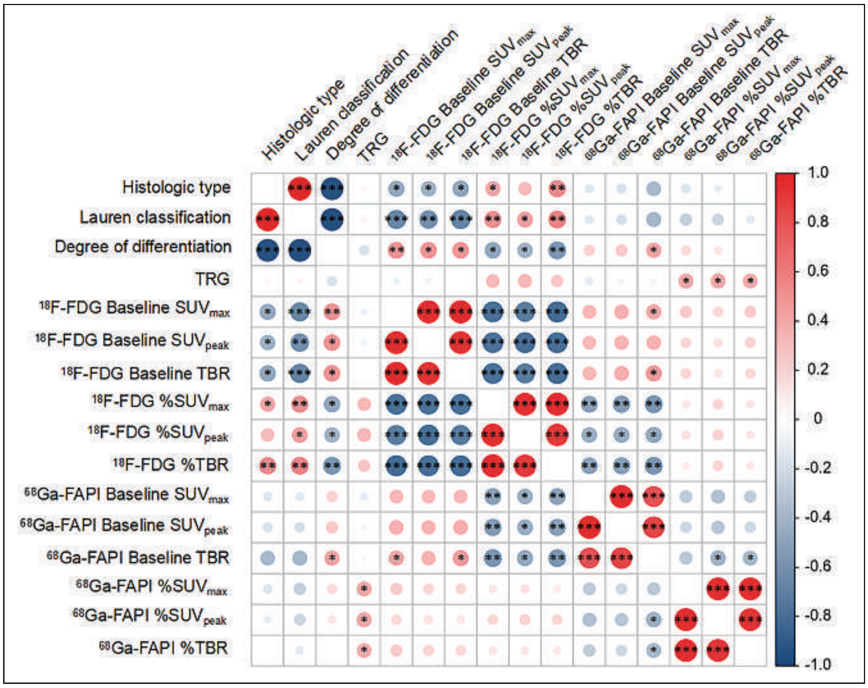

FIGURE 3. Correlations between PET parameters and pathologic features. Red circle denotes positive correlation between 2 factors, whereas blue circle denotes negative correlation. Darker color indicates stronger correlation. *P* values show statistical difference in correlation between 2 factors. *$P < 0.05$. **$P < 0.01$. ***$P < 0.001$.

^{18}F-FDG baseline and change rate parameters correlated with histologic type, Lauren classification, and differentiation degree, whereas most of the ^{68}Ga-FAPI-04 PET parameters did not correlate with the abovementioned pathologic characteristics. Second, TRG correlated with ^{68}Ga-FAPI-04 change rate parameters including %SUV$_{max}$, %SUV$_{peak}$, and %TBR but not with the baseline or change rate parameters of ^{18}F-FDG PET. Additionally, the ^{18}F-FDG PET parameters partially correlated with ^{68}Ga-FAPI-04 parameters, but there was no correlation between ^{18}F-FDG and ^{68}Ga-FAPI-04 PET change rate parameters.

Comparison of PET Parameters Between NAC Major and Minor Pathologic Responder Groups

Table 2 compares the ^{18}F-FDG and ^{68}Ga-FAPI PET parameters between the NAC major and minor pathologic responders in the whole cohort. The results showed that major pathologic responders had significantly lower ^{68}Ga-FAPI change rate parameters including %SUV$_{max}$, %SUV$_{peak}$, and %TBR ($P = 0.009$, $P = 0.022$, and $P = 0.007$, respectively) than minor pathologic responders, whereas both ^{18}F-FDG and ^{68}Ga-FAPI baseline PET parameters and ^{18}F-FDG change rate parameters showed no significant difference between the 2 groups. Supplemental Table 1 further compares the ^{18}F-FDG PET parameters between the 2 responder groups in 23 patients with ^{18}F-FDG–avid tumors (supplemental materials are available at http://jnm.snmjournals.org). The results were consistent with those of the overall cohort. Figure 4 displays representative cases of a major and a minor pathologic responder.

TABLE 2
Comparison of PET Parameters Between NAC Major and Minor Pathologic Responder Groups

	Major pathologic responder ($n = 6$)		Minor pathologic responder ($n = 22$)			
Parameter	Median	IQR	Median	IQR	Z	*P*
^{18}F-FDG						
Baseline SUV$_{max}$	12.98	5.43 to 16.71	11.19	8.96 to 26.37	−0.336	0.737
Baseline SUV$_{peak}$	7.89	3.41 to 11.19	6.59	5.09 to 14.03	−0.168	0.867
Baseline TBR	7.37	2.64 to 10.60	7.17	4.69 to 14.80	−0.672	0.502
%SUV$_{max}$	−49.54	−62.30 to −14.03	−35.96	−51.64 to −12.88	−0.840	0.401
%SUV$_{peak}$	−42.86	−74.92 to −22.87	−37.38	−59.84 to −22.73	−0.784	0.433
%TBR	−47.82	−64.05 to −12.65	−35.66	−52.60 to −17.36	−0.728	0.467
^{68}Ga-FAPI-04						
Baseline SUV$_{max}$	21.97	13.33 to 34.38	22.47	18.73 to 25.58	−0.224	0.823
Baseline SUV$_{peak}$	12.76	7.39 to 23.84	14.43	11.19 to 15.89	−0.056	0.955
Baseline TBR	24.22	13.98 to 39.25	23.01	18.43 to 28.92	−0.280	0.780
%SUV$_{max}$	−62.74	−65.63 to −42.29	−16.92	−37.26 to 1.03	−2.631	0.009*
%SUV$_{peak}$	−64.00	−66.35 to −46.52	−21.19	−52.71 to −10.30	−2.296	0.022†
%TBR	−65.06	−67.61 to −42.25	−25.46	−41.46 to 7.25	−2.687	0.007*

---

*$P < 0.01$.
$^{\dagger}P < 0.05$.
IQR = interquartile range.

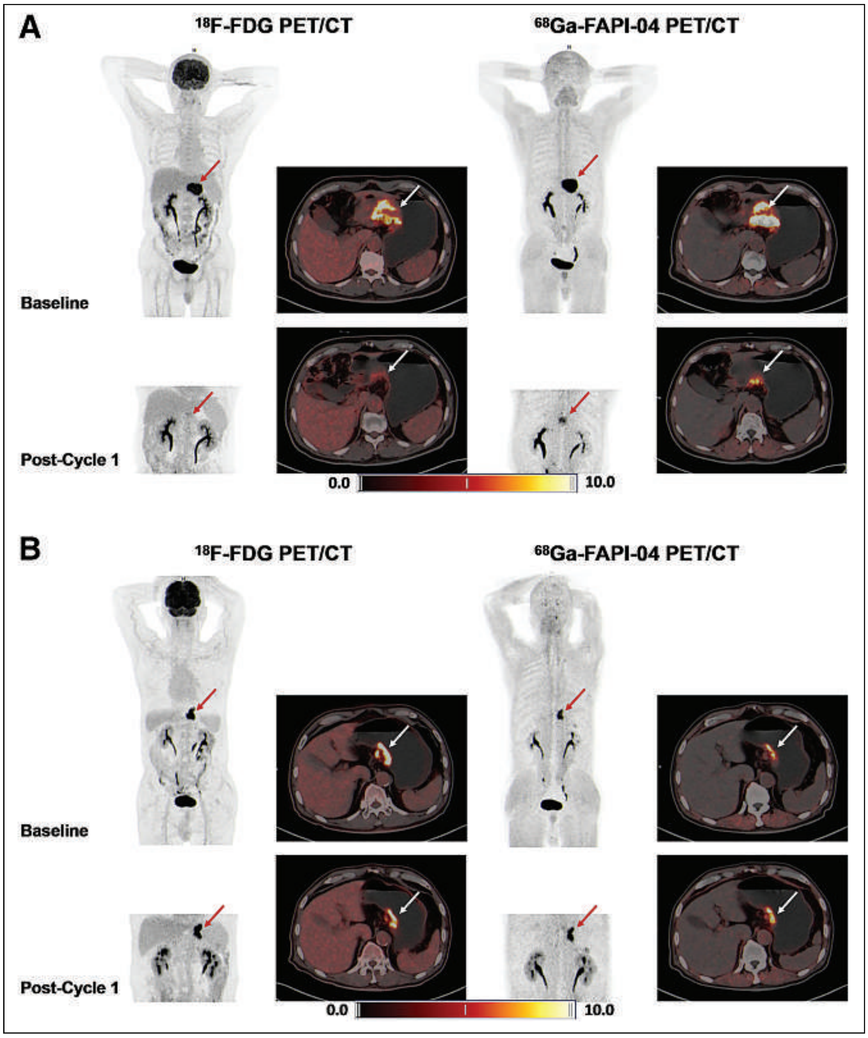

FIGURE 4. ^{18}F-FDG and ^{68}Ga-FAPI-04 PET/CT images at baseline and after 1 NAC cycle: major pathologic responder with TRG grade 0 (arrows, A) and minor pathologic responder with TRG grade 3 (arrows, B).

Performance of PET Parameters in Early Prediction of Pathologic Response to NAC

Supplemental Table 2 and Figure 5 present the receiver operating characteristic curves assessing the predictive accuracy of PET parameters in identifying major and minor pathologic responders to NAC. The AUCs for ^{68}Ga-FAPI %SUV$_{max}$, %SUV$_{peak}$, and %TBR were significant (0.856, 0.811, and 0.864, respectively) among the various PET parameters. Table 3 displays the predictive performance of significant PET parameters in early prediction of pathologic response to NAC. ^{68}Ga-FAPI %SUV$_{max}$, %SUV$_{peak}$, and %TBR had the same accuracy of 89.29%, with the thresholds of decrease to at least 52.43%, 60.46%, and 52.96%, respectively; the sensitivity, specificity, positive predictive value, and negative predictive value were 83.33%, 90.91%, 71.43%, and 95.24%, respectively.

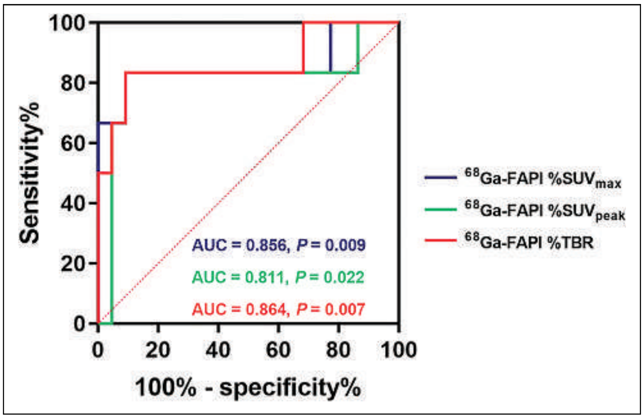

FIGURE 5. Receiver operating characteristic curves for ability of PET parameters to predict pathologic response to NAC early.

Comparison of PET Parameters Between Different NAC Regimens

Figure 6 further compares the ^{18}F-FDG and ^{68}Ga-FAPI change rate parameters among the 3 different regimens. The results showed that ^{68}Ga-FAPI %SUV$_{max}$ and %TBR were significantly lower in the SOX-plus-apatinib-plus-camrelizumab group than in the SOX group (P = 0.028 and 0.028, respectively). However, there were no significant differences between the other groups and for other PET parameters. According to the postoperative pathology, in the SOX, SOX-plus-apatinib, and SOX-plus-apatinib-plus-camrelizumab groups, there were 1 of 16, 0 of 4, and 5 of 8 patients, respectively, who achieved a major pathologic response.

DISCUSSION

In this study, TRG correlated with ^{68}Ga-FAPI change rate parameters including %SUV$_{max}$, %SUV$_{peak}$, and %TBR. Major pathologic responders had significantly lower ^{68}Ga-FAPI change rate parameters than minor pathologic responders. ^{68}Ga-FAPI %SUV$_{max}$, %SUV$_{peak}$, and %TBR could provide an early indication of pathologic response to NAC in LAGC and outperformed ^{18}F-FDG PET parameters. ^{68}Ga-FAPI %SUV$_{max}$ and %TBR may be better predictors of therapeutic response between different treatment regimens.

Considering the heterogeneity of gastric cancer, the therapeutic response to NAC is highly variable and is strongly associated with patient prognosis. A 2-center study found that the 3- and 5-y survival rates of patients with gastric cancer with TRG 0–1 after NAC plus surgery were 85.2% and 74.5%, respectively, compared with 28.2%–56.1% and 23%–44.1%, respectively, in patients with TRG 2–3 (*7*). An earlier metaanalysis of 17 studies on gastroesophageal cancer demonstrated that compared with no or minimal pathologic response after NAC, a major pathologic response is significantly associated with higher overall survival and disease-free survival (*8*). Therefore, we sought to obtain indirect prognostic information using PET/CT imaging techniques to predict pathologic response to NAC early.

Several studies have explored the value of ^{18}F-FDG PET for therapeutic monitoring in gastric cancer but obtained controversial findings (*21*). In our study, ^{18}F-FDG PET parameters did not

TABLE 3

Performance of PET Parameters in Early Prediction of Pathologic Response to NAC

Parameter	AUC	P	Threshold	Sensitivity (%)	Specificity (%)	PPV (%)	NPV (%)	Accuracy (%)
^{68}Ga-FAPI %SUV$_{max}$	0.856	0.009*	−52.43	83.33	90.91	71.43	95.24	89.29
^{68}Ga-FAPI %SUV$_{peak}$	0.811	0.022†	−60.46	83.33	90.91	71.43	95.24	89.29
^{68}Ga-FAPI %TBR	0.864	0.007*	−52.96	83.33	90.91	71.43	95.24	89.29

---

*$P < 0.01$.

$^{\dagger}P < 0.05$.

PPV = positive predictive value; NPV = negative predictive value.

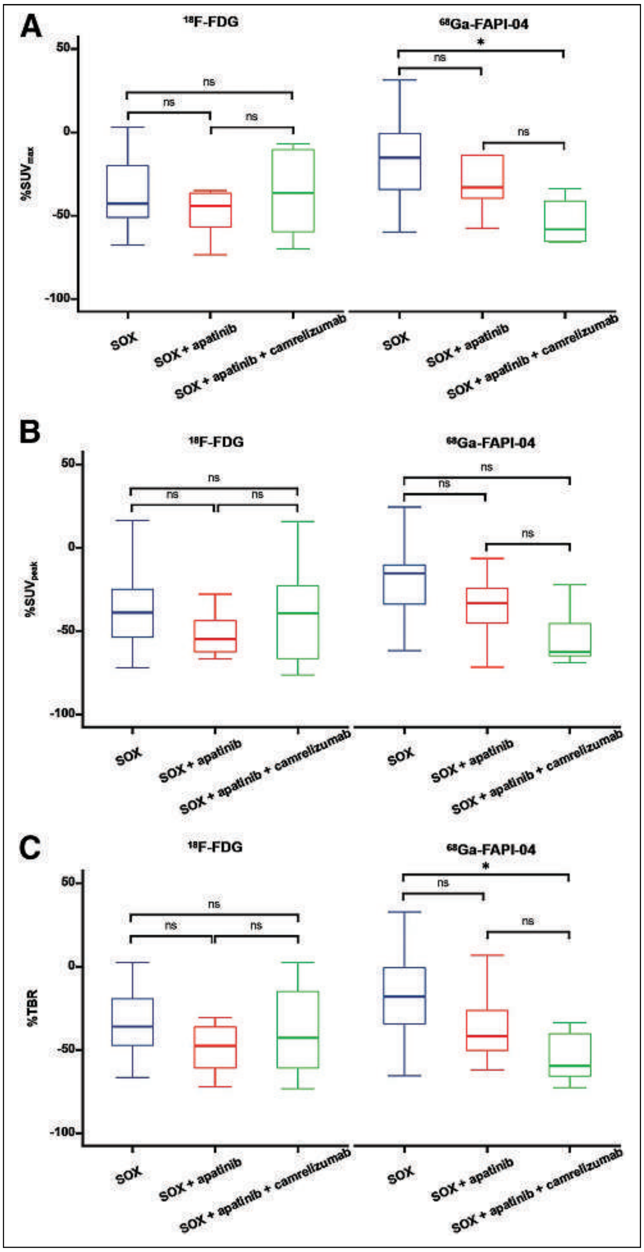

FIGURE 6. Comparison of change rate parameters between different NAC regimens: %SUV$_{max}$ (A), %SUV$_{peak}$ (B), and %TBR (C) from ^{18}F-FDG and ^{68}Ga-FAPI-04 PET. *$P < 0.05$. ns = not statistically significant.

correlate with TRG and were not significantly different between major and minor pathologic responders. This was further verified in ^{18}F-FDG–avid LAGC, as the assessment of metabolic response in non–^{18}F-FDG–avid gastric tumors was considered limited. For PCC (including SRCC), the incidence is on the rise, with a higher proportion of younger women and advanced-stage patients than for non-PCC subtypes, which tend to present as non–^{18}F-FDG–avid tumors, in part due to high mucus content, low tumor cell density, and low glucose transporter 1 expression (*22–24*). Given their poorer prognosis, effective assessment tools are needed.

Numerous studies revealed that ^{68}Ga-FAPI PET is preferable to ^{18}F-FDG in gastric cancer staging and restaging (*22,25–29*). Our previous study also confirmed the superiority of ^{68}Ga-FAPI PET over ^{18}F-FDG in detecting gastric cancer primary lesions and peritoneal metastases, especially in PCC including SRCC (*18*). As observed in our present study, most of the ^{68}Ga-FAPI-04 PET parameters had no significant correlation with the histologic type, Lauren classification, and degree of differentiation of the tumors, consistent with our previous finding (*18*). This may be because FAPI reflects the characteristics of the tumor stroma rather than the tumor cells. In addition, the value of ^{68}Ga-FAPI PET/CT in the early prediction of NAC treatment response in LAGC remains unclear.

Although previous case reports and series showed the initial value of FAPI PET in monitoring treatment response of breast myeloid sarcoma, peritoneal carcinomatosis, and gastric cancer, our prospective study further indicated that ^{68}Ga-FAPI PET change rate parameters (%SUV$_{max}$, %SUV$_{peak}$, and %TBR) could predict the pathologic response to NAC in LAGC early (*27,29–31*). Of these, ^{68}Ga-FAPI %SUV$_{max}$ and %TBR further discriminated the treatment response between different treatment regimens, suggesting that ^{68}Ga-FAPI PET may have potential applicability for monitoring the efficacy of different treatment regimens. However, baseline ^{68}Ga-FAPI PET parameters did not correlate with therapeutic response in our study—a finding that is inconsistent with the findings of Hu et al. (*32*). This may be attributed to different criteria used to evaluate the therapeutic response. Additionally, 5 patients with non–^{18}F-FDG–avid tumors (confirmed as PCC with partial SRCC) were all avid on ^{68}Ga-FAPI-04 PET, suggesting the potential of ^{68}Ga-FAPI PET parameters to predict NAC pathologic response early, especially in non–^{18}F-FDG–avid gastric cancer such as PCC (including SRCC). A typical case is shown in Figure 7. However, the fact that no significant changes in ^{68}Ga-FAPI PET parameters were observed in one of our major pathologic responders—possibly because of superimposition of inflammation or fibrosis after chemotherapy—may be a potential pitfall in predicting NAC efficacy that requires further investigation (*33*).

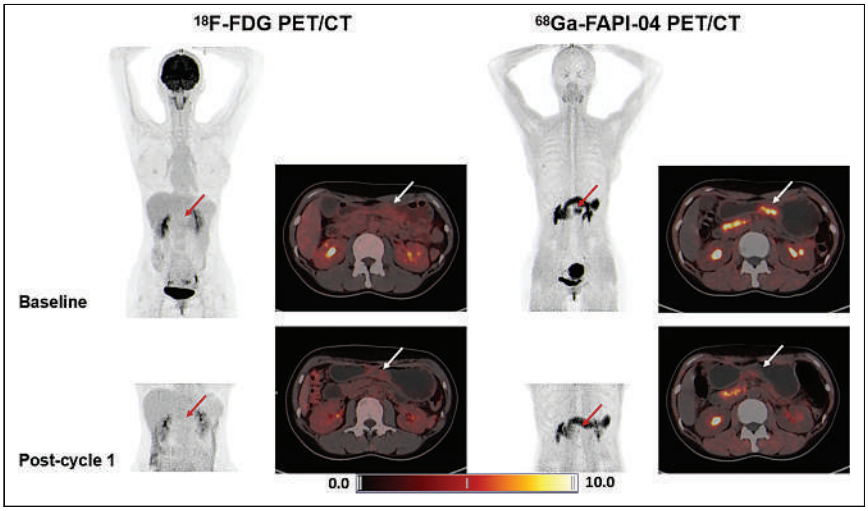

FIGURE 7. ^{18}F-FDG and ^{68}Ga-FAPI-04 PET/CT images at baseline and after 1 NAC cycle in major pathologic responder with TRG grade 1. Patient had non–^{18}F-FDG–avid LAGC (arrows), confirmed as PCC.

This study had several limitations. First, the sample size was relatively small. Especially, the number of patients showing a major response to NAC was limited, preventing further stratification analysis according to clinicopathologic characteristics. Second, an upper abdominal local PET/CT scan was used as an early evaluation scheme in our study; its use may contribute to underestimation because of the heterogeneity of tumor sensitivity to chemotherapy. For example, one of our patients had a new metastatic lesion in the pelvic peritoneum detected by laparoscopy after NAC completion, despite a significant reduction of ^{68}Ga-FAPI uptake in the primary lesion after 1 NAC cycle. In addition, our study was conducted at a single center; further large, multicenter clinical trials are needed to confirm our conclusion.

CONCLUSION

This preliminary study suggests that ^{68}Ga-FAPI-04 PET change rate parameters appear to be more predictive of the pathologic response at an early stage than ^{18}F-FDG PET parameters. ^{68}Ga-FAPI %SUV$_{max}$ and %TBR may be better predictors of therapeutic response between different treatment regimens, but this possibility needs to be verified in a larger cohort. This insight may help us understand the sensitivity of chemotherapy and thus optimize treatment regimens.

KEY POINTS

QUESTION: Can PET parameters from ^{18}F-FDG and ^{68}Ga-FAPI-04 PET/CT predict a pathologic response to NAC early in patients with LAGC?

PERTINENT FINDINGS: ^{68}Ga-FAPI PET parameters (including %SUV$_{max}$, %SUV$_{peak}$, and %TBR) could provide an early indication of pathologic response to NAC in LAGC and outperformed ^{18}F-FDG PET parameters. ^{68}Ga-FAPI %SUV$_{max}$ and %TBR may be better predictors of therapeutic response between different treatment regimens.

IMPLICATIONS FOR PATIENT CARE: Our preliminary findings may help optimize treatment for patients with LAGC.

DISCLOSURE

This work was supported by the Shanghai Municipal Key Clinical Specialty (shslczdzk03403); a joint research development project between Shenkang and United Imaging on clinical research and translation (SKLY2022CRT403); and the Shanghai Jiao Tong University "Star of Jiao Tong University" Program Medical–Industrial Intersection Research Foundation (YG2021QN15). No other potential conflict of interest relevant to this article was reported.

REFERENCES

1. Zhang X, Liang H, Li Z, et al. Perioperative or postoperative adjuvant oxaliplatin with S-1 versus adjuvant oxaliplatin with capecitabine in patients with locally advanced gastric or gastro-oesophageal junction adenocarcinoma undergoing D2 gastrectomy (RESOLVE): an open-label, superiority and non-inferiority, phase 3 randomised controlled trial. *Lancet Oncol.* 2021;22:1081–1092.
2. Cunningham D, Allum WH, Stenning SP, et al. Perioperative chemotherapy versus surgery alone for resectable gastroesophageal cancer. *N Engl J Med.* 2006;355:11–20.
3. Ychou M, Boige V, Pignon JP, et al. Perioperative chemotherapy compared with surgery alone for resectable gastroesophageal adenocarcinoma: an FNCLCC and FFCD multicenter phase III trial. *J Clin Oncol.* 2011;29:1715–1721.
4. Guan WL, He Y, Xu RH. Gastric cancer treatment: recent progress and future perspectives. *J Hematol Oncol.* 2023;16:57.
5. Japanese Gastric Cancer Association. Japanese gastric cancer treatment guidelines 2021 (6th edition). *Gastric Cancer.* 2023;26:1–25.
6. Iwasaki Y, Terashima M, Mizusawa J, et al. Gastrectomy with or without neoadjuvant S-1 plus cisplatin for type 4 or large type 3 gastric cancer (JCOG0501): an open-label, phase 3, randomized controlled trial. *Gastric Cancer.* 2021;24:492–502.
7. Xie JW, Lu J, Xu BB, et al. Prognostic value of tumor regression grading in patients treated with neoadjuvant chemotherapy plus surgery for gastric cancer. *Front Oncol.* 2021;11:587856.
8. Tomasello G, Petrelli F, Ghidini M, et al. Tumor regression grade and survival after neoadjuvant treatment in gastro-esophageal cancer: a meta-analysis of 17 published studies. *Eur J Surg Oncol.* 2017;43:1607–1616.
9. Martin-Romano P, Sola JJ, Diaz-Gonzalez JA, et al. Role of histological regression grade after two neoadjuvant approaches with or without radiotherapy in locally advanced gastric cancer. *Br J Cancer.* 2016;115:655–663.
10. Cascini GL, Avallone A, Delrio P, et al. ^{18}F-FDG PET is an early predictor of pathologic tumor response to preoperative radiochemotherapy in locally advanced rectal cancer. *J Nucl Med.* 2006;47:1241–1248.
11. Wang X, Yang W, Zhou Q, et al. The role of ^{18}F-FDG PET/CT in predicting the pathological response to neoadjuvant PD-1 blockade in combination with chemotherapy for resectable esophageal squamous cell carcinoma. *Eur J Nucl Med Mol Imaging.* 2022;49:4241–4251.
12. Davis JC, Daw NC, Navid F, et al. ^{18}F-FDG uptake during early adjuvant chemotherapy predicts histologic response in pediatric and young adult patients with osteosarcoma. *J Nucl Med.* 2018;59:25–30.
13. Avril S, Muzic RF Jr, Plecha D, Traughber BJ, Vinayak S, Avril N. ^{18}F-FDG PET/CT for monitoring of treatment response in breast cancer. *J Nucl Med.* 2016; 57(suppl 1):34S–39S.
14. Shimada H, Okazumi S, Koyama M, Murakami K. Japanese Gastric Cancer Association Task Force for Research Promotion: clinical utility of ^{18}F-fluoro-2-deoxyglucose positron emission tomography in gastric cancer. A systematic review of the literature. *Gastric Cancer.* 2011;14:13–21.
15. Hamson EJ, Keane FM, Tholen S, Schilling O, Gorrell MD. Understanding fibroblast activation protein (FAP): substrates, activities, expression and targeting for cancer therapy. *Proteomics Clin Appl.* 2014;8:454–463.
16. Peng D, He J, Liu H, Cao J, Wang Y, Chen Y. FAPI PET/CT research progress in digestive system tumours. *Dig Liver Dis.* 2022;54:164–169.
17. Huang D, Wu J, Zhong H, et al. [^{68}Ga]Ga-FAPI PET for the evaluation of digestive system tumors: systematic review and meta-analysis. *Eur J Nucl Med Mol Imaging.* 2023;50:908–920.

18. Miao Y, Feng R, Guo R, et al. Utility of [^{68}Ga]FAPI-04 and [^{18}F]FDG dual-tracer PET/CT in the initial evaluation of gastric cancer. *Eur Radiol.* 2023;33:4355–4366.
19. Wang L, Tang G. Comparison of ^{68}Ga-FAPI and ^{18}F-FDG PET/CT in the evaluation of advanced lung cancer. 2022:211424.
20. Sinnamon AJ, Savoldy M, Mehta R, et al. Tumor regression grade and overall survival following gastrectomy with preoperative therapy for gastric cancer. *Ann Surg Oncol.* 2023;30:3580–3589.
21. Tang L, Wang XJ, Baba H, Giganti F. Gastric cancer and image-derived quantitative parameters: part 2—a critical review of DCE-MRI and ^{18}F-FDG PET/CT findings. *Eur Radiol.* 2020;30:247–260.
22. Chen H, Pang Y, Li J, et al. Comparison of [^{68}Ga]Ga-FAPI and [^{18}F]FDG uptake in patients with gastric signet-ring-cell carcinoma: a multicenter retrospective study. *Eur Radiol.* 2023;33:1329–1341.
23. Mariette C, Carneiro F, Grabsch HI, et al. Consensus on the pathological definition and classification of poorly cohesive gastric carcinoma. *Gastric Cancer.* 2019;22:1–9.
24. Nakamura K, Eto K, Iwagami S, et al. Clinicopathological characteristics and prognosis of poorly cohesive cell subtype of gastric cancer. *Int J Clin Oncol.* 2022;27:512–519.
25. Gündoğan C, Komek H, Can C, et al. Comparison of ^{18}F-FDG PET/CT and ^{68}Ga-FAPI-04 PET/CT in the staging and restaging of gastric adenocarcinoma. *Nucl Med Commun.* 2022;43:64–72.
26. Jiang D, Chen X, You Z, et al. Comparison of [^{68}Ga]Ga-FAPI-04 and [^{18}F]-FDG for the detection of primary and metastatic lesions in patients with gastric cancer: a bicentric retrospective study. *Eur J Nucl Med Mol Imaging.* 2022;49:732–742.
27. Kuten J, Levine C, Shamni O, et al. Head-to-head comparison of [^{68}Ga]Ga-FAPI-04 and [^{18}F]-FDG PET/CT in evaluating the extent of disease in gastric adenocarcinoma. *Eur J Nucl Med Mol Imaging.* 2022;49:743–750.
28. Qin C, Shao F, Gai Y, et al. ^{68}Ga-DOTA-FAPI-04 PET/MR in the evaluation of gastric carcinomas: comparison with ^{18}F-FDG PET/CT. *J Nucl Med.* 2022;63:81–88.
29. Lin R, Lin Z, Chen Z, et al. [^{68}Ga]Ga-DOTA-FAPI-04 PET/CT in the evaluation of gastric cancer: comparison with [^{18}F]FDG PET/CT. *Eur J Nucl Med Mol Imaging.* 2022;49:2960–2971.
30. Wu S, Lin Z, Shang Q, Pang Y, Chen H. Use of ^{68}Ga-FAPI PET/CT for detecting myeloid sarcoma of the breast and assessing early response to chemotherapy. *Clin Nucl Med.* 2022;47:549–550.
31. Röhrich M, Naumann P, Giesel FL, et al. Impact of ^{68}Ga-FAPI PET/CT imaging on the therapeutic management of primary and recurrent pancreatic ductal adenocarcinomas. *J Nucl Med.* 2021;62:779–786.
32. Hu X, Zhou T, Ren J, et al. Response prediction using ^{18}F-FAPI-04 PET/CT in patients with esophageal squamous cell carcinoma treated with concurrent chemoradiotherapy. *J Nucl Med.* 2023;64:625–631.
33. Af Burén S, Tran TA, Klevebro F, Holstensson M, Axelsson RA. ^{68}Ga-FAPI-46 PET/CT imaging pitfall in assessing residual gastric cancer early after chemotherapy. *Clin Nucl Med.* 2022;47:644–645.

Summary: SNMMI Procedure Standard/EANM Practice Guideline for Estrogen Receptor Imaging of Patients with Breast Cancer Using 16α-[^{18}F]Fluoro-17β-Estradiol PET

David Mankoff*[1], Soňa Balogová*[2,3], Lisa Dunnwald[4], Farrokh Dehdashti[5], Erik DeVries[6], Laura Evangelista[7], Michel Van Kruchten[6], Sofia Carrilho Vaz[8,9], Amy Fowler[10], Hannah Linden[11], and Gary A. Ulaner[12]

[1]University of Pennsylvania, Philadelphia, Pennsylvania; [2]Comenius University, St. Elisabeth Oncology Institute, and NNG Bory, Bratislava, Slovakia; [3]AP-HP Hôpital Tenon, Université Sorbonne, Paris, France; [4]University of Iowa, Iowa City, Iowa; [5]Washington University, Saint Louis, Missouri; [6]University of Groningen, Groningen, The Netherlands; [7]University of Padova, Padova, Italy; [8]Champalimaud Center for the Unknown, Champalimaud Foundation, Lisbon, Portugal; [9]Leiden University Medical Center, Leiden, The Netherlands; [10]University of Wisconsin, Madison, Wisconsin; [11]University of Washington, Seattle, Washington; and [12]Hoag Family Cancer Institute, Newport Beach, California

The estrogen receptor (ER), a steroid hormone receptor important in female physiology, is a significant contributor to breast carcinogenesis and progression and, as such, is an important therapeutic target. Approximately 70% of breast cancers will express ER at presentation, and the determination of ER expression by tissue assay, usually by immunohistochemistry, is part of the standard of care for newly diagnosed breast cancer. ER expression is important in guiding the approach to treatment, especially with the increase in relevant systemic therapies. The ER-targeting imaging agent 16α-[^{18}F]fluoro-17β-estradiol ([^{18}F]FES) is approved for clinical use by regulatory agencies in France and the United States. Multiple studies suggest the advantages of [^{18}F]FES PET in assessing tumor ER expression, the ability of both qualitative and quantitative [^{18}F]FES PET measures to predict response to ER-targeted therapy, and the ability of [^{18}F]FES PET to clarify equivocal staging and restaging results in patients with ER-expressing cancers. [^{18}F]FES PET/CT may also be helpful in staging invasive lobular breast cancer and low-grade ER-expressing invasive ductal cancers and, in some cases, may be a substitute for biopsy. The Society of Nuclear Medicine and Molecular Imaging and the European Association of Nuclear Medicine in June 2023 released a procedure standard/practice guideline for [^{18}F]FES PET ER imaging of patients with breast cancer. The goal of the standard/guideline is to assist physicians in recommending, performing, interpreting, and reporting the results of [^{18}F]FES PET studies for patients with breast cancer and to provide clinicians with the best available evidence, inform them about areas where robust evidence is lacking, and help them deliver the best possible diagnostic efficacy and study quality for their patients. Also reviewed are standardized quality control, quality assurance, and imaging procedures for [^{18}F]FES PET. The authors emphasize the importance of precision, accuracy, repeatability, and reproducibility for both clinical management of patients and for use of [^{18}F]FES PET in multicenter trials. A standardized imaging procedure, in combination with already published appropriate-use criteria, will help promote the use of [^{18}F]FES PET and enhance subsequent research. This brief summary article reviews the content of the joint standard/guideline, which is available in its entirety at https://www.snmmi.org/ClinicalPractice/content.aspx?ItemNumber=6414&navItemNumbe=10790.

Key Words: breast cancer; estrogen receptor imaging; practice guidelines; [^{18}F]FES PET

J Nucl Med 2024; 65:221–223
DOI: 10.2967/jnumed.123.266938

Breast cancer is the most common nonskin cancer in women and remains an important cause of mortality. Systemic therapy of both early- and later-stage breast cancer is an important contributor to decreased breast cancer mortality, and advances in individualized and targeted therapy have improved outcomes and mitigated treatment toxicity. The estrogen receptor (ER), a steroid hormone receptor important in female physiology, is a significant contributor to breast carcinogenesis and progression and, as such, is a useful therapeutic target. Approximately 70% of breast cancers will express ER at presentation, and the determination of ER expression by tissue assay—most commonly using immunohistochemistry methods—is part of the standard of care of newly diagnosed breast cancer. ER expression carries both prognostic and predictive information and is important in guiding the approach to treatment, especially the use of ER-targeted systemic therapy. After a long development period and research by selective centers capable of generating novel imaging compounds, the ER-targeted PET imaging agent 16α-[18F]fluoro-17β-estradiol ([18F]FES) was approved for clinical use by regulatory agencies in France and the United States. Support for the use of [^{18}F]FES PET to diagnose ER-expressing breast cancer and guide ER-targeted therapy comes from several single-center studies and some recent prospective multicenter studies. These studies demonstrated the accuracy of [^{18}F]FES PET in assessing tumor ER expression compared with tissue assay reference standards, the ability of both qualitative and quantitative measures of [^{18}F]FES PET to predict response to ER-targeted therapy, and the ability of [^{18}F]FES PET to clarify equivocal staging and restaging results in patients with ER-expressing cancers. More recent data have suggested that [^{18}F]FES PET/CT may be helpful in the staging of invasive lobular breast cancer and low-grade ER-expressing invasive ductal cancers and may be a substitute for biopsy in some cases. More data are needed to better determine efficacy in these tasks.

Received Oct. 24, 2023; revision accepted Nov. 6, 2023.

For correspondence or reprints, contact David Mankoff (david.mankoff@pennmedicine.upenn.edu).

*Contributed equally to this work.

The Society of Nuclear Medicine and Molecular Imaging (SNMMI) and the European Association of Nuclear Medicine (EANM) in June 2023 released "SNMMI Procedure Standard/EANM Practice Guideline for Estrogen Receptor Imaging of Patients with Breast Cancer Using 16α-[^{18}F]Fluoro-17β-Estradiol PET." The goal of the guidance is to assist physicians in recommending, performing, interpreting, and reporting the results of [^{18}F]FES PET studies for patients with breast cancer. The document aims to provide clinicians with the best available evidence, to inform them of where robust evidence is lacking, and to help them deliver the best possible diagnostic efficacy and study quality for their patients. The guideline also presents standardized quality control, quality assurance, and imaging procedures for [^{18}F]FES PET. Adequate precision, accuracy, repeatability, and reproducibility are essential for the clinical management of patients and the use of [^{18}F]FES PET in multicenter trials. The availability of a standardized imaging procedure will help to promote the appropriate use of [^{18}F]FES PET and enhance subsequent research. This brief summary reviews the content of the joint standard/guideline, which is available in its entirety, including extensive reference citations, at https://www.snmmi.org/ClinicalPractice/content.aspx?ItemNumber=6414&navItemNumber=10790. The reader is referred to the complete guideline for appropriate limitations and considerations in applying these and similar practice guidelines.

DEFINITIONS AND COMMON CLINICAL INDICATIONS

The complete standard/guideline provides definitions of relevant terms, based on the EANM procedure guidelines for tumor PET imaging (version 2.0), including ranges of PET/CT anatomic focus. Common clinical indications, as previously detailed in SNMMI appropriate-use criteria (*1*), include assessing lesions that are difficult to biopsy or when biopsy is nondiagnostic, guiding therapy after

TABLE 1
Reporting ER Imaging of Breast Cancer Using [^{18}F]FES PET/CT

Category	Description
Required descriptions of findings on …	Quality of PET image, including any technical issues
	Visual analysis of clinically relevant findings, including …
	All sites of increased nonphysiologic focal uptake greater than local background suggestive of ER-positive lesions
	Any abnormal diffuse increased uptake
	Incidental findings with focal uptake, with further investigation suggested when needed
	Lesions identified by other imaging modalities as (suspected) tumor but not showing enhanced uptake (reported as [probable] ER-negative lesions)
	Quantitative analysis of sites of suspected disease, including where active disease is expected on basis of correlative imaging but visual inspection does not show uptake above background
	Detailed qualitative interpretation, specific to indication and individual clinical data, taking into consideration physiologic biodistribution of [^{18}F]FES
Synthesis of overall report impression	Summary of patient history, including current and prior medications targeted to ER-expressing breast cancer
	Summary of technical components of scan, including injected activity and uptake time
	Description of areas with physiologic uptake, metabolism, and excretion of [^{18}F]FES
	Identification and description of sites of qualitatively abnormal uptake above background that are suspected of being ER-expressing breast cancer, including anatomic localization on CT, qualitative level of uptake, and size of lesion by CT when relevant
	Quantitative uptake for sites identified by qualitative interpretation, noting that [^{18}F]FES $\text{SUV}_{\text{max}} > 1.5$ is suggestive of ER expression
	Description of suspected false-positive or nonspecific findings
	Description of sites where uptake may be absent in lesions observed by other available imaging techniques
	Summary of heterogeneity of uptake across sites of known disease with reference to other correlative imaging, and specific discussion of concordance with contemporaneous [^{18}F]FDG PET/CT findings when available
	Specific mention of qualitative and quantitative uptake by equivocal lesions, with conclusion on whether questioned lesions are ER-positive or -negative
	If [^{18}F]FES PET is acquired for therapy purposes, specific mention of overall qualitative and quantitative ER status of metastases, including heterogeneity of expression
	For interpreting physicians, section on limitations and pitfalls of [^{18}F]FES PET

This table is condensed from information in complete joint standard/guideline, available at https://www.snmmi.org/ClinicalPractice/content.aspx?ItemNumber=6414&navItemNumber=10790.

progression of metastatic disease, guiding therapy at initial presentation of metastatic disease, and detecting ER-expressing breast cancer sites when other imaging tests have equivocal or suggestive results. Other emerging indications under investigation include detecting ER-expressing lesions in patients with suspected or known recurrent or metastatic breast cancer; assessing ER status, in lieu of biopsy, in lesions that are easily accessible for biopsy; staging invasive lobular breast cancer and low-grade ER-expressing invasive ductal cancer; and routine staging of ER-expressing extraaxillary nodes and distant metastases. Other studies suggest that [^{18}F]FES PET can be used for detection and characterization of ER-expressing tumors other than breast cancer, such as ovarian and endometrial cancer.

The full standard/guideline details the qualifications and responsibilities of personnel performing [^{18}F]FES PET imaging, including physicians, technologists, and medical physicists. An overview of [^{18}F]FES properties and clinical pharmacology, as well as a review of [^{18}F]FES biodistribution and dosimetry, is included.

PROCEDURE SPECIFICATIONS

The full standard/guideline provides comprehensive consensus specifications for practice. Detailed recommendations cover patient referral and selection through dosimetry, the imaging procedure, and both qualitative and quantitative interpretation and reporting of findings.

PATIENT SELECTION AND PREPARATION

Scheduling, including nuclear pharmacy ordering and patient preparation and precautions, is reviewed, along with a useful table of clinical information required at the time of referral. Special considerations for patients taking drugs that block the ER and reduce uptake of [^{18}F]FES, such as tamoxifen and fulvestrant, are noted, with suggested required periods of withdrawal from these agents before [^{18}F]FES PET is attempted.

TRACER ADMINISTRATION AND IMAGING

The full standard/guideline details the administration process for [^{18}F]FES, the recommended administered activity (varying between 111 and 280 MBq [3–7.6 mCi]), and the mechanisms and timing of uptake for optimal imaging (usually 20–80 min after injection, with a 60-min uptake time suggested). PET/CT image acquisition considerations are reviewed, including recommended scan ranges and optional concurrent acquisition of CT images with contrast, as well as image reconstruction and processing.

IMAGE INTERPRETATION AND REPORTING

The most detailed portion of the full standard/guideline addresses the process of image interpretation and reporting of findings, with relevant recommendations specific to [^{18}F]FES breast imaging. Initial areas covered include technical details to be noted in the report and useful background information on expected [^{18}F]FES biodistribution and uptake in areas relevant to interpretation.

Recommended descriptions of findings and summary impressions are reviewed in the guideline and are condensed here in Table 1. Considerations of specific relevance to [^{18}F]FES and ER binding in determining and reporting both false-negative and false-positive findings are also addressed. Of special note are recommendations on reporting and interpreting quantitative measures, including what measures to record. Although qualitative assessment is usually sufficient to discriminate a positive from a negative scan, quantitative measurements may be of additional value. In particular, when qualitative assessment is equivocal, quantitative assessment can aid in defining whether a scan should be considered positive, although careful scanner calibration is needed to interpret SUV measures.

Current findings on the potential of [^{18}F]FES PET for quantitative prediction of treatment efficacy or failure and for serial assessment of ER-blocking drugs to assess the adequacy of receptor blockade are reviewed, as well as guidance in dosing of new drugs.

Correlative imaging, in addition to the CT component of PET/CT, is discussed as being especially important and helpful for guiding [^{18}F]FES PET/CT interpretation and evaluation of ER heterogeneity. When [^{18}F]FES PET is used in combination with correlative imaging that identifies sites of active disease, the combination can qualitatively assess the expression of ER in individual lesions and can therefore assess the heterogeneity of disease. This is one of several areas identified as needing further study. Overall, it is helpful to report [^{18}F]FES PET/CT results in the context of contemporaneous [^{18}F]FDG PET/CT results—both qualitatively and quantitatively—or the results of other conventional imaging.

SUMMARY

The complete "SNMMI Procedure Standard/EANM Practice Guideline for Estrogen Receptor Imaging of Patients with Breast Cancer Using 16α-[^{18}F]Fluoro-17β-Estradiol PET" provides the first comprehensive professional consensus specifications for practice, from patient referral and selection through dosimetry, the imaging procedure, and both qualitative and quantitative interpretation and reporting of findings. The availability of a standardized imaging procedure will help promote the appropriate clinical use of [^{18}F]FES PET and enhance subsequent research.

DISCLOSURE

No potential conflict of interest relevant to this article was reported.

REFERENCES

1. Ulaner GA, Mankoff DA, Clark AS, et al. Appropriate use criteria for estrogen receptor-targeted PET imaging with 16α-^{18}F-fluoro-17β-fluoroestradiol. Society for Nuclear Medicine and Molecular Imaging website. https://www.snmmi.org/ClinicalPractice/content.aspx?ItemNumber=42023. Accessed November 9, 2023.

The Imperative for Comparative Studies in Nuclear Medicine: Elevating ^{177}Lu-PSMA-617 in the Treatment Paradigm for mCRPC

Kambiz Rahbar[1,2] and Martin Boegemann[2,3]

[1]*Department of Nuclear Medicine, University Hospital Muenster, Muenster, Germany;* [2]*West German Cancer Centre, Muenster, Germany; and* [3]*Department of Urology, University Hospital Muenster, Muenster, Germany*

Nuclear medicine, with its ever-evolving spectrum of diagnostic and therapeutic interventions, plays a pivotal role in the multidisciplinary approach to cancer care. In recent years, the emergence of targeted radioligands, such as ^{177}Lu-PSMA-617, has offered renewed hope for patients with metastatic castration-resistant prostate cancer (mCRPC) (*1–3*). These agents have the potential to revolutionize the landscape of mCRPC treatment by offering targeted therapy that hones in on prostate-specific membrane antigen (PSMA)–expressing tumors. However, for these novel therapies to reach their full potential, we must take a meticulous and comparative approach. Herein, we underscore the need for robust comparative studies, acknowledging the reality of the treatment scenario and not comparing only with the easiest to beat and leaving out treatments such as docetaxel or poly(adenosine diphosphate ribose)polymerase (PARP) inhibitors that in the real world would be used in high percentage of patients.

Patients diagnosed with this advanced stage of prostate cancer face a daunting journey, often characterized by progression despite androgen deprivation therapy. Historically, the therapeutic armamentarium for mCRPC was limited. However, the landscape has been transformed with the advent of various treatment modalities, including docetaxel chemotherapy (*4*), abiraterone acetate (*5*), enzalutamide (*6*), ^{223}Ra (*7*), PARP inhibitors (*8*), and, more recently, targeted radioligands such as ^{177}Lu-PSMA-617 (*1*).

The PSMAfore trial, which was presented at the European Society for Medical Oncology congress in 2023, shines a light on the potential of ^{177}Lu-PSMA-617 (*9*). The trial results are undeniably encouraging, showcasing a substantial reduction in the risk of radiographic progression with ^{177}Lu-PSMA-617 compared with the androgen receptor pathway inhibitor (ARPI) switch. At a median follow-up of 15.9 mo, the trial reported a median radiographic progression-free survival of 12.02 mo for ^{177}Lu-PSMA-617 and 5.59 mo for the ARPI switch, with an impressive 84.2% crossover rate to ^{177}Lu-PSMA-617 for patients progressing on ARPI.

However, the PSMAfore trial carries a notable limitation: it does not include a direct comparison with docetaxel chemotherapy or PARP inhibitors, which remain a standard treatment of mCRPC. Patients included in this trial were not strictly patients unfit for chemotherapy. Therefore, the lack of such a comparator raises essential questions about the optimal treatment sequence and the potential role of ^{177}Lu-PSMA-617 in this context.

Comparative trials are fundamental in the world of oncology. They provide clinicians and researchers with the necessary data to evaluate the efficacy and safety of a new intervention in relation to a well-established standard of care. In the case of mCRPC, such a comparison with docetaxel chemotherapy and others would offer invaluable insights into the role of ^{177}Lu-PSMA-617 in patient management at this particular stage of disease.

A comprehensive comparative study addressing the omission of a direct comparison with docetaxel would undoubtedly have far-reaching implications for patient management in mCRPC.

A comparative study could elucidate the sequence that yields the best clinical outcomes. Is it more advantageous to initiate treatment with ^{177}Lu-PSMA-617, as suggested by the PSMAfore trial, followed by docetaxel? Or does the reverse sequence or another strategy prove superior? Answers to these questions would empower clinicians to individualize therapy for each patient.

As health care systems worldwide grapple with escalating costs, it is imperative to determine the cost-effectiveness of these treatments. A comparative analysis would provide insights into which treatment option offers the best value in terms of outcomes for the resources invested.

The absence of a direct comparison with docetaxel or others in the PSMAfore trial highlights the need for further research. Well-designed, comparative studies should be a top priority in the field of nuclear medicine. These studies could shed light on the potential for ^{177}Lu-PSMA-617 to take its place as a first-line or early-line therapy in mCRPC.

In summary, the landscape of mCRPC treatment is evolving rapidly, and nuclear medicine has a significant role to play. The potential of ^{177}Lu-PSMA-617, as demonstrated in the PSMAfore trial, is truly exciting. However, its full potential can be realized only through comparative studies that offer insights into how it measures up against established treatments such as docetaxel. With a commitment to rigorous, evidence-based research, nuclear medicine can lead the way in redefining patient management in mCRPC. It is only through such research that we can ensure that our patients receive the most effective and personalized care possible.

Received Oct. 26, 2023; revision accepted Dec. 4, 2023.

For correspondence or reprints, contact Kambiz Rahbar (rahbar@uni-muenster.de).

DOI: 10.2967/jnumed.123.266952

DISCLOSURE

Kambiz Rahbar reports honoraria from Advanced Accelerator Applications (AAA/Novartis), Bayer Healthcare, and SIRTEX and a consultancy/advisory role with ABX GmbH, ABX-CRO, Bayer, AAA, Pharmtrace, Jahnsen Cielag, Amgen, and AstraZeneca. Martin Boegemann receives honoraria from and has a consultancy/advisory role with Advanced Accelerator Applications (AAA/Novartis), Bayer, Janssen, Sanofi, Merck, MSD, BMS, Roche, Astellas, Exelixis, Pahrmtrace, Amgen, AstraZeneca, Eisai, Gilead, and EUSApharma. No other potential conflict of interest relevant to this article was reported.

REFERENCES

1. Sartor O, de Bono J, Chi KN, et al. Lutetium-177-PSMA-617 for metastatic castration-resistant prostate cancer. *N Engl J Med.* 2021;385:1091–1103.
2. Rahbar K, Ahmadzadehfar H, Kratochwil C, et al. German Multicenter Study investigating ^{177}Lu-PSMA-617 radioligand therapy in advanced prostate cancer patients. *J Nucl Med.* 2017;58:85–90.
3. Hofman MS, Violet J, Hicks RJ, et al. ^{177}Lu-PSMA-617 radionuclide treatment in patients with metastatic castration-resistant prostate cancer (LuPSMA trial): a single-centre, single-arm, phase 2 study. *Lancet Oncol.* 2018;19:825–833.
4. Tannok IF, de Wit R, Berry WR, et al. Docetaxel plus prednisone or mitoxantrone plus prednisone for advanced prostate cancer. *N Engl J Med.* 2004;351:1502–1512.
5. de Bono JS, Logothetis CJ, Molina A, et al. Abiraterone and increased survival in metastatic prostate cancer. *N Engl J Med.* 2011;364:1995–2005.
6. Scher HI, Fizazi K, Saad F, et al. Increased survival with enzulatamide in prostate cancer after chemotherapy. *N Engl J Med.* 2012;367:1187–1197.
7. Parker C, Nilsson S, Heinrich D, et al.; ALSYMPCA Investigators. Alpha emitter radium-223 and survival in metastatic prostate cancer. *N Engl J Med.* 2013;369: 213–223.
8. de Bono J, Mateo J, Fizazi K, et al. Olaparib for metastatic castration-resistant prostate cancer. *N Engl J Med.* 2020;382:2091–2102.
9. Sartor O, Castellano Gauna DE, Herrmann K, et al. Phase III trial of [^{177}Lu]Lu-PSMA-617 in taxane-naive patients with metastatic castration-resistant prostate cancer (PSMAfore) [abstract]. *Ann Oncol.* 2023;34(suppl 2):S1324–S1325.

Design Considerations in the PSMAfore Trial

Oliver Sartor[1], Karim Fizazi[2], Ken Herrmann[3], and Michael J. Morris[4]

[1]*Mayo Clinic, Rochester, Minnesota;* [2]*Institute Gustave Roussy, Paris, France;* [3]*University Hospital Essen, Essen, Germany; and* [4]*Memorial Sloan Kettering Cancer Center, New York, New York*

In their article entitled "The Imperative for Comparative Studies in Nuclear Medicine: Elevating ^{177}Lu-PSMA-617 in the Treatment Paradigm for mCRPC" in *The Journal of Nuclear Medicine,* Rahbar et al. make some important comments (*1*).

On behalf of the coauthors of the PSMAfore presentation at the 2023 congress of the European Society for Medical Oncology (*2*) in Madrid, we fully agree with Rahbar et al. that the landscape of metastatic castration-resistant prostate cancer (mCRPC) treatment is evolving rapidly and that nuclear medicine treatments have a significant role to play. As indicated by Rahbar et al., PSMAfore is not a perfect study that addresses all clinical questions—as indeed few are.

Many factors go into clinical trial design considerations, and we welcome the opportunity to discuss some of the critical factors involved when the PSMAfore trial was constructed. The use of ^{177}Lu-PSMA-617 in the mCRPC setting had already proven to be effective in the posttaxane, post–androgen receptor pathway inhibitor (ARPI) mCRPC setting as demonstrated by the phase III VISION trial (*3*). The VISION results led to widespread regulatory approvals.

Although VISION was clearly positive in this advanced setting, several criticisms were noted. First there was no crossover, and second patients were required to receive taxane before randomization. In addition, some criticized the nontaxane control arm, though approximately 40% of the patients had already received 2 taxane treatments.

The PSMAfore trial was designed to explore the activity of ^{177}Lu-PSMA-617 in an earlier mCRPC disease setting. In this case, the inclusion and exclusion criteria excluded prior taxane use unless applied in the adjuvant or neoadjuvant setting more than 1 y before trial enrollment. In addition, crossover to the isotopic therapy was allowed after documented radiographic progression on the control arm.

Docetaxel could be a logical comparator from several perspectives despite the fact that docetaxel has never been proven to be superior to a competitor in a randomized trial in the post-ARPI mCRPC space. Real-world data indicate that docetaxel use is limited in many counties in the mCRPC setting, especially as the first therapeutic choice in the initial post-ARPI mCRPC setting (*4–6*). As Rahbar et al. are likely aware, when given a choice, many physicians and patients clearly do not choose docetaxel as the initial treatment in the post-ARPI mCRPC disease state (*4,5*). The reasons for this choice are multifold, including dislike of the side effect profile of chemotherapy; progression declared by a rising prostate-specific antigen level only, without significant clinical or radiographic progression; the potential for long-term responsiveness to androgen-receptor–directed therapies; low disease burdens; and oligoprogressive disease, to name a few. The control arm of PSMAfore follows a common, real-world treatment paradigm.

We further note that all prerandomization patients could receive chemotherapy before entering the trial. If a taxane was deemed appropriate, patients and their physicians could readily choose that option and potentially receive commercial ^{177}Lu-PSMA-617 at a later date.

After randomization, if chemotherapy was deemed appropriate, patients and their physicians could choose that option at any time in either arm. Few chose that option. We note that a randomized phase II trial assigning post-ARPI, post-docetaxel patients to ^{177}Lu-PSMA-617 versus cabazitaxel found similar survival between the two arms but less adverse events with the isotope (*7*).

Other agents besides docetaxel might also be appropriate in selected patients in the post-ARPI mCRPC space. For instance, those with certain DNA repair defects may benefit from PARP inhibitors (*8*). These patients were required to seek such treatments rather than be randomized in the PSMAfore trial.

It is of notable interest that the patients enrolled in the PSMAfore trial were thought to be suitable for a second ARPI treatment by the enrolling investigators. The median radiographic progression-free survival in PSMAfore was 5.59 mo in the hormonal treatment arm. This compared with the median radiographic progression-free survival of 4.1 mo for the enzalutamide arm of the IMbassador250 trial (*9*), another post-ARPI mCRPC trial that did not allow taxanes in the control arm, suggesting indeed that patients with more indolent disease (and thus unlikely to be good candidates for immediate docetaxel) may have been selected to participate in PSMAfore. Another characteristic likely indicating the same selection phenomenon is the low incidence of visceral disease (3% liver metastases in the control arm) in men included in the trial.

The use of ^{177}Lu-PSMA-617 crossover for those randomized to the control arm, once they met the radiographic progression-free survival endpoint, further ensured the ethical nature of the trial. Given that 84.2% of the ARPI control arm patients eligible for crossover actually received ^{177}Lu-PSMA-617, most patients eligible for crossover actually received the isotopic therapy.

Taken together, the PSMAfore trial design carefully considered the suitability of patients for both arms of the trial. The trial enrolled briskly, indicating the acceptable nature of the trial design to both investigators and patients alike. Before and after randomization, various options were available to the patients, and choices were made to ensure that patient safety was a priority. Crossover was enthusiastically embraced in those with progression on the ARPI arm. We hope that these considerations may be more apparent to critics of the trial.

Received Nov. 28, 2023; revision accepted Jan. 5, 2024.

For correspondence or reprints, contact Oliver Sartor (osartor@tulane.edu).

DOI: 10.2967/jnumed.123.267034

REFERENCES

1. Rahbar K, Boegemann M. The imperative for comparative studies in nuclear medicine: elevating ^{177}Lu-PSMA-617 in the treatment paradigm for mCRPC. *J Nucl Med.* 2024;65:224–225.
2. Sartor O, Castellano Gauna DE, Herrmann K, et al. Phase III trial of [^{177}Lu]Lu-PSMA-617 in taxane-naive patients with metastatic castration-resistant prostate cancer (PSMAfore) [abstract]. *Ann Oncol.* 2023;34(suppl 2):S1324–S1325.
3. Sartor O, de Bono J, Chi KN, et al. Lutetium-177-PSMA-617 for metastatic castration-resistant prostate cancer. *N Engl J Med.* 2021;385:1091–1103.
4. George DJ, Sartor O, Miller K, et al. Treatment patterns and outcomes in patients with metastatic castration-resistant prostate cancer in a real-world clinical practice setting in the United States. *Clin Genitourin Cancer.* 2020;18:284–294.
5. Anton A, Pillai S, Semira MC, et al. Real-world first-line systemic therapy patterns in metastatic castration-resistant prostate cancer. *BJUI Compass.* 2021;14:205–213.
6. Barata PC, Leith A, Ribbands A, et al. Real-world treatment patterns among patients with metastatic castration-resistant prostate cancer: results from an international study. *Oncologist.* 2023;28:e737–e747.
7. Hofman MS, Emmett L, Sandhu S, et al. [^{177}Lu]Lu-PSMA-617 versus cabazitaxel in patients with metastatic castration-resistant prostate cancer (TheraP): a randomised, open-label, phase 2 trial. *Lancet.* 2021;397:797–804.
8. de Bono J, Mateo J, Fizazi K, et al. Olaparib for metastatic castration-resistant prostate cancer. *N Engl J Med.* 2020;382:2091–2102.
9. Powles T, Yuen KC, Gillessen S, et al. Atezolizumab with enzalutamide versus enzalutamide alone in metastatic castration-resistant prostate cancer: a randomized phase 3 trial. *Nat Med.* 2022;28:144–153.

PSMAFORE TRIAL DESIGN • Sartor et al. 227

Peptide Receptor Radionuclide Therapy Is Effective for Clinical Control of Symptomatic Metastatic Insulinoma: A Long-Term Retrospective Analysis

Liene Friebe*[1], Martin T. Freitag*[1–3], Martin Braun[1], Guillaume Nicolas[1,2], Andreas Bauman[1], David Bushnell[4], Emanuel Christ†[2,5], and Damian Wild†[1,2]

[1]Clinic of Radiology and Nuclear Medicine, University Hospital Basel, Basel, Switzerland; [2]ENETS Center of Excellence for Neuroendocrine and Endocrine Tumors, University Hospital Basel, Basel, Switzerland; [3]Clinic of Nuclear Medicine, University Hospital Freiburg, Freiburg, Germany; [4]Division of Nuclear Medicine, Department of Radiology, University of Iowa Hospitals and Clinics, Iowa City, Iowa; and [5]Department of Endocrinology, Diabetology, and Metabolism, University Hospital Basel, Basel, Switzerland

Metastatic insulinoma is a rare malignant neuroendocrine tumor characterized by inappropriate insulin secretion, resulting in life-threatening hypoglycemia, which is often difficult to treat. There is currently very limited information about the efficacy of peptide receptor radionuclide therapy (PRRT) for clinical control of hypoglycemia. The aim of this long-term retrospective study was to evaluate the therapeutic efficacy of PRRT for improving hypoglycemia, to evaluate the change of medication after PRRT, and to calculate progression-free survival (PFS) and overall survival (OS). **Methods:** Inclusion criteria were histologically proven somatostatin receptor–positive metastatic malignant insulinoma and at least 2 cycles of [^{90}Y]Y-DOTATOC or [^{177}Lu]Lu-DOTATOC therapy from early 2000 to early 2022. A semiquantitative scoring system was used to quantify the severity and frequency of hypoglycemic episodes under background antihypoglycemic therapy (somatostatin analog, diazoxide, everolimus, corticosteroids): score 0, no hypoglycemic episodes; score 1, hypoglycemic events requiring additional conservative treatment with optimization of nutrition; score 2, severe hypoglycemia necessitating hospitalization and combined medication or history of hypoglycemic coma. Hypoglycemic score before and after PRRT was analyzed. Time of benefit was defined as a time range of fewer hypoglycemic episodes in the observation period than at baseline. Information on antihypoglycemic medication before and after therapy, PFS, and OS was recorded. **Results:** Twenty-six of 32 patients with a total of 106 [^{90}Y]Y-DOTATOC/[^{177}Lu]Lu-DOTATOC cycles were included. The average observation period was 21.5 mo (range, 2.3–107.4 mo). Before therapy, 81% (n = 21) of the patients had a hypoglycemia score of 2 and 19% (n = 5) had a score of 1. After PRRT, 81% of patients (n = 21) had a decreased score, and the remaining 5 patients showed a stable situation. There was temporary worsening of hypoglycemia just after injection of [^{90}Y]Y-DOTATOC/[^{177}Lu]Lu-DOTATOC in 19% of patients. The average time of benefit in the observation period was 17.2 mo (range, 0–70.2 mo). Antihypoglycemic medication reduction was achieved in 58% (n = 15) of patients. The median OS and PFS after the start of PRRT were 19.7 mo (95% CI, 6.5–32.9 mo) and 11.7 mo (95% CI, 4.9–18.5 mo), respectively. **Conclusion:** To our knowledge, our study included the largest cohort of patients with malignant insulinoma to be evaluated. Long-lasting symptom control and reduction of antihypoglycemic medications were shown in most patients after late-line PRRT.

Key Words: malignant insulinoma; PRRT; [^{177}Lu]Lu-DOTATOC; [^{90}Y]Y-DOTATOC

J Nucl Med 2024; 65:228–235
DOI: 10.2967/jnumed.123.265894

Insulinoma is a rare insulin-secreting pancreatic neuroendocrine tumor (NET) clinically characterized by the Whipple triad including documented hypoglycemia, neuroglycopenic symptoms, and prompt relief of symptoms after the administration of carbohydrates (*1*). The severity of symptoms can range from mild to life-threatening hypoglycemic events, leading to coma and death. Most insulinomas are benign, but approximately 6% of insulinomas develop metastases and are therefore considered malignant. The estimated incidence of metastatic insulinoma is about 0.3 cases per 1 million person-years (*2*). Because the primary tumor and metastases secrete insulin in an unregulated manner (autonomy), the clinical symptoms worsen over time in parallel with the progression of metastatic disease. Because of the rarity of the disease, the treatment strategies for malignant metastatic disease are ill defined; the 2 pivotal aims are symptom and antiproliferative tumor control (*3*). The general treatment approaches include surgery, medicaments (everolimus, somatostatin analogs, sunitinib, diazoxide, corticosteroids), and chemotherapy (e.g., streptozocin and 5-fluorouracil), as well as other approaches such as transcatheter arterial (chemo) embolization, radiofrequency ablation, and peptide receptor radionuclide therapy (PRRT) (*3,4*). There is currently very limited information on PRRT efficacy in metastatic malignant insulinoma. Importantly, benign insulinomas express a high quantity of glucagonlike peptide-1 receptors but show a lower expression of somatostatin receptor subtype 2. For the malignant counterpart, there is a significant switch, with reduced glucagonlike peptide-1 receptor expression and increased somatostatin receptor subtype 2 expression (*5*). Hence, metastatic insulinoma can be treated with PRRT, and previous case studies demonstrated promising results in symptom control with PRRT (*5–7*).

Our hospital is specialized in the diagnosis and treatment of secreting and nonsecreting NETs and started PRRT in the late

---

Received Apr. 19, 2023; revision accepted Jul. 25, 2023.

For correspondence or reprints, contact Damian Wild (damian.wild@usb.ch).

*Contributed equally to this work.

†Contributed equally to this work.

TABLE 1
Inclusion and Exclusion Criteria

Inclusion criteria	Exclusion criteria
Histologically proven malignant insulinoma and inadequately increased insulin/C-peptide levels	Eastern Cooperative Oncology Group performance status > 3
Somatostatin receptor positivity in somatostatin receptor imaging prior therapy (Krenning score 3 or 4)	Pregnancy and breast feeding
Proven metastatic disease by imaging or biopsy	No observation period
Blood count	No available clinical data in observation period
Leukocytes $\geq$ 1,500/μL	
Hemoglobin $\geq$ 8 g/dL	
Platelets $\geq$ 70,000/μL	
Estimated glomerular filtration rate $\geq$ 30 mL/min/1.73 m^2	
Received at least 2 treatment cycles of [^{90}Y]Y-DOTATOC or [^{177}Lu]Lu-DOTATOC therapy	
Episodes of hypoglycemia in anamnesis	

1990s (*8*), resulting in treating a large patient collective with rare NETs. The goal of our study was to identify and evaluate all patients since 2000 who had malignant insulinoma treated with PRRT and to determine whether [^{90}Y]Y-DOTATOC or [^{177}Lu]Lu-DOTATOC therapy improved symptoms and hypoglycemia control.

MATERIALS AND METHODS

This retrospective single-center study was approved by the regional ethics committee (Ethikkommission Nordwest und Zentralschweiz). The requirement for written informed consent was waived by the institutional board because of the rarity of the disease, inclusion of international patients, the retrospective nature of the analysis, and anonymization of the data. All patients with histologically proven metastatic malignant insulinoma who received [^{90}Y]Y-DOTATOC or [^{177}Lu]Lu-DOTATOC therapy at University Hospital Basel from January 1, 2000, to March 21, 2022, were included. Inclusion and exclusion criteria are demonstrated in Table 1. To analyze the effect on hypoglycemia, we defined the observation period as the time range from the first to the last PRRT cycle. The clinical data of patients (sex, age), tumor characteristics (clinical stage, site of metastases, proliferation rate, previous treatment), and therapy data (number of PRRT cycles, radiotracer type received, activity per therapy cycle), as well as laboratory parameters (hemoglobin, white blood cells, platelet count, lymphocyte count, liver parameters [alanine aminotransferase, aspartate aminotransferase, alkaline phosphatase, γ-glutamyl transferase, albumin, blood bilirubin] and kidney parameters [creatinine, estimated glomerular filtration rate, glucose, potassium levels]), were collected during the observation period by reviewing the paper-based patient record and the electronic patient file. The adverse events were classified according to the Common Terminology Criteria for Adverse Events version 5.0 (https://ctep.cancer.gov/protocolDevelopment/electronic_applications/ctc.htm#ctc_50).

Manufacture of [^{90}Y]Y-DOTATOC and [^{177}Lu]Lu-DOTATOC and Posttherapeutic Imaging

[^{111}In]In-/[^{90}Y]Y-DOTATOC (referred to here as [^{90}Y]Y-DOTATOC) and [^{177}Lu]Lu-DOTATOC were synthesized as previously described (*9*). [^{90}Y]Y-DOTATOC was coinjected with approximately 111 MBq of [^{111}In]In-DOTATOC to increase the quality of posttherapeutic images. Posttherapeutic imaging was done 1 d later and included 1 whole-body scintigram and 1 coregistered SPECT/CT scan of the abdomen.

Treatment Efficiency

A semiquantitative scoring system was used to quantify the severity and frequency of hypoglycemic episodes under background antihypoglycemic therapy (somatostatin analogs, diazoxide, everolimus, or corticosteroids): score 0, no hypoglycemic episodes; score 1, some hypoglycemic events requiring additional conservative treatment with only optimization of nutritional intake; score 2, severe hypoglycemia requiring hospitalization and combined medication or history of hypoglycemic coma. The hypoglycemic scores before and after PRRT were compared. The duration of response (time of benefit) was defined as the time range of improvement in hypoglycemia score during the whole observation period from the first to the last PRRT cycle. The best response was defined as the lowest hypoglycemic score since the start of PRRT. We collected information on the hypoglycemic medications regularly taken before, during, and after therapy and determined whether—since the beginning of PRRT—additional medical therapy had been administered or medical therapy had been reduced.

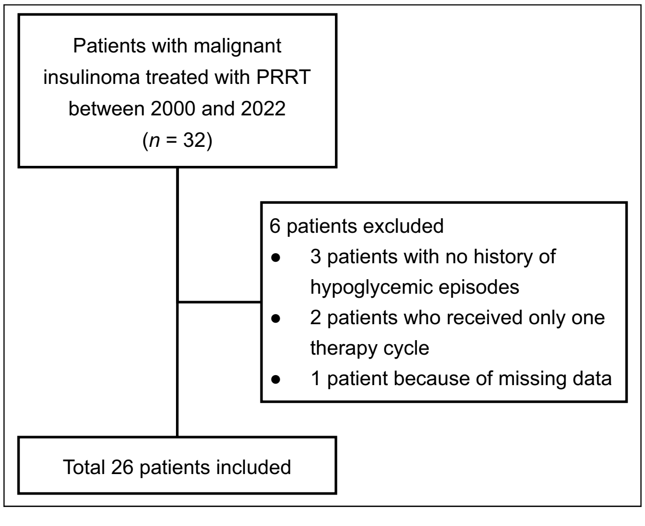

FIGURE 1. Flowchart of patient selection.

TABLE 2
Demographic Data of Study Population (n = 26)

Parameter	Data
Sex	
Female	12
Male	14
Mean age (±SD) at first treatment (y)	59.54 ± 14.64 (range, 25–78)
Site of metastasis	
Liver	100% (n = 26)
Bone	42% (n = 11)
Lymph node	35% (n = 9)
Lung	8% (n = 2)
Peritoneum	8% (n = 2)
Adrenal gland	4% (n = 1)
Previously received therapy	
Treatment-naïve	15% (n = 4)
Treated	85% (n = 22) (several therapeutic modalities per patient)
Surgery	15
Somatostatin analogs	7
Everolimus	7
TACE	7
Chemotherapy	4
Sunitinib	4
Diazoxide	4
Steroids	2
Glucagon	1
Other	3
Tumor grading (1–3) with Ki-67 values (maximal value)	
Grade 1, ≤ 2%	1
Grade 2, 3%–20%	10
Grade 3, >20%	5
Unknown	10

TACE = transarterial chemoembolization.

Progression-Free Survival (PFS) and Overall Survival (OS)

Information on patient survival and received therapy after the last PRRT was collected by reviewing paper-based and electronic patient records or by contacting the referring physician. PFS was defined as the time interval between the first PRRT cycle and either the start of disease progression (determined by imaging or worsening of hypoglycemia requiring another round of PRRT) or death. OS was defined as the time interval between the first PRRT cycle and death. The absolute

TABLE 3
PRRT Information of All 26 Included Patients

Parameter	Data
Mean ± SD number of therapy cycles delivered per patient	4.1 ± 2.2 (range, 2–10)
Received radiotracer	
Only [^{90}Y]Y-DOTATOC	7 patients
Only [^{177}Lu]Lu-DOTATOC	6 patients
Both	13 patients
Mean ± SD administered activity per therapy cycle (GBq)	[^{177}Lu]Lu 6.4 ± 1.1 (range, 3.7–7.4)
	[^{90}Y]Y 6.7 ± 0.7 (range, 4.8–8.1)

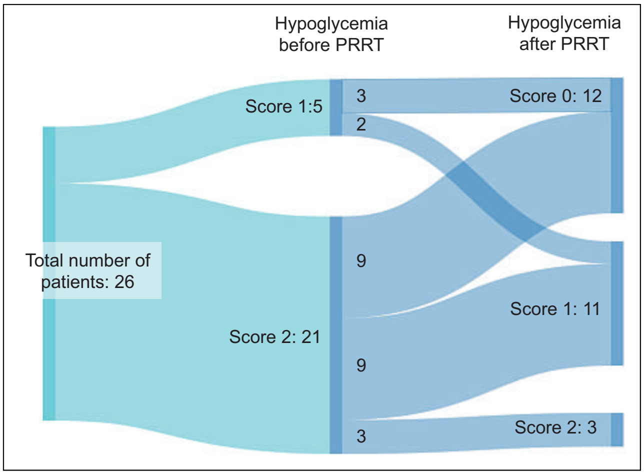

FIGURE 2. Sankey diagram of baseline hypoglycemic scores vs. best response.

survival rate was calculated as the percentage of patients who survived 5 y after the start of PRRT. The cutoff date of data collection was July 6, 2022.

Statistics

Data were collected in tabular form, and the IBM SPSS Statistics program (version 28.0) was used for statistical analysis. A Kaplan–Meier curve was used to demonstrate OS and PFS. In the survival analysis, censored patients were those who were alive (in the OS calculation) and those who did not experience disease progression (in the PFS calculation). A Sankey diagram for showing hypoglycemic episodes before and after therapy was created on the SankeyMATIC website (www.sankeymatic.com).

RESULTS

Study Population

There were 32 patients with malignant insulinoma treated with somatostatin receptor PRRT; 6 patients were excluded from the analysis (Fig. 1). Twenty-six patients with a total of 106 therapy cycles were finally included. All patients had stage IV disease with liver metastases. Of the patients, 85% were pretreated and 15% were treatment-naïve (Table 2; Supplemental Table 1; supplemental materials are available at http://jnm.snmjournals.org). The patients received an average of 4.1 ± 2.2 therapy cycles (range, 2–10 cycles per patient). Seven patients received 2 therapy cycles, 4 patients received 3 cycles, 8 patients received 4 cycles, 3 patients received 5 cycles, 1 patient received 6 cycles, 1 patient received 7 cycles, and 2 patients received 10 cycles. The mean administered radioactivity per cycle was 6.4 ± 0.9 GBq (range, 3.7–8.1 GBq) (Table 3; Supplemental Table 2).

Treatment Efficiency

Before the first cycle of therapy, 21 of 26 patients had a hypoglycemia score of 2 and 5 patients had a score of 1. In the long term, a total of 21 of 26 patients (81%) demonstrated improvement during the observation period (Fig. 2). The remaining 5 patients (3 patients with a score of 2 and 2 patients with a score of 1) were stable. Of the 26 patients, 5 (19%) experienced transient hypoglycemia after injection of [^{90}Y]Y-DOTATOC/[^{177}Lu]Lu-DOTATOC. In the long term, there were no cases of worsening symptoms compared with baseline during the observation period. A case presentation of 1 patient is shown in Figure 3.

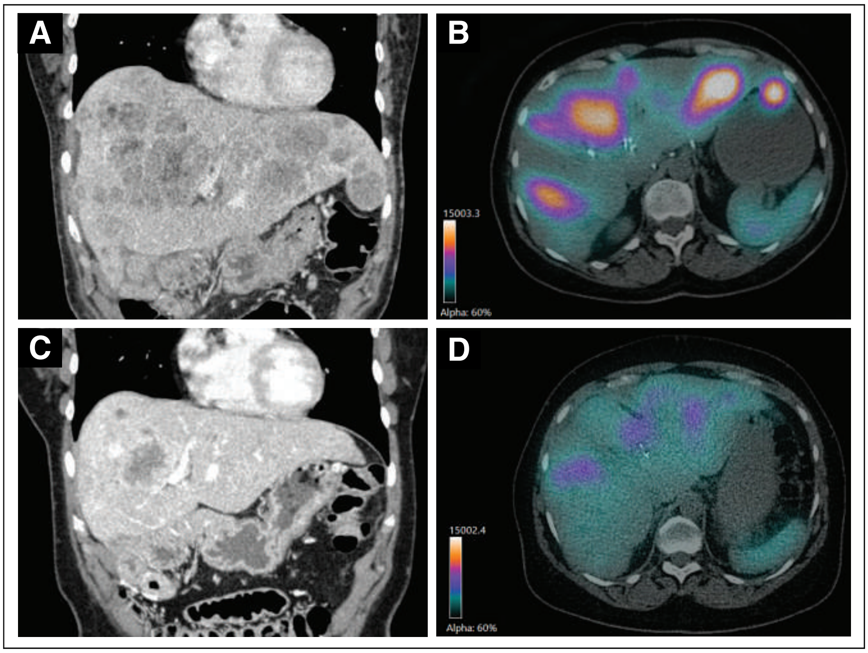

FIGURE 3. 62-y-old female patient who received 3 [^{90}Y]Y-DOTATOC and 1 [^{177}Lu]Lu-DOTATOC therapy cycles (total activity, 26.7 GBq) and benefited more than 15 of 18 mo of observation. Baseline CT scan (A) and intratherapeutic [^{90}Y]Y-DOTATOC SPECT/CT of second therapy cycle show multiple liver metastases (B). CT scan after second therapy cycle shows partial tumor response with significantly reduced tumor burden according to RECIST 1.1 (C). Intratherapeutic [^{90}Y]Y-DOTATOC SPECT/CT of fourth therapy cycle (D) shows reduced [^{90}Y]Y-DOTATOC uptake in liver metastases compared with [^{90}Y]Y-DOTATOC SPECT/CT of second therapy cycle (B), which also indicates treatment response.

After the first cycle of therapy, 17 patients showed an improved hypoglycemic score; 9 patients showed no improvement. Of these 9 patients who showed no improvement, 4 showed improvement after the second therapy cycle; 2 were stable since the start of PRRT, without improvement, and the remaining 3 received only 2 therapy cycles in total, with no follow-up available after the last PRRT.

The average observation period was 21.5 mo (range, 2.3–107.4 mo). The average time of benefit (improvement of hypoglycemia) was 17.2 mo (range, 0–70.2 mo), with no differences between tumor grade 1, 2, or 3: 12 of 26 patients had an improvement of hypoglycemic score during the whole (100%) observation period, 2 patients in 96%–97% of the observation period, 1 patient in 87% of the observation period, 3 patients in 62%–73% of the observation period, and 3 patients in 25%–42% of the observation period; 5 patients had no improvement (Fig. 4). In these 21 patients who showed improvement, the best response was observed at a median of 2.3 mo (interquartile range, 9.4 mo) after the start of PRRT.

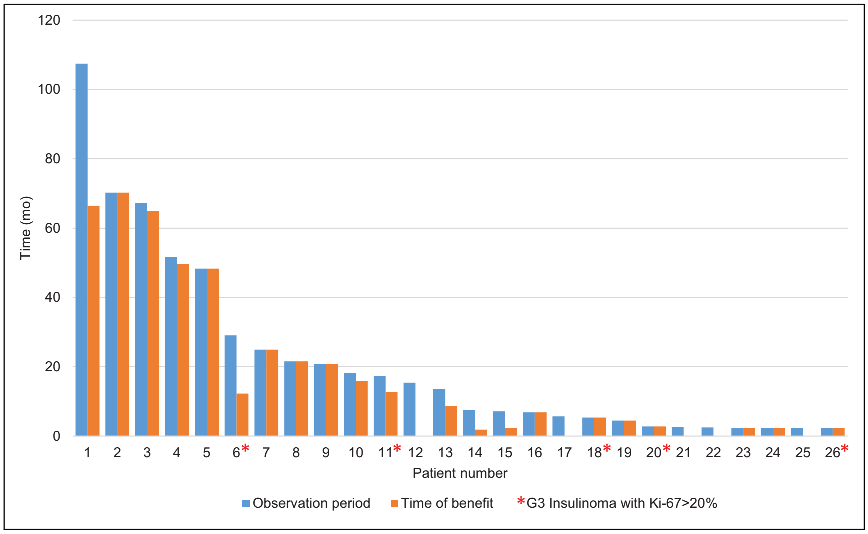

FIGURE 4. Observation period vs. time of benefit.

In total, 88% of patients (23/26) were using other medication to treat hypoglycemia during the observation period. In 58% of patients (15/26), a reduction of antihypoglycemic medication was achieved after PRRT during the observation period (Table 4). After the last PRRT cycle, 7 patients received no other therapy, 1 patient discontinued the previously received therapy, 13 patients received additional therapy, and 5 patients had no data available (Table 5).

OS and PFS

At the end of data collection, 20 patients had died, 4 patients were alive, and 2 patients had no information available. The median OS was 19.7 mo (95% CI, 6.5–32.9 mo) (Fig. 5). The survival rate since

TABLE 4

Detailed Information About Additional Hypoglycemic Medication Parallel to PRRT and Medication Reduction After PRRT

Parameter	Number of patients
Other medication to treat hypoglycemia (several therapeutic modalities per patient)	23
SSA	14
Diazoxide	12
Glucose	11
Everolimus	9
Steroids	8
Sunitinib	3
Cornstarch	2
Glucagon	1
Sirolimus	1
Reduction of antihypoglycemic medication after PRRT	15
Dose reduction of medication (diazoxide and steroids for ∼2 mo)	1
Discontinuation of medication (several therapeutic modalities per patient)	11
Diazoxide	7
Glucose infusion	5
Everolimus	2
SSA	2
Steroids	1
Sunitinib	1
Cornstarch	1
Dose reduction + discontinuation of medication	3
Dose reduction of steroids and discontinuation of everolimus	1
Dose reduction of everolimus and discontinuation of diazoxide and glucagon	1
Dose reduction of steroids and discontinuation of diazoxide	1

SSA = somatostatin analog.

TABLE 5
Therapy Information After Last PRRT

Parameter	Data
No other therapy	7
Discontinuation of previously received therapy (steroids)	1
Additional therapy (several therapeutic modalities per patient)	13
Everolimus	4
Glucose	2
SSA	2
Radiotherapy of metastatic lesion	2
Chemotherapy	2
Surgery	2
SIRT	2
Denosumab (monoclonal antibodies)	1
Cytostatic	1
Glucagon	1
Steroids	1
Sunitinib	1
No data available	5

SSA = somatostatin analog; SIRT = selective internal radiation therapy.

the start of therapy was 71% ($n = 17/24$) at 1 y, 42% ($n = 10$) at 2 y, 33% ($n = 8$) at 3 y, 29% ($n = 7$) at 4 y, and 29% ($n = 7$) at 5 y.

When the data collection ended, 25 patients had already experienced the first progression after the start of PRRT; 1 patient experienced no disease progression. The median PFS was 11.7 mo (95% CI, 4.9–18.5 mo) (Fig. 6).

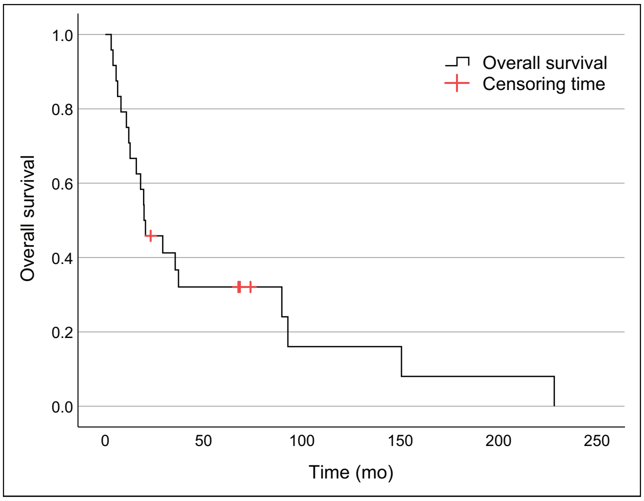

FIGURE 5. Kaplan–Meier survival analysis was performed for 24 patients with median OS of 19.7 mo (95% CI, 6.5–32.9 mo). Two patients were not included because of missing data, with 4 censored events (these patients are still alive).

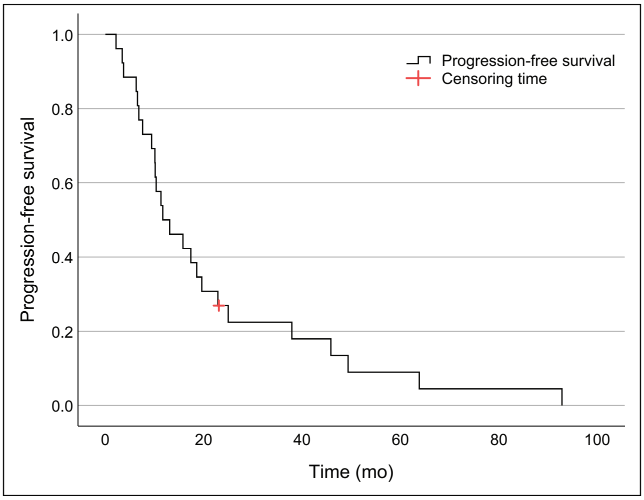

FIGURE 6. Kaplan–Meier survival analysis was performed for 26 patients with median PFS of 11.7 mo (95% CI, 4.9–18.5 mo), with 1 censored event due to patient who experienced no progression.

Side Effects

After at least 1 cycle of PRRT in patients without preexisting hematologic conditions, new grade 3 hematologic toxicity occurred in up to 15% of cases (12% anemia, 8% leukocytopenia, 15% lymphocytopenia, 0% thrombocytopenia), and new grade 4 hematotoxicity was observed in 4% of patients (1 patient with grade 4 lymphocytopenia, which improved to grade 3 at the time of the next PRRT) (Supplemental Table 3). Four patients with preexisting lymphocytopenia (grade 1 or 2) developed grade 3 lymphocytopenia after PRRT, and 1 patient progressed to grade 4. There was no new-onset grade 3 or 4 nephrotoxicity, although 1 patient with grade 1 renal disease at baseline progressed to grade 3 after 1 cycle of [^{90}Y]Y-DOTATOC and 2 cycles of [^{177}Lu]Lu-DOTATOC. Grade 3 hepatotoxicity developed in 19% of patients. No patients progressed to grade 4. Other symptoms reported included fatigue (3 patients), nausea (3 patients), fever (2 patients), and hair loss, insomnia, vomiting, dyspnea, and ankle edema (1 patient). One patient was diagnosed with acute myeloid leukemia 1 y after the last (fourth) PRRT cycle. During the hospital stay for PRRT, 19% of patients (5/26) experienced a temporary worsening of blood glucose, which was consistent with tumor lysis. Four patients with grade 1 or 2 hypoglycemia showed improvement within 1 day, 2 weeks, 1 month, and 1.5 months, respectively. One patient had grade 4 hypoglycemia (blood glucose level of 0.8 mmol/L); the episode was treated with 10% glucose infusion; corticosteroid therapy was started, and glucose levels returned to normal the next day. At the same time, there were no relevant changes in the potassium blood level (Supplemental Table 3).

DISCUSSION

To the best of our knowledge, this is the largest study to date of patients with metastatic malignant insulinoma treated with somatostatin-targeted PRRT. PRRT was effective in controlling hypoglycemia in 81% of the study population and enabled 58% of patients to reduce the use of other drugs to control hypoglycemic episodes, resulting in reduced potential drug side effects. OS and PFS were 19.7 and 11.7 mo, respectively.

The finding of controlled hypoglycemia in 81% of the patients after PRRT is similar to the finding of the second largest study, which included 14 patients with malignant insulinoma treated with PRRT and achieved hypoglycemic control in 93% of patients (*6*). However, the duration of the therapeutic effect of this study was not documented. Zandee et al. reported the efficacy of PRRT on functioning pancreatic NETs in 34 patients, including 14 insulinoma patients (*10*). Six of 9 (67%) insulinoma patients with uncontrolled symptoms at baseline showed a reduction of hypoglycemic events. The median PFS was 18.1 mo, with no subgroup differences (14 insulinomas, 7 gastrinomas, 5 vasoactive intestinal peptide tumors, and 8 glucagonomas among the 34 patients). This PFS is slightly longer than our finding and may be explained by differences in study populations (slightly different metastatic spread) and pretreatment (24% of treatment-naïve patients in Zandee et al., in contrast to 15% in the current study). Other authors presented case reports or case series suggesting the efficacy of PRRT to control hypoglycemic episodes (*11–13*).

When the effectiveness of other commonly used drugs to control hypoglycemia is compared, the results of PRRT are promising. The effectiveness of somatostatin analogs and diazoxide to treat hypoglycemia is estimated to be approximately 50% and 50%–60%, respectively (*14,15*). Everolimus is also used to control hypoglycemia, although data on its efficacy are scarce. A retrospective study including 12 patients with metastatic insulinoma treated with everolimus achieved hypoglycemic control in 92% of patients, and the median time to first progression was 6.5 mo (*16*). Some case reports and case series also indicated a decrease in hypoglycemic events with everolimus (*17–19*). There are few data suggesting the effectiveness of sunitinib in controlling excess hormone levels in functional NETs (*20,21*).

The current study showed lower OS and PFS (19.7 and 11.7 mo, respectively) than in patients with ileal or gastroenteropancreatic NETs treated with PRRT (*22–24*) and similar PFS but lower OS than for targeted therapy (sunitinib and everolimus) in pancreatic NETs (*25–28*). The underlying mechanisms for a worse prognosis are ill defined but may be related to the insulin secretion with the associated additional medical therapy, the specific biology of the malignant insulinoma itself, or a Ki-67 value of greater than 20% in about 20% of patients. According to the European Society for Medical Oncology and European Neuroendocrine Tumor Society guidelines, PRRT is the last-line therapy for metastatic pancreatic NETs (*20,29*). The current findings demonstrate that PRRT is indicated at an earlier time point (e.g., first- or second-line therapy) in the management of somatostatin receptor subtype 2–positive metastatic insulin-secreting grade 1–3 pancreatic NETs.

The documented side effects, including hematologic, renal, and liver toxicity, in the current study are consistent with data from other studies using PRRT (*30–32*). Hormonal crisis as a consequence of PRRT has been reported to be in the range of 1%–9% (*10,33*). In the case of insulinoma, the result may be severe hypoglycemia and hypokalemia due to the insulin-mediated shift of extracellular potassium into the cells. In the present study, there was only 1 patient (4%) who developed severe grade IV hypoglycemia during the hospital stay for PRRT, and no significant hypokalemia could be documented during PRRT. In our setting, the therapy was usually well tolerated, whereas hypoglycemia remains the most worrisome complication, for which regular glucose measurements during and after the in-hospital treatment are warranted.

This study has some limitations. Because of the rarity of the disease, this is a retrospective study with a limited number of patients. Some came from abroad, which led to limitations in the available clinical, imaging, and laboratory data. To mitigate this bias, we measured the symptom and hypoglycemic control only between those therapy cycles for which the patient was followed on a regular basis. Because 50% of patients received additional therapy cycles after initial progression, the time of benefit may be a better factor than PFS in demonstrating efficacy of therapy. Furthermore, because we could not document hypoglycemic events after the last therapy, the time of benefit is likely to be underestimated, as the benefit may have lasted beyond the last therapy. Since there was no uniform scheme to assess tumor burden after therapy, these findings cannot be reported in a reliable way. As a proxy, we used inter- and posttherapeutic SPECT/CT to determine tracer uptake. With this examination, significant progress can be excluded. Finally, there is a potential bias in PRRT's effectiveness in controlling hypoglycemia, as 88% of patients concomitantly received other drugs to control hypoglycemia. In addition, a potential interaction and counteraction between PRRT and other drugs cannot be fully excluded. However, the reduction in the number of drugs administered to control hypoglycemia with the improvement in hypoglycemic episodes serves as robust evidence of treatment efficacy in this retrospective setting for an orphan disease.

CONCLUSION

To our knowledge, our study included the largest cohort of patients with malignant insulinoma treated with PRRT as a late-line therapy. Long-lasting symptom control and reduction of antihypoglycemic medication was shown in more than 80% and approximately 60% of patients, respectively. OS and PFS were lower than in other NET studies administering PRRT, a finding that is possibly related to the associated hypoglycemia, the particular biology of the tumor, or the high Ki-67 value of more than 20% in about 20% of patients.

DISCLOSURE

This work was supported by a grant from the Swiss National Foundation (no. 320030-175544). No other potential conflict of interest relevant to this article was reported.

KEY POINTS

QUESTION: Does PRRT improve hypoglycemia and reduce antihypoglycemic medication in patients with hypoglycemic episodes due to an advanced metastatic insulinoma?

PERTINENT FINDINGS: This retrospective cohort study with symptomatic patients demonstrated long-lasting symptom control and reduction of antihypoglycemic medications in most patients after PRRT.

IMPLICATIONS FOR PATIENT CARE: This study demonstrated that PRRT is indicated at an earlier time point (e.g., first- or second-line therapy) for the treatment of patients with symptomatic somatostatin receptor subtype 2–positive metastatic insulin-secreting grade 1–3 pancreatic NETs.

REFERENCES

1. Okabayashi T, Shima Y, Sumiyoshi T, et al. Diagnosis and management of insulinoma. *World J Gastroenterol.* 2013;19:829–837.
2. Sada A, Yamashita TS, Glasgow AE, et al. Comparison of benign and malignant insulinoma. *Am J Surg.* 2021;221:437–447.

3. Baudin E, Caron P, Lombard-Bohas C, et al. Malignant insulinoma: recommendations for characterisation and treatment. *Ann Endocrinol (Paris).* 2013;74:523–533.
4. Yu J, Ping F, Zhang H, et al. Clinical management of malignant insulinoma: a single institution's experience over three decades. *BMC Endocr Disord.* 2018;18:92.
5. Wild D, Christ E, Caplin ME, et al. Glucagon-like peptide-1 versus somatostatin receptor targeting reveals 2 distinct forms of malignant insulinomas. *J Nucl Med.* 2011;52:1073–1078.
6. Veltroni A, Cosaro E, Spada F, et al. Clinico-pathological features, treatments and survival of malignant insulinomas: a multicenter study. *Eur J Endocrinol.* 2020;182:439–446.
7. Jansen TJP, van Lith SAM, Boss M, et al. Exendin-4 analogs in insulinoma theranostics. *J Labelled Compd Radiopharm.* 2019;62:656–672.
8. de Jong M, Bakker WH, Krenning EP, et al. Yttrium-90 and indium-111 labelling, receptor binding and biodistribution of [DOTA^{0},D-Phe^{1},Tyr^{3}]octreotide, a promising somatostatin analogue for radionuclide therapy. *Eur J Nucl Med.* 1997;24:368–371.
9. Villard L, Romer A, Marincek N, et al. Cohort study of somatostatin-based radiopeptide therapy with [^{90}Y-DOTA]-TOC versus [^{90}Y-DOTA]-TOC plus [^{177}Lu-DOTA]-TOC in neuroendocrine cancers. *J Clin Oncol.* 2012;30:1100–1106.
10. Zandee WT, Brabander T, Blazevic A, et al. Symptomatic and radiological response to ^{177}Lu-DOTATATE for the treatment of functioning pancreatic neuroendocrine tumors. *J Clin Endocrinol Metab.* 2019;104:1336–1344.
11. van Schaik E, van Vliet EI, Feelders RA, et al. Improved control of severe hypoglycemia in patients with malignant insulinomas by peptide receptor radionuclide therapy. *J Clin Endocrinol Metab.* 2011;96:3381–3389.
12. Magalhães D, Sampaio IL, Ferreira G, et al. Peptide receptor radionuclide therapy with ^{177}Lu-DOTA-TATE as a promising treatment of malignant insulinoma: a series of case reports and literature review. *J Endocrinol Invest.* 2019;42:249–260.
13. Iglesias P, Martínez A, Gajate P, Alonso T, Navarro T, Díez JJ. Long-term effect of ^{177}Lu-DOTATATE on severe and refractory hypoglycemia associated with malignant insulinoma. *AACE Clin Case Rep.* 2019;5:e330–e333.
14. Vezzosi D, Bennet A, Rochaix P, et al. Octreotide in insulinoma patients: efficacy on hypoglycemia, relationships with Octreoscan scintigraphy and immunostaining with anti-sst2A and anti-sst5 antibodies. *Eur J Endocrinol.* 2005;152:757–767.
15. Matej A, Bujwid H, Wroński J. Glycemic control in patients with insulinoma. *Hormones (Athens).* 2016;15:489–499.
16. Bernard V, Lombard-Bohas C, Taquet MC, et al. Efficacy of everolimus in patients with metastatic insulinoma and refractory hypoglycemia. *Eur J Endocrinol.* 2013;168:665–674.
17. Fiebrich H-B, Siemerink EJM, Brouwers AH, et al. Everolimus induces rapid plasma glucose normalization in insulinoma patients by effects on tumor as well as normal tissues. *Oncologist.* 2011;16:783–787.
18. Ong GSY, Henley DE, Hurley D, Turner JH, Claringbold PG, Fegan PG. Therapies for the medical management of persistent hypoglycaemia in two cases of inoperable malignant insulinoma. *Eur J Endocrinol.* 2010;162:1001–1008.
19. Baratelli C, Brizzi MP, Tampellini M, et al. Intermittent everolimus administration for malignant insulinoma. *Endocrinol Diabetes Metab Case Rep.* 2014;2014:140047.
20. Falconi M, Eriksson B, Kaltsas G, et al. ENETS consensus guidelines update for the management of patients with functional pancreatic neuroendocrine tumors and non-functional pancreatic neuroendocrine tumors. *Neuroendocrinology.* 2016;103:153–171.
21. Ito T, Lee L, Jensen RT. Treatment of symptomatic neuroendocrine tumor syndromes: recent advances and controversies. *Expert Opin Pharmacother.* 2016;17:2191–2205.
22. Strosberg J, El-Haddad G, Wolin E, et al. Phase 3 trial of ^{177}Lu-DOTATATE for midgut neuroendocrine tumors. *N Engl J Med.* 2017;376:125–135.
23. Strosberg JR, Caplin ME, Kunz PL, et al. ^{177}Lu-DOTATATE plus long-acting octreotide versus high-dose long-acting octreotide in patients with midgut neuroendocrine tumours (NETTER-1): final overall survival and long-term safety results from an open-label, randomised, controlled, phase 3 trial. *Lancet Oncol.* 2021;22:1752–1763.
24. Kwekkeboom DJ, de Herder WW, Kam BL, et al. Treatment with the radiolabeled somatostatin analog [^{177}Lu-DOTA^{0},Tyr^{3}]octreotate: toxicity, efficacy, and survival. *J Clin Oncol.* 2008;26:2124–2130.
25. Yao JC, Shah MH, Ito T, et al. Everolimus for advanced pancreatic neuroendocrine tumors. *N Engl J Med.* 2011;364:514–523.
26. Yao JC, Pavel M, Lombard-Bohas C, et al. Everolimus for the treatment of advanced pancreatic neuroendocrine tumors: overall survival and circulating biomarkers from the randomized, phase III RADIANT-3 study. *J Clin Oncol.* 2016;34:3906–3913.
27. Raymond E, Dahan L, Raoul J-L, et al. Sunitinib malate for the treatment of pancreatic neuroendocrine tumors. *N Engl J Med.* 2011;364:501–513.
28. Faivre S, Niccoli P, Castellano D, et al. Sunitinib in pancreatic neuroendocrine tumors: updated progression-free survival and final overall survival from a phase III randomized study. *Ann Oncol.* 2017;28:339–343.
29. Pavel M, Öberg K, Falconi M, et al. Gastroenteropancreatic neuroendocrine neoplasms: ESMO clinical practice guidelines for diagnosis, treatment and follow-up. *Ann Oncol.* 2020;31:844–860.
30. van der Zwan WA, Bodei L, Mueller-Brand J, de Herder WW, Kvols LK, Kwekkeboom DJ. Radionuclide therapy in neuroendocrine tumors. *Eur J Endocrinol.* 2015;172:R1–R8.
31. Waldherr C, Pless M, Maecke HR, et al. Tumor response and clinical benefit in neuroendocrine tumors after 7.4 GBq ^{90}Y-DOTATOC. *J Nucl Med.* 2002;43:610–616.
32. Bodei L, Kidd M, Paganelli G, et al. Long-term tolerability of PRRT in 807 patients with neuroendocrine tumours: the value and limitations of clinical factors. *Eur J Nucl Med Mol Imaging.* 2015;42:5–19.
33. de Keizer B, van Aken MO, Feelders RA, et al. Hormonal crises following receptor radionuclide therapy with the radiolabeled somatostatin analogue [^{177}Lu-DOTA^{0},Tyr^{3}]octreotate. *Eur J Nucl Med Mol Imaging.* 2008;35:749–755.

Prediction of ^{177}Lu-DOTATATE PRRT Outcome Using Multimodality Imaging in Patients with Gastroenteropancreatic Neuroendocrine Tumors: Results from a Prospective Phase II LUMEN Study

Magdalena Mileva[1], Gwennaëlle Marin[2], Hugo Levillain[2], Carlos Artigas[1], Camille Van Bogaert[3], Clémentine Marin[2], Rachele Danieli[2], Amelie Deleporte[4], Simona Picchia[5], Konstantinos Stathopoulos[5], Christiane Jungels[4], Bruno Vanderlinden[2], Marianne Paesmans[6], Lieveke Ameye[6], Gabriela Critchi[1], Loubna Taraji-Schiltz[1], Chloe Velghe[6], Zéna Wimana[1,7], Maria Bali[5], Alain Hendlisz[4], Patrick Flamen[1], and Ioannis Karfis[1]

[1]Nuclear Medicine Department, Institut Jules Bordet, ENETS Centre of Excellence, Hôpital Universitaire de Bruxelles, Université Libre de Bruxelles, Brussels, Belgium; [2]Medical Physics Department, Institut Jules Bordet, ENETS Centre of Excellence, Hôpital Universitaire de Bruxelles, Université Libre de Bruxelles, Brussels, Belgium; [3]Nuclear Medicine Department, CUB-Hôpital Erasme, ENETS Centre of Excellence, Hôpital Universitaire de Bruxelles, Université Libre de Bruxelles, Brussels, Belgium; [4]Medical Oncology Department, Institut Jules Bordet, ENETS Centre of Excellence, Hôpital Universitaire de Bruxelles, Université Libre de Bruxelles, Brussels, Belgium; [5]Radiology Department, Institut Jules Bordet, ENETS Centre of Excellence, Hôpital Universitaire de Bruxelles, Université Libre de Bruxelles, Brussels, Belgium; [6]Data Center, Institut Jules Bordet, ENETS Centre of Excellence, Hôpital Universitaire de Bruxelles, Université Libre de Bruxelles, Brussels, Belgium; and [7]Radiopharmacy Department, Institut Jules Bordet, ENETS Centre of Excellence, Hôpital Universitaire de Bruxelles, Université Libre de Bruxelles, Brussels, Belgium

---

Our objective was to predict the outcome of peptide receptor radionuclide therapy (PRRT) using multimodality imaging and tumor dosimetry on gastroenteropancreatic neuroendocrine tumor (GEP-NET) lesions and patients. **Methods:** This prospective study included patients with progressive GEP-NETs. Treatment consisted of 4 cycles of 7.4 GBq of ^{177}Lu-DOTATATE. Imaging parameters were measured on ^{68}Ga-DOTATATE PET/CT ($\text{SUV}_{\text{max/mean}}$, somatostatin receptor [SSTR] tumor volume [TV], total lesion SSTR expression, and tumor-to-blood and tumor-to-spleen ratios), ^{18}F-FDG PET/CT ($\text{SUV}_{\text{max/mean}}$, metabolically active TV, and total lesion glycolysis), and diffusion-weighted MRI (apparent diffusion coefficient) in a maximum of 5 target lesions per patient at approximately 10 wk after each injection. Tumor dosimetry was performed using SPECT/CT at 3 time points for every cycle. Baseline imaging parameters, their relative changes after PRRT cycle 1 (C1), and the tumor-absorbed dose at C1 were correlated with lesion morphologic outcome. The average values of the imaging parameters and the minimal, maximal, and mean C1 tumor-absorbed dose in each patient were tested for association with progression-free survival (PFS) and best objective response (RECIST 1.1). **Results:** In the 37 patients, the median PFS was 28 mo. Eleven of the 37 (30%) achieved a partial response (RECIST 1.1). After a median follow-up of 57 mo, the median time to lesion progression had not been reached in 84 morphologically evaluable lesions, with only 12 (14%) progressing (size increase $\geq$ 20% from baseline). Patients receiving a minimal C1 dose of 35 Gy in all target lesions exhibited a significantly longer PFS (48.1 vs. 26.2 mo; hazard ratio, 0.37; 95% CI, 0.17–0.82; $P = 0.02$). Volumetric ^{68}Ga-DOTATATE PET parameters correlated with lesion and patient outcome: patients with an SSTR TV decrease of more than 10% after C1 had a longer PFS (51.3 vs. 22.8 mo; hazard ratio, 0.35; 95% CI, 0.16–0.75; $P = 0.003$). There was no statistical evidence of an association between other dosimetric or imaging parameters and the lesion or patient outcome. **Conclusion:** Minimal tumor-absorbed dose at C1 is predictive of outcome in patients with GEP-NETs treated with PRRT, providing a basis for personalized dosimetry-guided treatment strategies. An SSTR TV decrease after C1 could be used for early therapy response assessment as a predictor of PRRT outcome.

Key Words: ^{68}Ga-DOTATATE; neuroendocrine tumors; peptide receptor radionuclide therapy; response prediction; dosimetry

J Nucl Med 2024; 65:236–244
DOI: 10.2967/jnumed.123.265987

Neuroendocrine neoplasms represent a challenging clinical entity with marked heterogeneity in phenotype, prognosis, and evolution over time. Approximately 55%–70% of cases arise from gastroenteropancreatic structures (*1*). Neuroendocrine neoplasms can range from well-differentiated neuroendocrine tumors (NETs) to poorly differentiated neuroendocrine carcinomas (*2*). NET cells frequently have increased somatostatin receptor (SSTR) expression, predominantly of the somatostatin 2A subtype (*3,4*). This feature constitutes the basis for molecular imaging and therapy using SSTR-targeting radiopharmaceuticals. Peptide receptor radionuclide therapy (PRRT) with ^{90}Y- and ^{177}Lu-radiolabeled SSTR agonists (e.g., DOTATOC and DOTATATE) has been successfully used for more than 2 decades in NETs (*5*). The regulatory approval of ^{177}Lu-DOTATATE PRRT followed the demonstration of significantly prolonged progression-free survival (PFS) compared with somatostatin analogs in patients with midgut NETs in the randomized phase 3 NETTER1 trial (*6*) and established a standard of care.

Maximizing the clinical benefit would require appropriate patient selection and adequate assessment of treatment response. In the last decade, PET/CT using ^{68}Ga-radiolabeled SSTR agonists

---

Received May 9, 2023; revision accepted Oct. 25, 2023.

For correspondence or reprints, contact Ioannis Karfis (ioannis.karfis@hubruxelles.be).

has almost completely replaced conventional SSTR scintigraphy as the fundamental step to assess SSTR status in vivo and evaluate the benefit likelihood for PRRT. Although PET/CT with ^{18}F-FDG is generally reserved for imaging of high-grade NETs and neuroendocrine carcinomas (*7,8*), studies have shown that low-grade NETs can also be ^{18}F-FDG–avid (*9*). Apart from assessing eligibility for PRRT, molecular imaging could potentially serve as a predictive biomarker of response to PRRT. Nevertheless, available data regarding the use of ^{68}Ga-SSTR PET/CT to predict PRRT response are mainly retrospective and somewhat conflicting (*10,11*). Additionally, as the absorbed dose is fundamental to the antitumor effect of PRRT (*12,13*), dosimetry of the tumor lesions could be used for outcome prediction and treatment personalization.

We conducted a prospective study enrolling patients who had progressive gastroenteropancreatic NETs (GEP-NETs) and were eligible for treatment with ^{177}Lu-DOTATATE PRRT. A series of multimodality imaging parameters derived from molecular imaging (i.e., ^{68}Ga-DOTATATE PET/CT and ^{18}F-FDG PET/CT) and from diffusion-weighted MRI was followed after every treatment cycle. Tumor dosimetry after each injection was also performed. We aimed to assess the value of the pretreatment imaging parameters and their relative changes after PRRT cycle 1 (C1), as well as the tumor-absorbed dose in C1, in predicting lesion and patient outcome.

MATERIALS AND METHODS

Patients and Treatment

The LuMEn trial (NCT01842165) is a single-arm, prospective, phase II clinical-imaging study enrolling patients with advanced, histologically proven well-differentiated GEP-NETs, progressive within 12 mo before study inclusion. The complete list of patient selection criteria is available in Supplemental Table 1 (supplemental materials are available at http://jnm.snmjournals.org). All procedures performed in the study were in accordance with the Declaration of Helsinki. The study was approved by the Jules Bordet Institute Ethics Committee (CE2034), and written informed consent was obtained from all participants. Treatment consisted of 4 ^{177}Lu-DOTATATE injections of 7.4 GBq (±5%) each, administered intravenously 10–12 wk apart, with concomitant infusion of a nephroprotective amino acid solution and preceded by an antiemetic regime. ^{177}Lu-DOTATATE was produced within the radiopharmacy facility of our nuclear medicine department as previously reported (*14*). All patients underwent baseline abdominopelvic MRI (or CT if MRI was contraindicated), ^{68}Ga-DOTATATE PET/CT, and ^{18}F-FDG PET/CT within 3 wk (± 1 wk) before the first PRRT injection. These imaging examinations were repeated approximately 10 wk after each ^{177}Lu-DOTATATE injection. Detailed acquisition parameters are available in Supplemental Table 2. After the last PRRT cycle, patients were followed clinically and radiologically every 3 mo until disease progression according to RECIST 1.1 (*15*).

Image Analysis

On side-by-side evaluation of baseline MRI (or CT), ^{68}Ga-DOTATATE PET/CT, and ^{18}F-FDG PET/CT, a maximum of 5 target lesions was selected by a radiologist and nuclear medicine physician. Selection of a lesion required that it be unequivocally neoplastic, be RECIST 1.1-measurable, have uptake higher than physiologic liver uptake on ^{68}Ga-DOTATATE PET/CT, and preferably be positive on ^{18}F-FDG PET/CT (uptake above the threshold as defined below). The lesions had to represent the global tumor burden, ideally be spheric, and be outside any prior radiation fields of view. Confluent extensive lesions or lesions adjacent to each other on the ^{68}Ga-DOTATATE PET/CT images were not included.

Tumors were delineated on ^{68}Ga-DOTATATE PET/CT images using a gradient-based method (PETEdge tool in MIM Encore, version 6.9; MIM Software) to measure specific uptake (SUV_{max}, SUV_{mean}, tumor-to-spleen ratio [tumor SUV_{max}/spleen SUV_{mean}], tumor-to-blood ratio [tumor SUV_{max}/blood SUV_{mean}]) and volumetric parameters (SSTR-expressing tumor volume [TV] and total lesion SSTR expression [$SUV_{mean} \times$ SSTR TV]). Spleen parenchyma was delineated using a fixed threshold of 50% of maximum spleen uptake to calculate the spleen SUV_{mean}, as previously defined by the group of Haug et al. (*16*). Blood SUV_{mean} was measured in a 1-cm-diameter cylindric volume of interest in the center of the descending thoracic aorta. ^{18}F-FDG–positive target lesions were delineated on ^{18}F-FDG PET/CT images using a PERCIST-based threshold (*17*) to measure SUV_{max}, SUV_{mean}, metabolically active TV, and total lesion glycolysis ($SUV_{mean} \times$ metabolically active TV). The apparent diffusion coefficient (ADC) map of the MR images was used to obtain the ADC of the target lesions (automatically calculated by the MRI scanner). The mean ADC (mm^2/s) was evaluated with a region of interest drawn inside the soft-tissue component of the lesion, avoiding necrosis or calcifications and without touching the borders. All parameters were measured for each lesion individually for the lesion-based analysis. The average values of the imaging parameters from the target lesions of one patient were used in a patient-based analysis.

For dosimetry purposes, SPECT/CT images were acquired 4, 24, and 168 h after each injection of ^{177}Lu-DOTATATE. Target lesions were segmented on all ^{177}Lu-DOTATATE SPECT/CT images using a region-growing tool (MIM Encore, version 6.9) to reach the same volume as the one obtained on the ^{68}Ga-DOTATATE PET/CT images. Detailed data about the tumor dosimetry procedure are available in Supplemental Table 3. A conversion factor (previously assessed by our group (*14*)) was used to convert counts into activity concentrations, which were then corrected for partial-volume effect using a recovery coefficient curve obtained at our institute using a National Electrical Manufacturers Association phantom with infinite contrast. The mean activity inside tumors was converted into dose rate using the sphere model (OLINDA/EXM 1.1) (*18*). To calculate the absorbed dose, dose rate was time-integrated using the trapezoidal method up to 24 h, and monoexponential decay was derived from the last 2 time points.

Response Assessment

On a lesion level, morphologic progression was defined as a size increase of at least 20% from baseline. A size decrease of more than 30% from baseline was defined as a partial response, and the complete disappearance of a lesion (or size $<$ 10 mm for lymph nodes) was defined as a complete response. Lesions showing neither a sufficient decrease nor a sufficient increase in size to qualify for progression or partial response were considered stable. For group comparisons, lesions with a complete or partial response were classified as responding lesions, whereas stable or progressive lesions were classified as nonresponding lesions. Morphologically evaluable lesions were those for which a response assessment after 4 PRRT cycles was available.

The patient-based response was assessed according to RECIST 1.1. Patients with a partial or complete response were classified as objective responders, whereas patients with stable or progressive disease were considered nonobjective responders.

Statistical Analysis

The primary endpoint of the study was lesion-based time to progression, calculated as the time between treatment initiation and the earliest documented lesion morphologic progression after completion of the treatment cycles. To get a power of 0.80 for a clinically relevant hazard ratio (HR) of 0.33, 37 progressive lesions needed to be documented. Differences in imaging parameters and tumor-absorbed dose between responding and nonresponding lesions were tested using the

Wilcoxon signed-rank test. Correlations were analyzed using the Spearman correlation coefficient. PFS was defined as the time between treatment initiation and disease progression or death resulting from any cause. Kaplan–Meier survival curves and the Cox proportional-hazards regression model were used to compare PFS among different groups. The objective response rate was calculated as the proportion of subjects with a partial or complete response. Average values of the imaging parameters and the minimal, maximal, and mean tumor-absorbed dose per patient in C1 were tested for association with PFS and best objective response using the log-rank test. The optimal cutoff for a continuous explanatory variable was determined with the method of Contal and O'Quigley (*19*). A *P* value of less than 0.05 was considered statistically significant in all cases. Statistical analyses were performed using SAS 9.4 (SAS Institute Inc.) and Prism 7.04 (GraphPad Software).

RESULTS

Patients and Treatment Data

Between July 2013 and January 2020, 37 consecutive patients with advanced GEP-NETs were included in the study. Patient demographics and tumor characteristics are detailed in Table 1. Overall, 140 ^{177}Lu-DOTATATE cycles were administered, with a mean cumulated administered activity of 27.9 GBq (range, 7.5–36.9 GBq). Twenty-eight patients completed 4 cycles of PRRT, with a mean administered activity of 7.5 GBq (±0.2 GBq) per cycle. In the remaining 9 patients, different numbers of PRRT cycles were administered, the reasons for which are detailed in Supplemental Table 4. Safety analysis for the study cohort will be the subject of a separate publication.

Outcomes

At baseline, 116 target lesions were selected. Eighty-four were morphologically evaluable, of which 22 (26%) showed a partial response. They were mostly liver lesions (15/22), identified in 13 patients. There were no target lesions with a complete response. Fifty lesions (60%) were stable, and 12 (14%) progressed morphologically. The median follow-up time (data cutoff, July 2022) was 57 mo (95% CI, 50–71 mo), during which the median lesion-based time to progression was not reached. The objective response rate was 30% (11 patients with a partial response and no patients with a complete response), and the median PFS for the whole cohort was 28.1 mo. The association between PFS and potential prognostic factors is detailed in Supplemental Table 5. Patients with pancreatic primary NETs had a shorter PFS (median, 19.4 mo) than that of patients with intestinal NETs (29.5 mo) ($P = 0.01$; HR, 2.96; 95% CI, 1.25–7.02).

Imaging Parameters and Association with Lesion Outcome

^{68}Ga-DOTATATE PET/CT. At baseline, ^{68}Ga-DOTATATE PET/CT parameters were available for 110 of the 116 target lesions (6 excluded because of PET/CT artifacts) for SUV_{max}, SUV_{mean}, tumor-to-blood ratio, SSTR TV, and total lesion SSTR expression and for 97 of the 116 target lesions for tumor-to-spleen ratio (additional 13 excluded because they were from 4 patients with prior splenectomy). Baseline SUV_{max}, SUV_{mean}, tumor-to-blood ratio, SSTR TV, and total lesion SSTR expression were not associated with lesion morphologic outcome (Table 2). Baseline tumor-to-spleen ratio was significantly lower in the responding lesions than in the nonresponding ones ($P = 0.03$); however, the Spearman rank coefficient was not statistically significant, as detailed in Table 3.

The changes in volumetric ^{68}Ga-DOTATATE PET/CT parameters—that is, SSTR TV and total lesion SSTR expression—after C1 from baseline were significantly associated with lesion morphologic outcome (Fig. 1; Table 4). The specific uptake parameters decreased significantly after C1 from baseline in all lesions (responding and nonresponding) (Supplemental Fig. 1); however, this decrease was not associated with lesion morphologic outcome (Table 3).

^{18}F-FDG PET/CT. At baseline, 21 target lesions from 12 patients were ^{18}F-FDG–positive. Baseline values of SUV_{max}, SUV_{mean}, metabolically active TV, and total lesion glycolysis showed no significant association with lesion morphologic outcome. A minor decrease in SUV_{max} was observed after C1 from baseline in all lesions (median, −10%; interquartile range [IQR], −20% to −8%; $P = 0.03$) but was not associated with lesion morphologic outcome, similarly to SUV_{mean}, metabolically active TV, and total lesion glycolysis. Nevertheless, the small number of ^{18}F-FDG–positive lesions prevents any meaningful statistical assessment.

Diffusion-Weighted MRI. Baseline ADC was available for 86 target lesions (6 excluded because of MR image artifacts; 24 were from patients followed by CT). The median value in all lesions was 859 (IQR, 718–1,002). ADC increased significantly after C1 from baseline in all evaluable lesions, with a median of 12% (IQR, 2%–27%; $P < 0.001$), and remained globally stable at the subsequent imaging time points. No statistically significant association was found between ADC (baseline or increase after C1) and lesion morphologic outcome ($P = 0.58$ and 0.71, respectively).

Imaging Parameters and Association with Patient Outcome

^{68}Ga-DOTATATE PET/CT. An SSTR TV decrease of more than 10% from baseline after C1 discriminated patients with a significantly longer median PFS (51.3 mo) than that (22.8 mo) of patients for whom SSTR TV increased or decreased by less than 10% ($P = 0.003$; HR, 0.35; 95% CI, 0.16–0.75) (Fig. 2A). The same parameter remained significantly associated with PFS when patients with pancreatic primary NET were excluded, as presented in Figure 2B (median PFS of 51.3 mo compared with 27.6 mo: $P = 0.008$; HR, 0.32; 95% CI, 0.13–0.81). A decrease in total lesion SSTR expression of more than 10% from baseline after C1 discriminated patients with a median PFS of 32.2 mo, compared with 26.2 mo ($P = 0.05$; HR, 0.42; 95% CI, 0.17–1.0).

The changes in SSTR TV and total lesion SSTR expression after C1 remained significantly associated with the best objective response according to RECIST 1.1: a median decrease of −9% (IQR, −36% to 9%; $P = 0.04$) and −34% (IQR, −52% to −10%; $P = 0.008$) for SSTR TV and total lesion SSTR expression, respectively, in the responding patients, compared with 8% (IQR, 3% to 30%) and −3% (IQR, −19% to 10%) in the nonresponding patients.

Because the baseline tumor-to-spleen ratio was significant in a lesion-based analysis, the average values per patient were tested for association with patient outcome. An optimal cutoff of 1.25 demonstrated no significant association with PFS ($P = 0.20$) or with best objective response ($P = 0.11$).

^{18}F-FDG PET/CT. Quantification of baseline ^{18}F-FDG PET/CT was available for only 10 patients. Because of the low number of patients and events, no statistical analysis for association with patient outcome was performed.

Diffusion-Weighted MRI. In 29 patients followed by MRI, there was no statistical evidence of an association between baseline ADC or its relative change after C1 and patient outcome.

TABLE 1
Patients' Demographics and Tumor Characteristics

Characteristic	Data
Sex	
Male	19 (51)
Female	18 (49)
Mean age at diagnosis (y)	61 ± 10
Mean age at inclusion (y)	66 ± 8.1
Median time since diagnosis (y)	3.4 (IQR, 1.7–7.7)
Primary tumor site	
Small intestinal	23 (62)
Pancreatic	10 (27)
Colorectal	4 (11)
Tumor grade	
1	12 (32)
2	22 (59)
3	3 (8)
Site of metastasis	
Liver	32 (86)
Lymph nodes	31 (84)
Bone	22 (59)
Peritoneum	12 (32)
Pancreas	3 (8)
Lung	2 (5)
Other*	6 (16)
Metastatic sites involved	
Median number	3 (range, 1–5)
≤3	25 (68)
>3	12 (32)
Symptoms	
Diarrhea	16 (43)
Pain	15 (41)
Fatigue	11 (30)
Flushing	9 (24)
No symptoms	12 (32)
^{18}F-FDG PET/CT–positive at baseline	15 (41)
Previous treatment lines	37 (100)
Previous treatments	
Surgery (including primary tumor resection)	27 (73)
Somatostatin analogs	36 (97)
Targeted therapy†	11 (30)
Chemotherapy	8 (22)
Liver-targeted therapy‡	8 (22)
Radiotherapy (external-beam radiation)	4 (11)
Interferon	1 (3)
Median number of previous treatment lines (all)	2 (range, 1–10)
Previous systemic treatment lines (excluding somatostatin analogs)	16 (43)
1	10 (27)
2	5 (13)
6	1 (3)

*Pleural, adrenal, ovarium, mesentery/pelvic.

†Including everolimus and sunitinib.

‡Including chemoembolization, radioembolization, and radiofrequency ablation.

Data are number followed by percentage in parentheses, unless otherwise indicated (n = 37 total patients).

Tumor Dosimetry

Dosimetry was performed for 83 target lesions from 35 patients (33 lesions were excluded; Supplemental Fig. 2). The median absorbed dose in C1 was 33 Gy (IQR, 22–50 Gy) and declined from the first to the last treatment cycles, reaching significance between C1 and cycle 3 (P = 0.002), C1 and cycle 4 (P < 0.001), and cycles 2 and 4 (P = 0.01), as presented in Figure 3.

The correlation between tumor-absorbed C1 dose and lesion outcome was tested for all target lesions treated with 4 PRRT cycles and in subgroups based on lesion size at baseline (inspired by a study by Ilan et al., in which accurate partial-volume effect correction was not possible for tumors < 22 mm in diameter, hence influencing the accuracy of activity measurement on SPECT images (*13*)) and on primary NET origin. As presented in Table 4, a significant correlation between tumor-absorbed C1 dose and lesion outcome was demonstrated for larger lesions (≥22 mm) and for the limited number of lesions of colorectal primary NET origin.

On a patient level, the minimal absorbed dose per target lesion in C1 ranged from 10 to 77 Gy. An optimal cutoff of 35 Gy (i.e., patients in whom all target lesions received at least a 35-Gy tumor-absorbed C1 dose) discriminated patients with a significantly longer median PFS (48.1 mo) than that of patients in whom at least 1 target lesion was treated with less than 35 Gy in C1 (26.2 mo) (P = 0.02; HR, 0.37; 95% CI, 0.17–0.82; P = 0.02) (Fig. 2C). The minimal absorbed dose per target lesion in C1 remained associated with PFS when patients with pancreatic primary NET were excluded, as presented in Figure 2D (median PFS of 48.1 compared with 27.6 mo: P = 0.05; HR, 0.40; 95% CI, 0.16–1.0).

Of the 26 patients who had a minimal absorbed dose of less than 35 Gy per target lesion in C1, 21 (81%) demonstrated an increase or decrease of less than 10% for SSTR TV on ^{68}Ga-DOTATATE PET/CT after C1. Subsequently, the combination of these 2 parameters showed a stronger association with PFS in all patients (P < 0.001; HR, 0.32; 95% CI, 0.14–0.71) and when patients with pancreatic primary NET were excluded (P = 0.001; HR, 0.28; 95% CI, 0.10–0.77), as presented in Figures 2E and 2F, respectively. No association with PFS was found for the maximal or mean C1 doses.

DISCUSSION

We conducted a prospective study, unique to the best of our knowledge, aiming to assess the value of a series of multimodality imaging parameters and tumor-absorbed dose as potential predictive biomarkers of lesion and patient outcome after PRRT. Serial imaging (^{68}Ga-DOTATATE PET/CT, ^{18}F-FDG PET/CT, and diffusion-weighted MRI) and SPECT/CT-based tumor dosimetry at every cycle were performed in a standardized mode for each ^{177}Lu-DOTATATE administration.

In 37 patients with advanced GEP-NETs, PRRT was confirmed to have high efficacy, with the median PFS reaching 28 mo and the best objective response rate being 30%, which line up with previous clinical trials (*6,20*). During a relatively long median follow-up (57 mo), our study's primary endpoint of lesion-based time to progression was not reached. Only a small fraction (14%) of the prospectively followed target lesions progressed according to the morphologic criteria, questioning their suitability as reliable outcome measurements in PRRT. Although widely used, criteria based on morphologic measurements, such as RECIST 1.1, have several limitations that are significant in the particular setting of slow-growing NETs (*21*). In the NETTER1 trial, objective RECIST-based

TABLE 2
Association Between Baseline ^{68}Ga-DOTATATE PET/CT Parameters and Morphologic Lesion Outcome

Parameter	Response	Lesions (*n*)	Median	IQR	*P**	Spearman ρ	*P*†
SUV_{max}	R	21	18.7	14.7 to 24.2	0.71		
	NR	59	18.6	14.8 to 25.4			
SUV_{mean}	R	21	11.4	9.7 to 13.1	0.99		
	NR	59	11.0	9.1 to 13.7			
Tumor-to-spleen ratio	R	16	1.3	0.8 to 1.9	0.03	0.04 (95% CI, −0.20 to 0.27)	0.73
	NR	54	1.8	1.3 to 2.7			
Tumor-to-blood ratio	R	21	59.8	51.1 to 82.1	0.37		
	NR	59	54.6	39.6 to 80.8			
SSTR TV	R	21	8.4	2.4 to 26.5	0.81		
	NR	59	7.6	3.9 to 20.9			
Total lesion SSTR expression	R	21	86	45 to 227	0.81		
	NR	59	108	39 to 247			

*Grouped analysis using Wilcoxon signed-rank test.
†Spearman rank correlation.
R = responding lesion; NR = nonresponding lesion.

tumor response was reached in only 18% of the patients treated in the ^{177}Lu-DOTATATE arm (*6*).

To our knowledge, this is the first report of the value of the lowest radiation dose received by tumors in C1 in predicting patient outcome. Patients receiving a minimum absorbed dose of 35 Gy in all measurable lesions showed a significantly longer median PFS than did patients in whom at least 1 target lesion received less than 35 Gy. This cutoff should ideally be confirmed in larger cohorts, especially in studies focusing on dose calculation for the entire tumor burden in the concept of personalized treatment regimes.

TABLE 3
Association Between Relative Change in ^{68}Ga-DOTATATE PET/CT Parameters After C1 from Baseline and Morphologic Lesion Outcome

Parameter	Response	Lesions (*n*)	Median	IQR	*P**	Spearman ρ	*P*†
SUV_{max}	R	19	−23%	−33% to 0%	0.48		
	NR	59	−16%	−33% to 0%			
SUV_{mean}	R	19	−21%	−39% to 3%	0.29		
	NR	59	−15%	−29% to 5%			
Tumor-to-spleen ratio	R	14	−32%	−41% to −8%	0.91		
	NR	54	−30%	−50% to −12%			
Tumor-to-blood ratio	R	19	−18%	−35% to 3%	0.44		
	NR	59	−16%	−31% to 19%			
SSTR TV	R	19	−9%	−36% to 20%	0.05	0.27 (95% CI, 0.05 to 0.47)	0.01
	NR	59	11%	−8% to 27%			
Total lesion SSTR expression	R	19	−27%	−46% to −3%	0.01	0.32 (95% CI, 0.11 to 0.51)	0.004
	NR	59	−6%	−24% to 11%			

*Grouped analysis using Wilcoxon signed-rank test.
†Spearman rank correlation.
R = responding lesion; NR = nonresponding lesion.

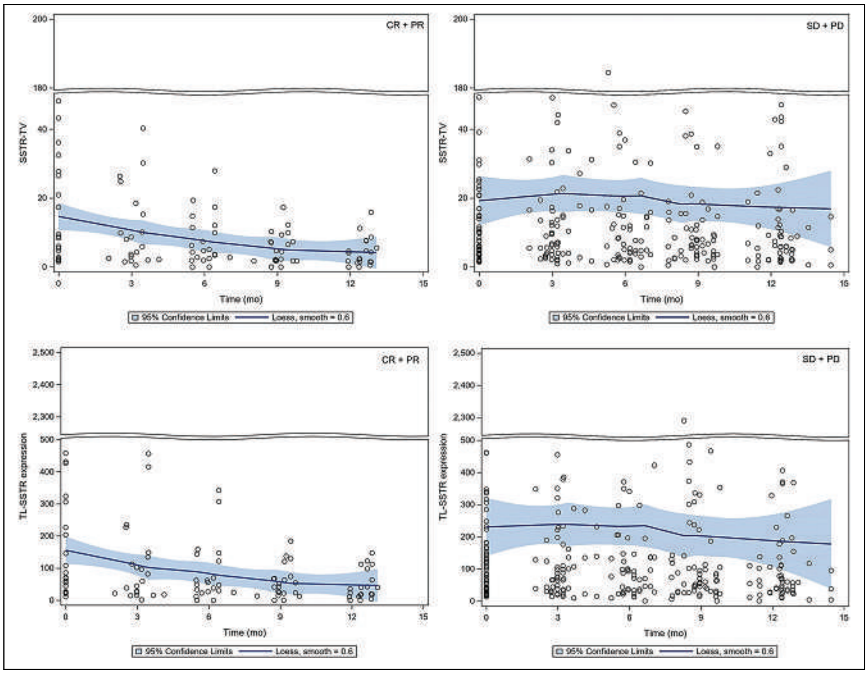

FIGURE 1. Scatterplot with locally weighted scatterplot smoothing and 95% CI of SSTR TV and total lesion SSTR expression on baseline ^{68}Ga-DOTATATE PET/CT and during subsequent treatment cycles. At left are morphologically responding lesions showing partial or complete response; at right are morphologically nonresponding lesions showing stable or progressive disease. CR = complete response; Loess = locally weighted scatterplot smoothing; PD = progressive disease; PR = partial response; SD = stable disease; TL = total lesion.

In a lesion-based analysis, our results demonstrate a correlation between absorbed dose in C1 and morphologic outcome only in the limited number of colorectal NET lesions but not for other primary NETs (i.e., pancreatic and small-intestinal). Direct comparison with previously published data, albeit scarce, on dose–response relationships in NETs treated with ^{177}Lu-DOTATATE is impractical because of differences in study methods. Aiming to predict morphologic lesion outcome during treatment, we evaluated the absorbed dose received by the tumors only in C1. In contrast, in the study of Ilan et al., including only pancreatic NETs, the absorbed dose until the best response correlated with tumor shrinkage at any time during the treatment, especially in large lesions measuring at least 4 cm (*13*). In a study from the same group, evaluating only tumors of small-intestinal primary origin, no relationship between tumor shrinkage and absorbed dose was demonstrated (*22*). This follows our findings, again stressing the weakness of morphologic measurements (i.e., tumor shrinkage) as response criteria, especially in small-intestinal NETs.

Three-time-point SPECT/CT-based dosimetry after each ^{177}Lu-DOTATATE injection revealed that the tumor-absorbed dose was higher in C1 and continuously decreased over the subsequent PRRT cycles. This observation supports the role of C1 and its impact on overall patient outcome. Furthermore, it could provide a basis for dosimetry-guided strategies in PRRT aiming at higher administered activities (to achieve higher tumor-absorbed doses) in the early therapy cycles. Several reports on the feasibility and safety of individualized dosimetry-based PRRT protocols in patients with NETs have been published so far. Two Swedish groups, using a similar study design, adjusted the

TABLE 4
Correlation Between Tumor-Absorbed C1 Dose and Lesion Morphologic Outcome in All Lesions and in Size-Based Subgroups According to Primary NET Origin

Origin	Lesions (*n*)	Spearman ρ	*P*
All lesions	61	−0.24 (−0.47 to 0.18)	0.06
Pancreatic	20	−0.35 (−0.69 to 0.11)	0.12
Small-intestinal	31	0.11 (−0.26 to 0.46)	0.53
Colorectal	10	−0.89 (−0.97 to −0.60)	<0.001
Lesions < 22 mm	27	−0.07 (−0.45 to 0.33)	0.72
Pancreatic	10	−0.58 (−0.89 to 0.08)	0.06
Small-intestinal	15	0.27 (−0.29 to 0.69)	0.32
Colorectal	2*	—	—
Lesions ≥ 22 mm	34	−0.41 (−0.67 to −0.08)	0.01
Pancreatic	10	−0.13 (−0.70 to 0.54)	0.71
Small-intestinal	16	−0.08 (−0.57 to 0.44)	0.75
Colorectal	8	−0.92 (−0.99 to −0.61)	<0.001

---

*Insufficient for analysis.

Data in parentheses are 95% CIs. Size groups are based on longest axial diameter on baseline MRI or CT.

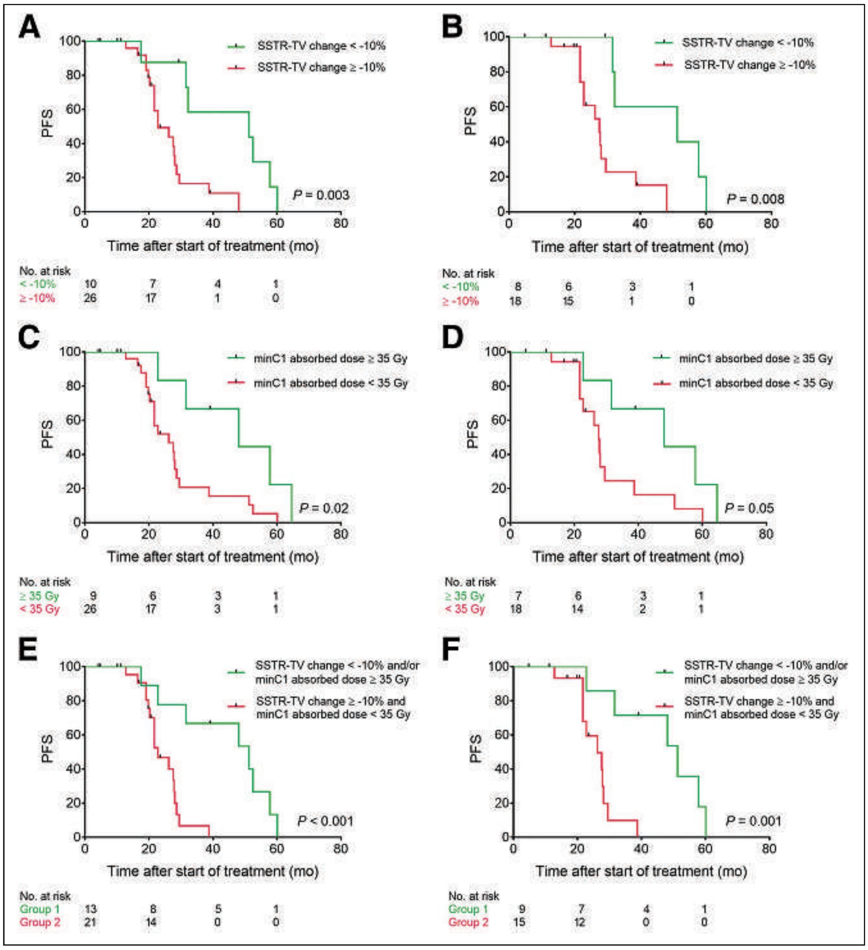

FIGURE 2. Kaplan–Meier curves of progression-free survival for SSTR TV change after C1 in all patients (A) and excluding patients with pancreatic primary NET (B), minimal absorbed dose per target lesion in C1 in all patients (C) and excluding patients with pancreatic primary NET (D), and combination of SSTR TV change after C1 and minimal absorbed dose per target lesion in C1 in all patients (E) and excluding patients with pancreatic primary NET (F). minC1 absorbed dose = minimal absorbed dose per target lesion in C1.

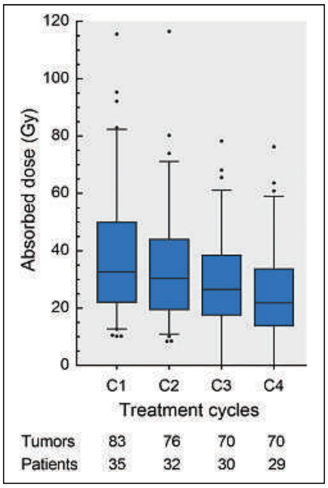

FIGURE 3. Tumor-absorbed dose as function of PRRT cycle across all target lesions. Whiskers indicate fifth and 95th percentiles.

number of PRRT cycles (each with a fixed injected activity of 7.4 GBq) to reach a maximum limit of absorbed dose to the kidneys. They achieved objective response rates of 24% (*23*) and 34% (*24*), without clinically significant toxicity. In contrast, Del Prete et al. personalized the administered activities in each cycle (median, 8.8 GBq) to deliver a prescribed absorbed dose to the kidneys over a fixed number of 4 PRRT cycles (*25*). They reported a high response rate of 59% and a significantly higher cumulative maximum tumor-absorbed dose, with a median 1.26-fold (maximum, 2.12-fold) increase compared with a simulated empiric regime. Because standard dosimetry protocols are generally burdensome for patients and personnel, implementing simplified procedures for such individualized tumor dosimetry is essential to expanding its availability in clinical routine. Methods of reducing the number of image acquisitions (single- or dual-time-point posttreatment SPECT/CT) are being explored by our group (*26*), as well as others (*27,28*), and they prove to be feasible and in agreement with standard dosimetry protocols.

SUV parameters measured on pretreatment SSTR PET/CT have been explored by many groups as predictors of PRRT outcome. In a study by Sharma et al., a baseline single-lesion SUV_{max} of more than 13 and an average SUV_{max} of more than 10.2 from up to 5 target lesions predicted RECIST 1.1 response to PRRT (*11*). Pauwels et al. found an SUV_{mean} higher than 13.7 (derived from the whole-tumor burden on baseline ^{68}Ga-DOTA-TOC PET/CT) to be associated with better overall survival (HR, 0.45; $P = 0.024$) (*29*). On a patient level, we could not identify any baseline ^{68}Ga-DOTATATE PET parameters associated with outcome. In a lesion-based analysis, only the tumor-to-spleen ratio was significantly lower in responding than nonresponding lesions ($P = 0.03$). Nonetheless, its value in predicting response and thus guiding treatment decisions should be carefully assessed. The tumor-to-spleen difference between the 2 groups of lesions could be influenced by the higher radiotracer uptake in the spleen in patients showing a RECIST 1.1 partial response (data not shown). This observation is possibly related to differences in overall tumor burden and, thus, peptide biodistribution (*30*).

We assessed the evolution of serial ^{68}Ga-DOTATATE PET/CT parameters after each treatment cycle with the intent to identify biomarkers of early outcome prediction using a rather complex design, which we do not recommend for implementation in clinical practice. Yet, this approach revealed that the changes in the volumetric ^{68}Ga-DOTATATE PET/CT parameters observed already at 10–12 wk after C1 correlated significantly with both lesion outcome and patient outcome. An even stronger association with patient PFS was demonstrated when the SSTR TV decrease after C1 was combined with the minimal absorbed dose per target lesion in C1 ($P < 0.001$; Fig. 2E). Identifying these patients early during the treatment course is essential, as implementing optimization strategies such as combination therapies, or even using new α-emitting radiopharmaceuticals, might further improve patient outcome and survival.

Treatments inducing cancer cell death, such as PRRT, lead to an increase in ADC due to the development of cell swelling, tumor lysis, and necrosis (*31*). In our study, this increase in ADC after C1 was not associated with lesion morphologic response or patient outcome. Similarly, in a small population of 18 patients with NETs, Weber et al. saw no significant differences in diffusion-weighted MRI parameters between responders and nonresponders to PRRT (*32*).

Restricting the analysis to 5 target lesions, with the resulting incomplete assessment of SSTR expression, is perhaps the most limiting factor of the present study. We recognize that this limitation affects the comprehensiveness of our findings. We are currently analyzing the entire tumor burden on ^{68}Ga-DOTATATE PET/CT in our prospectively followed cohort, aiming to evaluate how total tumor volumetric parameters and their change after C1 compare with the current methodology in predicting patient outcome. Additionally, target lesion selection can vary among observers, potentially affecting study results and their interpretation. Standardized criteria and involvement of more than one observer can significantly reduce intra- and interobserver variability. Enforcing these strategies minimized observer variability in our study.

Understanding the radiosensitivity of tumors is crucial in radiopharmaceutical therapies. Achieving this understanding involves various methods and techniques, including assessment of ^{18}F-FDG PET parameters to evaluate changes in tumor metabolism in response to radiation. However, our study's low number of ^{18}F-FDG–positive lesions and patients prevents us from drawing any meaningful conclusions. At our center, all patients undergo dual-tracer PET/CT with ^{68}Ga-DOTATATE and ^{18}F-FDG to evaluate whether PRRT would be appropriate. Consequently, when there is a high ^{18}F-FDG–positive tumor burden or ^{18}F-FDG–positive/^{68}Ga-DOTATATE–negative disease, other treatment modalities (e.g., chemotherapy) are preferred over PRRT.

Finally, the ^{68}Ga-DOTATATE PET/CT segmentation method might be considered another limitation of our study. Customized thresholds based on physiologic liver SUV_{max} have been proposed, as compared with the frequently used 50% threshold of SUV_{max} that impacts the DOTATATE-avid TV in cases of intense radiotracer uptake (*33*). However, it is not uncommon for patients with metastatic NETs to have diffuse liver infiltration, restricting the use of physiologic liver uptake and stressing the need for standardized segmentation criteria on SSTR PET/CT imaging. An example of such a case from our study cohort is presented in Supplemental Figure 3.

CONCLUSION

In this prospective study, patients in whom all target lesions received an absorbed dose of at least 35 Gy in C1 demonstrated a longer PFS. This finding provides a basis for treatment strategies focusing on higher administered activities and higher tumor-absorbed doses in the early therapy cycles. Changes in SSTR TV and total lesion SSTR expression in selected target lesions after C1 correlated with lesion morphologic outcome, PFS, and best objective response. These findings support the use of volumetric parameters on ^{68}Ga-DOTATATE PET/CT for early assessment of therapy response in GEP-NET patients treated with PRRT.

DISCLOSURE

A grant was provided by National Cancer Plan and Les Amis de l'Institut Bordet. No other potential conflict of interest relevant to this article was reported.

KEY POINTS

QUESTION: Can molecular imaging and tumor dosimetry predict response to ^{177}Lu-DOTATATE PRRT in patients with GEP-NETs?

PERTINENT FINDINGS: In a prospective study including 37 patients with advanced GEP-NETs, a decrease of more than 10% in volumetric parameters on ^{68}Ga-DOTATATE PET/CT after C1, and a minimal tumor-absorbed dose of at least 35 Gy in C1, were significantly associated with a longer PFS.

IMPLICATIONS FOR PATIENT CARE: ^{68}Ga-DOTATATE PET/CT and tumor lesion dosimetry could be used to predict patient outcome early in the course of PRRT, allowing implementation of strategies for further treatment optimization.

REFERENCES

1. Das S, Dasari A. Epidemiology, incidence, and prevalence of neuroendocrine neoplasms: are there global differences? *Curr Oncol Rep.* 2021;23:43.
2. Rindi G, Mete O, Uccella S, et al. Overview of the 2022 WHO classification of neuroendocrine neoplasms. *Endocr Pathol.* 2022;33:115–154.
3. Wängberg B, Nilsson O, Johanson VV, et al. Somatostatin receptors in the diagnosis and therapy of neuroendocrine tumor. *Oncologist.* 1997;2:50–58.
4. Oronsky B, Ma PC, Morgensztern D, Carter CA. Nothing but NET: a review of neuroendocrine tumors and carcinomas. *Neoplasia.* 2017;19:991–1002.
5. Kwekkeboom DJ, de Herder WW, Kam BL, et al. Treatment with the radiolabeled somatostatin analog [^{177}Lu-DOTA^0,Tyr^3]octreotate: toxicity, efficacy, and survival. *J Clin Oncol.* 2008;26:2124–2130.
6. Strosberg J, El-Haddad G, Wolin E, et al. Phase 3 trial of ^{177}Lu-DOTATATE for midgut neuroendocrine tumors. *N Engl J Med.* 2017;376:125–135.
7. Sundin A, Arnold R, Baudin E, et al. ENETS consensus guidelines for the standards of care in neuroendocrine tumors: radiological, nuclear medicine & hybrid imaging. *Neuroendocrinology.* 2017;105:212–244.
8. Hope TA, Bergsland EK, Bozkurt MF, et al. Appropriate use criteria for somatostatin receptor PET imaging in neuroendocrine tumors. *J Nucl Med.* 2018;59:66–74.
9. Severi S, Nanni O, Bodei L, et al. Role of ^{18}FDG PET/CT in patients treated with ^{177}Lu-DOTATATE for advanced differentiated neuroendocrine tumours. *Eur J Nucl Med Mol Imaging.* 2013;40:881–888.
10. Gabriel M, Oberauer A, Dobrozemsky G, et al. ^{68}Ga-DOTA-Tyr^3-octreotide PET for assessing response to somatostatin-receptor–mediated radionuclide therapy. *J Nucl Med.* 2009;50:1427–1434.
11. Sharma R, Wang WM, Yusuf S, et al. ^{68}Ga-DOTATATE PET/CT parameters predict response to peptide receptor radionuclide therapy in neuroendocrine tumours. *Radiother Oncol.* 2019;141:108–115.
12. Pauwels S, Barone R, Walrand S, et al. Practical dosimetry of peptide receptor radionuclide therapy with ^{90}Y-labeled somatostatin analogs. *J Nucl Med.* 2005;46(suppl 1):92S–98S.
13. Ilan E, Sandstrom M, Wassberg C, et al. Dose response of pancreatic neuroendocrine tumors treated with peptide receptor radionuclide therapy using ^{177}Lu-DOTATATE. *J Nucl Med.* 2015;56:177–182.
14. Marin G, Vanderlinden B, Karfis I, et al. A dosimetry procedure for organs-at-risk in ^{177}Lu peptide receptor radionuclide therapy of patients with neuroendocrine tumours. *Phys Med.* 2018;56:41–49.
15. Eisenhauer EA, Therasse P, Bogaerts J, et al. New response evaluation criteria in solid tumours: revised RECIST guideline (version 1.1). *Eur J Cancer.* 2009;45:228–247.
16. Haug AR, Auernhammer CJ, Wangler B, et al. ^{68}Ga-DOTATATE PET/CT for the early prediction of response to somatostatin receptor–mediated radionuclide therapy in patients with well-differentiated neuroendocrine tumors. *J Nucl Med.* 2010;51:1349–1356.
17. Wahl RL, Jacene H, Kasamon Y, Lodge MA. From RECIST to PERCIST: evolving considerations for PET response criteria in solid tumors. *J Nucl Med.* 2009;50(suppl 1):122S–150S.
18. Stabin MG, Sparks RB, Crowe E. OLINDA/EXM: the second-generation personal computer software for internal dose assessment in nuclear medicine. *J Nucl Med.* 2005;46:1023–1027.
19. Contal C, O'Quigley J. An application of changepoint methods in studying the effect of age on survival in breast cancer. *Computational Statistics & Data Analysis.* 1999;30:253–270.

20. Brabander T, van der Zwan WA, Teunissen JJM, et al. Long-term efficacy, survival, and safety of [^{177}Lu-DOTA^{0},Tyr^{3}]octreotate in patients with gastroenteropancreatic and bronchial neuroendocrine tumors. *Clin Cancer Res.* 2017;23:4617–4624.
21. Liberini V, Huellner MW, Grimaldi S, et al. The challenge of evaluating response to peptide receptor radionuclide therapy in gastroenteropancreatic neuroendocrine tumors: the present and the future. *Diagnostics (Basel).* 2020;10:1083.
22. Jahn U, Ilan E, Sandstrom M, Garske-Roman U, Lubberink M, Sundin A. ^{177}Lu-DOTATATE peptide receptor radionuclide therapy: dose response in small intestinal neuroendocrine tumors. *Neuroendocrinology.* 2020;110:662–670.
23. Garske-Román U, Sandstrom M, Fross Baron K, et al. Prospective observational study of ^{177}Lu-DOTA-octreotate therapy in 200 patients with advanced metastasized neuroendocrine tumours (NETs): feasibility and impact of a dosimetry-guided study protocol on outcome and toxicity. *Eur J Nucl Med Mol Imaging.* 2018;45:970–988.
24. Sundlöv A, Gleisner KS, Tennvall J, et al. Phase II trial demonstrates the efficacy and safety of individualized, dosimetry-based ^{177}Lu-DOTATATE treatment of NET patients. *Eur J Nucl Med Mol Imaging.* 2022;49:3830–3840.
25. Del Prete M, Buteau FA, Arsenault F, et al. Personalized ^{177}Lu-octreotate peptide receptor radionuclide therapy of neuroendocrine tumours: initial results from the P-PRRT trial. *Eur J Nucl Med Mol Imaging.* 2019;46:728–742.
26. Danieli R, Marin G, Mileva M, et al. Implementation of simplified protocol for tumour dosimetry in molecular radiotherapy with ^{177}Lu-DOTATATE [abstract]. *Eur J Nucl Med Mol Imaging.* 2022;49(suppl 1):S127.
27. Sundlöv A, Gustafsson J, Brolin G, et al. Feasibility of simplifying renal dosimetry in ^{177}Lu peptide receptor radionuclide therapy. *EJNMMI Phys.* 2018;5:12.
28. Chicheportiche A, Sason M, Godefroy J, et al. Simple model for estimation of absorbed dose by organs and tumors after PRRT from a single SPECT/CT study. *EJNMMI Phys.* 2021;8:63.
29. Pauwels E, Van Binnebeek S, Vandecaveye V, et al. Inflammation-based index and ^{68}Ga-DOTATOC PET–derived uptake and volumetric parameters predict outcome in neuroendocrine tumor patients treated with ^{90}Y-DOTATOC. *J Nucl Med.* 2020;61:1014–1020.
30. Beauregard JM, Hofman MS, Kong G, Hicks RJ. The tumour sink effect on the biodistribution of ^{68}Ga-DOTA-octreotate: implications for peptide receptor radionuclide therapy. *Eur J Nucl Med Mol Imaging.* 2012;39:50–56.
31. Galbán CJ, Hoff BA, Chenevert TL, Ross BD. Diffusion MRI in early cancer therapeutic response assessment. *NMR Biomed.* 2017;30:10.1002/nbm.3458.
32. Weber M, Kessler L, Schaarschmidt B, et al. Treatment-related changes in neuroendocrine tumors as assessed by textural features derived from ^{68}Ga-DOTATOC PET/MRI with simultaneous acquisition of apparent diffusion coefficient. *BMC Cancer.* 2020;20:326.
33. Thuillier P, Liberini V, Grimaldi S, et al. Prognostic value of whole-body PET volumetric parameters extracted from ^{68}Ga-DOTATOC PET/CT in well-differentiated neuroendocrine tumors. *J Nucl Med.* 2022;63:1014–1020.

Beyond Average: α-Particle Distribution and Dose Heterogeneity in Bone Metastatic Prostate Cancer

Nadia Benabdallah[1], Peng Lu[1,2], Diane S. Abou[1], Hanwen Zhang[1], David Ulmert[3,4], Robert F. Hobbs[5], Hiram A. Gay[6], Brian W. Simons[7], Muhammad A. Saeed[8], Buck E. Rogers[6], Abhinav K. Jha[1,2], Yuan-Chuan Tai[1], Christopher D. Malone[1], Joseph E. Ippolito[1], Jeff Michalski[6], Jack W. Jennings[1], Brian C. Baumann[6,9], Russell K. Pachynski[8], and Daniel L.J. Thorek[1,2,10]

[1]Mallinckrodt Institute of Radiology, Washington University in St. Louis School of Medicine, St. Louis, Missouri; [2]Department of Biomedical Engineering, Washington University in St. Louis, St. Louis, Missouri; [3]Department of Molecular and Medical Pharmacology, UCLA, Los Angeles, California; [4]Division of Oncology and Pathology, Department of Clinical Sciences, Lund University, Lund, Sweden; [5]Department of Radiation Oncology, Johns Hopkins University, Baltimore, Maryland; [6]Department of Radiation Oncology, Washington University in St. Louis School of Medicine, St. Louis, Missouri; [7]Center for Comparative Medicine, Baylor University, Houston, Texas; [8]Department of Medicine, Washington University in St. Louis School of Medicine, St. Louis, Missouri; [9]Department of Radiation Oncology, Springfield Clinic, Springfield, Illinois; and [10]Oncologic Imaging Program, Siteman Cancer Center, Washington University in St. Louis School of Medicine, St. Louis, Missouri

---

α-particle emitters are emerging as a potent modality for disseminated cancer therapy because of their high linear energy transfer and localized absorbed dose profile. Despite great interest and pharmaceutical development, there is scant information on the distribution of these agents at the scale of the α-particle pathlength. We sought to determine the distribution of clinically approved [^{223}Ra]RaCl$_2$ in bone metastatic castration-resistant prostate cancer at this resolution, for the first time to our knowledge, to inform activity distribution and dose at the near-cell scale. **Methods:** Biopsy specimens and blood were collected from 7 patients 24 h after administration. ^{223}Ra activity in each sample was recorded, and the microstructure of biopsy specimens was analyzed by micro-CT. Quantitative autoradiography and histopathology were segmented and registered with an automated procedure. Activity distributions by tissue compartment and dosimetry calculations based on the MIRD formalism were performed. **Results:** We revealed the activity distribution differences across and within patient samples at the macro- and microscopic scales. Microdistribution analysis confirmed localized high-activity regions in a background of low-activity tissue. We evaluated heterogeneous α-particle emission distribution concentrated at bone–tissue interfaces and calculated spatially nonuniform absorbed-dose profiles. **Conclusion:** Primary patient data of radiopharmaceutical therapy distribution at the small scale revealed that ^{223}Ra uptake is nonuniform. Dose estimates present both opportunities and challenges to enhance patient outcomes and are a first step toward personalized treatment approaches and improved understanding of α-particle radiopharmaceutical therapies.

Key Words: α-particle; dosimetry; ^{223}Ra; biopsy; autoradiography

J Nucl Med 2024; 65:245–251
DOI: 10.2967/jnumed.123.266571

Prostate cancer is the second most frequently diagnosed malignancy in men, and an estimated 30,000 men were projected to die of the disease in the United States in 2023 alone (*1,2*). Early treatment for localized disease can be curative; however, locally advanced and disseminated prostate cancer is incurable. Bone metastatic castration-resistant prostate cancer (bmCRPC) is a frequent form of late-stage disease that is challenging to manage. Recently approved adoptive cell therapy, taxanes, DNA repair, and novel androgen-receptor-axis inhibitors have limited effects on bone lesions, which are associated with decreased survival and difficult-to-palliate pain (*3*).

α-particle radiopharmaceutical therapy (α-RPT), delivering megaelectronvolt energies over only several cell diameters directly to sites of disease, has garnered intense academic and clinical interest (*4,5*). At the vanguard of this class of potent agents is ^{223}Ra-dichloride ([^{223}Ra]RaCl$_2$ citrate [Xofigo; Bayer]), the first and only approved α-RPT (*6*). Studies demonstrate improved overall survival, increased time to the first skeleton-related event, and reduced symptomatic pain (*7–12*). Although volumetric effects are limited, the ablative impact must be viewed in the context of the disease stage for which the drug has been approved and is comparable with other therapeutic modalities. Without an understanding of the local activity profile, we can only speculate that modest efficacy may be due to insufficient local dose.

Conventional external-beam radiotherapy produces uniform absorbed-dose fields. These contrast with radiopharmaceutical therapy, which can accumulate heterogeneously at any site. However, current methods assume unrealistic uniform activity distributions, often informed by noninvasive imaging. [^{223}Ra]RaCl$_2$ distribution studies have focused on organ-scale pharmacokinetics using scintigraphy and emerging SPECT methodologies that are incapable of resolving α-RPT distribution at a cellular resolution (*13–17*). It is at these dimensions that the doses are deposited, resulting in uneven distributions that are relevant for both tumor effects and marrow toxicity for this bone-seeking ion (*18,19*). Clinical trials involving [^{223}Ra]RaCl$_2$ have revealed that average absorbed-dose estimates to the red marrow do not accurately predict suppression (*20*).

Received Aug. 22, 2023; revision accepted Oct. 23, 2023.

For correspondence or reprints, contact Daniel L.J. Thorek (thorek.lab@wustl.edu).

It is imperative to develop advanced methodologies that enable optimization of individual patient treatment plans while concurrently strengthening the robustness of radiobiologic studies. Small-scale characterization is necessary to understand the clinical effects of these potent radioactive emissions in healthy and diseased tissues. This can be used to precisely assess dose (*21,22*) and to guide optimized use of these potent therapies (*23,24*). There is a dearth of data at this scale, with no primary data on the activity distribution of α-RPT clinically needed to improve small-scale models or inform personalized treatment approaches (*25–27*).

To define the distribution and absorbed doses at bmCRPC sites, we acquired multimodal imaging and high-resolution quantitative ^{223}Ra autoradiography of patient biopsy specimens. We observed heterogeneous distribution of the α-emitter, primarily localized at the bone–tissue interface within lesions, leading to spatially nonuniform absorbed-dose profiles. These data provide insight into the complex microstructure of pathologic bone metastases and variability in the magnitude and spatial distribution across patients and across lesions, providing a basis to measure effects of ^{223}Ra and other investigational α-RPT.

MATERIALS AND METHODS

Patients and Biopsy

Patients diagnosed with bmCRPC were treated with [^{223}Ra]RaCl$_2$ citrate at the standard activity of 55 kBq/kg. Written informed consent was obtained for all patients ($n = 7$) under Institutional Review Board protocol 201411115. Patients received pretreatment ^{99m}Tc-methyl diphosphonate bone scans, and candidate osseous lesions were identified. Blood samples were collected 24 h after therapy, followed by CT-guided percutaneous drill-assisted biopsy using the coaxial OnControl system (Teleflex Arrow).

Sample Preparation and Counting

Samples were weighed on a microbalance (XP204; Mettler Toledo) and subsequently fixed (4% paraformaldehyde and 30% sucrose, each for 24 h). Biopsy and blood (triplicate, 2 mL) samples were γ-counted using an open-window protocol for 10 min using a National Institute of Standards and Technology source–calibrated system (Wizard^2; Perkin Elmer) (*28*). Spectral acquisitions of biopsy specimens and pooled blood were conducted for 1 h on a high-purity germanium system (GEM-50195-S and Gamma-Vision version 8.0; Ametek). Samples were placed directly on the aluminum endcap, enclosed in a 10-cm lead shield (HPLBS1; Ametek). Finally, biopsy specimens were cryoembedded (optimal cutting temperature compound; Sakura Finetek) without decalcification, as per our previous radium-preserving protocols (*29,30*).

Micro-CT

Optimal cutting temperature compound–embedded biopsy specimens were scanned by high-resolution micro-CT (VivaCT40; Scanco). Samples were secured in a cylindric insert with dry ice and scanned at an isotropic voxel size of 12.5 μm (70 kVp, 114 μA) and analyzed in Amira (version 5.3.3; Thermo Scientific).

Microdistribution and Histology

Cryoembedded biopsy specimens were sectioned onto an adhesive support and affixed to 2.54 × 7.62 cm (1 × 3 in) glass slides (8 μm; CM1860; Leica), within 48 h of biopsy. Approximately 100 sections per biopsy specimen were exposed on storage phosphor for digital autoradiography (DAR; CyclonePlus; Perkin Elmer), coexposed with [^{223}Ra]RaCl$_2$ activity standards, read out at 600 dpi (approximately 40-μm resolution; OptiQuant version 5.0; PerkinElmer), and further processed in ImageJ (*31*). Subsequently, sections were stained with hematoxylin and eosin (H&E) and scanned with a ×10 objective (Eclipse Ti2; Nikon).

We built an image-processing pipeline to segment H&E acquisitions and register to DAR (Supplemental Fig. 1; supplemental materials are available at http://jnm.snmjournals.org). H&E images were converted to the International Commission on Illumination color space, and 4 statistical features (mean, SD, skewness, and kurtosis) were extracted from each channel from image subtiles (*30*). K-means clustering of features defined nonosseous tissues, and a deep convolutional neural network was trained from 20 manually defined sections to segment the bone surface. Coregistration was accomplished by downsampling H&E micrographs to DAR resolution, determining bounding boxes of each section, and performing an initial automated registration (including scaling, rotation, and translation), as described previously (*30*). A finer automated alignment was then conducted to maximize the mutual information between the images. We defined the bone–tissue interface as 50 μm within each compartment.

Small-Scale Dosimetry

Absorbed-dose distribution was assessed according to MIRD methodology using $D = \tilde{A} \times \Delta \times \phi/\text{mass}$, where $\tilde{A}$ is cumulated activity, Δ is mean α-energy, and ϕ is the absorbed fraction, with extrapolation to infinity, yielding a maximally conservative estimate (*32*). Activity in each voxel was calibrated using coimaged standards. Activity was decay-corrected to the time of biopsy. Finally, $\tilde{A}$ was calculated by assuming that ^{223}Ra and its daughters (^{219}Rn, ^{215}Po, and ^{211}Bi) were fixed in the bone (*18*), that all decays occurred within the same voxel, and that all α-energy is deposited locally ($\phi = 1$) with a voxel size of 43.2 × 43.2 × 8 μm. Energy values were sourced from International Commission on Radiological Protection publication 107 (*33*), yielding $\Delta = 4.23 \times 10^{-12}$ J/(Bq·s) for ^{223}Ra and its daughters. The density of bone was set to 1.92 g/cm^3 and that of soft tissue and the bone–tissue interface to 1.03 g/cm^3 (*34*).

Analyses and Statistics

Several figures of merit were selected from the accumulated activity distribution and dose information. For each section, activity per voxel per tissue compartment was determined. Representative DAR and fusion of the tissue compartment and dose-map images are reported in digital light units or voxel dose values (Gy), respectively. Interactive Data Language (version 8.7.2; Harris Geospatial Solutions, Inc.), MATLAB (version R2016B; MathWorks), and Prism (version 10; GraphPad) were used for computations and statistical analyses.

RESULTS

Macrodistribution

The present study involved 7 patients with bmCRPC treated with [^{223}Ra]RaCl$_2$. Men with a median age of 70 y (range, 66–78 y) and weight of 102 kg (range, 70–138 kg) underwent standard-of-care biopsy 24 h after α-RPT, with individual patient characteristics presented in Table 1. Prior bone scans were used to identify regions of active bone remodeling indicating a lesion, and both appendicular and axial skeletal sites were sampled (Fig. 1A).

Bone content at these pathologic sites varied, as seen in volume-rendered high-resolution micro-CT (Fig. 1B). These scans were used to measure the bone volume present in each biopsy specimen (Fig. 2A). Typically, the pathologic biopsy specimen dimensions were 2 mm in diameter by 7 mm in length. The cores were composed of a mixture of cancer cells, soft tissue, and bone compartments, reflected in the differences in bone volume and microbalance measures of total biopsy specimen mass (Figs. 2A and 2B). Bone volume and mass of biopsy specimen from patient 5 (0.07 mm^3 and 14.7 mg, respectively) and patient 7 (27.8 mm^3

TABLE 1
Patient and Biopsy Information

Pt.	Age (y)	Weight (kg)	Bx. at fraction	Activity injected (MBq)	Biopsy site	Number of cores
1	70	104	4	5.7	R ilium	2
2	70	117	2	6.5	L ilium	6
3	78	81	1	4.6	T12 vertebra	2
4	66	102	1	5.8	L5 vertebra	2
5	69	138	1	7.8	R humeral head	2
6	67	86	1	4.8	R ilium	2
7	73	70	2	3.9	L2 vertebra	1

Pt. = patient; Bx. = biopsy.

and 73.3 mg, respectively) represent the bounds of the bone-volume range sampled.

Activity in each biopsy specimen was assessed by γ-counting and verified by high-purity germanium (Supplemental Fig. 2). There is significant variability in the activity per sample at the subkilobecquerel level across patients and across samples (Fig. 2C). Biopsy specimen activities range from the limit of detection (0.0037 Bq) to 133 Bq. Blood samples were also collected before the biopsy. We observed circulating activity at 24 h of 5–13 Bq/mL and of 1–3 Bq/mL/MBq, when normalized to the administered activity (Fig. 2D). High-purity germanium γ-spectroscopy revealed that parent ^{223}Ra was detected at or near secular equilibrium (measured <4 h after venipuncture; Supplemental Fig. 3).

A weak Pearson correlation coefficient between biopsy specimen activity and bone volume can be distinguished, despite the sublesion sampling ($n = 12$, Fig. 2E). By contrast, no clear correlation between the biopsy specimen and blood activity levels was discerned (Fig. 2F). Across samples, activity concentrations ranged from 0 to 27.1 Bq/mm^3, with a median value of 1.7 Bq/mm^3. Data for each biopsy specimen are included in Supplemental Figure 4, along with the bone biopsy specimen activity normalized to administered activity, which averages nearly 0.6 Bq/mm^3/MBq. The individual blood concentration values (nonnormalized) are included for completeness (Supplemental Fig. 4C).

Microdistribution

We next sought to determine the activity distribution within each biopsy specimen using an undecalcified sectioning technique and DAR (*29,30*). Approximately 100 sections were acquired for each sample along with a quantitation standard (DAR of first 42 sections of patient 3, biopsy 2 as an example dataset; Supplemental Fig. 5). Representative DAR and H&E micrographs are shown in Figure 3. H&E was used to define 3 compartments for bone, soft tissue (including marrow and prostate cancer), and the bone–tissue interface. Using a manually defined training set, we used an automated delineation of bone and soft-tissue compartments to segment the histologic data and coregister with the spatial distribution of radioactivity (Supplemental Fig. 1). The bone–tissue interface compartment was established as the boundary between the bone and the soft tissue and masks, and coregistered images are shown in Figure 3.

Fused high-resolution imaging reveals several features of the activity distribution near the cell scale. There is focused uptake of ^{223}Ra along the bone–tissue interface, with nonuniform labeling displaying areas of both hot regions and no activity (Fig. 3). Intensity of the uptake decreases with distance from the bone–tissue interface. An extremely low signal was measured in the sections from the biopsy specimen of patient 5. Indeed, the biopsy specimen contains minimal calcified material (Fig. 1B; Fig. 2) and insignificant activity (Supplemental Fig. 6).

To assess patterns of distribution, we determined the spatial activity profiles for each defined region across all evaluated biopsy sections. A representative compartmentalization of the whole section and segmented compartments is included (Fig. 4A), along with activity histograms for each (Fig. 4B). These data were normalized as volume per 8-μm section in tranches of first or second SD from the mean activity to evaluate heterogeneity of the ^{223}Ra distribution (Fig. 4C). Bone and the bone–tissue interface are the regions that are distinguished as being above the mean. Soft-tissue regions consistently have the lowest activity profile and lack hot spots. Across the sections from a biopsy specimen, separated by hundreds of micrometers in depth, there is a clustering of the activity distribution profile; however, variability in these sample-normalized quantifications remains large.

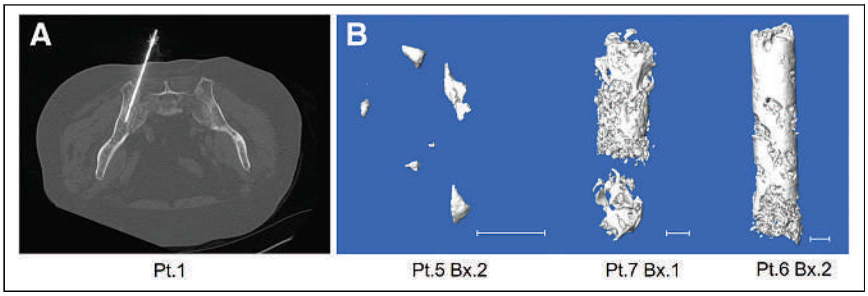

FIGURE 1. (A) Axial slice at collection from CT-guided biopsy of representative patient. Sample collection and biopsy needle location are shown entering ilium. (B) Micro-CT of biopsy (Bx.) 2 of patient (Pt.) 5, Bx. 1 of Pt. 7, and Bx. 2 of Pt. 6 (from left to right). Scale bar is 1 mm.

Small-Scale Dosimetry

We next undertook novel measures of the absorbed dose at the small scale from these patient samples. Calibrated activity per voxel values from the sampled tissues

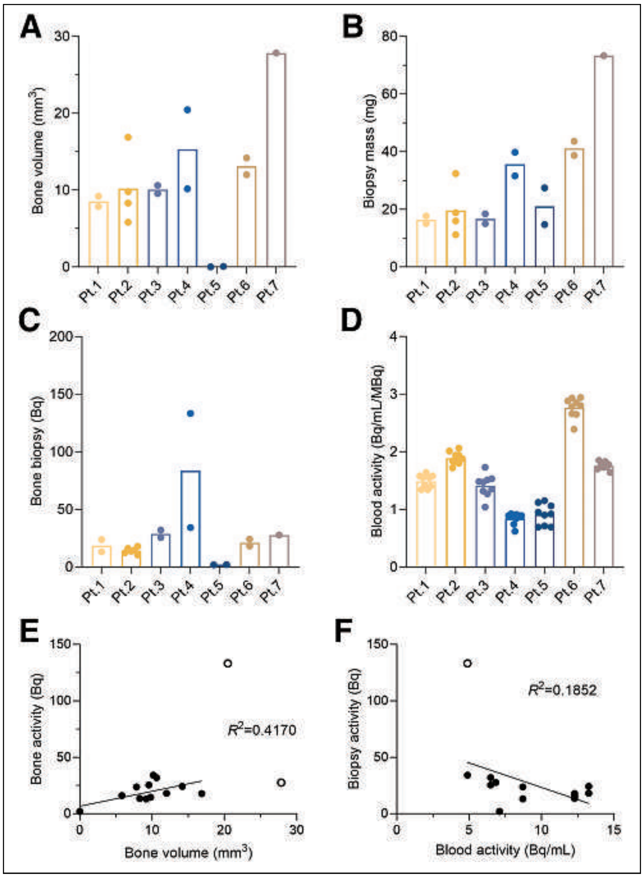

FIGURE 2. (A and B) Bone volume from micro-CT scan (A) and mass of each biopsy specimen (B). Mass of biopsy specimens from patients 1 and 2 was estimated using bone and tissue volumes measured from micro-CT. (C) Activity of ^{223}Ra in biopsy specimens for each patient. (D) Concentration of ^{223}Ra in blood samples for each patient's normalized to administered activity. (E and F) Correlation of biopsy activity and bone volume (E) and blood activity (F). Open circles in E and F are outliers removed from correlation. Pt. = patient.

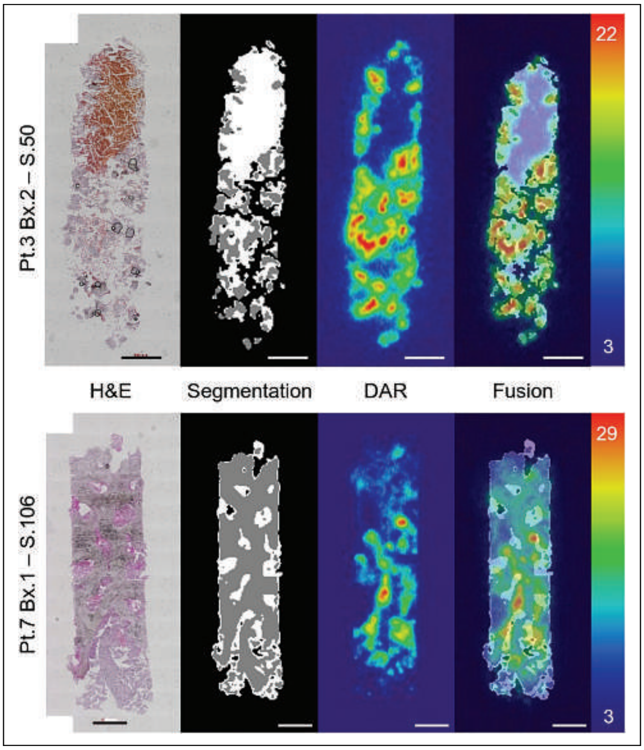

FIGURE 3. Representative workflow of 1 section from patient (Pt.) 3 (top) and Pt. 7 (bottom). From left to right, H&E acquisition; segmented compartments of soft tissue (white), bone (gray), and background (black); registered DAR; and fused result with autoradiography of sections matching. Scale is in digital light units × 10^4. Training, segmentation, and autoregistration workflow schema are explained in Supplemental Figure 1. Bx. = biopsy; S. = section.

at 24 h was used with the assumption that ^{223}Ra localized to the bone and daughters decayed in place (*18,29*). We report mean and maximum absorbed-dose values for representative sections across patient biopsy specimens for whole samples and compartmentalized regions of bone, soft tissue, and the bone–tissue interface (Figs. 5A and 5B).

The highest absorbed dose values correlate with regions of greatest ^{223}Ra localization, namely the bone–tissue interface. Values varied across patient samples in a range from 20.1 ± 3.2 to 1.9 ± 0.1 Gy at this surface (Supplemental Table 1). Modest differences between the mean absorbed doses measured in the bone–tissue interface were observed across sections of the same biopsy specimen, suggesting consistency within a bone metastatic core sample. Predictably, maximum absorbed-dose values have a greater range from 38.3 ± 4.8 to 7.5 ± 1.5 Gy at the surface (Supplemental Table 2). Most maximum dose voxels were found within this bone–tissue interface compartment, and thus maximum values of the whole section and bone surface values are concordant.

DISCUSSION

The general approach of using mean activity concentrations to compute cumulated activity of a radiopharmaceutical as input for dosimetry calculations does not reflect the reality of highly localized distribution. Although adequate for γ-emitters in many contexts, these are insufficient to capture absorbed-dose profiles from spatially circumscribed interactions of α- and β-particle emitters at tens of micrometers and millimeters, respectively. The nonuniform cellular distribution of target cells and of ^{223}Ra uptake and irradiation complicates the interpretation of the macroscopically averaged absorbed dose in terms of the biologic effect, and similarly, there are as yet no definitive evidence-based values for the relative biological effects of this therapy. [^{223}Ra]RaCl$_2$-treated biopsy specimens collected and analyzed here provide novel insight into α-RPT in metastases and to existing data of β-particle distribution in renal tissues and hepatocellular carcinoma (*21,22,35*).

Prior preclinical work has shown foci of ^{223}Ra at sites of active bone turnover (*29,36*). Most ^{223}Ra was localized to the bone–tissue interface in these clinical specimens, confirming this pattern of uptake at pathologic sites and underlining the role of lesional bone structure in activity distribution. Bulk measures of activity per mass of core, an accurate assessment of activity concentration, do not reflect the complexity of the activity or dose-distribution profiles. Mean absorbed-dose estimates vary from more than 20 Gy to (ostensibly) 0 Gy across bone surfaces of the samples (Fig. 5). With the caveat that we have sampled lesions rather than marrow sites specifically, this variability in primary data helps to substantiate the good safety profile with mild reversible myelosuppression despite model-based study estimates of endosteal cell and marrow mean doses of 16 and 1.5 Gy, respectively (*18,37*). This is, in turn, consistent with

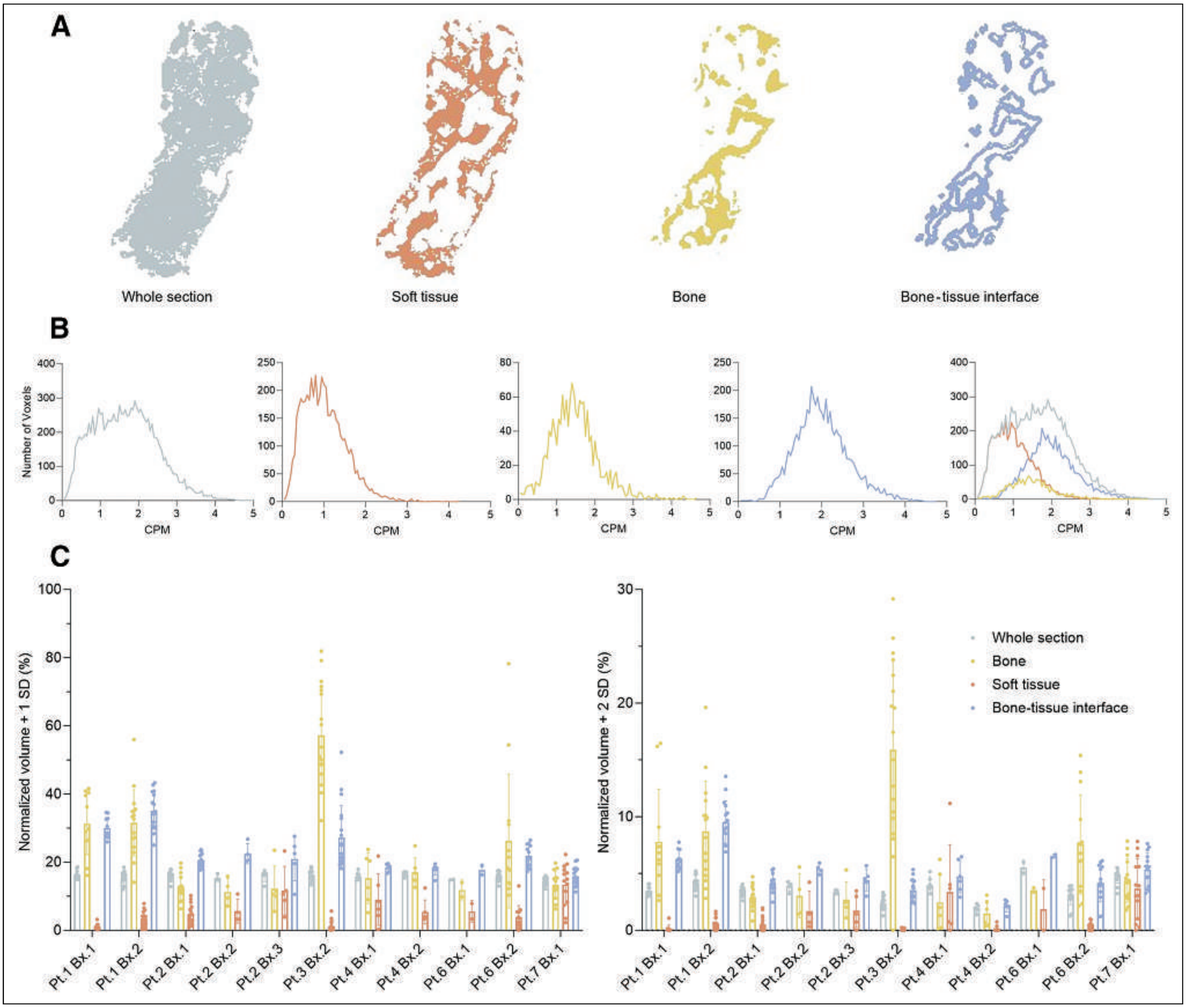

FIGURE 4. (A) Representative compartments for analysis, using section 77 of patient (Pt.) 1, biopsy (Bx.) 1, for soft tissue, bone, and bone–tissue interface. (B) Histogram of CPM measured in each compartment for same section. (C) Volume of each compartment over mean + 1 or 2 SDs for each patient biopsy. CPM = counts per minute; STD = SD.

and confirms predictions from small-scale marrow modeling (*25*). Indeed, the results of this study can be implemented in bone-marrow models (*2,3*). Furthermore, dosimetry estimates based on patient-specific data could guide the optimal administered activity and personalization of [^{223}Ra]RaCl$_2$ therapy.

Absorbed-dose values in high-activity regions would be sufficient to ablate most metastatic and supporting cell types for many of the samples, considering the relative damage done by high linear energy transfer radiation. The computed values are for a single administration of [^{223}Ra]RaCl$_2$ (approved for use in 4 cycles separated by 6 wk). The information from the activity distribution and structural data suggests that for some metastases, a reduced number of treatments may be sufficient to control disease sites and that a subset of metastases will not benefit from either increased administered activities or increased cycles.

Histomorphometry is a core methodology for structure–function analyses in orthopedics; however, abnormal and diseased bone sites are rarely evaluated at this resolution. This is an interesting yet understudied area for which these samples provide additional value. The novel structural (micro-CT and H&E) and activity distribution (DAR) data collected here can further be used to inform small-scale dosimetry, essential to improving our understanding of anticancer and normal-tissue effects (*38,39*).

Nuclear and anatomic imaging localized sites for CT-guided sampling. The low bone content and absence of detectable activity in patient 5 at both macro- and microscopic scales do not imply a low-quality biopsy but rather underline the tissue complexity found at sites of bmCRPC. Biopsy provides a subsample of the lesion, which may reflect only the tissue directly collected and not the greater lesion, let alone the total patient burden. Further, anatomic location, structural features, and prior therapy to bmCRPC sites may influence local uptake and global response (*40*), directions of future research. Advances in high-resolution imaging, Monte Carlo dose modeling, and measures of biologic impact can

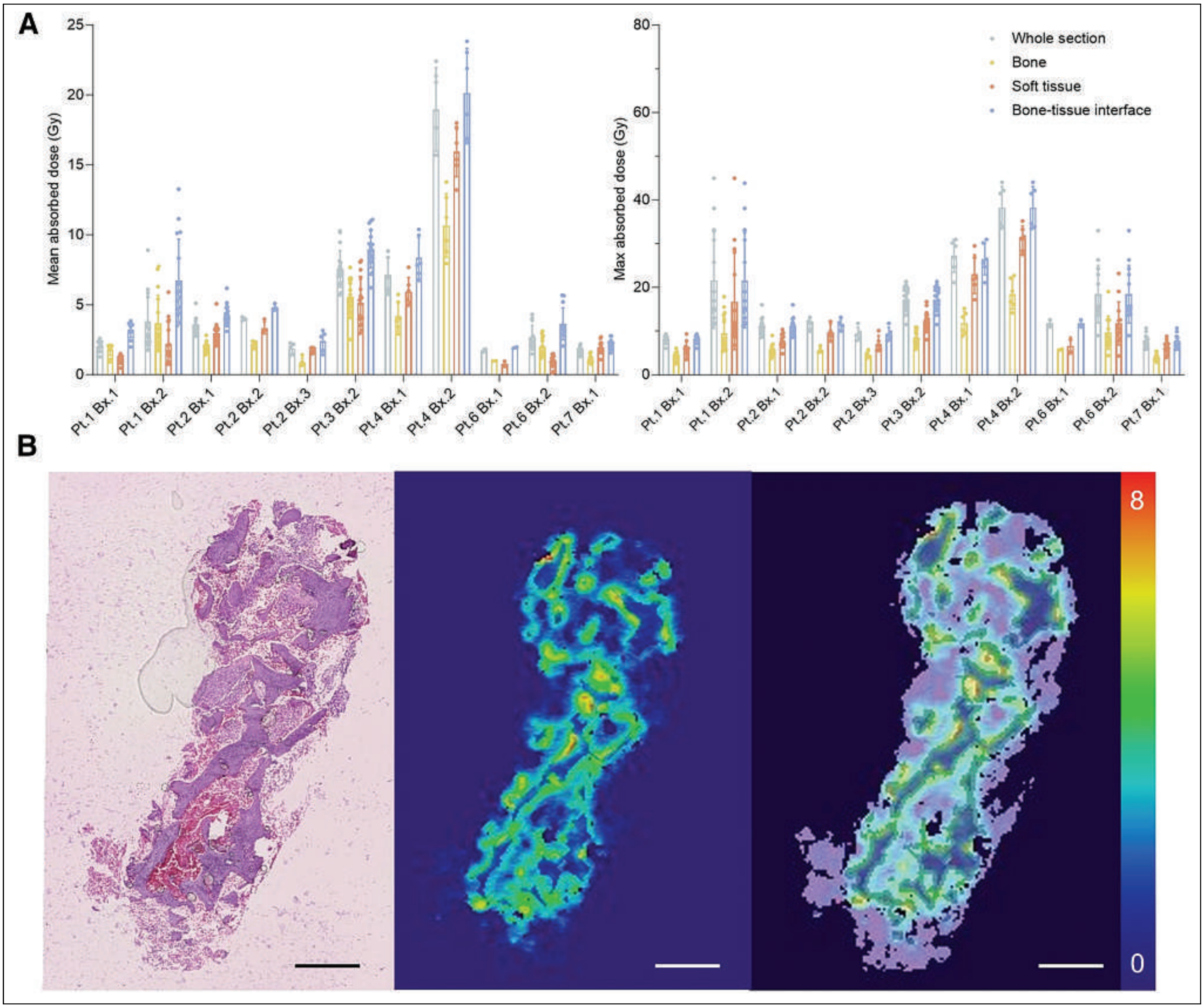

FIGURE 5. (A) Mean and maximum absorbed dose to compartment from direct measures of ^{223}Ra distribution by patient and biopsy section ($n \geq 8$) at left and right, respectively. (B) Representative biopsy specimen from patient 1 including H&E staining, computed absorbed dose distribution, and fused dose to compartment model segmentation. Scale is in Gy. Pt. = patient; Bx. = biopsy.

also be used to guide optimal use of α-RPT with the presented data (*25,30,41*).

We have demonstrated high-resolution α-distribution in affected tissues at the length scale of the interactions within clinical samples. Our studies confirm highly localized uptake of ^{223}Ra across samples from multiple skeletal sites of metastasis, with a low-activity background in adjacent soft tissue. Although onerous, direct assessment distribution can be implemented to estimate the dose within days after sampling, and implementation of such data for treatment decision-making may be feasible in the future. Limitations of this study include cohort size and the fundamental limitation that a site can only be biopsied once. We also assumed that ^{223}Ra and its daughters are fixed from the 24-h time-point measurement and have assumed disintegrations and α-particle deposition occur within single voxels. To further our understanding of cellular-scale effects of clinical α-RPT, samples from a wider cohort are being assembled, with rapid processing to determine the potential for local diffusion of daughters and with cell-scale multiomics to link the dose with tumor and marrow responses.

CONCLUSION

We addressed the lack of primary information of α-RPT activity distribution at the scale of its effect via high-throughput evaluation of bone-lesion specimens. These results provide the first patient sample small-scale values for ^{223}Ra. Highly nonuniform distribution and absorbed dose present opportunities and challenges to improved outcomes for patients receiving α-RPT. Further, these data serve as a benchmark for comparison with other bone-lesion–targeted and molecular radiotherapies.

DISCLOSURE

This work was supported by NCI R01CA201035, R01CA229893, and R01CA240711 (to Daniel Thorek) and R01EB031962 (to Abhinav Jha). The Siteman Cancer Center is funded by NCI Cancer

Center Support Grant P30CA091842. We thank the Washington University Musculoskeletal Research Center (P30AR074992) for micro-CT expertise. No other potential conflict of interest relevant to this article was reported.

KEY POINTS

QUESTION: Can we improve our understanding and application of α-particle emitter therapies by learning small-scale distribution and absorbed dose from patient samples?

PERTINENT FINDINGS: In a cohort of 7 patients with bmCRPC treated with [^{223}Ra]RaCl$_2$ citrate, we evaluated the distribution of ^{223}Ra in primary bone biopsy specimens. Autoradiography and histology were analyzed to reveal predominant localization at the bone–tissue interface in clinical specimens. Computed mean absorbed-dose estimates ranged from more than 20 Gy to 0 Gy, displaying distribution differences across and within patient samples.

IMPLICATIONS FOR PATIENT CARE: This study highlights that macroscopic measurements inadequately capture the intricacies of lesion-scale activity distribution, establishing a foundation for enhancing treatment response through the development of more realistic dosimetry models.

REFERENCES

1. Siegel RL, Miller KD, Wagle NS, Jemal A. Cancer statistics, 2023. *CA Cancer J Clin.* 2023;73:17–48.
2. Ferlay J, Colombet M, Soerjomataram I, et al. Cancer statistics for the year 2020: an overview. *Int J Cancer.* 2021;149:778–789.
3. Teo MY, Rathkopf DE, Kantoff P. Treatment of advanced prostate cancer. *Annu Rev Med.* 2019;70:479–499.
4. Baidoo KE, Yong K, Brechbiel MW. Molecular pathways: targeted α-particle radiation therapy. *Clin Cancer Res.* 2013;19:530–537.
5. Bruland ØS, Larsen RH, Baum RP, Juzeniene A. Editorial: targeted alpha particle therapy in oncology. *Front Med (Lausanne).* 2023;10:1165747.
6. Kluetz PG, Pierce W, Maher VE, et al. Radium Ra 223 dichloride injection: U.S. Food and Drug Administration drug approval summary. *Clin Cancer Res.* 2014;20:9–14.
7. Nilsson S, Larsen RH, Fossa SD, et al. First clinical experience with alpha-emitting radium-223 in the treatment of skeletal metastases. *Clin Cancer Res.* 2005;11:4451–4459.
8. Parker C, Nilsson S, Heinrich D, et al. Alpha emitter radium-223 and survival in metastatic prostate cancer. *N Engl J Med.* 2013;369:213–223.
9. Parker CC, Coleman RE, Sartor O, et al. Three-year safety of radium-223 dichloride in patients with castration-resistant prostate cancer and symptomatic bone metastases from phase 3 randomized Alpharadin in Symptomatic Prostate Cancer trial. *Eur Urol.* 2018;73:427–435.
10. Sartor O, Coleman R, Nilsson S, et al. Effect of radium-223 dichloride on symptomatic skeletal events in patients with castration-resistant prostate cancer and bone metastases: results from a phase 3, double-blind, randomised trial. *Lancet Oncol.* 2014;15:738–746.
11. Hoskin P, Sartor O, O'Sullivan JM, et al. Efficacy and safety of radium-223 dichloride in patients with castration-resistant prostate cancer and symptomatic bone metastases, with or without previous docetaxel use: a prespecified subgroup analysis from the randomised, double-blind, phase 3 ALSYMPCA trial. *Lancet Oncol.* 2014;15:1397–1406.
12. Higano CS, George DJ, Shore ND, et al. Clinical outcomes and treatment patterns in REASSURE: planned interim analysis of a real-world observational study of radium-223 in metastatic castration-resistant prostate cancer. *EClinicalMedicine.* 2023;60:101993.
13. Chittenden SJ, Hindorf C, Parker CC, et al. A phase 1, open-label study of the biodistribution, pharmacokinetics, and dosimetry of ^{223}Ra-dichloride in patients with hormone-refractory prostate cancer and skeletal metastases. *J Nucl Med.* 2015;56:1304–1309.
14. Carrasquillo JA, O'Donoghue JA, Pandit-Taskar N, et al. Phase I pharmacokinetic (PK) and biodistribution study of radium-223 chloride in patients with castration resistant prostate cancer (CRPC) metastatic to bone. *J Clin Orthod.* 2010;28(suppl):4680.
15. Li Z, Benabdallah N, Abou DS, et al. A projection-domain low-count quantitative SPECT method for α-particle-emitting radiopharmaceutical therapy. *IEEE Trans Radiat Plasma Med Sci.* 2023;7:62–74.
16. Owaki Y, Nakahara T, Kosaka T, et al. Ra-223 SPECT for semi-quantitative analysis in comparison with Tc-99m HMDP SPECT: phantom study and initial clinical experience. *EJNMMI Res.* 2017;7:81.
17. Gustafsson J, Rodeño E, Mínguez P. Feasibility and limitations of quantitative SPECT for ^{223}Ra. *Phys Med Biol.* 2020;65:085012.
18. Lassmann M, Nosske D. Dosimetry of ^{223}Ra-chloride: dose to normal organs and tissues. *Eur J Nucl Med Mol Imaging.* 2013;40:207–212.
19. Woliner-van der Weg W, Schoffelen R, Hobbs RF, et al. Tumor and red bone marrow dosimetry: comparison of methods for prospective treatment planning in pretargeted radioimmunotherapy. *EJNMMI Phys.* 2015;2:5.
20. Sciuto R, Rea S, Ungania S, et al. The role of dosimetry and biological effects in metastatic castration-resistant prostate cancer (mCRPC) patients treated with ^{223}Ra: first in human study. *J Exp Clin Cancer Res.* 2021;40:281.
21. De Jong M, Valkema R, Van Gameren A, et al. Inhomogeneous localization of radioactivity in the human kidney after injection of [^{111}In-DTPA]octreotide. *J Nucl Med.* 2004;45:1168–1171.
22. Konijnenberg M, Melis M, Valkema R, Krenning E, de Jong M. Radiation dose distribution in human kidneys by octreotides in peptide receptor radionuclide therapy. *J Nucl Med.* 2007;48:134–142.
23. Sgouros G, Bolch WE, Chiti A, et al. ICRU REPORT 96, dosimetry-guided radiopharmaceutical therapy. *J ICRU.* 2021;21:1–212.
24. Tronchin S, Forster JC, Hickson K, Bezak E. Dosimetry in targeted alpha therapy. A systematic review: current findings and what is needed. *Phys Med Biol.* 2022;67:9.
25. Hobbs RF, Song H, Watchman CJ, et al. A bone marrow toxicity model for ^{223}Ra alpha-emitter radiopharmaceutical therapy. *Phys Med Biol.* 2012;57:3207–3222.
26. Tranel J, Feng FY, James SS, Hope TA. Effect of microdistribution of alpha and beta-emitters in targeted radionuclide therapies on delivered absorbed dose in a GATE model of bone marrow. *Phys Med Biol.* 2021;66:035016.
27. Strigari L, Konijnenberg M, Chiesa C, et al. The evidence base for the use of internal dosimetry in the clinical practice of molecular radiotherapy. *Eur J Nucl Med Mol Imaging.* 2014;41:1976–1988.
28. Hasson A, Jiang W, Benabdallah N, et al. Radiochemical quality control methods for radium-223 and thorium-227 radiotherapies. *Cancer Biother Radiopharm.* 2023;38:15–25.
29. Abou DS, Ulmert D, Doucet M, Hobbs RF, Riddle RC, Thorek DLJ. Whole-body and microenvironmental localization of radium-223 in naive and mouse models of prostate cancer metastasis. *J Natl Cancer Inst.* 2016;108:djv380.
30. Peng L, Nadia B, Wen J, et al. Blind image restoration enhances digital autoradiographic imaging of radiopharmaceutical tissue distribution. *J Nucl Med.* 2022;63:591–597.
31. Schneider CA, Rasband WS, Eliceiri KW. NIH Image to ImageJ: 25 years of image analysis. *Nat Methods.* 2012;9:671–675.
32. Sgouros G, Roeske JC, McDevitt MR, et al. MIRD pamphlet no. 22 (abridged): radiobiology and dosimetry of α-particle emitters for targeted radionuclide therapy. *J Nucl Med.* 2010;51:311–328.
33. Eckerman K, Endo A. ICRP publication 107: nuclear decay data for dosimetric calculations. *Ann ICRP.* 2008;38:5–265.
34. Valentin J. Basic anatomical and physiological data for use in radiological protection: reference values: ICRP Publication 89. *Ann ICRP.* 2002;32:1–277.
35. Hemmingsson J, Högberg J, Mölne J, et al. Autoradiography and biopsy measurements of a resected hepatocellular carcinoma treated with 90 yttrium radioembolization demonstrate large absorbed dose heterogeneities. *Adv Radiat Oncol.* 2018;3:439–446.
36. Abou DS, Fears A, Summer L, et al. Improved ^{223}Ra therapy with combination epithelial sodium channel blockade. *J Nucl Med.* 2021;62:1751–1758.
37. ICRP. Age-dependent doses to members of the public from intake of radionuclides: part 2 ingestion dose coefficients (ICRP publication 67). *Ann ICRP.* 1992;23:1–167.
38. Hobbs RF, Baechler S, Fu DX, et al. A model of cellular dosimetry for macroscopic tumors in radiopharmaceutical therapy. *Med Phys.* 2011;38:2892–2903.
39. Humphreys ER, Humm JL. A Monte-Carlo approach to the microdosimetry of ^{224}Ra in murine compact and cancellous bone. *Health Phys.* 1988;54:607–615.
40. Armstrong AJ, Gupta S, Healy P, et al. Pharmacodynamic study of radium-223 in men with bone metastatic castration resistant prostate cancer. *PLoS One.* 2019;14:e0216934.
41. Miller BW, Bowen JM, Morrison EC. High-resolution, single-particle digital autoradiography of actinide sources using microcapillary array collimators and the iQID camera. *Appl Radiat Isot.* 2020;166:109348.

Fibroblast Activation Protein α–Directed Imaging and Therapy of Solitary Fibrous Tumor

Rainer Hamacher[1,2], Kim M. Pabst[2,3], Phyllis F. Cheung[4,5], Christoph E. Heilig[6,7], Jennifer Hüllein[8], Sven-Thorsten Liffers[4,5], Sabrina Borchert[2,9], Pedro Fragoso Costa[2,3], Benedikt M. Schaarschmidt[2,10], Lukas Kessler[2,3], Monika A. Miera[1,4], Margret Droste[4,5], Merve Akbulut[1], Johanna Falkenhorst[1,2], Fadi Zarrad[2,3], Karina Kostbade[1,2], Ilektra A. Mavroeidi[1,2], Hanno Glimm[11–16], Lale Umutlu[2,10], Martin Schuler[1,2], Daniel Hübschmann[7,8,17], Sebastian Bauer[1,2], Stefan Fröhling[6,7], Ken Herrmann[2,3], Jens T. Siveke[1,2,4,5], Hans-Ulrich Schildhaus*[2,9], and Wolfgang P. Fendler*[2,3]

[1]Department of Medical Oncology, West German Cancer Center, University Hospital Essen, Essen, Germany; [2]German Cancer Consortium, Partner site University Hospital Essen, Essen, Germany; [3]Department of Nuclear Medicine, West German Cancer Center, University Hospital Essen, Essen, Germany; [4]Bridge Institute of Experimental Tumor Therapy, West German Cancer Center, University Hospital Essen, Essen, Germany; [5]Division of Solid Tumor Translational Oncology, German Cancer Consortium (Partner Site Essen) and German Cancer Research Center, Heidelberg, Germany; [6]Department of Translational Medical Oncology, National Center for Tumor Diseases, Heidelberg and German Cancer Research Center, Heidelberg, Germany; [7]German Cancer Consortium, Core Center Heidelberg, Heidelberg, Germany; [8]Computational Oncology, Molecular Precision Oncology Program, German Cancer Research Center and National Center for Tumor Diseases, Heidelberg, Germany; [9]Institute of Pathology, West German Cancer Center, University Hospital Essen, Essen, Germany; [10]Department of Diagnostic and Interventional Radiology and Neuroradiology, West German Cancer Center, University Hospital Essen, Essen, Germany; [11]Department for Translational Medical Oncology, National Center for Tumor Diseases (NCT/UCC), Dresden, Germany; [12]German Cancer Research Center, Heidelberg, Germany; [13]Faculty of Medicine and University Hospital Carl Gustav Carus, Technische Universität Dresden, Dresden, Germany; [14]Helmholtz-Zentrum Dresden–Rossendorf, Dresden, Germany; [15]Translational Medical Oncology, Faculty of Medicine and University Hospital Carl Gustav Carus, Technische Universität Dresden, Dresden, Germany; [16]German Cancer Consortium, Dresden, Germany; and [17]Heidelberg Institute for Stem Cell Technology and Experimental Medicine, Heidelberg, Germany

---

Fibroblast activation protein α (FAPα) is expressed at high levels in several types of tumors. Here, we report the expression pattern of FAPα in solitary fibrous tumor (SFT) and its potential use as a radiotheranostic target. **Methods:** We analyzed FAPα messenger RNA and protein expression in biopsy samples from SFT patients using immunohistochemistry and multiplexed immunofluorescence. Tracer uptake and detection efficacy were assessed in patients undergoing clinical ^{68}Ga-FAPα inhibitor (FAPI)–46 PET, ^{18}F-FDG PET, and contrast-enhanced CT. ^{90}Y-FAPI-46 radioligand therapy was offered to eligible patients with progressive SFT. **Results:** Among 813 patients and 126 tumor entities analyzed from the prospective observational MASTER program of the German Cancer Consortium, SFT (n = 34) had the highest median FAPα messenger RNA expression. Protein expression was confirmed in tumor biopsies from 29 of 38 SFT patients (76%) in an independent cohort. Most cases showed intermediate to high FAPα expression by immunohistochemistry (24/38 samples, 63%), which was located primarily on the tumor cell surface. Nineteen patients who underwent ^{68}Ga-FAPI-46 PET imaging demonstrated significantly increased tumor uptake, with an SUV_{max} of 13.2 (interquartile range [IQR], 10.2), and an improved mean detection efficacy of 94.5% (SEM, 4.2%), as compared with ^{18}F-FDG PET (SUV_{max}, 3.2 [IQR, 3.1]; detection efficacy, 77.3% [SEM, 5.5%]). Eleven patients received a total of 34 cycles (median, 3 cycles [IQR, 2 cycles]) of ^{90}Y-FAPI-46 radioligand therapy, which resulted in disease control in 9 patients (82%). Median progression-free survival was 227 d (IQR, 220 d). **Conclusion:** FAPα is highly expressed by SFT and may serve as a target for imaging and therapy. Further studies are warranted to define the role of FAPα-directed theranostics in the care of SFT patients.

Key Words: FAPI; radioligand; sarcoma; SFT; theranostic

J Nucl Med 2024; 65:252–257
DOI: 10.2967/jnumed.123.266411

Theranostics is an emerging approach in precision oncology using tumor-specific targets for diagnosis and treatment (*1*). A novel pan-tumor target is fibroblast activation protein α (FAPα), which is expressed in activated fibroblasts during stromal remodeling and in cancer-associated fibroblasts in most epithelial tumors but is absent in normal adult tissues (*2*). With a recently developed series of quinolone-based FAPα inhibitors (FAPIs), FAPα is a promising target for theranostic approaches in various tumor entities (*3*).

We recently demonstrated the safety and efficacy of ^{90}Y-FAPI-46 radioligand therapy (RLT) in a cohort of 21 patients with advanced sarcoma and other cancer entities. Here, most subentities were attributable to sarcomas, particularly solitary fibrous tumor (SFT) (*4*). It was reported that sarcoma cancer cells themselves often aberrantly express high levels of FAPα (*5–7*) and that PET revealed high sarcoma uptake of the ligand ^{68}Ga-FAPI (*3,8–10*). Indeed, the tumoral uptake intensity on ^{68}Ga-FAPI-46 PET correlates with histopathologic FAPα expression in biopsy and surgical specimens (*9*).

Received Jul. 24, 2023; revision accepted Nov. 7, 2023.

For correspondence or reprints, contact Rainer Hamacher (rainer.hamacher@uk-essen.de).

*Contributed equally to this work.

SFT is a rare spindle cell tumor of mesenchymal origin with an incidence of about 3.5 per million each year (*11*). Although SFTs typically demonstrate benign behavior, with a 5-y disease-specific survival rate of 93%, high-risk groups present a considerable risk of recurrence and metastasis, with a 5-y survival rate of 60% (*12*). In advanced disease, the outcome is less satisfactory; there are no prospective data on the efficacy of chemotherapy for SFTs, and variable median progression-free survival (PFS) is reported to be between 3 and 11 mo (*13*). Retrospective case series and prospective phase II data on vascular endothelial growth factor receptor–targeted therapies using tyrosine kinase inhibitors, particularly pazopanib or sunitinib, or the combination of temozolomide and bevacizumab, found a median PFS of around 5–10 mo (*13*).

Therefore, better diagnosis and efficacious treatment are urgently needed. On the basis of our previous findings (*4*), here we systematically explore FAPα as a theranostic target in SFT.

MATERIALS AND METHODS

Study Design and Patient Cohorts

Details on ethics approval and consent to participate are reported in the supplemental methods (supplemental materials are available at http://jnm.snmjournals.org) (*14–16*). In 3 independent cohorts, with a minor overlap of patients, we were addressing ex vivo FAPα expression in tumor tissue, in vivo tumor uptake of the FAPα-targeting radioligand ^{68}Ga-FAPI-46 on PET/CT, and efficacy of FAPα-targeting RLT using ^{90}Y-FAPI-46 (Fig. 1). We assessed messenger RNA (mRNA) data from the National Center for Tumor Diseases/German Cancer Research Center/German Cancer Consortium Molecularly Aided Stratification for Tumor Eradication Research (MASTER) program of the National Center for Tumor Diseases, Heidelberg, Germany, a prospective, continuously recruiting, multicenter observational study for biology-driven stratification of adults with advanced cancer across various histologies (*14*). The cohort of 813 patients (the MASTER cohort) consists of 779 non-SFT and 15 SFT cases that were published previously (*17*). In addition, 19 other SFT cases, which had been analyzed until October 2021, were included and analyzed in the same way.

We analyzed FAPα expression with immunohistochemical staining in archived formalin-fixed, paraffin-embedded blocks of tumor tissue from an independent cohort of 38 SFT patients (the tissue cohort; Supplemental Table 1) treated at the West German Cancer Center of the University Hospital Essen, Germany. Moreover, we performed multiplexed immunofluorescence (mIF).

In 19 patients who underwent clinical ^{68}Ga-FAPI-46 and ^{18}F-FDG PET as well as contrast-enhanced CT (the theranostic cohort; Supplemental Table 2), we assessed imaging findings. Examinations took place during participation in a prospective observational trial at University Hospital Essen (NCT04571086) (*8,9*). Within the theranostic cohort, 11 of 19 patients (58%) received ^{90}Y-FAPI-46 RLT on a compassionate-use basis. The patient flow diagram is shown in Figure 1C. Data on 9 of 11 patients have been shown previously in a report on our study on safety and efficacy in patients with advanced sarcoma and other cancer entities (*4*). Here, we performed a subgroup analysis and follow-up of these patients and present data on 2 additional patients.

Quantification of Gene Expression

Expression levels were determined per gene and sample as transcripts per million mapped reads. Extraction of RNA, RNA sequencing, and data processing were described previously (*17*). The difference in transcripts per million mapped reads in SFT versus non-SFT cases was evaluated using a Student *t* test.

Sequential mIF and Computer-Aided Quantification

mIF was performed using the Opal multiplex system (Akoya Biosciences) according to the manufacturer's instructions. Details on the multiplexed staining conditions are reported in the supplemental methods.

Imaging

Clinical PET/CT scans with ^{18}F-FDG and ^{68}Ga-FAPI-46 as well as contrast-enhanced CT were performed in the craniocaudal orientation on a Biograph mCT or Biograph mCT Vision (Siemens Healthineers) as previously described (*9*). Details of the radiosynthesis are presented in the supplemental methods. The mean (±SD) injected activities were 244 ± 77 MBq for ^{18}F-FDG and 116 ± 35 MBq for ^{68}Ga-FAPI-46.

Detection Efficacy

Detection efficacy was assessed by an independent lesion-based evaluation of ^{68}Ga-FAPI-46 PET, ^{18}F-FDG PET, and contrast-enhanced CT by 2 masked nuclear medicine physicians and 1 masked radiologist. Disagreement was resolved by a joint consensus read. Across all imaging modalities, a total of 388 lesions was detected. On PET, areas with focal uptake above the surrounding background level, not attributable to physiologic findings, were rated positive. On CT, lymph nodes that were larger than 1 cm in short diameter and had suggestive features (contrast enhancement and a round shape, among others) were considered positive, as were organ lesions (including features such as morphologic delineation, necrosis, or hyperarterialization). Follow-up imaging (CT or PET/CT), clinical data, or histologic confirmation was used as the standard of truth.

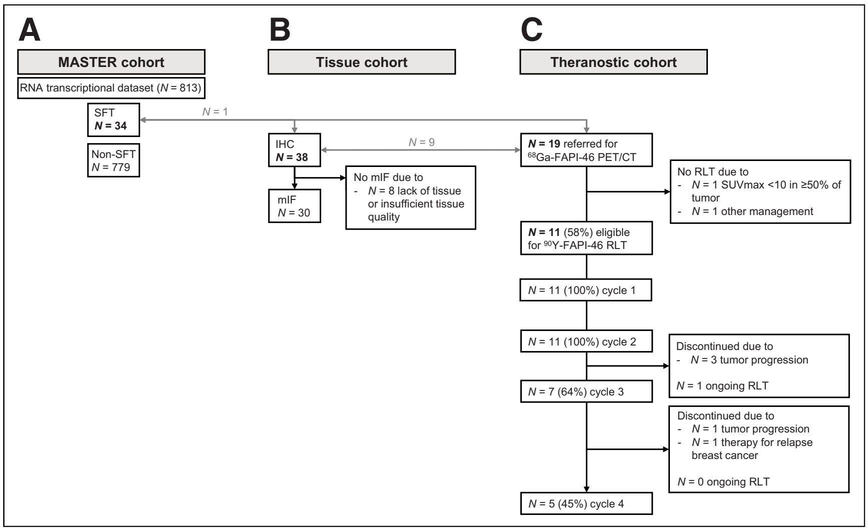

FIGURE 1. Patient flow diagram and overview of the 3 study cohorts: MASTER (A), tissue (B), and theranostic (C). Numbers of overlapping patients are indicated in gray. IHC = immunohistochemistry.

^{90}Y-FAPI-46 RLT

The ^{90}Y-FAPI-46 administration protocol and eligibility criteria have been reported previously (*4,18*). Details on the radiosynthesis are shown in the supplemental methods. Ten patients received a scout dose of 3.7 ± 0.1 GBq of ^{90}Y-FAPI-46 (except patient 3, who received a first-cycle high dose of 8.9 GBq) with PET-based dosimetry. Patients manifesting focal ^{90}Y-FAPI-46 uptake in

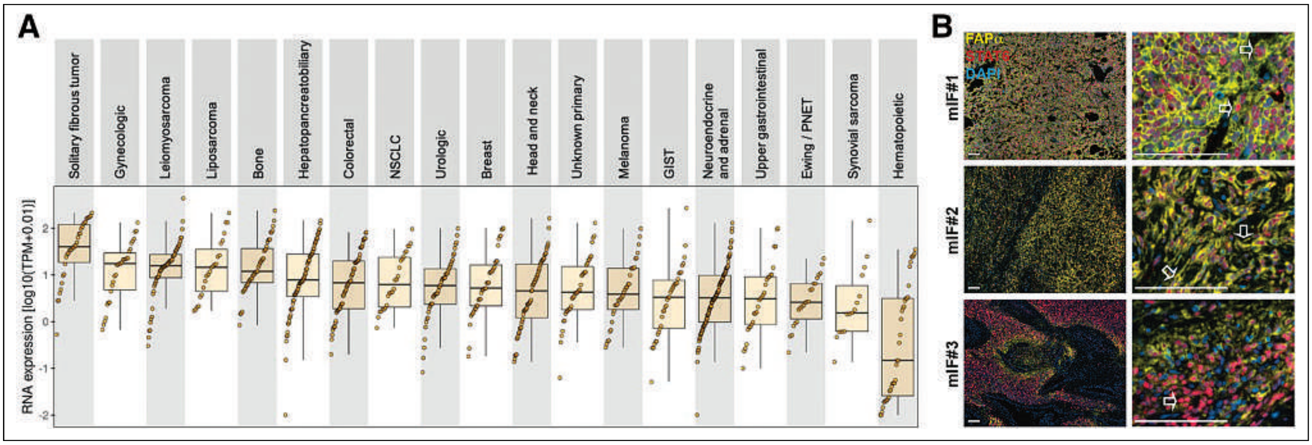

FIGURE 2. RNA and protein expression of FAPα in SFT tissue. (A) mRNA expression of FAPα in MASTER cohort (813 patients; 126 different morphology codes [International Classification of Diseases for Oncology, third revision] categorized into subcohorts). (B) Representative mIF from tissue cohort demonstrating staining with FAPα, STAT6, and DAPI. mIF 1 shows FAPα-positive tumor cells (FAPα-positive/STAT6-positive; arrow), mIF 2 shows FAPα-positive stroma cells (FAPα-positive/STAT6-negative; arrow), and mIF 3 shows FAPα-negative tumor cells (FAPα-negative/STAT6-positive; arrow). GIST = gastrointestinal stromal tumor; NSCLC = non–small cell lung carcinoma; PNET = primitive neuroectodermal tumor; STAT6 = signal transducer and activator of transcription 6; TPM = transcripts per million mapped reads.

more than 50% of tumor lesions on posttherapy ^{90}Y-FAPI-46 bremsstrahlung scintigraphy, and if otherwise clinically indicated, were eligible to receive 3 further cycles every 4–6 wk with 7.4 ± 0.5 GBq of ^{90}Y-FAPI-46 (high dose), split into 2 intravenous applications administered 4 h apart (except for patients 4 and 11, who received a second-cycle single application of ^{90}Y-FAPI-46 at a dose of 1.0 and 3.8 GBq, respectively). Bremsstrahlung scintigraphy was performed within 24 h of scout dosing. Details on the posttherapeutic dosimetry are presented in the supplemental methods.

Response Evaluation

^{18}F-FDG PET with morphologic imaging follow-up was performed as per clinical routine at 2- to 3-mo intervals during and after ^{90}Y-FAPI-46 treatment. The median follow-up time was 270 d. Imaging response was defined according to RECIST version 1.1 for CT and PERCIST version 1.0 for ^{18}F-FDG PET/CT (*19,20*). Two nuclear medicine physicians analyzed the follow-up imaging through unmasked, independent rereadings. For calculating disease control rate, disease control was defined as a complete response or complete metabolic response, a partial response or partial metabolic response, and stable disease or stable metabolic disease. For calculating the overall response rate, response was defined as a complete response or complete metabolic response or as a partial response or partial metabolic response. PFS was defined from the first ^{90}Y-FAPI-46 treatment to the time of progressive disease or death.

Statistical Considerations

Descriptive statistics, that is, the frequency of occurrence, percentage, median, and interquartile range (IQR), were calculated for each of the independent variables. An unpaired *t* test with Welch correction was used for statistical analysis. PFS was calculated using the Kaplan–Meier method. Statistical analyses were performed with SPSS Statistics version 27 (IBM) and Prism version 9 (GraphPad).

RESULTS

High Expression of Theranostic Target FAPα in SFT Tumor Tissue

We assessed FAPα mRNA pan-tumor expression levels in the MASTER cohort with available RNA sequencing data (*17*). Among the 813 patients with 126 different morphology codes (International Classification of Diseases for Oncology, third revision), we identified 34 patients with a diagnosis of SFT. Interestingly, SFT showed the highest median FAPα mRNA expression among all histologies (median transcripts per million mapped reads: 40.18 for SFT vs. 5.98 for non-SFT; $P < 0.0001$) (Fig. 2A). Next, we aimed to verify FAPα protein expression in the tissue cohort. By visual analysis of FAPα in immunohistochemistry, 8 of 38 (21%) SFT samples were rated negative and 30 (79%) were rated positive (Supplemental Fig. 1A, upper graph). Supplemental Figure 2 depicts representative hematoxylin and eosin and FAPα staining with negative, low, intermediate, and high expression. Semiquantitative assessment of FAPα staining in the entire tumor section, as percentage of FAPα-positive cells, indicated high expression in 32% of the patients, intermediate expression in 34%, and absent or low expression in only 34% (Supplemental Fig. 1A, lower graph).

To address which cell type in SFT expresses FAPα, we performed mIF in 30 of the 38 tumor samples of the tissue cohort, using computer-aided analysis of signal transducer and activator of transcription 6 as a marker for tumor cells. Here, we distinguished tumor cells with expression of FAPα (mIF 1), stromal cells with expression of FAPα (mIF 2), and tumor cells without FAPα expression (mIF 3) (Fig. 2B). The overall median expression of FAPα was 34.6% (IQR, 38.5%) of all cells in the tumor tissue, with a median FAPα positivity of tumor cells of 27.3% (IQR, 33.1%), which significantly exceeded the FAPα positivity of stroma cells (12.7%; IQR, 11.2%; $P < 0.001$) (Supplemental Fig. 1B).

High In Vivo Uptake of FAPα-Directed Radioligand with Improved Detection Efficacy

We investigated the diagnostic value of ^{68}Ga-FAPI-46 in the theranostic cohort. All patients underwent ^{68}Ga-FAPI-46 PET/CT, ^{18}F-FDG PET/CT, and diagnostic contrast-enhanced CT within a short interval of no more than 3 d (Fig. 3A; Supplemental Fig. 3). Tumor uptake was significantly higher for ^{68}Ga-FAPI-46 than for ^{18}F-FDG (respectively, 13.2 [IQR, 10.2] vs. 3.2 [IQR, 3.1] [$P < 0.01$] for median SUV$_{max}$ and 7.6 [IQR, 6.4] vs. 2.0 [IQR, 2.0] [$P < 0.01$] for median SUV$_{mean}$) (Fig. 3B). Also, the patient-based detection efficacy of tumor lesions was highest for ^{68}Ga-FAPI-46 PET by

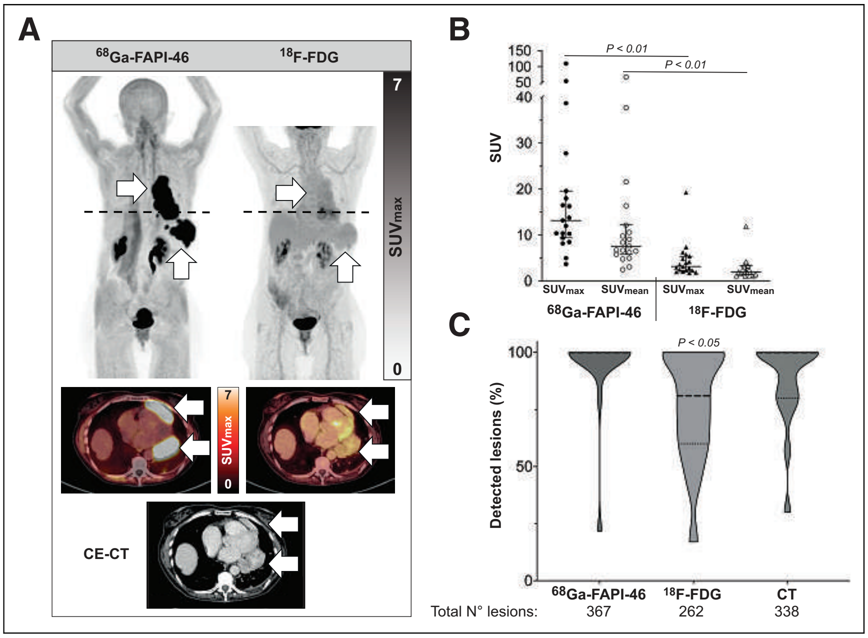

FIGURE 3. Comparison of ^{68}Ga-FAPI-46 PET uptake intensity and detection efficacy in theranostic cohort (n = 19). (A) 85-y-old patient with metastatic SFT. Shown are representative maximum-intensity projection (top) and axial PET images (left, ^{68}Ga-FAPI-46 PET; right, ^{18}F-FDG PET), as well as axial CT image (bottom). Tumor lesions are indicated by arrows. (B) Column scatter graph comparing uptake intensity using mean SUV_{max} and mean SUV_{mean} of ^{68}Ga-FAPI-46 PET and ^{18}F-FDG PET in patients with localized and metastatic SFT. (C) Truncated violin plots showing patient-based detected tumor lesion as percentage of maximum detected lesions for all modalities (total number of lesions, 388), for ^{68}Ga-FAPI-46 PET, for ^{18}F-FDG PET, and for CT. Statistical significance is defined as $P < 0.05$ with Welch t test. CE-CT = contrast-enhanced CT.

detecting 367 of a total of 388 tumor lesion over all modalities (94.5%; SEM, 4.2%). This was higher than standard imaging with contrast-enhanced CT, which detected 338 lesions (87.8%; SEM, 4.3%), and significantly superior to ^{18}F-FDG PET, which detected only 262 lesions (77.3%; SEM, 5.5%; $P < 0.05$) (Fig. 3C).

Efficacy of FAPα-Directed RLT

Eleven of the 19 patients (58%) in the theranostic cohort subsequently received ^{90}Y-FAPI-46 RLT. The patients received a total of 34 cycles of ^{90}Y-FAPI-46 RLT, with a median of 3 cycles (IQR, 2 cycles) per patient (Supplemental Table 3). The distribution of cycles and reasons for discontinuation in the 11 patients receiving RLT, as well as reasons for not receiving RLT in the other 8 patients, are displayed in Figure 1C. The median maximal absorbed radiation dose was 2.9 Gy/GBq (IQR, 3.9 Gy/GBq; range, 0.5–24.7 Gy/GBq) in tumor (Supplemental Table 3). Both RECIST and PERCIST response during or after therapy revealed a partial response in 3 patients (27%) and stable disease in 6 patients (55%), leading to a disease control rate of 82% (Supplemental Table 3). Representative images of 2 patients with a partial response are shown in Figure 4. A swimmer plot in Figure 5A displays the course of treatment: 3 patients were in follow-up without progression, 1 patient was still under RLT, 1 patient died because of relapse of concomitant breast cancer without progression of SFT, 1 patient was lost to follow-up after progression, and 5 patients received subsequent systemic treatment after progression. Kaplan–Meier plots illustrate PFS of the therapy before RLT (PFS1), of ^{90}Y-FAPI-46 RLT (PFS2), and of the first subsequent therapy after RLT (PFS3) (Fig. 5B). The observed median PFS for ^{90}Y-FAPI-46 RLT was 227 d (Supplemental Table 3).

DISCUSSION

To our knowledge, this was the first study systematically investigating FAPα as a theragnostic target in SFT to report high expression level of FAPα on the tumor cell surface, enabling superior tumor detection by FAPα-directed PET. Moreover, we report on efficacy and survival after ^{90}Y-FAPI-46 RLT in a patient subgroup.

Our analysis showed that SFT samples demonstrated the highest median mRNA expression of FAPα in the MASTER cohort. Likewise, we confirmed FAPα cell surface expression by immunohistochemistry and mIF in the tissue cohort. The high FAPα expression, particularly in tumor cells of SFT, is in contrast to previous reports on epithelial cancers, where FAPα expression was concentrated in cancer-associated fibroblasts, with low levels in the tumor cells (*2,21,22*).

In line with the observed high FAPα mRNA and protein expression, 18 of the 19 patients (95%) with SFT from the theranostic cohort showed high uptake of the FAPα-directed radioligand ^{68}Ga-FAPI-46 in tumor lesions. Also, tumor detection efficacy was better for ^{68}Ga-FAPI-46 PET than for contrast-enhanced CT and significantly better than for ^{18}F-FDG PET. Our data are supported by recent studies showing similarly high ^{68}Ga-FAPI PET uptake in 4 SFT patients and 2 studies reporting high FAPα protein expression in tumor tissue as well (*23–26*).

FAPα-associated RLT is an emerging approach for targeted systemic therapy against solid tumors (*27*). We recently demonstrated that ^{90}Y-FAPI-46-RLT was safe and led to disease control in 8 of 16 (50%) evaluable patients, which was associated with improved overall survival (*4*). Noteworthy, 7 of 8 patients (88%) with disease control had metastatic sarcoma, including 5 patients with SFT (*4*). Here, we report expanded follow-up in 11 patients with SFT, including 9 patients (patients 1–9) of the previous study (*4*) and 2 new patients. We observed disease control in 9 patients (82%): partial response in 3 and stable disease in 6. When all other available therapeutic options fail, development of a novel therapy has a primary goal of achieving disease control.

This study was limited by its retrospective design, short follow-up for the theranostic cohort, and small sample size of treated patients due to low incidence. Moreover, the study lacked a direct correlation of RNA/protein expression, FAPI uptake, dosimetry, and treatment response. Another question, which should be addressed in future studies, is the mechanism regulating FAPα expression in SFT. Nevertheless, for such a rare disease our numbers are high and the data are consistent across 3 independent cohorts using different endpoints. In rare diseases, solid retrospective data are important since they are often the only available evidence-based data and form a basis for prospective research.

CONCLUSION

Screening of tissue mRNA and protein expression by immunohistochemistry identified FAPα as hallmark theranostic target for

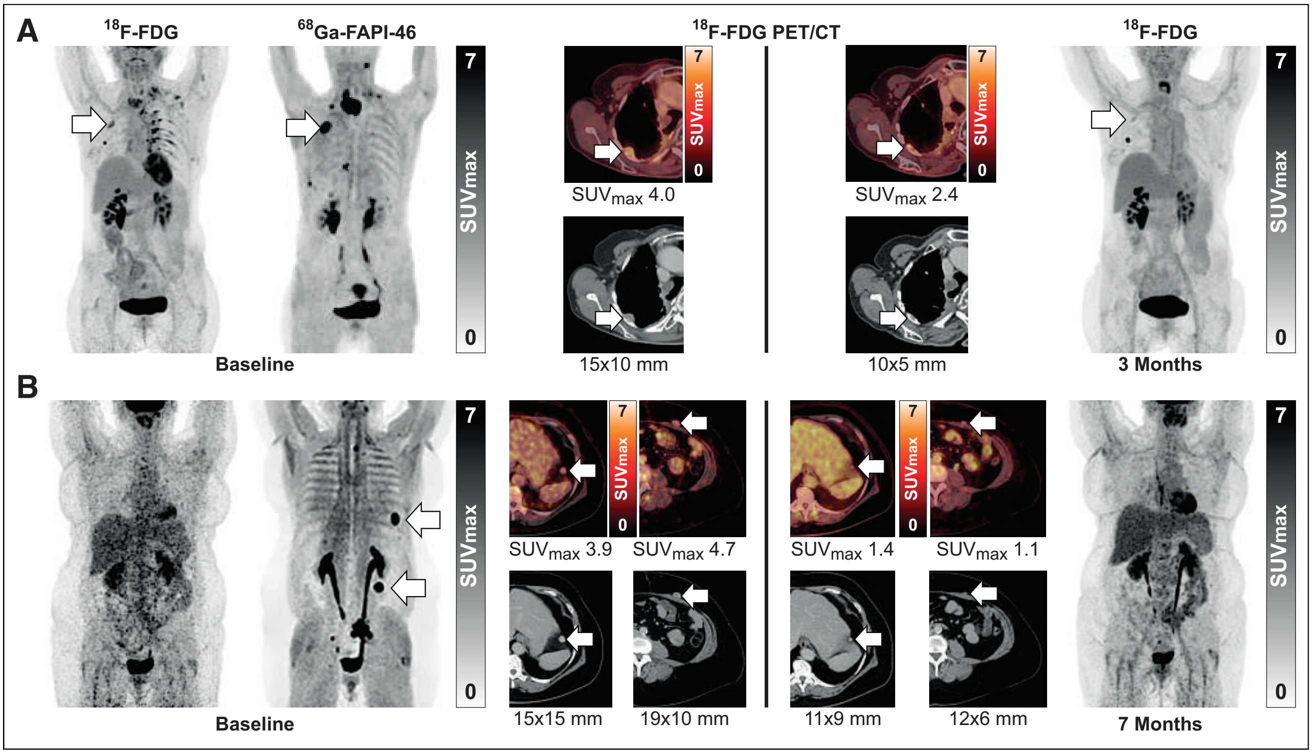

FIGURE 4. Patients with partial response after ^{90}Y-FAPI-46 RLT. At far left and right are maximum-intensity PET projections, and at center are axial ^{18}F-FDG PET/CT (top rows) and CT (bottom rows) images, with $\mathrm{SUV_{max}}$ and tumor diameter, respectively, before therapy (left) and at time point of best response (right). (A) 67-y-old woman (patient 2) with metastatic SFT who progressed under 3 lines of systemic therapy, with RECIST partial response and PERCIST partial metabolic response under RLT. ^{90}Y-FAPI-46 RLT was discontinued because of relapse of metastatic breast cancer in liver and lung. (B) 57-y-old woman (patient 5) with metastatic SFT who progressed under 2 lines of systemic therapy, with RECIST partial response and PERCIST stable metabolic disease under RLT.

SFT. In line with this finding, ^{68}Ga-FAPI-46 PET demonstrated SFT detection superior to that of ^{18}F-FDG PET and contrast-enhanced CT. Finally, ^{90}Y-FAPI-46 RLT of SFT led to disease control in more than 80% of cases. These data strongly support future prospective evaluation of FAPα-directed radioligand imaging and therapy in SFT and potentially other sarcomas.

DISCLOSURE

Rainer Hamacher was supported by the Clinician Scientist Program of the University Medicine Essen Clinician Scientist Academy (UMEA; Faculty of Medicine and Deutsche Forschungsgemeinschaft [DFG]); reports travel grants from Lilly, Novartis, and PharmaMar; and reports personal fees from Lilly and PharmaMar outside the submitted work. Kim Pabst has received a Junior Clinician Scientist Stipend from the University Medicine Essen Clinician Scientist Academy (UMEA; Faculty of Medicine and Deutsche Forschungsgemeinschaft [DFG]); reports travel fees from IPSEN; and reports research funding from Bayer. Phyllis Cheung is supported by the Deutsche Forschungsgemeinschaft (DFG) (CH 2320/2-3). Lukas Kessler is a consultant for AAA and BTG and received fees from Sanofi. Sabrina Borchert reports fees from Brystol Myers Squibb (research funding) outside the submitted work. Martin Schuler reports personal fees as a consultant from Amgen, AstraZeneca, Boehringer Ingelheim, Bristol Myers Squibb, GlaxoSmithKline, Janssen, Merck Serono, Novartis, Roche, Sanofi, and Takeda; honoraria for continuing medical education presentations from Amgen, Boehringer Ingelheim, Bristol Myers Squibb, Janssen, MSD, and Novartis; and research funding (to the institution) from AstraZeneca and Bristol Myers Squibb—all outside the submitted work. Sebastian Bauer reports personal fees from Bayer, Eli Lilly, Novartis, Pfizer, and PharmaMar; serves in an advisory/consultancy role for

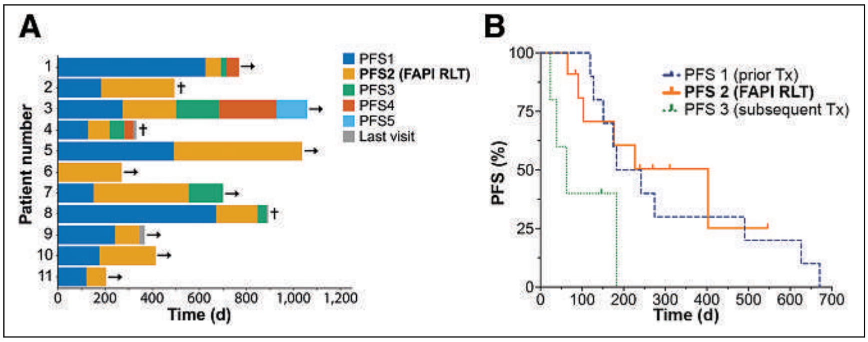

FIGURE 5. Response and survival under ^{90}Y-FAPI-46 RLT (n = 11). (A) Swimmer plot showing PFS for therapy before RLT (PFS1), for RLT (PFS2), and for subsequent therapies after RLT (PFS3–PFS5). Death of patient 2 was due to relapse of breast cancer. (B) Corresponding Kaplan–Meier plot for PFS. Arrows denote ongoing treatment or follow-up. †Death. Tx = treatment.

ADC Therapeutics, Bayer, Blueprint Medicines, Daiichi Sankyo, Deciphera, Eli Lilly, Exelixis, Janssen-Cilag, Nanobiotix, Novartis, PharmaMar, Plexxikon, and Roche; reports research funding from Novartis; and serves as a member of the external advisory board of the Federal Ministry of Health for off-label use in oncology—all outside the submitted work. Stefan Fröhling reports personal fees from Amgen, Bayer, Eli Lilly, Illumina, PharmaMar, and Roche and research funding from AstraZeneca, Boehringer Ingelheim, Pfizer, PharmaMar, and Roche. Ken Herrmann reports personal fees from Bayer, SOFIE Biosciences, SIRTEX, Adacap, Curium, Endocyte, IPSEN, Siemens Healthineers, GE Healthcare, Amgen, Novartis, ymabs, Aktis, Oncology, and Pharma15; nonfinancial support from ABX; and grants and personal fees from BTG. Jens Siveke is supported by German Cancer Aid (grant 70112505, PIPAC; grant 70113834, PREDICT-PACA), the Wilhelm-Sander Foundation (grant 2019.008.1), the DFG through grant SI1549/3-1 (Clinical Research Unit KFO337) and SI1549/4-1, and the Federal Ministry of Education and Research (BMBF; SATURN3 consortium); receives honoraria as a consultant or for continuing medical education presentations from AstraZeneca, Bayer, Immunocore, Roche, and Servier; receives research funding (to the institution) from Bristol Myers Squibb, Celgene, and Roche; and holds ownership and serves on the board of directors of Pharma15—all outside the submitted work. Wolfgang Fendler reports fees from SOFIE Biosciences (research funding), Janssen (consultant, speaker), Calyx (consultant, image review), Bayer (consultant, speaker, research funding), Novartis (speaker, consultant), Telix (speaker), GE Healthcare (speaker), Eczacıbaşı Monrol (speaker), Abx (speaker), and Amgen (speaker)—all outside the submitted work. No other potential conflict of interest relevant to this article was reported.

ACKNOWLEDGMENTS

We thank Ulrike Winter and Katja Beck from the Department of Translational Medical Oncology at the National Center for Tumor Diseases Heidelberg for coordination and logistic support within the National Center for Tumor Diseases/German Cancer Research Center/German Cancer Consortium MASTER program. We thank Yvonne Krause and Sophia Berger from the Schildhaus Laboratory, as well as the technicians from the Institute of Pathology, for technical support. We thank all the nurses and technicians of the nuclear medicine team for ongoing logistic support.

KEY POINTS

QUESTION: Does FAPα serve as a suitable target for radiotheranostic applications in SFT?

PERTINENT FINDINGS: In this translational study, we demonstrated high expression of FAPα in SFT, particularly in tumor cells, with superiority of FAPα-targeting PET imaging and efficacy of FAPα-targeting RLT.

IMPLICATIONS FOR PATIENT CARE: These results form the basis and rationale for exploring SFT FAPα-directed radioligand imaging and therapy in future prospective trials.

REFERENCES

1. Sgouros G, Bodei L, McDevitt MR, Nedrow JR. Radiopharmaceutical therapy in cancer: clinical advances and challenges. *Nat Rev Drug Discov.* 2020;19:589–608.
2. Xin L, Gao J, Zheng Z, et al. Fibroblast activation protein-α as a target in the bench-to-bedside diagnosis and treatment of tumors: a narrative review. *Front Oncol.* 2021;11:648187.
3. Kratochwil C, Flechsig P, Lindner T, et al. ^{68}Ga-FAPI PET/CT: tracer uptake in 28 different kinds of cancer. *J Nucl Med.* 2019;60:801–805.
4. Fendler WP, Pabst KM, Kessler L, et al. Safety and efficacy of ^{90}Y-FAPI-46 radioligand therapy in patients with advanced sarcoma and other cancer entities. *Clin Cancer Res.* 2022;28:4346–4353.
5. Dohi O, Ohtani H, Hatori M, et al. Histogenesis-specific expression of fibroblast activation protein and dipeptidylpeptidase-IV in human bone and soft tissue tumours. *Histopathology.* 2009;55:432–440.
6. Dolznig H, Schweifer N, Puri C, et al. Characterization of cancer stroma markers: in silico analysis of an mRNA expression database for fibroblast activation protein and endosialin. *Cancer Immun.* 2005;5:10.
7. Rettig WJ, Garin-Chesa P, Beresford HR, Oettgen HF, Melamed MR, Old LJ. Cell-surface glycoproteins of human sarcomas: differential expression in normal and malignant tissues and cultured cells. *Proc Natl Acad Sci USA.* 1988;85:3110–3114.
8. Hirmas N, Hamacher R, Sraieb M, et al. Fibroblast-activation protein PET and histopathology in a single-center database of 324 patients and 21 tumor entities. *J Nucl Med.* 2023;64:711–716.
9. Kessler L, Ferdinandus J, Hirmas N, et al. ^{68}Ga-FAPI as a diagnostic tool in sarcoma: data from the ^{68}Ga-FAPI PET prospective observational trial. *J Nucl Med.* 2022;63:89–95.
10. Koerber SA, Finck R, Dendl K, et al. Novel FAP ligands enable improved imaging contrast in sarcoma patients due to FAPI-PET/CT. *Eur J Nucl Med Mol Imaging.* 2021;48:3918–3924.
11. de Pinieux G, Karanian M, Le Loarer F, et al. Nationwide incidence of sarcomas and connective tissue tumors of intermediate malignancy over four years using an expert pathology review network. *PLoS One.* 2021;16:e0246958.
12. Demicco EG, Park MS, Araujo DM, et al. Solitary fibrous tumor: a clinicopathological study of 110 cases and proposed risk assessment model. *Mod Pathol.* 2012; 25:1298–1306.
13. Martin-Broto J, Mondaza-Hernandez JL, Moura DS, Hindi N. A comprehensive review on solitary fibrous tumor: new insights for new horizons. *Cancers (Basel).* 2021;13: 2913.
14. Henry LR, Lee HO, Lee JS, et al. Clinical implications of fibroblast activation protein in patients with colon cancer. *Clin Cancer Res.* 2007;13:1736–1741.
15. Nader M, Valla DF, Vriamont C, et al. [^{68}Ga]/[^{90}Y]FAPI-46: automated production and analytical validation of a theranostic pair. *Nucl Med Biol.* 2022;110–111:37–44.
16. Stabin MG, Sparks RB, Crowe E. OLINDA/EXM: the second-generation personal computer software for internal dose assessment in nuclear medicine. *J Nucl Med.* 2005;46:1023–1027.
17. Horak P, Heining C, Kreutzfeldt S, et al. Comprehensive genomic and transcriptomic analysis for guiding therapeutic decisions in patients with rare cancers. *Cancer Discov.* 2021;11:2780–2795.
18. Ferdinandus J, Costa PF, Kessler L, et al. Initial clinical experience with ^{90}Y-FAPI-46 radioligand therapy for advanced-stage solid tumors: a case series of 9 patients. *J Nucl Med.* 2022;63:727–734.
19. Eisenhauer EA, Therasse P, Bogaerts J, et al. New response evaluation criteria in solid tumours: revised RECIST guideline (version 1.1). *Eur J Cancer.* 2009;45: 228–247.
20. Wahl RL, Jacene H, Kasamon Y, Lodge MA. From RECIST to PERCIST: evolving considerations for PET response criteria in solid tumors. *J Nucl Med.* 2009;50(suppl 1):122s–150s.
21. Garin-Chesa P, Old LJ, Rettig WJ. Cell surface glycoprotein of reactive stromal fibroblasts as a potential antibody target in human epithelial cancers. *Proc Natl Acad Sci USA.* 1990;87:7235–7239.
22. Liu F, Qi L, Liu B, et al. Fibroblast activation protein overexpression and clinical implications in solid tumors: a meta-analysis. *PLoS One.* 2015;10:e0116683.
23. Liu H, Liu L, Chen L, et al. [^{68}Ga]Ga-DOTA-FAPI-04 PET/CT imaging of benign pulmonary solitary fibrous tumour. *Eur J Nucl Med Mol Imaging.* 2021;48:2053–2054.
24. Wang R, Liu Q, Sui H, Zhang M, Zhu Z, Cui R. ^{68}Ga-FAPI outperforms ^{18}F-FDG PET/CT in identifying solitary fibrous tumor. *Eur J Nucl Med Mol Imaging.* 2021; 48:2055–2056.
25. Zhang A, Zhang H, Zhou X, Li Z, Li N. Solitary fibrous tumors of the pleura shown on ^{18}F-FDG and ^{68}Ga-DOTA-FAPI-04 PET/CT. *Clin Nucl Med.* 2021;46:e534–e537.
26. Zhang Y, Cai J, Wu Z, Yao S, Miao W. Intense [^{68}Ga]Ga-FAPI-04 uptake in solitary fibrous tumor/hemangiopericytoma of the central nervous system. *Eur J Nucl Med Mol Imaging.* 2021;48:4103–4104.
27. Privé BM, Boussihmad MA, Timmermans B, et al. Fibroblast activation protein-targeted radionuclide therapy: background, opportunities, and challenges of first (pre)clinical studies. *Eur J Nucl Med Mol Imaging.* 2023;50:1906–1918.

Outcome on Mesenteric Mass Response of Small-Intestinal Neuroendocrine Tumors Treated by ^{177}Lu-DOTATATE Peptide Receptor Radionuclide Therapy: The MesenLuth Study, a National Study from the French Group of Endocrine Tumors and Endocan-RENATEN Network

Laure Al Mansour[1], Louis De Mestier[2], Magalie Haissaguerre[3], Pauline Afchain[4], Julien Hadoux[5], Thierry Lecomte[6], David Morland[7], Anne Segolene Cottereau[8], Ophelie De Rycke[2], Ghoufrane Tlili[9], Jérémie Tordo[10], Marc Janier[1], Agathe Deville[1], and Thomas Walter[11,12]

[1]Service de Médecine Nucléaire, Hôpital Louis Pradel, Hospices Civils de Lyon, Bron, France; [2]Service de Pancréatologie et Oncologie Digestive, Hôpital Beaujon, Assistance Publique-Hôpitaux de Paris, Université Paris-Cité, Clichy, France; [3]Service d'Endocrinologie, Hôpital Haut-Lévêque, Université de Bordeaux, Pessac, France; [4]Service d'Oncologie, Hôpital Saint Antoine, Assistance Publique-Hôpitaux de Paris, Paris, France; [5]Service d'Oncologie, Institut Gustave Roussy, Université Paris Saclay, Villejuif, France; [6]Service de d'Hépato-gastro-entérologie et de Cancérologie Digestive, CHRU Hôpitaux de Tours, Tours, France; [7]Service de Médecine Nucléaire et Centre de Recherche en STIC EA 3804, Institut Godinot, Université de Reims Champagne-Ardenne, Reims, France; [8]Service de Médecine Nucléaire, Hôpital Cochin, Assistance Publique-Hôpitaux de Paris, Université René Descartes, Paris, France; [9]Service de Médecine Nucléaire, CHU de Bordeaux, Bordeaux, France; [10]Service de Médecine Nucléaire, Hôpital Lyon Sud, Hospices Civils de Lyon, Pierre-Bénite, France; [11]Service d'Oncologie Digestive, Hôpital Edouard Herriot, Hospices Civils de Lyon, Lyon, France; and [12]Gastro-entérologie et Technologies pour la Santé, Unité de Recherche, Centre de Recherche en Cancérologie de Lyon, INSERM, Lyon, France

A mesenteric mass (MM), characterized by fibrotic reaction, is present in most small-intestinal neuroendocrine tumors (SI-NETs). ^{177}Lu-DOTATATE peptide receptor radionuclide therapy (PRRT) has shown its efficacy in patients with progressive SI-NETs. However, because of specific tissue characteristics of desmoplastic MMs, we hypothesize that these lesions may be refractory to ^{177}Lu-DOTATATE PRRT. **Methods:** From the national French Groupe d'étude des Tumeurs Endocrines database, we identified patients with an advanced SI-NET and a MM ($\geq$2 cm with a retractile aspect) of a SI-NET treated by at least 1 course of ^{177}Lu-DOTATATE PRRT. The primary endpoint was a MM objective response rate (ORR) of less than 5%. Secondary endpoints were metabolic response, MM-related safety, and clinical response, as well as MM progression-free survival (PFS) and non-MM PFS. **Results:** In total, 52 patients were included. The MM ORR was 4% ($n = 2$), and the non-MM ORR was 8% ($n = 4$). No patient had a MM metabolic response, and the non-MM metabolic response rate was 12% ($n = 6$). Among the 26 patients with baseline MM-related symptoms, 46% had a clinical response. Four patients presented with gastrointestinal complications during PRRT. The median MM-related PFS was not reached, and the non-MM PFS was 50.3 mo (95% CI, 38.2–61.7 mo). **Conclusion:** This study confirms that ^{177}Lu-DOTATATE PRRT does not lead to morphologic response on MMs (ORR $<$ 5%). However, it allows MM stability, with few MM-related side effects, and has a relevant impact on MM-related symptoms.

Key Words: neuroendocrine tumor; mesenteric mass; objective response; ^{177}Lu-DOTATATE; PRRT

J Nucl Med 2024; 65:258–263
DOI: 10.2967/jnumed.123.266063

Small-intestinal neuroendocrine tumors (SI-NETs) are the most common well-differentiated metastatic NETs (*1*). These tumors often metastasize, especially to the mesenteric lymph nodes and the liver. SI-NETs generally produce serotonin and other vasoactive substances that can lead to carcinoid syndrome (CS). The distant action of serotonin can cause fibrosis of right-sided heart valves, potentially leading to carcinoid heart disease (*2*,*3*). In addition, mesenteric lymph node metastases are often affected by fibrosis because of local serotonin secretion. In certain cases, this can lead to dense desmoplastic fibrosis, causing tethering of the bowel and mesenteric ischemia (*3*,*4*).

The efficacy of peptide receptor radionuclide therapy (PRRT) using radiolabeled somatostatin analog ^{177}Lu-DOTATATE for progressive SI-NETs has been demonstrated (*5*). In the phase III NETTER-1 trial, PRRT (associated with 30 mg of long-acting release octreotide) led to a higher objective response rate (ORR, 18%), according to RECIST version 1.1; increased progression-free survival (PFS); and improved quality of life compared with a high dose of long-acting release octreotide alone (60 mg every 4 wk) in a population of patients with progressive SI-NETs (*5*,*6*). However, because of the specific tissue characteristics of desmoplastic mesenteric metastases, it was hypothesized that these lesions may be particularly refractory to PRRT, as suggested by recent studies that investigated their morphologic response (*2*,*3*) but did not set specific criteria to define a retractile mesenteric mass (MM). Furthermore,

---

Received May 25, 2023; revision accepted Oct. 25, 2023.

For correspondence or reprints, contact Thomas Walter (thomas.walter@chu-lyon.fr).

none of these studies investigated the metabolic response of MMs to PRRT, the clinical impact on MM-related symptoms, or MM-related safety. Therefore, the aim of the present retrospective study was to evaluate the ORR, according to RECIST version 1.1, on precisely defined MMs in patients with SI-NET treated with ^{177}Lu-DOTATATE PRRT. We also evaluated the metabolic response, clinical response, and toxicity of PRRT on MMs.

MATERIALS AND METHODS

Population

Among patients treated in the 25 participant centers of the national database of the Groupe d'étude des Tumeurs Endocrines (GTE), we retrospectively identified patients with a SI-NET and a mesenteric lymph node metastasis at the time of the first dose of PRRT from January 2001 to October 2021 and managed within the national French network dedicated to NET (Endocan-RENATEN [Reseau National de Prise en Charge des Tumeurs Endocrines]-GTE). This observational study was approved on February 21, 2023, by the medical ethics research committee of the Hospices Civils de Lyon (number 22_5425). The national database of the GTE was approved on January 5, 2021, by the national data protection commission (Commission Nationale de l'Informatique et des Libertés, number 2219168). The medical records of these patients were retrospectively sought, and patients were included if they presented with a mesenteric lymph node metastasis measuring at least 2 cm in the minor axis at the time of the first PRRT use, according to RECIST version 1.1, and if they had a retractile aspect (tumor surrounded by linear bands radiating into the mesenteric fat; Fig. 1) that we defined as a MM. Other inclusion criteria were a histologically confirmed grade 1 to grade 3 SI-NET (there was no central review of the pathologic specimen, but diagnosis was made by expert pathologists from the Endocan-TENpath-GTE national network), functioning or nonfunctioning; receipt of at least 1 course of PRRT (^{177}Lu-DOTATATE); and an available morphologic evaluation by CT or MRI performed before and after PRRT. The exclusion criteria were NETs of non–small-intestinal origin, poorly differentiated carcinomas, the absence of a MM, or a prior course of PRRT.

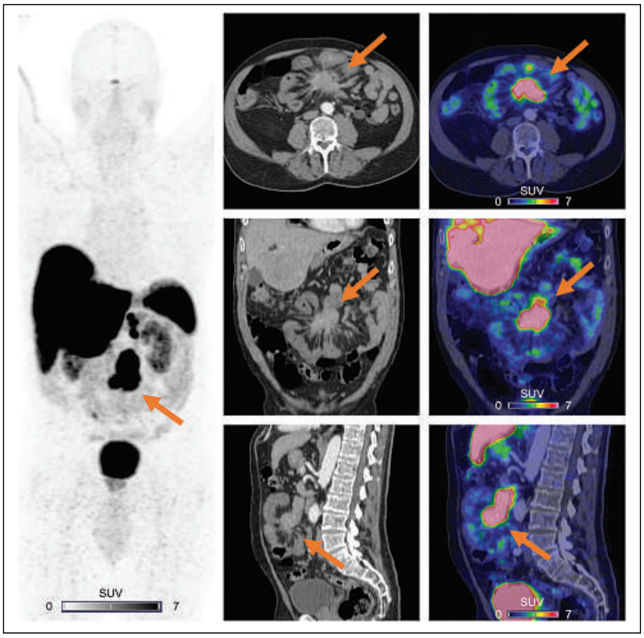

FIGURE 1. Baseline ^{68}Ga-DOTATOC PET (left), CT (middle), and PET/CT (right) images of 61-y-old patient presenting with typical retractile MM surrounded by linear bands radiating into mesenteric fat (arrows) that were intensely hypermetabolic (Krenning score 4).

Parameters

We collected morphologic and metabolic imaging for central review to evaluate the potential resectability of the MM and to evaluate MM response. The resectability of the MM was based on the classification proposed by Lardière-Deguelte et al. (*7*) for the involvement of the superior mesenteric artery and on the study reported by Bertani et al. (*8*) to also include the degree of superior mesenteric venous involvement and the presence or not of mesenteric fibrosis retraction. As described by these authors, the MM was considered unresectable if the involvement of the superior mesenteric artery was classified as stage IIIup or higher (*7*), if proximal infiltration of the superior mesenteric vein was seen, or if there were signs of severe mesenteric fibrosis retraction (*8*).

The following parameters were also collected at the time of first PRRT: age, sex, NET primary location, World Health Organization classification with grading, Ki-67 index, Eastern Cooperative Oncology Group performance status (0–1 or ≥2), clinical CS, carcinoid heart disease, MM-related symptoms, number and location of metastatic sites, uptake on somatostatin receptor imaging (either ^{111}In-octreotide scintigraphy or ^{68}Ga-DOTATOC PET/CT), serum plasma chromogranin A (CgA) concentration (considered elevated if >2 times the upper limit of normal value at baseline), oncology treatments received before PRRT, and MM morphologic progression (according to RECIST version 1.1) before PRRT.

The characteristics and effectiveness of PRRT were collected: number of cycles, dose (full dose or reduced dose), reason for discontinuation (general health deterioration, toxicity, scheduled, or unknown), occurrence of gastrointestinal complications during PRRT (bowel obstruction, abdominal pain, motility disorders, or perforation), and corticosteroids because of the occurrence of a PRRT-related complication.

Endpoints

The primary endpoint was MM morphologic response to ^{177}Lu-DOTATATE PRRT, according to RECIST version 1.1. A response was defined as a reduction of at least 30% in lesion diameter between the images made before and those made after PRRT. We hypothesized that the MM ORR would be less than 5% based on the study reported by Pelle et al. (*2*) that found no response. For 80% nominal power and an α-level of 5%, the sample size required was estimated to be 42 patients.

The secondary endpoints were MM-related safety of PRRT (occurrence of gastrointestinal complications during PRRT or need for corticosteroids), MM morphologic response in comparison to other metastatic sites (liver, adenopathy, peritoneum, etc.) for the same patient (according to RECIST version 1.1), metabolic response on MMs and on other metastatic sites, clinical response on MM-related symptoms, CS clinical response, CgA laboratory response, MM-related and non–MM-related PFS, overall survival since the first dose of PRRT, long-term clinical MM outcome (symptom response and complications), and cause of death (MM-related, NET-related but non–MM-related, non–NET-related, or unknown).

The metabolic response was defined as a decrease of at least 1 point on the Krenning scale, for ^{111}In-octreotide scintigraphy, or according to European Organization for Research and Treatment of Cancer criteria, for ^{68}Ga-DOTATOC PET/CT (*9*), on imaging before versus after PRRT. The clinical MM response was determined in patients with MM-related symptoms because of a MM at baseline and was defined as complete (no symptoms), partial (if ≥50% of baseline symptom improvement based on intensity on a 1–10 scale or frequency of the symptom), progression (if >50% of symptom aggravation based on intensity or frequency of the symptom), or stability (in case of neither response nor progression). The CS clinical response was determined in patients with baseline CS symptoms and was defined as complete, partial (if ≥50% of baseline symptom improvement based on intensity on a 1–10 scale or frequency of the symptom), progression (if >50% of symptom aggravation based on intensity or frequency of the symptom), or stability (in case of neither response nor progression). CgA laboratory response was defined as a decrease of at least 50% of the CgA level in patients with elevated baseline CgA.

Long-term gastrointestinal complications and long-term clinical MM response were both defined at the time of last news, at least 6 mo after the last PRRT dose. We also estimated the median follow-up time between the last dose of PRRT and the last news. Images were reviewed by an independent observer, who reassessed the morphologic and metabolic responses on MM and non-MM metastatic sites.

Statistical Analysis

Categoric data are expressed as number and percentage, and continuous variables are expressed as median and range. PFS was calculated from the first dose of PRRT to the date of first morphologic progression or death. Overall survival was calculated from the first dose of PRRT to the date of death or last follow-up. Survival curves for PFS and overall survival were estimated using the Kaplan–Meier method. All statistical analyses were performed using SPSS version 17.0 (IBM).

RESULTS

Patient Characteristics

Among the 25 participant centers of the GTE database, 8 centers agreed to include patients. In total, 52 patients were included; 46% were women, and the median age was 70 y (range, 47–89 y). Ileum was the primary SI-NET site in most patients (73%). SI-NETs were grade 1 (48%) or grade 2 (42%), and median Ki-67 was 2.5%. There were no grade 3 SI-NETs, but 5 patients had SI-NETs of an unknown grade. Most patients (62%) had at least 2 other metastatic sites. These metastases were mainly located in the liver (87%), distant lymph nodes (37%), peritoneum (33%), or bone (27%; Table 1). In total, 29 patients were classified as stage IIIup ($n = 15$) or stage IV ($n = 14$), according to the Lardière-Deguelte et al. (*7*) classification; therefore, the MM was considered unresectable. According to Bertani et al. (*8*), 27 patients had proximal superior mesenteric venous involvement and 18 patients had severe mesenteric fibrosis. In total, 32 (65%) patients had an unresectable MM at the time of PRRT (missing data, $n = 3$; Supplemental Table 1 [supplemental materials are available at http://jnm.snmjournals.org]).

Almost half (46%) of patients had previously undergone primary tumor resection, and 31% of patients had previously undergone liver embolization. Concerning systemic therapies, 90% of patients received prior somatostatin analogs and 19% of patients received prior everolimus (Table 1). Of the 24 patients who underwent resection of the primary tumor without resection of the MM, 14 (64%) patients had at least 1 nonresectability criterion. The other 8 patients had a potentially resectable MM, but all had synchronous metastases and all but 1 patient presented with minimal mesenteric fibrosis or peripheral superior mesenteric venous infiltration; therefore, no reoperation was performed (Supplemental Table 1). Almost all patients had an Eastern Cooperative Oncology Group performance status of 0–1 (96%) before PRRT, and

TABLE 1
Patient Characteristics at Time of First PRRT Dose, $n = 52$

Characteristic	Data
Women	24 (46)
Age (y)	70 (47–89)
NET primary location	
Ileum	38 (73)
Jejunum	6 (12)
Not available	8 (15)
WHO classification	
NET-G1	25 (48)
NET-G2	22 (42)
Unknown	5 (10)
Ki-67 (%) in 44 patients	2.5 (1–16)
Non-MM metastatic sites	
0	3 (5)
1	17 (33)
2	16 (31)
>2	16 (31)
Location of metastatic sites	
Liver	45 (87)
Distant lymph node	19 (37)
Peritoneum	17 (33)
Bone	14 (27)
Other*	8 (15)
Treatment received before PRRT	
Primary tumor resection	24 (46)
Liver surgery	5 (10)
Liver embolization	16 (31)
Somatostatin analogs	47 (90)
Targeted therapy with everolimus	10 (19)
Chemotherapy	8 (15)
ECOG performance status	
0–1	50 (96)
≥2	2 (4)
Clinical CS	39 (75)
Carcinoid heart disease	7 (13)
MM-related symptoms	
No symptoms on MM	26 (50)
Abdominal pain	20 (38)
Diarrhea	14 (27)
Occlusive syndrome	8 (15)
Mesenteric ischemia symptoms	5 (10)
Constipation	3 (6)
Vomiting	1 (2)
MM uptake on SRI	
Krenning 2 or equivalent for PET	1 (2)
Krenning 3 or equivalent for PET	4 (8)
Krenning 4 or equivalent for PET	47 (90)
CgA > 2 ULN	15 (29)
MM RECIST progression before PRRT	20 (38)

---

*Other metastatic sites were ovary ($n = 3$), pancreas ($n = 1$), breast ($n = 1$), lung ($n = 1$), pericardium ($n = 2$), testis ($n = 1$), and muscle ($n = 1$).

WHO = World Health Organization; ECOG = Eastern Cooperative Oncology Group; SRI = somatostatin receptor imaging; ULN = upper limit of normal.

Categoric data are number and percentage; continuous data are median and range.

75% of patients presented with a clinical CS. Half of them had MM-related symptoms; the most frequent symptoms were mainly abdominal pain (38%), diarrhea (27%), occlusive syndrome (15%), or mesenteric ischemia symptoms (10%). All but 1 patient had a MM Krenning score of 3 (8%) or 4 (90%) at baseline somatostatin receptor imaging. More than a third (38%) of patients presented with a morphologic progression on the MM, according to RECIST version 1.1, at the time of the first PRRT dose (Table 1).

Effectiveness and Safety of PRRT

Imaging (CT or MRI) was done at a mean of 2.0 mo (range, 1 d to 7 mo) before PRRT and a mean of 4.6 mo (range, 2–11.7 mo) after PRRT. Images and both morphologic and metabolic evaluations were centrally reviewed for 43 (83%) patients, and no difference was found with the first reading. With regard to the primary endpoint, the MM ORR was 4%, and no patient had a metabolic response. The non-MM ORR was 8%, and the non-MM metabolic response rate was 12%. Among the 26 patients with baseline MM-related symptoms, 12 (46%) patients had clinical response (complete in 3 patients and partial in 9 patients). Among the 39 patients presenting with a CS, 18 (46%) patients had a complete or partial response (Table 2). Only 5 (10%) patients presented with MM RECIST progression on a median follow-up of 30.2 mo. The median MM-related PFS was not reached (Fig. 2A; Table 2) and was 50.3 mo (95% CI, 38.2–61.7 mo) on non–MM-related PFS (Fig. 2B; Table 2). The median overall survival was 55.0 mo (95% CI, 39.5–80.8 mo; Table 2). Of the patients who showed MM-related symptoms before PRRT, 42% presented with long-term persistence of partial or complete clinical response.

Most patients (83%) received 4 cycles of ^{177}Lu-DOTATATE. For those who discontinued PRRT prematurely, the main reason was the occurrence of toxicity (8% of the total population): cholestasis ($n = 1$), cytopenia ($n = 1$), and renal insufficiency ($n = 2$; Table 3). Four patients presented with gastrointestinal complications during PRRT: bowel obstruction and abdominal pain ($n = 1$), abdominal pain only ($n = 1$), diarrhea because of mesenteric ischemia ($n = 1$), or vomiting ($n = 1$). Two received a short course of corticosteroids (Table 3). In 6 (12%) patients, long-term gastrointestinal complications occurred (bowel obstruction, abdominal pain, constipation, perforation, or mesenteric ischemia). Two (4%) patients died from MM-related complications, which resulted from a digestive perforation for 1 of the patients (Table 3). Among the 9 patients presenting with early or late complications, 2 patients were theoretically resectable on the MM. The 2 patients who died from MM-related complications were clearly unresectable (stage IV superior mesenteric artery involvement, proximal superior mesenteric venous infiltration, and severe mesenteric fibrosis; Supplemental Table 1).

DISCUSSION

The present study confirms that MM does not respond morphologically to PRRT, which is concordant with the suggestions of Pelle et al. (*2*), who reported 0 of 21 (0%) ORR on mesenteric metastasis, and Blažević et al. (*3*), who reported 5 of 132 (4%) ORR on mesenteric metastasis. The strength of the present study is that it is a multicenter, national study with a retrospective central review of most morphologic and metabolic imaging that pays specific attention to MM outcomes during and after PRRT.

TABLE 2
Effectiveness of ^{177}Lu-DOTATATE PRRT, $n = 52$

Characteristic	Data
Cycles	
<4	9 (17)
4	43 (83)
Dose	
Full	49 (94)
Reduced	3 (6)
MM best morphologic response	
ORR	2 (4)
Stable disease	50 (96)
Non-MM best morphologic response	
ORR	4 (8)
Stable disease	44 (90)
Progressive disease	1 (2)
MM best metabolic response	
ORR	0 (0)
Stable disease	52 (100)
Non-MM best metabolic response	
ORR	6 (12)
Stable disease	43 (88)
MM-related symptom clinical response	
Complete	3/26 (11)
Partial	9/26 (35)
Stability	14/26 (54)
Progression	0/26 (0)
CS clinical response	
Complete or partial	18 (46)
Stability	19 (49)
Progression	0 (0)
Not available	2 (5)
MM-related symptom long-term clinical response	
Complete	3 (11)
Partial	8 (31)
Stability	8 (31)
Progression	3 (11)
Missing data	4 (16)
MM-related PFS (mo)	Not reached
Non-MM PFS (mo)	50.3 (38.2–61.7)
Overall survival (mo)	55.0 (39.5–80.8)

Categoric data are number or number per subpopulation, with percentage in parentheses. Continuous data are median, with 95% CI range in parentheses.

Although the MM ORR was low, only a few patients presented with radiologic MM progression during the follow-up, whereas more than a third of them had progressive MM disease before initiating PRRT; furthermore, the median MM-related PFS was longer than the median non–MM-related PFS. Altogether, this suggests that PRRT

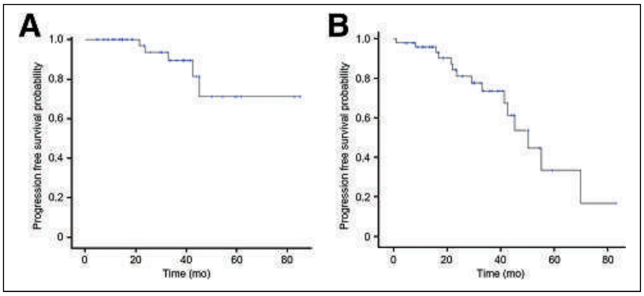

FIGURE 2. Patients' estimated MM-related PFS (A) and non–MM-related PFS (B) since first dose of PRRT.

TABLE 3
Safety of ^{177}Lu-DOTATATE PRRT, $n = 52$

Characteristic	Data
Reason for early discontinuation of PRRT	
General health deterioration	2 (4)
Toxicity	4 (8)
Cholestasis	1 (2)
Cytopenia	1 (2)
Renal insufficiency	2 (4)
Unknown	3 (6)
Occurrence of gastrointestinal complications during PRRT	4* (8)
Bowel obstruction	1 (2)
Abdominal pain	2 (4)
Diarrhea because of mesenteric ischemia	1 (2)
Emesis	1 (2)
Patients receiving short course of corticosteroid therapy	2 (4)
Occurrence of long-term gastrointestinal complications	6* (12)
Bowel obstruction	3 (6)
Abdominal pain	3 (6)
Constipation	2 (4)
Perforation	1 (2)
Mesenteric ischemia	1 (2)
Cause of death in affected patients	
MM-related	2 (4)
Occlusive syndrome with digestive perforation	1 (2)
Missing data	1 (2)
NET-related but non–MM-related	7 (13)
Altered general condition with cachexia	4 (8)
Missing data	3 (6)
Non–NET-related	3 (6)
Unknown	2 (4)

*One patient presented with both gastrointestinal complications during PRRT and long-term gastrointestinal complications.

Data are number and percentage.

could lead to long-term stabilization of the MM. However, this may also be explained by the relatively static growth behavior of mesenteric metastases, as suggested by Blažević et al. (*3*), who found a mesenteric metastasis progression rate close to that reported herein (13.5%). The authors also suggested potential underestimation of disease progression and PRRT response on MMs resulting from the exclusive use of RECIST in this context (*3*). Concerning clinical effectiveness, PRRT significantly affected symptomatic patients. For instance, there was improvement of clinical CS in almost half of the patients, which is concordant with the literature: Zandee et al. (*10*) reported improvement of CS symptoms in at least 50% of patients with NET treated with PRRT. It is also concordant with the results of the NETTER-1 study, which demonstrate significant improvement in the quality of life of patients presenting with a NET treated with PRRT compared with results from high-dose octreotide, partly related to CS improvement (*6*). We also noted clinical improvement in almost half of patients presenting with baseline MM-related clinical symptoms, which reinforces the clinical value of PRRT. This is all the more important because almost half of baseline MM-related symptomatic patients presented with persistence of partial or complete clinical response more than 6 mo after the end of PRRT, suggesting a possible long-term clinical impact of PRRT. However, because 9 patients presented with early or late gastrointestinal complications and 2 patients died from MM-related complications, removal of the MM (when resectable) before PRRT should be discussed in a multidisciplinary tumor board dedicated to NETs.

The present study also indicates that PRRT can be used in patients presenting with baseline MM-related symptoms, because none of the patients in the study presented with progression of symptoms under PRRT. Moreover, relatively few gastrointestinal complications were observed during PRRT in the total population, and only 1 patient presented with bowel obstruction. There are concerns with regard to the potential occurrence of such complications, given Strosberg et al. (*11*) reported that PRRT can lead to bowel obstruction in patients with a mesenteric metastasis by inducing inflammation. However, Laskaratos et al. (*12*) suggested that there is no relationship between the severity of mesenteric fibrosis and the onset of an obstructive symptomatology. It was also suggested by Strosberg et al. (*11*) that a short course of corticosteroids during PRRT could potentially prevent the occurrence of gastrointestinal complications. In the present study, the patient who experienced bowel obstruction did not receive a preventive course of corticosteroids, possibly overestimating the occurrence of gastrointestinal complications if a preventive course of corticosteroids to prevent these symptoms becomes routine practice. Still, a prospective randomized study would be helpful to determine whether such prophylactic treatment would be useful in avoiding locoregional complications of PRRT without altering its efficacy. Moreover, we noted few occurrences of long-term gastrointestinal complications, which provides reassurance on the feasibility of PRRT.

An interesting aside is the finding herein that the non-MM ORR was twice as high as the MM ORR. However, this rate remains lower than that reported in the literature for patients without a mesenteric metastasis; for instance, in the NETTER-1 study, ORR was 18% (*4*), whereas the non-MM ORR reported by Blažević et al. (*3*) was closer (13%) to that found herein. This difference may be explained, at least partly, by differences in the rates of G1 SI-NET, which were higher in the NETTER-1 study (72% vs. 48% herein) (*4*) and closer in the study reported by Blažević et al. (52% vs. 48% herein) (*3*). We could also hypothesize that SI-NETs with MMs have a different carcinogenesis from NETs without MMs that is associated with a lower ORR on the non-MM metastatic sites; this has to be confirmed in prospective studies comparing patients treated by PRRT with versus without a MM.

The limitation of this study, given its retrospective nature based on patient medical records, is that the data may not be accurate among the different centers; a prospective study would be interesting to reinforce the results. In addition, 5-hydroxyindoleacetic acid was not collected; therefore, it was not possible to evaluate the biologic response on CS under PRRT in correlation with the clinical, morphologic, and metabolic responses.

CONCLUSION

This study confirms that ^{177}Lu-DOTATATE PRRT does not lead to morphologic response on MMs (ORR $<$ 5%). However, it allows MM stability, with few MM-related side effects, and has a relevant clinical impact on MM-related symptoms.

DISCLOSURE

This study did not receive specific grants from funding agencies in the public, commercial, or not-for-profit sectors; however, patients were identified from the French national database of the GTE, which is partially supported by IPSEN-pharma. Louis De Mestier is supported by AAA/Novartis, Esteve, IPSEN-pharma, and Sirtex; Magalie Haissaguerre is supported by Novartis, AAA, and IPSEN-pharma; Pauline Afchain is supported by IPSEN-pharma and Novartis; Julien Hadoux is supported by Lilly, AAA, IPSEN-pharma, Roche, Pharma Mar, EISAI, and Novartis; Thierry Lecomte is supported by IPSEN-pharma, AAA, and Novartis; and Thomas Walter is supported by Novartis, IPSEN-pharma, Keocyt, and Sirtex. No other potential conflict of interest relevant to this article was reported.

ACKNOWLEDGMENTS

We thank the patients and their association (APTED) for their participation. We also thank the French organization for neuroendocrine neoplasm management, the Endocan-RENATEN clinical network (constructed and supported by the GTE), and Philip Robinson (DRS, Hospices Civils de Lyon) for his help in article preparation.

KEY POINTS

QUESTION: Is it relevant to propose ^{177}Lu-DOTATATE PRRT to patients with progressive SI-NETs and a retractile MM?

PERTINENT FINDINGS: In a study involving 52 patients, our data confirm that ^{177}Lu-DOTATATE PRRT does not lead to morphologic response on MMs (ORR $<$ 5%); however, it allows MM stability, with few MM-related side effects, and a relevant clinical impact on MM-related symptoms in some patients.

IMPLICATIONS FOR PATIENT CARE: There was improvement of clinical CS in almost half of the patients and clinical improvement in almost half of patients presenting with baseline MM-related clinical symptoms, which reinforces the clinical value of PRRT. This is all the more important because almost half of baseline MM-related symptomatic patients presented with persistence of partial or complete clinical response more than 6 mo after the end of PRRT, suggesting a possible long-term clinical impact of PRRT.

REFERENCES

1. Frilling A, Akerström G, Falconi M, et al. Neuroendocrine tumor disease: an evolving landscape. *Endocr Relat Cancer.* 2012;19:R163–R185.
2. Pelle E, Al-Toubah T, Morse B, El-Haddad G, Strosberg J. Desmoplastic mesenteric lesions do not respond radiographically to peptide receptor radionuclide therapy. *J Neuroendocrinol.* 2021;33:e12936.
3. Blažević A, Brabander T, Zandee WT, et al. Evolution of the mesenteric mass in small intestinal neuroendocrine tumours. *Cancers (Basel).* 2021;13:443.
4. Cives M, Strosberg JR. Gastroenteropancreatic neuroendocrine tumors. *CA Cancer J Clin.* 2018;68:471–487.
5. Strosberg J, El-Haddad G, Wolin E, et al. Phase 3 trial of ^{177}Lu-DOTATATE for midgut neuroendocrine tumors. *N Engl J Med.* 2017;376:125–135.
6. Strosberg J, Wolin E, Chasen B, et al. Health-related quality of life in patients with progressive midgut neuroendocrine tumors treated with ^{177}Lu-DOTATATE in the phase III NETTER-1 trial. *J Clin Oncol.* 2018;36:2578–2584.
7. Lardière-Deguelte S, De Mestier L, Appéré F, et al. Toward a preoperative classification of lymph node metastases in patients with small intestinal neuroendocrine tumors in the era of intestinal-sparing surgery. *Neuroendocrinology.* 2016;103:552–559.
8. Bertani E, Zugni F, Radice D, et al. Predicting resectability of primary tumor and mesenteric lymph-node masses in patients with small-intestine neuroendocrine tumors. *Updates Surg.* 2022;74:1697–1704.
9. Young H, Baum R, Cremerius U, et al. Measurement of clinical and subclinical tumour response using [^{18}F]-fluorodeoxyglucose and positron emission tomography: review and 1999 EORTC recommendations. European Organization for Research and Treatment of Cancer (EORTC) PET Study Group. *Eur J Cancer.* 1999;35:1773–1782.
10. Zandee WT, Brabander T, Blažević A, et al. Peptide receptor radionuclide therapy with ^{177}Lu-DOTATATE for symptomatic control of refractory carcinoid syndrome. *J Clin Endocrinol Metab.* 2021;106:e3665–e3672.
11. Strosberg JR, Al-Toubah T, Pellè E, et al. Risk of bowel obstruction in patients with mesenteric or peritoneal disease receiving peptide receptor radionuclide therapy. *J Nucl Med.* 2021;62:69–72.
12. Laskaratos F, Cox N, Woo WL, et al. Assessment of changes in mesenteric fibrosis (MF) after peptide receptor radionuclide therapy (PRRT) in midgut neuroendocrine tumours (NETs) [abstract]. *Neuroendocrinology.* 2019;108(suppl 1):217.

Long-Term Overall Survival After Selective Internal Radiation Therapy for Locally Advanced Hepatocellular Carcinomas: Updated Analysis of DOSISPHERE-01 Trial

Etienne Garin[1,2], Lambros Tselikas[3], Boris Guiu[4], Julia Chalaye[5], Yan Rolland[1,6], Thierry de Baere[3], Eric Assenat[4], Vania Tacher[5], Xavier Palard[1], Desirée Déandreis[3], Denis Mariano-Goulart[4], Giuliana Amaddeo[5], Karim Boudjema[7], Antoine Hollebecque[3], Mohamad Azhar Meerun[4], Helen Regnault[5], Eric Vibert[8], Boris Campillo-Gimenez[1,6], and Julien Edeline[1,9]

[1]Cancer Institute Eugene Marquis, Rennes, France; [2]University of Rennes, INSERM, INRAE, Nutrition Métabolismes et Cancer U1317, Rennes, France; [3]Gustave Roussy, University of Paris-Saclay, Villejuif, France; [4]Montpellier University Hospital, Montpellier, France; [5]AP-HP, Hopitaux Universitaires Henri Mondor, Creteil, France; [6]University of Rennes, INSERM, LTSI–UMR 1099, Rennes, France; [7]Department of Hepatobiliary and Digestive Surgery, CHU Rennes, Rennes, France; [8]Centre Hepato-Biliaire, Paul Brousse Hospital, AP-HP, Paris Saclay University, Villejuif, France; and [9]University of Rennes, INSERM, COSS–UMR_S 1242, Rennes, France

Interim analysis of the DOSISPHERE-01 study demonstrated a strong improvement in response and overall survival (OS) on using ^{90}Y-loaded glass microspheres with personalized dosimetry compared with standard dosimetry in patients with nonoperable locally advanced hepatocellular carcinoma. This report sought to provide a long-term analysis of OS. **Methods:** In this phase II study (ClinicalTrials.gov identifier NCT02582034), treatment was randomly assigned (1:1) with the goal to deliver either at least 205 Gy (if possible >250–300 Gy) to the index lesion in the personalized dosimetry approach (PDA) or 120 ± 20 Gy to the treated volume in the standard dosimetry approach (SDA). The 3-mo response of the index lesion was the primary endpoint, with OS being one of the secondary endpoints. This report is a post hoc long-term analysis of OS. **Results:** Overall, 60 hepatocellular carcinoma patients with at least 1 lesion larger than 7 cm and more than 30% of hepatic reserve were randomized (intent-to-treat population: PDA, $n = 31$; SDA, $n = 29$), with 56 actually treated (modified intent-to-treat population: $n = 28$ in each arm). The median follow-up for long-term analysis was 65.8 mo (range, 2.1–73.1 mo). Median OS was 24.8 mo and 10.7 mo (hazard ratio [HR], 0.51; 95% CI, 0.29–0.9; $P = 0.02$) for PDA and SDA, respectively, in the modified intent-to-treat population. Median OS was 22.9 mo for patients with a tumor dose of at least 205 Gy, versus 10.3 mo for those with a tumor dose of less than 205 Gy (HR, 0.42; 95% CI, 0.22–0.81; $P = 0.0095$), and was 22.9 mo for patients with a perfused liver dose of 150 Gy or higher, versus 10.3 mo for those with a perfused liver dose of less than 150 Gy (HR, 0.42; 95% CI, 0.23–0.75; $P = 0.0033$). Lastly, median OS was not reached in patients who were secondarily resected ($n = 11$, 10 in the PDA group and 1 in the SDA group), versus 10.8 mo in those without secondary resection ($n = 45$) (HR, 0.17; 95% CI, 0.065–0.43; $P = 0.0002$). Only resected patients displayed favorable long-term OS rates, meaning an OS of more than 50% at 5 y. **Conclusion:** After longer follow-up, personalized dosimetry sustained a meaningful improvement in OS, which was dramatically improved for patients who were accurately downstaged toward resection, including most portal vein thrombosis patients.

Key Words: hepatocellular carcinoma; ^{90}Y-loaded glass microspheres; personalized dosimetry; downstaged; portal vein thrombosis

J Nucl Med 2024; 65:264–269
DOI: 10.2967/jnumed.123.266211

Hepatocellular carcinoma is the most common primary liver cancer, being the third leading cause of cancer-related death worldwide, with approximately 745,000 deaths reported annually (*1*). Selective internal radiation therapy (SIRT) using ^{90}Y-loaded glass microspheres can be used for patients with early-stage to locally advanced hepatocellular carcinoma (*2,3*).

Despite the negativity of all randomized trials comparing ^{90}Y-loaded resin microspheres versus sorafenib (*4–6*), without any personalized dosimetry used, the interest in SIRT for locally advanced hepatocellular carcinoma is returning because of the results of the randomized DOSISPHERE-01 study (*7*). This randomized phase II trial using ^{90}Y-loaded microspheres sought to compare the effectiveness of ^{90}Y-loaded microspheres using a personalized dosimetry approach (PDA) versus a standard dosimetry approach (SDA), which was stopped at the interim analysis because of the pronounced superiority of PDA in primary endpoint terms. Indeed, the 3-mo response of the index lesion was 71% in PDA versus only 36% in SDA ($P = 0.0074$) (*7*). On study analysis, median overall survival (OS) was significantly improved in the intent-to-treat population in the PDA group: 26.6 mo (95% CI, 11.7 mo to not reached) versus 10.7 mo (95% CI, 6.0–16.8 mo) in the SDA group (hazard ratio [HR], 0.42; 95% CI, 0.21–0.83; $P = 0.0096$) (*7*). However, at that time, OS evaluation was performed with a short follow-up time of 27.2 mo because of early trial termination at interim analysis. Moreover, a description of long-term follow-up of patients who could be resected after downsizing is important.

Received Jun. 22, 2023; revision accepted Nov. 7, 2023.

For correspondence or reprints, contact Etienne Garin (e.garin@rennes.unicancer.fr).

Our main objective here was to report the OS evaluation after updated longer-term follow-up in the DOSISPHERE-01 cohort.

MATERIALS AND METHODS

Study Design and Population

The study design and population have been published previously (*7*). Briefly, eligible patients were randomly assigned (1:1) to the PDA and SDA groups. Treatment was scheduled to deliver a tumor dose (TD) of at least 205 Gy (if possible $>$250–300 Gy) to the index lesion in the PDA group or 120 ± 20 Gy to the treated volume in the SDA group. The response rate of the index lesion at 3 mo, according to the criteria of the European Association for the Study of the Liver, was the primary endpoint, with OS being one of the secondary endpoints. Some of the most specific eligibility criteria applied in the DOSISPHERE-01 trial were at least 1 lesion larger than 7 cm; the ability to spare at least 30% of the liver volume from radiation; exclusion based on treatment simulation, including a high lung shunt leading to an excessive lung dose (providing $>$30 Gy); a digestive shunt; and poor tumor and/or poor portal vein thrombosis (PVT) targeting.

All patients provided written informed consent before undergoing study-specific procedures. The study was performed in accordance with the Declaration of Helsinki principles. The study protocol was approved by the ethics committee of the University Hospital La Cavalle Blanche (IRB-ID approval 2015-A00894-45) and registered on ClinicalTrials.gov (NCT02582034).

Procedures

^{90}Y-loaded glass microspheres were used with a lobar approach. The dosimetry evaluation was based on ^{99m}Tc-macroaggregated albumin SPECT/CT (quantification as previously described (*8*)).

Statistics

Results were presented according to the modified intent-to-treat population, defined as the overall treated patients. Long-term follow-up was estimated using the reverse Kaplan–Meier approach. OS curves were estimated by means of the Kaplan–Meier methodology and compared using log-rank tests. Product-limit estimates were presented by arm using median times and 1- to 5-y survival rates with the corresponding 2-sided 95% CI. HRs were computed using univariable Cox regression. A priori subgroup analyses were conducted as recorded in the initial DOSISPHERE protocol (*7*). Post hoc comparisons were added comparing survival curves according to TD ($<$205 Gy vs. $\geq$205 Gy), perfused liver dose (PLD) ($<$150 Gy vs. $\geq$150 Gy), and secondary resection (resected vs. not resected). A multivariable analysis of OS was also performed including these 3 additional variables and all previous subgroup factors. A Cox proportional-hazards model was fitted using significant variables (threshold < 0.15) from the univariate analysis. An ascending and descending stepwise procedure was used to select variables, minimizing the Akaike criteria. Data were analyzed using R version 4.2.1 (2022-06-23 ucrt; https://www.R-project.org/).

RESULTS

The main individual characteristics of the study population are presented in Table 1. Median follow-up was 65.8 mo (range, 2.1–73.1 mo).

As shown in Figure 1, median OS was 24.8 mo (95% CI, 11–36.5 mo) in the PDA group versus 10.7 mo (95% CI, 6–14.9 mo) in the SDA group (HR, 0.51; 95% CI, 0.29–0.9; $P = 0.020$). The effect of personalized dosimetry was generally consistent across subgroups according to baseline characteristics (Fig. 2).

Censored at time of surgery, median OS was 11.7 mo (95% CI, 8.12–22.9 mo) in the PDA group versus 10.8 mo (95% CI, 6–16.8 mo) in the SDA group (HR, 0.77; 95% CI, 0.44–1.4; $P = 0.37$) (Fig. 1).

TABLE 1
Summary of Main Demographic and Baseline Characteristics of Patients in Modified Intent-to-Treat Population

Characteristic	PDA (*n* = 28)	SDA (*n* = 28)
Age (y)	64.8 ± 10.1	62.5 ± 63.7
Child classification		
A5	22 (78.6%)	22 (78.6%)
A6/B7	6 (21.4%)	6 (21.4%)
ECOG performance status		
0	16 (57.1%)	13 (46.4%)
1	12 (42.9%)	15 (53.6%)
BCLC classification		
B	3 (10.7%)	2 (7.1%)
C	25 (89.3%)	26 (92.9%)
Portal vein invasion		
Present	18 (64.3%)	21 (75%)
Absent	10 (35.7%)	7 (25%)
Cirrhosis etiology		
Alcohol	9 (32.1%)	9 (32.1%)
Viral hepatitis	7 (25%)	9 (32.1%)
Hemochromatosis	1 (3.6%)	0
NASH	3 (10.7%)	3 (10.7%)
Mixture (alcohol + other)	4 (14.3%)	3 (10.7%)
No cirrhosis	4 (14.3%)	4 (14.3%)
Tumor size (cm)	10.54 ± 2.43	10.92 ± 2.57

ECOG = Eastern Cooperative Oncology Group; BCLC = Barcelona Clinic of Liver Cancer; NASH = nonalcoholic steatohepatitis.

Qualitative data are number and percentage; continuous data are mean ± SD.

In patients with PVT, which was a patient subgroup of particular interest (*n* = 39), median OS was 22 mo (95% CI, 10.3–36.5 mo) in the PDA group versus 9.4 mo (95% CI, 5.3–17.6 mo) in the SDA group (HR, 0.52; 95% CI, 0.26–0.1; $P = 0.058$) (Fig. 1).

Concerning post hoc comparison (Fig. 3), median OS was 22.9 mo (95% CI, 11–48.1 mo) in patients with a TD of 205 Gy or higher versus 10.3 mo in those with a TD of less than 205 Gy (95% CI, 5.9–17.6 Gy; HR, 0.42; 95% CI, 0.22–0.81; $P = 0.010$). Median OS was 22.9 mo (95% CI, 11–48.1 mo) in patients with a PLD of 150 Gy or higher versus 10.3 mo in those with a PLD of less than 150 Gy (95% CI, 5.9–17.6 Gy; HR, 0.42; 95% CI, 0.23–0.75; $P = 0.003$). Lastly, median OS was not reached (95% CI, 21.2 mo to not reached) in patients who were secondarily resected (*n* = 11; 10 in the PDA group and 1 in the SDA group) versus 10.8 mo (95% CI, 7.9–14 mo) in those without secondary resection (*n* = 45) (HR, 0.17; 95% CI, 0.06–0.43; $P < 0.001$).

Estimated survival rates, by years, in the modified intent-to-treat population and subgroup population reported above have been presented in Table 2.

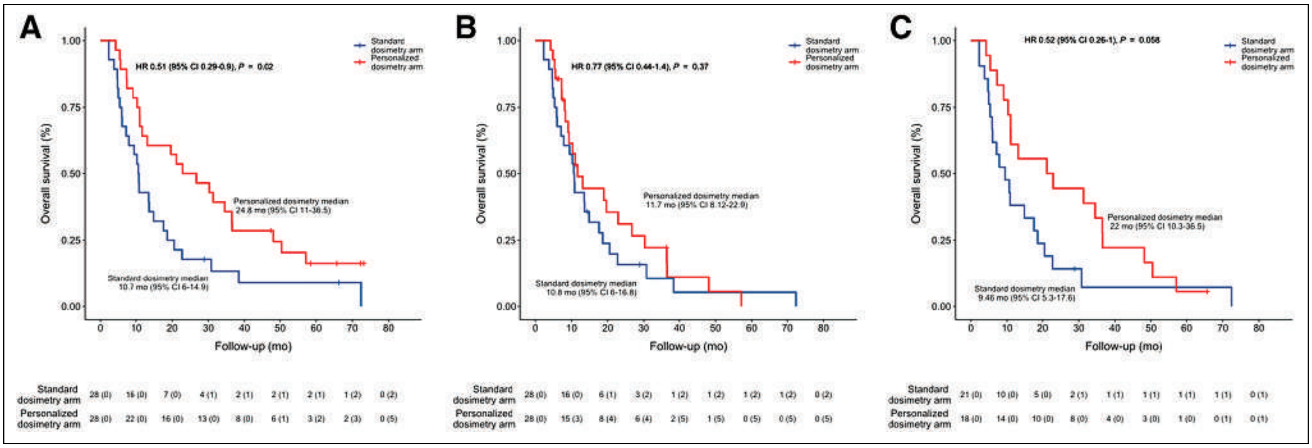

FIGURE 1. OS curves according to randomization for modified intent-to-treat population: median OS for global population (A), global population censored at time of surgery (B), and PVT patient subgroup (C).

In multivariate analysis (Table 3), only 2 parameters were significantly associated with long-term OS: secondary resection (adjusted HR, 0.15; 95% CI, 0.06–0.43; adjusted $P < 10^{-3}$) and bilobar disease (adjusted HR, 2.3; 95% CI, 1.24–4.37; adjusted $P = 0.008$).

DISCUSSION

After analysis of long-term 65.8-mo follow-up, improvement in median OS was shown to be sustained in the PDA group. The 22.9-mo (95% CI, 11–36.5 mo) median OS reached in the PDA group was observed in a population with severely advanced disease, including PVT involvement for 65% of them and a mean tumor size of 10.6 cm (*7*). These results compare favorably with results obtained in immunotherapy trials in which the reported median OS was 19.4 mo (95% CI, 11–36.5 mo) with atezolizumab plus bevacizumab (*9*) and 16.4 mo (95% CI, 14.1–19.5 mo) with durvalumab plus tremelimumab (*10*).

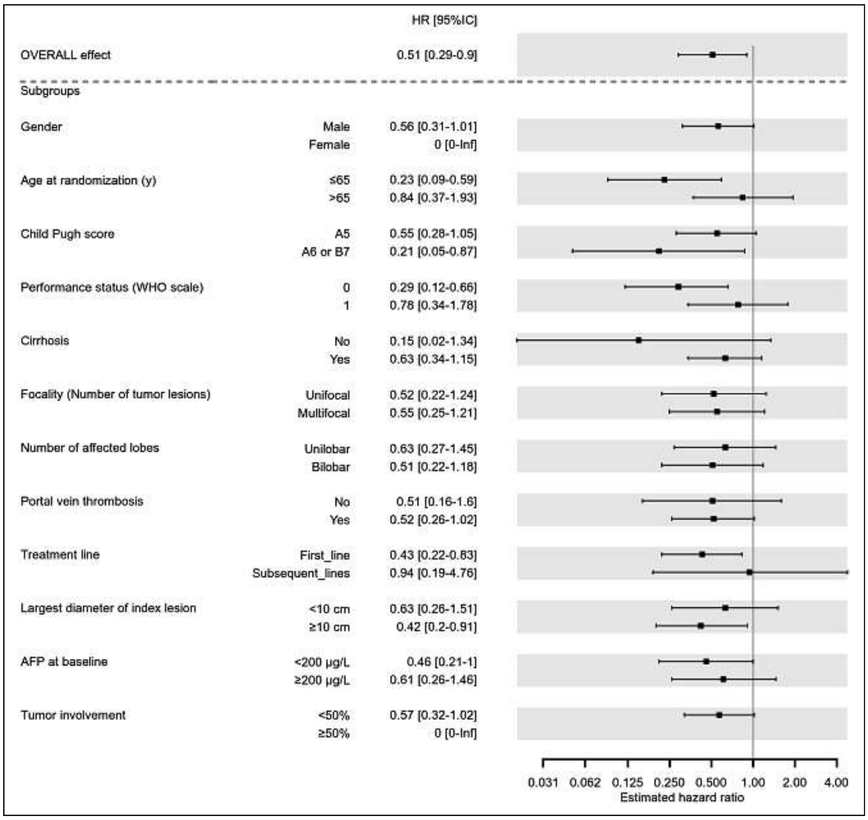

FIGURE 2. Forest plot analysis of HRs regarding treatment arms, for prespecified subgroups of interest in modified intent-to-treat population. AFP = α-fetoprotein; WHO = World Health Organization.

However, it must be mentioned that a direct comparison between SIRT studies and studies using systemic drugs turns out to be hazardous, especially on account of differences in the patient populations included. Indeed, in SIRT trials, PVT was shown to be more common (∼65% in DOSISPERE-01 (*7*) vs. only 26%–38% in immunotherapy trials (*9,10*)); SIRT patients did not exhibit any extrahepatic spread, whereas 53%–63% of immunotherapy-treated patients exhibited distant metastases (*9,10*); additionally, underlying cirrhosis characteristics and etiology differed (hepatitis B was reported in only 26% of SIRT-treated patients (*7*) vs. 31%–49% of immunotherapy-treated ones (*9,10*)).

Results for PVT patients deserve to be further highlighted, given that this patient population is of specific interest. Indeed, PVT patients were classified as advanced patients according to the Barcelona Clinic of Liver Cancer classification (*2*), similarly to patients with extrahepatic spread, despite portal vein invasion representing only a locoregional spread, which is thus accessible to SIRT (*3,11,12*), unlike distant metastasis. On the basis of this classification, the recommended treatment of PVT patients is systemic therapy rather than locoregional therapy such as SIRT (*2*). Although the statistically significant difference in OS for PVT patients was lost in this long-term analysis, this was most likely due to a lack of power, as this study was stopped by

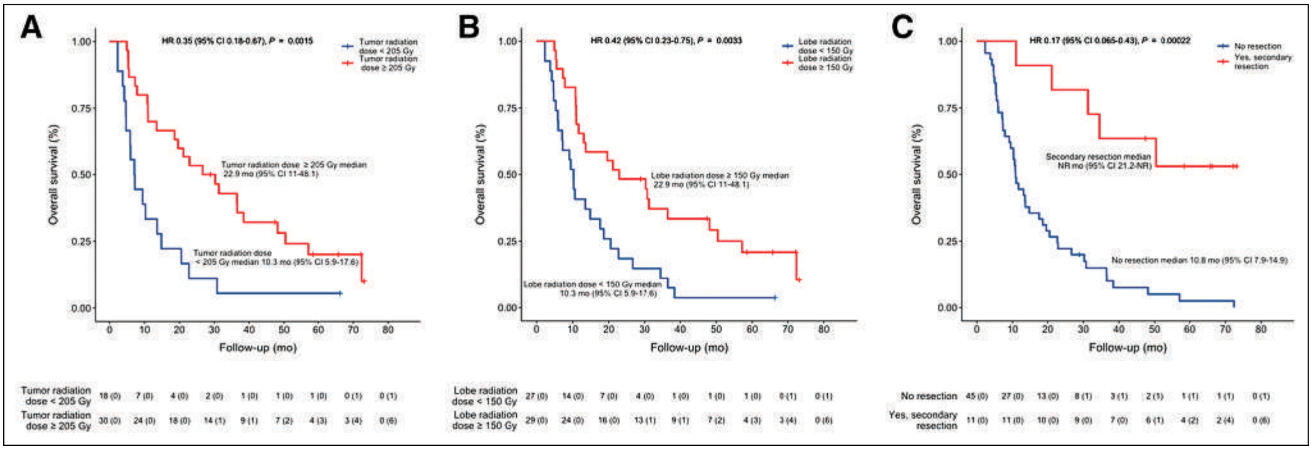

FIGURE 3. Median OS based on group of interest: TD (A), PLD (B), and secondary resection status (C). NR = not reached.

anticipation, whereas the trends are still striking, with a median OS of 22 mo (95% CI, 10.3–36.5 mo) in the PDA group versus 9.5 mo (95% CI, 5.3–17.6 mo) in the SDA group (HR, 0.52; 95% CI, 0.26–0.1; $P = 0.058$). Here, again, the median OS of 22 mo (95% CI, 10.3–36.5 mo) that was reached in the PDA group in PVT patients compares favorably with that obtained in immunotherapy-treated patients, for whom the median OS in the event of macrovascular invasion was 14.2 mo (95% CI, 11–19.4 mo) under atezolizumab plus bevacizumab (*9*) but was not reported for the durvalumab-plus-tremelimumab combination (*10*).

Regarding dosimetry parameters, the impact of TD on OS remains significant. Furthermore, this study revealed a significant impact exerted by PLD on OS (not reported in the first report). Indeed, median OS was 22.9 mo (95% CI, 11–48.1 mo) for patients receiving a PLD of 150 Gy or more versus 10.3 mo (95% CI, 5.9–17.6 mo) for those treated with a PLD of less than 150 Gy. Although TD and PLD are not independent prognostic indicators, this point is of particular interest for technical reasons when personalized dosimetry based on TD is difficult to perform. This can be the case given that tumor segmentation can turn out to be challenging in several instances (disease not well delineated, infiltrative disease, or multiple lesions), as when there is a large lesion with multiple feeders. In this situation, ^{99m}Tc-macroaggregated albumin dosimetry would often require, to be accurate, 1 injection of ^{99m}Tc-macroaggregated albumin for each feeder, separated by at least 24 h. In those situations, a PDA based on the PLD is doable, as for radiation segmentectomy (*13,14*), in this specific patient population exhibiting good liver function and at least 30% of hepatic reserve.

The analysis of OS rates from 2 to 5 y likewise discloses additional information of interest. For patients with poor features, namely those randomly assigned to SDA, receiving a TD of less than 205 Gy or a PLD of less than 150 Gy, or not downstaged to resection, OS rates were dramatically decreased, from 13% to 22% at 2 y and to less than 10% at 4 y. For patients with good features, besides those who were resected, OS rates were between 44% and 50% at 2 y and between 33% and 37% at 3 y. Only resected patients displayed an OS rate of more than 50% at 5 y.

The huge prognostic impact of secondary surgery on long-term OS in this population of patients with large lesions and often PVT, even with PDA, is highlighted by the loss of difference in median OS censored at the time of surgery between arms, as by the

TABLE 2
OS Rates from 2 to 5 Years in Modified Intent-to-Treat Population

Parameter	2 y	3 y	5 y
PDA	50.0 (34.5–72.4)	35.7 (21.7–58.7)	16.4 (6.8–38.9)
SDA	17.8 (8–39.5)	13.3 (5–35.5)	8.9 (2.5–31.5)
PVT+ (PDA)	44.4 (26.5–74.5)	33.3 (17.3–64.1)	5.6 (0.8–37.3)
PVT+ (SDA)	14.2 (5–40.7)	7.1 (1.2–40.6)	7.1 (1.2–40.6)
TD ≥ 205 Gy	48.5 (34.1–68.9)	35.7 (22.4–56.8)	18.3 (8.5–39.1)
TD < 205 Gy	13.3 (3.6–48.4)	13.3 (3.6–48.4)	6.7 (1–44.3)
PLD ≥ 150 Gy	48.3 (33.1–70.4)	37.1 (22.9–60)	20.9 (9.8–44.2)
PLD < 150 Gy	18.5 (8.3–40.9)	11.1 (3.8–32.3)	3.7 (0.5–25.3)
Resected	81.8 (61.9–100)	63.6 (40.7–99.5)	53.0 (29.9–94)
Not resected	22.2 (12.8–38.4)	15 (7.8–30.5)	2.5 (0.3–17.1)

Data in parentheses are 95% CIs.

TABLE 3
Multivariate Analysis of Factors Associated with OS

Factor	HR	*P*	Adjusted HR	Adjusted *P*
PDA vs. SDA	0.51 (0.29–0.9)	0.018	—	—
Resection after SIRT, yes vs. no	0.17 (0.06–0.43)	$<10^{-3}$	0.15 (0.06–0.4)	$<10^{-3}$
Sex, female vs. male	0.86 (0.27–2.77)	0.797	—	—
Age, >65 y vs. ≤65 y	1.13 (0.63–2)	0.684	—	—
Child Pugh score, A6 or B7 vs. A5	1.61 (0.84–3.1)	0.151	—	—
ECOG, 1 vs. 0	1.23 (0.69–2.19)	0.471	—	—
Cirrhosis, yes vs. no	2.4 (0.94–6.12)	0.059	—	—
Multifocal vs. unifocal	20.3 (1.13–3.65)	0.016	—	—
Bilobar vs. unilobar	2.1 (1.17–3.76)	0.011	2.33 (1.24–4.37)	0.008
PVT, yes vs. no	1.88 (0.98–3.63)	0.054	—	—
Treatment line, subsequent vs. first	1.09 (0.54–2.21)	0.808	—	—
Index lesion size, ≥10 cm vs. <10 cm	0.99 (0.56–1.76)	0.968	—	—
AFP, ≥200 μg/L vs. <200 μg/L	1.6 (0.91–2.83)	0.098	—	—
Tumor involvement, ≥50% vs. <50%	0.95 (0.29–3.07)	0.927	—	—
TD, ≥205 Gy vs. <205 Gy	0.42 (0.22–0.81)	0.007	—	—
PLD, ≥150 Gy vs. <150 Gy	0.42 (0.23–0.75)	0.002	—	—

ECOG = Eastern Cooperative Oncology Group; AFP = α-fetoprotein.
Data in parentheses are 95% CIs.

multivariate analysis. This result, the major impact of secondary resection to achieve prolonged long-term OS even with personalized dosimetry with large lesions and PVT, was not necessarily intuitive as it is not the case for small lesions. Indeed, in the LEGACY study (*15*), with 94% of lesions smaller than 5 cm (and 62% < 3 cm), OS was not driven by secondary surgery. Indeed, for patients who received SIRT as a unique treatment, OS was similar to that of patients with resection or transplantation (3-y OS rate of 86.6% without secondary surgery vs. 92.8% for patients with resection or transplantation) (*15*). The difference in the impact of surgery between these 2 kinds of populations can be explained by the fact that complete pathologic response is more frequently observed for small lesions, that is, in 67% of the patients of the LEGACY study who underwent resection or transplantation (*14*) versus only 10% for large lesions with often PVT in the DOSISPHERE-01 study (*7*). Furthermore, patients with large lesions and often PVT have a much higher risk of recurrence (median PFS was only 6 mo in the DOSISPHERE-01 study vs. not reached at 24 mo in the Legacy study (*15*)), then SIRT allowed to accurately evaluate the biological test of time, allowing surgery to be performed only on patients with a low risk of recurrence.

Two key messages arise from these observations. First, everything possible has to be done with SIRT to downstage patients to surgery, even including PVT patients, as it is the only way to achieve acceptable prolonged median OS rates, including an OS of more than 50% at 5 y. Such prolongation of median OS has recently been described after post-SIRT surgery performed for initially unresectable patients (*16*). In that study, including 18 patients who were accurately downstaged and then resected, 78% of whom presented with PVT, median OS was 61.8 mo (95% CI, 31.4 mo to not reached) (*16*). Thus, SIRT is most likely to optimize preparation and accurate selection of good PVT candidates who are eligible for surgery on account of its strong debulking effect (including portal vein complete response and revascularization) (*7,11*) and its ability to ensure contralateral liver hypertrophy, which is usually attained within 3–6 mo (*17,18*). In addition, biological tests performed in a timely manner permit exclusion of patients with early relapse after SIRT.

The second key message arising from our analysis is that even for patients with good features, excepting the resected ones, the OS rates were seen to decrease quite rapidly between 2 and 4 y, which is another strong argument to evaluate SIRT delivered in combination with immunotherapy in this patient population. Indeed, several arguments are in favor of combining SIRT with immunotherapy, including the strong debulking effect of SIRT in the treated area, even in the presence of large lesions (*7*). The systemic action of immunotherapy will be complementary to the local action of SIRT. Furthermore, a potential synergy between both approaches is awaited as SIRT is known to induce an immune response (*19,20*). Additional arguments for these combinations could be situations in which immunotherapy efficacy is likely diminished, such as in patients without viral hepatitis, in whom the HR was found to be 1.05 with atezolizumab plus bevacizumab versus sorafenib (*9*) but 0.58 for patients with viral hepatitis B. This may also apply to large lesions. Indeed, the response rate (modified RECIST) for the atezolizumab-plus-bevacizumab arm was significantly ($P = 0.0097$) lower in the presence of lesions larger than 5 cm than in the presence of lesions smaller than 5 cm, being 26.1% versus 40.9%, respectively (data calculation based on results presented in Fig. 1 (*21*)).

In addition to the rather small number of patients included, a major limitation of this study is that SIRT using personalized dosimetry was not randomized to this population's standard treatment, consisting of atezolizumab plus bevacizumab or double immunotherapy. Therefore, drawing definite conclusions about the role of SIRT in this specific population is not possible. Thus, further randomized studies are warranted to better define this role.

CONCLUSION

After a long-term follow-up period, a meaningful improvement in OS was sustained after personalized dosimetry. OS was dramatically improved for patients who were accurately downstaged toward resection and then resected, including most PVT patients. However, except for resected patients, the 5-y survival rates remain quite low. Randomized trials comparing SIRT with personalized dosimetry plus immunotherapy versus immunotherapy alone are now warranted in this specific patient population to better define the place of SIRT for this indication.

DISCLOSURE

Etienne Garin reports receiving a grant, personal fees, and nonfinancial support from Boston Scientific during the conduct of the study. Lambros Tselikas reports personal fees from Boston Scientific, Sirtex, and GE Healthcare; grants from Terumo and the Bristol Myers Squibb Foundation; and nonfinancial support from GE Healthcare during the conduct of the study. Boris Guiu reports personal fees from Boston Scientific during the conduct of the study. Julien Edeline reports receiving a grant from Boston Scientific during the conduct of the study; personal fees from Boston Scientific, Bayer, Roche, Eisai, Merck Sharpe & Dohme, AstraZeneca, and Ipsen; grants and personal fees from Bristol Myers Squibb; and nonfinancial support from Amgen outside the submitted work. Thierry de Baere reports grants from Terumo and personal fees from Guerbet and Terumo during the conduct of the study. Antoine Hollebecque reports nonfinancial support from Servier, Incyte, and Lilly and personal fees from Amgen, Eisai, and Gritstone Oncology outside the submitted work. Helen Regnault reports personal fees from Boston Scientific outside the submitted work. Xavier Palard, Boris Campillo-Gimenez, and Yan Rolland report receiving a grant from Boston Scientific during the conduct of the study. No other potential conflict of interest relevant to this article was reported.

KEY POINTS

QUESTION: Does long-term analysis maintain substantial OS improvement for locally advanced hepatocellular carcinoma patients treated with SIRT using personalized dosimetry?

PERTINENT FINDINGS: In this randomized study comparing personalized dosimetry versus a standard dosimetry, OS improvement was maintained during long-term analysis of 5 y. This is particularly true for patients accurately downstaged to resection, whose OS rate at 5 y was higher than 50%.

IMPLICATIONS FOR PATIENT CARE: SIRT must be used with personalized dosimetry for locally advanced hepatocellular carcinoma, and SIRT with personalized dosimetry may become the standard care for well-selected patients with advanced hepatocellular carcinoma.

REFERENCES

1. Sung H, Ferlay J, Siegel RL, et al. Global cancer statistics 2020: GLOBOCAN estimates of incidence and mortality worldwide for 36 cancers in 185 countries. *CA Cancer J Clin.* 2021;71:209–249.
2. Reig M, Forner A, Rimola J, et al. BCLC strategy for prognosis prediction and treatment recommendation: the 2022 update. *J Hepatol.* 2022;76:681–693.
3. Salem R, Gabr A, Riaz A, et al. Institutional decision to adopt Y90 as primary treatment for hepatocellular carcinoma informed by a 1000-patient 15-year experience. *Hepatology.* 2018;68:1429–1440.
4. Vilgrain V, Pereira H, Assenat E, et al. Efficacy and safety of selective internal radiotherapy with yttrium-90 resin microspheres compared with sorafenib in locally advanced and inoperable hepatocellular carcinoma (SARAH): an open-label randomised controlled phase 3 trial. *Lancet Oncol.* 2017;18:1624–1636.
5. Chow PKH, Gandhi M, Tan S-B, et al. SIRveNIB: selective internal radiation therapy versus sorafenib in Asia-Pacific patients with hepatocellular carcinoma. *J Clin Oncol.* 2018;36:1913–1921.
6. Ricke J, Klümpen HJ, Amthauer H, et al. Impact of combined selective internal radiation therapy and sorafenib on survival in advanced hepatocellular carcinoma. *J Hepatol.* 2019;71:1164–1174.
7. Garin E, Tselikas L, Guiu B, et al. Selective internal radiation therapy (SIRT) using personalised dosimetry for locally advanced hepatocellular carcinoma (HCC) patients: a multicentre randomised phase 2 study (DOSISPHERE-01 trial). *Lancet Gastroenterol Hepatol.* 2021;6:17–29.
8. Garin E, Lenoir L, Yan Rolland Y, et al. ^{99m}Tc-MAA SPECT/CT based dosimetry accurately predicts tumour response and survival in HCC patients treated with ^{90}Y-loaded glass microspheres: preliminary results. *J Nucl Med.* 2012;53:255–263.
9. Cheng AL, Qin S, Ikeda M, et al. Updated efficacy and safety data from IMbrave150: atezolizumab plus bevacizumab vs. sorafenib for unresectable hepatocellular carcinoma. *J Hepatol.* 2022;76:862–873.
10. Abou-Alfa GK, Lau G, Kudo M, et al. Tremelimumab plus durvalumab in unresectable hepatocellular carcinoma. *NEJM Evid.* 2022;1:1–12.
11. Garin E, Rolland Y, Edeline J, et al. Personalized dosimetry and intensification concept with ^{90}Y-loaded glass microsphere radioembolization induce prolonged overall survival in hepatocellular carcinoma patients with portal vein thrombosis. *J Nucl Med.* 2015;56:339–346.
12. Spreafico C, Sposito C, Vaiani M, et al. Development of a prognostic score to predict response to yttrium-90 radioembolization for hepatocellular carcinoma with portal vein invasion. *J Hepatol.* 2018;68:724–732.
13. Vouche M, Habib A, Ward TJ, et al. M. Unresectable solitary hepatocellular carcinoma not amenable to radiofrequency ablation: multicenter radiology-pathology correlation and survival of radiation segmentectomy. *Hepatology.* 2014;60:192–201.
14. Gabr A, Riaz A, Johnson GE, et al. Correlation of Y90-absorbed radiation dose to pathological necrosis in hepatocellular carcinoma: confirmatory multicenter analysis in 45 explants. *Eur J Nucl Med Mol Imaging.* 2021;48:580–583.
15. Salem R, Johnson GE, Kim E, et al. Yttrium-90 radioembolization for the treatment of solitary, unresectable HCC: the LEGACY study. *Hepatology.* 2021;74:2342–2352.
16. Meerun MA, Allimant C, Rivière B, et al. Large, multifocal or portal vein-invading HCCs downstaged by Y90 using personalized dosimetry: safety, pathological results and outcomes after surgery. *Hepatobiliary Surg Nutr.* 2023;1:351–365.
17. Gaba RC, Lewandowski RJ, Kulik LM, et al. Radiation lobectomy: preliminary findings of hepatic volumetric response to lobar yttrium-90 radioembolization. *Ann Surg Oncol.* 2009;16:1587–1596.
18. Palard X, Edeline J, Rolland Y, et al. Dosimetric parameters predicting contralateral liver hypertrophy after unilobar radioembolization of hepatocellular carcinoma. *Eur J Nucl Med Mol Imaging.* 2018;45:392–401.
19. Chew V, Lee YH, Pan L, et al. Immune activation underlies a sustained clinical response to yttrium-90 radioembolisation in hepatocellular carcinoma. *Gut.* 2019; 68:335–346.
20. Craciun L, de Wind R, Demetter P, et al. Retrospective analysis of the immunogenic effects of intra-arterial locoregional therapies in hepatocellular carcinoma: a rationale for combining selective internal radiation therapy (SIRT) and immunotherapy. *BMC Cancer.* 2020;20:135.
21. Salem R, Li D, Sommer N, et al. Characterization of response to atezolizumab + bevacizumab versus sorafenib for hepatocellular carcinoma: results from the IMbrave150 trial. *Cancer Med.* 2021;10:5437–5447.

Clinical Outcomes After Personalized Dosimetry for ^{90}Y Radioembolization of Advanced Hepatocellular Carcinoma: Defining the Role of a Device in a Pharma-Centric Landscape

Michael C. Soulen[1] and William S. Rilling[2]

[1]*Interventional Oncology, Abramson Cancer Center, University of Pennsylvania, Philadelphia, Pennsylvania; and*
[2]*Interventional Radiology, Medical College of Wisconsin, Milwaukee, Wisconsin*

In the United States, ^{90}Y microspheres have been approved for more than 20 y for treatment of hepatic malignancies. Glass microspheres (TheraSphere; Boston Scientific) received a humanitarian device exemption for treatment of hepatocellular carcinoma (HCC) from the Food and Drug Administration (FDA) Center for Devices and Radiologic Health in 1999 on the basis of 3 single-arm studies each with 7–24 patients (*1*). SIR-Spheres (Sirtex) received FDA premarket approval for treatment of metastatic colon cancer in combination with intraarterial chemotherapy in 2002 after a single randomized trial in which 35 patients received ^{90}Y microspheres through a surgically implanted hepatic artery infusion pump (*1*).

The process for FDA approval of devices is markedly different from that for pharmaceuticals. New anticancer drugs undergo highly regulated phase 3 randomized trials involving hundreds or thousands of patients to obtain approval by the Center for Drug Evaluation and Research. Most drugs enter clinical practice with level 1 evidence that qualifies them for inclusion into guidelines and for reimbursement. In contrast, 95%–98% of medical devices come to market through the FDA 510k approval process without requiring a definitive clinical trial, making adoption and reimbursement challenging (*2*).

The vulnerability of devices to the standards of approval used by the Center for Devices and Radiologic Health is particularly felt in oncology, where radiologists work as part of multidisciplinary disease management teams and are held to the same levels of evidence as those used by other oncologic specialties. Because the studies used for FDA approval of ^{90}Y microspheres were underpowered for efficacy assessment, acceptance in cancer guidelines has been limited. To address this obstacle, multiple large, randomized, controlled trials of ^{90}Y microspheres for HCC and metastatic colorectal cancer were completed. The SIRFLOX, FOXFIRE, and FOXFIRE Global trials collectively randomized more than 1,000 patients with liver-dominant metastatic colorectal cancer to first-line chemotherapy with or without SIR-Spheres and found no improvement in progression-free survival or overall survival (OS) (*3*). Similarly, the SARAH, SIRveNIB, and SORAMIC trials randomized patients with HCC to TheraSphere or sorafenib and found no significant difference in progression-free survival or OS (*4*). A subsequent systematic review and metaanalysis of 1,439 patients in 8 studies concluded that transarterial radioembolization (TARE) does not improve OS in patients with unresectable HCC (*5*). In contrast to these disappointing outcomes in advanced HCC, TARE has been utilized in early-stage HCC and shown high and durable complete response rates using a radiation segmentectomy approach in which an ablative dose is given into the arterial supply of the tumor-bearing segment. In 2021, the Center for Devices and Radiologic Health granted TheraSphere a premarket approval for HCC based on a multicenter retrospective report of objective response rate and duration in solitary tumors (*6*).

Given the high reported response rates to TARE, the lack of clinical efficacy in advanced HCC was a surprise to the radiologic community and stimulated investigation into how the treatment could be improved. The original dosimetry guidelines for both microspheres were simplistic. TheraSphere used a MIRD model in which a fixed dose of 120 Gy was delivered to the target volume of liver regardless of the tumor burden or tumor-to-liver uptake ratio. SIR-Spheres extrapolated the target volume from the patient's body surface area and hence was vulnerable to both over- and underdosing depending on the actual size of the tumor-bearing liver relative to the patient's body habitus.

Recent approaches to personalized dosimetry use ^{99m}Tc-macroaggregated albumin SPECT and cone-beam CT images to segment actual tumor and liver volumes and calculate the liver and tumor activity using partition models or voxel-based dosimetry. These approaches ensure an adequate or boosted dose to the tumor while keeping the normal-liver dose below an acceptable threshold. The DOSISPHERE-01 phase 2 trial randomized patients with unresectable HCC to personalized versus standard dosimetry (*7*). It was stopped at the first interim analysis after reaching its primary endpoint of response rate by European Association for the Study of the Liver criteria, which were 71% for personalized dosimetry versus 36% with standard dosimetry.

Objective response rate is an appealing early surrogate for treatment efficacy but in fact tells us what happened only to the patients' images, not to the patients. It is an insidious heuristic to associate the two when the correlation is quite poor. Among 146 randomized chemotherapy trials for colorectal cancer, the correlation between objective response rate and OS was only 0.1 (*8*). Novel classes of drugs such as tyrosine kinase inhibitors and immune checkpoint inhibitors have low objective response rates yet generate prolonged disease stabilization that translates to

---

Received Dec. 8, 2023; revision accepted Dec. 19, 2023.

For correspondence or reprints, contact Michael C. Soulen (michael.soulen@pennmedicine.upenn.edu).

DOI: 10.2967/jnumed.123.267035

meaningful survival benefit. Hence, it is essential to report clinically meaningful survival outcomes for all trials of new therapeutic approaches.

In *The Journal of Nuclear Medicine*, Garin et al. update the DOSISPHERE-01 trial to report the long-term survival outcomes (*9*). The treated cohorts had advanced disease with a median tumor size of more than 10 cm: 65% had portal vein tumor invasion, and 85% were Barcelona clinic liver cancer class C. At a median follow-up exceeding 5 y, median OS was better with personalized dosimetry for the group as a whole (25 vs. 11 mo), and even the subset with macroscopic portal vein tumor invasion did well (22 vs. 9 mo). Importantly, the rate of adverse events did not differ between the 2 arms.

However, multivariate analysis revealed that the survival benefit was limited to those patients who subsequently underwent resection. When such patients were censored in the survival analysis, median OS dropped to 11.7 mo in the personalized dosimetry arm versus 10.7 mo with standard dosimetry ($P = 0.23$). Hence, personalized dosimetry was beneficial among patients downstaged to resection even with portal vein invasion but not among never-resectable patients such as those with bilobar disease.

The ability to downstage is a critical outcome. Eleven of 31 (32%) patients in the personalized dosimetry arm were downstaged to resection, resulting in improved survival in this subset. Recent guidelines from the European Society of Organ Transplantation recommend that all HCC patients without extrahepatic disease or macrovascular invasion be considered for downstaging (*10*). More data are required, but advanced HCC patients with unilobar disease and adequate hepatic reserve should be afforded the opportunity to be downstaged to either resection or transplantation. Ongoing and future studies will investigate the role of combining TARE with immunotherapy in this patient population.

There are a few take-home messages from this paper. First, whereas objective response rate is a routinely reported outcome measure in the early assessment of new therapies, it is an unreliable surrogate, and a clinically meaningful outcome measure should be primary. Second, the DOSISPHERE trial supports use of personalized dosimetry in the neoadjuvant setting when resection or transplantation is the ultimate therapeutic goal. Third, evidence for a survival benefit from TARE outside the neoadjuvant setting remains elusive. The role for TARE in the advanced HCC population has yet to be determined, and studies combining TARE and immunotherapy will help to further define future treatment algorithms.

DISCLOSURE

Michael Soulen reports grants and personal fees from Guerbet LLC, grants from Sirtex Medical, grants from Pfizer, personal fees from Genetech, and personal fees from AstraZeneca, outside the submitted work. William Rilling reports consulting fees from Boston Scientific, Terumo, BD/Bard, Varian, Astra Zeneca, and Eisai. No other potential conflict of interest relevant to this article was reported.

REFERENCES

1. Westcott MA, Coldwell DM, Liu DM, Zikria JF. The development, commercialization, and clinical context of yttrium-90 radiolabeled resin and glass microspheres. *Adv Radiat Oncol.* 2016;1:351–364.
2. Silvestrini E. FDA 510(k) clearance process. Drugwatch website. https://www.drugwatch.com/fda/510k-clearance/. Modified September 5, 2023. Accessed December 21, 2023.
3. Wasan HS, Gibbs P, Sharma NK, et al. First-line selective internal radiotherapy plus chemotherapy versus chemotherapy alone in patients with liver metastases from colorectal cancer (FOXFIRE, SIRFLOX, and FOXFIRE-Global): a combined analysis of three multicentre, randomised, phase 3 trials. *Lancet Oncol.* 2017;18:1159–1171.
4. Walton M, Wade R, Claxton L, et al. Selective internal radiation therapies for unresectable early-, intermediate- or advanced-stage hepatocellular carcinoma: systematic review, network meta-analysis and economic evaluation. *Health Technol Assess.* 2020;24:1–264.
5. Lemieux S, Buies A, Turgeon AF, et al. Effect of yttrium-90 transarterial radioembolization in patients with non-surgical hepatocellular carcinoma: a systematic review and meta-analysis. *PLoS One.* 2021;16:e0247958.
6. Salem R, Johnson GE, Kim E, et al. Yttrium-90 radioembolization for the treatment of solitary, unresectable HCC: the LEGACY study. *Hepatology.* 2021;74:2342–2352.
7. Garin E, Tselikas L, Guiu B, et al. Selective internal radiation therapy (SIRT) using personalised dosimetry for locally advanced hepatocellular carcinoma (HCC) patients: a multicentre randomised phase 2 study (DOSISPHERE-01 trial). *Lancet Gastroenterol Hepatol.* 2021;6:17–29.
8. Johnson KR, Ringland C, Stokes BJ, et al. Response rate or time to progression as predictors of survival in trials of metastatic colorectal cancer or non-small-cell lung cancer: a meta-analysis. *Lancet Oncol.* 2006;7:741–746.
9. Garin E, Tselikas L, Guiu B, et al. Long-term survival after selective internal radiation therapy for locally advanced hepatocellular carcinomas: updated analysis of DOSISPHERE-01 trial. *J Nucl Med.* 2024;65:264–269.
10. Claasen MPAW, Sneider D, Rakké YS, et al. European Society of Organ Transplantation (ESOT) consensus report on downstaging, bridging and immunotherapy in liver transplantation for hepatocellular carcinoma. *Transpl Int.* 2023;36:11648.

Comparison of 3 Different Therapeutic Particles in Radioembolization of Locally Advanced Intrahepatic Cholangiocarcinoma

Martijn E.H.M. Wagemans[1], Britt Kunnen[1,2], Martina Stella[1], Rob van Rooij[1], Maarten Smits[1], Rutger Bruijnen[1], Marnix G.E.H. Lam[1], Hugo W.A.M. de Jong[1], and Arthur J.A.T. Braat[1]

[1]Department of Radiology and Nuclear Medicine, UMC Utrecht, Utrecht, The Netherlands; and [2]Image Sciences Institute, UMC Utrecht and University Utrecht, Utrecht, The Netherlands

Our objective was to compare 3 different therapeutic particles used for radioembolization in locally advanced intrahepatic cholangiocarcinoma. **Methods:** ^{90}Y-glass, ^{90}Y-resin, and ^{166}Ho-labeled poly(L-lactic acid) microsphere prescribed activity was calculated as per manufacturer recommendations. Posttreatment quantitative ^{90}Y PET/CT and quantitative ^{166}Ho SPECT/CT were used to determine tumor-absorbed dose, whole-normal-liver–absorbed dose, treated-normal-liver–absorbed dose, tumor-to-nontumor ratio, lung-absorbed dose, and lung shunt fraction. Response was assessed using RECIST 1.1 and the [^{18}F]FDG PET–based change in total lesion glycolysis. Hepatotoxicity was assessed using the radioembolization-induced liver disease classification. **Results:** Six ^{90}Y-glass, 8 ^{90}Y-resin, and 7 ^{166}Ho microsphere patients were included for analysis. The mean administered activity was 2.6 GBq for ^{90}Y-glass, 1.5 GBq for ^{90}Y-resin, and 7.0 GBq for ^{166}Ho microspheres. Tumor-absorbed dose and treated-normal-liver–absorbed dose were significantly higher for ^{90}Y-glass than for ^{90}Y-resin and ^{166}Ho microspheres (mean tumor-absorbed dose, 197 Gy for ^{90}Y-glass vs. 73 Gy for ^{90}Y-resin and 50 Gy for ^{166}Ho; mean treated-normal-liver–absorbed dose, 79 Gy for ^{90}Y-glass vs. 37 Gy for ^{90}Y-resin and 31 Gy for ^{166}Ho). The whole-normal-liver–absorbed dose and tumor-to-nontumor ratio did not significantly differ between the particles. All patients had a lung-absorbed dose under 30 Gy and a lung shunt fraction under 20%. The 3 groups showed similar toxicity and response according to RECIST 1.1 and [^{18}F]FDG PET–based total lesion glycolysis changes. **Conclusion:** The therapeutic particles used for radioembolization differed from each other and showed significant differences in absorbed dose, whereas toxicity and response were similar for all groups. This finding emphasizes the need for separate dose constraints and dose targets for each particle.

Key Words: intrahepatic cholangiocarcinoma; radioembolization; microspheres; ^{90}Y; ^{166}Ho

J Nucl Med 2024; 65:272–278
DOI: 10.2967/jnumed.123.265597

Intrahepatic cholangiocarcinoma (ICC) is the second most common liver malignancy, with surgery as its only curative option (*1*). Most patients (68%) cannot undergo surgery at diagnosis, because of unresectable (70%) or metastatic (30%) disease (*1*). Radioembolization is a promising treatment for locally advanced ICC (*2–6*). During radioembolization treatment, microspheres are injected into the hepatic artery and will preferentially lodge in and around the tumor, providing local irradiation. Currently, 3 types of microspheres are commercially available: ^{90}Y-glass (TheraSpheres; Boston Scientific), ^{90}Y-resin (SIR-Spheres; Sirtex Medical), and ^{166}Ho-labeled poly(L-lactic acid) (QuiremSpheres; Quirem Medical B.V.) microspheres. Their physical characteristics are listed in Table 1.

Prescribed activity calculation methods vary. For ^{90}Y-glass and ^{166}Ho microspheres, a MIRD monocompartment model is typically used, aiming for an average absorbed dose in the target volume. The prescribed activity formula for ^{166}Ho microspheres is based on a 60-Gy average absorbed dose to the whole liver (*7*). For ^{90}Y-glass microspheres, the recommended dose varies with liver volume, ranging from 80 to 150 Gy, as determined by the treating physician's evaluation (*7*). For ^{90}Y-resin microspheres, the body surface area method is most commonly used, in which the prescribed activity is based on body surface area and fraction of tumor involvement (*7*). However, the actual dose distribution is heterogeneous. The so-called partition model takes into account differences in activity concentration in different compartments, including the tumor-to-nontumor ratio. Nonetheless, heterogeneous activity distribution within the specified compartments is not considered (*8*).

Dose–response and dose–toxicity studies improve personalized treatments by establishing tumor-absorbed dose targets and normal-liver–absorbed dose limits. Despite recommendations for ICC treatment in radioembolization guidelines, these recommendations are not supported by consistent evidence (*7*). In the literature, a wide variety of dose thresholds is reported (*9–12*). The reason for this variety includes differences in response criteria, absorbed dose calculations, scan modalities, tumor types, and microsphere types (*8*). This study compared the 3 radioembolization particles to understand the differences in dosimetric thresholds, efficacy, and toxicity for ICC patients.

MATERIALS AND METHODS

Treatment Procedures and Planning

Patients with unresectable, chemorefractory locally advanced ICC, with an Eastern Cooperative Oncology Group performance score of 2 or less and a Child–Pugh score of less than B8, treated with radioembolization after pretreatment [^{18}F]FDG PET/CT, were included in this retrospective study. The medical ethics committee of the University Medical Center Utrecht waived the need for informed consent.

Received May 16, 2023; revision accepted Nov. 7, 2023.

For correspondence or reprints, contact Martijn E.H.M. Wagemans (m.e.h.wagemans-2@umcutrecht.nl).

TABLE 1

Microsphere Characteristics (*7,31,32*)

Characteristic	^{90}Y-glass	^{90}Y-resin	^{166}Ho
Mean diameter (μm)	25	30	30
Range of diameter (μm)	20–30	20–60	15–60
Specific activity (Bq/sphere)	4,354*	40–70†	200–400
Mean β-energy (MeV)	0.94	0.94	0.71
Maximum β-energy (MeV)	2.28	2.28	1.85 (50.0%), 1.77 (48.7%)
Mean range of β-energy in tissue (mm)	4.1	4.1	2.2
Maximum range of β-energy in tissue (mm)	11.3	11.3	8.7
Half-life (h)	64.2	64.2	26.8

*At calibration, Pasciak et al. reported 4,354 Bq (*24*). Instructions for use indicate 2,500 Bq, but value can differ because of physical decay and administration timing.

†Value may vary because FLEXdose (Sirtex) option allows injection up to 3 d before calibration, when vial activity is 10 GBq.

The standard radioembolization work-up included [^{18}F]FDG PET/CT and multiphasic liver CT, followed by pretreatment planar scintigraphy and SPECT/CT with administration of about 150 MBq of ^{99m}Tc-labeled macroaggregated albumin ([^{99m}Tc]MAA) (TechneScan LyoMAA [Mallinckrodt Medical B.V.] or Pulmocis [Curium Pharma]) to assess lung shunt fraction (LSF) and exclude extrahepatic depositions. The treating physician determined the microsphere type on the basis of [^{99m}Tc]MAA SPECT/CT and target volume. The prescribed activity was based on manufacturer guidelines. The target region dose for ^{90}Y-glass microspheres was based on visual assessment of activity accumulation in the tumor on [^{99m}Tc]MAA SPECT: 120 Gy for good targeting, 80–100 Gy for moderate to poor targeting, or 200 Gy for radiation segmentectomy. In all cases, a target dose of 60 Gy to the whole liver was planned for ^{166}Ho microspheres. The target dose for ^{90}Y-resin microspheres was determined using the body surface area method.

Posttreatment Imaging

Posttreatment quantitative imaging of ^{90}Y-glass and ^{90}Y-resin was performed within 24 h after microsphere administration. ^{90}Y PET images were acquired on a Biograph mCT PET/CT scanner (Siemens Medical Solutions). An acquisition time of 15 min/bed position at 2 bed positions was used. Images were reconstructed using an iterative algorithm (4 iterations and 21 subsets) including (relative scaling method) scatter correction, resolution recovery, and low-dose CT-based attenuation correction (40 mAs, 100–120 kV). A gaussian postreconstruction filter of 5 mm was applied, and a 200 × 200 matrix was used, resulting in a pixel size of 4 × 4 × 3 mm.

Quantitative imaging of ^{166}Ho microspheres was performed with SPECT/CT on a Symbia T16 (Siemens Medical Solutions) at 3–6 d after microsphere administration. The acquisition time was 15 s/view, and the number of projections was 120. A Monte Carlo–based reconstruction algorithm (Utrecht Monte Carlo System) was used (*13*). Technical details with respect to the reconstruction were described by Elschot et al. (*13*).

Three months after treatment, all patients underwent multiphasic CT, and 16 of them also underwent [^{18}F]FDG PET/CT on the same scanner. The [^{18}F]FDG PET/CT acquisition and reconstruction were according to the method of the European Association of Nuclear Medicine Research Ltd., version 1.0 (*14*).

Intrahepatic Dosimetry

Tumors were segmented on baseline [^{18}F]FDG PET/CT using an SUV$_{mean}$ (normalized for lean body mass) higher than 2 times that in the aortic blood pool, excluding volumes under 5 cm^3. For each tumor, metabolic activity was recorded as total lesion glycolysis (TLG), computed by multiplying metabolic tumor volume by tumor SUV$_{mean}$ normalized for lean body mass. Tumor volumes of interest (VOIs) were transferred from [^{18}F]FDG PET/CT to ^{90}Y PET/CT or ^{166}Ho SPECT/CT using rigid registration based on low-dose CT scans (*15*). Whole-liver and treated-liver segments were manually delineated using 3D Slicer (Fig. 1) (*16*).

Reconstructed ^{90}Y and ^{166}Ho microsphere activity concentrations were converted into absorbed dose maps through PET and SPECT calibration properties using the local deposition method, which we preferred because ^{90}Y is a 99.9% β-emitter and there are limited γ-photons from ^{166}Ho (*17,18*). The mean absorbed dose was recorded for all tumors, whole-normal-liver tissue (defined as whole-liver VOI minus all tumor VOIs), and treated-normal-liver tissue (defined as treated-liver VOI minus all tumor VOIs). For tumor and liver tissue, a density of 1.04 g/cm^3 was assumed (*19*). The tumor-to-nontumor ratio was defined as tumor-absorbed dose divided by treated-normal-liver–absorbed dose.

Lung Dosimetry

The posttreatment lung-absorbed dose (LD) was determined on ^{90}Y PET/CT or ^{166}Ho SPECT/CT by segmenting the lungs on the associated CT scan (excluding the basal lung regions $<$ 2 cm from the liver; Fig. 1), assuming a lung density of 0.3 g/cm^3 (*19*). Posttreatment LSF, defined as total lung activity divided by total-liver–plus–lung activity, was determined by extrapolating activity in the part of the lungs inside the field of view to the lung volume as measured on the pretreatment [^{18}F]FDG PET/CT scan and using activity in the previously delineated liver.

For comparison, the estimated LSF and LD based on pretreatment planar [^{99m}Tc]MAA scintigraphy was calculated. The clinically used estimated LSF was based on the geometric mean of posterior and anterior planar images of [^{99m}Tc]MAA. This estimated LSF was converted to a pretreatment estimated LD by multiplying the estimated LSF by the net administered activity (corrected for residual activity measurement), assuming a lung mass of 1 kg.

Response and Toxicity

Per-lesion response was determined using pre- and posttreatment multiphasic CT according to RECIST 1.1 (*20*). For patients with follow-up [^{18}F]FDG PET/CT, metabolic response was defined per-lesion by percentage change in TLG between pre- and posttreatment [^{18}F]FDG PET/CT, adhering to PERCIST. Over a 45% reduction in

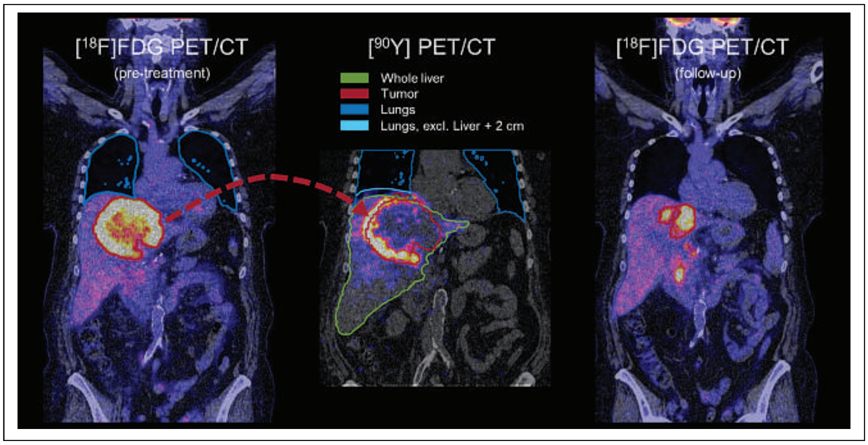

FIGURE 1. VOIs: tumor (red) segmented by [^{18}F]FDG PET/CT thresholding, transferred to ^{90}Y PET/CT (or ^{166}Ho SPECT/CT). Lungs (blue) are segmented by thresholding of associated CT of [^{18}F]FDG PET/CT for lung volume measurement and by associated CT of ^{90}Y PET/CT (or ^{166}Ho SPECT/CT) for dosimetry where lung portions within 2 cm of liver boundary are excluded (light blue). Liver (green) and treated liver (in this example same as liver) are manually delineated on associated CT. For response assessment, tumor (red) is segmented by [^{18}F]FDG PET/CT thresholding (follow-up).

TLG was regarded as a partial response, over a 75% increase in TLG was regarded as progressive disease, and anything in between was regarded as stable disease (*21*). The radioembolization-induced liver disease classification by Braat et al. was used for hepatotoxicity classification (Table 2) (*22*).

Statistics

Microsphere groups were compared using the Kruskal–Wallis test, and significant metrics were further analyzed using the Mann–Whitney *U* test. A 5% significance level was assumed. [^{99m}Tc]MAA-based lung dosimetry and posttreatment lung dosimetry relationships were tested using linear regression. CIs for low numbers were determined using the Agresti–Coull formula.

RESULTS

From June 2011 to March 2020, 23 patients with advanced ICC received treatment with different microspheres: 7 with ^{90}Y-glass, 8 with ^{90}Y-resin, and 8 with ^{166}Ho. One ^{166}Ho patient was excluded because the activity at the time of the SPECT acquisition was too high for adequate quantitative imaging (1,739 MBq) (*23*), and 1 ^{90}Y-glass patient was excluded because of an [^{18}F]FDG-negative tumor. Table 3 shows the characteristics of the remaining patients. Three patients received first-week ^{90}Y-glass microspheres: 2 at 4 d and 1 at 3 d after calibration. Another 3 patients were treated with second-week microspheres: 1 at 9 d and 2 at 11 d after calibration. Significant group differences were observed in the type of radioembolization treatment, between ^{90}Y-glass and ^{90}Y-resin (P = 0.01), and in median administered activity and median activity at posttreatment imaging, between the ^{166}Ho group and both ^{90}Y groups (P = 0.01 each).

Figure 2 shows the tumor-to-nontumor ratio, tumor-absorbed dose, treated-normal-liver–absorbed dose, and whole-normal-liver–absorbed dose for each group of microspheres. ^{90}Y-glass microspheres differed significantly from ^{90}Y-resin and ^{166}Ho microspheres for tumor-absorbed dose (mean of 197 Gy vs. 73 Gy and 50 Gy, respectively; P = 0.006) and treated-healthy-liver–absorbed dose (mean of 79 Gy vs. 37 Gy and 31 Gy, respectively; P = 0.001). No microspheres differed for whole-normal-liver–absorbed dose (mean of 41, 37, and 28 Gy, respectively) or tumor-to-nontumor ratio (mean of 2.5, 2.1, and 3.0, respectively).

All patients had an LD under 30 Gy and an LSF under 20% (Fig. 3). LD and LSF differences among groups were insignificant on planar [^{99m}Tc]MAA scintigraphy but were significant on posttreatment imaging. For LD, all microsphere groups were significantly different from each other (mean, 0.1 Gy for ^{166}Ho vs. 5.0 Gy for ^{90}Y-glass vs. 1.3 Gy for ^{90}Y-resin; P = 0.001). For LSF, all patients in both the ^{90}Y-glass and the ^{90}Y-resin groups exhibited an LSF greater than 0% after treatment. However, in the ^{166}Ho microsphere group, 71% (5/7) patients displayed an LSF above 0%. The mean LSF of ^{166}Ho microspheres differed significantly from that of ^{90}Y-glass and ^{90}Y-resin microspheres (mean of 0.2% for ^{166}Ho vs. 3.7% for ^{90}Y-glass and 1.5% for ^{90}Y-resin; P = 0.002). None of the particles showed a linear trend with

TABLE 2
Hepatotoxicity Classification (*22*)

Hepatotoxicity grade	Description
0	No liver toxicity
1	Minor liver toxicity, limited to increased aspartate aminotransferase, alanine aminotransferase, alkaline phosphatase, or γ-glutamyl transpeptidase levels (not exceeding grade 1 CTCAE toxicity)
2	Moderate liver toxicity, with self-limiting course; no medical intervention necessary
3	REILD manageable with noninvasive treatments such as diuretics, ursodeoxycholic acid, and steroids
4	REILD necessitating invasive medical treatment such as paracentesis, transfusions, hemodialysis, or TIPS
5	Fatal REILD

CTCAE = common terminology criteria for adverse events; TIPS = transjugular intrahepatic portosystemic shunt; REILD = radioembolization-induced liver disease.

TABLE 3
Patient Characteristics

Characteristic	^{90}Y-glass	^{90}Y-resin	^{166}Ho	*P**	Significant pair
Patients	6	8	7		
Age (y)	64.5 (32–80)	61.5 (43–81)	59 (45–83)	0.87	
Sex				0.94	
Male	24	3	2		
Female		5	5		
Liver volume (cm^3)	2,077 (1,636–2,631)	1,842 (1,231–2,182)	2,261 (1,725–4,019)	0.22	
Tumors	7	24	11	0.31	
Tumor volume (cm^3)	100 (10–470)	156 (36–398)	146 (16–2,655)	0.73	
Total TLG (10^6)	0.60 (0.09–5.8)	1.2 (0.27–5.6)	1.2 (0.11–24)	0.77	
Type of radioembolization treatment				0.01	^{90}Y-glass vs. ^{90}Y-resin
Whole liver	0	8	4		
Lobar	5	0	2		
Superselective	1	0	1		
Previous treatments				0.38	
Chemotherapy	2	4	5		
Surgery	1	0	0		
Chemotherapy + surgery	1	3	0		
Chemotherapy + radioembolization	1	0	0		
Surgery + radioembolization	0	0	1		
None	1	1	1		
ECOG performance status				0.71	
0	5	7	5		
1	1	1	1		
2	0	0	1		
Administered activity (MBq)	2,273 (894–4,503)	1,541 (729–1,943)	6,568 (2,391–12,897)	0.01	^{90}Y-glass vs. ^{166}Ho; ^{90}Y-resin vs. ^{166}Ho
Activity at posttreatment acquisition (MBq)	1,818 (735–3,536)	1,397 (596–1,697)	324 (156–374)	0.01	^{90}Y-glass vs. ^{166}Ho; ^{90}Y-resin vs. ^{166}Ho
LSF on planar [^{99m}Tc]MAA imaging	3.5% (1.9%–11.7%)	2.2% (0.8%–14.8%)	4.4% (1.6%–13.4%)	0.15	

---

*Numeric variables were assessed with Kruskal–Wallis H and Mann–Whitney *U* tests. For categoric variables, χ^2 tests were used.
ECOG = Eastern Cooperative Oncology Group.
Qualitative data are number; continuous data are median and range.

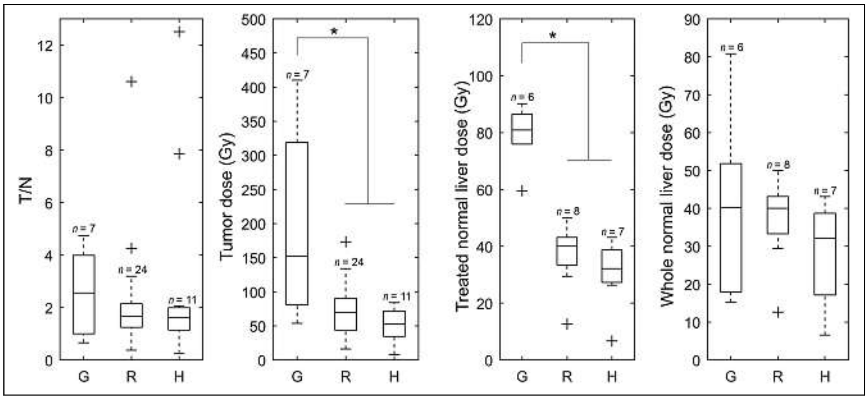

FIGURE 2. Microsphere posttreatment dosimetry. Numbers above box plots indicate number of included tumors or patients. $^{*}P < 0.05$. G = ^{90}Y-glass; H = ^{166}Ho; R = ^{90}Y-resin; T/N = tumor-to-nontumor activity concentration ratio.

[^{99m}Tc]MAA prediction—either for LD or for LSF (all 95% CIs for slope include 0 and all $R^2 < 0.5$).

RECIST 1.1 was assessed in 20 patients. Evaluation was impeded for 1 patient because of intrahepatic edema after treatment (Fig. 4) and for another because of surgical clip artifacts. Sixteen patients underwent 3 mo of follow-up [^{18}F]FDG PET/CT for per-lesion response assessment (Fig. 5). The number of tumors included for RECIST 1.1 and TLG change were 6 and 6 for ^{90}Y-glass, 22 and 9 for ^{90}Y-resin, and 11 and 11 for ^{166}Ho, respectively. Response differences were not significant per RECIST 1.1. TLG change showed that ^{166}Ho differed significantly from ^{90}Y-glass but not from ^{90}Y-resin (median TLG change of −29% [range, 220% to −79%] for ^{166}Ho, −84% [range, −49% to −100%] for ^{90}Y-glass, and −84% [range, 391% to −100%] for ^{90}Y-resin; $P = 0.02$). On a per-patient basis according to RECIST 1.1, 2 of 20 patients showed a partial response, 14 of 20 showed stable disease, and 4 of 20 showed progressive disease.

^{90}Y-glass, ^{90}Y-resin, and ^{166}Ho microspheres showed no significant differences in hepatotoxicity classification with respect to whole-normal-liver–absorbed dose and treated-normal-liver–absorbed dose (Fig. 6). Fatal radioembolization-induced liver disease, grade 5, occurred only once.

DISCUSSION

This study compared the commercially available microspheres for radioembolization in locally advanced ICC. Despite dosimetric differences, the microspheres showed similar toxicity and response. The differences in microsphere-specific activities cause variations in the administered number of microspheres. Pasciak et al. showed that greater microsphere quantities result in a more homogeneous dose distribution, leading to receipt of a potentially toxic absorbed dose by a greater volume fraction of the treated liver (*24*) and potentially explaining the lesser toxicity of ^{90}Y-glass than of ^{90}Y-resin at the same average absorbed dose (*9*). Administered microsphere numbers for ^{166}Ho resembled those for ^{90}Y-resin but were considerably less than for ^{90}Y-glass.

^{90}Y-glass microspheres delivered a higher tumor-absorbed dose because of a higher total administered activity than for ^{90}Y-resin microspheres. However, all ^{90}Y-glass microsphere patients received partial-liver treatment, resulting in a significant difference in the choice of radioembolization treatment between the ^{90}Y-glass and ^{90}Y-resin microspheres. Although no significant difference in the previous treatments and Eastern Cooperative Oncology Group performance status were found, these physician-induced group differences are

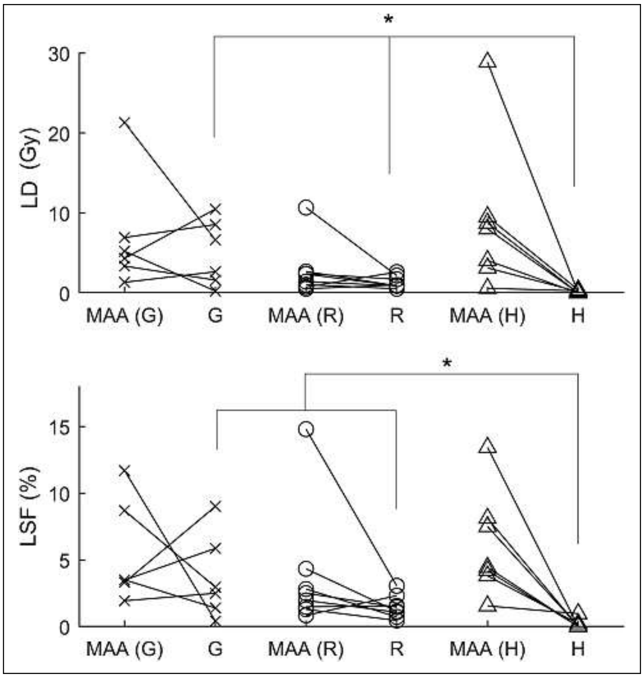

FIGURE 3. Lung dosimetry. Individual patient data are connected by line. $^{*}P < 0.05$. G = ^{90}Y-glass; H = ^{166}Ho; R = ^{90}Y-resin.

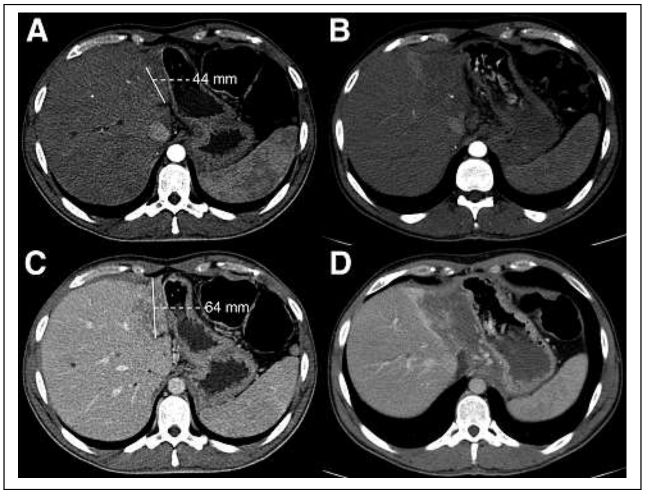

FIGURE 4. Extensive intrahepatic edema and necrosis after left lobar treatment with ^{90}Y-glass microspheres. Shown are multiphase contrast-enhanced CT at baseline (A and C) and 3 mo after treatment (B and D). At baseline, primary tumor invades left liver lobe on portal venous CT (C) and shows enhancement in arterial phase (A). Posttreatment images show intrahepatic edema and necrosis, masking tumor for RECIST 1.1 assessment. However, disappearance of arterial enhancement suggests complete response according to modified RECIST.

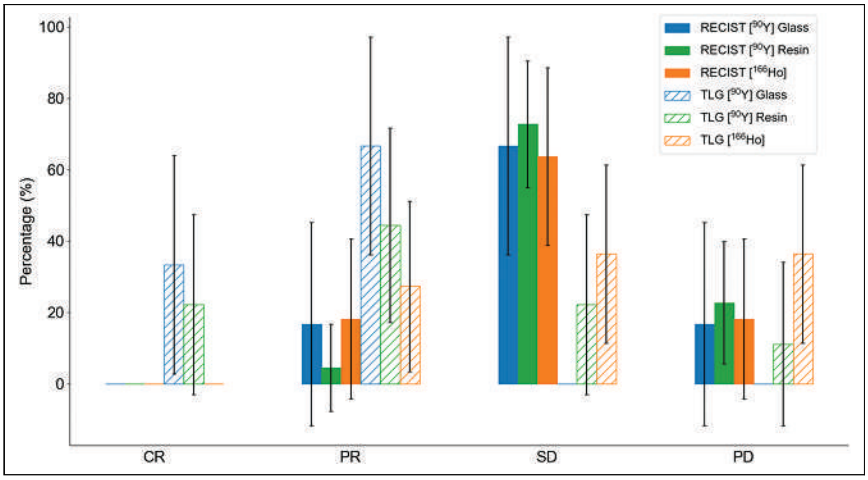

FIGURE 5. Response according to RECIST 1.1 and TLG change. CR = complete response; PD = progressive disease; PR = partial response; SD = stable disease.

inherent in retrospective research and consistent with day-to-day practice.

The per-tumor response analysis revealed distinct response profiles between TLG and RECIST 1.1., partly because RECIST 1.1 does not differentiate necrotic from nonnecrotic tissue. Although there is no consensus on the preferred response criteria for ICC treated with radioembolization, and although determining this preference was outside the scope of this study, Figure 4 suggests greater suitability of modified RECIST (not used in this work), in which contrast enhancement in the arterial phase represents viable tumor parts. However, modified RECIST cannot be used for hypovascular ICC, and [^{18}F]FDG PET/CT and TLG change can depict the viable tissue proportion in both hypervascular and hypovascular tumors. The latter method is not perfect either, however, as 1 patient in this study was excluded because of [^{18}F]FDG-negative disease.

Consistent with prior studies on ICC and radioembolization, hepatotoxicity was modest (*3,6,25,26*). Grade 5 radioembolization-induced liver disease occurred in 1 patient, who received a whole-liver treatment (mean liver-absorbed dose of 81 Gy). The injection position differed from the [^{99m}Tc]MAA procedure, leading to a poor tumor dose and a high normal-liver dose.

Planar [^{99m}Tc]MAA scintigraphy showed similar lung dosimetry for the entire population, confirming the similarity of the groups at baseline, but posttreatment lung dosimetry showed differences between therapeutic particles, where ^{166}Ho stood out for both LSF and LD. This observation is at least partially due to the different imaging modalities. ^{166}Ho images were acquired on a SPECT system, combined with Monte Carlo reconstruction. ^{90}Y images were acquired on a PET system, which suffers from a low count rate and a high random fraction. This is known to cause a positive bias in the reconstruction, especially in regions with low counts (e.g., the lungs), resulting in an overestimation of the LSF (*27,28*). Hence, these observed differences may be more reflective of the technical aspects of scanning and of significant differences in treatment approaches and volumes (whole liver vs. selective) than of any physiologic variations.

Contrary to other publications on dosimetry in radioembolization, calculation of absorbed dose was based on posttreatment imaging, not on pretreatment [^{99m}Tc]MAA SPECT/CT. In addition, reconstructed activity was not scaled on the basis of net administered activity. This introduces errors in ^{90}Y PET/CT and ^{166}Ho SPECT/CT quantification but avoids errors introduced by scaling and residual activity measurement of administered net activity (*29*). Although commonly used, the rigid coregistration method for transferring tumor VOIs from [^{18}F]FDG PET/CT to SPECT/CT relies on low-dose CT, not on the molecular images themselves, introducing errors. Additionally, the use of rigid coregistration for a deformable organ is known to induce errors to some degree.

Dosimetric outcomes adhere closely to the instructions for use outlined by each manufacturer, complicating direct comparison among the 3 microsphere types. Still, following these instructions enhances the real-world applicability of our results. However, patients were treated before the release of the 2022 European Association of Nuclear Medicine guidelines (*7*), possibly limiting comparisons with current clinical practice.

A limitation of this study was the small population, which impedes our ability to draw generalizable conclusions. In addition, follow-up [^{18}F]FDG PET/CT was not available for all patients, and modified RECIST could not be assessed in most patients because of hypovascular tumors. Therefore, conclusions on dose–response and dose–toxicity relationships cannot be drawn. Overall, irrespective of the particle used, and on a per-patient basis, our results were in line with the literature (*3,6,26*).

Another limitation was the bias regarding type of treatment. In our institute, all particles are used for whole-liver treatments, but for selective treatments ^{90}Y-glass microspheres are preferred because of high specific activity. In the presented patients with locally advanced ICC, this difference resulted in a ^{90}Y-glass group with only partial-liver treatments, a ^{90}Y-resin group with only whole-liver treatments, and a mixed ^{166}Ho microsphere group. Moreover, ^{90}Y-glass microspheres were injected at different times after calibration, that is, with a different specific activity per sphere. This variability within the ^{90}Y-glass group may limit comparisons of this group with the other treatment groups.

Finally, because many patients had discrepancies between the [^{99m}Tc]MAA procedure and treatment (e.g., different injection positions or additional coiling), we could not use [^{99m}Tc]MAA SPECT/CT data to compare intrahepatic dose metrics with posttreatment PET/CT or SPECT/CT. (*30*). We did use [^{99m}Tc]MAA planar data for lung dosimetry, as a different catheter position would barely influence these results.

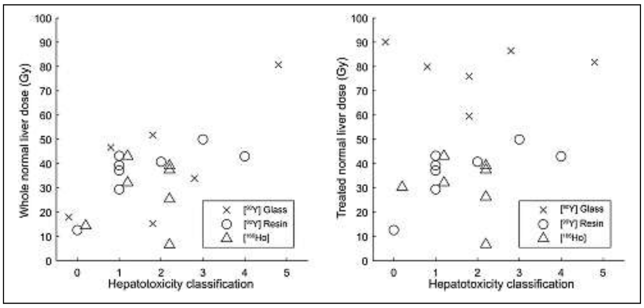

FIGURE 6. Hepatotoxicity classification with respect to dose absorbed by whole normal liver (left) and treated normal liver (right).

CONCLUSION

In the present study, 3 available microspheres were compared in locally advanced ICC. The particles differed in physical characteristics and methods for calculating prescribed activity, resulting in significant differences in absorbed dose. However, toxicity and response were similar for all groups. This finding emphasizes the need for separate dose constraints and dose targets for each particle.

DISCLOSURE

The UMC Utrecht Department of Radiology and Nuclear Medicine receives royalties from Terumo. Marnix Lam is a consultant for Boston Scientific and Terumo and receives research support from Boston Scientific and Novartis. Arthur Braat is a consultant for Boston Scientific and Terumo and receives research support from Ariceum Therapeutics. Maarten Smits is a consultant for Philips, Terumo/Quirem Medical, and Swedish Orphan Biovitrum. He also serves as a speaker for Medtronic. No other potential conflict of interest relevant to this article was reported.

KEY POINTS

QUESTION: How do different therapeutic particles for SIRT compare in the treatment of advanced ICC?

PERTINENT FINDINGS: The therapeutic particles used for radioembolization significantly differ from each other in terms of absorbed dose, yet they show similar toxicity and response across all groups.

IMPLICATIONS FOR PATIENT CARE: The findings emphasize the need for distinct dose constraints and targets for each therapeutic particle, optimizing patient outcomes in ICC treatment.

REFERENCES

1. Endo I, Gonen M, Yopp AC, et al. Intrahepatic cholangiocarcinoma: rising frequency, improved survival, and determinants of outcome after resection. *Ann Surg.* 2008;248:84–96.
2. Edeline J, Touchefeu Y, Guiu B, et al. Radioembolization plus chemotherapy for first-line treatment of locally advanced intrahepatic cholangiocarcinoma: a phase 2 clinical trial. *JAMA Oncol.* 2020;6:51–59.
3. Swinburne NC, Biederman DM, Besa C, et al. Radioembolization for unresectable intrahepatic cholangiocarcinoma: review of safety, response evaluation criteria in solid tumors 1.1 imaging response and survival. *Cancer Biother Radiopharm.* 2017;32:161–168.
4. Filippi L, Pelle G, Cianni R, Scopinaro F, Bagni O. Change in total lesion glycolysis and clinical outcome after ^{90}Y radioembolization in intrahepatic cholangiocarcinoma. *Nucl Med Biol.* 2015;42:59–64.
5. Mouli S, Memon K, Baker T, et al. Yttrium-90 radioembolization for intrahepatic cholangiocarcinoma: safety, response, and survival analysis. *J Vasc Interv Radiol.* 2013;24:1227–1234.
6. Gangi A, Shah J, Hatfield N, et al. Intrahepatic cholangiocarcinoma treated with transarterial yttrium-90 glass microsphere radioembolization: results of a single institution retrospective study. *J Vasc Interv Radiol.* 2018;29:1101–1108.
7. Weber M, Lam M, Chiesa C, et al. EANM procedure guideline for the treatment of liver cancer and liver metastases with intra-arterial radioactive compounds. *Eur J Nucl Med Mol Imaging.* 2022;49:1682–1699.
8. Bastiaannet R, Kappadath SC, Kunnen B, Braat AJAT, Lam MGEH, de Jong HWAM. The physics of radioembolization. *EJNMMI Phys.* 2018;5:22.
9. Chiesa C, Mira M, Maccauro M, et al. Radioembolization of hepatocarcinoma with ^{90}Y glass microspheres: development of an individualized treatment planning strategy based on dosimetry and radiobiology. *Eur J Nucl Med Mol Imaging.* 2015; 42:1718–1738.
10. van den Hoven AF, Rosenbaum CE, Elias SG, et al. Insights into the dose-response relationship of radioembolization with resin ^{90}Y-microspheres: a prospective cohort study in patients with colorectal cancer liver metastases. *J Nucl Med.* 2016;57:1014–1019.
11. Kappadath SC, Mikell J, Balagopal A, et al. Hepatocellular carcinoma tumor dose response after ^{90}Y-radioembolization with glass microspheres using ^{90}Y-SPECT/CT-based voxel dosimetry. *Int J Radiat Oncol Biol Phys.* 2018;102:451–461.
12. Garin E, Lenoir L, Rolland Y, et al. Dosimetry based on ^{99m}Tc-macroaggregated albumin SPECT/CT accurately predicts tumor response and survival in hepatocellular carcinoma patients treated with ^{90}Y-loaded glass microspheres: preliminary results. *J Nucl Med.* 2012;53:255–263.
13. Elschot M, Smits ML, Nijsen JF, et al. Quantitative Monte Carlo-based holmium-166 SPECT reconstruction. *Med Phys.* 2013;40:112502.
14. Boellaard R, O'Doherty MJ, Weber WA, et al. FDG PET and PET/CT: EANM procedure guidelines for tumour PET imaging: version 1.0. *Eur J Nucl Med Mol Imaging.* 2010;37:181–200.
15. Klein S, Staring M, Murphy K, Viergever MA, Pluim JP. elastix: a toolbox for intensity-based medical image registration. *IEEE Trans Med Imaging.* 2010;29: 196–205.
16. Fedorov A, Beichel R, Kalpathy-Cramer J, et al. 3D Slicer as an image computing platform for the Quantitative Imaging Network. *Magn Reson Imaging.* 2012;30: 1323–1341.
17. Stella M, Braat AJAT, van Rooij R, de Jong HWAM, Lam MGEH. Holmium-166 radioembolization: current status and future prospective. *Cardiovasc Intervent Radiol.* 2022;45:1634–1645.
18. Knešaurek K. Comparison of posttherapy ^{90}Y positron emission tomography/computed tomography dosimetry methods in liver therapy with ^{90}Y microspheres. *World J Nucl Med.* 2020;19:359–365.
19. Yu N, Srinivas SM, Difilippo FP, et al. Lung dose calculation with SPECT/CT for ^{90}yttrium radioembolization of liver cancer. *Int J Radiat Oncol Biol Phys.* 2013; 85:834–839.
20. Eisenhauer EA, Therasse P, Bogaerts J, et al. New response evaluation criteria in solid tumours: revised RECIST guideline (version 1.1). *Eur J Cancer.* 2009;45: 228–247.
21. O JH, Lodge MA, Wahl RL. Practical PERCIST: a simplified guide to PET response criteria in solid tumors 1.0. *Radiology.* 2016;280:576–584.
22. Braat MN, van Erpecum KJ, Zonnenberg BA, van den Bosch MA, Lam MG. Radioembolization-induced liver disease: a systematic review. *Eur J Gastroenterol Hepatol.* 2017;29:144–152.
23. Elschot M, Nijsen JF, Dam AJ, de Jong HW. Quantitative evaluation of scintillation camera imaging characteristics of isotopes used in liver radioembolization. *PLoS One.* 2011;6:e26174.
24. Pasciak AS, Abiola G, Liddell RP, et al. The number of microspheres in Y90 radioembolization directly affects normal tissue radiation exposure. *Eur J Nucl Med Mol Imaging.* 2020;47:816–827.
25. Manceau V, Palard X, Rolland Y, et al. A MAA-based dosimetric study in patients with intrahepatic cholangiocarcinoma treated with a combination of chemotherapy and ^{90}Y-loaded glass microsphere selective internal radiation therapy. *Eur J Nucl Med Mol Imaging.* 2018;45:1731–1741.
26. Buettner S, Braat AJAT, Margonis GA, et al. Yttrium-90 radioembolization in intrahepatic cholangiocarcinoma: a multicenter retrospective analysis. *J Vasc Interv Radiol.* 2020;31:1035–1043.e2.
27. Kunnen B, Beijst C, Lam MGEH, Viergever MA, de Jong HWAM. Comparison of the Biograph Vision and Biograph mCT for quantitative ^{90}Y PET/CT imaging for radioembolisation. *EJNMMI Phys.* 2020;7:14.
28. Kunnen B, Dietze MMA, Braat AJAT, Lam MGEH, Viergever MA, de Jong HWAM. Feasibility of imaging 90 Y microspheres at diagnostic activity levels for hepatic radioembolization treatment planning. *Med Phys.* 2020;47:1105–1114.
29. Ebbers SC, Kunnen B, van Nierop BJ, et al. Verification study of residual activity measurements after yttrium-90 radioembolization with glass microspheres. *Cardiovasc Intervent Radiol.* 2020;43:1378–1383.
30. Wondergem M, Smits ML, Elschot M, et al. ^{99m}Tc-macroaggregated albumin poorly predicts the intrahepatic distribution of ^{90}Y resin microspheres in hepatic radioembolization. *J Nucl Med.* 2013;54:1294–1301.
31. Westcott MA, Coldwell DM, Liu DM, Zikria JF. The development, commercialization, and clinical context of yttrium-90 radiolabeled resin and glass microspheres. *Adv Radiat Oncol.* 2016;1:351–364.
32. Cremonesi M, Ferrari M, Bodei L, Tosi G, Paganelli G. Dosimetry in peptide radionuclide receptor therapy: a review. *J Nucl Med.* 2006;47:1467–1475.

Hemodynamic Insights into Combined Fractional Flow Reserve and Instantaneous Wave-Free Ratio Assessment Through Quantitative [^{15}O]H$_2$O PET Myocardial Perfusion Imaging

Ruben W. de Winter[1], Pepijn A. van Diemen[1], Stefan P. Schumacher[1], Ruurt A. Jukema[1], Yvemarie B.O. Somsen[1], Roel Hoek[1], Albert C. van Rossum[1], Jos W.R. Twisk[2], Guus A. de Waard[1], Alexander Nap[1], Pieter G. Raijmakers[3], Roel S. Driessen[1], Paul Knaapen[1], and Ibrahim Danad[1]

[1]Department of Cardiology, Amsterdam UMC, Vrije Universiteit Amsterdam, Amsterdam, The Netherlands; [2]Department of Epidemiology and Data Science, Amsterdam UMC, Vrije Universiteit Amsterdam, Amsterdam, The Netherlands; and [3]Department of Radiology, Nuclear Medicine, and PET Research, Amsterdam UMC, Vrije Universiteit Amsterdam, Amsterdam, The Netherlands

In patients evaluated for obstructive coronary artery disease (CAD), guidelines recommend using either fractional flow reserve (FFR) or instantaneous wave-free ratio (iFR) to guide coronary revascularization decision-making. The hemodynamic significance of lesions with discordant FFR and iFR measurements is debated. This study compared [^{15}O]H$_2$O PET–derived absolute myocardial perfusion between vessels with concordant and discordant FFR and iFR measurements. **Methods:** We included 197 patients suspected of obstructive CAD who had undergone [^{15}O]H$_2$O PET perfusion imaging and combined FFR/iFR interrogation in 468 vessels. Resting myocardial blood flow (MBF), hyperemic MBF, and coronary flow reserve (CFR) were compared among 4 groups: FFR low/iFR low (n = 79), FFR high/iFR low (n = 22), FFR low/iFR high (n = 22), and FFR high/iFR high (n = 345). Predefined [^{15}O]H$_2$O PET thresholds for ischemia were 2.3 $\text{mL}\cdot\text{min}^{-1}\cdot\text{g}^{-1}$ or less for hyperemic MBF and 2.5 or less for CFR. **Results:** Hyperemic MBF was lower in the concordant low (2.09 ± 0.67 $\text{mL}\cdot\text{min}^{-1}\cdot\text{g}^{-1}$), FFR high/iFR low ($2.41 \pm 0.80$ $\text{mL}\cdot\text{min}^{-1}\cdot\text{g}^{-1}$), and FFR low/iFR high (2.40 ± 0.69 $\text{mL}\cdot\text{min}^{-1}\cdot\text{g}^{-1}$) groups compared with the concordant high group (2.91 ± 0.84 $\text{mL}\cdot\text{min}^{-1}\cdot\text{g}^{-1}$) ($P < 0.001$, $P = 0.004$, and $P < 0.001$, respectively). A lower CFR was observed in the concordant low (2.37 ± 0.76) and FFR high/iFR low (2.64 ± 0.84) groups compared with the concordant high group (3.35 ± 1.07, $P < 0.01$ for both). However, for vessels with either low FFR or low iFR, quantitative hyperemic MBF and CFR values exceeded the ischemic threshold in 38% and 49%, respectively. In addition, resting MBF exhibited a negative correlation with iFR ($P < 0.001$) and was associated with FFR low/iFR high discordance compared with concordant low FFR/low iFR measurements, independent of clinical and angiographic characteristics, as well as hyperemic MBF (odds ratio [OR], 0.41; 95% CI, 0.26–0.65; $P < 0.001$). **Conclusion:** We found reduced myocardial perfusion in vessels with concordant low and discordant FFR/iFR measurements. However, FFR/iFR combinations often inaccurately classified vessels as either ischemic or nonischemic when compared with hyperemic MBF and CFR. Furthermore, a lower resting MBF was associated with a higher iFR and the occurrence of FFR low/iFR high discordance. Our study showed that although combined FFR/iFR assessment can be useful to estimate the hemodynamic significance of coronary lesions, these pressure-derived indices provide a limited approximation of [^{15}O]H$_2$O PET–derived quantitative myocardial perfusion as the physiologic standard of CAD severity.

Key Words: fractional flow reserve; instantaneous wave-free ratio; [^{15}O]H$_2$O PET; absolute myocardial perfusion

J Nucl Med 2024; 65:279–286
DOI: 10.2967/jnumed.123.265973

Fractional flow reserve (FFR)–guided revascularization improves patient outcome compared with an angiography-guided approach, with the additional benefit of percutaneous coronary intervention (PCI) on top of optimal medical therapy for FFR-defined significant coronary artery disease (CAD) (*1–3*). The nonhyperemic instantaneous-wave free ratio (iFR) was proposed as an alternative to FFR, as randomized studies reported comparable event-free survival after an iFR- or FFR-guided revascularization strategy (*4*,*5*). In accordance, current revascularization guidelines recommend using either FFR or iFR to assess the hemodynamic impact of coronary lesions in patients with undocumented ischemia (*6*,*7*). However, iFR and FFR are both pressure-derived indices reflecting simulated relative regional differences in flow and flow reserve (*8–11*). Furthermore, iFR is calculated during a specific phase in cardiac diastole during which resting microvascular resistance was asserted to be constant and relatively minimized, yet this fundamental physiologic principle has been disputed (*12–14*). Indeed, although binary thresholds of 0.80 or less for FFR and 0.89 or less for iFR have been validated to guide revascularization decision-making, discrepancy is reported in up to 20% of cases (*6*,*7*,*15–17*). These findings have triggered a debate on the functional significance of lesions with discordant FFR and iFR values (*18–20*). Studies using intracoronary Doppler and thermodilution suggested that the coronary flow characteristics in vessels with FFR below despite iFR above established thresholds were comparable to those of nonobstructed reference vessels (*18*,*20*). In addition, a study with ^{13}NH$_3$ PET reported higher perfusion values in the left anterior descending coronary artery with low FFR and high iFR compared with concordant abnormal pressure indices (*19*). To our knowledge, studies comparing absolute quantitative myocardial perfusion in vessels with concordant low, discordant, and concordant

---

Received May 3, 2023; revision accepted Nov. 1, 2023.

For correspondence or reprints, contact Paul Knaapen (p.knaapen@amsterdamumc.nl).

high FFR and iFR measurements have not been conducted. Therefore, the present study sought to provide insights into the hemodynamic significance of agreement and discrepancy between FFR and iFR in patients evaluated for obstructive CAD, using [^{15}O]H_2O PET perfusion indices as the physiologic standard of CAD severity.

MATERIALS AND METHODS

Study Population

This was a substudy of the PACIFIC I (Comparison of Cardiac Imaging Techniques for Diagnosing Coronary Artery Disease) and II (Functional Stress Imaging to Predict Abnormal Coronary Fractional Flow Reserve) prospective clinical trials comparing the diagnostic performance of multiple cardiac imaging modalities for the detection of FFR-defined significant CAD (*21*,*22*). The study protocols and the inclusion and exclusion criteria have been previously described (*21*,*22*). All patients included in the PACIFIC studies underwent [^{15}O]H_2O PET perfusion imaging followed by invasive coronary angiography within 2 wk. Invasive physiologic assessment of all coronary arteries was performed if anatomically feasible, irrespective of imaging results. Whereas FFR interrogation was routinely performed in the PACIFIC trials, iFR evaluation was added to both study protocols at a later stage during the enrollment period. Patients were eligible for inclusion in the present study if combined FFR/iFR measurements were obtained in at least 1 coronary artery. Both PACIFIC trials were approved by the local Medical Ethics Committee and were performed in accordance with the Declaration of Helsinki. Written informed consent was obtained from all participants.

[^{15}O]H_2O PET Perfusion Imaging Acquisition

A hybrid PET/CT device (Gemini TF 64 or Ingenuity TF 128; Philips Healthcare) was used. A detailed description of the acquisition protocol and quantitative perfusion assessment has been previously reported (*23*). Briefly, dynamic PET perfusion images were acquired during rest and vasodilator stress (intravenous adenosine, $140\,\mu g \cdot kg^{-1} \cdot min^{-1}$) using 370 MBq of [^{15}O]H_2O as the PET tracer. In-house–developed software (Cardiac VUer) was used to construct parametric images allowing for quantitative assessment of absolute myocardial blood flow (MBF, expressed in $mL \cdot min^{-1} \cdot g^{-1}$). Resting and hyperemic MBF was obtained for each of the 3 vascular territories (right coronary artery, left anterior descending coronary artery, and circumflex coronary artery) according to the standardized 17-segment model of the American Heart Association (*24*). Coronary flow reserve (CFR) was defined as the ratio of hyperemic to resting MBF. Ischemic thresholds for [^{15}O]H_2O PET perfusion imaging, which have been validated in prior work, were $2.3\,mL \cdot min^{-1} \cdot g^{-1}$ or less for hyperemic MBF and 2.5 or less for CFR (*23*). To take into account the variation in hemodynamic conditions, we additionally corrected the resting MBF for the rate–pressure product using the following equation: [mean rate–pressure product × resting MBF]/rate–pressure product in the individual patient (*25*). Corrected CFR was calculated by taking the ratio of hyperemic MBF to corrected resting MBF.

Invasive Coronary Angiography and Physiologic Pressure Measurements

Patients underwent invasive coronary angiography according to standard practice. Angiography images were acquired using a monoplane cardiovascular x-ray system (Allura Xper FD 10/10; Philips Healthcare). Intracoronary administration of nitroglycerin ($200\,\mu g$) was used to induce coronary vasodilation before contrast injection. A minimum of 2 orthogonal projections was obtained for each evaluated coronary artery. Subsequently, invasive pressure measurements were obtained in all major coronary arteries (>2.0 mm) independent of stenosis severity. FFR and iFR were defined as the time-averaged ratio of mean distal coronary pressure to aortic pressure and calculated with an automated MATLAB script (MathWorks) with an integrated iFR algorithm (Volcano Corp.). iFR was obtained during resting conditions; hence, caution was exercised to avoid measurement directly after any preceding intracoronary contrast or saline injection. FFR was measured during maximal hyperemia, which was induced by administration of intracoronary ($150\,\mu g$) or intravenous ($140\,\mu g \cdot kg^{-1} \cdot min^{-1}$) adenosine. Established thresholds for low FFR (≤ 0.80) and low iFR (≤ 0.89) were used to stratify vessels into 4 groups: FFR low/iFR low, FFR high/iFR low, FFR low/iFR high, and FFR high/iFR high (*3*,*5*–*7*). Gray-zone FFR was defined as an FFR value at least 0.75 but no more than 0.85 (*26*).

Statistical Analysis

Categoric variables, expressed as frequencies with percentages, were compared using the χ^2 test. Continuous variables, shown as mean ± SD or median and interquartile range, were analyzed with 1-way ANOVA or the Kruskal–Wallis test, depending on the normality of the data distribution. Correlations were quantified using either the Pearson or the Spearman rank correlation test, as appropriate. We used generalized estimating equation analyses with an independent working correlation structure to compare quantitative resting MBF, hyperemic MBF, and CFR values among the 4 FFR/iFR groups, adjusting for multiple vessel comparisons within the same patient. Similar generalized estimating equation analyses were performed to compare corrected resting MBF and CFR between vessels with concordant and discordant FFR and iFR measurements. Furthermore, in line with common clinical practice, in which the resting pressure gradient is calculated first, we used generalized estimating equation models to compare clinical characteristics (age, sex, body mass index, hypertension, hypercholesterolemia, diabetes mellitus, smoking, a family history of CAD, prior PCI, prior myocardial infarction, and ventricular function) and angiographic characteristics (vascular territory, percentage diameter stenosis, minimal lumen diameter, and lesion length) between the concordant low and discordant group with high FFR and between the concordant high and discordant group with low FFR. We constructed a similar multivariable model that also included resting and hyperemic MBF, to assess the independent relationship between resting MBF and FFR low/iFR high discordance, in comparison to concordant low FFR/iFR measurements. Analyses were performed on a per-vessel basis using SPSS (version 26.0; IBM). A 2-sided *P* value of less than 0.05 was considered statistically significant.

RESULTS

Study Population

[^{15}O]H_2O PET perfusion imaging–derived resting and hyperemic MBF values were available in 197 patients in whom combined FFR and iFR interrogation was performed in a total of 468 coronary arteries. Clinical characteristics are presented in Table 1. Vessel characteristics, intracoronary pressure measurements, and [^{15}O]H_2O PET results are shown in Table 2. Supplemental Table 1 provides a comparison of clinical characteristics between patients with and without combined FFR/iFR measurements included in the PACIFIC trials (supplemental materials are available at http://jnm.snmjournals.org).

Correlation and Agreement Between FFR and iFR

The distribution of FFR and iFR indices is illustrated in Figure 1. The correlation coefficient between FFR and iFR was 0.82. FFR and iFR agreement was observed in 424 (91%) vessels, whereas discordance occurred in 44 (9%) vessels. Specifically, 79 (17%) vessels showed concordant low, 22 (5%) FFR high/iFR low, 22 (5%) FFR low/iFR high, and 345 (74%) concordant high FFR/iFR measurements. Supplemental Table 2 shows the clinical and vessel characteristics compared among the 4 FFR/iFR groups. Variables that were independently associated with FFR/iFR

TABLE 1
Baseline Characteristics ($n = 197$)

Characteristic	Data
Demographics	
Age (y)	61 ± 9
Male sex	139 (71)
Body mass index (kg/m^2)	27 ± 4
Cardiovascular risk factors	
Hypertension	104 (53)
Hypercholesterolemia	101 (51)
Diabetes mellitus	34 (17)
Smoking	32 (16)
Family history of CAD	105 (53)
Cardiac history	
No prior cardiac history	118 (60)
Prior PCI	40 (20)
Prior myocardial infarction	71 (36)
LVEF (%)	62 ± 9
≥55	162 (82)
45–54	28 (14)
31–44	4 (2)
≤30	0 (0)
Medication	
Platelet inhibitor	180 (91)
β-blocker	119 (60)
ACE inhibitor/ARB	89 (45)
Statin	150 (76)
Calcium channel blockers	58 (29)
Symptoms	
Typical angina	76 (39)
Atypical angina	82 (41)
Nonspecific chest discomfort	39 (20)

ACE = angiotensin-converting enzyme, ARB = angiotensin II receptor blocker, LVEF = left ventricular ejection fraction.

Qualitative data are number and percentage; continuous data are mean ± SD.

discordance are presented in Table 3. Prior myocardial infarction was the only independent predictor for FFR high/iFR low discordance (OR, 1.21; 95% CI, 1.02–1.44). Meanwhile, FFR low/iFR high discordance was associated with male sex (OR, 1.06; 95% CI, 1.01–1.10), stenosis in the LAD territory (OR, 1.10; 95% CI, 1.03–1.17), and percentage diameter stenosis (OR, 1.05; 95% CI, 1.02–1.09). A list of all variables included in this analysis is provided in Supplemental Table 3.

Absolute Myocardial Perfusion

Figure 2 illustrates [^{15}O]H_2O PET myocardial perfusion indices stratified according to FFR/iFR classification. The FFR low/iFR high group showed a significantly lower resting MBF compared with the concordant low, FFR high/iFR low, and concordant high FFR/iFR groups. Hyperemic MBF was significantly lower in the concordant low, FFR high/iFR low, and FFR low/iFR high groups than in the concordant high group. CFR in the FFR high/iFR low group was similar to that in the concordant low group and was significantly lower than that in the concordant high group. In contrast, CFR in the FFR low/iFR high group was similar to that in the concordant high group and was significantly higher compared with the concordant low group. Analyses using corrected resting MBF and CFR yielded equivalent results (Supplemental Fig. 1). Furthermore, we found a stepwise decrease in the percentage of vessels with hyperemic MBF and CFR below the ischemic [^{15}O]H_2O PET thresholds in the concordant low, FFR high/iFR low, FFR low/iFR high, and concordant high FFR/iFR groups (Fig. 1). Within these groups, hyperemic MBF values of $2.3\,\mathrm{mL{\cdot}min^{-1}{\cdot}g^{-1}}$ or less were observed in 68%, 59%, 41%, and 26% of vessels, respectively. Likewise, CFR was 2.5 or less in 59%, 41%, 32%, and 19% across vessels within these respective groups. Additionally, in the discordant FFR/iFR groups, resting MBF negatively correlated with iFR ($P < 0.001$), whereas no correlation between iFR and percentage diameter stenosis was found. Conversely, resting MBF showed no correlation with FFR, whereas a negative correlation between FFR and percentage diameter stenosis was observed ($P = 0.025$) (Supplemental Fig. 2). Finally, a lower resting MBF was independently associated with the occurrence of FFR low/iFR high discordance compared with concordant low FFR/iFR measurements, independent of clinical and angiographic characteristics, as well as hyperemic MBF (OR, 0.41; 95% CI, 0.26–0.65; $P < 0.001$). Figure 3 shows 4 case examples demonstrating invasive coronary angiography and [^{15}O]H_2O PET myocardial perfusion images.

DISCUSSION

This post hoc analysis of the PACIFIC trials investigated the value of combined FFR and iFR pressure ratio measurements for the assessment of CAD severity, using [^{15}O]H_2O PET–derived quantitative myocardial perfusion as the physiologic reference standard. Significant myocardial perfusion differences were observed according to FFR/iFR classification, with diminished MBF in vessels with concordant low and discordant FFR/iFR indices. However, FFR/iFR combinations often inaccurately classified vessels as either ischemic or nonischemic when compared with quantitative hyperemic MBF and CFR. Finally, a lower resting MBF was found to correlate with higher iFR values and independently predicted FFR low/iFR high discordance.

Invasive Pressure Ratio Measurements in Clinical Practice

Demand ischemia is the result of reduced coronary blood flow to the myocardial tissue, rather than changes in perfusion pressure across a coronary lesion (*27*). Nonetheless, various studies showed a correlation between a significant transstenotic pressure gradient and myocardial ischemia, with equivalent diagnostic performance for both FFR and iFR (*28*,*29*). Randomized trials have confirmed the clinical value of these pressure-based indices to facilitate safe deferral of revascularization, resulting in a class IA recommendation in revascularization guidelines to use either FFR or iFR for the hemodynamic assessment of coronary stenosis in patients with undocumented ischemia (*3–7*). However, whereas one of these pressure indices currently suffices for physiology-driven decisions in the catheterization laboratory, using either FFR or iFR may result in differences in patient selection for revascularization deferral (*15–17*). Indeed, as FFR and iFR rely on different physiologic mechanisms to estimate coronary flow impairment—that is, the

TABLE 2
Procedural Characteristics and PET Measurements

Characteristic	FFR low/iFR low (n = 79)	FFR high/iFR low (n = 22)	FFR low/iFR high (n = 22)	FFR high/iFR high (n = 345)
Vessel				
Right coronary artery	16 (20)	1 (5)	6 (27)	120 (35)
Left anterior descending coronary artery	47 (60)	16 (73)	13 (59)	91 (26)
Left circumflex coronary artery	16 (20)	5 (23)	3 (14)	134 (39)
Diameter stenosis (%)	52 ± 14	43 ± 11	49 ± 15	34 ± 13
Minimal lumen diameter (mm)	1.3 ± 0.4	1.5 ± 0.4	1.5 ± 0.5	1.9 ± 0.6
Lesion length (mm)	19 ± 10	15 ± 10	17 ± 11	16 ± 12
Physiologic indices				
FFR	0.67 (0.58–0.75)	0.84 (0.82–0.86)	0.77 (0.72–0.77)	0.95 (0.90–0.98)
Gray-zone FFR (0.75–0.85)	23 (29)	17 (77)	13 (59)	38 (11)
iFR	0.81 (0.66–0.85)	0.88 (0.85–0.89)	0.92 (0.90–0.93)	0.98 (0.95–1.00)
[^{15}O]H$_2$O PET measurements				
Baseline heart rate (beats/min)	63 ± 9	65 ± 10	61 ± 8	63 ± 10
Baseline systolic pressure (mm Hg)	121 (112–128)	115 (111–127)	121 (109–140)	122 (110–135)
Baseline diastolic pressure (mm Hg)	66 (60–74)	62 (58–74)	71 (64–76)	69 (62–75)
Rate–pressure product	7,675 ± 1,760	7,488 ± 1,823	7,614 ± 1,757	7,819 ± 1,990
Hyperemic heart rate (beats/min)	82 ± 12	84 ± 13	85 ± 15	83 ± 13
Hyperemic systolic pressure (mm Hg)	113 (102–129)	113 (96–126)	118 (105–129)	119 (105–129)
Hyperemic diastolic pressure (mm Hg)	60 (55–70)	60 (54–71)	70 (59–78)	65 (58–72)
Resting MBF (mL·min^{-1}·g^{-1})	0.90 ± 0.19	0.93 ± 0.25	0.80 ± 0.16	0.90 ± 0.24
Hyperemic MBF (mL·min^{-1}·g^{-1})	2.09 ± 0.67	2.41 ± 0.80	2.40 ± 0.69	2.91 ± 0.84
Hyperemic MBF $\leq$ 2.3 mL·min^{-1}·g^{-1}	54 (68)	13 (59)	9 (41)	91 (26)
CFR	2.37 ± 0.76	2.64 ± 0.84	3.05 ± 0.84	3.35 ± 1.07
CFR $\leq$ 2.5	47 (59)	9 (41)	7 (32)	65 (19)
Corrected resting MBF (mL·min^{-1}·g^{-1})	0.93 ± 0.19	0.99 ± 0.19	0.83 ± 0.13	0.92 ± 0.20
Corrected CFR	2.30 ± 0.78	2.51 ± 1.04	2.94 ± 0.95	3.27 ± 1.06

Qualitative data are number and percentage; continuous data are mean ± SD or median and interquartile range.

induction of maximal hyperemia versus measurement in resting conditions during the wave-free period—incongruence between these methods may be anticipated (*13*,*18*). The iFR, measured during a phase in cardiac diastole when microvascular resistance was presumed to equal mean hyperemic resistance, was proposed as an alternative to FFR without the need for vasodilatory agents (*12*). However, subsequent studies showed that administering adenosine during the wave-free period significantly reduced microvascular resistance, whereas other diastolic resting pressure indices and the full-cycle resting ratio of distal coronary pressure to aortic pressure were found to be numerically identical to iFR (*13*,*30*). These observations clarify that the diagnostic agreement between FFR and iFR, reported to be approximately 80%, was found to be significantly influenced by variations in the rest-to-stress myocardial resistance ratio, which challenged the concept that FFR and iFR can be used interchangeably to identify ischemia-inducing coronary stenosis in all cases (*13*,*15*). There has been debate on whether iFR's advantage of avoiding hyperemia would outweigh the potential risk of misclassifying functional lesion significance in selected patients (*17*,*27*). This prompted efforts to enhance the understanding of coronary hemodynamics, implications for the subtending myocardium, etiologic factors, and clinical outcomes related to FFR and iFR discordance (*17*,*28*). Our study adds to these efforts, as we compared [^{15}O]H$_2$O PET–derived absolute myocardial perfusion among vessels with concordant low, discordant, and concordant high FFR and high iFR indices.

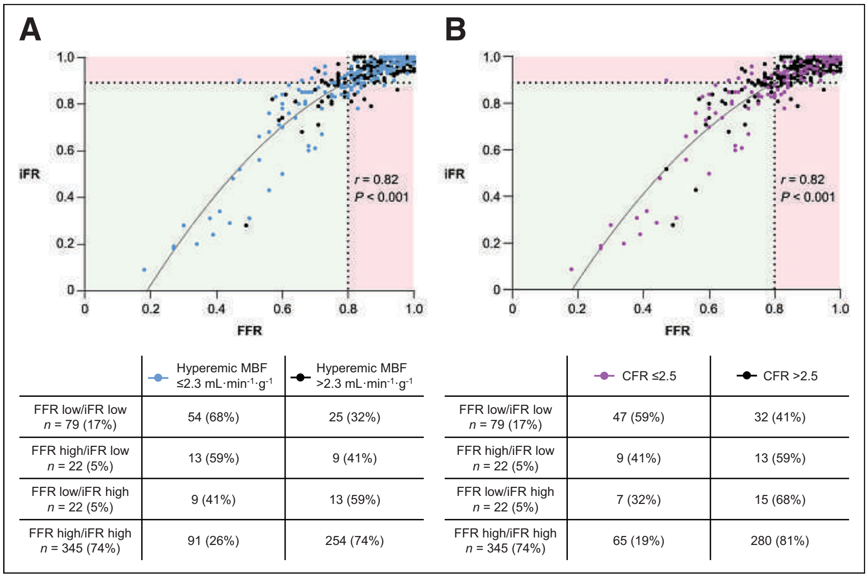

	🔵 Hyperemic MBF ≤2.3 mL·min^{-1}·g^{-1}	● Hyperemic MBF >2.3 mL·min^{-1}·g^{-1}
FFR low/iFR low *n* = 79 (17%)	54 (68%)	25 (32%)
FFR high/iFR low *n* = 22 (5%)	13 (59%)	9 (41%)
FFR low/iFR high *n* = 22 (5%)	9 (41%)	13 (59%)
FFR high/iFR high *n* = 345 (74%)	91 (26%)	254 (74%)

	🟣 CFR ≤2.5	● CFR >2.5
FFR low/iFR low *n* = 79 (17%)	47 (59%)	32 (41%)
FFR high/iFR low *n* = 22 (5%)	9 (41%)	13 (59%)
FFR low/iFR high *n* = 22 (5%)	7 (32%)	15 (68%)
FFR high/iFR high *n* = 345 (74%)	65 (19%)	280 (81%)

FIGURE 1. Scatterplots demonstrating correlation between FFR and iFR in 468 vessels, including Spearman-defined correlation coefficient ($r = 0.82$, $P < 0.001$). Solid black lines depicts polynomial best-of-fit curve to second order, whereas dotted lines represent thresholds for low FFR (≤0.80) and low iFR (≤0.89). (A) Vessels with hyperemic MBF below and above ischemic [^{15}O]H_2O PET threshold (≤2.3 mL·min^{-1}·g^{-1}). (B) Vessels with CFR below and above ischemic [^{15}O]H_2O PET threshold (≤2.5).

Relationship Between Intracoronary Pressure Indices and Absolute Myocardial Perfusion

Several studies explored the association between combined FFR and iFR measurements with coronary blood flow as an external reference (*18–20*). Cook et al. (*18*) used intracoronary Doppler measurements and reported that flow values in discordant vessels with FFR below and iFR above interventional thresholds were comparable to those in angiographically unobstructed vessels. In addition, the FFR high/iFR low group yielded similar coronary flow characteristics to the concordant low FFR/iFR group. Because a similar baseline flow velocity was observed, the authors concluded that differences in coronary flow between resting and hyperemic pressure indices were the result of hyperemic flow velocity variation. Subsequent work demonstrated comparable results for intracoronary thermodilution-derived CFR values, which corroborates prior work showing that iFR provides a stronger correlation and agreement with coronary flow velocity reserve than FFR (*20*,*31*). It has been well established that a strong hyperemic response in patients with preserved microvascular function may lead to a substantial increase in coronary flow velocity, which in turn causes an increased pressure drop across a coronary lesion, resulting in low FFR values with normal coronary flow characteristics (*18*,*29*). The results of previous flow studies are to be interpreted in this context (*18*,*20*). In the present study, we assessed absolute MBF with ^{15}O-water as the PET perfusion tracer, which is freely diffusible and extracted linear to perfusion from the arterial blood pool, independent of coronary pressure or flow (*27*). In accordance with prior work, CFR did not differ between the FFR low/iFR high and the concordant high FFR/iFR group and was also similar in the FFR high/iFR low and the concordant low FFR/iFR group. However, in contrast to previous work by Cook et al. (*18*), hyperemic MBF in the present study was equivalent between the 2 discordant FFR/iFR groups and lower than in vessels with concordant high FFR/iFR measurements. As such, the comparable CFR values in the FFR low/iFR high group and the concordant high FFR/iFR group were driven by resting MBF, rather than hyperemic MBF, illustrated by the significantly lower value of resting MBF in FFR low/iFR high vessels, even after correcting for the rate–pressure product. We further explored the correlation between resting MBF and iFR and found a significant negative correlation between these indices. In addition,

TABLE 3

Independent Clinical and Angiographic Significant Predictors of FFR Discordance Stratified to Low- and High-iFR Cohorts

Predictor of discordance	OR	95% CI	*P*
With iFR low (*n* = 101) (iFR ≤ 0.89 and FFR > 0.80)			
Cardiac history			
Prior myocardial infarction	1.21	1.02–1.44	0.027
With iFR high (*n* = 367) (iFR > 0.89 and FFR ≤ 0.80)			
Demographics			
Male sex	1.06	1.01–1.10	0.010
Vessel characteristics			
LAD territory	1.10	1.03–1.17	0.005
Diameter stenosis, 10%	1.05	1.02–1.09	<0.001

LAD = left anterior descending coronary artery.

Variables included in multivariable generalized estimating equation analysis were age, sex, body mass index, hypertension, hypercholesterolemia, diabetes mellitus, smoking, family history of CAD, prior PCI, prior myocardial infarction, left ventricular function, LAD territory, percentage diameter stenosis, minimal lumen diameter, and lesion length.

resting MBF was a significant predictor of the occurrence of FFR low/iFR high discordance, independent of clinical characteristics, stenosis severity, and hyperemic MBF. The female sex has been associated with a higher baseline flow in multiple PET studies; hence, this may in part account for the observed differences (*32*). Furthermore, an increased resting flow has been described in the setting of coronary microvascular dysfunction, whereas healthy microcirculatory function is assumed in the physiologic explanation of FFR low/iFR high discordant pressure measurements with preserved flow characteristics (*29*,*33*). Previously, Dérimay et al. (*16*) also suggested an association between resting flow and iFR as a simulation of relative resting perfusion distribution, noting an association between heart rate, β-blocker use, and FFR/iFR discrepancy. As such, resting coronary pressure gradients, and hence iFR, may depend on highly variable rest flow, potentially limiting its value for the hemodynamic assessment of intermediate coronary lesions in certain patient subgroups (e.g., in tachycardic or bradycardic patients). Interestingly, in the present study, quantitative hyperemic MBF was diminished in discordant vessels, regardless of either FFR or iFR values in the reference range. Several PET studies indicated that lower stress perfusion is associated with adverse patient outcome, even after adjusting for the concurrent CFR value (*34*). Additionally, higher hyperemic MBF values after revascularization therapy have been related to a significant reduction in angina symptoms (*35*). Driessen et al. (*10*) reported a significant correlation between the post-PCI alterations in intracoronary pressure and the enhancement of [^{15}O]H_2O PET stress perfusion, suggesting that the positive prognostic impact of post-PCI pressure restoration might be attributed to the normalization of myocardial perfusion. Importantly, however, in the present study mean hyperemic MBF and CFR values exceeded ischemic [^{15}O]H_2O PET thresholds in both discordant FFR/iFR groups. Moreover, in vessels with either low FFR or low iFR, hyperemic MBF and CFR values above the threshold for myocardial ischemia were found in 38% and 49%, respectively. On the other hand, hyperemic MBF and CFR showed myocardial ischemia in, respectively, 26% and 19% of vessels with concordant high FFR/iFR measurements. These results are in line with prior work reporting discordance between FFR and CFR in approximately 40% of lesions (*9*). Absolute quantitative myocardial perfusion imaging provides encompassing pathophysiologic information on the extent of CAD by integrating the impact of focal stenosis, diffuse atherosclerotic disease, and associated microvascular dysfunction through the evaluation of MBF expressed in mL/min/g of myocardial tissue (*9*,*11*). Conversely, pressure-derived physiologic indices reflect simulated relative regional differences in flow and flow reserve over an epicardial coronary stenosis (*9*,*10*). Indeed, discordance between coronary pressure and flow measurements has been shown to be related to the relative contribution of focal and diffuse disease, which is commonly observed in patients being evaluated for obstructive CAD, reflecting the underlying pathophysiology (*8*–*10*). Our study expands on this observation, as we found that pressure-derived indices provide a limited approximation of [^{15}O]H_2O PET–derived quantitative myocardial perfusion as the physiologic standard of CAD severity.

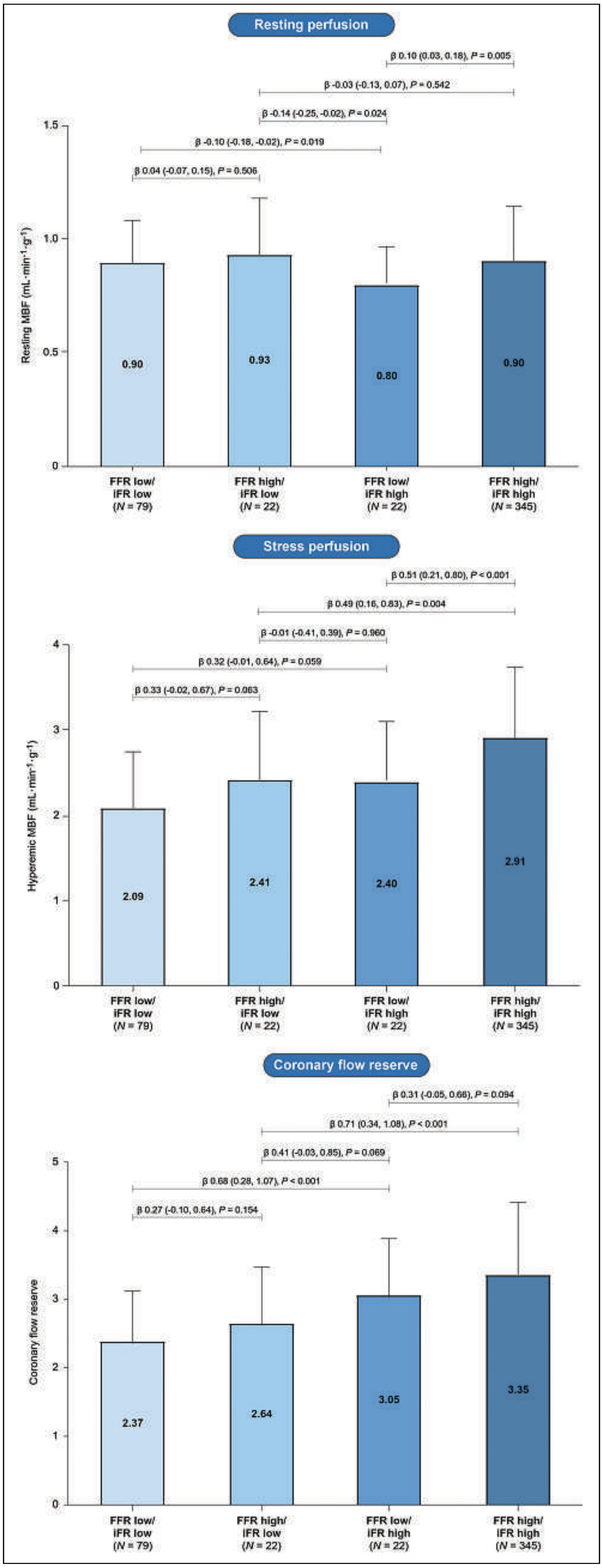

FIGURE 2. [^{15}O]H_2O PET–derived resting MBF, hyperemic MBF and CFR stratified according to FFR/iFR classification. Perfusion values in box plots are presented as mean ± SD. β values are followed by 95% CIs in parentheses.

Clinical Implications

Focal epicardial stenosis is usually treated with PCI, and multiple studies have shown that deferring revascularization for discordant FFR/iFR lesions was not associated with an increased risk of adverse outcomes (*20*,*36*). Conversely, 5-y follow-up data from a retrospective registry indicated an increased risk of target vessel

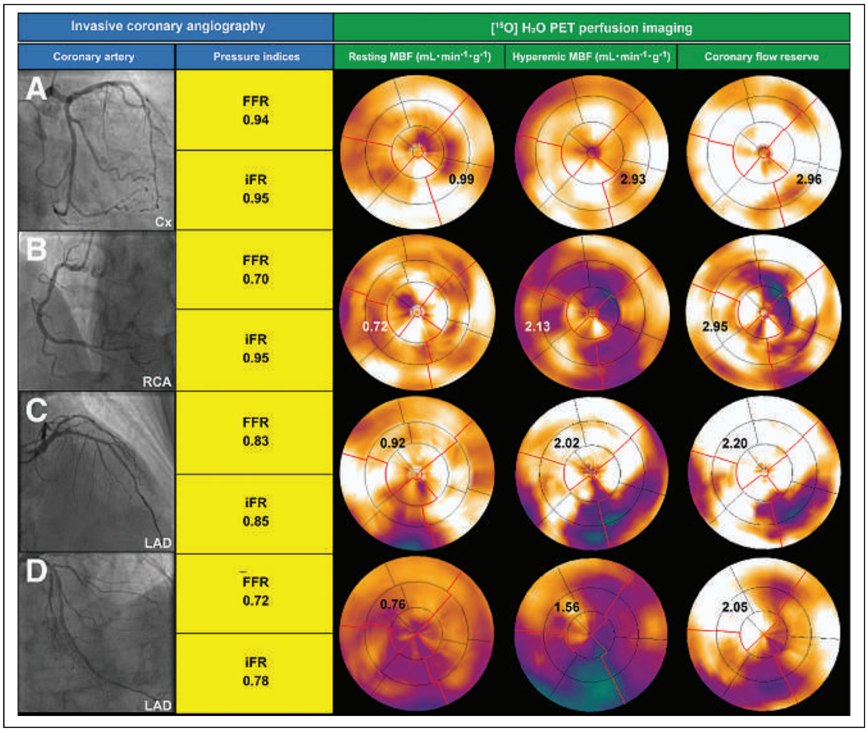

FIGURE 3. Example coronary angiography images of vessels with concordant high (A), FFR low/iFR high (B), FFR high/iFR low (C), and concordant low (D) FFR/iFR measurements. Corresponding resting MBF, hyperemic MBF, and CFR values are depicted in PET perfusion images. Cx = circumflex coronary artery; LAD = left anterior descending coronary artery; RCA = right coronary artery.

failure in vessels with either FFR or a resting ratio of distal coronary pressure to aortic pressure below the threshold, suggesting that combined hyperemic and nonhyperemic pressure ratio application could refine revascularization decisions (*37*). In addition, recent studies have raised concerns regarding higher event rates in the iFR-guided revascularization group, particularly an increased 5-y (cardiovascular) mortality risk, which may be attributed to discordant iFR values when compared with FFR (*5*,*38*,*39*). To date, limited evidence is available to select the optimal treatment strategy for lesions with discordant resting and hyperemic pressure indices. The current study does not include patient outcome but does support prior work suggesting significant differences in coronary hemodynamics between vessels with discordant and concordant high FFR and iFR indices. Furthermore, in line with previous studies exploring physiologic or pathophysiologic factors contributing to FFR/iFR discordance, we found several patient and vessel characteristics to be independently associated with the occurrence of FFR discordance after measurement of the iFR, which can aid the clinician to determine whether additional invasive or noninvasive functional assessment or intravascular imaging may be warranted before making a final treatment decision (*16*,*17*). Importantly, our study indicated that although pressure-derived indices and [^{15}O]H$_2$O PET–derived absolute perfusion measurements are physiologically related, the detection of myocardial ischemia might vary within the same vascular region, potentially impacted by the integrated effects of segmental stenosis, diffuse disease, and microvascular dysfunction on coronary vasodilator capacity and microcirculatory autoregulation reserve, collectively defining CAD severity.

Limitations

First, this was a post hoc analysis of the PACIFIC studies, in which invasive functional assessment was performed in all coronary arteries, regardless of stenosis severity. This explains the relatively low number of discordant FFR/iFR vessels included in the present study. Second, our study did not incorporate clinical follow-up, nor did it capture data on quality of life or angina status after treatment or deferral for FFR/iFR discordant lesions. Third, the PACIFIC I study, involving patients without a prior cardiac history, comprised a larger proportion of patients who underwent combined pressure measurements than did the PACIFIC II study. Last, in the present study, [^{15}O]H$_2$O PET perfusion imaging allowed for quantification of MBF in mL/min/g of viable, water-perfusable myocardial tissue, which was evaluated for the 3 major vascular regions according to the standardized 17-segment model of the American Heart Association (*24*). Although this standard methodology may facilitate interpretation of our results, it does not account for the individual patient variation in coronary artery distribution, as opposed to a more advanced segmental model calculating the regional size-severity classification of CAD by assessment of the artery-specific pixel perfusion distribution of the left ventricle (*11*).

CONCLUSION

This study showed significant differences in absolute myocardial perfusion across vessels with concordant low, discordant, and concordant high FFR and iFR indices in patients evaluated for obstructive CAD. Specifically, reduced MBF was observed in vessels with concordant low and discordant FFR/iFR measurements. However, FFR/iFR combinations often inaccurately characterized vessels as either ischemic or nonischemic when compared with [^{15}OH$_2$O PET–derived quantitative hyperemic MBF and CFR. Furthermore, a lower resting MBF was associated with elevated iFR and independently predicted the occurrence of FFR low/iFR high discordance. Our findings indicate that although combined FFR/iFR assessment can be useful to estimate the hemodynamic significance of coronary lesions, these pressure-derived indices provide a limited approximation of [^{15}O]H$_2$O PET–derived quantitative myocardial perfusion as the standard physiologic metric of CAD severity.

DISCLOSURE

No potential conflict of interest relevant to this article was reported.

KEY POINTS

QUESTION: What is the value of combined FFR and iFR measurements for assessing CAD severity, as compared with the physiologic standard of quantitative myocardial perfusion derived from [^{15}O]H_2O PET perfusion imaging that accounts for the integrated effects of both diffuse CAD and focal stenosis?

PERTINENT FINDINGS: Reduced MBF was observed in vessels with concordant low and discordant FFR/iFR measurements. However, low FFR or iFR did not invariably correspond with hyperemic MBF and CFR below the ischemic PET thresholds. Furthermore, iFR values negatively correlated with resting MBF, whereas resting MBF independently predicted the occurrence of FFR low/iFR high discordance.

IMPLICATIONS FOR PATIENT CARE: Clinicians should be aware that iFR values may be influenced by a highly variable resting MBF, potentially limiting its value for the hemodynamic assessment of intermediate coronary lesions in certain patient subgroups. Importantly, combined FFR/iFR assessment integrates pressure-derived relative regional differences in flow and flow reserve, which can be useful to estimate the hemodynamic impact of coronary lesions, yet its value to assess CAD severity is limited when compared with absolute quantitative myocardial stress perfusion and CFR as the physiologic reference standard.

REFERENCES

1. Tonino PA, De Bruyne B, Pijls NH, et al. Fractional flow reserve versus angiography for guiding percutaneous coronary intervention. *N Engl J Med.* 2009;360:213–224.
2. De Bruyne B, Pijls NHJ, Kalesan B, et al. Fractional flow reserve–guided PCI versus medical therapy in stable coronary disease. *N Engl J Med.* 2012;367:991–1001.
3. Xaplanteris P, Fournier S, Pijls NHJ, et al. Five-year outcomes with PCI guided by fractional flow reserve. *N Engl J Med.* 2018;379:250–259.
4. Davies JE, Sen S, Dehbi H-M, et al. Use of the instantaneous wave-free ratio or fractional flow reserve in PCI. *N Engl J Med.* 2017;376:1824–1834.
5. Götberg M, Berntorp K, Rylance R, et al. 5-year outcomes of PCI guided by measurement of instantaneous wave-free ratio versus fractional flow reserve. *J Am Coll Cardiol.* 2022;79:965–974.
6. Neumann F-J, Sousa-Uva M, Ahlsson A, et al. 2018 ESC/EACTS guidelines on myocardial revascularization. *Eur Heart J.* 2019;40:87–165.
7. Lawton JS, Tamis-Holland JE, Bangalore S, et al. 2021 ACC/AHA/SCAI guideline for coronary artery revascularization. *J Am Coll Cardiol.* 2022;79:e21–e129.
8. Johnson NP, Kirkeeide RL, Gould KL. Is discordance of coronary flow reserve and fractional flow reserve due to methodology or clinically relevant coronary pathophysiology? *JACC Cardiovasc Imaging.* 2012;5:193–202.
9. Gould KL, Johnson NP, Bateman TM, et al. Anatomic versus physiologic assessment of coronary artery disease: role of coronary flow reserve, fractional flow reserve, and positron emission tomography imaging in revascularization decision-making. *J Am Coll Cardiol.* 2013;62:1639–1653.
10. Driessen RS, Danad I, Stuijfzand WJ, et al. Impact of revascularization on absolute myocardial blood flow as assessed by serial [^{15}O]H_2O positron emission tomography imaging: a comparison with fractional flow reserve. *Circ Cardiovasc Imaging.* 2018;11:e007417.
11. Gould KL, Nguyen TT, Kirkeeide R, et al. Coronary physiology and quantitative myocardial perfusion. In: Dilsizian V, Narula J, eds. *Atlas of Nuclear Cardiology.* Springer International Publishing; 2021:161–259.
12. Sen S, Escaned J, Malik IS, et al. Development and validation of a new adenosine-independent index of stenosis severity from coronary wave-intensity analysis: results of the ADVISE (ADenosine Vasodilator Independent Stenosis Evaluation) study. *J Am Coll Cardiol.* 2012;59:1392–1402.
13. Johnson NP, Kirkeeide RL, Asrress KN, et al. Does the instantaneous wave-free ratio approximate the fractional flow reserve? *J Am Coll Cardiol.* 2013;61:1428–1435.
14. Gould KL, Johnson NP, Kirkeeide RL. Approximate truth. *J Am Coll Cardiol.* 2017;70:3097–3101.
15. Jeremias A, Maehara A, Généreux P, et al. Multicenter core laboratory comparison of the instantaneous wave-free ratio and resting Pd/Pa with fractional flow reserve: the RESOLVE study. *J Am Coll Cardiol.* 2014;63:1253–1261.
16. Dérimay F, Johnson NP, Zimmermann FM, et al. Predictive factors of discordance between the instantaneous wave-free ratio and fractional flow reserve. *Catheter Cardiovasc Interv.* 2019;94:356–363.
17. Fogelson B, Tahir H, Livesay J, et al. Pathophysiological factors contributing to fractional flow reserve and instantaneous wave-free ratio discordance. *Rev Cardiovasc Med.* 2022;23:70.
18. Cook CM, Jeremias A, Petraco R, et al. Fractional flow reserve/instantaneous wave-free ratio discordance in angiographically intermediate coronary stenoses: an analysis using doppler-derived coronary flow measurements. *JACC Cardiovasc Interv.* 2017;10:2514–2524.
19. Lee JM, Hwang D, Park J, et al. Physiologic mechanism of discordance between instantaneous wave-free ratio and fractional flow reserve: Insight from ^{13}N-ammonium positron emission tomography. *Int J Cardiol.* 2017;243:91–94.
20. Lee SH, Choi KH, Lee JM, et al. Physiologic characteristics and clinical outcomes of patients with discordance between FFR and iFR. *JACC Cardiovasc Interv.* 2019;12:2018–2031.
21. Danad I, Raijmakers PG, Driessen RS, et al. Comparison of coronary CT angiography, SPECT, PET, and hybrid imaging for diagnosis of ischemic heart disease determined by fractional flow reserve. *JAMA Cardiol.* 2017;2:1100–1107.
22. Driessen RS, van Diemen PA, Raijmakers PG, et al. Functional stress imaging to predict abnormal coronary fractional flow reserve: the PACIFIC 2 study. *Eur Heart J.* 2022;43:3118–3128.
23. Danad I, Uusitalo V, Kero T, et al. Quantitative assessment of myocardial perfusion in the detection of significant coronary artery disease: cutoff values and diagnostic accuracy of quantitative [^{15}O]H_2O PET imaging. *J Am Coll Cardiol.* 2014;64:1464–1475.
24. Cerqueira MD, Weissman NJ, Dilsizian V, et al. Standardized myocardial segmentation and nomenclature for tomographic imaging of the heart. A statement for healthcare professionals from the Cardiac Imaging Committee of the Council on Clinical Cardiology of the American Heart Association. *Circulation.* 2002;105:539–542.
25. Uren NG, Melin JA, De Bruyne B, et al. Relation between myocardial blood flow and the severity of coronary-artery stenosis. *N Engl J Med.* 1994;330:1782–1788.
26. Petraco R, Sen S, Nijjer S, et al. Fractional flow reserve-guided revascularization: practical implications of a diagnostic gray zone and measurement variability on clinical decisions. *JACC Cardiovasc Interv.* 2013;6:222–225.
27. de Waard GA, Danad I, Petraco R, et al. Fractional flow reserve, instantaneous wave-free ratio, and resting Pd/Pa compared with [^{15}O]H_2O positron emission tomography myocardial perfusion imaging: a PACIFIC trial sub-study. *Eur Heart J.* 2018;39:4072–4081.
28. De Rosa S, Polimeni A, Petraco R, et al. Diagnostic performance of the instantaneous wave-free ratio: comparison with fractional flow reserve. *Circ Cardiovasc Interv.* 2018;11:e004613.
29. van de Hoef TP, Lee JM, Echavarria-Pinto M, et al. Non-hyperaemic coronary pressure measurements to guide coronary interventions. *Nat Rev Cardiol.* 2020;17:629–640.
30. Van't Veer M, Pijls NHJ, Hennigan B, et al. Comparison of different diastolic resting indexes to iFR: are they all equal? *J Am Coll Cardiol.* 2017;70:3088–3096.
31. Petraco R, van de Hoef TP, Nijjer S, et al. Baseline instantaneous wave-free ratio as a pressure-only estimation of underlying coronary flow reserve: results of the JUSTIFY-CFR Study (Joined Coronary Pressure and Flow Analysis to Determine Diagnostic Characteristics of Basal and Hyperemic Indices of Functional Lesion Severity-Coronary Flow Reserve). *Circ Cardiovasc Interv.* 2014;7:492–502.
32. Schindler TH. Myocardial blood flow: putting it into clinical perspective. *J Nucl Cardiol.* 2016;23:1056–1071.
33. Guerraty MA, Rao HS, Anjan VY, et al. The role of resting myocardial blood flow and myocardial blood flow reserve as a predictor of major adverse cardiovascular outcomes. *PLoS One.* 2020;15:e0228931.
34. Bom MJ, van Diemen PA, Driessen RS, et al. Prognostic value of [^{15}O]H_2O positron emission tomography-derived global and regional myocardial perfusion. *Eur Heart J Cardiovasc Imaging.* 2020;21:777–786.
35. Schumacher SP, Stuijfzand WJ, de Winter RW, et al. Ischemic burden reduction and long-term clinical outcomes after chronic total occlusion percutaneous coronary intervention. *JACC Cardiovasc Interv.* 2021;14:1407–1418.
36. Lee JM, Lee SH, Hwang D, et al. Long-term clinical outcomes of nonhyperemic pressure ratios: resting full-cycle ratio, diastolic pressure ratio, and instantaneous wave-free ratio. *J Am Heart Assoc.* 2020;9:e016818.
37. Boerhout CKM, de Waard GA, Lee JM, et al. Combined use of hyperemic and non-hyperemic pressure ratios for revascularization decision-making: from the ILIAS registry. *Int J Cardiol.* 2023;370:105–111.
38. Berry C, McClure JD, Oldroyd KG. Meta-analysis of death and myocardial infarction in the DEFINE-FLAIR and iFR-SWEDEHEART trials. *Circulation.* 2017;136:2389–2391.
39. Escaned JPM, Serruys P, Davies J. DEFINE-FLAIR: five-year follow-up. In: *2023 EuroPCR Course Programme.* PCR; 2023:88.

Toward Quantitative Multisite Preclinical Imaging Studies in Acute Myocardial Infarction: Evaluation of the Immune-Fibrosis Axis

Maja Strunk*[1], Gyu Seong Heo*[2], Annika Hess[1], Hannah Luehmann[2], Tobias L. Ross[1], Robert J. Gropler[2], Frank M. Bengel[1], Yongjian Liu[2], and James T. Thackeray[1]

[1]Department of Nuclear Medicine, Hannover Medical School, Hannover, Germany; and [2]Department of Radiology, Washington University School of Medicine, St. Louis, Missouri

The immune-fibrosis axis plays a critical role in cardiac remodeling after acute myocardial infarction. Imaging approaches to monitor temporal inflammation and fibroblast activation in mice have seen wide application in recent years. However, the repeatability of quantitative measurements remains challenging, particularly across multiple imaging centers. We aimed to determine reproducibility of quantitative inflammation and fibroblast activation images acquired at 2 facilities after myocardial infarction in mice. **Methods:** Mice underwent coronary artery ligation and sequential imaging with ^{68}Ga-DOTA-ECL1i to assess chemokine receptor type 2 expression at 3 d after myocardial infarction and ^{68}Ga-FAPI-46 to assess fibroblast activation protein expression at 7 d after myocardial infarction. Images were acquired at 1 center using either a local or a consensus protocol developed with the second center; the protocols differed in the duration of isoflurane anesthesia and the injected tracer dose. A second group of animals were scanned at the second site using the consensus protocol. Image analyses performed by each site and just by 1 site were also compared. **Results:** The uptake of ^{68}Ga-DOTA-ECL1i in the infarct territory tended to be higher when the consensus protocol was used ($P = 0.03$). No difference was observed between protocol acquisitions for ^{68}Ga-FAPI-46. Compared with the local protocol, the consensus protocol decreased variability between individual animals. When a matched consensus protocol was used, the ^{68}Ga-DOTA-ECL1i infarct territory percentage injected dose per gram of tissue was higher on images acquired at site B than on those acquired at site A ($P = 0.006$). When normalized to body weight as SUV, this difference was mitigated. Both the percentage injected dose per gram of tissue and the SUV were comparable between sites for ^{68}Ga-FAPI-46. Image analyses at the sites differed significantly, but this difference was mitigated when all images were analyzed at site A. **Conclusion:** The application of a standardized acquisition protocol may lower variability within datasets and facilitate comparison of molecular radiotracer distribution between preclinical imaging centers. Like clinical studies, multicenter preclinical studies should use centralized core-based image analysis to maximize reproducibility across sites.

Key Words: myocardial infarction; inflammation; fibroblast activation; reproducibility; macrophage

J Nucl Med 2024; 65:287–293
DOI: 10.2967/jnumed.123.266526

The immune-fibrosis axis has emerged as a prognostic imaging biomarker and therapeutic target for the progression of heart failure after acute myocardial infarction (*1*). For example, radiotracer molecular imaging of chemokine receptors, including C-C chemokine receptor type 2 (CCR2), provides a sensitive indication of local inflammation after myocardial injury that correlates with the severity of functional decline (*2*). Similarly, fibroblast activation protein (FAP) imaging reveals transient upregulation of activated fibroblasts early after myocardial infarction and predicts the subsequent functional outcome (*3–5*).

However, given the technical specialization involved in image acquisition, reconstruction, and analysis, obtaining reproducible quantitative values for radiotracer uptake can be challenging. Few studies have compared the reproducibilities of quantitative small-animal radiotracer images acquired at different imaging facilities. Mannheim et al. reported widely different whole-body biodistributions of ^{18}F-FDG in healthy mice when images were acquired and analyzed at 4 different imaging centers (*6*). Cardiac uptake alone varied by 120%. Even when variables were minimized using identical procedures, operators, and equipment, there remained considerable differences in quantitative cardiac ^{18}F-FDG uptake (*6*). Importantly, such studies have focused on ^{18}F-FDG, the uptake of which is governed by the metabolic state—which can be difficult to control, particularly under continuous anesthesia (*7–9*). The quantitative comparability of newer molecular imaging radiotracers across multiple laboratories has not been investigated. Given the growing emphasis on data integrity and reproducibility in preclinical research (*10,11*) and the rapid rollout of preclinical imaging studies, a direct assessment of the reproducibility of quantitative cardiac radiotracer uptake is desirable.

We hypothesized that a standardized acquisition protocol applied at 2 distinct imaging laboratories with cardiac expertise would reduce the variability in quantitative image analysis. We selected 2 preclinically established radioligands targeting aspects of the immune-fibrosis axis: ^{68}Ga-DOTA-ECL1i, targeting CCR2 expressed by proinflammatory monocytes/macrophages, and ^{68}Ga-FAPI-46, targeting FAP expressed by activated cardiac fibroblasts.

MATERIALS AND METHODS

Animals

Male C57BL/6N mice (*n* = 25) were purchased from Charles River Germany for site A. For site B, male and female CCR2$^{+/gfp}$ heterozygous mice (*n* = 4 of each) with a C57BL/6J background were used.

Received Aug. 10, 2023; revision accepted Nov. 9, 2023.

For correspondence or reprints, contact James T. Thackeray (Thackeray.James@mh-hannover.de).

*Contributed equally to this work.

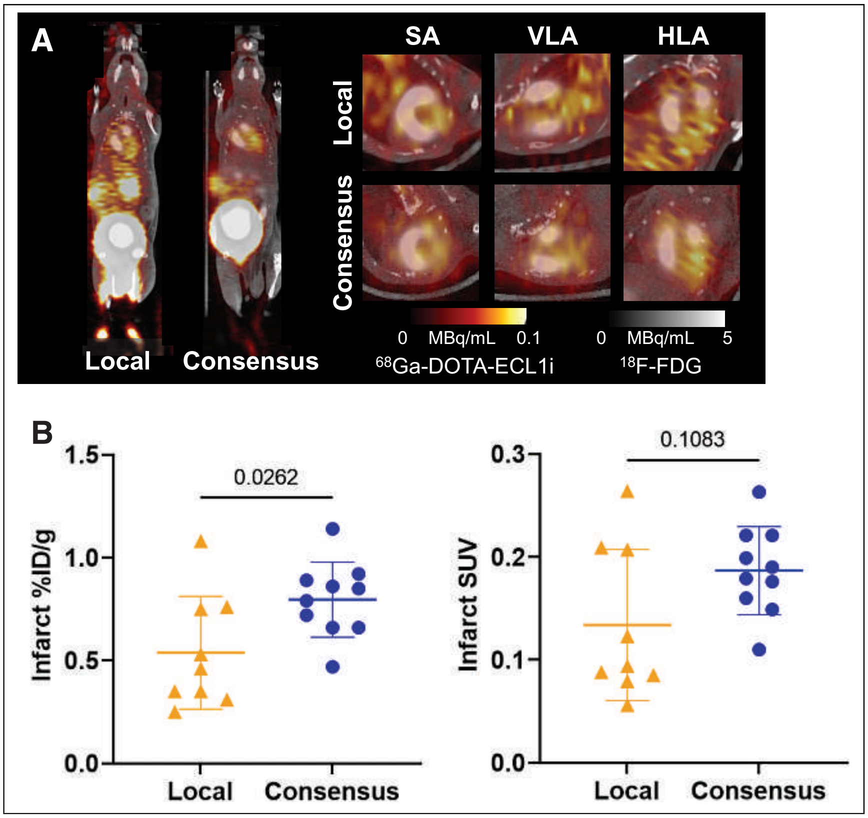

FIGURE 1. (A) Representative cardiac ^{68}Ga-DOTA-ECL1i images at 3 d after myocardial infarction and acquired using local and consensus imaging protocols. (B) Quantitative tracer uptake in infarct myocardium as %ID/g (left) and SUV (right) on images acquired using local or consensus acquisition protocol. Statistical analysis performed using Mann–Whitney *U* test. HLA = horizontal long axis; SA = short axis; VLA = vertical long axis.

In these mice, 1 CCR2 allele is replaced by green fluorescence protein, and these mice do not exhibit differences in inflammatory cell behavior relative to wild-type mice. Animals were housed in groups under temperature-controlled conditions and a 12-h light/12-h dark cycle, and a standard laboratory diet and water were freely available. All animal experiments were approved by the local state authority (Landesamt für Verbraucherschutz und Lebensmittelsicherheit or Washington University Institutional Animal Care and Use Committee) and conducted in accordance with European, U.S. (National Institutes of Health Office of Laboratory Animal Welfare), and international guidelines.

Surgery

Surgical myocardial infarction was induced at 8–10 wk of age at each site as described previously (*1*), with minor variations between sites. After analgesic pretreatment, mice were anesthetized, intubated, and mechanically ventilated. A left thoracotomy and pericardiotomy exposed the left anterior descending coronary artery, which was ligated ∼1 mm distal to the left auricle. The chest wall was then closed, anesthesia was discontinued, and animals recovered with continued postoperative analgesia treatment. Surgical details for each site are provided in Supplemental Table 1 (supplemental materials are available at http://jnm.snmjournals.org).

Study Design

At site A, animals were assigned to either the local acquisition protocol ($n = 9$) or the consensus acquisition protocol ($n = 10$). At site B, mice ($n = 8$) underwent imaging using the consensus protocol. Sequential imaging was performed to assess inflammation at 3 d after myocardial infarction using ^{68}Ga-DOTA-ECL1i and fibroblast activation at 7 d after myocardial infarction using ^{68}Ga-FAPI-46.

Radiosynthesis

^{68}Ga-DOTA-ECL1i and ^{68}Ga-FAPI-46 were produced as described previously (*12,13*), with minor deviations between centers, as noted in Supplemental Table 2. FAPI-46 precursor was provided by Sofie Biosciences. Radiochemical purity (>95%) was confirmed by high-performance liquid chromatography, and the product was diluted in isotonic saline for injection. The average cold doses administered were 0.92 ± 0.19 (mean ± SD) nmol for ^{68}Ga-DOTA-ECL1i and 0.99 ± 0.64 nmol for ^{68}Ga-FAPI-46.

Image Acquisition

Site A Local Protocol. PET and CT images were acquired in pairs using dedicated small-animal cameras (Inveon DPET and CT; Siemens) as described previously (*1*). Mice were anesthetized under isoflurane (2%; 0.8 L of O_2/min), and a 27-gauge catheter was inserted into a lateral tail vein. ^{68}Ga-DOTA-ECL1i (12.5 ± 0.8 MBq) or ^{68}Ga-FAPI-46 (12.5 ± 0.6 MBq) was administered as a 150-μL bolus in heparinized saline. Animals then recovered on a heating pad in a holding cage to allow conscious distribution of the radiotracer. After 40 min, animals were reanesthetized under isoflurane and placed prone on the scanner bed (Minerve) with continuous warm air circulation and respiration monitoring. Images were acquired from 45–60 min after radiotracer administration. At the conclusion of the PET scan, a low-dose CT scan was acquired for radiotracer colocalization. To define the infarct size and location, ^{18}F-FDG (18.3 ± 2.1 MBq) was administered as a 200-μL bolus by intraperitoneal injection subsequent to ^{68}Ga image acquisition with the animal in the identical position of the scanner bed. A static image was acquired 20–30 min after ^{18}F-FDG injection. Images were histogrammed to a single frame and reconstructed using an iterative ordered-subset expectation maximization (2 iterations) fast maximum a posteriori (18 iterations) algorithm with a target resolution of 1.5 mm and scanner-based corrections for scatter and dead time. A transmission scan with paired ^{57}Co sources was used for attenuation correction.

Consensus Protocol. The consensus protocol followed the same sequence as the site A local protocol, with some exceptions. First, a lower administered dose was used for ^{68}Ga-DOTA-ECL1i (8.5 ± 1.7 MBq) or ^{68}Ga-FAPI-46 (7.9 ± 2.6 MBq). Second, animals were maintained under isoflurane anesthesia throughout the radiotracer uptake phase and for the full duration of the experiment. Third, a low-dose CT scan was used for attenuation correction rather than a transmission scan. All other parameters were kept identical. Images at site B were acquired using the consensus protocol and a Mediso dedicated small-animal PET/CT camera. Images were reconstructed using the manufacturer's iterative TeraTomo 3DOSEM algorithm (6 subsets, 4 iterations). At site B, ^{18}F-FDG was administered using the same intravenous catheter as for the ^{68}Ga-labeled radiotracer administration, and images were acquired directly after the conclusion of the low-dose CT scan.

Image Analysis

At site A, regions of interest (ROIs) were drawn using ^{18}F-FDG images and imported to colocalized ^{68}Ga images as described

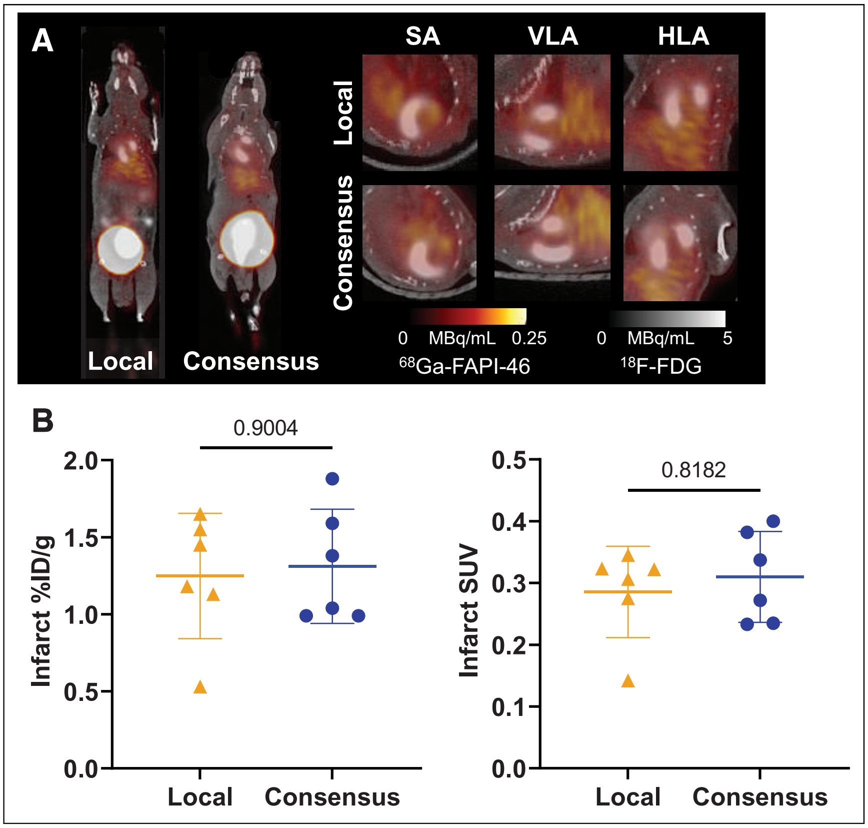

FIGURE 2. (A) Representative cardiac ^{68}Ga-FAPI-46 images at 7 d after myocardial infarction and acquired using local and consensus imaging protocols. (B) Quantitative tracer uptake in infarct myocardium as %ID/g (left) and SUV (right) in images acquired using local or consensus acquisition protocol. Statistical analysis performed using Mann–Whitney *U* test. HLA = horizontal long axis; SA = short axis; VLA = vertical long axis.

previously (*1*). ^{18}F-FDG and ^{68}Ga images were coregistered by alignment to the common CT image. Minimal manual adjustment following the anatomy was required, because the anesthetized animal was not moved between acquisitions. Briefly, an ROI for viable noninfarcted myocardium was defined by interactive thresholding on the ^{18}F-FDG scan and cross-applied to each matched ^{68}Ga scan. The infarct territory was defined by manual placement of an ROI covering the full anterolateral wall without ^{18}F-FDG uptake superior to the liver (Supplemental Fig. 1). With the colocalization CT image as a guide, additional ROIs were defined for the liver and quadriceps femoris skeletal muscle as nonspecific control regions. At site B, the infarct region was defined similarly, but a spheric ROI of fixed size (~20 mm^3) was manually positioned in the anterolateral wall or the inferoseptal wall.

Radiotracer uptake was quantified as the percentage injected dose per gram of tissue (%ID/g), where a uniform tissue density of 1 g/mL was assumed, and—to account for variable body weight—also as the SUV. Infarct size was calculated from polar map analysis using MunichHeart software (*1*). To assess whether variability in image analysis could be reduced, 2 individuals at site A analyzed imaging datasets from that site.

Statistics

All data are presented as mean ± SD. Statistical analysis was performed using GraphPad Prism (version 9.3). Quantitative radiotracer uptake was compared between imaging protocols or between sites using the Mann–Whitney test. Three groups for infarct sizes and body weights were compared using the Kruskal–Wallis test. Pearson product moment correlation was used to assess the relationship between parameters. Bland–Altman analysis was used to determine the intercenter and interoperator comparabilities of quantitative image analyses. Statistical significance was considered at a *P* value of less than 0.05.

RESULTS

Permanent Coronary Artery Ligation Generates Range of Scar Sizes at Different Imaging Sites

Infarct sizes were determined by polar map analysis of ^{18}F-FDG images acquired at 3 d after coronary occlusion, where scar was defined as less than 60% of the normalized maximum signal. Animals at site A exhibited a median infarct extent of 22% of the left ventricle (range, 8%–41%). There was no statistical difference in infarct size between mice assigned to different acquisition protocols (Supplemental Fig. 2A). By contrast, site B infarct sizes tended to be modestly larger (median, 29%; range, 18%–40%), but the differences from the site A infarct sizes were not statistically significant. Although there was no difference in body mass between protocols at site A (24 ± 2 vs. 23 ± 1 g; $P = 0.411$), CCR2$^{+/gfp}$ mice at site B had lower body mass (18 ± 2 g; $P < 0.001$), which may have affected radiotracer biodistribution (Supplemental Fig. 2B).

Standardized Acquisition Protocol Limits Variability of Inflammation Imaging Signal at Site A

To determine the impact of standardized acquisition on quantitative image analysis, we first acquired images using either the local or the consensus protocol in mice after coronary artery occlusion. ^{68}Ga-DOTA-ECL1i uptake was observed in the anterolateral nonviable infarct region of the left ventricle at 3 d after coronary artery occlusion (Fig. 1A). Quantitative analysis of the infarct region demonstrated significantly higher %ID/g and a trend toward higher SUV$_{\text{mean}}$ in mice scanned with the consensus protocol than in those scanned with the local protocol (Fig. 1B). Population variability in cardiac radiotracer uptake was lower among animals scanned with the consensus protocol than among those scanned with the local protocol ($\sigma = 0.51$ vs. 0.21) (Table 1). Radiotracer uptake values in nontarget organs, including remote noninfarcted myocardium, liver, and skeletal muscle, were similar in local and consensus protocol acquisitions (Supplemental Fig. 3).

Standardized Acquisition Has Limited Impact on Quantification of Fibroblast Activation at Site A

The uptake of ^{68}Ga-FAPI-46 at 7 d after coronary artery occlusion was generally elevated in the anterolateral infarct region and remote noninfarcted myocardium (Fig. 2A). Quantitative analysis demonstrated directly comparable radiotracer uptake in the infarct territory using either the local or the consensus protocol when calculated as %ID/g or SUV$_{\text{mean}}$ (Fig. 2B). The variabilities of the radiotracer signal in the infarct region were similar between protocols ($\sigma = 0.33$ vs. 0.31) (Table 1). In nontarget organs, the radiotracer signal was consistently low, although there was a tendency toward higher liver accumulation with the local protocol than with the consensus protocol (Supplemental Fig. 4).

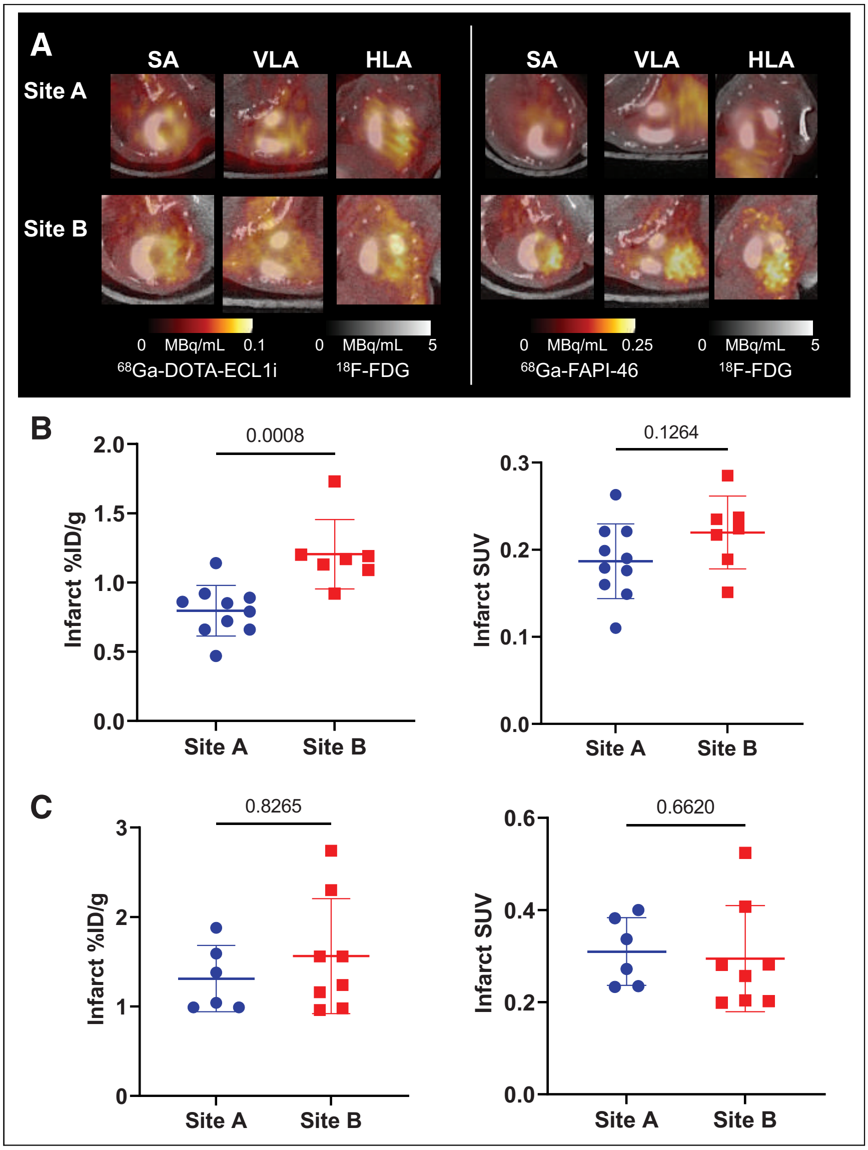

FIGURE 3. (A) Representative cardiac ^{68}Ga-DOTA-ECL1i and ^{68}Ga-FAPI-46 images acquired using consensus imaging protocol at site A and site B. (B) Quantitative uptake of ^{68}Ga-DOTA-ECL1i in infarct myocardium as %ID/g (left) and SUV (right). (C) Quantitative uptake of ^{68}Ga-FAPI-46 in infarct myocardium as %ID/g (left) and SUV (right). Statistical analysis performed using Mann–Whitney *U* test. HLA = horizontal long axis; SA = short axis; VLA = vertical long axis.

Standardized Acquisition Protocol Facilitates Direct Comparison of Quantitative Imaging Data Between Sites

To evaluate the consistency of imaging measurements across centers, 2 imaging sites acquired CCR2 and FAP PET images after coronary artery ligation using the consensus protocol, analyzed at site A. Radiotracer distributions were comparable, with localized cardiac accumulation of ^{68}Ga-DOTA-ECL1i at 3 d and ^{68}Ga-FAPI-46 at 7 d (Fig. 3A). A quantitative assessment revealed a consistently higher infarct region %ID/g CCR2 PET signal in images acquired at site B than in those acquired at site A using identical protocols (Fig. 3B). When uptake was normalized to body weight using SUV_{mean}, the difference between protocols was dampened. A similar pattern was observed in other peripheral organs, including the quadriceps skeletal muscle. By contrast, semiquantitative uptake of infarct region ^{68}Ga-FAPI-46 was more consistent between imaging sites using %ID/g and SUV_{mean} (Fig. 3C). Distribution to other peripheral organs was unaffected by the acquisition site. This discrepancy could not be explained by differences in infarct size, as there was no correlation between ^{18}F-FDG–defined infarct size and the intensity of the CCR2 PET signal (r = 0.205; P = 0.482) or the intensity of the FAP PET signal (r = 0.200; P = 0.494).

Image Quantification Is More Reproducible with Centralized Single-Site Analysis Than with Multisite Image Analysis

All images acquired at each site and with each protocol were analyzed independently by operators at site A and site B. Pairwise comparisons demonstrated consistently higher infarct territory %ID/g and SUV_{mean} for CCR2 images analyzed at site B than for those analyzed at site A (Fig. 4A). Bland–Altman analysis identified a strong correlation between these images (r = 0.940; P = 0.001), with consistent bias between sites (−0.24 ± 0.11 %ID/g) (Supplemental Fig. 5A). For FAP images, there was more variability in pairwise comparisons, but the average radiotracer uptake tended to be calculated at a higher value at site B than at site A (Fig. 4B). Bland–Altman analysis demonstrated a smaller bias in the infarct territory FAP signal (−0.17 ± 0.18 %ID/g) (Supplemental Fig. 5B). By contrast, Bland–Altman analysis demonstrated a high correlation and a smaller bias in CCR2 and FAP images between operators at site A alone (Supplemental Fig. 6). Because the radiotracer signal was calculated as an average for the total volume of interest, we evaluated the consistency of the sizes of the analyzed volumes of interest between centers. The average size of the volume of interest was smaller at site B than at site A (28 ± 5 vs. 22 ± 1 mm^3; P = 0.014); this finding may have contributed to the difference in the quantitative values (Supplemental Fig. 7). Notably, when image analysis was performed by 2 operators at site A, the quantitative values tended to be more similar, reflecting the similarity of the sizes of the volumes of interest for analysis.

DISCUSSION

The exponential growth of cardiac radionuclide-based molecular imaging applications, such as using inflammation- and FAP-targeted radiotracers, has generated extensive data; however, the lack of harmonized image acquisition and analysis procedures hinders comparison of data between studies, especially when undertaken by distinct imaging laboratories. Standardization of imaging protocols in clinical practice facilitates multicenter imaging trials, but implementation of similar procedures in small-animal imaging is lacking. With growing recognition of the importance of data

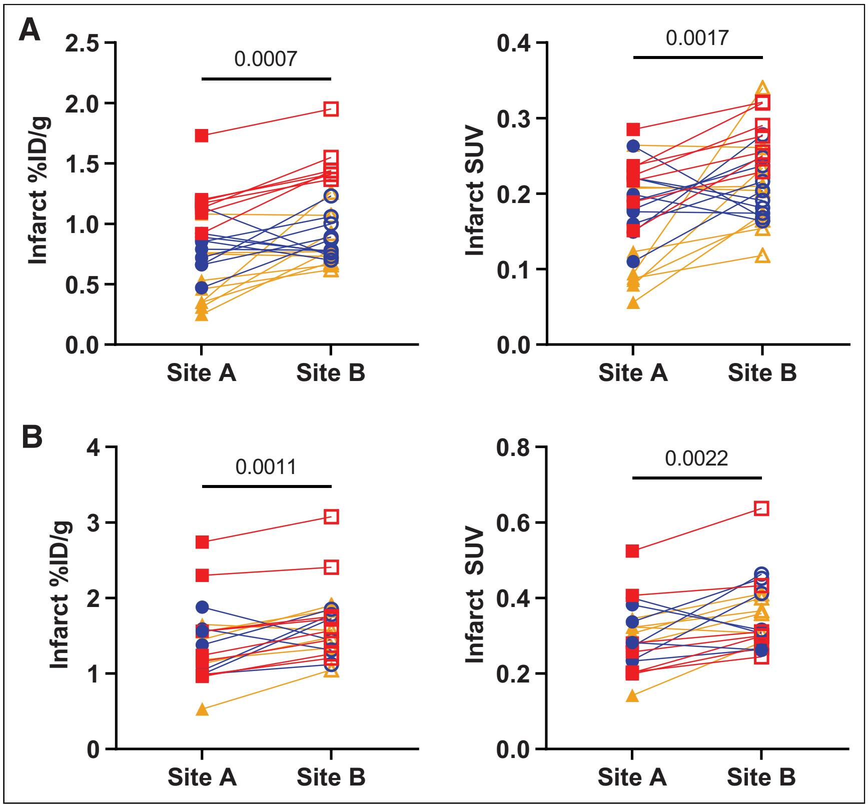

FIGURE 4. (A) Comparison of quantitative ^{68}Ga-DOTA-ECL1i uptake in infarct region on all images analyzed at site A or site B as %ID/g (left) or SUV (right). (B) Comparison of ^{68}Ga-FAPI46 uptake in infarct region on all images analyzed at site A or site B as %ID/g (left) or SUV (right). Statistical analysis performed using Student's paired *t* test.

reproducibility, there is an obligation in the imaging community to assess the impact of laboratory-imposed imaging protocols on quantitative measurements. Here, we compared distinct imaging protocols using 2 emerging molecular imaging markers of inflammation and fibroblast activation in the setting of experimental myocardial infarction in mice. This analysis revealed 3 key observations: first, changes in the image acquisition protocol regarding anesthesia duration and administered dose have a minimal impact on quantitative measurements acquired at the same institution; second, a harmonized imaging protocol reduces variability in images acquired in 2 different laboratories; and third, image analysis may represent a greater source of variability than image acquisition, suggesting a benefit to core lab–style centralized quantitative image analysis.

Although there has been widespread interest in the scientific community regarding the reproducibility of preclinical experiments, there remain hindrances to the adoption of standardized practices for data acquisition and analysis to facilitate interlaboratory comparisons. In molecular imaging, the confluence of biologic, radiochemical, and technical factors presents unique challenges to the comparability of quantitative measurements. Semiquantitative cardiac PET signals of chemokine receptor CXCR4 ligands after myocardial infarction diverge by up to 2-fold in %ID/g values (*14–17*). Likewise, the recent explosion of ^{68}Ga-FAPI-46 preclinical experiments has generated wide ranges of quantitative uptake values in the myocardium (*3,4,18,19*). Although some of this variability may be ascribed to species, radiotracer, or camera differences, there is no standardization in the methods used for acquisition and analysis.

In the present study, we observed a significant difference in ^{68}Ga-DOTA-ECL1i uptake in the infarct region between imaging protocols at the same site; this result was not apparent with ^{68}Ga-FAPI-46. This finding may reflect differences in the temporal dynamics of inflammation and fibroblast activation; that is, earlier postinfarction imaging of inflammation may be more sensitive to a change in the acquisition protocol than later postinfarction imaging of fibrosis. This notion may reflect differences in tracer blood clearance between the 2 compounds or differences in the tracer substrate between mobile blood-derived leukocytes and myocardium-derived activated fibroblasts. Blood activity of ^{68}Ga-DOTA-ECL1i also tends to be higher at 50–60 min after administration than that of ^{68}Ga-FAPI-46, which may be influenced by continuous isoflurane anesthesia affecting spillover to the infarct region.

Desire for reproducible preclinical imaging data has stimulated comparison studies across imaging centers, but many previous studies focused solely on the performance of different scanners. Phantom studies of the 2 scanners used in the present study showed similar spatial resolutions in hot rods, with comparable uniformity and spillover ratios (*20*). Nonequal SUV suggested higher variation with filtered backprojection reconstruction, but the phantom studies did not assess iterative reconstruction (*20*). Filtered backprojection reconstruction poorly resolves the myocardium (*8*), necessitating iterative algorithms like those used in the present study to differentiate between the infarct and remote noninfarcted myocardium.

One multicenter preclinical imaging study addressed the variability of quantitative ^{18}F-FDG biodistribution in healthy mice (*6*). Across 4 imaging laboratories, myocardial uptake of ^{18}F-FDG was widely divergent across laboratories. Further, image acquisition by the same personnel using different protocols led to minor differences in cardiac ^{18}F-FDG %ID/g (*6*). Metabolic preparation is crucial for ^{18}F-FDG imaging, such that fluctuations in blood glucose affect myocardial glucose transport (*7,8*). In the present study, despite different camera systems and personnel, the variation in quantitative imaging was reduced by use of a common acquisition protocol.

A major factor contributing to the difference in quantitative imaging values between centers appears to derive from image analysis. Interoperator %ID/g was more consistent in the automatically defined remote noninfarcted myocardium defined by the threshold of the colocalized ^{18}F-FDG image. Conversely, the infarct region required manual definition of boundaries, resulting in greater disparity of the ROI volume and quantitative uptake for both ^{68}Ga-DOTA-ECL1i and ^{68}Ga-FAPI-46. Although site A used the full region of the infarct territory for average radiotracer uptake, site B used a smaller region of consistent size across animals. The results suggest that restriction of the analysis area may emphasize regions of high radiotracer uptake that may not be

TABLE 1

Variability of Quantitative Tracer Uptake in Infarct Region

Tracer	Protocol	Variability in σ (SD/mean)
^{68}Ga-ECL1i	Site A local	0.511
	Site A consensus	0.214
	Site B consensus	0.152
^{68}Ga-FAPI-46	Site A local	0.326
	Site A consensus	0.310
	Site B consensus	0.351

representative of the entire infarct territory. By contrast, larger volumes of interest may lack sensitivity to subtle changes. Focal uptake of ^{68}Ga-DOTA-ECL1i in the infarct territory was consistently higher when analyzed by site B than by site A, irrespective of the location or image acquisition protocol, whereas the FAP signal was more dispersed between analyses. This result may reflect the larger area of FAP upregulation after infarction, as demonstrated in clinical studies (*5*), making it less susceptible to regional sampling bias. The larger size of the infarct ROI also counteracts potential partial-volume effects, which are more pronounced with smaller structures. The wider affected area of FAP expression may also suggest a value to global myocardium quantification, although further study is warranted. Taken together, the comparability of quantitative molecular imaging measurements likely requires centralized core facility–based image analysis at a single center, similar to the model used in clinical studies (*21*). One advantage of standardized protocols across multiple sites is the ability to increase sample sizes in imaging studies, as exemplified in a recent MRI study of stroke across 6 centers in more than 2,500 animals (*22*). That study demonstrated the feasibility of standardized procedures and centralized analysis to facilitate preclinical multicenter evaluation of therapeutics.

Some limitations to the present study should be acknowledged. First, biologic factors could not be standardized between centers. Specifically, the relative infarct sizes tended to be larger in the smaller mice operated at site B as compared with site A. Larger infarct size is associated with a stronger inflammatory response (*1*), which could contribute to the difference in subsequent fibroblast activation (*23*). When analysis was restricted to only animals with infarct sizes of greater than 20% of the left ventricle, the same pattern of tracer uptake site to site was apparent for both CCR2 and FAP imaging. Moreover, the difference in mouse strains may have contributed to variable inflammation after myocardial infarction. Although the CCR2$^{+/gfp}$ mice exhibit similar inflammatory cell content compared with the wild type, the difference between C57BL/6N and C57BL/6J mice may influence postinfarction healing (*24*). Likewise, we cannot discount an influence of sex on the observed uptake patterns. Initial analysis suggests no difference in male and female uptake of either ^{68}Ga-DOTA-ECL1i ($P = 0.857$) or ^{68}Ga-FAPI-46 ($P = 0.457$), but dedicated analysis in both sexes has not yet been pursued. Second, differences in pain management in the first 1–5 d after surgical infarction, particularly the use at site B of carprofen, which has antiinflammatory activity, may affect leukocyte dynamics and infarct healing postinfarction. We are heartened that the imaging signal of ^{68}Ga-DOTA-ECL1i remained comparable to mice at site A that were treated with the lesser antiinflammatory tramadol over the first days after infarction, suggesting that this action of carprofen postoperatively does not adversely impact healing. Third, because images at different sites were acquired using different commercial scanners, image reconstruction could not be completely standardized. Variability in the reconstruction algorithm can affect quantitative measurements (*25*), although the iterative reconstructions applied here have been widely validated against ex vivo measurements. Nonetheless, further investigation of multisite reproducibility of different reconstruction methods is warranted. Finally, we have only addressed in vivo imaging measurements without further validation by ex vivo autoradiography, γ-counting or protein measurements. It should be noted that correlation of in vivo image measurements have been directly correlated to the expression of CCR2 and FAP in prior studies (*2,4*).

CONCLUSION

The adoption of a common acquisition protocol may lower the variability of quantitative image analysis and facilitate comparison of radiotracer uptake between different imaging centers in preclinical imaging. Despite robust image acquisition, these findings suggest that multisite preclinical imaging studies would benefit from centralized image analysis, similar to clinical study design, to facilitate comparison of radiotracer uptake in images acquired at multiple sites.

DISCLOSURE

This work was supported by grants from the Leducq Foundation (to Robert J. Gropler, Frank M. Bengel, Yongjian Liu, and James T. Thackeray), the National Institutes of Health (P41EB025815), and the German Research Foundation (Heisenberg TH 2161/3–1, to James T. Thackeray). No other potential conflict of interest relevant to this article was reported.

KEY POINTS

QUESTION: Does the protocol for image acquisition in small animals affect quantitative reproducibility in cardiac imaging at multiple sites?

PERTINENT FINDINGS: The adoption of a standardized consensus acquisition protocol lowered variability in ^{68}Ga-DOTA ECL1i (CCR2) and ^{68}Ga-FAPI-46 (FAP) uptake values compared with a local acquisition protocol and enabled direct comparison of images acquired at a second facility. Quantitative analysis was more reproducible when conducted at a single center, supporting a core analysis model for multicenter preclinical imaging studies.

IMPLICATIONS FOR PATIENT CARE: Achieving reproducible quantitative measurements of radiotracer uptake across multiple institutions will increase the reliability of preclinical research, providing more robust biologic information, and may streamline translation to clinical applications.

REFERENCES

1. Hess A, Thackeray JT, Wollert KC, Bengel FM. Radionuclide image-guided repair of the heart. *JACC Cardiovasc Imaging.* 2020;13:2415–2429.
2. Heo GS, Kopecky B, Sultan D, et al. Molecular imaging visualizes recruitment of inflammatory monocytes and macrophages to the injured heart. *Circ Res.* 2019; 124:881–890.

3. Langer LBN, Hess A, Korkmaz Z, et al. Molecular imaging of fibroblast activation protein after myocardial infarction using the novel radiotracer [^{68}Ga]MHLL1. *Theranostics.* 2021;11:7755–7766.
4. Varasteh Z, Mohanta S, Robu S, et al. Molecular imaging of fibroblast activity after myocardial infarction using a ^{68}Ga-labeled fibroblast activation protein inhibitor, FAPI-04. *J Nucl Med.* 2019;60:1743–1749.
5. Diekmann J, Koenig T, Thackeray JT, et al. Cardiac fibroblast activation in patients early after acute myocardial infarction: integration with MR tissue characterization and subsequent functional outcome. *J Nucl Med.* 2022;63:1415–1423.
6. Mannheim JG, Mamach M, Reder S, et al. Reproducibility and comparability of preclinical PET imaging data: a multicenter small-animal PET study. *J Nucl Med.* 2019;60:1483–1491.
7. Kreissl MC, Stout DB, Wong KP, et al. Influence of dietary state and insulin on myocardial, skeletal muscle and brain [^{18}F]-fluorodeoxyglucose kinetics in mice. *EJNMMI Res.* 2011;1:8.
8. Thackeray JT, Bankstahl JP, Bengel FM. Impact of image-derived input function and fit time intervals on PATLAK quantification of myocardial glucose uptake in mice. *J Nucl Med.* 2015;56:1615–1621.
9. Toyama H, Ichise M, Liow JS, et al. Evaluation of anesthesia effects on [^{18}F]FDG uptake in mouse brain and heart using small animal PET. *Nucl Med Biol.* 2004;31: 251–256.
10. Begley CG, Ioannidis JP. Reproducibility in science: improving the standard for basic and preclinical research. *Circ Res.* 2015;116:116–126.
11. Pusztai L, Hatzis C, Andre F. Reproducibility of research and preclinical validation: problems and solutions. *Nat Rev Clin Oncol.* 2013;10:720–724.
12. Heo GS, Bajpai G, Li W, et al. Targeted PET imaging of chemokine receptor 2–positive monocytes and macrophages in the injured heart. *J Nucl Med.* 2021;62: 111–114.
13. Loktev A, Lindner T, Burger EM, et al. Development of fibroblast activation protein–targeted radiotracers with improved tumor retention. *J Nucl Med.* 2019;60: 1421–1429.
14. Cifarelli V, Kuda O, Yang K, et al. Cardiac immune cell infiltration associates with abnormal lipid metabolism. *Front Cardiovasc Med.* 2022;9:948332.
15. Hess A, Derlin T, Koenig T, et al. Molecular imaging-guided repair after acute myocardial infarction by targeting the chemokine receptor CXCR4. *Eur Heart J.* 2020;41:3564–3575.
16. Thackeray JT, Derlin T, Haghikia A, et al. Molecular imaging of the chemokine receptor CXCR4 after acute myocardial infarction. *JACC Cardiovasc Imaging.* 2015;8:1417–1426.
17. Zacherl MJ, Todica A, Wangler C, et al. Molecular imaging of cardiac CXCR4 expression in a mouse model of acute myocardial infarction using a novel ^{68}Ga-MCXCL12 PET tracer. *J Nucl Cardiol.* 2021;28:2965–2975.
18. Qiao P, Wang Y, Zhu K, et al. Noninvasive monitoring of reparative fibrosis after myocardial infarction in rats using ^{68}Ga-FAPI-04 PET/CT. *Mol Pharm.* 2022;19:4171–4178.
19. Wang G, Yang Q, Wu S, et al. Molecular imaging of fibroblast activity in pressure overload heart failure using [^{68}Ga]Ga-FAPI-04 PET/CT. *Eur J Nucl Med Mol Imaging.* 2023;50:465–474.
20. McDougald W, Vanhove C, Lehnert A, et al. Standardization of preclinical PET/CT imaging to improve quantitative accuracy, precision, and reproducibility: a multicenter study. *J Nucl Med.* 2020;61:461–468.
21. Fahey FH, Kinahan PE, Doot RK, Kocak M, Thurston H, Poussaint TY. Variability in PET quantitation within a multicenter consortium. *Med Phys.* 2010;37:3660–3666.
22. Lyden PD, Diniz MA, Bosetti F, et al. A multi-laboratory preclinical trial in rodents to assess treatment candidates for acute ischemic stroke. *Sci Transl Med.* 2023;15:eadg8656.
23. Hartupee J, Mann DL. Role of inflammatory cells in fibroblast activation. *J Mol Cell Cardiol.* 2016;93:143–148.
24. Gao XM, Xu Q, Kiriazis H, Dart AM, Du XJ. Mouse model of post-infarct ventricular rupture: time course, strain- and gender-dependency, tensile strength, and histopathology. *Cardiovasc Res.* 2005;65:469–477.
25. Constantinescu CC, Mukherjee J. Performance evaluation of an Inveon PET preclinical scanner. *Phys Med Biol.* 2009;54:2885–2899.

Noninvasive PET Detection of CD69-Positive Immune Cells Before Signs of Clinical Disease in Inflammatory Arthritis

Emmi Puuvuori*[1], Yunbing Shen*[2], Gry Hulsart-Billström[1], Bogdan Mitran[1,3], Bo Zhang[1], Pierre Cheung[1], Olivia Wegrzyniak[1], Sofie Ingvast[4], Jonas Persson[1,5], Stefan Ståhl[5], Olle Korsgren[4], John Löfblom[5], Fredrik Wermeling†[2], and Olof Eriksson†[1,3]

[1]Science for Life Laboratory, Department of Medicinal Chemistry, Uppsala University, Uppsala, Sweden; [2]Center for Molecular Medicine, Division of Rheumatology, Department of Medicine, Solna, Karolinska Institutet and Karolinska University Hospital, Stockholm, Sweden; [3]Antaros Medical AB, Mölndal, Sweden; [4]Department of Immunology, Genetics and Pathology, Uppsala University, Uppsala, Sweden; and [5]Department of Protein Science, Division of Protein Engineering, KTH Royal Institute of Technology, Stockholm, Sweden

Rheumatoid arthritis (RA) is the most common inflammatory joint disease, and early diagnosis is key for effective disease management. CD69 is one of the earliest cell surface markers seen at the surface of activated immune cells, and CD69 is upregulated in synovial tissue in patients with active RA. In this study, we evaluated the performance of a CD69-targeting PET agent, [^{68}Ga]Ga-DOTA-Z$_{\text{CAM241}}$, for early disease detection in a model of inflammatory arthritis. **Methods:** A model of inflammatory arthritis was induced by transferring splenocytes from KRN T-cell receptor transgenic B6 mice into T-cell–deficient I-A^{g7} major histocompatibility complex class II–expressing recipient mice. The mice were examined longitudinally by [^{68}Ga]Ga-DOTA-Z$_{\text{CAM241}}$ PET/CT before and 3, 7, and 12 d after induction of arthritis. Disease progression was monitored by clinical parameters, including measuring body weight and scoring the swelling of the paws. The uptake of [^{68}Ga]Ga-DOTA-Z$_{\text{CAM241}}$ in the paws was analyzed and expressed as SUV$_{\text{mean}}$. Tissue biopsy samples were analyzed for CD69 expression by flow cytometry or immunostaining for a histologic correlate. A second group of mice was examined by a nonbinding, size-matched Affibody molecule as the control. **Results:** Clinical symptoms appeared 5–7 d after induction of arthritis. The uptake of [^{68}Ga]Ga-DOTA-Z$_{\text{CAM241}}$ in the joints was negligible at baseline but increased gradually after disease induction. An elevated PET signal was found on day 3, before the appearance of clinical symptoms. The uptake of [^{68}Ga]Ga-DOTA-Z$_{\text{CAM241}}$ correlated with the clinical score and disease severity. The presence of CD69-positive cells in the joints and lymph nodes was confirmed by flow cytometry and immunostaining. The uptake of the nonbinding tracer that was the negative control also increased gradually with disease progression, although to a lesser extent than with [^{68}Ga]Ga-DOTA-Z$_{\text{CAM241}}$. **Conclusion:** The uptake of [^{68}Ga]Ga-DOTA-Z$_{\text{CAM241}}$ in the inflamed joints preceded the clinical symptoms in the KRN T-cell transfer model of inflammatory arthritis, in accordance with immunostaining for CD69. [^{68}Ga]Ga-DOTA-Z$_{\text{CAM241}}$ is thus a promising PET imaging marker of activated immune cells in tissue during RA onset.

Key Words: rheumatoid arthritis; inflammatory arthritis; PET; CD69; inflammation

J Nucl Med 2024; 65:294–299
DOI: 10.2967/jnumed.123.266336

Rheumatoid arthritis (RA) affects 0.5%–1% of the global population, making it the most common inflammatory arthropathy worldwide (*1*). It is a complex autoimmune disease characterized by chronic inflammatory changes, including synovium hyperplasia, hypertrophy, and joint destruction. The chronic inflammation can cause the destruction of cartilage and bone, eventually leading to limitations, disabilities, loss of function, decreased quality of life, and possibly shortened life expectancy, mainly because of increased risk of cardiovascular disease and lymphoma (*2,3*).

The etiology of RA is linked to a complex combination of genetic and environmental factors. The strongest identified environmental influences are smoking and other forms of lung stress (*4*). Of the genetic risk factors, the most important for RA development are the shared epitope alleles, which reside in the major histocompatibility complex class II region (*5*). The major histocompatibility complex class II molecules are expressed at high levels on professional antigen-presenting cells, including dendritic cells, B cells, and macrophages that play a crucial role in adaptive immune responses such as T-cell activation (*6,7*).

Although cytokine inhibitors can alleviate the symptoms of RA, there is no available cure, making early identification and accurate monitoring of the disease activity the keys to effective personalized treatment to slow disease progression (*8*). The diagnosis of RA uses a combination of medical history, physical examination, and blood tests of, for example, erythrocyte sedimentation rate, C-reactive protein, rheumatoid factor, and anticyclic citrullinated peptides (*9*). However, disease progress is not similar in all patients, and the early changes in joint activity might not be detectable in blood samples. Established clinical imaging modalities such as radiographs, CT, ultrasound, and MRI visualize secondary changes in bone and joint structures, which usually occur at later stages of the disease. None of these modalities provide information about molecular alterations or the role of specific immune cells during disease development (*10*). To overcome these issues, molecular imaging approaches could be used to detect early molecular changes and alterations in the local inflammatory milieu that precede structural changes. PET is a noninvasive molecular imaging modality that is

---

Received Jul. 12, 2023; revision accepted Oct. 10, 2023.

For correspondence or reprints, contact Fredrik Wermeling (fredrik.wermeling@ki.se) or Olof Eriksson (olof.eriksson@ilk.uu.se).

*Contributed equally to this work.

†Contributed equally to this work.

used in clinical routine for detection and staging in the oncologic setting. However, its applications in RA and inflammatory diseases are not widespread, mainly because of the lack of PET probes selective for immune cells. The metabolic PET marker [^{18}F]FDG has been the most widely used so far for imaging of inflammation in RA patients (*11,12*). [^{18}F]FDG studies have demonstrated the detection and quantification of several types of arthritis activity and displayed uptake in fibroblasts, neutrophils, and macrophages when exposed to the inflammatory cytokines tumor necrosis factor and interleukin 1. However, almost no uptake in T cells has been observed, and in nonsevere and remission patients, the results have been inconclusive (*11,12*). As a general marker for glucose metabolism, the common limitations of [^{18}F]FDG include nonspecificity and false-positive findings in areas with high metabolic activity, such as the brain, heart, activated muscles, or brown adipose tissue and tumors.

Several other radiotracers, including those targeting macrophages, bone metabolism, vascular adhesion protein 1, angiogenesis, and cell proliferation, have been evaluated in RA (*11–14*). However, most of these radiotracers have been evaluated only in small patient cohorts or tested only preclinically and thus require further clinical evaluation (*13–16*). Thus, despite intense efforts in this area, there is an urgent need for PET imaging probes specific for noninvasive detection of immune cell activation in RA.

CD69 is an early activation antigen expressed by immune cells during activation. Limited expression is seen in peripheral blood leukocytes of healthy individuals. In contrast, increased expression is seen in T cells, B cells, and neutrophils in synovial tissue of RA patients, making it a promising target for studying aspects of the adaptive and innate immune reactions during RA onset and progression (*17–20*). Recently, radiolabeled antibodies directed toward CD69 were described and evaluated as imaging agents for detection of tumor-infiltrating activated immune cells in the oncologic context (*21,22*). However, antibodies are not ideal PET imaging agents because of their large size and slow clearance. Therefore, we have developed Z_{CAM241}, a small protein based on the Affibody (Affibody AB) molecule scaffold with nanomolar affinity for human and murine CD69 (*23*).

In this study, we examined the potential of ^{68}Ga-labeled Z_{CAM241} for early PET detection of activated immune cells in tissue in a mouse model of induced inflammatory arthritis.

MATERIALS AND METHODS

Chemical Synthesis and Radiolabeling of Affibody Molecules

Z_{CAM241} is an Affibody molecule selected for binding to the extracellular domain of human recombinant CD69 (Supplemental Table 1 [supplemental materials are available at http://jnm.snmjournals.org]) (*23,24*). The chemical synthesis and the ^{68}Ga radiolabeling of DOTA-conjugated Z_{CAM241} and the nonbinding, size-matched Affibody molecule DOTA-Z_{AM106} as the control are described in detail in the supplemental materials.

In Vitro and In Vivo Characterization of [^{68}Ga]Ga-DOTA-Z_{CAM241}

Unlabeled Z_{CAM241} has been evaluated in detail, such as with respect to affinity toward CD69 (*23*). DOTA-Z_{CAM241} labeled with ^{111}In has been studied for in vivo biodistribution and has demonstrated binding to, for example, activated human peripheral blood mononuclear cells (*23*). Here, we verified that radiolabeled [^{68}Ga]Ga-DOTA-Z_{CAM241} retained the biodistribution, stability, and binding of previously evaluated radiolabeled analogs (supplemental materials; Supplemental Figs. 1–3).

Adoptive T-Cell Transfer and Joint Evaluation

Experiments used 8- to 12-wk-old sex- and age-matched mice. KRN.B6 mice were generated and provided by Diane Mathis and Christophe Benoist (Harvard Medical School) (*25*). KRN.B6.CD45.1 mice were generated by crossing KRN.B6 mice with CD45.1 mice (stock number 002014, Jackson Laboratories). TCRb$^{-/-}$I-A$^{b+/-}$I-A$^{g7+/-}$ mice were generated by crossing B6.TCRb mice (TCRb$^{-/-}$ on C57BL/6 background; stock number 002118) with nonobese diabetic mice (stock number 001976, Jackson Laboratories). Primers used for genotyping are detailed in the supplemental materials. To induce disease, KRN.B6 splenocytes were prepared by pressing the spleen through a 40-μm cell strainer with a 3-mL syringe plunger. Roughly 2×10^7 cells were injected via the tail vein into TCRb$^{-/-}$I-A$^{b+/-}$I-A$^{g7+/-}$ recipient mice. The severity of arthritis was scored every 2–3 d by clinical examination of each paw and ankle (0, no swelling; 3, maximal swelling), adding up to a total clinical score (0–12) per mouse. The weight of the animals was monitored every 2–3 d. At the end of each experiment, different organs and blood were collected for further analysis.

[^{68}Ga]Ga-DOTA-Z_{CAM241} PET/CT Imaging of Arthritic Mice

The animal experiments were authorized by the Animal Ethics Committee of the Swedish Animal Welfare Agency and performed according to institutional guidelines (Uppsala University Guidelines on Animal Experimentation, UFV 2007/724) and ARRIVE 2.0 guidelines.

The study design was a longitudinal imaging study to follow each mouse through 4 PET scans over 12 d, from before disease induction and during disease progression. The detailed ethical considerations and the in vivo study design are described in the supplemental materials.

Each mouse (5 female mice; weight, 20–23 g at the start of the study) was imaged by [^{68}Ga]Ga-DOTA-Z_{CAM241} (target dose of 2 MBq) PET 4 times: before (baseline) and then 3, 7, and 12 d after induction of inflammatory arthritis (Supplemental Fig. 1B). The mice were euthanized after the last PET scan, and biopsy samples were taken.

A control study was conducted separately with the nonbinding Affibody molecule [^{68}Ga]Ga-DOTA-Z_{AM106}, using the same protocols for imaging, disease induction, and monitoring of clinical symptoms as described earlier for [^{68}Ga]Ga-DOTA-Z_{CAM241}. Briefly, [^{68}Ga]Ga-DOTA-Z_{AM106} was evaluated by PET/CT (target injected dose, 2 MBq; same scanning protocol in 4 female mice; weight, 20–23 g at the start of the control study) at 4 time points (baseline and 3, 7, and 10 d after disease induction).

The PET scanning protocol, the image analysis methodology, and the histologic analysis of postmortem biopsy samples are described in detail in the supplemental materials.

Flow Cytometry

Single-cell suspensions from lymph organs were collected by pressing through a 40-μm cell strainer with a 3-mL syringe plunger. Single cells from the ankle joints of the hind paws were prepared by cutting joint tissue into small pieces in cold phosphate-buffered saline, vortexing, and filtering through a 40-μm cell strainer. Cells were filtered and stained with BioLegend's CD19-Alexa647 (catalog number 115522), CD45.1-BV605 (catalog number 110738), CD45.2-BV785 (catalog number 109839), TCRβ-BV711 (catalog number 109243), and CD69-PE (catalog number 310905), as well as the Fixable Aqua Dead Cell Stain Kit (catalog number L34965; Invitrogen), for 30 min. After staining, cells were acquired using BD LSRFortessa. Generated flow cytometry standard files were analyzed by FlowJo version 10 (FlowJo).

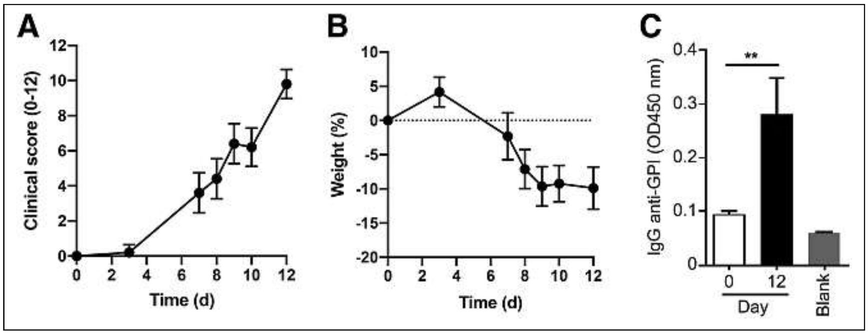

FIGURE 1. (A) Quantification of joint inflammation (clinical score, 0–12; 0–3 points per paw) as part of characterizing induced joint inflammation in KRN T-cell adoptive transfer model. (B) Weight change presented as percentage of weight at day 0. (C) Serum IgG anti-GPI levels comparing day 0 and day 12. $^{**}P < 0.01$, by unpaired *t* test ($n = 5$). GPI = glucose phosphate isomerase; OD = optical density.

RESULTS

Progression of Joint Disease

The disease development of the mice was monitored by scoring the swelling of the paws, including the ankle, and measuring the weight of the animals. The clinical score started to increase 7 d after injection of the model (Fig. 1A). Weight decreased 5 d after injection (Fig. 1B), reaching a maximum drop of approximately 10%. IgG anti-glucose phosphate isomerase (GPI) levels were significantly different between baseline and day 12 (Fig. 1C). The uptake in PET images was already visibly increasing on rear paws 3 d after injection (Fig. 2A) and in line with corresponding CD69 staining (Fig. 2B).

[^{68}Ga]Ga-DOTA-Z$_{\text{CAM241}}$ Uptake Increased During Progression of Inflammatory Arthritis

The in vitro and in vivo characterization of [^{68}Ga]Ga-DOTA-Z$_{\text{CAM241}}$ in healthy animals demonstrated suitable biodistribution (Supplemental Figs. 2 and 3A–3C; details in supplemental materials) and retained binding toward CD69 (Supplemental Fig. 3D). These results guided the design of the imaging protocol in the arthritic mice.

The PET images were quantified by calculating the SUV$_{\text{mean}}$ of the rear joints. As seen visually in Figure 2, the SUV increased gradually and almost linearly from day 0 (SUV$_{\text{mean}}$, 0.21 ± 0.04, $n = 5$) to day 3 (SUV$_{\text{mean}}$, 0.69 ± 0.25, $n = 5$), day 7 (SUV$_{\text{mean}}$, 1.06 ± 0.09, $n = 5$), and day 12 (SUV$_{\text{mean}}$, 1.53 ± 0.12, $n = 5$; Fig. 3A). The SUV$_{\text{mean}}$ of each mouse is displayed in Figure 3B, where all animals followed similar uptake pattern. Most variation was noticeable at the day 3 time point, where 1 animal (mouse 2; Fig. 3B) exhibited a higher increase in joint uptake than the rest of the animals. The ratio of [^{68}Ga]Ga-DOTA-Z$_{\text{CAM241}}$ uptake to baseline demonstrated a similar increase with time from induction of disease (Fig. 3C). In addition, the ratio of [^{68}Ga]Ga-DOTA-Z$_{\text{CAM241}}$ uptake to baseline demonstrated a positive correlation with the clinical score of the joints ($r = 0.82$, $P < 0.0001$; Fig. 3D).

Uptake of the Control Nonbinding Peptide [^{68}Ga]Ga-DOTA-Z$_{\text{AM106}}$ in Inflammatory Arthritis

The ratio of [^{68}Ga]Ga-DOTA-Z$_{\text{AM106}}$ uptake to baseline also increased over time (Supplemental Fig. 4A), although to a lesser extent than for [^{68}Ga]Ga-DOTA-Z$_{\text{CAM241}}$. The correlation between [^{68}Ga]Ga-DOTA-Z$_{\text{AM106}}$ uptake ratio to baseline and clinical score of the joints indicated a positive connection ($r = 0.87$, $P < 0.0001$; Supplemental Fig. 4B) but was less pronounced than for [^{68}Ga]Ga-DOTA-Z$_{\text{CAM241}}$. The disease progression in the mice being investigated with the control nonbinding peptide [^{68}Ga]Ga-DOTA-Z$_{\text{AM106}}$ was similar to that monitored by clinical symptoms such as swelling of the paws and weight changes (Supplemental Figs. 4C and 4D). Histology of the joints demonstrated the presence of CD69-positive cells after euthanasia at the day 10 time point (Supplemental Fig. 4D).

Expression of CD69 in the Lymph Nodes Was Higher Than in the Joints

Besides analysis in the joints, CD69 expression levels were analyzed in different cell populations and organs (axillary, brachial, inguinal, mesenteric, and popliteal lymph nodes, as well as the spleen and joints) on day 12. The representative histogram gating is presented as viable singlets in Figure 4A, and quantification of the plots is presented in Figure 4B. The frequency of B cells and T cells in the CD69-positive viable singlet gate is shown in Figure 4C, and the quantification of plots is shown in Figure 4D. Fluorescence staining of the lymph nodes at baseline (Supplemental Fig. 4A) and 12 d after injection of arthritis induction (Supplemental Fig. 4B) demonstrated increased expression of CD69, in line with flow cytometry results. [^{68}Ga]Ga-DOTA-Z$_{\text{CAM241}}$ uptake of the right (SUV$_{\text{mean}}$, 3.6 ± 1.09) and left (SUV$_{\text{mean}}$, 3.3 ± 0.72) axillary lymph nodes was strong 12 d after disease induction, higher than the background uptake in muscle (SUV$_{\text{mean}}$, 0.45 ± 0.34; Fig. 4E) and consistent with the presence of CD69-positive cells seen by flow cytometry at the same time point.

DISCUSSION

Appropriate diagnosis and prediction of the disease progression of the individual RA patient are fundamental for successful

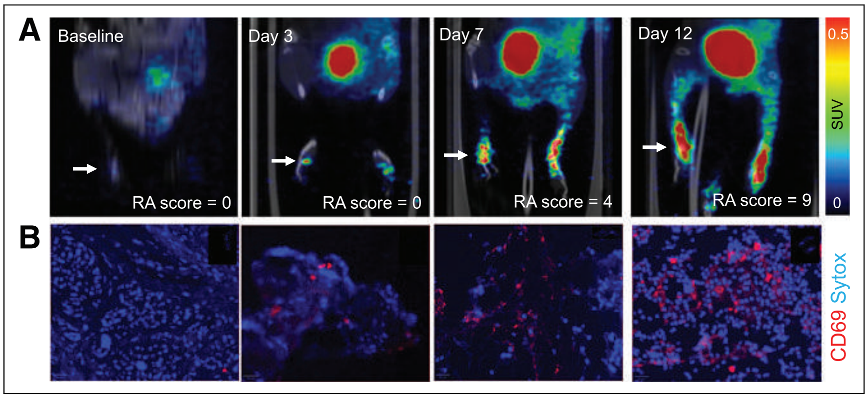

FIGURE 2. (A) PET images of [^{68}Ga]Ga-DOTA-Z$_{\text{CAM241}}$ uptake at baseline and 3, 7, and 12 d after injection as inflammatory arthritis developed in single representative individual mouse. Images are normalized to SUV of 0.5 for direct comparison between time points. (B) CD69 immunofluorescence Sytox (Thermo Fisher Scientific) staining of joints of representative animals during matching time points.

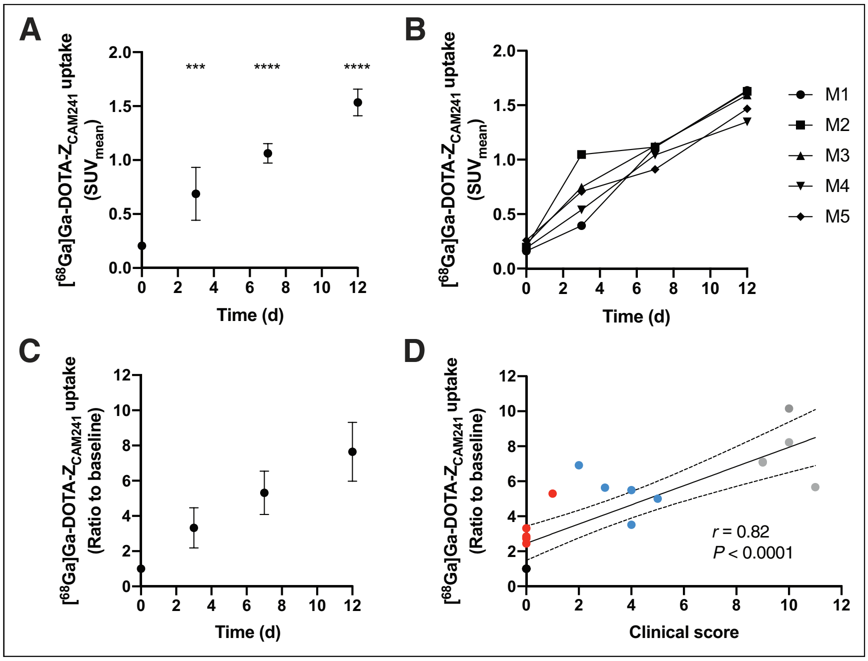

FIGURE 3. [^{68}Ga]Ga-DOTA-Z$_{CAM241}$ uptake expressed as SUV$_{mean}$ (each point represents average and SD of 5 scans) over time in joints either at group level (A) or in individuals (B). Error bars for day 0 time point in A are too small to be visualized. Asterisks indicate significance compared with baseline at day 0. (C) Uptake of [^{68}Ga]Ga-DOTA-Z$_{CAM241}$ expressed as ratio at each time point compared with baseline in individuals. (D) Correlation of uptake of [^{68}Ga]Ga-DOTA-Z$_{CAM241}$ in joints with clinical score. ***$P < 0.001$. ****$P < 0.0001$. M1–M5 = mouse 1 to mouse 5.

treatment, because the outcome of RA can be vastly heterogeneous. New drugs and treatment modalities, such as emerging biologics, are associated with high costs and potential serious side effects for the patient. An established PET tracer for sensitive detection of activated immune cells in RA could offer prognostic value by identifying subclinical activity in individuals at an early stage of disease development, predicting flares in patients with established disease, and serving as a tool for early monitoring of drug response. Early detection is central to the development of potential preventative and curative treatments. To accomplish this, several immune cell activation markers could be considered potential targets for probes, such as surface markers for T-cell subpopulations (*26*). Accordingly, PET radiotracers have been developed to enable preclinical in vivo detection of, for example, CD69 (*21–23*), inducible T-cell costimulator (*27*), OX40 (*28*), granzyme B (*29*), and interferon-γ (*30*). So far, these techniques have not been applied specifically in models of inflammatory arthritis.

In this study, we wanted to assess PET tracer [^{68}Ga]Ga-DOTA-Z$_{CAM241}$ uptake in a mouse model of inflammatory arthritis. The model we used is a KRN T-cell transfer model, in which splenic KRN T cells are injected into T-cell–deficient mice. The KRN T-cell transfer model has been reported to be reproducible and show clinical signs of disease onset 7 d after the transfer, with infiltration of macrophages and neutrophils into the joints, as well as cartilage damage and bone resorption. T cells have not been detected in the joints but have been reported to be present in the popliteal lymph nodes (*23*). Disease severity usually reaches a maximum peak after around 2 wk of induction (*23*). Similarly, in this study, we observed that the mice developed clinical symptoms in the form of swelling of the joints around day 7, but the average weight decreased a little earlier, on day 5. The uptake of [^{68}Ga]Ga-DOTA-Z$_{CAM241}$ in the joints was already visually apparent on PET images 3 d after induction of the model, which is earlier than the clinical signs started appearing. The largest variability in SUV uptake between individual animals was also on day 3, which could refer to the variation in magnitude of the initial immune reaction. Otherwise, the animals followed approximately the same pattern of disease progression. [^{68}Ga]Ga-DOTA-Z$_{CAM241}$ uptake gradually increased with time, which is consistent with the increasing severity of the inflammation and the correlation between SUV ratio and clinical score.

The uptake of [^{68}Ga]Ga-DOTA-Z$_{CAM241}$ was low in or absent from the joints before disease induction (SUV$_{mean}$, ∼0.2; Fig. 3A), but it increased almost 10-fold 12 d after injection (SUV$_{mean}$, ∼1.5). The uptake of [^{68}Ga]Ga-DOTA-Z$_{CAM241}$ in the lymph nodes on day 12 was even stronger, with SUV$_{mean}$ greater than 3 (Fig. 4E). However, because of the small size of the animal model compared with the resolution of the scanner, as well as the proximity of high focal uptake in the kidneys, it was difficult to measure the CD69 signal from the lymph nodes in vivo. Thus, the absolute values of the uptake of [^{68}Ga]Ga-DOTA-Z$_{CAM241}$ in the lymph nodes should be considered with caution. Still, the relative uptake patterns are in agreement with the flow cytometry data, which indicate a higher proportion of CD69-positive immune cells in the lymph nodes than in the joints (Fig. 4B). In addition, flow cytometry analysis of the lymph nodes identified that the main CD69-expressing cells were B cells, followed by T cells. This is in line with the interaction of autoreactive B cells and T cells, resulting in IgG anti-GPI production that is central to this disease model (*25*).

Strong inflammation in tissue involves not only recruitment of immune cells but also increased perfusion and vascular permeability. The last 2 factors are known to potentially contribute to increased nonspecific PET tracer uptake in tissue. Thus, it is important to control for nonspecific uptake in sites of inflammation.

After analysis of [^{68}Ga]Ga-DOTA-Z$_{CAM241}$, we proceeded to investigate in another batch of animals the uptake of the nonbinding Affibody molecule [^{68}Ga]Ga-DOTA-Z$_{AM106}$ as a control, using the same experimental setup. The uptake of [^{68}Ga]Ga-DOTA-Z$_{AM106}$ followed the same pattern by increasing in the joints with time, but it was lower than with [^{68}Ga]Ga-DOTA-Z$_{CAM241}$. This indicates that there is a separate mechanism for nonspecific uptake, likely because of increased perfusion and permeability resulting from the inflammatory environment. Therefore, there is most likely a nonspecific component for the uptake of [^{68}Ga]Ga-DOTA-Z$_{CAM241}$, in addition to binding to CD69-positive immune cells in tissue. However, the animal model of inflammatory arthritis used in this study exhibits stronger and more acute inflammation than the usually chronic and low-intensive process seen in RA in humans. Thus, it can be expected that the nonspecific uptake of [^{68}Ga]Ga-DOTA-Z$_{CAM241}$ resulting from increased perfusion and vascular permeability would be less pronounced in patients.

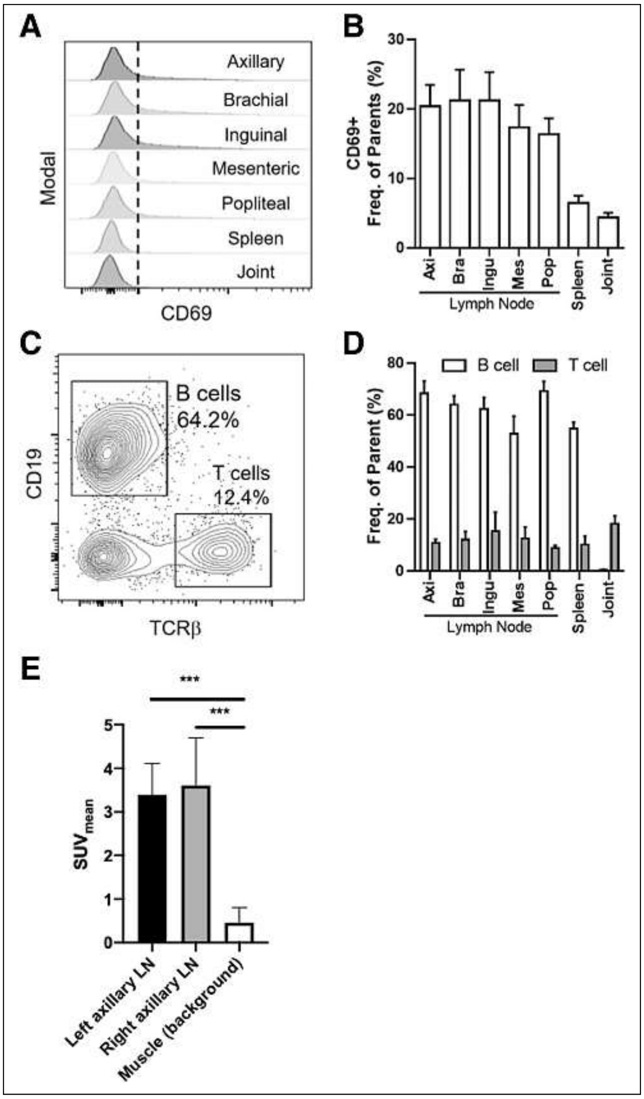

FIGURE 4. CD69 expression analysis in different cell populations on day 12. (A) Representative histogram plot of CD69 expression in different lymph organs (axillary, brachial, inguinal, mesenteric, and popliteal lymph nodes, as well as spleen and joints). Gate shows viable singlets. (B) Quantification of plots in A, with CD69-positive percentage of viable singlets ($n = 3$). (C) Representative plot showing frequency of B cells and T cells in CD69-positive viable singlet gate. (D) Quantification of plots in C, with percentage of B cells and T cells in CD69-positive viable singlet gate ($n = 3$). (E) SUV$_{\text{mean}}$ uptake of left and right axillary lymph nodes and muscle at day 12. ***$P < 0.001$, by ANOVA ($n = 5$). Axi = axillary; Bra = brachial; Freq. = frequency; Ingu = inguinal, LN = lymph node; Mes = mesenteric; Pop = popliteal; TCRβ = T-cell receptor β.

Limitations of the current study include the lack of blocking studies in a subset of animals. However, there is a lack of available CD69-specific binders and inhibitors or endogenous ligands, and before the discovery of Z$_{\text{CAM241}}$, only monoclonal or polyclonal antibodies toward CD69 were available. Thus, no ligands are suitable for in vivo blocking, except for the CD69-targeting Affibody molecule Z$_{\text{CAM241}}$. Z$_{\text{CAM241}}$ may also block potential off-target binding; thus, blocking with an unrelated binder is usually recommended for validation of PET tracers. Because of the lack of a suitable blocking ligand different from the Affibody molecule, we opted to use the nonbinding, size-matched Affibody molecule [^{68}Ga]Ga-DOTA-Z$_{\text{AM106}}$ to estimate the nonspecific uptake, as is often done in similar situations.

Another limitation is that the [^{68}Ga]Ga-DOTA-Z$_{\text{CAM241}}$ and [^{68}Ga]Ga-DOTA-Z$_{\text{AM106}}$ PET scans were performed on different groups of animals, which may have different severity levels of inflammatory arthritis. This was done to decrease the number of PET scans and tracer injections to which each animal was subjected. It was considered better for the study design to obtain tracer uptake at 4 time points in 2 groups than to obtain 2 scans using 2 tracers (the active and the control nonbinding PET probes). However, the selected model is known for its reproducibility, which was confirmed by the similar outcome of clinical scores; thus, the PET data from both groups should be comparable.

For future studies, binding of [^{68}Ga]Ga-DOTA-Z$_{\text{CAM241}}$ should be further investigated with blocking studies to confirm the proportion of binding in the inflamed joints that is specific and the proportion that results from nonspecific capillary leakage. In addition, a study in a larger animal model, such as a pig, could provide more information about lymph node uptake because of the larger distance between tissues, minimizing the spillover from excretory organs.

CONCLUSION

Increased uptake of the CD69-directed peptide [^{68}Ga]Ga-DOTA-Z$_{\text{CAM241}}$ was seen in the paws of mice with induced inflammatory arthritis, which preceded the appearance of clinical symptoms. [^{68}Ga]Ga-DOTA-Z$_{\text{CAM241}}$ is thus a potential candidate for PET imaging of activated immune cells during RA onset.

KEY POINTS

QUESTION: Can activated immune cells be visualized in inflammatory arthritis using a CD69-targeting PET tracer?

PERTINENT FINDINGS: CD69-directed peptide [^{68}Ga]Ga-DOTA-Z$_{\text{CAM241}}$ displayed increased uptake in the paws of mice with induced inflammatory arthritis, which preceded the appearance of clinical symptoms. [^{68}Ga]Ga-DOTA-Z$_{\text{CAM241}}$ accumulation in the paws was strong and consistent with disease duration, whereas a nonspecific control peptide demonstrated only low binding.

IMPLICATIONS FOR PATIENT CARE: [^{68}Ga]Ga-DOTA-Z$_{\text{CAM241}}$ is a potential candidate for clinical PET imaging of activated immune cells in the joints during onset of, for example, RA.

DISCLOSURE

The study was funded by JDRF (1-SRA-2020-973-S-B), the Science for Life Laboratory, the Swedish Research Council (2020-02312 to Olof Eriksson, 2019-05115 to John Löfblom, 2019-01415 to Olle Korsgren, and 2021-03178 to Fredrik Wermeling), the Swedish Cancer Society (CAN 2017/649 and 20 1090 PjF to John Löfblom and 20 1114 PjF and 22 0546 SIA to Fredrik Wermeling), Vinnova (2019/00104 to John Löfblom), the China Scholarship Council (to Yunbing Shen), ExoDiab, the Novo Nordisk Foundation, an EFSD/Novo Nordisk grant, the Ernfors Family Fund, Barndiabetesfonden, Diabetesfonden, Diabetes Wellness, the Sten A. Olssons Foundation, Helmsley Charitable Trust, and the Juvenile Diabetes Foundation International. John Löfblom, Jonas Persson, Stefan Ståhl, Olof Eriksson, and Olle Korsgren are inventors of a patent covering Z$_{\text{CAM241}}$. Bogdan Mitran and Olof Eriksson are employees of Antaros Medical AB. Olof Eriksson and Olle

Korsgren are shareholders of Antaros Tracer AB. No other potential conflict of interest relevant to this article was reported.

ACKNOWLEDGMENTS

The Preclinical PET/MRI Platform, Sofie Ingvast, Athanisios Bitzios, and Bogdan Mitran are acknowledged for expert technical assistance.

REFERENCES

1. Almutairi K, Nossent J, Preen D, Keen H, Inderjeeth C. The global prevalence of rheumatoid arthritis: a meta-analysis based on a systematic review. *Rheumatol Int.* 2021;41:863–877.
2. Catrina AI, Svensson CI, Malmström V, Schett G, Klareskog L. Mechanisms leading from systemic autoimmunity to joint-specific disease in rheumatoid arthritis. *Nat Rev Rheumatol.* 2017;13:79–86.
3. de Almeida DE, Ling S, Holoshitz J. New insights into the functional role of the rheumatoid arthritis shared epitope. *FEBS Lett.* 2011;585:3619–3626.
4. Klareskog L, Catrina AI. Autoimmunity: lungs and citrullination. *Nat Rev Rheumatol.* 2015;11:261–262.
5. Scherer HU, Häupl T, Burmester GR. The etiology of rheumatoid arthritis. *J Autoimmun.* 2020;110:102400.
6. Klareskog L, Forsum U, Scheynius A, Kabelitz D, Wigzell H. Evidence in support of a self-perpetuating HLA-DR-dependent delayed-type cell reaction in rheumatoid arthritis. *Proc Natl Acad Sci USA.* 1982;79:3632–3636.
7. Ting JPY, Trowsdale J. Genetic control of MHC class II expression. *Cell.* 2002; 109(suppl):S21–S33.
8. van der Krogt JMA, van Binsbergen WH, van der Laken CJ, Tas SW. Novel positron emission tomography tracers for imaging of rheumatoid arthritis. *Autoimmun Rev.* 2021;20:102764.
9. Kay J, Upchurch KS. ACR/EULAR 2010 rheumatoid arthritis classification criteria. *Rheumatology (Oxford).* 2012;51(suppl 6):Svi5–Svi9.
10. Heidari B. Rheumatoid arthritis: early diagnosis and treatment outcomes. *Caspian J Intern Med.* 2011;2:161–170.
11. Jamar F, van der Laken CJ, Panagiotidis E, et al. Update on imaging of inflammatory arthritis and related disorders. *Semin Nucl Med.* 2023;53:287–300.
12. Matsui T, Nakata N, Nagai S, et al. Inflammatory cytokines and hypoxia contribute to ^{18}F-FDG uptake by cells involved in pannus formation in rheumatoid arthritis. *J Nucl Med.* 2009;50:920–926.
13. Narayan N, Owen DR, Taylor PC. Advances in positron emission tomography for the imaging of rheumatoid arthritis. *Rheumatology.* 2017;56:1837–1846.
14. Fuchs K, Kohlhofer U, Quintanilla-Martinez L, et al. In vivo imaging of cell proliferation enables the detection of the extent of experimental rheumatoid arthritis by 3′-deoxy-3′-^{18}F-fluorothymidine and small-animal PET. *J Nucl Med.* 2013;54: 151–158.
15. Brenner W. ^{18}F-FDG PET in rheumatoid arthritis: there still is a long way to go. *J Nucl Med.* 2004;45:927–929.
16. Viitanen R, Moisio O, Lankinen P, et al. First-in-humans study of ^{68}Ga-DOTA-Siglec-9, a PET ligand targeting vascular adhesion protein 1. *J Nucl Med.* 2021;62: 577–583.
17. Rincón-Arévalo H, Burbano C, Atehortúa L, et al. Modulation of B cell activation by extracellular vesicles and potential alteration of this pathway in patients with rheumatoid arthritis. *Arthritis Res Ther.* 2022;24:169.
18. Afeltra A, Galeazzi M, Ferri GM, et al. Expression of CD69 antigen on synovial fluid T cells in patients with rheumatoid arthritis and other chronic synovitis. *Ann Rheum Dis.* 1993;52:457–460.
19. Ortiz AM, Laffon A, Gonzalez-Alvaro I. CD69 expression on lymphocytes and interleukin-15 levels in synovial fluids from different inflammatory arthropathies. *Rheumatol Int.* 2002;21:182–188.
20. Atzeni F, Del Papa N, Sarzi-Puttini P, Bertolazzi F, Minonzio F, Capsoni F. CD69 expression on neutrophils from patients with rheumatoid arthritis. *Clin Exp Rheumatol.* 2004;22:331–334.
21. Nisnboym M, Vincze SR, Xiong Z, et al. Immuno-PET imaging of CD69 visualizes T-cell activation and predicts survival following immunotherapy in murine glioblastoma. *Cancer Res Commun.* 2023;3:1173–1188.
22. Edwards KJ, Chang B, Babazada H, et al. Using CD69 PET imaging to monitor immunotherapy-induced immune activation. *Cancer Immunol Res.* 2022;10:1084–1094.
23. Persson J, Puuvuori E, Zhang B, et al. Discovery, optimization and biodistribution of an Affibody molecule for imaging of CD69. *Sci Rep.* 2021;11:19151.
24. Ståhl S, Gräslund T, Eriksson Karlström A, Frejd FY, Nygren PÅ, Löfblom J. Affibody molecules in biotechnological and medical applications. *Trends Biotechnol.* 2017;35:691–712.
25. LaBranche TP, Hickman-Brecks CL, Meyer DM, et al. Characterization of the KRN cell transfer model of rheumatoid arthritis (KRN-CTM), a chronic yet synchronized version of the K/BxN mouse. *Am J Pathol.* 2010;177:1388–1396.
26. Shipkova M, Wieland E. Surface markers of lymphocyte activation and markers of cell proliferation. *Clin Chim Acta.* 2012;413:1338–1349.
27. Xiao Z, Mayer AT, Nobashi TW, Gambhir SS. ICOS is an indicator of T-cell-mediated response to cancer immunotherapy. *Cancer Res.* 2020;80:3023–3032.
28. Alam IS, Mayer AT, Sagiv-Barfi I, et al. Imaging activated T cells predicts response to cancer vaccines. *J Clin Invest.* 2018;128:2569–2580.
29. Larimer BM, Wehrenberg-Klee E, Dubois F, et al. Granzyme B PET imaging as a predictive biomarker of immunotherapy response. *Cancer Res.* 2017;77:2318–2327.
30. Gibson HM, McKnight BN, Malysa A, et al. IFNγ PET imaging as a predictive tool for monitoring response to tumor immunotherapy. *Cancer Res.* 2018;78:5706–5717.

Identification of (*R*)-[^{18}F]YH134 for Monoacylglycerol Lipase Neuroimaging and Exploration of Its Use for Central Nervous System and Peripheral Drug Development

Yingfang He[1], Stefanie D. Krämer[1], Uwe Grether[2], Matthias B. Wittwer[2], Ludovic Collin[2], Bernd Kuhn[2], Andreas Topp[2], Dominik Heer[2], Fionn O'Hara[2], Michael Honer[2], Anto Pavlovic[2], Hans Richter[2], Martin Ritter[2], Didier Rombach[2], Claudia Keller[1], Luca Gobbi[2], and Linjing Mu[1]

[1]Center for Radiopharmaceutical Sciences, Institute of Pharmaceutical Sciences, Department of Chemistry and Applied Biosciences, ETH Zurich, Zurich, Switzerland; and [2]Pharma Research and Early Development, Roche Innovation Center Basel, F. Hoffmann-La Roche Ltd., Basel, Switzerland

This study aimed to evaluate (*R*)-[^{18}F]YH134 as a novel PET tracer for imaging monoacylglycerol lipase (MAGL). Considering the ubiquitous expression of MAGL throughout the whole body, the impact of various MAGL inhibitors on (*R*)-[^{18}F]YH134 brain uptake and its application in brain–periphery crosstalk were explored. **Methods:** MAGL knockout and wild-type mice were used to evaluate (*R*)-[^{18}F]YH134 in in vitro autoradiography and PET experiments. To explore the impact of peripheral MAGL occupancy on (*R*)-[^{18}F]YH134 brain uptake, PET kinetics with an arterial input function were studied in male Wistar rats under baseline and blocking conditions. **Results:** In in vitro autoradiography, (*R*)-[^{18}F]YH134 revealed a heterogeneous distribution pattern with high binding to MAGL-rich brain regions in wild-type mouse brain slices, whereas the radioactive signal was negligible in MAGL knockout mouse brain slices. The in vivo brain PET images of (*R*)-[^{18}F]YH134 in wild-type and MAGL knockout mice demonstrated its high specificity and selectivity in mouse brain. A Logan plot with plasma input function was applied to estimate the distribution volume (V_T) of (*R*)-[^{18}F]YH134. V_T was significantly reduced by a brain-penetrant MAGL inhibitor but was unchanged by a peripherally restricted MAGL inhibitor. The MAGL target occupancy in the periphery was estimated using (*R*)-[^{18}F]YH134 PET imaging data from the brain. **Conclusion:** (*R*)-[^{18}F]YH134 is a highly specific and selective PET tracer with favorable kinetic properties for imaging MAGL in rodent brain. Our results showed that blocking of the peripheral target influences brain uptake but not the V_T of (*R*)-[^{18}F]YH134. (*R*)-[^{18}F]YH134 can be used for estimating the dose of MAGL inhibitor at half-maximal peripheral target occupancy.

Key Words: monoacylglycerol lipase; PET imaging; plasma input function; drug occupancy studies

J Nucl Med 2024; 65:300–305
DOI: 10.2967/jnumed.123.266426

Monoacylglycerol lipase (MAGL) is a serine hydrolase that belongs to the endocannabinoid system. It is expressed in various organs, including the brain, heart, liver, kidney, adipose tissue, and adrenal gland (*1,2*). MAGL plays a key role in hydrolyzing endocannabinoid 2-arachidonoylglycerol to arachidonic acid, the main precursor for proinflammatory eicosanoids (*3,4*). The dual role of MAGL in the regulation of neuroinflammation and endocannabinoid signaling makes it a promising therapeutic target for several neurologic disorders. Pharmacologic inhibition of MAGL led to therapeutic effects in animal models of Alzheimer disease (*4,5*), Parkinson disease (*6*), and multiple sclerosis (*7*), as well as psychiatric disorders, among others (*8–10*). In addition, peripheral MAGL was suggested to serve as a critical hub in lipid signaling under physiologic and oncologic conditions (*11,12*). Moreover, peripherally restricted MAGL inhibitors may be of use for treatments against metabolic disorders, obesity, and cancer (*8*).

PET imaging of MAGL enzymes in the central nervous system (CNS) enables precision pharmacology to address elemental questions during drug development (*13*). A suitable MAGL PET tracer can provide quantitative information about drug–target interactions and facilitate the assessment of target alterations under disease conditions (*14,15*). So far, [^{18}F]T-401 has been the only tracer shown capable of visualizing MAGL in the human brain (*16*). [^{11}C]PF-06809247 revealed promising results in a target occupancy study in the brain of nonhuman primates (*17*). Recently, we disclosed the discovery of (*R*)-[^{18}F]YH149 (Fig. 1), an [^{18}F]T-401 derivative that exhibits improved brain penetration and appropriate clearance from the brain target in vivo (*18*). However, in subsequent work, a radiometabolite was detected in mouse brain, which complicates quantitative PET and kinetic modeling. This study set out to investigate a novel compound, (*R*)-YH134, the *meta*-fluorine–substituted analog of (*R*)-[^{18}F]YH149. In comparison to (*R*)-YH149, (*R*)-YH134 revealed 1.3-fold and 2-fold lower clearance in mouse and human liver microsomes, respectively. This finding suggests an improved stability of (*R*)-YH134 against cytochrome P450 oxidation in phase I metabolism. Further in vivo characterization of (*R*)-[^{18}F]YH134 (Fig. 1) revealed an improved kinetic profile, particularly regarding the absence of radiometabolites in rodent brain. Encouraged by these promising results, kinetic modeling was performed with an arterial input function (IF). Considering the ubiquitous and high expression of MAGL in the CNS and periphery, we further explored the brain–periphery crosstalk in CNS tracer and drug development, and we attempted to answer the following questions: How does peripheral MAGL inhibition influence brain uptake of (*R*)-[^{18}F]YH134 for neuroimaging? Can a MAGL CNS PET tracer facilitate the characterization

---

Received Aug. 3, 2023; revision accepted Nov. 7, 2023.

For correspondence or reprints, contact Linjing Mu (linjing.mu@pharma.ethz.ch).

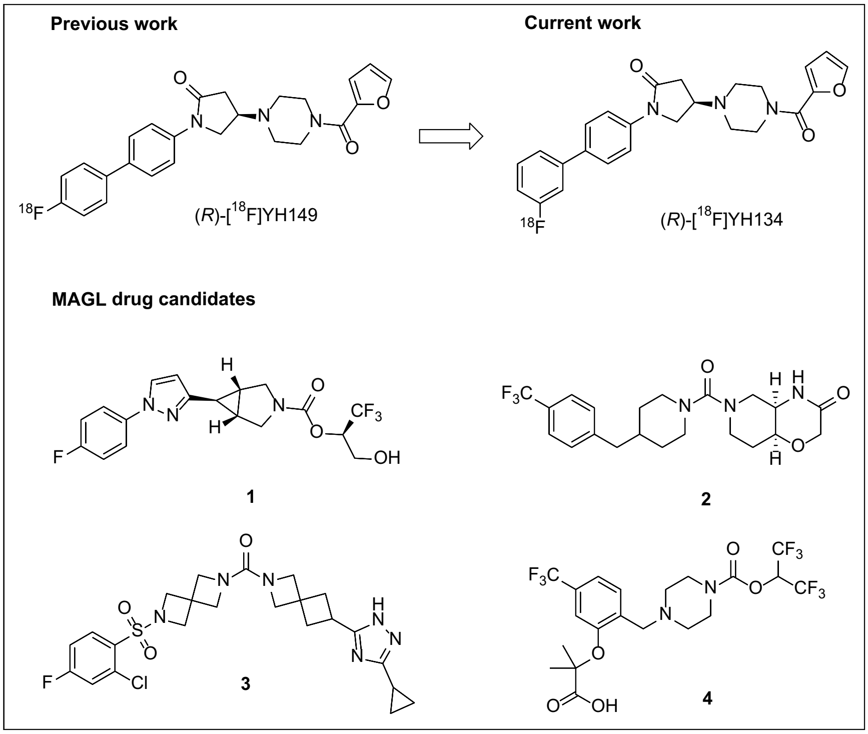

FIGURE 1. Chemical structures of (*R*)-[^{18}F]YH149, (*R*)-[^{18}F]YH134, and 4 MAGL blockers for in vivo studies.

of peripherally restricted MAGL inhibitors during drug development? As illustrated in Figure 1, 4 MAGL drug candidates were selected for the studies (*19–21*). The impact of peripheral MAGL inhibition on (*R*)-[^{18}F]YH134 brain kinetics was further examined using elevating doses of compound **3** (Fig. 1).

MATERIALS AND METHODS

The study was approved by the institutional review board. All animal studies were conducted in accordance with ARRIVE guidelines (Animal Research: Reporting of In Vivo Experiments) and Swiss animal protection and welfare legislation and were approved by the Veterinary Office of Canton Zurich. MAGL knockout and wild-type mice were from Taconic Biosciences, and Wistar rats were from Charles River. The husbandry of animals was conducted under standard conditions as previously reported (*22*). The apical efflux ratios from P-glycoprotein (P-gp) of MAGL inhibitors were measured as previously reported (*23*). A CEREP screen consisting of 50 receptors or enzymes was performed using radioligand binding displacement or enzymic assays (*24*). The detailed synthetic procedures for (*R*)-YH134 and its boronic ester precursor are presented in Supplemental Scheme 1, and experimental details on (*R*)-YH134 plasma protein binding, in vitro autoradiography, and in vivo animal studies can be found in the supplemental data (supplemental materials are available at http://jnm.snmjournals.org).

MAGL Inhibition Constants, Radiochemistry, and In Vitro Characterization

The MAGL inhibition constants (half-maximal inhibitory concentrations) of both the (*R*)- and the (*S*)-YH134 enantiomers and the microsomal and hepatic clearance of (*R*)-YH134 in different species were measured as previously reported (*22*). ^{18}F-labeled YH134 was produced via copper-mediated radiofluorination of the boronic pinacol ester precursor (*25*). Lipophilicity and in vitro stability were evaluated according to published procedures (*18*).

PET Experiments and Biodistribution After Dissection of MAGL Knockout and Wild-Type Mice

MAGL knockout ($n = 4$) or wild-type ($n = 4$) mice were anesthetized with isoflurane for PET/CT (*26*). Tracer biodistribution was investigated after dissection. Awake MAGL knockout and wild-type mice (4 for each group) were injected intravenously with (*R*)-[^{18}F]YH134 (4.32–11.85 MBq, 2.13–2.51 nmol/kg) and euthanized under isoflurane (5%) anesthesia by decapitation at 30 min after injection. The organs of interest were dissected and weighed, and radioactivity was measured in a γ-counter (Wizard; Perkin Elmer). PET and dissection data are reported as SUV and percentage normalized injected dose per gram of tissue, respectively. Mean values are shown with SD.

In Vivo Radiometabolite Analyses and Tracer Plasma–to–Whole-Blood Ratio

The radiometabolite analyses were performed on C57BL/6 mice and Wistar rats. All samples were analyzed by radio–ultra performance liquid chromatography (UPLC; Waters). The mice were injected with 38–81 MBq of (*R*)-[^{18}F]YH134 ($n = 2$). Brain and plasma samples were collected at 45 and 90 min after injection. The rats were assigned to a baseline ($n = 2$) or a blockade ($n = 2$) group. The blockade group was pretreated with compound **3** to investigate whether the blocker affected tracer plasma–to–whole-blood distribution and metabolism.

Rat PET Scans Without Arterial IF

PET scans were conducted on anesthetized male Wistar rats (301–355 g) with 8.33–47.90 MBq of (*R*)-[^{18}F]YH134 (0.40–4.48 nmol/kg). Under blockade conditions, the animals were pretreated with a 2 mg/kg dose of compound **1,** a 1 mg/kg dose of compound **2,** various doses of compound **3** (1, 3, 5, or 10 mg/kg), or a 3 mg/kg dose of compound **4.** Blood from the rats receiving compound **3** was collected at 100 min after injection on completion of the PET scans, and plasma was separated by centrifugation and stored at −80°C before being analyzed by liquid chromatography tandem mass spectrometry to determine the concentration of compound **3** in plasma.

Rat PET Scans with Arterial IF

PET kinetics with an arterial IF were determined in male Wistar rats (344–427 g; Supplemental Table 1). For the arterial plasma IF, blood activity was determined from an arteriovenous shunt simultaneously with acquisition of the PET data (*27*). During PET scanning, blood from either the cannulated tail artery (minimally invasive protocol) or a femoral artery (invasive protocol) was guided through a Twilite coincidence counter (Swisstrace) and a peristaltic pump and then was transferred back to a cannulated lateral tail vein or a femoral vein.

Logan Plot Analysis to Determine Distribution Volume (V_T) of Total Tracer

IF was generated from the blood coincidences by correcting the data with a biexponential function describing the plasma–to–whole-blood ratios. The parent tracer was the only detectable radioactivity in rat plasma up to 60 min after injection; no further correction was therefore required for the IF. V_T was calculated as the slope of the linear part of the Logan plot generated from the IF and the PET data (*28*).

Statistical Analysis

Data were compared by a homoscedastic, 2-tailed Student's *t* test in Excel (version 2013; Microsoft) or R (version 4.2.2; The R Project for Statistical Computing), assuming equal variance (comparison of 2 conditions) or by ANOVA with post hoc correction for multiple comparisons (the Tukey honestly significant difference test; functions aov and TukeyHSD in R), as indicated. A *P* value of less than 0.05 was considered statistically significant.

RESULTS

Properties of (*R*)-YH134

(*R*)-YH134 exhibited potent inhibition, with a similar half-maximal inhibitory concentration of 11 nM toward mouse and human MAGL enzyme. However, (*S*)-YH134 showed significant loss of MAGL-inhibiting activity, with half-maximal inhibitory concentrations of 397 nM in mice and 197 nM in humans. The apparent intrinsic clearance of (*R*)-YH134 was determined as 93, 71, and 10 μL/min/mg in mouse, rat, and human liver microsomes, respectively. A similar tendency was found using hepatocytes from mice (133 μL/min/10^6 cells), rats (45 μL/min/10^6 cells), and humans (10 μL/min/10^6 cells). An in vitro screening assay using unlabeled (*R*)-YH134 showed no significant binding of the compound to any of the tested targets (Supplemental Table 2).

Radiochemistry and In Vitro Characterization

The enantiomerically pure *S*- or *R*-form of boronic ester was used as the precursor for copper-mediated radiofluorination to produce (*S*)- or (*R*)-[^{18}F]YH134. High radiochemical purity was achieved after semipreparative high-performance liquid chromatography purification (>99%). The molar activities of (*R*)-[^{18}F]YH134 were in the range of 102–277 GBq/μmol at the end of the syntheses ($n = 13$). The distribution coefficient of (*R*)-[^{18}F]YH134 was 2.52 ± 0.18 ($n = 3$). No radioactive degradation products of (*R*)-[^{18}F]YH134 were observed in rodent or human plasma for up to 2 h (Supplemental Fig. 1). Its unbound fractions in rat and human plasma were 8% ± 1% and 14% ± 2%, respectively ($n = 3$). (*R*)-[^{18}F]YH134 revealed a heterogeneous distribution in rat brain slices in in vitro autoradiography studies (Fig. 2A). The highest radioactivity accumulation appeared in the cortex, hippocampus, and striatum, regions known to express high levels of MAGL (*29,30*). Coincubation with MAGL inhibitors, either SAR127303 or PF-06809247, or with the reference compound (*R*)-YH134 substantially reduced the radioactive signal in the MAGL-rich brain regions. (*R*)-[^{18}F]YH134 demonstrated negligible binding in MAGL knockout mouse brain sections compared with that in wild-type mice (Fig. 2C, top). These results suggest high selectivity and specificity of (*R*)-[^{18}F]YH134 toward MAGL in vitro.

PET Scans and Biodistribution in MAGL Knockout and Wild-Type Mice

Figure 2B depicts the time–activity curves of PET scans of (*R*)-[^{18}F]YH134 and (*S*)-[^{18}F]YH134 in wild-type and MAGL knockout mice. As expected, (*S*)-[^{18}F]YH134, with modest MAGL half-maximal inhibitory concentrations, displayed no distinguishable differences between MAGL knockout and wild-type mice, whereas time–activity curves of (*R*)-[^{18}F]YH134 were substantially higher in wild-type than MAGL knockout mice over the whole scanning period (Fig. 2B). The significantly higher averaged SUV (1–91 min [SUV_{av}]) of (*R*)-[^{18}F]YH134 PET in wild-type than in MAGL knockout mice confirmed the high selectivity and specificity of (*R*)-[^{18}F]YH134 for MAGL in vivo (SUV_{av}, 0.84 ± 0.03 vs. 0.51 ± 0.02; $P < 0.001$). The representative sagittal and coronal PET images of (*R*)-[^{18}F]YH134 are in accordance with its in vitro autoradiography on wild-type and MAGL knockout mouse brain slices as shown in Figure 2C. To assess the whole-body distribution of radioactivity, we conducted biodistribution experiments after dissection of wild-type and MAGL knockout mice at 30 min after injection. The data are summarized in Supplemental Table 3. The radioactivity accumulation of (*R*)-[^{18}F]YH134 in MAGL knockout mouse brain was significantly lower than that in wild-type mice (1.31% vs. 1.75% injected dose/g, $P = 0.0225$). In the periphery, wild-type mice showed significantly higher radioactivity in a set of MAGL-expressing organs (*2*), such as the heart, brown adipose tissue, and adrenal gland. Regarding excretory pathways, radioactivity was high in both urine and bile.

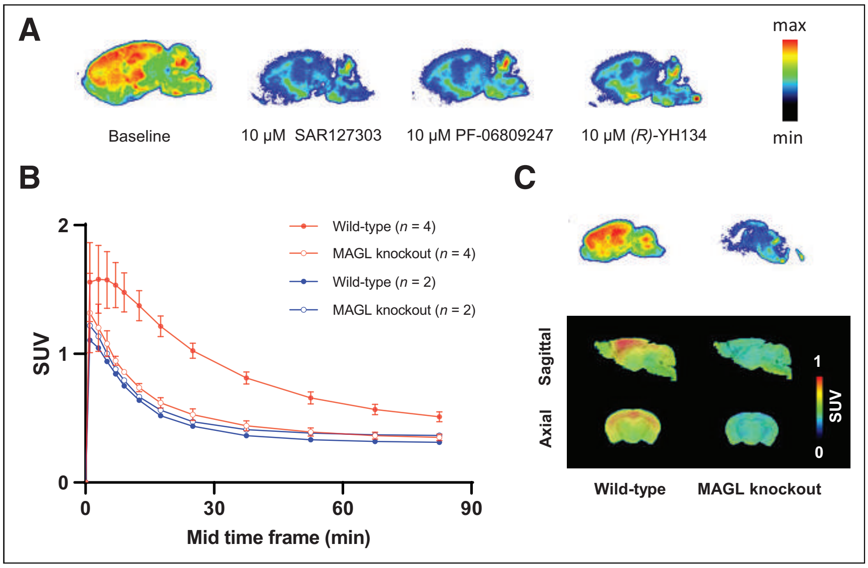

FIGURE 2. (A) In vitro autoradiography of (*R*)-[^{18}F]YH134 on rat brain sections. Baseline (13 nM (*R*)-[^{18}F]YH134 only) and blocking conditions are as indicated. (B) Brain time–activity curves of (*R*)-[^{18}F]YH134 (red) and (*S*)-[^{18}F]YH134 (blue) in MAGL knockout and wild-type mice. Mean values are given. Error bars indicate SD for $n = 4$. (C) In vitro autoradiograms (top) and in vivo brain PET images (bottom) of (*R*)-[^{18}F]YH134 averaged from 9.0 until 60 min after injection in wild-type and MAGL knockout mice. PET data are overlaid on MRI template.

In Vivo Metabolism and Plasma-to-Whole-Blood Ratio in Rats

The percentages of intact radiotracer in brain homogenates and plasma samples are summarized in Supplemental Table 4. Only intact radiotracer with a retention time of about 3.7 min was detected in mouse and rat brain homogenates up to 90 min after injection. In mouse plasma, a polar radiometabolite (retention time, 0.3 min) was detected at 45 and 90 min after injection. In contrast, the parental radiotracer remained the sole detectable

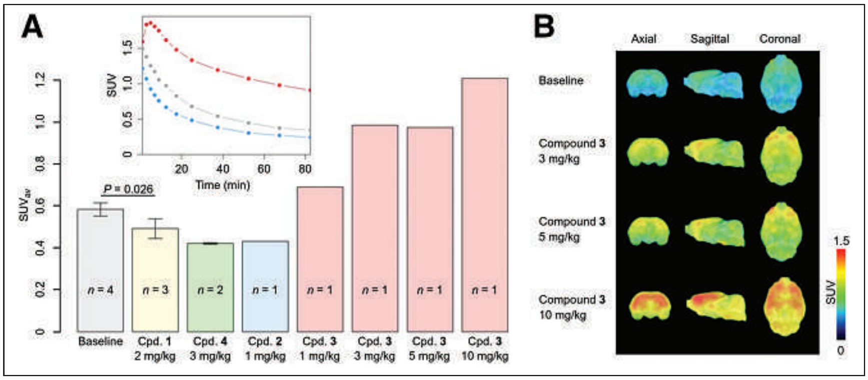

FIGURE 3. (A) SUV_{av} from PET brain time–activity curves of (*R*)-[^{18}F]YH134 in Wistar rats under various blocking conditions. Significant blocking effect was revealed using compound **1** as blocker at 2 mg/kg ($P = 0.026$). Inset shows representative time–activity curves from baseline condition (gray), 1 mg/kg dose of compound **2** (blue), and 10 mg/kg dose of compound **3** (red). (B) Representative PET images of (*R*)-[^{18}F]YH134 averaged from 8.0 to 90 min after injection with increasing doses of MAGL inhibitor **3.** Cpd. = compound.

radioactive species in rat plasma for up to 60 min after injection. Pretreatment with a 10 mg/kg dose of compound **3** did not alter the metabolic profile of (*R*)-[^{18}F]YH134 in rat brain and blood. The plasma–to–whole-blood ratios in rats at defined time points under control and blockade conditions and their simulation with a biexponential function are shown in Supplemental Figure 2.

Effects of MAGL Blocking on (*R*)-[^{18}F]YH134 PET in Rats

PET experiments were further performed on Wistar rats to evaluate the CNS binding of (*R*)-[^{18}F]YH134 in the presence of the various MAGL drug candidates. The SUV_{av} calculated from PET brain time–activity curves is depicted in Figure 3A. Under blockade conditions with either MAGL inhibitor **1** or **2** (*19,21*), tracer accumulation in the brain was reduced, as expected for compounds competing with tracer binding to MAGL in rat brain. The blocking effect of a 2 mg/kg dose of compound **1** was significant, compared with the baseline SUV_{av} ($P = 0.026$). The presumably peripherally restricted MAGL inhibitor **4** containing a carboxylic acid group surprisingly reduced brain uptake of (*R*)-[^{18}F]YH134 to the same level as for a 1 mg/kg dose of compound **2.** Pretreatment with compound **3,** a P-gp substrate with an efflux ratio of 7.65 (Supplemental Table 5), increased the SUV_{av} in a dose-dependent manner (1, 3, 5, and 10 mg/kg; Fig. 3A). Therefore, we selected compound **2** as a brain-penetrant blocker but compound **3** as a peripherally restricted MAGL inhibitor for further kinetic studies. The respective PET images averaged from 8 to 90 min after injection are shown in Figure 3B.

Logan Plot and SUV_{av} Brain-to-Plasma Ratio to Quantify (*R*)-[^{18}F]YH134 Distribution to Rat Brain

PET kinetic modeling with an IF was further performed to quantify brain uptake of (*R*)-[^{18}F]YH134 and interpret the observed effects of compounds **2** and **3** on the brain SUV of (*R*)-[^{18}F]YH134. Rats were injected with vehicle ($n = 3$), compound **2,** or compound **3** before tracer injection. (*R*)-[^{18}F]YH134 brain uptake was analyzed by Logan plots of the PET data and the IF (V_T) and from the ratio between the SUV_{av} of brain and plasma (PET SUV_{av}/IF SUV_{av}). Representative Logan plots are shown in Supplemental Figure 3.

In agreement with the previous section, compound **2** reduced the SUV_{av} of (*R*)-[^{18}F]YH134 in rat brain. The effect of **2** (at 1 mg/kg) on brain uptake was significant (SUV_{av} at baseline, 0.560 ± 0.033 [$n = 3$], vs. SUV_{av} with **2,** 0.414 ± 0.036 [$n = 3$]; $P < 0.01$). The SUV_{av} of the IF was not reduced by compound **2** ($P = \sim 0.6$). However, the V_T and SUV_{av} brain-to-plasma ratios were significantly reduced by compound **2** (Figs. 4C and 4D), indicating significant competition between **2** and (*R*)-[^{18}F]YH134 binding in rat brain. Administration of the peripheral blocker **3** (1–10 mg/kg) resulted in a significantly increased SUV_{av} in both brain and IF compared with baseline conditions (all doses included; $P < 0.0001$; Figs. 4A and 4B). However, the uptake-enhancing effect was cancelled out when V_T or SUV_{av} brain-to-plasma ratios were compared, in agreement with a lack of competition for MAGL binding in the brain.

Peripheral Target Occupancy Determined by (*R*)-[^{18}F]YH134 PET

As concluded from the previous section, compound **3** enhanced (*R*)-[^{18}F]YH134 SUV_{av} in rat brain and IF by occupying peripheral MAGL. We investigated whether we can estimate the dose of **3** at half-maximal MAGL blocking (D_{50}) in the periphery. Figure 5 shows the brain PET SUV_{av} and the IF SUV_{av} of plasma plotted

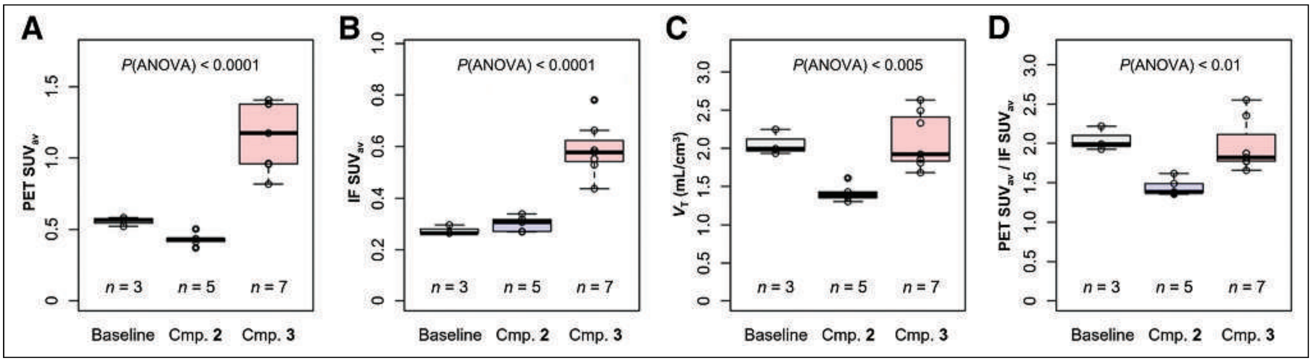

FIGURE 4. (A) (*R*)-[^{18}F]YH134 SUV_{av} in rat brain. (B) (*R*)-[^{18}F]YH134 SUV_{av} in rat plasma. (C) V_T in rat brain as determined by Logan plot analysis. (D) Ratio of SUV_{av} in rat brain and SUV_{av} in plasma. *P* values are shown for ANOVA. Injected doses of compounds **2** and **3** were neglected in this figure (doses are shown in Supplemental Table 1). Baseline = (*R*)-[^{18}F]YH134 with vehicle; Cmp. **2** = blocking with compound **2** at doses from 1 to 3 mg/kg; Cmp. **3** = blocking with compound **3** at doses from 1 to 10 mg/kg.

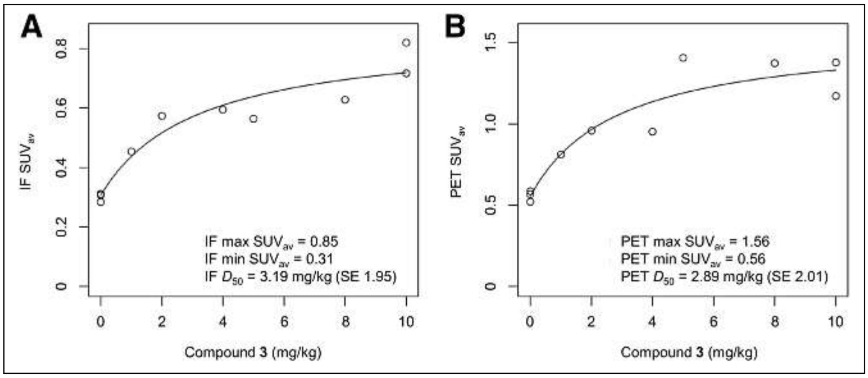

FIGURE 5. Peripheral MAGL occupancy by compound **3** determined with (*R*)-[^{18}F]YH134. SUV$_{av}$ in rat plasma (A, IF SUV$_{av}$) and brain (B, PET SUV$_{av}$) after injection of (*R*)-[^{18}F]YH134 alone (0 mg/kg blocker) and after varying doses of compound **3** is indicated. Data were fit with 1:1 saturation function; fitted values are indicated in plots. Dose of (*R*)-[^{18}F]YH134 at 0 mg/kg blocker was ∼1 nmol/kg (<1 µg/kg).

against the blocker doses (same data as shown in Fig. 4). Analysis with a saturation function revealed D_{50} to be approximately 3 mg/kg in both cases. This is in line with the D_{50} of approximately 4 mg/kg estimated from the calculated percentage target occupancy at the averaged (0–100 min) plasma concentrations of **3,** back-calculated from the quantified plasma concentrations at 100 min at the various dose levels (Supplemental Fig. 4).

DISCUSSION

Moving the fluorine atom of (*R*)-YH149 from the *para*- to the *meta*-position of the phenyl ring resulted in (*R*)-YH134, with increased in vitro and in vivo stability. Our newly developed (*R*)-[^{18}F]YH134 demonstrated increased MAGL in vivo specificity (Supplemental Fig. 5). Potential off-target binding of the tracer in mice was largely excluded on the basis of the low radioactive signal seen on in vitro autoradiography and in vivo PET studies on MAGL knockout mouse brain. These features suggest that (*R*)-[^{18}F]YH134 is a promising MAGL PET tracer in rodents, and further studies on nonhuman primates are ongoing.

(*R*)-[^{18}F]YH134 uptake in rat brain, expressed as V_T, SUV$_{av}$, or SUV$_{av}$ ratio between brain and plasma, was significantly reduced by a 1 mg/kg dose of compound **2,** a potent MAGL brain-penetrant inhibitor (Supplemental Table 5). Compound **3,** a MAGL inhibitor with a high in vitro P-gp efflux ratio of 7.65 and therefore negligible distribution to the brain, affected brain SUV$_{av}$ more than V_T or the SUV$_{av}$ brain-to-plasma ratio. As for (*R*)-YH134, efflux ratios of 1.05 and 1.13 were obtained with mouse and human P-gp, respectively (Supplemental Table 5), indicating it is not a P-gp substrate. We therefore concluded that the radioactivity elevation in the brain was caused by blocking of peripheral MAGL binding sites rather than inhibition of P-gp–mediated efflux. The SUV$_{av}$ brain-to-plasma ratio, because of its similarity to V_T determined with the Logan plot from PET data and IF, is a good surrogate for the V_T of (*R*)-[^{18}F]YH134 in rat brain. Therefore, when MAGL in brain is targeted, tracer blood activity should be determined in addition to brain uptake. Our results, together with those of previous studies (*31–33*) on in vivo PET imaging of histone deacetylases and heat shock protein 90—targets expressed in both the CNS and the periphery—highlight the importance of normalization of radiotracer brain uptake to metabolite-corrected plasma radiotracer levels to verify tracer-specific binding in blockade studies in vivo.

We further investigated whether our tracer can support the characterization of drug candidates targeting peripheral MAGL. The increasing brain uptake of (*R*)-[^{18}F]YH134 in the presence of compound **3** was driven by the increased concentrations of free tracer in the blood. We therefore concluded that compound **3** bound mainly to peripheral MAGL, in agreement with its high P-gp efflux ratio determined in vitro. Indeed, the SUV$_{av}$ of both brain and IF followed saturation functions, allowing fitting of D_{50} values for the saturation of peripheral MAGL by **3.** The result agrees with the D_{50} value obtained by measuring the plasma concentration of **3** using the traditional method, liquid chromatography tandem mass spectrometry.

MAGL is not the only target expressed both in the CNS and in the periphery; this dual expression is also true for a variety of other targets, such as acetylcholine receptors (*34*), γ-aminobutyric acid receptors (*35*), heat shock protein 90 (*33*), and σ-receptors (*36*). Our current work demonstrates the utility of a CNS PET tracer in both brain and peripheral drug development. As whole-body PET scanners advance (*37*), a suitable PET tracer may help elucidate the complicated connections between the CNS and the periphery.

CONCLUSION

Our data suggest that (*R*)-[^{18}F]YH134 is a promising PET tracer for noninvasive visualization and quantification of MAGL in preclinical studies. The V_T or SUV$_{av}$ brain-to-plasma ratio of (*R*)-[^{18}F]YH134 allows quantification of available MAGL binding sites in the brain, unaffected by peripheral MAGL blocking. Apart from being used to evaluate target engagement and the half-maximal MAGL occupancy of brain-penetrant MAGL inhibitors, (*R*)-[^{18}F]YH134 brain PET can also be used to estimate the D_{50} of a peripherally restricted MAGL inhibitor. In our opinion, these promising preclinical results warrant the evaluation of (*R*)-[^{18}F]YH134 as a MAGL PET tracer in a clinical setting. We believe that advances in whole-body PET scanners will enable a more comprehensive analysis of the endocannabinoid system under pathologic conditions or therapeutic intervention.

DISCLOSURE

This work was partially supported by the Swiss National Science Foundation (205321_192409/1). No other potential conflict of interest relevant to this article was reported.

ACKNOWLEDGMENTS

We sincerely thank Dr. Neil Parrott (Roche Innovation Center Basel) for fruitful discussions; Marie-Thérèse Miss, Isabelle Kaufmann, Roland Humm, Pawel Dzygiel, and Carina Cantrill (Roche Innovation Center Basel) for technical assistance; and Bruno Mancosu and Annette Krämer (ETH Zurich) for cyclotron support. Figdraw provided the material for the graphical abstract.

KEY POINTS

QUESTIONS: Is (*R*)-[^{18}F]YH134 a suitable PET tracer for imaging MAGL in rodent brain? How does peripheral MAGL influence brain uptake of (*R*)-[^{18}F]YH134 under blocking conditions?

PERTINENT FINDINGS: (*R*)-[^{18}F]YH134 is a highly specific and selective PET tracer for MAGL brain imaging. V_T and SUV brain-to-plasma ratio are better suited than SUV to quantify MAGL binding in the brain under blocking conditions, and (*R*)-[^{18}F]YH134 can be used to estimate the dose of MAGL inhibitor at half-maximal peripheral target occupancy.

IMPLICATIONS FOR PATIENT CARE: Our results warrant clinical translation of (*R*)-[^{18}F]YH134. Clinical imaging of MAGL and advances in whole-body PET scanners will enable a more comprehensive analysis of the endocannabinoid system under pathologic conditions or therapeutic intervention.

REFERENCES

1. Tornqvist H, Belfrage P. Purification and some properties of a monoacylglycerol hydrolyzing enzyme of rat adipose tissue. *J Biol Chem.* 1976;251:813–819.
2. Karlsson M, Contreras JA, Hellman U, Tornqvist H, Holm C. cDNA cloning, tissue distribution, and identification of the catalytic triad of monoglyceride lipase. *J Biol Chem.* 1997;272:27218–27223.
3. Nomura DK, Morrison BE, Blankman JL, et al. Endocannabinoid hydrolysis generates brain prostaglandins that promote neuroinflammation. *Science.* 2011;334: 809–813.
4. Piro JR, Benjamin DI, Duerr JM, et al. A dysregulated endocannabinoid-eicosanoid network supports pathogenesis in a mouse model of Alzheimer's disease. *Cell Rep.* 2012;1:617–623.
5. Chen R, Zhang J, Wu Y, et al. Monoacylglycerol lipase is a therapeutic target for Alzheimer's disease. *Cell Rep.* 2012;2:1329–1339.
6. Pasquarelli N, Porazik C, Bayer H, et al. Contrasting effects of selective MAGL and FAAH inhibition on dopamine depletion and GDNF expression in a chronic MPTP mouse model of Parkinson's disease. *Neurochem Int.* 2017;110:14–24.
7. Hernández-Torres G, Cipriano M, Hedén E, et al. A reversible and selective inhibitor of monoacylglycerol lipase ameliorates multiple sclerosis. *Angew Chem Int Ed Engl.* 2014;53:13765–13770.
8. Gil-Ordóñez A, Martín-Fontecha M, Ortega-Gutiérrez S, López-Rodríguez ML. Monoacylglycerol lipase (MAGL) as a promising therapeutic target. *Biochem Pharmacol.* 2018;157:18–32.
9. Tuo W, Leleu-Chavain N, Spencer J, Sansook S, Millet R, Chavatte P. Therapeutic potential of fatty acid amide hydrolase, monoacylglycerol lipase, and N-acylethanolamine acid amidase inhibitors. *J Med Chem.* 2017;60:4–46.
10. Fowler CJ. Monoacylglycerol lipase: a target for drug development? *Br J Pharmacol.* 2012;166:1568–1585.
11. Blankman JL, Simon GM, Cravatt BF. A comprehensive profile of brain enzymes that hydrolyze the endocannabinoid 2-arachidonoylglycerol. *Chem Biol.* 2007;14: 1347–1356.
12. Nomura DK, Long JZ, Niessen S, Hoover HS, Ng SW, Cravatt BF. Monoacylglycerol lipase regulates a fatty acid network that promotes cancer pathogenesis. *Cell.* 2010;140:49–61.
13. Matthews PM, Rabiner EA, Passchier J, Gunn RN. Positron emission tomography molecular imaging for drug development. *Br J Clin Pharmacol.* 2012;73:175–186.
14. Lee C-M, Farde L. Using positron emission tomography to facilitate CNS drug development. *Trends Pharmacol Sci.* 2006;27:310–316.
15. Phelps ME. Positron emission tomography provides molecular imaging of biological processes. *Proc Natl Acad Sci USA.* 2000;97:9226–9233.
16. Takahata K, Seki C, Kimura Y, et al. First-in-human in vivo imaging and quantification of monoacylglycerol lipase in the brain: a PET study with ^{18}F-T-401. *Eur J Nucl Med Mol Imaging.* 2022;49:3150–3161.
17. Arakawa R, Takano A, Nag S, et al. Target occupancy study and whole-body dosimetry with a MAGL PET ligand [^{11}C]PF-06809247 in non-human primates. *EJNMMI Res.* 2022;12:13.
18. He Y, Schild M, Grether U, et al. Development of high brain-penetrant and reversible monoacylglycerol lipase PET tracers for neuroimaging. *J Med Chem.* 2022;65: 2191–2207.
19. McAllister LA, Butler CR, Mente S, et al. Discovery of trifluoromethyl glycol carbamates as potent and selective covalent monoacylglycerol lipase (MAGL) inhibitors for treatment of neuroinflammation. *J Med Chem.* 2018;61:3008–3026.
20. Grice CA, Buzard DJ, Shaghafi MB, inventors; Abide Therapeutics Inc., assignee. Magl inhibitors. Patent WO2019222266A1. November 21, 2019.
21. Bell C, Benz J, Gobbi L, et al., inventors; Hoffmann-La Roche Inc., assignee. New heterocyclic compounds as monoacylglycerol lipase inhibitors. Patent WO2020035424A1. February 20, 2020.
22. He Y, Gobbi LC, Herde AM, et al. Discovery, synthesis and evaluation of novel reversible monoacylglycerol lipase radioligands bearing a morpholine-3-one scaffold. *Nucl Med Biol.* 2022;108-109:24–32.
23. Fischer H, Senn C, Ullah M, Cantrill C, Schuler F, Yu L. Calculation of an apical efflux ratio from P-glycoprotein (P-gp) in vitro transport experiments shows an improved correlation with in vivo cerebrospinal fluid measurements in rats: impact on P-gp screening and compound optimization. *J Pharmacol Exp Ther.* 2021;376: 322–329.
24. Bendels S, Bissantz C, Fasching B, et al. Safety screening in early drug discovery: an optimized assay panel. *J Pharmacol Toxicol Methods.* 2019;99:106609.
25. Tredwell M, Preshlock SM, Taylor NJ, et al. A general copper-mediated nucleophilic ^{18}F fluorination of arenes. *Angew Chem Int Ed Engl.* 2014;53:7751–7755.
26. Goertzen AL, Bao Q, Bergeron M, et al. NEMA NU 4-2008 comparison of preclinical PET imaging systems. *J Nucl Med.* 2012;53:1300–1309.
27. Müller Herde A, Keller C, Milicevic Sephton S, et al. Quantitative positron emission tomography of mGluR5 in rat brain with [^{18}F]PSS232 at minimal invasiveness and reduced model complexity. *J Neurochem.* 2015;133:330–342.
28. Logan J, Fowler JS, Volkow ND, et al. Graphical analysis of reversible radioligand binding from time–activity measurements applied to [*N*-^{11}C-methyl]-(−)-cocaine PET studies in human subjects. *J Cereb Blood Flow Metab.* 1990;10:740–747.
29. Dinh TP, Carpenter D, Leslie FM, et al. Brain monoglyceride lipase participating in endocannabinoid inactivation. *Proc Natl Acad Sci USA.* 2002;99:10819–10824.
30. Yamasaki T, Mori W, Zhang Y, et al. First demonstration of in vivo mapping for regional brain monoacylglycerol lipase using PET with [^{11}C]SAR127303. *Neuroimage.* 2018;176:313–320.
31. Wang C, Schroeder FA, Wey HY, et al. In vivo imaging of histone deacetylases (HDACs) in the central nervous system and major peripheral organs. *J Med Chem.* 2014;57:7999–8009.
32. Van de Bittner GC, Ricq EL, Hooker JM. A philosophy for CNS radiotracer design. *Acc Chem Res.* 2014;47:3127–3134.
33. Vermeulen K, Cools R, Briard E, et al. Preclinical evaluation of [^{11}C]YC-72-AB85 for in vivo visualization of heat shock protein 90 in brain and cancer with positron emission tomography. *ACS Chem Neurosci.* 2021;12:3915–3927.
34. Peralta EG, Ashkenazi A, Winslow JW, Smith DH, Ramachandran J, Capon DJ. Distinct primary structures, ligand-binding properties and tissue-specific expression of four human muscarinic acetylcholine receptors. *EMBO J.* 1987;6:3923–3929.
35. Ben-Ari Y. Excitatory actions of gaba during development: the nature of the nurture. *Nat Rev Neurosci.* 2002;3:728–739.
36. Rousseaux CG, Greene SF. Sigma receptors [σRs]: biology in normal and diseased states. *J Recept Signal Transduct Res.* 2016;36:327–388.
37. Badawi RD, Shi H, Hu P, et al. First human imaging studies with the Explorer total-body PET scanner. *J Nucl Med.* 2019;60:299–303.

Early-Frame [^{18}F]Florbetaben PET/MRI for Cerebral Blood Flow Quantification in Patients with Cognitive Impairment: Comparison to an [^{15}O]Water Gold Standard

Ates Fettahoglu*[1,2], Moss Zhao*[1,3], Mehdi Khalighi[1], Hillary Vossler[4], Maria Jovin[1], Guido Davidzon[1], Michael Zeineh[1], Fernando Boada[1], Elizabeth Mormino[4], Victor W. Henderson[4], Michael Moseley[1], Kevin T. Chen†[5], and Greg Zaharchuk†[1]

[1]Department of Radiology, Stanford University, Stanford, California; [2]Radiology and Biomedical Imaging, Yale School of Medicine, New Haven, Connecticut; [3]Stanford Cardiovascular Institute, Stanford University, Stanford, California; [4]Department of Neurology and Neurological Sciences, Stanford University, Stanford, California; and [5]Department of Biomedical Engineering, National Taiwan University, Taipei, Taiwan

Cerebral blood flow (CBF) may be estimated from early-frame PET imaging of lipophilic tracers, such as amyloid agents, enabling measurement of this important biomarker in participants with dementia and memory decline. Although previous methods could map relative CBF, quantitative measurement in absolute units (mL/100 g/min) remained challenging and has not been evaluated against the gold standard method of [^{15}O]water PET. The purpose of this study was to develop and validate a minimally invasive quantitative CBF imaging method combining early [^{18}F]florbetaben (eFBB) with phase-contrast MRI using simultaneous PET/MRI. **Methods:** Twenty participants (11 men and 9 women; 8 cognitively normal, 9 with mild cognitive impairment, and 3 with dementia; 10 β-amyloid negative and 10 β-amyloid positive; 69 ± 9 y old) underwent [^{15}O]water PET, phase-contrast MRI, and eFBB imaging in a single session on a 3-T PET/MRI scanner. Quantitative CBF images were created from the first 2 min of brain activity after [^{18}F]florbetaben injection combined with phase-contrast MRI measurement of total brain blood flow. These maps were compared with [^{15}O]water CBF using concordance correlation (CC) and Bland–Altman statistics for gray matter, white matter, and individual regions derived from the automated anatomic labeling (AAL) atlas. **Results:** The 2 methods showed similar results in gray matter ([^{15}O]water, 55.2 ± 14.7 mL/100 g/min; eFBB, 55.9 ± 14.2 mL/100 g/min; difference, 0.7 ± 2.4 mL/100 g/min; $P = 0.2$) and white matter ([^{15}O]water, 21.4 ± 5.6 mL/100 g/min; eFBB, 21.2 ± 5.3 mL/100 g/min; difference, −0.2 ± 1.0 mL/100 g/min; $P = 0.4$). The intrasubject CC for AAL-derived regions was high (0.91 ± 0.04). Intersubject CC in different AAL-derived regions was similarly high, ranging from 0.86 for midfrontal regions to 0.98 for temporal regions. There were no significant differences in performance between the methods in the amyloid-positive and amyloid-negative groups as well as participants with different cognitive statuses. **Conclusion:** We conclude that eFBB PET/MRI can provide robust CBF measurements, highlighting the capability of simultaneous PET/MRI to provide measurements of both CBF and amyloid burden in a single imaging session in participants with memory disorders.

Key Words: [^{18}F]florbetaben PET; phase-contrast MRI; PET/MRI; cerebral blood flow

J Nucl Med 2024; 65:306–312
DOI: 10.2967/jnumed.123.266273

Cerebral blood flow (CBF) is an important biomarker in many neurologic disorders, including neurodegenerative and cerebrovascular diseases, and has been associated with changes in cognitive status (*1–5*). Subsequent work identified reduced CBF as a key component in early pathologic mechanisms and prognosis of Alzheimer disease (AD) and cognitive decline as well as in normal aging (*6–9*). Preclinical AD has been conceptualized as a synaptic disease, primarily driven by β-amyloid (Aβ) plaque and tau tangle deposition (*10*), yet cognitively normal individuals can present with elevated amyloid levels identical to those seen in AD pathology (*11*). Other biomarkers, including perfusion, may be relevant to neurodegeneration and cognitive decline (*12*). [^{15}O]water PET is the gold standard for quantitative CBF measurements but is primarily limited to research facilities with an on-site cyclotron due to the tracer's extremely short half-life (~2 min).

Conceptually, early-frame PET imaging of lipophilic radiotracers with a high extraction fraction offers the potential to measure CBF using tracer kinetic methods, in which it is usually referred to as K_1. However, such quantification requires measurement of an arterial input function, which may require invasive arterial cannulation. This analysis method may be limited by uncertainties introduced by downstream radiotracer metabolites. Furthermore, the requirement for high temporal resolution leads to a lower signal-to-noise ratio in the individual frames. Despite these challenges, this dual use of a single PET agent is attractive because of the potential for simultaneously measuring both CBF and molecular binding information.

Previous studies using a range of tracers showed good correlation between early-frame PET imaging and CBF, but no studies have proposed a method to move from relative to absolute CBF measurements (*13–16*). One agent that has been proposed for such dual use is [^{18}F]florbetaben, a tracer that in late time windows can image β-amyloid burden within the cerebral cortex, a necessary but nonsufficient condition for a diagnosis of AD (*17*). As such, [^{18}F]florbetaben could be used to image 2 critical biomarkers in a single study evaluation, revealing a more complete picture of the

---

Received Jul. 2, 2023; revision accepted Oct. 24, 2023.

For correspondence or reprints, contact Kevin T. Chen (chenkt@ntu.edu.tw).

*Contributed equally to this work.

†Contributed equally to this work.

vascular and molecular profiles of participants with cognitive decline. The aim of this study was to develop a method to quantify CBF by combining early [^{18}F]florbetaben (eFBB) PET with phase-contrast MRI using simultaneous PET/MRI. The results were validated against gold standard [^{15}O]water PET CBF measurements acquired in the same session.

MATERIALS AND METHODS

Study Design and Participants

This study was approved by the Stanford Institutional Review Board. All participants or their legally appointed representatives provided written informed consent before the imaging session. Participants were recruited through the Stanford Alzheimer Disease Research Center. This center reaches out to participants with memory issues and older, cognitively normal adults for the purposes of better understanding the pathophysiologic changes related to dementia.

PET Image Acquisition and Reconstruction

All PET and MR images were acquired on a simultaneous time-of-flight–enabled 3-T PET/MRI scanner (Signa; GE Healthcare). Each participant received an intravenous injection of [^{15}O]water (775 MBq) through the antecubital vein. Images were reconstructed using a time-of-flight ordered-subset expectation maximization algorithm with 3 iterations and 28 subsets, a nominal matrix size of 192 × 192, a field of view of 300 mm, and a slice thickness of 2.78 mm. At 20 min after the [^{15}O]water PET imaging session, [^{18}F]florbetaben (330 MBq) was injected in the same manner, and list-mode PET was acquired for a 20-min period. After the completion of the early-frame PET acquisition, participants were kept outside the scanner until the beginning of late-phase standard imaging in accordance with the [^{18}F]florbetaben protocol. Static reconstructions were performed on list-mode data acquired between injection and 30, 60, 120, and 300 s to determine the optimal early-frame duration. The eFBB PET reconstruction was performed with the time-of-flight ordered-subset expectation maximization algorithm (3 iterations, 28 subsets) using the vendor's zero-echo-time method for attenuation correction and a 4-mm gaussian postreconstruction filter. Late-phase static [^{18}F]florbetaben scans were also acquired between 90 and 110 min after injection to assess the amyloid burden of each participant.

MR Image Acquisition

Phase-contrast MRI was acquired for the quantitative measurement of blood flow velocity and vessel area in the internal carotid arteries and vertebral arteries simultaneously with the [^{15}O]water PET session. A single-slice cardiac-gated fast low-angle gradient-echo sequence with the following parameters was used: TR/TE, 12/4.6 ms; flip angle, 20°; matrix size, 480 × 384; voxel size, 0.375 × 0.375 mm; slice thickness, 3 mm; number of averages, 2; and velocity encoding, 100 cm/s in the inferior to posterior direction. The placement of the imaging slices at the flexion of the vertebral artery at the second cervical vertebra, perpendicular to the internal carotid arteries and vertebral arteries, was confirmed by a noncontrast cervical MR angiogram. Fast spoiled gradient-echo T1-weighted anatomic MRI was simultaneously performed for estimating the whole brain volume, with the following parameters: TR/TE, 9.6/3.8 ms; flip angle, 13°; and voxel size, 0.94 × 0.94 × 1.0 mm.

CBF Quantification

Phase-contrast MRI flow data were analyzed with the Arterys platform (Arterys) using a region-growing algorithm to define the borders of the arterial lumen of the bilateral internal carotid and vertebral arteries. The blood flow in each vessel was determined by multiplying the flow velocity and area for each vessel and summing the measurements to yield the total brain blood flow in units of mL/min. Total brain weight was derived from the volume measured by the T1-weighted anatomic image using the FSL Brain Extraction Toolbox (Analysis Group, FMRIB), assuming a brain tissue density of 1.1 g/mL, which included the ventricular and cerebrospinal fluid spaces. Mean whole-brain CBF was calculated from the total blood inflow divided by the total brain weight, yielding the traditional units of mL of blood/100 g/min (*18*). This value was used to scale both [^{15}O]water PET and [^{18}F]florbetaben early uptake to yield quantitative CBF maps (PC-eFBB).

Clinical Diagnosis and Amyloid Status

On the basis of the Uniform Dataset Clinician Diagnosis Form D1 (naccdata.org/data-collection/forms-documentation/uds-3), each participant's cognitive status and etiology were determined by Alzheimer Disease Research Center–affiliated neurologists. The cognitive status was established using the following classifications: normal cognition, mild cognitive impairment (MCI), and dementia. Because participants can have multiple cognitive statuses that may change throughout the years of enrollment at the Alzheimer Disease Research Center, the diagnosis date closest to the scan date was used for data analysis purposes. Amyloid status (Aβ positive [Aβ+] vs. Aβ negative [Aβ−]) was determined by the majority determination of 3 physicians trained to interpret [^{18}F]florbetaben imaging (2 neuroradiologists with 17 and 13 y of experience and 1 nuclear medicine physician with 9 y of experience; all trained on interpreting amyloid PET imaging), on the basis of the 90- to 110-min [^{18}F]florbetaben images.

Image Processing and Analysis

PC-eFBB and [^{15}O]water PET images were preprocessed with FSL 6.0.5 (Analysis Group, FMRIB) using the following steps. The brain extraction tool was used to extract brain data from T1-weighted images, followed by FLIRT (FMRIB's Linear Image Registration Tool) rigid-body registration to the native T1-weighted images and finally nonlinear affine registration to the Montreal Neurologic Institute (MNI) 152 (MNI152) template space. Separation of gray matter and white matter volumes was performed by FAST (FMRIB's Automated Segmentation Tool) segmentation on T1-weighted images after the removal of cerebellum data. The automated anatomic labeling (AAL) atlas was overlaid on the MNI152 template–registered images using MRIcroGL (version 12.3; https://www.nitrc.org/projects/mricrogl). Eight regions of interest (ROIs) corresponding to the cerebellar vermis, bilateral cerebellar hemispheres, midfrontal cortex, superior frontal cortex, inferior frontal cortex, occipital cortex, parietal cortex, and temporal cortex were extracted. Finally, voxel-by-voxel cross-correlation was performed for the purposes of determining the optimal early-frame length for [^{18}F]florbetaben (between 30 s and 5 min). The optimal duration of the early frame for early [^{18}F]florbetaben was selected on the basis of the highest correlation coefficient between eFBB and [^{15}O]water CBF.

To obtain a voxelwise CBF difference map, the following steps were performed. [^{15}O]water and PC-eFBB images of all of the participants were averaged in the template space. The averaged PC-eFBB images were then subtracted to obtain an error map. Two thresholds were applied to the error map (−5 to −25 and 5 to 25 mL/100 g/min) to avoid the near-zero noise floor, yielding under- and overestimation maps, respectively, which were overlaid on the T1-weighted structural image in the MNI152 template space. Data generated or analyzed during the study are available from the corresponding author by request, with a formal data sharing agreement and approval from the requesting researcher's local ethics committee.

Statistical Analyses

Statistical analyses were performed in Stata (version 17.0; https://www.stata.com). The Lin concordance correlation (CC) and Bland–Altman analysis with measurement of 95% limits of agreement were used to assess CBF measurements in ROIs defined by the AAL atlas, and a paired 2-tailed t test was applied to determine significance using a P value of 0.05. Correlations within regions in separate individuals and between regions within individuals were both determined. For the latter, a summary statistic representing the median correlation and interquartile range was determined. The CC was calculated for white and gray matter measurements along with regression analysis by dividing the cohort according to cognition and amyloid burden. Regression analysis was used to determine whether there were significant differences in performance among patients with normal cognition, MCI, and dementia and between amyloid-positive and amyloid-negative participants.

RESULTS

Participant Demographics

Participants who were enrolled in the Stanford Alzheimer Disease Research Core program, which included patients with known or suspected neurodegenerative disease and healthy age-matched controls, and who had agreed to receive an amyloid PET/MRI study were offered the opportunity to participate in this additional [^{15}O]water substudy. Of the 26 participants who enrolled in this substudy, 20 participants (9 women; mean age, 69 y [SD = 9 y]; 10 Aβ+ and 10 Aβ−) were included in the analysis. Six subjects did not complete the full imaging protocol, for the following reasons: 3 due to radiotracer delivery failure and 3 due to claustrophobia (Fig. 1). On the basis of the National Alzheimer Coordinating Center consensus criteria, 8 participants were cognitively normal, 9 had MCI, and 3 had dementia. The patients with cognitive impairment (MCI and dementia) had the following clinical diagnoses: AD (n = 5), corticobasilar degeneration (n = 2), dementia with Lewy bodies (n = 4), and cognitive impairment due to substance abuse (n = 1).

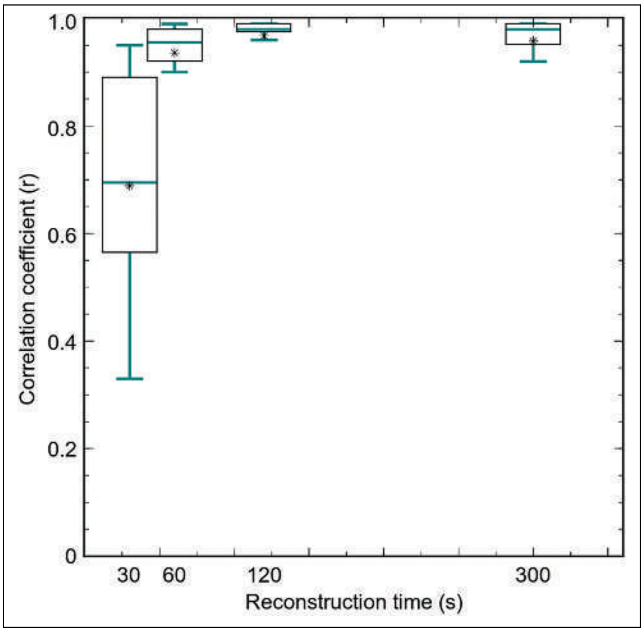

FIGURE 2. Whole-brain voxelwise cross-correlation (r) between [^{15}O]water and eFBB CBF as function of eFBB reconstruction duration (30 s, 1 min, 2 min, and 5 min) after injection. Asterisk indicates mean, bar indicates median, box indicates first and third quartiles, error bars indicate ±1 SD from mean.

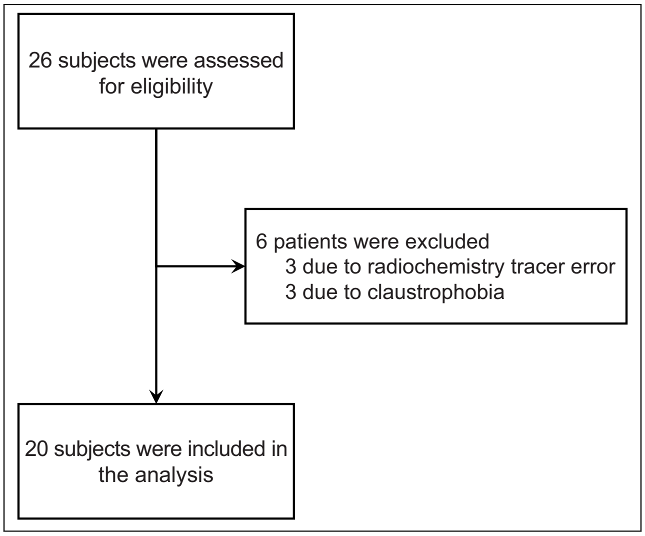

FIGURE 1. Flowchart for participant inclusion.

Determining Optimal Frame Length for eFBB

Voxelwise whole-brain correlation between [^{15}O]water PET and eFBB CBF measurements are shown for different eFBB frame lengths (30 s, 1 min, 2 min, and 5 min) after injection in Figure 2; a 2-min frame length was chosen for subsequent analyses.

Comparison of [^{15}O]Water and eFBB CBF

Mean whole-brain CBF measurements determined by [^{15}O]water PET and eFBB were 40.1 ± 20.7 and 39.6 ± 19.9 mL/100 g/min, respectively. A comparison of CBF measurements using the 2 modalities in the 8 summarized AAL atlas ROIs is shown in Figure 3. CC coefficient values between [^{15}O]water and eFBB for different AAL-based regions ranged from 0.86 to 0.98 (Table 1). There was no significant difference in the CC when the population was subdivided into amyloid-negative and amyloid-positive participants (CC, 0.90 vs. 0.87).

Mean whole-brain CBF measurements determined by the 2 methods were similar for gray matter (55.2 ± 14.7 mL/100 g/min vs. 55.9 ± 14.2 mL/100 g/min; $P > 0.2$) and white matter (21.4 ± 5.6 mL/100 g/min vs. 21.2 ± 5.1 mL/100 g/min; $P > 0.4$). Bland–Altman analysis demonstrated a bias of 0.7 ± 2.4 mL/100 g/min with 95% limits of agreement of 5.4 and −4.0 mL/100 g/min and −0.2 ± 1.0 mL/100 g/min with 95% limits of agreement of −2.2 and 1.8 mL/100 g/min for measurements in gray matter and white matter regions, respectively.

Regression analysis showed no statistical significance among different cognitive statuses with respect to measurements in gray matter (CC for cognitively normal, 0.98; CC for MCI, 0.98; CC for dementia, 0.98) and white matter (CC for cognitively normal, 0.99; CC for MCI, 0.98; CC for dementia, 0.99). Table 2 shows the correlation for the 115 AAL-generated regions for each participant in our study, demonstrating a median correlation of 0.92 (interquartile range, 0.87–0.93).

CBF images for representative participants with the 2 methods are shown in Figure 4, demonstrating similar visual appearances. An averaged CBF difference map measured on a voxel-by-voxel level is shown in Figure 5, demonstrating only small, scattered regions with absolute differences between the measurement methods on the order of 5–10 mL/100 g/min.

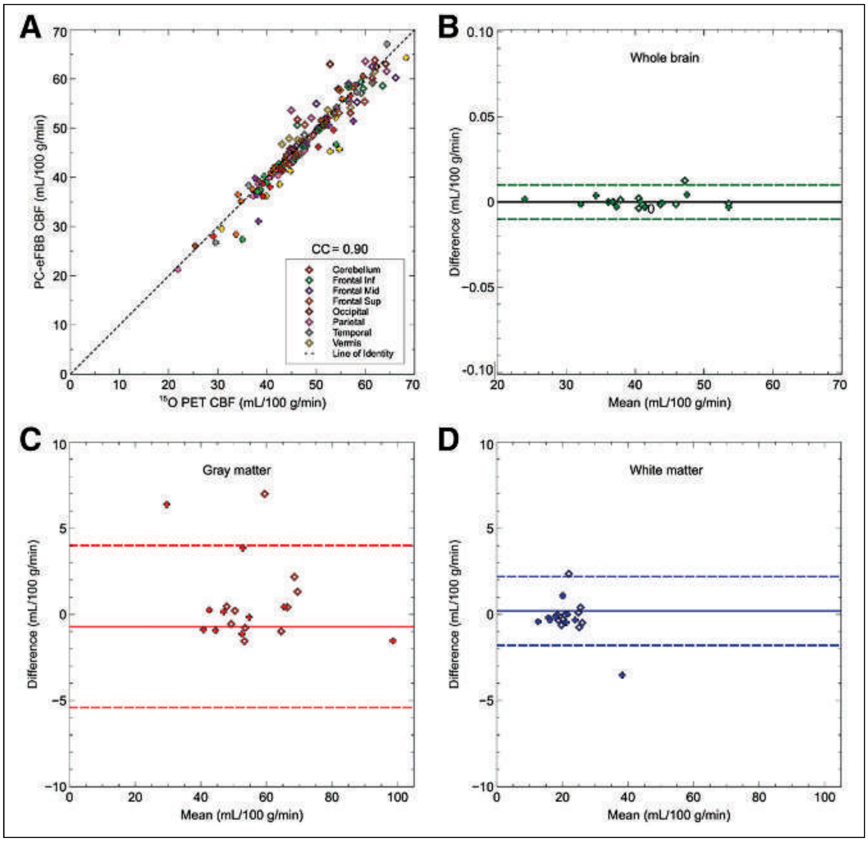

FIGURE 3. (A) Scatterplot of [^{15}O]water and eFBB CBF measurements for all regions in all subjects. (B–D) Bland–Altman analysis for whole brain (B), gray matter (C), and white matter (D) for all subjects. Bias is indicated by solid lines, and dashed lines represent 95% limits of agreement. Diamonds and plus symbols represent β-amyloid–negative and –positive cases, respectively. Inf = inferior; Sup = superior.

DISCUSSION

In the present study, we described and validated the use of eFBB imaging combined with MRI to determine quantitative CBF measurements. We first used voxel-by-voxel correlational analysis to determine an optimal early time frame for the eFBB measurement from our PET scanner. Although shorter frame lengths will be more highly CBF weighted, they will also have higher noise levels. To optimally trade off these 2 considerations, we chose a 2-min interval as opposed to other possible time frames (*19,20*). We then demonstrated equivalence in a cohort that included participants with normal cognition, MCI, and dementia, with equal representation of Aβ− and Aβ+ participants. There was a strong correlation between [^{15}O]water and eFBB CBF measurements in whole brain, gray matter, white matter, and AAL-defined reference regions. Bland–Altman analysis revealed small biases of 0.7 and −0.2 mL/100 g/min between the measurements in gray matter and white matter, respectively. Given natural variability in blood flow in humans, this difference is negligible. Even variability as expressed by the 95% CI range was relatively small, from 5.4 to −4.0 mL/100 g/min. We did not see any difference in performance between Aβ− and Aβ+ participants or in different groups based on cognitive status.

PC-eFBB is an absolute quantification method that uses phase-contrast MRI as a robust method to scale the relative perfusion map obtained from the initial eFBB PET images. Another method to calculate CBF from early-frame PET tracer data would be to use kinetic analysis with either arterial blood sampling or an image-derived input function (IDIF) (*21*). Arterial sampling is invasive, carries risk to the participant, and requires estimation of delay and dispersion, and prior studies suggested frequent failures due to blood clotting within arterial catheters (*19,22*). The use of an IDIF obviates the need for invasive sampling but introduces additional variability due to the selection of the ROI and the relatively high noise of individual short-temporal-frame PET images required for capturing the early time points. Also, the need to set multiple parameters in the kinetic analysis adds additional variability. A scaling factor derived from phase-contrast MR images that measure whole-brain CBF is simple to use and

TABLE 1
Comparison of CBF Measurements Obtained with [^{15}O]Water and eFBB in Different AAL-Derived Regions

	[^{15}O]water		eFBB		
ROI	Mean	SD	Mean	SD	CC
Vermis	49.4	8.0	49.7	8.0	0.92
Cerebellum	48.6	8.4	48.5	8.8	0.90
Inferior frontal	47.3	8.3	49.2	8.8	0.86
Midfrontal	52.3	8.3	51.4	8.4	0.86
Superior frontal	47.4	8.1	48.3	8.3	0.90
Occipital	50.9	9.3	52.9	10.6	0.90
Parietal	46.9	9.4	47.8	9.8	0.92
Temporal	47.8	8.2	47.1	8.0	0.98

TABLE 2
CC of 115 AAL-Derived Regions in Individual Participants

Participant	Classification (NACC diagnosis)	Amyloid	CC*
1	MCI_LBD	Positive	0.95
2	Dementia_AD	Positive	0.95
3	Normal	Negative	0.93
4	MCI_LBD	Negative	0.95
5	Normal	Positive	0.87
6	Normal	Positive	0.76
7	MCI_CBD	Positive	0.70
8	Normal	Positive	0.93
9	MCI_IMPSUB	Negative	0.85
10	Normal	Positive	0.85
11	MCI_AD	Negative	0.90
12	Normal	Negative	0.93
13	MCI_LBD	Negative	0.91
14	MCI_CBD	Negative	0.88
15	Dementia_AD	Positive	0.93
16	Dementia_AD	Positive	0.87
17	MCI_LBD	Negative	0.93
18	MCI_AD	Positive	0.84
19	Normal	Negative	0.95
20	Normal	Negative	0.94

*Median = 0.92 (interquartile range, 0.87–0.93).

NACC = National Alzheimer Coordinating Center; LBD = dementia with Lewy bodies; CBD = corticobasilar degeneration; IMPSUB = cognitive impairment due to substance abuse.

has high reproducibility (*23*). The method highlights the value of simultaneous PET/MRI, with which simultaneous relative CBF images and the scaling factor for quantitation can be obtained to reduce physiologic variability. The range of whole-brain CBF values was as expected from an elderly population with mixed cognitive statuses. A recent review of CBF measurement comparisons between PET and arterial spin labeling reported that the correlation between the 2 methods was heavily influenced by the time interval between separate imaging sessions (*24*), emphasizing the day-to-day variability of CBF and the value of simultaneous data acquisition.

Previous research evaluated the suitability of eFBB for estimating CBF, but it yielded only relative measures (*15–17,20,25*). Kwon et al. investigated the optimal reference region for eFBB and reported a high correlation (*r*, 0.90) with ethyl cysteinate dimer SPECT using a cerebellar gray matter normalization approach (*15*). Daerr et al. compared images created from the first 5 or 10 min after [^{18}F]florbetaben injection with [^{18}F]FDG PET images, which demonstrated an appearance similar to CBF due to the relationship between blood flow and metabolism (*20*). They found correlations between 0.81 and 0.92 for a variety of ROIs through normalization to the global mean SUV ratio (*20*). Similar results were observed by Seiffert et al. in a comparison of 0- to 1-min amyloid images from 3 different ^{18}F tracers to [^{18}F]FDG images (*25*). Ottoy et al. evaluated 0- to 2-min early-frame [^{18}F]AV45 directly against several other tracers and metrics, including [^{15}O]water, [^{18}F]FDG, and R1 (tracer delivery rate) estimated from [^{18}F]AV45 using tracer kinetics in a population similar to ours (*16*). They found correlations of 0.70–0.94 for different regions between early-frame [^{18}F]AV45 and [^{15}O]water PET but concluded that R1 better reflected disease severity than early-frame [^{18}F]AV45. It is important to note that all of these methods provided only correlations and, unlike our study, none was capable of deriving quantitative CBF from the amyloid images.

Heeman et al. reported variability in R1 measurements derived from kinetic modeling with [^{18}F]florbetapir and [^{18}F]flortaucipir in individuals with AD and cognitively normal individuals, where the latter tracer showed better repeatability (*26*). This was not the case for PC-eFBB, as we were able to demonstrate equivalence between A$\beta-$ and A$\beta+$ participants and among different cognitive groups. Bullich et al. demonstrated a noninvasive kinetic modeling approach with [^{18}F]florbetaben in a dual-time-window acquisition protocol similar to our experimental design (*27*). Alongside kinetic modeling, they applied an SUV ratio-based approach and concluded that the latter would be sufficient for most clinical applications, in which a compromise in accuracy is reasonable in favor of simplicity. Our approach showed high correlation as well as quantitative accuracy between the methods, likely due to our use of a simultaneous PET/MRI system. Although voxelwise differences in PC-eFBB and [^{15}O]water CBF were not reported at an individual level, AAL atlas ROIs were defined in 115 subregions, which sampled the CBF maps with

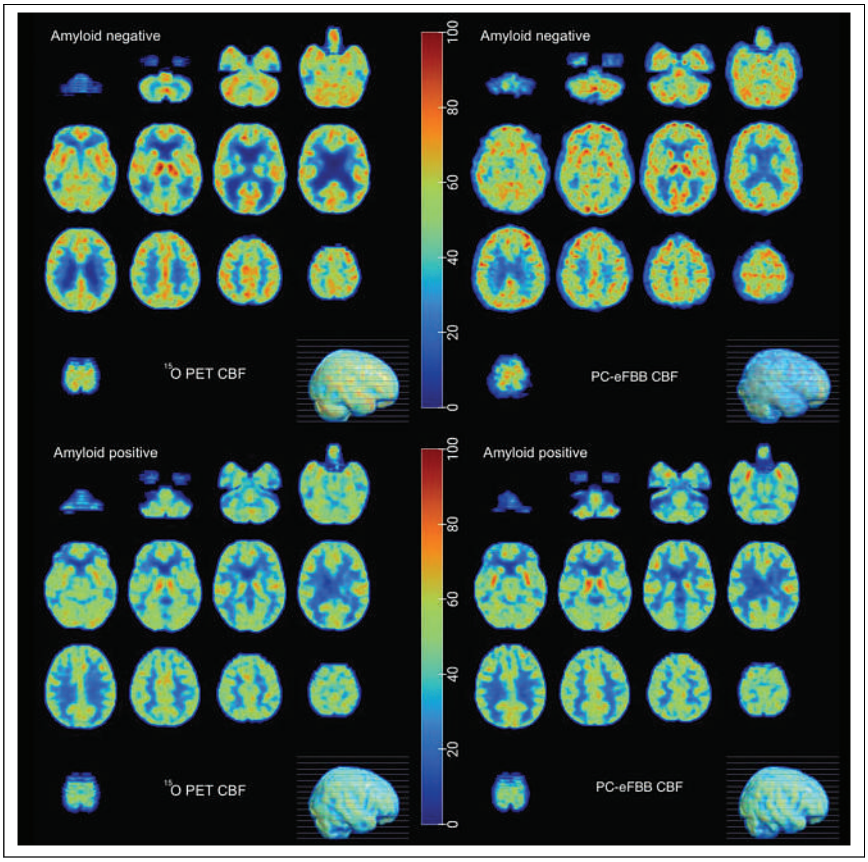

FIGURE 4. Representative [^{15}O]water PET and phase-contrast scaled eFBB CBF (PC-eFBB CBF) for representative β-amyloid–negative and –positive participants. Amyloid-positive participant had dementia that was ascribed to Alzheimer disease pathology. Amyloid-negative participant had normal cognition. Units of color bars measuring CBF are mL/100 g/min.

nearly voxelwise resolution and had the benefit of being more robust against complications such as small misalignment errors. As such, this approach will enable the measurement of both quantitative CBF and late-stage amyloid in the same participant with a single injection during a single imaging examination.

Our study has several limitations. eFBB could be validated in a larger and more diverse cohort, including more patients with dementia. Only a single PET/MRI scanner was used to acquire the imaging data and to derive the optimal early-frame reconstruction duration. This optimal time duration could vary with different PET scanners on the basis of their sensitivities. Next, we did not perform arterial sampling or obtain an IDIF to measure [^{15}O]water CBF. The latter was partially due to logistic limitations at our site surrounding arterial cannulation and our experience that these IDIF-based tracer kinetic measurements tend to be relatively unstable compared with phase-contrast MRI. Furthermore, our experimental protocol was not designed around the IDIF reconstruction method, and prior images (i.e., PET angiogram) were not rigorously validated during the acquisition.

The CBF quantification pipelines for [^{15}O]water and [^{18}F]florbetaben both depend on the Arterys-derived phase-contrast MRI measurements of the flow velocity and area in the bilateral internal carotid and vertebral arteries and are therefore limited by their accuracy (*28*). Other MRI-based CBF proxies, such as arterial spin labeling, could also be considered to normalize the relative PET CBF acquisitions. A final question might be why such a method is valuable at all, given that arterial spin labeling can measure CBF in studies that include MRI. Although arterial spin labeling can be used as a proxy for flow, its accuracy can be affected by susceptibility artifacts, unknown variations in labeling efficiency, changes in hematocrit that affect the T1 of the blood and, probably most importantly, prolonged arterial transit times (*12*). For these reasons, we believe that the eFBB approach could be more robust.

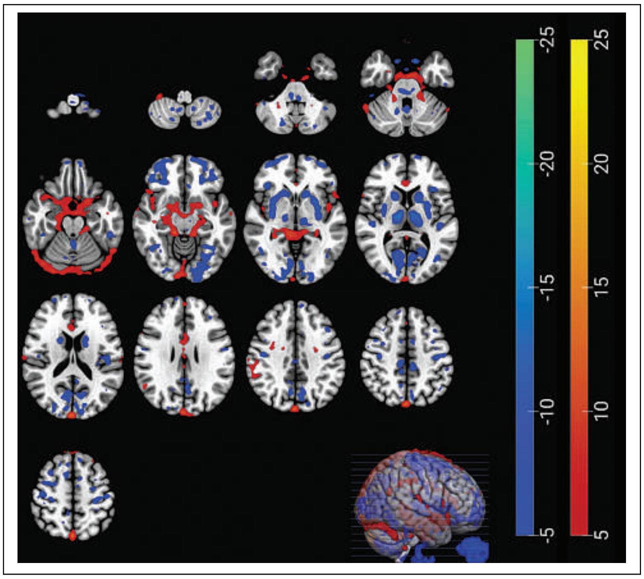

FIGURE 5. Voxelwise difference in CBF values measured using [^{15}O]water and eFBB averaged for all participants in units of mL/100 g/min. Red and blue represent regions where eFBB over- and underestimated CBF as measured by [^{15}O]water PET, respectively.

CONCLUSION

We have described and validated a hybrid PET/MRI method using eFBB and phase-contrast MRI to provide quantitative CBF measurements to complement late-phase amyloid assessment. As such, 2 important biomarkers may be measured in a single session in participants with memory concerns, enabling improved characterization of dementia pathophysiology with reduced cost and inconvenience to participants and their caregivers. Future studies could explore the use of other early-frame PET tracers and a similar methodology to provide additional quantitative CBF measurements in a wide range of diseases.

DISCLOSURE

This project was supported by National Institutes of Health grants P41-EB015891, R01-EB025220, K99-AG068310, R01-AG048076, and R21-AG058859; Stanford Alzheimer's Disease Research Center (P30-AG06615); Yushan Fellow Program by the Ministry of Education (Taiwan) NTU-112V1015-3; National Science and Technology Council (Taiwan) grant 110-2222-E-002-015-MY3; the Alzheimer's Association (AARFD-21-849349); GE Healthcare; Life Molecular Imaging; and American Heart Association grant 826254. Outside the submitted work, Greg Zaharchuk is a cofounder of and has an equity relationship with Subtle Medical Inc.; grant funding was supplied by GE Healthcare; and consulting fees were received from Biogen. No other potential conflict of interest relevant to this article was reported.

ACKNOWLEDGMENT

We thank Tie Liang for the statistical analysis.

KEY POINTS

QUESTION: Can a PET/MRI method for CBF measurement be developed using static early-frame [^{18}F]florbetaben PET and phase-contrast MRI and validated with the reference standard [^{15}O]water?

PERTINENT FINDINGS: When a CBF quantification method using eFBB and phase-contrast MRI was compared with the reference standard [^{15}O]water, a high regional mean CBF CC (median CC, 0.92) was found in an elderly cohort including patients with a range of cognitive disorders. The eFBB CBF quantification method was accurate irrespective of amyloid pathology, and the optimal time frame for perfusion quantification was observed to be the first 2 min after injection.

IMPLICATIONS FOR PATIENT CARE: This approach is likely applicable to other lipophilic radiotracers, enabling CBF and molecular information to be measured in 1 setting in a dual-phase static PET/MRI acquisition.

REFERENCES

1. de Heus RA, de Jong DL, Sanders ML, et al. Dynamic regulation of cerebral blood flow in participants with Alzheimer disease. *Hypertension.* 2018;72:139–150.
2. Vestergaard MB, Lindberg U, Aachmann-Andersen NJ, et al. Comparison of global cerebral blood flow measured by phase-contrast mapping MRI with ^{15}O-H$_2$O positron emission tomography. *J Magn Reson Imaging.* 2017;45:692–699.
3. Kety SS, Schmidt CF. The effects of altered arterial tensions of carbon dioxide and oxygen on cerebral blood flow and cerebral oxygen consumption of normal young men. *J Clin Invest.* 1948;27:484–492.
4. Appelman AP, van der Graaf Y, Vincken KL, et al. Total cerebral blood flow, white matter lesions and brain atrophy: the SMART-MR study. *J Cereb Blood Flow Metab.* 2008;28:633–639.
5. Sabayan B, van der Grond J, Westendorp RG, et al. Total cerebral blood flow and mortality in old age: a 12-year follow-up study. *Neurology.* 2013;81:1922–1929.
6. Korte N, Nortley R, Attwell D. Cerebral blood flow decrease as an early pathological mechanism in Alzheimer's disease. *Acta Neuropathol (Berl).* 2020;140:793–810.
7. Benedictus MR, Leeuwis AE, Binnewijzend MA, et al. Lower cerebral blood flow is associated with faster cognitive decline in Alzheimer's disease. *Eur Radiol.* 2017;27:1169–1175.
8. Martin AJ, Friston KJ, Colebatch JG, Frackowiak RS. Decreases in regional cerebral blood flow with normal aging. *J Cereb Blood Flow Metab.* 1991;11:684–689.
9. Albrecht D, Isenberg AL, Stradford J, et al. Associations between vascular function and tau PET are associated with global cognition and amyloid. *J Neurosci.* 2020;40:8573–8586.
10. Braak H, Braak E. Neuropathological staging of Alzheimer-related changes. *Acta Neuropathol (Berl).* 1991;82:239–259.
11. Esparza TJ, Zhao H, Cirrito JR, et al. Amyloid-beta oligomerization in Alzheimer dementia versus high-pathology controls. *Ann Neurol.* 2013;73:104–119.
12. Haller S, Zaharchuk G, Thomas D, et al. Arterial spin labeling perfusion of the brain: emerging clinical applications. *Radiology.* 2016;281:337–356.
13. Blomquist G, Engler H, Nordberg A, et al. Unidirectional influx and net accumulation of PIB. *Open Neuroimag J.* 2008;2:114–125.
14. Dishino DD, Welch M, Kilbourn M, Raichle M. Relationship between lipophilicity and brain extraction of C-11 labeled radiopharmaceuticals. *J Nucl Med.* 1983;24:1030–1038.
15. Kwon SJ, Ha S, Yoo SW, et al. Comparison of early F-18 florbetaben PET/CT to Tc-99m ECD SPECT using voxel, regional, and network analysis. *Sci Rep.* 2021;11:16738.
16. Ottoy J, Verhaeghe J, Niemantsverdriet E, et al. ^{18}F-FDG PET, the early phases and the delivery rate of ^{18}F-AV45 PET as proxies of cerebral blood flow in Alzheimer's disease: validation against ^{15}O-H$_2$O PET. *Alzheimers Dement.* 2019;15:1172–1182.
17. Yoon HJ, Kim BS, Jeong JH, et al. Dual-phase ^{18}F-florbetaben PET provides cerebral perfusion proxy along with beta-amyloid burden in Alzheimer's disease. *Neuroimage Clin.* 2021;31:102773.
18. Ishii Y, Thamm T, Guo J, et al. Simultaneous phase-contrast MRI and PET for noninvasive quantification of cerebral blood flow and reactivity in healthy participants and participants with cerebrovascular disease. *J Magn Reson Imaging.* 2020;51:183–194.
19. Heijtel DF, Mutsaerts HJ, Bakker E, et al. Accuracy and precision of pseudo-continuous arterial spin labeling perfusion during baseline and hypercapnia: a head-to-head comparison with ^{15}O H$_2$O positron emission tomography. *Neuroimage.* 2014;92:182–192.
20. Daerr S, Brendel M, Zach C, et al. Evaluation of early-phase [^{18}F]-florbetaben PET acquisition in clinical routine cases. *Neuroimage Clin.* 2016;14:77–86.
21. Khalighi MM, Deller TW, Fan AP, et al. Image-derived input function estimation on a TOF-enabled PET/MR for cerebral blood flow mapping. *J Cereb Blood Flow Metab.* 2018;38:126–135.
22. Ssali T, Anazodo UC, Thiessen JD, et al. A noninvasive method for quantifying cerebral blood flow by hybrid PET/MRI. *J Nucl Med.* 2018;59:1329–1334.
23. Thunberg P, Karlsson M, Wigstrom L. Accuracy and reproducibility in phase contrast imaging using SENSE. *Magn Reson Med.* 2003;50:1061–1068.
24. Fan AP, Jahanian H, Holdsworth SJ, Zaharchuk G. Comparison of cerebral blood flow measurement with [^{15}O]-water positron emission tomography and arterial spin labeling magnetic resonance imaging: a systematic review. *J Cereb Blood Flow Metab.* 2016;36:842–861.
25. Seiffert AP, Gomez-Grande A, Villarejo-Galende A, et al. High correlation of static first-minute-frame (FMF) PET imaging after ^{18}F-labeled amyloid tracer injection with [^{18}F]FDG PET imaging. *Sensors (Basel).* 2021;21:1–14.
26. Heeman F, Visser D, Yaqub M, et al. Precision estimates of relative and absolute cerebral blood flow in Alzheimer's disease and cognitively normal individuals. *J Cereb Blood Flow Metab.* 2023;43:369–378.
27. Bullich S, Barthel H, Koglin N, et al. Validation of noninvasive tracer kinetic analysis of ^{18}F-florbetaben PET using a dual-time-window acquisition protocol. *J Nucl Med.* 2018;59:1104–1110.
28. Wen B, Tian S, Cheng J, et al. Test–retest multisite reproducibility of neurovascular 4D flow MRI. *J Magn Reson Imaging.* 2019;49:1543–1552.

Tumor Location Relative to the Spleen Is a Prognostic Factor in Lymphoma Patients: A Demonstration from the REMARC Trial

Kibrom B. Girum[1], Anne-Ségolène Cottereau[2], Laetitia Vercellino[3], Louis Rebaud[1,4], Jérôme Clerc[2], Olivier Casasnovas[5], Franck Morschhauser[6], Catherine Thieblemont[7], and Irène Buvat[1]

[1]LITO Laboratory, U1288 Inserm, Institut Curie, University Paris-Saclay, Orsay, France; [2]Department of Nuclear Medicine, Cochin Hospital, AP-HP, Paris Descartes University, Paris, France; [3]Department of Nuclear Medicine, Saint Louis Hospital, AP-HP, Paris, France; [4]Research and Clinical Collaborations, Siemens Medical Solutions USA, Knoxville, Tennessee; [5]Department of Hematology, University Hospital of Dijon, Dijon, France; [6]Research Group on Injectable Forms and Associated Technologies, Department of Hematology, Claude Huriez Hospital, University Lille, Lille, France; and [7]Department of Hematology, Saint Louis Hospital, AP-HP, Paris, France

Baseline [^{18}F]FDG PET/CT radiomic features can improve the survival prediction in patients with diffuse large B-cell lymphoma (DLBCL). The purpose of this study was to investigate whether characterizing tumor locations relative to the spleen location in baseline [^{18}F]FDG PET/CT images predicts survival in patients with DLBCL and improves the predictive value of total metabolic tumor volume (TMTV) and age-adjusted international prognostic index (IPI). **Methods:** This retrospective study included 301 DLBCL patients from the REMARC (NCT01122472) cohort. Physicians delineated the tumor regions, whereas the spleen was automatically segmented using an open-access artificial intelligence algorithm. We systematically measured the distance between the centroid of the spleen and all other lesions, defining the SD of these distances as the lesion spread (SpreadSpleen). We calculated the maximum distance between the spleen and another lesion (Dspleen) for each patient and normalized it with the body surface area, resulting in standardized Dspleen (sDspleen). The predictive value of each PET/CT feature for progression-free survival (PFS) and overall survival (OS) was evaluated through univariate and multivariate time-dependent Cox models and Kaplan–Meier analysis. **Results:** In total, 282 patients (mean age, 68.33 ± 5.41 y; 164 men) were evaluated. The artificial intelligence algorithm successfully segmented the spleen in 96% of the patients. SpreadSpleen, Dspleen, and sDspleen were correlated neither with TMTV (Pearson $\rho < 0.23$) nor with IPI (Pearson $\rho < 0.15$). When median values were used as the cutoff, SpreadSpleen, Dspleen, and sDspleen all significantly classified patients into 2 risk groups for PFS and OS ($P < 0.001$). They complemented TMTV and IPI to classify the patients into 3 risk groups for PFS and OS ($P < 0.001$). Integrating SpreadSpleen, Dspleen, or sDspleen into a Cox model on the basis of TMTV, IPI, and TMTV combined with IPI significantly improved the concordance index for PFS and OS ($P < 0.05$). **Conclusion:** Baseline PET/CT features that characterize tumor spread and dissemination relative to the spleen strongly predicted survival in patients with DLBCL. Integrating these features with TMTV and IPI further improved survival prediction.

Key Words: tumor location; FDG; CT; DLBCL; artificial intelligence

J Nucl Med 2024; 65:313–319
DOI: 10.2967/jnumed.123.266322

Whole-body [^{18}F]FDG PET/CT is a standard of care for staging and assessing responses of patients with diffuse large B-cell lymphoma (DLBCL). The CT images are often preferred to view the anatomic structures, and the [^{18}F]FDG PET images are used to capture the molecular activities of the tumor. Despite the widespread use of the age-adjusted international prognostic index (IPI) in DLBCL, recent literature suggests that image-based biomarkers could also be used for this purpose (*1*). Baseline [^{18}F]FDG PET–based features that characterize the tumor burden, such as the total metabolic tumor volume (TMTV), have been shown to predict survival in DLBCL patients (*1–4*). Recently introduced tumor dissemination features, such as the distance between the 2 farthest lesions (Dmax) and the maximum distance between the largest lesion and another lesion (Dbulk), have shown promising results for predicting survival (*5–9*). Their simplicity, intuitive interpretation, and value in predicting the outcome inspired this study.

Given that the spleen plays a particular role in the lymphatic system and particularly in DLBCL (*10*), we assumed that the spleen could serve as a reference organ to model the disease distribution and dissemination over the whole body.

The purpose of this study was to investigate whether tumor distribution and dissemination measured relative to the spleen from baseline [^{18}F]FDG PET/CT images had prognostic values independent of that of TMTV and IPI and improved survival prediction in DLBCL patients. The individual prognostic values of these new image-based features were evaluated in terms of progression-free survival (PFS) and overall survival (OS). We also assessed the added prognostic value of these biomarkers when they are combined with TMTV and age-adjusted IPI.

MATERIALS AND METHODS

Patients

A retrospective analysis of 301 DLBCL patients with a baseline [^{18}F]FDG PET/CT scan from the REMARC trial (NCT01122472) was conducted. The REMARC trial study started including patients in 2010 and was a double-blind, international, multicenter, randomized phase II study. Patients included in this study were 60–80 y old and

---

Received Jul. 12, 2023; revision accepted Oct. 23, 2023.

For correspondence or reprints, contact Irène Buvat (irene.buvat@curie.fr).

had an Ann Arbor stage of I–IV and age-adjusted IPI of at least 1 at diagnosis, with histologically proven CD20-positive DLBCL according to the 2008 World Health Organization criteria (*11*). Detailed characteristics of the patients were reported elsewhere (*2*). The survival outcomes (PFS and OS) were recorded as defined by the revised National Cancer Institute criteria (*12*). Figure 1 summarizes the flow diagram of the data. Patient data were anonymized before any analysis. All patients gave written informed consent, and institutional review board approval, including ancillary studies, was obtained. The demographics and staging of the DLBCL patients used for the survival analysis are summarized in Table 1.

TABLE 1
Population Characteristics (n = 282)

Parameter	Number
Men	164 (58.2%)
Women	118 (41.8%)
Median age (y)	68.33 (64.0–73.0)
Median weight (kg)	72 (63.0–83.0)
Median height (cm)	168 (160.0–175.0)
Ann Arbor stage	
<I	1 (0.4%)
≥II	281 (99.6%)
Performance status	
0	114 (40.4%)
1	120 (42.6%)
2	41 (14.5%)
3	2 (0.7%)
4	2 (0.7%)
Missing	3 (1.1%)

Qualitative data are number and percentage; continuous data are median and interquartile ranges (quartile 1 to quartile 3).

Image Analysis and Feature Extraction

Two experienced nuclear medicine physicians (with 7 and 10 y of experience) delineated the lesion regions semiautomatically from the baseline 3-dimensional PET/CT images. The exact delineation procedure has been previously described (*2*). All lesion segmentations were visually verified to include pathologic lesions and to exclude physiologic uptake. The total volume of the lesions for each patient was then calculated as TMTV. Two recently introduced lesion dissemination features, Dmax (*6*) and Dbulk (*7*), were calculated from each lesion's centroid.

Automatic Spleen Segmentation on CT Images. An artificial intelligence (AI) method called TotalSegmentator was used to segment the spleen from 3-dimensional CT images (*13*). This method was initially developed to segment 104 anatomic structures from CT images, but in our work, we focused on spleen segmentation only. A postprocessing method was developed to check the quality of the spleen segmentation and correct it when needed. The postprocessing method included 2 criteria to trigger a warning, ensuring that the spleen segmentation had a single connected component and was not outside the whole-body field of view. If the spleen included more than 1 connected component, the largest one was automatically selected as the spleen. After postprocessing, all segmentations were visually verified and manually adjusted using the LIFEx software whenever needed (*14*). As the CT and PET images were aligned from the PET/CT acquisition, for each patient, the spleen segmentation result obtained from the AI was superimposed onto the lesion segmentation obtained from the experts. Figure 2 illustrates the proposed image-processing pipeline.

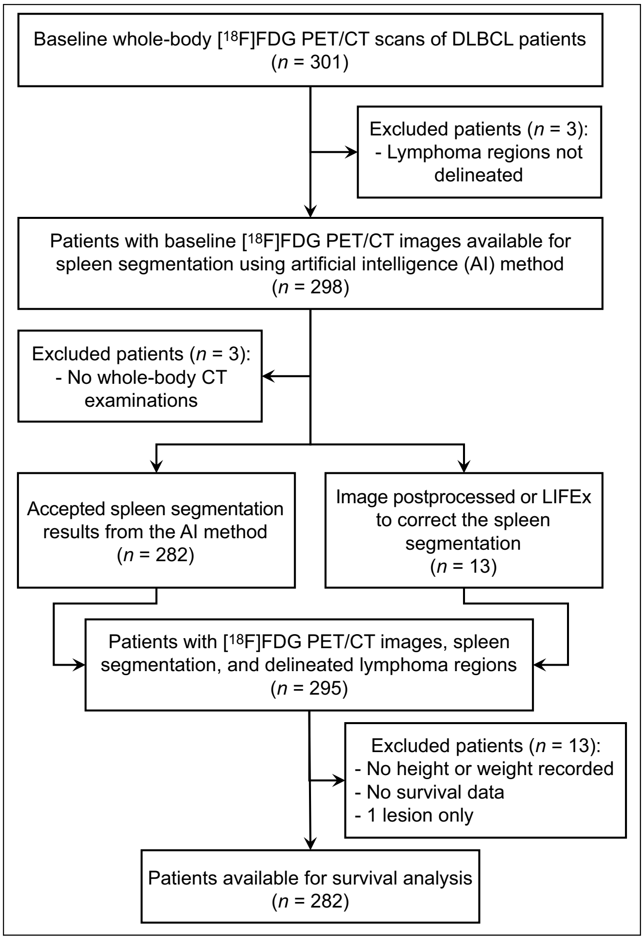

FIGURE 1. Study flowchart.

PET/CT Feature Extraction. The superimposed spleen and lesion 3-dimensional regions were used to calculate the tumor location relative to the spleen. From the 3-dimensional coordinates of the spleen region, the centroid was automatically calculated and defined the spleen location. For each patient, the distance between the centroid of the spleen, $A = (x_a, y_a, z_a)$, and all other detected lesion centroids ($B_i = x_{bi}, y_{bi}, z_{bi}$, centroid of the ith lesion) was measured using the Euclidean distance formula $\sqrt{(x_{bi} - x_a)^2 + (y_{bi} - y_a)^2 + (z_{bi} - z_a)^2}$, $i = 1, 2, 3 \ldots, N$ for N detected lesions. The SD of the distance between the spleen centroid and all lesions was calculated for each patient as $\sigma = \sqrt{\frac{\sum_{i=1}^{N} (ABi - \mu)^2}{N}}$ and was referred to as lesion spread relative to the spleen (SpreadSpleen), where $\mu = \sum_{i=1}^{N} (AB_i)/N$. The distance between the spleen and the farthest lesion from the spleen (Dspleen) was deduced for each patient and normalized by the patient's body surface area, given by body surface area $= \frac{\sqrt{\text{weight (kg)} \times \text{height (cm)}}}{60}$, and named hereafter the standardized distance of the farthest lesion from the spleen (sDspleen) (*15*). Supplemental Figure 1 illustrates the definitions of the new features relative to the spleen (supplemental materials are available at http://jnm.snmjournals.org). The image-processing pipeline, including the AI-based spleen segmentation, feature extraction, and survival

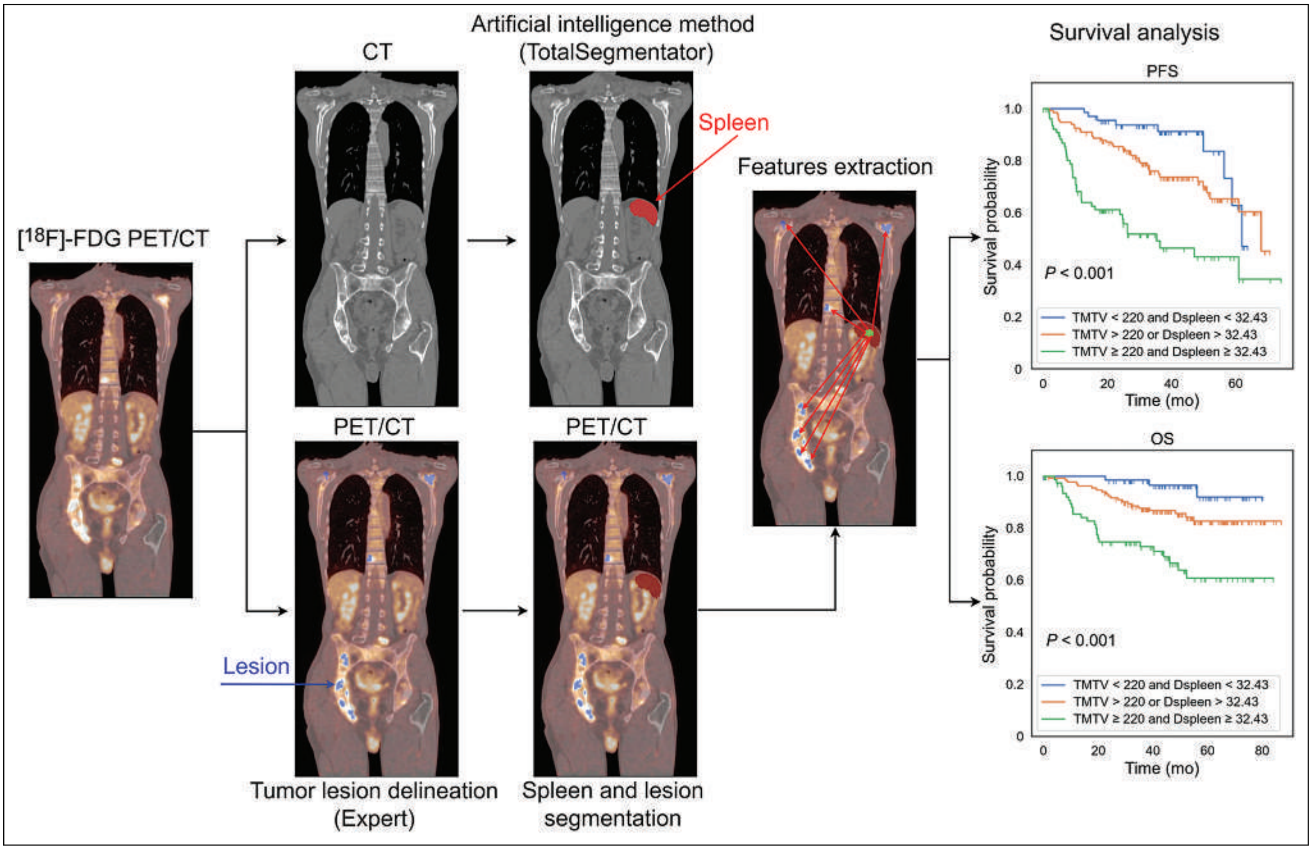

FIGURE 2. Overview of image-processing pipeline to calculate tumor locations relative to spleen from [^{18}F]FDG PET/CT images. Deep learning–based whole-body segmentation was used to segment spleen from CT images. From overlapped tumor and spleen segmentations, we extracted whole-body radiomic features, including TMTV and Dspleen. Extracted radiomic features were used to predict OS and PFS.

analysis, is publicly available at https://github.com/KibromBerihu/TumorLocationProfiler.

The exact same analysis was performed using the liver as a reference organ, as described in the supplemental materials.

Statistical Analysis

The predictive power of the calculated features was evaluated in univariate and multivariate analyses. First, we evaluated if each of the calculated biomarkers was predictive of the PFS and OS using Kaplan–Meier survival analysis and a time-dependent area under the receiver operating characteristics curve (AUC), and the results obtained for the different features were compared. Correlations between the biomarkers were calculated using the Pearson correlation coefficient (ρ). Second, we evaluated the added values of the predictive biomarkers combined with known predictive biomarkers, including the TMTV and the IPI. A multivariate Cox regression analysis with a bootstrap resampling at the patient level was used to associate CIs to the Cox model hazard ratio and the concordance index. The empiric 95% CI was reported with a bootstrap of 5,000 random samplings with replacement. Cox proportional hazard models were used to analyze univariate and multivariate results. *P* values less than 0.05 were interpreted as statistically significant.

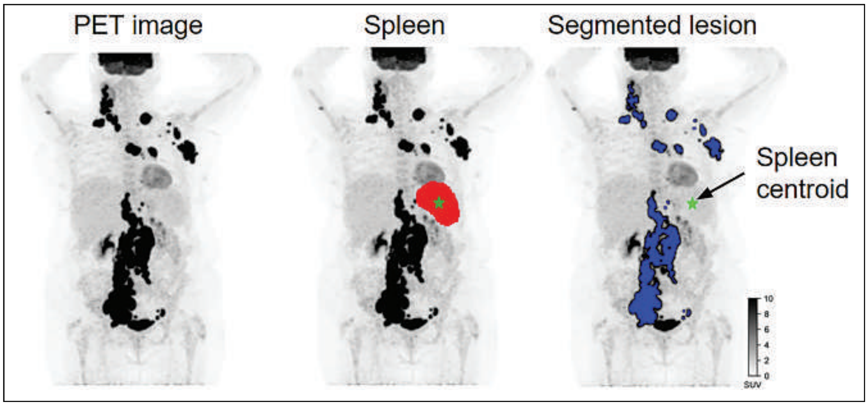

FIGURE 3. Maximum-intensity projection of PET images with spleen segmentation by AI model and lesion segmentations by expert. Cross hair indicates centroid of spleen.

RESULTS

Among the 301 patients from the REMARC cohort, 282 patients (mean age, 68.33 ± 5.41 y; 164 men) were included for the biomarker and survival analysis. [^{18}F]FDG PET/CT quality control and other criteria described in Figure 1 excluded 19 patients. The characteristics of the 282 patients included for the survival analysis are shown in Table 1.

Spleen Segmentation

Among the 295 patients available for PET/CT segmentations (regardless of the availability of survival data; Fig. 1), the TotalSegmentator AI method correctly

TABLE 2
Statistics of PET/CT Features

PET/CT feature	Mean	SD	Median	Interquartile range 1–3
TMTV (cm^3)	434.43	569.52	240.02	78.24 – 551.08
SpreadSpleen (cm)	6.30	3.03	6.67	3.99–8.41
Dspleen (cm)	32.02	9.57	32.43	25.92–38.73
sDspleen × 100 (m^{-1})	17.59	5.45	18.05	13.80–21.29
Dmax (cm)	44.08	23.05	44.62	23.84–64.17
Dbulk (cm)	31.63	18.62	31.73	15.63–44.40

detected and segmented the spleen in 282 patients (96%); the postprocessing method yielded a warning in 13 patients (4%) and automatically corrected the segmentation in 12 of 13 patients. The spleen segmentation of 1 patient only had to be manually corrected using the LIFEx software. The median size of the spleen was 256.15 cm^3 (interquartile range, 169–395 cm^3). A total of 101 (34%) patients had lesions segmented by the expert in the spleen. Figure 3 shows the coronal maximum-intensity projection views of the PET image of 1 patient, the PET image overlapped with the spleen segmentation by the AI model, and the lesion segmentations by the expert. The automatically calculated centroid of the spleen is shown as a cross hair.

PET/CT Features

Table 2 shows the descriptive statistics of the baseline PET/CT features in 282 patients. Neither the sDspleen nor the SpreadSpleen was correlated with TMTV ($\rho = 0.14$ and 0.21, respectively) or IPI ($\rho = 0.12$ and 0.15, respectively). The correlation between sDspleen and SpreadSpleen was 0.68. All dissemination features were moderately correlated pairwise ($\rho = 0.60$–0.78). The correlogram between all PET/CT features is given in Supplemental Figure 2.

Univariate Survival Analysis

The median values of Dspleen, sDspleen, and SpreadSpleen shown in Table 2 were used as cutoff values for the Kaplan–Meier survival analysis. Each feature reflecting the tumor location relative to the spleen (Dspleen, sDspleen, and SpreadSpleen) classified the patients into 2 risk groups (high risk and low risk) significantly for both PFS and OS (log-rank test, $P < 0.001$; Supplemental Fig. 3). When the optimal cutoff values obtained by maximizing the Youden index of an AUC were used, all biomarkers were predictive of PFS and OS (log-rank test, $P < 0.05$). Of the 73 (26%) patients with PFS less than 4 y, 51 (70%) patients also had a Dspleen greater than the median value (32.43 cm), and 52 (71%) patients had a TMTV greater than the median value (242 cm^3). The Harrell concordance indices for PFS and OS were 0.66 and 0.66 for TMTV, 0.64 and 0.60 for Dmax, 0.62 and 0.60 for Dbulk, 0.65 and 0.63 for SpreadSpleen, 0.66 and 0.64 for Dspleen, 0.65 and 0.64 for sDspleen, 0.63 and 0.63 for tumor spread measured from the liver, 0.63 and 0.63 for the distance between the liver and the farthest lesion from the liver, 0.63 and 0.63 for the standardized distance from the liver, and 0.59 and 0.61 for IPI, respectively.

The time-dependent AUC and hazard ratios with 95% CI of the image-based biomarkers are shown in Table 3. The sDspleen feature scored the highest for predicting both OS and PFS in terms of hazard ratios. All PET features and the IPI were predictive of survival in patients with DLBCL, as indicated by their AUC (≥0.60), and their predictive values were all statistically significant ($P < 0.05$).

Multivariate Survival Analysis

Three risk categories can be significantly distinguished by combining the TMTV with the Dspleen or sDspleen (Fig. 4). Supplemental

TABLE 3
Univariate Analysis of the Predictive Value of PET/CT Features in Time-Dependent AUC and Hazard Ratios

	PFS		OS	
Clinical and PET/CT feature	AUC	HR	AUC	HR
Known features				
IPI	0.60 (0.54–0.66)	3.45 (1.09–8.66)	0.61 (0.53–0.69)	6.18 (1.47–17.44)
TMTV	0.67 (0.59–0.74)	12.03 (2.15–57.56)	0.67 (0.58–0.76)	18.16 (2.63–108.20)
Dmax	0.64 (0.58–0.70)	7.87 (2.04–18.87)	0.62 (0.53–0.70)	7.39 (1.43–18.38)
Dbulk	0.63 (0.55–0.69)	5.59 (1.56–14.15)	0.62 (0.53–0.70)	6.96 (1.25–18.24)
New features				
SpreadSpleen	0.64 (0.57–0.70)	5.85 (1.63–15.16)	0.63 (0.54–0.70)	9.87 (1.66–31.45)
Dspleen	0.66 (0.59–0.74)	17.49 (3.62–60.47)	0.64 (0.55–0.72)	18.18 (2.30–54.66)
sDspleen	0.66 (0.60–0.72)	53.28 (10.01–181.01)	0.65 (0.57–0.73)	32.51 (2.18–348.53)

HR = hazard ratio.
Data are mean with 95% CI.

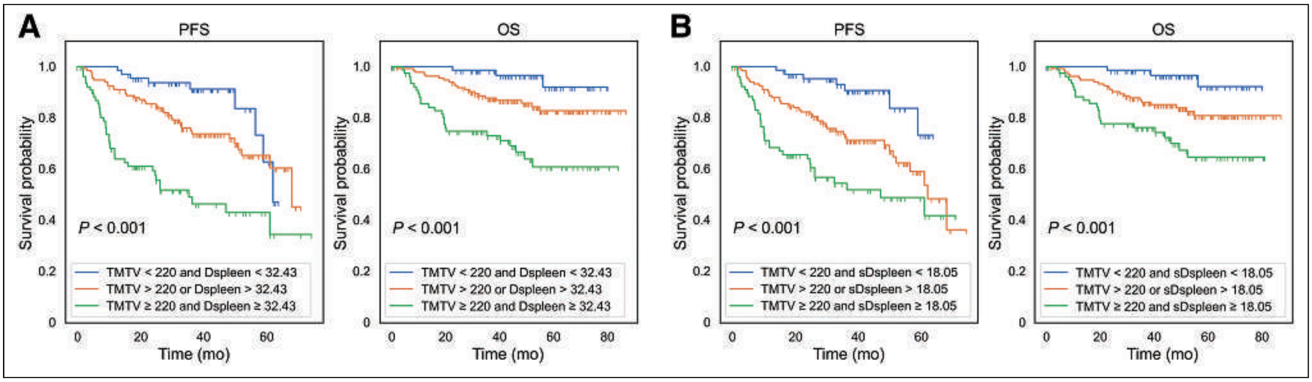

FIGURE 4. Three-risk category Kaplan–Meier curves of OS and PFS according to TMTV (cm^3) with Dspleen (A) and sDspleen (×100 m^{-1}) (B).

Figure 4 shows the features for SpreadSpleen, Dmax, and Dbulk. For simplicity, we used the median values as the cutoff values in the Kaplan–Meier analysis for these 3 features, whereas the optimal TMTV value of 220 cm^3 previously published was used (*9*). The sDspleen values were scaled by 100 for computational purposes.

Results from multivariate Cox regression analyses are shown in Table 4. We consider 3 baseline models to evaluate the added predictive value of the new PET/CT features with respect to the known biomarkers. The baseline models were based on TMTV, IPI, and TMTV combined with IPI. The added survival predictive values were evaluated using the concordance index. Only Dbulk had no significant change in the concordance index ($P > 0.05$) when combined with the TMTV for OS prediction. In all scenarios, regardless of the baseline model, the tumor location relative to the spleen (Dspleen, sDspeen, and SpreadSpleen) features significantly improved the predictive power of the IPI, TMTV, and TMTV combined with IPI ($P < 0.05$). The highest concordance indices were achieved when the spleen location-based features (SpreadSpleen, Dspleen, and sDspleen) were combined with TMTV and with the association of TMTV and IPI.

Supplemental Figure 3D demonstrates that lymphoma splenic invasion is also a poor-prognosis factor, with a log-rank test showing a *P* value of 0.03 for PFS and OS. In the subgroup of patients without splenic invasion ($n = 185$), the proposed spleen-based

TABLE 4
Predictive Value of PET/CT Features, Combined with Known Features (TMTV and IPI) as Baseline Cox Model

PET/CT features	PFS (C-index)	Increase in C-index	OS (C-index)	Increase in C-index
IPI (baseline)	0.58 (0.53–0.64)		0.61 (0.53–0.68)	
IPI + TMTV	0.65 (0.58–0.71)	0.07	0.67 (0.59–0.75)	0.07
IPI + Dmax	0.65 (0.59–0.70)	0.07	0.65 (0.56–0.72)	0.04
IPI + Dbulk	0.65 (0.59–0.69)	0.06	0.66 (0.57–0.73)	0.05
IPI + SpreadSpleen	0.67(0.59–0.72)	0.08	0.68 (0.59–0.76)	0.08
IPI + Dspleen	**0.68 (0.62–0.73)**	0.09	**0.69 (0.59–0.77)**	0.08
IPI + sDspleen	0.67 (0.61–0.73)	0.09	0.68(0.59–0.76)	0.08
TMTV (baseline)	0.66 (0.59–0.72)		0.67 (0.6–0.8)	
TMTV + Dmax	0.67 (0.58–0.72)	0.01	0.67 (0.58–0.74)	−0.01
TMTV + Dbulk	0.67 (0.59–0.72)	0.01	0.67 (0.59–0.75)	0.00
TMTV + SpleenSpread	0.69 (0.62–0.74)	0.03	0.70 (0.61–0.78)	0.03
TMTV + Dspleen	0.69 (0.62–0.74)	0.03	0.70 (0.63–0.77)	0.03
TMTV + sDspleen	**0.69 (0.62–0.75)**	0.03	**0.71 (0.64–0.78)**	0.04
TMTV + IPI (baseline)	0.65 (0.58–0.71)		0.67 (0.59–0.75)	
TMTV + IPI + Dmax	0.67 (0.60–0.72)	0.02	0.68 (0.61–0.75)	0.00
TMTV + IPI + Dbulk	0.67 (0.60–0.72)	0.02	0.68 (0.61–0.75)	0.01
TMTV + IPI + SpreadSpleen	0.69 (0.61–0.74)	0.04	0.71 (0.62–0.79)	0.03
TMTV + IPI + Dspleen	**0.69 (0.63–0.74)**	**0.04**	**0.71 (0.63–0.78)**	**0.03**
TMTV + IPI + sDspleen	0.69 (0.63–0.75)	0.04	0.71 (0.59–0.75)	0.04

C-index = concordance index.
Data are mean with 95% CI. Bold font indicates highest C-index.

biomarkers were prognosticators (Supplemental Fig. 5). The results in Supplemental Table 1 further confirm the improved added predictive values of the spleen-based features to the combined model of TMTV with IPI in patients without splenic invasion.

DISCUSSION

We developed and evaluated a new framework to extract novel PET/CT features that characterize how tumors spread and disseminate relative to the spleen in patients diagnosed with DLBCL and demonstrated the additional prognostic values of these features compared with known prognostic features. Lymphoma is a cluster of blood cancers that develop from lymphocytes and can spread to various body parts through the circulatory system. The spleen, an essential organ in blood filtration, plays a crucial role in removing old or damaged red blood cells, pathogens, and other foreign particles. The spleen also acts as a reservoir for the immune cells and platelets, which are critical for fighting infections and blood clotting.

The specific role of the spleen in the lymphatic system (*10*) was the primary motivation for considering the spleen as a reference organ to model disease spread and dissemination. We therefore investigated the possibility of simple and interpretable features that could characterize the location of the lesions relative to the spleen in patients with DLBCL. Lesion location–based features are often less sensitive to variations in imaging modalities or imaging devices and segmentation methods once the lesions are identified, which is an asset to transfer from academic research to routine clinical practice (*8*).

This study introduces 3 new features (SpreadSpleen, Dspleen, and sDspleen) extracted from baseline PET/CT images to quantify tumor locations relative to the spleen. Previous studies have proven that PET/CT-based features can be used for patient management on different DLBCL cohorts (*9*). To the best of our knowledge, no previous studies have been conducted to model the disease distribution and dissemination relative to a reference organ. Here, we used an open-access fully automated AI algorithm to segment the spleen from the CT images (*13*). The segmentation results were carefully assessed, and in 96% (282/295) of the patients, the spleen segmentation was acceptable. A correction was needed for only 4% (13/295) of the patients. Our new features are based on the centroid of the spleen, which makes them barely sensitive to the precise delineation of the spleen. We checked this lack of sensitivity to the exact delineation of the spleen by randomly shifting the spleen centroid by 2 cm and observed no substantial changes in prognostic values of the spleen-based biomarkers (results provided in the supplemental material). Experts performed lesion segmentations in our study. However, to fully automate the process, the pipeline could be integrated with existing AI-based automatic lesion segmentations from PET/CT images (*16–19*).

Univariate and multivariate Kaplan–Meier and Cox model analyses showed that SpreadSpleen, Dspleen, and sDspleen are strong predictors of PFS and OS. They can significantly classify patients with DLBCL into 2 risk groups (high risk and low risk) using the median values as cutoff values. Experimental results showed that Dspleen predicts PFS and OS like sDspleen. In cases of missed body surface area in clinical information, Dspleen could be used. SpreadSpleen, Dspleen, and sDspleen features can be calculated for any patient, including those with a single lesion. They consistently and significantly improved the predictive power of the IPI, TMTV, and IPI combined with TMTV. The improvements were more significant than those brought by other lesion dissemination–based features (Dmax and Dbulk). It demonstrates that the spleen-based features can complement TMTV and IPI to better characterize the disease at an early stage.

The proposed spleen-based features (SpreadSpleen, Dspleen, and sDspleen) are simple to calculate and intuitive to interpret. The spleen was chosen as the reference organ because of its role in the lymphatic system. Lymphoma splenic invasion is also a poor prognosis factor. In subgroups of patients without splenic invasion, the spleen-based features were prognosticators, suggesting that the spleen-based features code more than just a patient's splenic invasion. The bladder and liver were also tested as reference organs for evaluating tumor distribution and dissemination features. The predictive value from the bladder-based features was low for both PFS and OS (AUC < 0.60, data not shown). Although liver-based features were correlated with spleen-based features because of their relative anatomic proximity and were also predictive (data in the supplemental material), spleen-based features always had significantly higher predictive values ($P < 0.05$).

The main limitation of our study is the need for further evaluation of the proposed new features, ideally in multicenter cohorts, to confirm our findings. In addition, developing a machine-learning model that would best combine all PET/CT prognostic features to improve the prediction of PFS and OS warrants further investigation.

CONCLUSION

In this study, we introduced 3 predictive biomarkers extracted from baseline PET/CT images in patients with DLBCL. To our knowledge, this is the first study showing that characterizing tumor location relative to a reference organ predicts survival in a large series of DLBCL patients. We demonstrated that characterizing how the tumor spreads and disseminates relative to the spleen can improve survival prediction (PFS and OS) compared with the internationally accepted risk-score method, age-adjusted IPI, and PET/CT image-based biomarker, TMTV, for patients with DLBCL.

DISCLOSURE

The REMARC clinical studies and analyses were sponsored by the Lymphoma Academic Research Organization (LYSARC) of France. Kibrom Girum and Irène Buvat received a research grant given to the Institut Curie by ANR (ANR-19-SYME-0005-03). Louis Rebaud was employed by Siemens Medical Solutions. No other potential conflict of interest relevant to this article was reported.

KEY POINTS

QUESTION: Do baseline [^{18}F]FDG PET/CT features that characterize the tumor location relative to a reference organ predict survival in patients with DLBCL, and can they improve the predictive value of the TMTV and age-adjusted IPI?

PERTINENT FINDINGS: New baseline PET/CT features characterizing tumor spread and dissemination relative to the spleen predicted PFS and OS in DLBCL patients. The new biomarkers significantly enhanced the predictive value of TMTV and IPI for both PFS and OS.

IMPLICATIONS FOR PATIENT CARE: Tumor spread and dissemination features relative to the spleen calculated from baseline [^{18}F]FDG PET/CT are prognostic biomarkers in patients with DLBCL.

REFERENCES

1. Mikhaeel NG, Heymans MW, Eertink JJ, et al. Proposed new dynamic prognostic index for diffuse large B-cell lymphoma: international metabolic prognostic index. *J Clin Oncol.* 2022;40:2352–2360.
2. Vercellino L, Cottereau A, Casasnovas O, et al. High total metabolic tumor volume at baseline predicts survival independent of response to therapy. *Blood.* 2020;135:1396–1405.
3. Thieblemont C, Chartier L, Dührsen U, et al. A tumor volume and performance status model to predict outcome before treatment in diffuse large B-cell lymphoma. *Blood Adv.* 2022;6:5995–6004.
4. Eertink JJ, Zwezerijnen GJ, Heymans M, et al. Baseline PET radiomics outperform the IPI risk score for prediction of outcome in diffuse large B-cell lymphoma. *Blood.* 2023;141:3055–3064.
5. Ceriani L, Zucca E. D_{max}: a simple and reliable PET/CT-derived new biomarker of lymphoma outcome? *Hematol Oncol.* 2022;40:843–845.
6. Cottereau A-S, Nioche C, Dirand A, et al. ^{18}F-FDG PET dissemination features in diffuse large B-cell lymphoma are predictive of outcome. *J Nucl Med.* 2020;61:40–45.
7. Eertink JJ, van de Brug T, Wiegers SE, et al. ^{18}F-FDG PET baseline radiomics features improve the prediction of treatment outcome in diffuse large B-cell lymphoma. *Eur J Nucl Med Mol Imaging.* 2022;49:932–942.
8. Albano D, Treglia G, Dondi F, et al. ^{18}F-FDG PET/CT maximum tumor dissemination (Dmax) in lymphoma: a new prognostic factor? *Cancers (Basel).* 2023;15:2494.
9. Cottereau A-S, Meignan M, Nioche C, et al. Risk stratification in diffuse large B-cell lymphoma using lesion dissemination and metabolic tumor burden calculated from baseline PET/CT. *Ann Oncol.* 2021;32:404–411.
10. Mebius RE, Kraal G. Structure and function of the spleen. *Nat Rev Immunol.* 2005;5:606–616.
11. Thieblemont C, Tilly H, Gomes da Silva M, et al. Lenalidomide maintenance compared with placebo in responding elderly patients with diffuse large B-cell lymphoma treated with first-line rituximab plus cyclophosphamide, doxorubicin, vincristine, and prednisone. *J Clin Oncol.* 2017;35:2473–2481.
12. Cheson BD, Pfistner B, Juweid ME, et al. Revised response criteria for malignant lymphoma. *J Clin Oncol.* 2007;25:579–586.
13. Wasserthal J, Breit H-C, Meyer MT, et al. TotalSegmentator: robust segmentation of 104 anatomic structures in CT images. *Radiol Artif Intell.* 2023;5:e230024.
14. Nioche C, Orlhac F, Boughdad S, et al. LIFEx: a freeware for radiomic feature calculation in multimodality imaging to accelerate advances in the characterization of tumor heterogeneity. *Cancer Res.* 2018;78:4786–4789.
15. Mosteller RD. Simplified calculation of body-surface area. *N Engl J Med.* 1987;317:1098.
16. Blanc-Durand P, Jégou S, Kanoun S, et al. Fully automatic segmentation of diffuse large B cell lymphoma lesions on 3D FDG-PET/CT for total metabolic tumour volume prediction using a convolutional neural network. *Eur J Nucl Med Mol Imaging.* 2021;48:1362–1370.
17. Sibille L, Seifert R, Avramovic N, et al. ^{18}F-FDG PET/CT uptake classification in lymphoma and lung cancer by using deep convolutional neural networks. *Radiology.* 2020;294:445–452.
18. Girum KB, Rebaud L, Cottereau A-S, et al. ^{18}F-FDG PET maximum-intensity projections and artificial intelligence: a win-win combination to easily measure prognostic biomarkers in DLBCL patients. *J Nucl Med.* 2022;63:1925–1932.
19. Jemaa S, Fredrickson J, Carano RAD, Nielsen T, de Crespigny A, Bengtsson T. Tumor segmentation and feature extraction from whole-body FDG-PET/CT using cascaded 2D and 3D convolutional neural networks. *J Digit Imaging.* 2020;33:888–894.

Dynamic Human Brain Imaging with a Portable PET Camera: Comparison to a Standard Scanner

Elizabeth A. Bartlett[1,2], Mohammad Lesanpezeshki[1], Sergey Anishchenko[3], Ilia Shkolnik[3], R. Todd Ogden[1,2,4], J. John Mann[1,2,5], David Beylin[3], Jeffrey M. Miller[1,2], and Francesca Zanderigo[1,2]

[1]Molecular Imaging and Neuropathology Area, New York State Psychiatric Institute, New York, New York; [2]Department of Psychiatry, Columbia University Medical Center, New York, New York; [3]Brain Biosciences, Inc., Rockville, Maryland; [4]Department of Biostatistics, Mailman School of Public Health, Columbia University, New York, New York; and [5]Department of Radiology, Columbia University Medical Center, New York, New York

Portable, cost-effective PET cameras can radically expand the applicability of PET. We present here a within-participant comparison of fully quantified [^{18}F]FDG dynamic scans in healthy volunteers using the standard Biograph mCT scanner and portable CerePET scanner. **Methods:** Each of 20 healthy volunteers underwent dynamic [^{18}F]FDG imaging with both scanners (1–154 d apart) and concurrent arterial blood sampling. Tracer SUV, net influx rate (K_i), and the corresponding cerebral metabolic rate of glucose (CMR_{glu}) were quantified at regional and voxel levels. **Results:** At the regional level, CerePET outcome measure estimates within participants robustly correlated with Biograph mCT estimates in the neocortex, wherein the average Pearson correlation coefficients across participants ± SD were 0.83 ± 0.07 (SUV) and 0.85 ± 0.08 (K_i and CMR_{glu}). There was also strong agreement between CerePET and Biograph mCT estimates, wherein the average regression slopes across participants were 0.84 ± 0.17 (SUV), 0.83 ± 0.17 (K_i), and 0.85 ± 0.18 (CMR_{glu}). There was similar bias across participants but higher correlation and less variability in subcortical regions than in cortical regions. Pearson correlation coefficients for subcortical regions equaled 0.97 ± 0.02 (SUV) and 0.97 ± 0.03 (K_i and CMR_{glu}), and average regression slopes equaled 0.79 ± 0.14 (SUV), 0.83 ± 0.11 (K_i), and 0.86 ± 0.11 (CMR_{glu}). In voxelwise assessment, CerePET and Biograph mCT estimates across outcome measures were significantly different only in a cluster of left frontal white matter. **Conclusion:** Our results indicate robust correlation and agreement between semi- and fully quantitative brain glucose metabolism measurements from portable CerePET and standard Biograph mCT scanners. The results obtained with a portable PET scanner in this comparison in humans require follow-up but lend confidence to the feasibility of more flexible and portable brain imaging with PET.

Key Words: portable PET; metabolic rate of glucose; net influx rate; SUV; human

J Nucl Med 2024; 65:320–326
DOI: 10.2967/jnumed.122.265309

PET imaging allows in vivo quantification of brain metabolism and levels of neurotransmitter system components. There are barriers to entry to PET that hinder its use in research and clinics, including the scanner size, cost for siting and maintenance, complexity of current scanners and acquisition protocols, radiotracer cost and availability, and radiation shielding considerations. To overcome some of these obstacles, cost-effective, portable scanners have been developed (*1–6*).

Brain-dedicated PET scanners were designed with detector geometry to enhance sensitivity and resolution (*7–12*). Modern portable scanners have leveraged these improvements to provide high-resolution, cost-effective devices with the potential to transform the PET field by offering options beyond traditional supine scanning, including seated or standing configurations. This allows imaging while participants are engaged more naturalistically in tasks or interacting with their environment. Furthermore, these scanners have the potential to image proximal to real-world events (e.g., brain injury at sports venues, in intensive care units, outpatient drug abuse treatment centers, rural areas, and in vulnerable populations, such as homebound and incarcerated individuals). However, validation of portable scanners is required to support widespread use.

NeuroPET/CT (Photo Diagnostic Systems, Inc.), a brain-dedicated scanner with wheels supporting portability within a center or hospital, has recently shown good correspondence of SUVs of [^{18}F]FDG, a ubiquitously used glucose analog, relative to the standard ECAT HR+ scanner (Siemens) (*8*). To our knowledge, dynamic acquisition with full quantification of tracer uptake/binding (for [^{18}F]FDG, this yields estimates of tracer net influx rate (K_i) into brain tissue and corresponding cerebral metabolic rate of glucose (CMR_{glu}) (*13*,*14*)) has yet to be analyzed in the human brain across portable and standard scanners. Here, we compare outcomes from the portable CerePET scanner (Brain Biosciences, Inc.) and the standard Biograph mCT scanner (Siemens).

CerePET is a high-resolution, brain-dedicated PET scanner that weighs approximately 22.7 kg (50 pounds), plugs into a standard power outlet, and requires only a laptop computer as the console. Figure 1 shows its setup in this study, with a fixed patient table, and Table 1 describes its performance characteristics. The PET detector consists of 15,210 crystals of 2 × 2 × 13 mm cerium-doped lutetium yttrium orthosilicate arranged in a full ring with a 22-cm field-of-view (FOV) diameter and an 8.6-cm axial FOV (*2–4*). The detector can continuously translate along the z-axis during acquisition to cover an axial FOV up to 22.5 cm, allowing full brain coverage (*2–4*), which is how it was used in this study. CerePET can function as a stand-alone device with integrated attenuation correction using a model-based approach (model-AC) or can import an external CT for AC (CT-AC).

As part of a larger project (National Institute of Biomedical Imaging and Bioengineering R01EB026481) whose primary aim is to develop noninvasive brain glucose metabolism estimation

---

Received Dec. 12, 2022; revision accepted Oct. 19, 2023.

For correspondence or reprints, contact Elizabeth A. Bartlett (elizabeth.bartlett@nyspi.columbia.edu).

FIGURE 1. CerePET shown in research setup used in this study.

approaches with both standard and portable PET scanners (*15*), we performed dynamic acquisitions with CerePET, with accompanying Biograph mCT [^{18}F]FDG scans in 20 healthy volunteers. Concurrent arterial blood sampling during both scans allowed us to examine within-participant relationships between fully quantified K_i and CMR_{glu} regionally and voxelwise across scanners. Exploratory analyses tested for sources of biologic variance between acquisitions (e.g., scan-day heart rate).

MATERIALS AND METHODS

Participants

Healthy volunteers ($n = 20$, 18–60 y old, with absence of major psychiatric illness) provided written informed consent (inclusion and exclusion in supplemental materials [supplemental materials are available at http://jnm.snmjournals.org]). The New York State Psychiatric Institute Institutional Review Board and the Joint Radiation Safety Committee at Columbia University Irving Medical Center approved this study.

MRI Acquisition and Processing

Each participant received a 3-T T1-weighted, magnetization-prepared rapid gradient-echo MRI (details in supplemental materials), and the MRI was processed through FreeSurfer version 7.1.1 (Laboratory for Computational Neuroimaging, Athinoula A. Martinos Center for Biomedical Imaging; http://surfer.nmr.mgh.harvard.edu/).

PET Acquisition and Reconstruction

All participants were imaged at rest with both scanners on separate days (12 participants had a CerePET scan first) and agreed to a prescan 6-h fast. At each scan, 1 intravenous catheter sampled the nonradioactively tagged blood glucose concentration (cold glucose) before the scans. Contralaterally, an arterial catheter measured the total radioactivity of [^{18}F]FDG in arterial whole blood and plasma throughout the scans. [^{18}F]FDG was injected as an intravenous bolus over 30 s ($\leq$185 MBq), and dynamic PET data were acquired for 60 min. Participants were instructed to keep their eyes closed and head as still as possible and to rest.

CerePET. The Brain Biosciences team brought the CerePET scanner to the Columbia University PET center for 7 multiday sessions between October 2018 and June 2021. The day before each session, CerePET was set up in a shielded room, adjacent to the Biograph mCT room. CerePET quality assurance was performed before each session with a rotating ^{68}Ge line source (PET-220/0.5; Sanders Medical Products) for energy and timing calibration and for verification of crystal map stability, as per the established protocol at Brain Biosciences.

For further calibration, the uniform section of an American College of Radiology accreditation phantom was filled with 18.13 MBq (0.49 mCi) of ^{18}F, corresponding to a 221.63-MBq (5.99-mCi) injection in a 70-kg patient, and imaged a single time for 20 min with both scanners during the first session of CerePET acquisitions. Biograph mCT phantom scans were reconstructed with time-of-flight ordered-subset expectation maximization with 4 iterations and 21 subsets, as is standard for phantoms at the Columbia University PET center. CerePET phantom scans were reconstructed in the same way as CerePET human scans (as described later), both with CT-AC. A calibration factor was then derived for CerePET scans and applied across all human scans in the study.

Human CerePET scans used stand-alone model-AC and CT-AC with the coregistered CT data acquired at the beginning of each participant's Biograph mCT scan in Brain Biosciences' Galatea software.

TABLE 1
CerePET and Biograph mCT Performance Characteristics

Characteristic	CerePET	Biograph mCT (*31*)
Crystal material	Cerium-doped lutetium yttrium orthosilicate	Lutetium oxyorthosilicate
Crystal pixel size	2 × 2 × 13 mm	4 × 4 × 20 mm
Detectors	Photomultiplier tube	Photomultiplier tube
Axial FOV	8.6 cm (stationary), 22.5 cm (translating)	22.1 cm
Transaxial FOV	22 cm	70 cm
Detector ring diameter	26 cm	84.2 cm
Time coincidence window	4 ns	4.1 ns
System time resolution	1 ns	540 ps
Energy window	430–650 keV	435–650 keV
Axial resolution		
At 1 cm	Up to 2 mm	4.4 mm
At 10 cm	Up to 2 mm	5.7 mm
Transverse resolution		
At 1 cm	Up to 2.1 mm	4.4 mm
At 10 cm	Up to 3.1 mm	4.9 mm

Model-based attenuation maps were created by segmenting CerePET images with background having zero coefficient and head and neck having the same coefficient as water. Calculated headrest attenuation was added to model-AC and CT-AC. Reconstruction was performed with 25 iterations of maximum-likelihood expectation maximization (MLEM), as established by Brain Biosciences (*2–4*), on a 200 × 200 × 192 grid (1.2 × 1.2 × 1.2 mm voxels) with 3 × 3 × 3 voxel gaussian filtering. The binning scheme for CerePET was 10 × 30 s, 5 × 1 min, 4 × 5 min, and 3 × 10 min. Because CerePET detectors move instead of the patient table, 30 s is the minimum frame duration for the CerePET detectors to cover 22.5 cm.

Biograph mCT. In our group's standard Biograph mCT acquisition protocol, motion was minimized with an individual polyurethane head mold (Soule Medical); this served as a gold standard to be compared with CerePET scans, which were acquired without motion minimization as they would be in real-world applications. A low-dose CT scan was acquired, and reconstruction was performed with CT-AC using the same binning scheme and MLEM parameters as those of CerePET (as described earlier). For comparison, Biograph mCT scans were also reconstructed with the standard parameters of our group: a 256 × 256 matrix, filtered backprojection, a 2.5-mm Shepp reconstruction filter, and a binning scheme of 9 × 15 s, 5 × 30 s, 1 × 45 s, 4 × 1 min, 1 × 3 min, 4 × 5 min, 1 × 7.5 min, and 2 × 10 min. Unless otherwise noted, comparisons used Biograph mCT and CerePET with CT-AC, MLEM, and the same binning scheme.

Preprocessing and Quantification

As validated (*16*), for motion correction, PET frames were registered to the eighth frame using FMRIB's Linear Image Registration Tool (FMRIB Image Analysis Group) and coregistered to the MRI. Bilateral average time–activity curves were extracted from the FreeSurfer Desikan–Killiany and subcortical atlases (*17,18*) and analyzed separately, given the differing spatial locations and functions of the regions.

SUVs were calculated as the frame duration–weighted average of all PET frames, multiplied by body weight, and divided by injected dose. Weighting by frame duration ensures SUVs are not skewed toward the many, short frames driven by perfusion at the beginning of the scan.

To generate an arterial input function, tracer total radioactivity in arterial plasma was fit with a sum of 3 decreasing exponentials via nonlinear least squares, with interpolation until the plasma peak. The same was repeated with whole-blood measurements for vascular correction, assuming a blood volume fraction of 5%. The arterial input function served as the input to the Patlak approach (*19*). For voxelwise analyses, each participant's MRI was normalized to Montreal Neurologic Institute space using Advanced Normalization Tools (*20*). The corresponding warps were applied to MRI-coregistered SUV, K_i, and CMR_{glu} maps, and the resultant images were smoothed with a 6-mm gaussian kernel for group-level analysis.

Statistics

Pearson correlation coefficient (*r*), percent difference (PD = [CerePET − Biograph mCT]/average [CerePET, Biograph mCT] × 100), and linear regression assessed within-participant CerePET-to-Biograph mCT correspondence (across regions) and within-region correspondence (across participants). To assess motion with and without an individualized head holder in Biograph mCT and CerePET scans, respectively, total motion in each frame was calculated as the root of sum of squares across the 6 motion correction affine transform parameters (*21*). This framewise measure was summed across all PET frames to produce a metric of total motion per scan (*21*) and compared between scanners with 2-tailed paired *t* tests. Linear mixed-effects models tested for scanner differences in SUV, K_i, and CMR_{glu} (1 model per outcome measure), with scanner and region as fixed effects, participant and scan nested within participant as random effects (allowing for participant-level random variation), and log-transformed PET outcomes (to satisfy normality assumptions) from 8 brain regions, representing [^{18}F]FDG's widespread uptake, as the model outcome (putamen, hippocampus, and amygdala, and caudal anterior cingulate, lateral occipital, middle temporal, rostral middle frontal, and superior parietal cortices).

Statistical parametric mapping (SPM12; Functional Imaging Laboratory, Queen Square Institute of Neurology, University College London) was used for voxelwise analyses with a familywise error rate of 0.05 and clusterwise multiple-comparisons correction with 3DClustSim in Analysis of Functional NeuroImages (National Institute of Mental Health Scientific and Statistical Computing Core; $P < 0.05$; cluster-forming threshold, $P < 0.001$) (*22,23*).

Exploratory analyses testing for biologic variance between scans are detailed in supplemental materials and Supplemental Figure 2.

RESULTS

Participant and scanning characteristics are detailed in Supplemental Table 1. We validated use of a glucometer instead of a blood-based laboratory assay for cold glucose measurement (required for CMR_{glu}; Supplemental Fig. 1). Although the difference between cold glucose measurements was small, it did reach statistical significance ($F_{1,38} = 5.09$, $P = 0.03$). Because portability and simplification were goals, given the degree of correlation between measures, glucometer measurements were used for all analyses. Intraparticipant cold glucose PD between CerePET and Biograph mCT scans was 2.88% ± 8.04%, with CerePET cold glucose equal to 90.8 ± 6.91 mg/dL and Biograph mCT cold glucose equal to 88.20 ± 6.38 mg/dL. Intraparticipant PDs in input functions, calculated as the area under the curve after converting radioactivity counts to SUV, between CerePET and Biograph mCT scans were −0.96% ± 14.51% (minimum, −26.74%; maximum, 24.79%). In the comparison of Biograph mCT scans with and CerePET scans without a custom head holder, CerePET scans had greater total motion than Biograph mCT scans (57.28 ± 31.43 and 44.44 ± 35.47 mm, respectively), but the difference was not statistically significant ($P = 0.18$).

Regionwise Analyses by Participant

CerePET cortical SUV, K_i, and CMR_{glu} estimates robustly correlated with Biograph mCT estimates: average *r* values within participant, across regions, were 0.83 (SUV) and 0.85 (K_i and CMR_{glu}). CerePET-to-Biograph mCT correlation for subcortical regions within participant was higher such that the average *r* values within a participant, across regions, for SUV, K_i, and CMR_{glu} were all 0.97, with coefficients of variation of 2.39% (SUV) and 3.04% (K_i and CMR_{glu}) (Fig. 2; Table 2).

CerePET SUV, K_i, and CMR_{glu} estimates were, on average, slightly underestimated relative to Biograph mCT for PDs across all regions and participants (SUV, −0.48 ± 16.20; K_i, −3.54% ± 16.42%; CMR_{glu}, −0.69% ± 16.05%). Average regression slopes between CerePET and Biograph mCT estimates across participants were similar for cortical and subcortical regions (range, 0.79–0.86; Table 2). However, cortical regions had higher coefficients of variation across individual participants' regression slopes than did subcortical regions (Table 2). Proportional bias was observed across outcomes, except cortical SUVs (Fig. 3, top). This effect was more dramatic for K_i and CMR_{glu} than for SUV partly because 1 participant had high K_i and CMR_{glu} Biograph mCT estimates (well above those of all other participants) that were not observed in the corresponding CerePET scan (Fig. 3, bottom). Evidence for

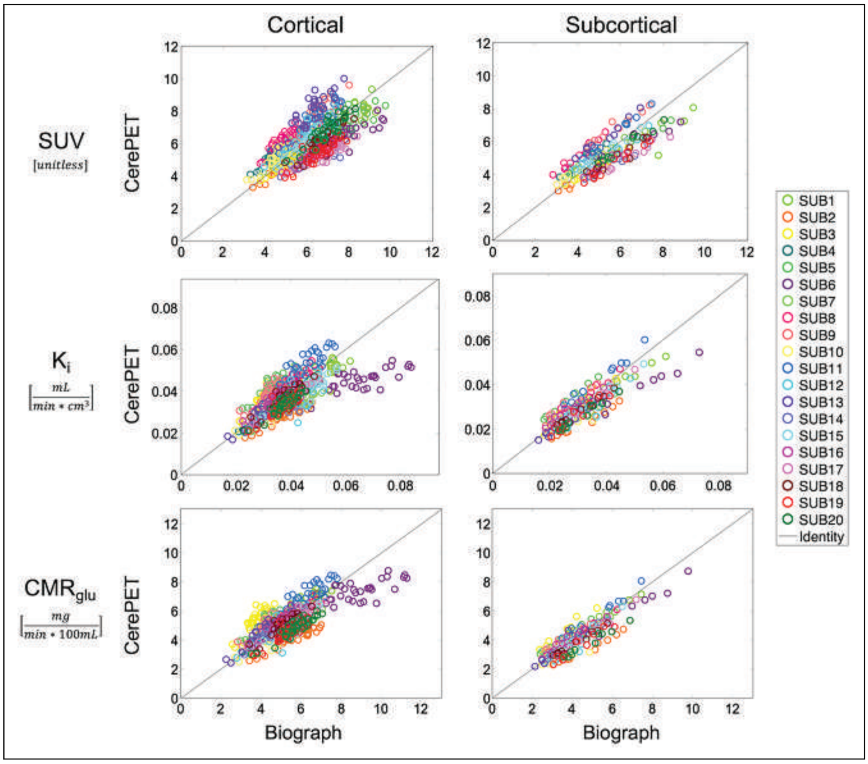

FIGURE 2. Regionwise estimates of SUV, K_i, and CMR_{glu} plotted for CerePET vs. Biograph mCT. All brain regions from FreeSurfer Desikan–Killiany and subcortical atlases are shown (listed in supplemental materials). SUB = subject.

proportional bias was diminished when this participant was excluded (Fig. 3, bottom).

CerePET's stand-alone model-AC yielded absolute PDs (to account for expected over- and underestimations across regions with model-AC) of 5.86% ± 14.45% (SUV) and 5.09% ± 22.83% (K_i and CMR_{glu}) from CT-AC, demonstrating feasibility for portable CerePET imaging without separate CT acquisition. Estimates from Biograph mCT data reconstructed with filtered backprojection were comparable to MLEM: the average PD across participants and regions was 0.21% ± 2.53% (SUV) and −0.81% ± 3.11% (K_i and CMR_{glu}), lending confidence to the choice of MLEM reconstruction parameters for quantitative accuracy. Correspondence of CerePET and Biograph mCT was generally better, with lower variability, using matching reconstruction and AC (SUV, −0.48 ± 16.20; K_i, −3.54% ± 16.42%; CMR_{glu}, −0.69% ± 16.05%), as reported in the prior paragraph, than when MLEM model-AC was used for CerePET and filtered backprojection CT-AC for Biograph mCT (SUV, 5.09 ± 22.83; K_i, 3.59% ± 19.08%; CMR_{glu}, 6.44% ± 19.63%). CerePET versus Biograph mCT correspondence was similar whether SUVs were calculated as the frame duration–weighted average across all frames (average correlation coefficient, 0.83 ± 0.07; average regression slopes, 0.84 ± 0.17; Table 2) or as the raw average across the last 3 frames (30–60 min into scanning; $r = 0.84 \pm 0.07$; average regression slopes, 0.84 ± 0.18).

Regionwise Analyses by Region

Within region, across participants, CerePET performed similarly across subcortical and cortical regions, with slightly better agreement subcortically for K_i and CMR_{glu} than cortically (Table 3). Average PD maps for Desikan–Killiany regions are shown in Supplemental Figure 3. Visually, there was an anterior-to-posterior gradient of differences that was more dramatic in white matter than in gray matter, with CerePET tending to underestimate outcome measures anteriorly and overestimate outcome measures posteriorly.

Collectively, across a priori regions, SUV, K_i, and CMR_{glu} estimates from CerePET did not differ significantly from Biograph mCT estimates. However, there was a region-by-scanner interaction for all 3 outcomes ($P < 0.001$). In post hoc analyses, lateral occipital cortex SUVs were higher with CerePET than with Biograph mCT ($P = 0.030$). Rostral middle frontal cortex and putamen K_i and CMR_{glu} estimates were higher with Biograph mCT than with CerePET (K_i, $P = 0.013$ and 0.028; CMR_{glu}, $P = 0.017$ and 0.038, respectively); none of these post hoc findings survived Bonferroni adjustment for 8 regions.

Voxelwise Analyses

Representative individual and averaged CerePET and Biograph mCT outcome measures, PDs, and statistical maps are shown in Figure 3. Voxelwise analyses paralleled regionwise analyses, with good agreement between scanners. All 3 outcomes showed larger

TABLE 2
Within-Participant, Across-Region Comparison of CerePET and Biograph mCT

		r			Regression slope		
Atlas	Data type	SUV	K_i	CMR_{glu}	SUV	K_i	CMR_{glu}
DK	Mean ± SD	0.83 ± 0.07	0.85 ± 0.08	0.85 ± 0.08	0.84 ± 0.17	0.83 ± 0.17	0.85 ± 0.18
	COV	8.74%	9.15%	9.15%	20.70%	20.62%	21.62%
Subcortical	Mean ± SD	0.97 ± 0.02	0.97 ± 0.03	0.97 ± 0.03	0.79 ± 0.14	0.83 ± 0.11	0.86 ± 0.11
	COV	2.39%	3.04%	3.04%	17.27%	13.02%	12.32%

DK = Desikan–Killiany; COV = coefficient of variation.

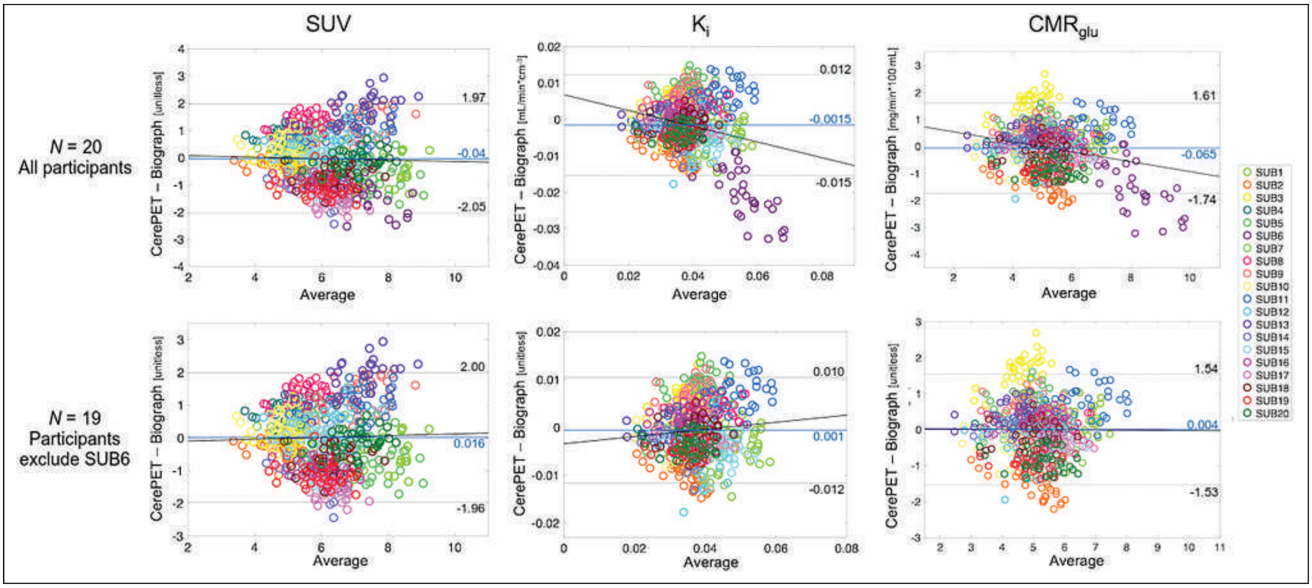

FIGURE 3. Bland–Altman plots for SUV, K_i, and CMR_{glu} for all participants (top) and excluding 1 participant with high Biograph mCT K_i and CMR_{glu} values (bottom). Not considering this 1 participant yields diminished proportional bias. Means are shown as blue lines, 95% limits of agreement are shown as thin black lines, and regression lines are shown as thick black lines. SUB = subject.

average PDs in white matter than in gray matter. Statistical parametric mapping revealed a cluster of higher uptake in left anterior white matter with Biograph mCT than with CerePET that survived multiple-comparisons correction (644, 653, and 583 voxels for SUV, K_i, and CMR_{glu}, respectively; Fig. 4; Supplemental Fig. 4).

DISCUSSION

This is a quantitative description of [^{18}F]FDG dynamic imaging of the human brain by portable CerePET, comparing its performance with that of Biograph mCT. We found good correlation and agreement of SUV, K_i, and CMR_{glu} estimates by CerePET relative to Biograph mCT within-participant. Subcortical regionwise CerePET estimates were more closely correlated within-participant with Biograph mCT estimates compared with cortical estimates. The only significant difference between scanners in voxelwise analysis was in a cluster in the left frontal white matter. Some variability in portable scanner performance might have been expected given CerePET's small, lightweight, and cost-effective design, as well as potential effects from acquisitions on the 2 scanners on different days. However, the absence of statistically significant differences in fully quantified dynamic outcomes in cortical and subcortical areas between the 2 scanners indicates the capacity of the CerePET scanner for implementation in imaging human subjects. The CerePET has potential for future applications not just in portable PET imaging (e.g., combat zones, sports fields, and intensive care units) but also in scenarios with limited space or budget (e.g., outpatient treatment centers, rural medical centers, and penitentiaries) and for research uses (e.g., seated or standing PET during more naturalistic experimental tasks).

To our knowledge, NeuroPET/CT is the only other PET scanner designed for mobility that has been validated in humans (*8*). Although CerePET does not have the integrated CT capability of NeuroPET/CT (*24*), we found that CerePET's stand-alone model-AC generated [^{18}F]FDG outcomes within about 5% of CT-AC. The high level of agreement between CT-AC and model-AC was surprising; given that a single value was used for nonbackground in model-AC, larger biases were expected. This expands the range of CerePET applicability, because obtaining a separate CT scan would not be possible in many applications that might take advantage of CerePET's portability.

TABLE 3
Within-Region, Across-Participant Comparison of CerePET and Biograph mCT

Atlas	Data type	*r*			Regression slope		
		SUV	K_i	CMR_{glu}	SUV	K_i	CMR_{glu}
DK	Mean ± SD	0.55 ± 0.07	0.58 ± 0.07	0.66 ± 0.08	0.54 ± 0.07	0.50 ± 0.10	0.55 ± 0.09
	COV	12.62%	11.45%	11.54%	13.31%	21.18%	16.29%
Subcortical	Mean ± SD	0.55 ± 0.08	0.71 ± 0.07	0.74 ± 0.07	0.52 ± 0.09	0.68 ± 0.13	0.75 ± 0.11
	COV	14.87%	9.22%	8.77%	16.74%	19.33%	14.39%

DK = Desikan–Killiany; COV = coefficient of variation.

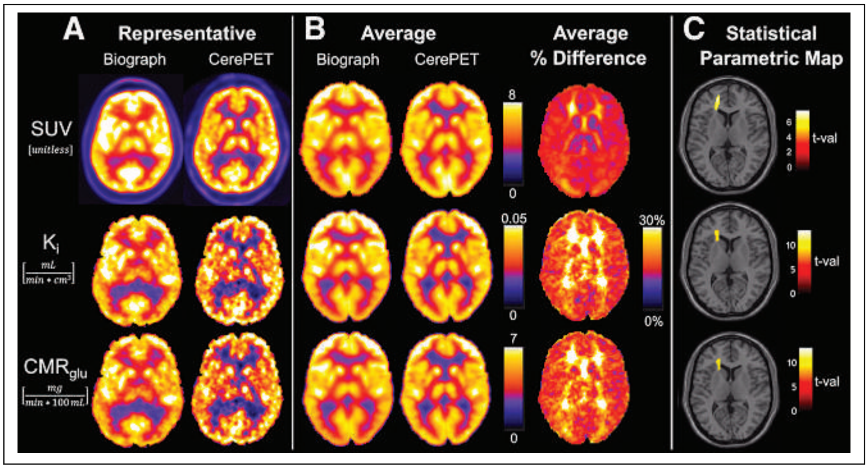

FIGURE 4. Voxelwise maps for CerePET and Biograph mCT for SUV, K$_i$, and CMR$_{glu}$. (A) Representative participant in participant MRI space. (B) Average maps across 20 healthy volunteers in Montreal Neurologic Institute space (left), and average absolute PD maps across 20 healthy volunteers (right). Color maps apply within outcome measures in A and B. (C) Statistical parametric mapping multiple-comparisons–corrected *t*-value maps showing single significant cluster with familywise error rate of $P = 0.05$ and cluster-size thresholds of 546 (SUV), 408 (K$_i$), and 410 voxels (CMR$_{glu}$). t-val = *t* value.

Whereas we found average slopes of 0.84 for SUV and 0.83 for K$_i$ and CMR$_{glu}$ across participants when comparing CerePET to Biograph mCT, NeuroPET/CT generated SUV estimates with a slope of 1.07 when compared with the ECAT Exact HR+ (Siemens) (*8*). NeuroPET/CT and CerePET had similar participant-wise variability in performance, with regression slope SD across participants of 0.18 for NeuroPET/CT (*8*) and 0.17, 0.17, and 0.19 for SUV, K$_i$, and CMR$_{glu}$, respectively, for CerePET. Some variability in scanner performance across participants was expected given uncertainties in, for example, tracer biodistribution and preprocessing steps (*8*).

The observed slight underestimation with CerePET but relatively small between-participant variability could result from differences in spatial resolution, sensitivity, noise equivalent counting rate, scatter fraction, dead-time correction, uniformity, the interval of about 1 wk between scans, or contrast recovery. Formal follow-up analyses are planned, including National Electrical Manufacturers Association measurements, which will be published on completion. Other factors, such as detector geometry and spatial resolution drop-off from the center of the FOV, may also contribute. Furthermore, the required movement of the CerePET detector for whole-brain coverage means that the signal in each voxel is detected for only part of the time, unlike the Biograph mCT scanner. This could contribute to the observed underestimation and will be investigated.

[^{18}F]FDG test–retest (TRT) repeatability could play a role in the participantwise variability in CerePET performance. [^{18}F]FDG TRT studies in humans, mostly published more than 20 y ago using data from scanners with a spatial resolution greater than 8 mm, reveal a surprising degree of CMR$_{glu}$ variability. Average TRT PDs ranged from 7% (same day) (*25*) to 7.9% (1–12 wk apart) (*26*) and 24.5% (1–6 wk apart) (*27*), and same-day and 1-wk-apart scans had correlation coefficients of 0.61–0.89 across regions (*25,28*). To our knowledge, 2 studies have been performed in the last 20 y that report TRT correlations of 0.17–0.93 (6 mo apart) (*29*) and average PD of 8.75% (17 ± 44 d apart) (*30*) across regions. Despite the widespread use of SUV in oncology, we did not come across TRT studies reporting SUV in normal brain tissue. Altogether, inherent biologic and instrumental variance of [^{18}F]FDG measurements from the scanners on different days may have contributed to the participant-level variance of CerePET versus Biograph mCT correspondence.

In exploratory analyses investigating biologic sources of variance between acquisitions, we found positive correlations between K$_i$ and CMR$_{glu}$ values and injected dose for CerePET but not for Biograph mCT (supplemental materials; Supplemental Fig. 2). Optimization of CerePET's dead-time correction may ameliorate this injected dose effect.

This study had some limitations. There was a large range in the number of days between within-participant PET scans and in the variability in the scan time of day. Although these factors are not significantly related to scanner differences, they could induce variability. In addition, no standard [^{18}F]FDG TRT studies with CerePET or Biograph mCT scanners have been published to assess variability within repeated scans using the same scanner. The phantom for calibration was scanned once on each scanner at the start of the study to derive a studywide calibration factor, so the long-term stability of the CerePET-to-Biograph mCT phantom calibration is not known and the results cannot account for changes in dead-time correction at each imaging session. It takes 30 s for the moving detector rings to cover the 22.5-cm axial FOV. This means that activity from different brain regions is detected at different times throughout each frame, which might influence results. Future work can explore voxelwise quantification with custom mid-time vectors to reflect the exact location of the detector rings, an approach that may potentially enhance CerePET performance. This work sought to match reconstruction, preprocessing, and quantification approaches across CerePET and Biograph mCT. Future work can further optimize these and other factors for CerePET if closer correspondence is desired. A National Electrical Manufacturers Association study is required for CerePET and is planned.

CONCLUSION

This study characterizes the portable CerePET scanner with semi- and full quantification of human [^{18}F]FDG scans and includes within-participant comparisons to Biograph mCT. Outcome measures were well correlated and highly agreed across scanners, with expected levels of between-participant variability in the relationship between CerePET and Biograph mCT estimates. Future work will focus on more detailed scanner performance characterization, followed by application of CerePET to novel PET scanning scenarios.

DISCLOSURE

The National Institute of Biomedical Imaging and Bioengineering funded this study (R01EB026481; principle investigator, Francesca Zanderigo). J. John Mann receives royalties from the Research Foundation for Mental Hygiene for the commercial use of the Columbia Suicide Severity Rating Scale. Ilia Shkolnik (senior software developer), Sergey Anishchenko (computational scientist), and David Beylin (chief executive officer) have financial interests as employees and shareholders at Brain Biosciences. No other potential conflict of interest relevant to this article was reported.

KEY POINTS

QUESTION: How do outcome measures from dynamic [^{18}F]FDG human brain scans obtained with a portable PET scanner compare with those from a standard scanner?

PERTINENT FINDINGS: In 20 healthy volunteers, [^{18}F]FDG outcome measures were well correlated and highly agreed across scanners, with expected levels of interparticipant variability.

IMPLICATIONS FOR PATIENT CARE: We demonstrate feasibility of portable PET imaging scanning in humans, with follow-up required for further performance characterization.

REFERENCES

1. Zeng T, Zheng J, Xia X, et al. Design and system evaluation of a dual-panel portable PET (DP-PET). *EJNMMI Phys.* 2021;8:47.
2. Spriet M, Edwards L, Arndt S, et al. Validation of a dedicated positron emission tomography scanner for imaging of the distal limb of standing horses. *Vet Radiol Ultrasound.* 2022;63:469–477.
3. Spriet M, Espinosa P, Kyme AZ, et al. Positron emission tomography of the equine distal limb: exploratory study. *Vet Radiol Ultrasound.* 2016;57:630–638.
4. McLarty E, Spriet M, Beylin D, et al. Comparison of ^{18}F-sodium fluoride positron emission tomography and CT: an exploratory study in 12 dogs with elbow pain. *Vet Radiol Ultrasound.* 2021;62:498–506.
5. Kinahan P, Majewski S, Elston B, et al. Design considerations for AMPET: the ambulatory micro-dose, wearable PET brain imager [abstract]. *J Nuclear Med.* 2015;56(suppl 3):S1540.
6. González AJ, Majewski S, Sánchez F, et al. The MINDView brain PET detector, feasibility study based on SiPM arrays. *Nucl Instrum Methods Phys Res A.* 2016; 818:82–90.
7. Wang Z, Yu W, Xie S. A dedicated PET system for human brain and head/neck imaging. Paper presented at: IEEE Nuclear Science Symposium and Medical Imaging Conference; 2013; Seoul, Korea.
8. Grogg KS, Toole T, Ouyang J, et al. National Electrical Manufacturers Association and clinical evaluation of a novel brain PET/CT scanner. *J Nucl Med.* 2016;57: 646–652.
9. Wienhard K, Schmand M, Casey M, et al. The ECAT HRRT: performance and first clinical application of the new high resolution research tomograph. *IEEE Trans Nucl Sci.* 2002;49:104–110.
10. Braem A, Llatas MC, Chesi E, et al. Feasibility of a novel design of high resolution parallax-free Compton enhanced PET scanner dedicated to brain research. *Phys Med Biol.* 2004;49:2547–2562.
11. Yamaya T, Yoshida E, Obi T, Ito H, Yoshikawa K, Murayama H. First human brain imaging by the jPET-D4 prototype with a pre-computed system matrix. *IEEE Trans Nucl Sci.* 2008;55:2482–2492.
12. Moliner L, Rodríguez-Alvarez MJ, Catret JV, González A, Ilisie V, Benlloch JM. NEMA performance evaluation of CareMiBrain dedicated brain PET and comparison with the whole-body and dedicated brain PET systems. *Sci Rep.* 2019;9:15484.
13. Sokoloff L, Reivich M, Kennedy C, et al. The [^{14}C] deoxyglucose method for the measurement of local cerebral glucose utilization: theory, procedure, and normal values in the conscious and anesthetized albino rat. *J Neurochem.* 1977;28:897–916.
14. Phelps ME, Huang SC, Hoffman EJ, Selin C, Sokoloff L, Kuhl DE. Tomographic measurement of local cerebral glucose metabolic rate in humans with (F-18)2-fluoro-2-deoxy-D-glucose: validation of method. *Ann Neurol.* 1979;6:371–388.
15. Bartlett EA, Ogden RT, Mann JJ, Zanderigo F. Source-to-Target Automatic Rotating Estimation (STARE): a publicly-available, blood-free quantification approach for PET tracers with irreversible kinetics—theoretical framework and validation for [^{18}F] FDG. *Neuroimage.* 2022;249:118901.
16. Sullivan GM, Oquendo MA, Simpson N, Van Heertum RL, Mann JJ, Parsey RV. Brain serotonin1A receptor binding in major depression is related to psychic and somatic anxiety. *Biol Psychiatry.* 2005;58:947–954.
17. Desikan RS, Ségonne F, Fischl B, et al. An automated labeling system for subdividing the human cerebral cortex on MRI scans into gyral based regions of interest. *Neuroimage.* 2006;31:968–980.
18. Khan AR, Wang L, Beg MF. FreeSurfer-initiated fully-automated subcortical brain segmentation in MRI using large deformation diffeomorphic metric mapping. *Neuroimage.* 2008;41:735–746.
19. Patlak CS, Blasberg RG, Fenstermacher JD. Graphical evaluation of blood-to-brain transfer constants from multiple-time uptake data. *J Cereb Blood Flow Metab.* 1983;3:1–7.
20. Avants BB, Tustison NJ, Wu J, Cook PA, Gee JC. An open source multivariate framework for *n*-tissue segmentation with evaluation on public data. *Neuroinformatics.* 2011;9:381–400.
21. Mazaika P, Whitfield-Gabrieli S, Reiss A, Glover G. Artifact repair for fMRI data from high motion clinical subjects. *Hum Brain Mapp.* 2007;47:70238-1.
22. Forman SD, Cohen JD, Fitzgerald M, Eddy WF, Mintun MA, Noll DC. Improved assessment of significant activation in functional magnetic resonance imaging (fMRI): use of a cluster-size threshold. *Magn Reson Med.* 1995;33:636–647.
23. Cox RW. AFNI: software for analysis and visualization of functional magnetic resonance neuroimages. *Comput Biomed Res.* 1996;29:162–173.
24. Grogg KS, Toole T, Ouyang J, et al. National Electrical Manufacturers Association and clinical evaluation of a novel brain PET/CT scanner. *J Nucl Med.* 2016;57: 646–652.
25. Bartlett EJ, Barouche F, Brodie JD, et al. Stability of resting deoxyglucose metabolic values in PET studies of schizophrenia. *Psychiatry Res.* 1991;40:11–20.
26. Maquet P, Dive D, Salmon E, et al. Cerebral glucose utilization during sleep-wake cycle in man determined by positron emission tomography and [^{18}F] 2-fluoro-2-deoxy-D-glucose method. *Brain Res.* 1990;513:136–143.
27. Duara R, Gross-Glenn K, Barker WW, et al. Behavioral activation and the variability of cerebral glucose metabolic measurements. *J Cereb Blood Flow Metab.* 1987; 7:266–271.
28. Holcomb HH, Cascella NG, Medoff DR, et al. PET-FDG test–retest reliability during a visual discrimination task in schizophrenia. *J Comput Assist Tomogr.* 1993; 17:704–709.
29. Schaefer SM, Abercrombie HC, Lindgren KA, et al. Six-month test–retest reliability of MRI-defined PET measures of regional cerebral glucose metabolic rate in selected subcortical structures. *Hum Brain Mapp.* 2000;10:1–9.
30. Sundar LK, Muzik O, Rischka L, et al. Towards quantitative [^{18}F] FDG-PET/MRI of the brain: automated MR-driven calculation of an image-derived input function for the non-invasive determination of cerebral glucose metabolic rates. *J Cereb Blood Flow Metab.* 2019;39:1516–1530.
31. Jakoby BW, Bercier Y, Conti M, Casey ME, Bendriem B, Townsend DW. Physical and clinical performance of the mCT time-of-flight PET/CT scanner. *Phys Med Biol.* 2011;56:2375–2389.

Dual Role for L-[Methyl-^{11}C]-Methionine PET in Acromegaly: Confirming Remission and Detecting Recurrence

Linus Haberbosch[1,2], Daniel Gillett[1], James MacFarlane[1], Olympia Koulouri[1], Knut Mai[2], Joachim Spranger[2], Richard Mannion[1], Heok Cheow[1], Jonathan Jones[1], and Mark Gurnell[1]

[1]Wellcome-MRC Institute of Metabolic Science and Addenbrooke's Hospital, Cambridge, United Kingdom; and
[2]Charité–Universitätsmedizin Berlin, Berlin, Germany

Molecular imaging using the amino acid PET tracer L-[methyl-^{11}C]-methionine (^{11}C-Met PET) is emerging as an important addition to the armamentarium of clinicians treating pituitary disease. In acromegaly cases, ^{11}C-Met PET can accurately localize sites of residual tumors to guide (further) surgery or radiotherapy (*1*,*2*). However, ^{11}C-Met PET can also help confirm remission. Here, we illustrate both roles in a single patient.

A 31-y-old woman with recently diagnosed acromegaly (insulin-like growth factor 1, 103.0 nmol/L; upper limit of normal, 45.0) underwent endoscopic transsphenoidal surgery for a macroadenoma (21 mm). Gross total resection was achieved, with complete biochemical remission (insulin-like growth factor 1, 21.3 nmol/L; nadir growth hormone, 0.33 μg/L). Although postoperative MRI suggested a possible right-sided tumor remnant, ^{11}C-Met PET demonstrated only physiologic uptake in the remaining normal gland (Fig. 1A).

Nine years later, the patient experienced clinical and biochemical recurrence (insulin-like growth factor 1, 44.9 nmol/L; upper limit of normal, 35.5; nadir growth hormone, 1.75 μg/L). However, the contemporaneous MRI was unchanged. Therefore, a second ^{11}C-Met PET study was performed, which revealed a new focus of radiotracer uptake in the right sella adjacent to, but distinct from, the normal gland (Fig. 1B). The patient underwent repeat surgery, and the tumor was resected from the site identified on the ^{11}C-Met PET scan. The patient reentered remission (insulin-like growth factor 1, 15.6 nmol/L; upper limit of normal, 28.0; nadir growth hormone, <0.05 μg/L), with repeat ^{11}C-Met PET demonstrating uptake only in the residual normal gland (Fig. 1C), consistent with otherwise preserved pituitary function. This report therefore illustrates the dual role of ^{11}C-Met PET in acromegaly, confirming remission and detecting recurrence (*1*).

DISCLOSURE

No potential conflict of interest relevant to this article was reported.

REFERENCES

1. Koulouri O, Kandasamy N, Hoole AC, et al. Successful treatment of residual pituitary adenoma in persistent acromegaly following localisation by ^{11}C-methionine PET co-registered with MRI. *Eur J Endocrinol.* 2016;175:485–498.
2. Bashari WA, Senanayake R, Koulouri O, et al. PET-guided repeat transsphenoidal surgery for previously deemed unresectable lateral disease in acromegaly. *Neurosurg Focus.* 2020;48:E8.

Received Aug. 1, 2023; revision accepted Sep. 12, 2023.

For correspondence or reprints, contact Mark Gurnell (mg299@medschl.cam.ac.uk).

DOI: 10.2967/jnumed.123.266446

^{11}C-MET PET IN ACROMEGALY • Haberbosch et al. 327

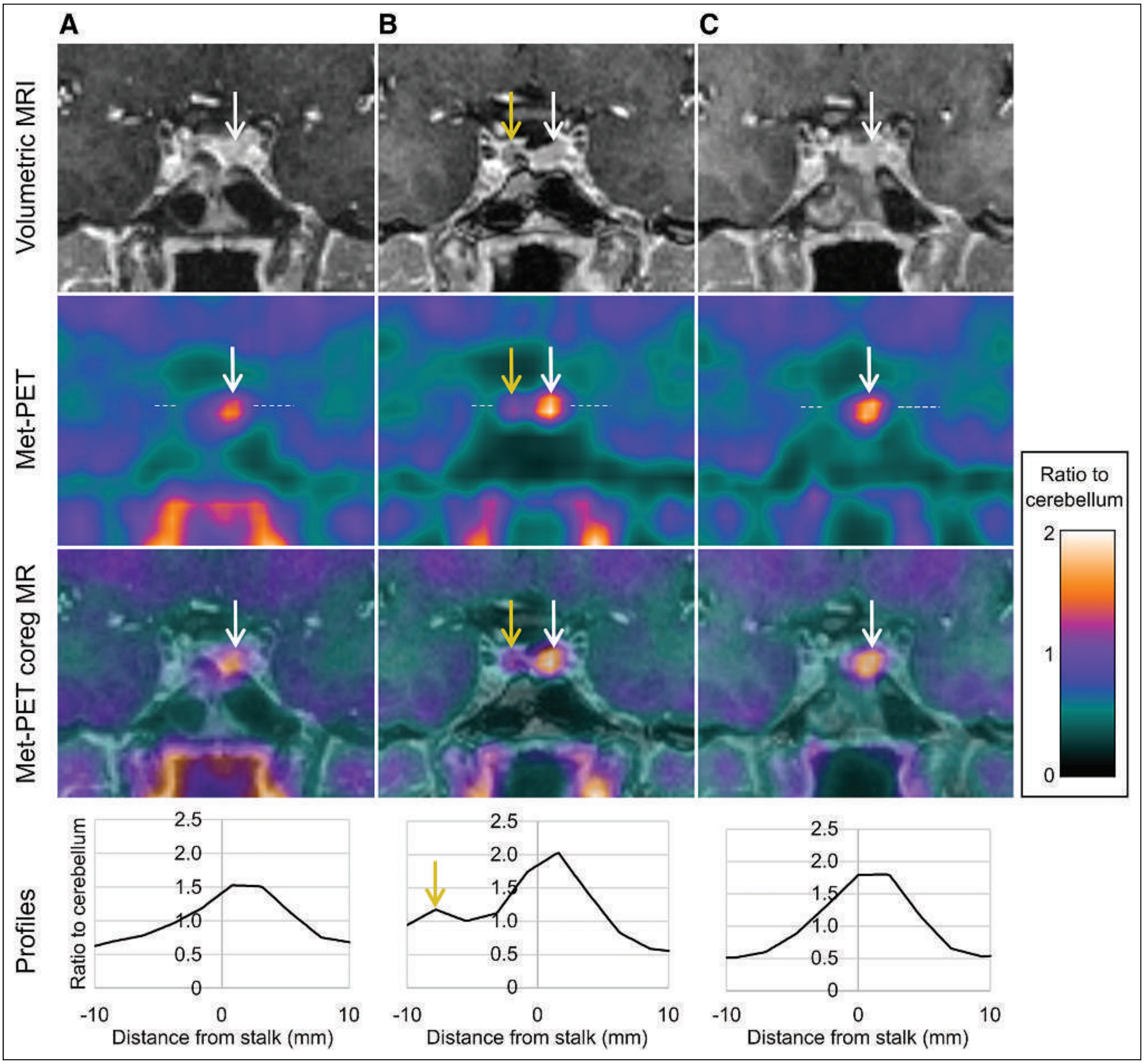

FIGURE 1. MRI, ^{11}C-Met PET, and coregistered images during initial remission (A), at recurrence (B), and after successful repeat surgery (C). Normal pituitary gland (demonstrating typical variability in uptake between scans) is indicated by white arrows; recurrence (visually appreciated on second scan only) is indicated by yellow arrows. (A) MRI showing indeterminate appearance in right sella but with ^{11}C-methionine uptake confined to residual normal gland in left side of sella. (B) MRI unchanged despite disease relapse; ^{11}C-Met PET reveals discrete, new focus of ^{11}C-methionine uptake in right sella. (C) Normalization of insulin-like growth factor 1 after repeat surgery correlates with absence of right-sided tracer uptake. Coronal MRI of T1-weighted fast-spoiled gradient echo images: repetition time, 11.5 ms; echo time, 4.2 ms; isotropic voxel spacing of 1 mm × 1 mm (256 × 256 matrix size) × 1 mm (slice thickness). ^{11}C-Met PET static images acquired on GE Discovery-690 20–40 min after administration of ^{11}C-Met. Ordered-subset expectation maximization reconstruction: attenuation correction, time-of-flight, point-spread function, 3 iterations, 24 subsets, and gaussian postprocessing filter (3.2 mm in 2011, 2 mm in 2020–2021). coreg = coregistered.

Recent Evidence on Cardiac ^{99m}Tc-DPD Uptake After Therapy with Tafamidis May Reveal the Road to an Ultra-Early Diagnosis in Patients with ATTR Amyloidosis

TO THE EDITOR: In recent years, the management of patients with amyloid transthyretin–related (ATTR) cardiac amyloidosis (CA) has undergone major changes because of the validation of effective therapies. For example, new treatment with antibodies such as N1006 showed promise in depleting ATTR CA (*1*), and gene editing strategies showed promise in reducing levels of serum TTR protein in the hereditary forms of the disease (*2*).

In this context, tafamidis has secured an important role in the treatment of ATTR CA and has now been included in international guidelines (*3*), which underline the need for a timely start of therapy, as efficacy is reduced in more advanced stages of the disease (*4*). In this regard, it is undoubtedly clear that a prompt diagnosis is essential to yield favorable outcome in ATTR CA patients, and a reliable imaging modality able to provide an early and accurate diagnosis is essential.

Counterintuitively, guidance on where to direct our attention for early diagnosis of ATTR CA should be sought not in literature on the diagnostic accuracy of imaging modalities but in recent data on the use of these modalities for follow-up after tafamidis. In line with recent reports, a study recently published in *The Journal of Nuclear Medicine* (*5*) has shown that the degree of cardiac uptake in ^{99m}Tc-3,3-diphosphono-1,2 propanodicarboxylic acid (^{99m}Tc-DPD) SPECT decreases after therapy.

The most intriguing finding of this study was the somewhat unexpected decrease in ^{99m}Tc-DPD uptake. In fact, tafamidis essentially reduces deposition of amyloid fibrils within the myocardium rather than degrading them. Consistent with this concept, studies featuring cardiac MRI showed stabilization of extracellular volume after treatment (*6*). Hence, it is conceivable that a cardiac MRI–based calculation of extracellular volume reflects amyloid burden within the myocardium, whereas ^{99m}Tc-DPD SPECT reflects not the burden of amyloid but the degree of active deposition. This concept is consistent with the observation that ^{99m}Tc-DPD binds directly not to amyloid fibrils but to microcalcifications within amyloid (*7*). As happens with bone scans, only calcifications with active metabolism are expected to take up ^{99m}Tc-DPD, and the same concept pertains to amyloid imaging.

As such, if we aim to detect ATTR CA early, when the amyloid burden can be small but active deposition rapid, ^{99m}Tc-DPD may be preferred to yield an accurate diagnosis. In this regard, the most conceivable pattern of ^{99m}Tc-DPD uptake may not be diffuse and mild but rather moderate to intensive and localized in the left ventricular myocardial regions known to be affected first—that is, basal regions, with sparing of apical regions.

In this context, it is clear that planar ^{99m}Tc-DPD imaging should no longer be considered sufficient to make an early diagnosis. In fact, whereas small areas of mildly to moderately increased ^{99m}Tc-DPD uptake are likely to be missed on planar imaging, sensitivity is expected to be higher with SPECT. Furthermore, SPECT-based quantification of myocardial uptake may provide important information on the degree of active amyloid deposition at baseline and, thus, on prognosis (*8*). Although quantification of bone tracers with SPECT has shown little evidence of a prognostic role in later stages of the disease (*9*), the role may be more robust in earlier stages. This concept is also consistent with published recommendations (*10*), highlighting the importance of screening for ATTR CA in selected patients.

If future studies show ^{99m}Tc-DPD SPECT to have prognostic value in ATTR CA, this modality may become the gatekeeper to select patients more likely to benefit from tafamidis, thus optimizing allocation of resources in this increasingly prevalent disease. Hence, ^{99m}Tc-DPD SPECT may be the protagonist of this change in paradigm in the management of patients with ATTR CA. The nuclear medicine community should be ready to take up this challenge.

DISCLOSURE

Federico Caobelli is supported by a research grant by Siemens Healthineers and receives speaker honoraria from Bracco AG and Pfizer AG for matters not related to the present letter. No other potential conflict of interest relevant to this article was reported.

REFERENCES

1. Garcia-Pavia P, Aus dem Siepen F, Donal E, et al. Phase 1 trial of antibody NI006 for depletion of cardiac transthyretin amyloid. *N Engl J Med.* 2023;389:239–250.
2. Gillmore JD, Gane E, Taubel J, et al. CRISPR-Cas9 in vivo gene editing for transthyretin amyloidosis. *N Engl J Med.* 2021;385:493–502.
3. Garcia-Pavia P, Rapezzi C, Adler Y, et al. Diagnosis and treatment of cardiac amyloidosis: a position statement of the ESC Working Group on Myocardial and Pericardial Diseases. *Eur Heart J.* 2021;42:1554–1568.
4. Elliott P, Drachman BM, Gottlieb SS, et al. Long-term survival with tafamidis in patients with transthyretin amyloid cardiomyopathy. *Circ Heart Fail.* 2022;15:e008193.
5. Papathanasiou M, Kessler L, Bengel FM, et al. Regression of myocardial ^{99m}Tc-DPD uptake after tafamidis treatment of cardiac transthyretin amyloidosis. *J Nucl Med.* 2023;64:1083–1086.
6. Rettl R, Mann C, Duca F, et al. Tafamidis treatment delays structural and functional changes of the left ventricle in patients with transthyretin amyloid cardiomyopathy. *Eur Heart J Cardiovasc Imaging.* 2022;23:767–780.
7. Stats MA, Stone JR. Varying levels of small microcalcifications and macrophages in ATTR and AL cardiac amyloidosis: implications for utilizing nuclear medicine studies to subtype amyloidosis. *Cardiovasc Pathol.* 2016;25:413–417.
8. Caobelli F, Braun M, Haaf P, Wild D, Zellweger MJ. Quantitative ^{99m}Tc-DPD SPECT/CT in patients with suspected ATTR cardiac amyloidosis: feasibility and correlation with visual scores. *J Nucl Cardiol.* 2020;27:1456–1463.
9. Miller RJH, Cadet S, Mah D, et al. Diagnostic and prognostic value of technetium-99m pyrophosphate uptake quantitation for transthyretin cardiac amyloidosis. *J Nucl Cardiol.* 2021;28:1835–1845.
10. Seferovic PM, Ponikowski P, Anker SD, et al. Clinical practice update on heart failure 2019: pharmacotherapy, procedures, devices and patient management. An expert consensus meeting report of the Heart Failure Association of the European Society of Cardiology. *Eur J Heart Fail.* 2019;21:1169–1186.

Federico Caobelli
University of Bern
Bern, Switzerland
E-mail: federico.caobelli@insel.ch

DOI: 10.2967/jnumed.123.266676

REPLY: We read with great interest the letter from Dr. Caobelli, which referred to our recent article in *The Journal of Nuclear Medicine* on using bone scintigraphy to monitor patients with amyloid transthyretin–related (ATTR) cardiac amyloidosis (CA) under tafamidis therapy (*1*).

For a long time, ATTR CA was a disease for which there was no effective therapy, making it frustrating for the treating physicians, particularly in light of the morbidity and mortality of the disease (mean life expectancy of ∼2.5 y for certain hereditary forms and 3.6 y for wild-type ATTR CA without therapy) (*2,3*). The community was therefore all the more enthusiastic about the recent introduction of an effective therapy that could at least halt disease progression, as demonstrated in the ATTR-ACT trial (*4*). As pointed out by Dr. Caobelli, we observed a reduction in cardiac ^{99m}Tc-3,3-diphosphono-1,2 propanodicarboxylic acid (^{99m}Tc-DPD) accumulation in most of our patients under ongoing tafamidis therapy, a finding that was unexpected for us. Including our study, there are now several publications that support this observation (*1,5–7*), but the reason for the decreased accumulation of bone-avid tracers in the heart is still unclear. To our knowledge, it is still not fully understood why bone-avid tracers bind to the heart of patients with ATTR CA. One of the most frequently raised theories, which was also mentioned by Dr. Caobelli, is that the tracers bind to microcalcifications that form in the area of amyloid deposits in the heart. This theory is supported, inter alia, by the fact that electron microscopic studies detected these microcalcifications in the heart (referred to in the cited publication as "dust-like calcifications") (*8*). Interestingly, they were found not only in the vicinity of amyloid but also in areas where there were no amyloid deposits—a fact that could in a way support the hypothesis of Dr. Caobelli that binding of bone-avid tracers could be more an (early) indicator of active amyloid deposition than of persisting deposits.

Moreover, it could be assumed that a decrease in tracer accumulation in the heart is associated with a decrease in calcifications, but to our knowledge there are no studies on this. It is known from the ATTR-ACT trial that patients undergoing tafamidis therapy, which stabilizes transthyretin, experience a slowing of disease progression compared with placebo therapy. In MRI studies, this is reflected in a stabilization of the extracellular volume (*9*), whereas in the ATTR-ACT trial there was a less severe deterioration of, for example, the 6-min walk test or the Kansas City cardiomyopathy questionnaire overall summary score (*4*). In the APOLLO-B trial, in which patients with ATTR CA received either the small interfering RNA-based patisiran (inhibiting hepatic production of transthyretin) or placebo, all patients receiving patisiran showed a reduction in cardiac tracer uptake, whereas none of the patients in the placebo arm did (*10*). In this context, the idea that uptake of bone-avid tracers to the heart is reduced under tafamidis therapy because microcalcifications form on only fresh and active amyloid deposits is interesting. However, since there is still a lack of data on this, the idea must be classified as (at least in part) speculative. Further considerations as to why the binding is lower relate to a possible reduction in amyloid deposition (*11*). This hypothesis is supported by the fact that we observed a clinical improvement in the patients with reduced cardiac ^{99m}Tc-DPD uptake (*1*). Furthermore, other researchers, who also saw a decrease in tracer accumulation in the heart on bone scans, observed a decrease in N-terminal pro–brain natriuretic peptide levels and an improvement in, for example, the global longitudinal strain on echocardiography with tafamidis therapy (*5*).

In our opinion, one of the most important ways to clarify this current mystery could be to perform amyloid-specific imaging. In contrast to cardiac MRI and bone scintigraphy, amyloid-specific PET tracers bind directly to the amyloid (*12*) and, hence, can visualize cardiac amyloid burden. Using these amyloid-specific PET tracers, it should therefore be possible to investigate whether there is a real decrease in the amyloid load in the heart under tafamidis therapy; however, no such study has been conducted so far to the best of our knowledge (*13*). If this is not the case, the idea put forward by Dr. Caobelli could certainly provide a potential explanation. Moreover, explaining the mechanism of cardiac binding of bone-specific scintigraphy tracers in patients could shed light on the question of whether they can be used for early detection as well as monitoring of therapy response. In summary, many questions remain unanswered, and research on ATTR CA still represents a highly interesting field for imagers and clinicians alike.

REFERENCES

1. Papathanasiou M, Kessler L, Bengel FM, et al. Regression of myocardial ^{99m}Tc-DPD uptake after tafamidis treatment of cardiac transthyretin amyloidosis. *J Nucl Med.* 2023;64:1083–1086.
2. Gillmore JD, Damy T, Fontana M, et al. A new staging system for cardiac transthyretin amyloidosis. *Eur Heart J.* 2018;39:2799–2806.
3. Grogan M, Scott CG, Kyle RA, et al. Natural history of wild-type transthyretin cardiac amyloidosis and risk stratification using a novel staging system. *J Am Coll Cardiol.* 2016;68:1014–1020.
4. Maurer MS, Schwartz JH, Gundapaneni B, et al. Tafamidis treatment for patients with transthyretin amyloid cardiomyopathy. *N Engl J Med.* 2018;379:1007–1016.
5. Rettl R, Wollenweber T, Duca F, et al. Monitoring tafamidis treatment with quantitative SPECT/CT in transthyretin amyloid cardiomyopathy. *Eur Heart J Cardiovasc Imaging.* 2023;24:1019–1030.
6. Rettl R, Calabretta R, Duca F, et al. Reduction in ^{99m}Tc-DPD myocardial uptake with therapy of ATTR cardiomyopathy. *Amyloid.* August 20, 2023 [Epub ahead of print].
7. Tingen HSA, Tubben A, Bijzet J, et al. Cardiac [^{99m}Tc]Tc-hydroxydiphosphonate uptake on bone scintigraphy in patients with hereditary transthyretin amyloidosis: an early follow-up marker? *Eur J Nucl Med Mol Imaging.* October 16, 2023 [Epub ahead of print].
8. Thelander U, Westermark GT, Antoni G, et al. Cardiac microcalcifications in transthyretin (ATTR) amyloidosis. *Int J Cardiol.* 2022;352:84–91.
9. Rettl R, Mann C, Duca F, et al. Tafamidis treatment delays structural and functional changes of the left ventricle in patients with transthyretin amyloid cardiomyopathy. *Eur Heart J Cardiovasc Imaging.* 2022;23:767–780.
10. Kale P, Maurer MS, Fontana M, et al. Exploratory analyses from the APOLLO-B, a phase 3 study of patisiran in patients with ATTR amyloidosis with cardiomyopathy [abstract]. *J Card Failure.* 2022;29:P552.
11. Tsai C-H, Chao C-C, Hsieh S-T, et al. Tafamidis decreased cardiac amyloidosis deposition in patients with Ala97Ser hereditary transthyretin cardiomyopathy: a 12-month follow-up cohort study. *Orphanet J Rare Dis.* 2023;18:289.
12. Dorbala S, Vangala D, Semer J, et al. Imaging cardiac amyloidosis: a pilot study using ^{18}F-florbetapir positron emission tomography. *Eur J Nucl Med Mol Imaging.* 2014;41:1652–1662.
13. Tingen HSA, Tubben A, van 't Oever JH, et al. Positron emission tomography in the diagnosis and follow-up of transthyretin amyloid cardiomyopathy patients: a systematic review. *Eur J Nucl Med Mol Imaging.* 2023;51:93–109.

Christoph Rischpler*
David Kersting
Lukas Kessler
Zohreh Varasteh
Peter Luedike
Alexander Carpinteiro
Tienush Rassaf
Ken Herrmann
Maria Papathanasiou
**Klinikum Stuttgart*
Stuttgart, Germany
E-mail: c.rischpler@klinikum-stuttgart.de

DOI: 10.2967/jnumed.123.266767

Good Voxel Dosimetry with a Simplified Study Design Resulted in Improvable Safety Limits

TO THE EDITOR: In a paper recently published by *The Journal of Nuclear Medicine,* Watanabe et al. claimed theirs was "the first study to show superiority for voxel-based dosimetry over multicompartment dosimetry in the prediction of liver decompensation of [hepatocellular carcinoma] patients undergoing radioembolization with ^{90}Y glass microspheres" (*1*). As dosimetrists we cannot be anything but glad for this success, which pursued a methodology that Carlo Chiesa defended in a point–counterpoint debate with objective difficulty due to the scarce available evidence (*2*). As a matter of fact, previous efforts by our group (*3*) were not able to demonstrate a significant "superiority for voxel-based dosimetry in the pretherapeutic prediction of hepatotoxicity in [hepatocellular carcinoma] patients undergoing radioembolization of the whole liver," as written by Watanabe et al. (*1*), nor in the prediction of response (*4*). Therefore, the achievement by Watanabe et al. might be regarded as an important step forward not only in dosimetric planning in radioembolization but also in nuclear medicine dosimetry in general, as one of the first evidences of superiority of voxel dosimetry over the mean-dose approach.

However, as often happens in science, opening new scenarios raises additional questions and the need for further clarification. We think that the nuclear medicine community would appreciate some general clarification to properly compare results to progress as a community. Some additional notes by Watanabe et al. would be welcome, since the rather simplified design of their study might have led to improvable safety thresholds.

Let us focus first on the whole-liver treatment subgroup of 98 patients, in which Watanabe et al. obtained a brilliant area under the curve (AUC) of 0.84 with a 40-Gy volume (V40) variable in terms of separation between toxic and nontoxic treatments. Then, with a standard methodology in the receiver-operating-characteristic curve analysis (Youden index), they found the best toxicity threshold at a 40-Gy volume of 72%. In their dose volume histogram, the 40-Gy volume variable is the percent volume of whole nontumoral liver tissue receiving an absorbed dose higher than 40 Gy. The obtained threshold means that if this percentage is larger than 72%, there is a certain risk of liver decompensation. The other limit of an absorbed dose to 30% of volume (AD30) means that we have risk if 30% of the nontumoral liver volume receives an absorbed dose of at least 43 Gy (AUC, 0.823). Using the mean absorbed dose on whole nontumoral liver tissue (AD-WNTLT), they obtained an apparently less brilliant AUC value of 0.633, with a safety threshold of 55.6 Gy.

Watanabe et al., however, did not report the uncertainty nor the 95% CI of the AUC values. Without this error estimate, it is impossible to demonstrate the significance of differences between different AUC values. Their mean AD-WNTLT can be compared with our finding, in contrast to the 40-Gy volume and 30% absorbed dose, which were not calculated in our work (*5*). The result, 55.6 Gy, is quite close to our 59 Gy, and the authors' AUC of 0.633 is not so different from our AUC of 0.68.

Neither sensitivity nor specificity associated with such thresholds was mentioned.

The toxicity endpoint definition was different from our definition. We included other symptoms as indicators of liver decompensation: a prothrombin time international normalized ratio greater than 2.2, clinically detectable ascites, encephalopathy, esophageal varices bleeding, and death. The timeline was the same (≤6 mo).

All our patients were Child–Pugh A, whereas Watanabe et al.'s Table 1 reports that 109 patients were Child–Pugh A, 6 were Child–Pugh B7, and the remaining 61 were undefined. Should these patients be Child–Pugh C? This could explain toxicity at low AD-WNTLT.

We treated 96% of our patients with the lobar approach, and we extrapolated the tolerance to a whole-liver approach according to the Lyman formalism for a pure parallel organ. In our analysis, we censored patients on the day of the second treatment, in order to observe the effect and to calculate the dose for a single administration. Watanabe et al. obtained their best results in the group whose whole liver was treated, but "in cases of whole-liver treatment with 2 or more injections (e.g., separate injections for left and right lobes), injections were performed in 2 sessions, approximately 4–6 wk apart" (*1*). This whole-liver approach is therefore a sort of hybrid between a real simultaneous whole-liver treatment and 2 sequential right lobe–left lobe treatments, separated by a time interval insufficient to fully obtain radioinduced contralateral hypertrophy (5.9 ± 3.4 mo (*6*)). The dosimetric tolerance calculation is biased by this interval because we cannot rigorously consider the treatment as a single one, nor could we assume to have a new organ, as we assume once contralateral hypertrophy is completed. When considering these 2 models, one would choose the former because a time frame of 4–6 wk is short compared with 5.9 mo. Therefore, these 2-step treatments could (hardly) be considered as whole-liver treatments.

Watanabe et al. did not apply any analysis of the cause of toxicity introduced by Garin et al. (*7*). This aspect is important. In a hepatocellular carcinoma patient, liver decompensation happens, even without treatment, as a natural progression of cirrhosis or tumor growth. Furthermore, hyperbilirubinemia could derive from bile-duct compression by the tumor. Without a cause analysis, the authors included as toxicity cases those not derived from treatment. These events are observed even at a low absorbed dose. For this reason, the optimal threshold determination is impaired. Confirmation is provided by the normal-tissue complication probability experimental points reported by Strigari et al. (*8*). They also did not apply analysis of toxicity causes. Their point at the lowest biologic effective liver dose (20 Gy, corresponding to a 16-Gy whole-liver–absorbed dose) gave about a 20% risk of toxicity of at least grade 2 according to Common Terminology Criteria for Adverse Events (version 4; National Cancer Institute). In our experience (*5*), almost half of the observed liver decompensations within 6 mo were not related to treatment.

The second important aspect is that Watanabe et al. did not stratify patients on the basal bilirubin level. This risk factor is stronger than with AD-WNTLT (*5*) and heavily influences the safety threshold obtained. In Table 1, Watanabe et al. report a baseline bilirubin distribution of 0.8 ± 0.4 mg/dL. This means that, within 1 SD, 68% of the bilirubin level was within the interval of 0.4 and 1.2 mg/dL, whereas 32% are outside such an interval, with a nonnegligible percentage above 1.2 mg/dL (16% if the distribution was normal, that is, symmetric). In our steps toward optimal planning criteria, we started with a safety limit of 75 Gy (*9*), but after advances in knowledge, we were forced to split this limit into 50 Gy versus 90 Gy after we observed the importance of basal bilirubin levels greater than or less than 1.1 mg/dL, respectively (*5*).

The normal-tissue complication probability analysis is absent. This is the standard in external-beam radiobiologic modeling. Once the normal-tissue complication probability curve is obtained, it is possible to predict the quantitative level of risk of liver decompensation given an intended AD-WNTLT value. We decided to fix the limits to keep the liver decompensation risk lower than 15%. Just to clarify the difference, our receiver-operating-characteristic curve analysis with this bilirubin stratification gave optimal thresholds of 59 and 65 Gy, whereas the normal-tissue complication probability–based limits are 50 and 90 Gy.

In the lobar treatment group, Watanabe et al. reported 4 of 78 toxicity cases (5%) and 74 nontoxic cases. In the whole-liver approach, they had 16 of 98 liver decompensations (16%) versus 82 nontoxic treatments. Note that the difference in toxicity incidence was found to be significant using the exact Fisher test ($P = 0.03$). The mean AD-WNTLT was 42 Gy in the lobar treatment group (lower than our more conservative limit of 50 Gy), whereas it was 70 Gy in the whole-liver group. In addition, without a second contralateral treatment, radioinduced hypertrophy was free to develop. Therefore, the combination of lower AD-WNTLT and partial treatment resulted in a significantly lower toxicity incidence in the lobar approach. It was so low that the authors could not obtain statistical significance, nor was a meaningful threshold found, given the small number of toxic treatments, as was our experience with lobar treatment (*4*).

In conclusion, the voxel dosimetry method by Watanabe et al. might be an important advance to safely plan radioembolization. However, before being used in clinics by other centers, the proposed safety thresholds for whole-liver treatment (hybrid) should be revised according to the above comments, mainly introducing analysis of causes, stratification on the basal bilirubin value, and normal-tissue complication probability analysis.

DISCLOSURE

In the last 3 y, Carlo Chiesa and Marco Maccauro were consultants for Boston Scientific, the producer of ^{90}Y glass microspheres; for Terumo, the producer of ^{166}Ho microspheres; and for AAA, the producer of Lutathera (^{177}Lu-DOTATATE). He received a research grant from Boston Scientific. Matteo Bagnalasta is a resident supported by a scholarship from Boston Scientific. No potential conflict of interest relevant to this article was reported.

REFERENCES

1. Watanabe M, Grafe H, Theysohn J, et al. Voxel-based dosimetry predicts hepatotoxicity in hepatocellular carcinoma patients undergoing radioembolization with ^{90}Y glass microspheres. *J Nucl Med.* 2023;64:1102–1108.
2. Chiesa C, Bardies M, Zaidi H. Voxel-based dosimetry is superior to mean-absorbed dose approach for establishing dose–effect relationship in targeted radionuclide therapy. *Med Phys.* 2019;46:5403–5406.
3. Chiesa C, Mira M, Maccauro M, et al. Radioembolization of hepatocarcinoma with ^{90}Y glass microspheres: development of an individualized treatment planning strategy based on dosimetry and radiobiology. *Eur J Nucl Med Mol Imaging.* 2015;42:1718–1738.
4. Romanò C, Mazzaglia S, Maccauro M, et al. Radioembolization of hepatocellular carcinoma with ^{90}Y glass microspheres: no advantage of voxel dosimetry with respect to mean dose in dose–response analysis with two radiological methods. *Cancers (Basel).* 2022;14:959.
5. Chiesa C, Mira M, Bhoori S, et al. Radioembolization of hepatocarcinoma with ^{90}Y glass microspheres: treatment optimization using the dose–toxicity relationship. *Eur J Nucl Med Mol Imaging.* 2020;47:3018–3032.
6. Palard X, Edeline J, Rolland Y, et al. Dosimetric parameters predicting contralateral liver hypertrophy after unilobar radioembolization of hepatocellular carcinoma. *Eur J Nucl Med Mol Imaging.* 2018;45:392–401.
7. Garin E, Rolland Y, Laffont S, Edeline J. Clinical impact of ^{99m}Tc-MAA SPECT/CT-based dosimetry in the radioembolization of liver malignancies with ^{90}Y-loaded microspheres. *Eur J Nucl Med Mol Imaging.* 2016;43:559–575.
8. Strigari L, Sciuto R, Rea S, et al. Efficacy and toxicity related to treatment of hepatocellular carcinoma with ^{90}Y SIR spheres: radiobiologic considerations. *J Nucl Med.* 2010;51:1377–1385.
9. Chiesa C, Mira M, Maccauro M, et al. A dosimetric treatment planning strategy in radioembolization of hepatocarcinoma with ^{90}Y glass microspheres. *Q J Nucl Med Mol Imaging.* 2012;56:503–508.

Carlo Chiesa*
Matteo Bagnalasta
Marco Maccauro
**Foundation IRCCS Istituto Nazionale Tumori*
Milan, Italy
E-mail: carlo.chiesa@istitutotumori.mi.it

DOI: 10.2967/jnumed.113.129353

Unraveling the Hypocalcemic Response to ^{177}Lu-Prostate-Specific Membrane Antigen Therapy

TO THE EDITOR: We read with great interest the recent article by Kumar et al. published in *The Journal of Nuclear Medicine* (*1*). The authors presented an intriguing finding of clinically significant hypocalcemia and osteosclerosis as rare but important side effects of ^{177}Lu-PSMA-I&T therapy in patients with high-volume osseous metastatic disease who showed a significant treatment response. The paper provides valuable insights and stimulates thought; however, there are still certain aspects that require further clarification and discussion. Although Kumar et al. shed light on the potential side effects of ^{177}Lu-PSMA-I&T therapy, additional investigation is necessary to fully comprehend the underlying mechanisms and optimize patient management.

Hungry bone syndrome was initially described by Albright and Reifenstein in relation to the removal of parathyroid adenomas (*2*). This procedure triggers an increase in osteoblastic activity, resulting in excessive deposition of calcium and phosphate in the bones (*3*). The calcium sink effect in metastatic prostate cancer, which is also associated with hungry bone syndrome, is actually caused by tumor-induced osteoblastic activity (*4*). These cases generally do not respond well to aggressive medical treatment but may show improvement after successful tumor control (*1,5,6*).

We posit that the findings of Kumar et al. may differ from the tumor-induced calcium sink effect. According to their study, patients who were previously normocalcemic experienced hypocalcemia after ^{177}Lu-PSMA therapy, specifically when there was significant tumor suppression. The authors hypothesized that the remaining minority of tumoral cells may have increased the release of osteoblastogenic growth factors. However, we propose that the underlying pathophysiology might be explained by considering the fact that prostate cancer cells have the ability to secrete parathyroid hormone–related peptide, thereby stimulating osteoclast activity. Tumor suppression consequently results in significant suppression of parathyroid hormone–related peptide in the microenvironment, leading to hypocalcemia that closely resembles hungry bone syndrome (*7,8*). Unfortunately, Kumar et al. did not provide any data regarding the levels of parathyroid hormone–related peptide in the cases to assess this hypothesis. Furthermore, it would have been valuable to evaluate whether changes in calcium levels correlate with changes in prostate-specific antigen and prostate-specific membrane antigen levels in the bone-only metastatic subgroup.

Kumar et al. have also introduced intriguing concepts regarding the Tyr phenomenon and its potential impact on bone marrow reserve. However, their report lacks supportive data on this matter. The authors propose that an excessive osteoblastic reaction may lead to a decrease in the bone marrow reserve. To substantiate this assertion, it would have been beneficial if they had presented the changes in hemoglobin levels among patients experiencing albumin-corrected hypocalcemia after ^{177}Lu-PSMA therapy and compared them with the original dataset.

In their approach to mitigate the undesired exaggerated osteoblastic reaction, the authors used glucocorticoid therapy, which appears to be a reasonable strategy. However, it is worth considering ^{223}Ra therapy as a potential alternative since it can inhibit osteoblastic activity and has demonstrated its efficacy in controlling refractory tumor-induced hypocalcemia (*9,10*).

REFERENCES

1. Kumar S, Crumbaker M, Harvey C, et al. The Tyr phenomenon: a hypocalcemic response in high-volume treatment responders to ^{177}Lu-prostate-specific membrane antigen therapy. *J Nucl Med.* 2023;64:1412–1416.
2. Albright F, Reifenstein EC. *The Parathyroid Glands and Metabolic Bone Disease.* Williams & Wilkins; 1948:103–114.
3. Sakr MF. Hungry bone syndrome (HBS). In: *Parathyroid Gland Disorders: Controversies and Debates.* Springer; 2022:233–249.
4. Abramson EC, Gajardo H, Kukreja SC. Hypocalcemia in cancer. *Bone Miner.* 1990; 10:161–169.
5. Drekolias D, Gonuguntla K, Gadela NV, et al. A rare case of severe sequestrational hypocalcemia in patient with metastatic prostate cancer [abstract]. *Chest.* 2020; 158(suppl):A842–A843.
6. Hariharan V, Vallepu SR, Bantu S, Garg M. ODP134 resistant hypocalcemia in prostate cancer with osteoblastic metastasis [abstract]. *J Endocr Soc.* 2022;6(suppl): A182–A183.
7. Roato I, D'Amelio P, Gorassini E, et al. Osteoclasts are active in bone forming metastases of prostate cancer patients. *PLoS One.* 2008;3:e3627.
8. Archer Goode E, Wang N, Munkley J. Prostate cancer bone metastases biology and clinical management. *Oncol Lett.* 2023;25:163.
9. Morris MJ, Corey E, Guise TA, et al. Radium-223 mechanism of action: implications for use in treatment combinations. *Nat Rev Urol.* 2019;16:745–756.
10. Garla VV, Salim S, Kovvuru KR, Subauste A. Hungry bone syndrome secondary to prostate cancer successfully treated with radium therapy. *BMJ Case Rep.* 2018;2018: bcr2018225039.

Emran Askari
Sara Harsini*
**BC Cancer Research Institute*
Vancouver, British Columbia, Canada
E-mail: sharsini@bccrc.ca

DOI: 10.2967/jnumed.123.266368

REPLY: We have reviewed the letter to the editor entitled, "Unraveling the Hypocalcemic Response to ^{177}Lu-Prostate-Specific Membrane Antigen Therapy," which refers to our published article, "The Tyr Phenomenon: A Hypocalcemic Response in High-Volume Treatment Responders to ^{177}Lu-Prostate-Specific-Membrane Antigen Therapy" (*1*). We thank the authors for their interest in our article.

We describe a novel phenomenon of severe hypocalcemia in patients with high-volume bone metastatic prostate cancer who respond to ^{177}Lu-prostate-specific membrane antigen (PSMA) treatment. Patients who developed hypocalcemia ($<$2.10 mmol/L) during ^{177}Lu-PSMA had significantly higher markers of pretreatment disease burden, including baseline SPECT total tumor volume (median, 3,249 cm^3 [interquartile range (IQR), 1,856–3,852 cm^3] vs. 465 cm^3 [IQR, 135–1,172 cm^3]; $P = 0.002$), baseline prostate-specific antigen concentration (median, 471 ng/mL [IQR, 108–1,380 ng/mL] vs. 76 ng/mL [IQR, 22–227 ng/mL]; $P = 0.008$), and baseline alkaline phosphatase concentration (median, 311 U/L [IQR, 195–2,046] vs. 114 U/L [IQR, 69–184 U/L]; $P < 0.001$). Patients who developed hypocalcemia also demonstrated a greater prostate-specific antigen response between the first- and third-dose ^{177}Lu-PSMA (median, 85% [IQR, 53%–91%] vs. 47% [IQR, 1%–77%]; $P = 0.022$).

We suspect that an exaggerated osteoblastic response drove the hypocalcemia in our 2 most severe cases given the markedly elevated alkaline phosphatase and procollagen type 1 N-propeptide concentrations at hypocalcemia onset and the rapid response of serum calcium and bone formation markers to high-dose prednisone therapy, which is known to suppress osteoblastogenesis and promote osteoblast apoptosis (*2,3*). It is unclear whether this osteoblastic response is specifically occurring in the osteoblastic bone metastases or is a more generalized skeletal response. Interrogation of further cases with transiliac bone biopsy, including histomorphometric indices of bone turnover and micro-CT assessment of trabecular and cortical bone morphology, will likely provide important insights. We agree that our cases differ from those with hypocalcemia in the setting of progressive bone metastases (*4*), as the hypocalcemia occurred in association with excellent responses to treatment.

The authors postulate whether parathyroid hormone–related protein suppression in the tumor microenvironment and subsequent reduction in osteoclastic activity may have been the driving factor for hypocalcemia. This is a reasonable hypothesis, which we did not examine. However, given the evidence for an exaggerated osteoblastic response, we suspect parathyroid hormone–related protein suppression was not a major underlying factor for the hypocalcemia, particularly given that the 2 more severe cases had recent high-dose denosumab, which is already a potent suppressant of osteoclast activity (*5*). Indeed, one of our patients had a low-normal serum C-terminal telopeptide of type 1 collagen at the onset of hypocalcemia (113 μg/L; normal range, 100–750 ug/L). Further, we were unable to identify any cases in the literature describing hypocalcemia secondary to parathyroid hormone–related protein suppression. Most patients in our cohort had underlying bone metastases ($>$95%), and we demonstrated that onset of hypocalcemia during ^{177}Lu-PSMA treatment correlated with greater prostate-specific antigen response.

Patients who developed hypocalcemia in our cohort had a significantly lower hemoglobin nadir between the first and third doses of ^{177}Lu-PSMA (median, 95 g/L [IQR, 76–114 g/L] vs. 112 g/L [IQR, 102–122 g/L]; $P = 0.029$). There is concern that an osteoblastic hypersclerotic reaction may compromise marrow reserve; however, various factors can contribute to anemia in such patients. Further, whereas our data suggest a short-term decline in hemoglobin, a long-term persistent hemoglobin reduction is more clinically relevant and would require a longer follow-up period.

We commenced high-dose prednisone in the 2 most severe cases of hypocalcemia to suppress the exaggerated osteoblastic response. ^{223}Ra is a calcium mimetic that facilitates α-radiation preferentially to osteoblastic bone metastases exhibiting high bone turnover (*6*). However, as mentioned, the hypocalcemic phenotype we describe occurred in excellent treatment responders, and hence, administering alternative treatment with ^{223}Ra at the onset of hypocalcemia would not have been considered suitable.

REFERENCES

1. Kumar S, Crumbaker M, Harvey C, et al. The Tyr phenomenon: a hypocalcemic response in high-volume treatment responders to ^{177}Lu-prostate-specific membrane antigen therapy. *J Nucl Med.* 2023;64:1412–1416.
2. Chotiyarnwong P, McCloskey EV. Pathogenesis of glucocorticoid-induced osteoporosis and options for treatment. *Nat Rev Endocrinol.* 2020;16:437–447.
3. Lane NE. Glucocorticoid-induced osteoporosis: new insights into the pathophysiology and treatments. *Curr Osteoporos Rep.* 2019;17:1–7.
4. Garla VV, Salim S, Kovvuru KR, Subauste A. Hungry bone syndrome secondary to prostate cancer successfully treated with radium therapy. *BMJ Case Rep.* 2018; 2018:bcr2018225039.
5. Lipton A, Fizazi K, Stopeck AT, et al. Superiority of denosumab to zoledronic acid for prevention of skeletal-related events: a combined analysis of 3 pivotal, randomised, phase 3 trials. *Eur J Cancer.* 2012;48:3082–3092.
6. Parker C, Nilsson S, Heinrich D, et al. Alpha emitter radium-223 and survival in metastatic prostate cancer. *N Engl J Med.* 2013;369:213–223.

Shejil Kumar
Megan Crumbaker
Louise Emmett*
**St. Vincent's Hospital Sydney,*
New South Wales, Australia
E-mail: louise.emmett@svha.org.au

DOI: 10.2967/jnumed.123.266768

Rudolf Höfer, MD, 1923–2023

Rudolf Höfer, MD, professor emeritus at the University of Vienna (Austria) and a lead figure in nuclear medicine in Europe, died on November 9, 2023, after a long, fulfilling, and impactful life. He was born on March 18, 1923, into a family of physicians in Vienna. His early education included attendance at the Theresian Academy. His studies at the Medical Faculty of the University of Vienna were interrupted by military service and a 5-y postwar imprisonment in Africa. He ultimately received his doctorate in general medicine on July 3, 1953, before joining the second Medical University Clinic in Vienna, led by Karl Fellinger, who had been a student of the 1927 Nobel Laureate in Physiology, Julius Wagner-Jauregg.

Höfer was fascinated by the then new field of nuclear medicine. In an interview on the occasion of his 95th birthday, he said, “I was born into nuclear medicine, for the year of my birth was when George de Hevesy published his first results from the applications of radioactive isotopes in biology and medicine.” Shortly after joining the Medical University Clinic, Höfer received a Fulbright scholarship that took him to the Donner Laboratory in Berkeley, CA. After his return, he took over management of the Medical University isotope ward in 1958. Later he said, “I was a nobody to arrive in Berkeley and return 3 mo later as a so-called specialist, which was considered enough to engage in the introduction of radioisotope methods” in Vienna.

The Vienna activities of Höfer and colleagues, such as Herbert Vetter and Fritz Hawliczek, were initially focused on research, diagnosis, and therapy of thyroid diseases, which ultimately led to Höfer’s formal qualification (habilitation) in internal medicine in 1966. In the 1960s, nuclear medicine at the University of Vienna was housed in a 3-story barrack built with funds recovered from donations received by Fellinger as University Rektor at the school’s 600th anniversary. Nuclear medicine was on the ground floor, squeezed between a computer hub in the basement and gastroenterology on the first floor.

Höfer was one of the leading forces in establishing the subject of nuclear medicine as its own distinct subject area. In 1973, nuclear medicine was launched as an independent department before it became an integral part of the Vienna General Hospital, where it relocated physically in 1992. The nuclear medicine clinic hosted an extraordinary array of 12 γ-cameras, 2 total-body counters (not to be confused with total-body PET), radiochemistry labs, a small cyclotron, and a therapy ward.

On October 1, 1983, Höfer was appointed the first full professor of nuclear medicine at the University of Vienna, a position he held until 1993. The early foundations of nuclear medicine in Austria were further supported by the close engagement of his mentor Herbert Vetter with the International Atomic Energy Agency and their Atoms for Peace program, as well as the activities of Georg Riccabona in Innsbruck, Otto Eber in Graz, and Gerhard Mostbeck in Vienna in advancing the clinical use of radioisotopes.

In addition to his many clinical and national activities, Höfer was entrusted in January 1972 with the founding of the European Nuclear Medicine Society, which took place on June 8, 1974, in Clermont-Ferrand, France, and for which he became first secretary. This society was merged in the 1980s with the European Society of Nuclear Medicine into the European Association of Nuclear Medicine. In addition, he was secretary and president of the Austrian Nuclear Medicine Society (ÖGNMB) from 1972 to 1978.

One of Höfer’s most notable accomplishments in broadening the nuclear medicine landscape was the foundation of the Radioactive Isotopes in Clinics and Research symposium in 1954. This meeting was held on a biannual basis in Bad Gastein, Austria, and brought together a growing number of international advocates for clinical and biologic applications of radioisotopes. Dr. Höfer organized this symposium from 1954 to 1993 and helped it to develop quickly into a leading international congress in the field of diagnostic and therapeutic nuclear medicine. It is noteworthy that, despite the restrictions of the Cold War, each of the Gastein meetings was attended by scientists from Eastern Europe, most likely because of the neutrality of Austria. At their peak, these symposia brought together 400 attendees from almost 40 countries, encouraging lively exchanges and lifelong friendships. Without a doubt these meetings made an important contribution to East–West rapprochement and serve as an example of the power and obligation of scientists to remain in touch in times of global turmoil. Höfer was later awarded honorary membership in the ÖGNMB for his service to the professional society.

Höfer was spokesperson for the Curia of Professors and vice dean of the Medical Faculty at the University of Vienna from 1992 to 1993. As a member of the “New Vienna General” building commission, he played a key role in designing the nuclear medicine facility as one of the largest and best equipped in European university hospitals.

Höfer was one of the founding fathers of Austrian and European nuclear medicine. His commitment to nuclear medicine in Vienna and beyond came at a time when this field of medicine was in its infancy. Without Höfer, nuclear medicine development in Austria and Europe would likely have been delayed. What made him a truly inspiring and commendable person was his wit, modesty, and pride. A few years ago, when asked about his retirement, he responded, “I am very happy that people remember me after I left my professional career.” We visited him occasionally after accepting our respective positions as professors of nuclear medicine and physics of medical imaging. He would serve platters of food, much of which he prepared himself, followed by lively and humorous conversations. He was a pioneer of nuclear medicine and a welcoming host to many.

Commenting on the place of our field in the larger medical landscape, Höfer said, “The use of radioactive isotopes in the clinic and research grew on the grounds of theoretical and clinical subjects. In recent years, the combination of radiological and nuclear medicine techniques has gained a permanent place in imaging diagnostics. Given this success, cooperation at eye level is both required and a guarantee for continued success. However, to conclude from this that nuclear medicine is a part of radiology is just as absurd as it would be to declare radiology a branch of nuclear medicine in the future.” We are honored to have known this special person, friend, and mentor and extend our condolences to his family at this difficult time.

Marcus Hacker*
Thomas Beyer
Medical University of Vienna
Vienna, Austria
**E-mail: marcus.hacker@meduniwien.ac.at*

DOI: 10.2967/jnumed.123.267216


Innovate. Illuminate.

WHAT IS AN SNMMI RPT **CENTER OF EXCELLENCE?**

To learn more and apply, visit
www.snmmi.org/RPTCOE

SNMMI created the Radiopharmaceutical Therapy (RPT) Center of Excellence (COE) Program to allow centers with expertise in RPT to showcase their capabilities and services, including research. A designation means that your site has the personnel, expertise, and equipment to manage the care of patients requiring RPT. The designations levels are Comprehensive, Clinical, or Basic Therapy Center.

Targeted RPTs are changing the way patients with cancer are treated. These advances have allowed providers to treat and manage a multitude of other cancers and diseases. Not all sites have the expertise to use these agents clinically or in clinical trials.

If your site has experience with one or more radiopharmaceutical therapies, we encourage you to apply for the SNMMI RPTCOE designation.

COMPREHENSIVE RPT CENTER

An application fee of $1,500 for members and $2,500 for non-members is required for a 2-year designation.

SCAN QR CODE TO APPLY

CLINICAL RPT CENTER

An application fee of $900 for members and $1,500 for non-members is required for a 2-year designation.

SCAN QR CODE TO APPLY

BASIC RPT CENTER

The designation does not require any application fee and is valid for a 2-year designation.

SCAN QR CODE TO APPLY

012024-9

Now Available!

Radiopharmaceutical Therapy Accreditation

The new program offers facilities a mechanism for demonstrating their commitment to quality and patient safety in radiopharmaceutical therapy and **augments the existing IAC accreditation areas of Nuclear Cardiology, General Nuclear Medicine and PET**.

Radiopharmaceutical Therapy Accreditation Program

SNMMI SOCIETY OF NUCLEAR MEDICINE & MOLECULAR IMAGING | IAC INTERSOCIETAL ACCREDITATION COMMISSION

SNMMI and IAC are pleased to announce the first three facilities to be awarded the new Radiopharmaceutical Therapy Accreditation:

BAMF Health
Grand Rapids, MI

Carilion Clinic Targeted Therapy Center
Roanoke, VA

Stanford Health Care
Stanford, CA

First to Earn Accreditation Discuss Value ...

"Being among the first organizations to receive Radiopharmaceutical Therapy accreditation is a way to demonstrate our commitment to best practice while providing high quality patient care and a framework for safety to patient's family and friends. **The IAC's accreditation process is very thorough and demonstrates our organization's commitment to continuous improvement in the areas of quality, safety and excellent patient outcomes**."

Todd Faasse, MPH, CNMT, PET RT(N) (CT)
Nuclear Medicine Operations Specialist
BAMF Health

"**Preparation for accreditation made us stronger requiring >40 hours of technical support and allowed for improvement in several areas with new standards.** It is important for these standards to be embraced to solidify our utility in our patients' care pathways. We are very grateful for the recognition you have given our program and look forward to continuing to help define the path for excellence in these therapies in conjunction with the IAC."

Jackson W. Kiser, MD
Medical Director and Section Chief Molecular Imaging and Theranostics
Carilion Clinic Targeted Therapy Center

IAC
Improving health care through accreditation®
intersocietal.org | 800.838.2110

Scan the QR code to complete an interest form or visit **intersocietal.org/nuclear**.

2/24

The Journal of Nuclear Medicine

February 2024 ▪ Vol. 65 ▪ Pages 167–335